Magmatic / Hydrothermal Interactions at Fast Spreading Mid-Ocean Ridges: Implications on the Dynamics of the Axial Melt Lens

Lydéric France

UNIVERSITE MONTPELLIER II
SCIENCES ET TECHNIQUES DU LANGUEDOC

T H E S E

pour obtenir le grade de

DOCTEUR DE L'UNIVERSITE MONTPELLIER II

Discipline : Sciences de la Terre

Ecole Doctorale : SIBAGHE

présentée et soutenue publiquement

par

Lydéric France

Le 8 décembre 2009

Titre :

Interactions entre processus magmatiques et hydrothermaux aux dorsales océaniques à expansion rapide: implications pour la dynamique de la lentille magmatique axiale

Magmatic / Hydrothermal Interactions at Fast Spreading Mid-Ocean Ridges: Implications on the Dynamics of the Axial Melt Lens

JURY

M Benoit Ildefonse	Directeur de Recherche (CNRS UMII)	(Directeur de thèse)
M Juergen Koepke	Assistant Professeur (Hannover University)	(Co-directeur de thèse)
Mme Catherine Mével	Directeur de Recherche (CNRS, IPGP)	(Rapporteur)
M Bruno Scaillet	Directeur de Recherche (CNRS, ISTO)	(Rapporteur)
Mme Andrea Tommasi	Directeur de Recherche (CNRS UMII)	(Examinateur)
M Wolfgang Bach	Professeur (MARUM, Bremen University)	(Examinateur)
M Yves Lagabrielle	Directeur de Recherche (CNRS, UMII)	(Invité)
Mme Françoise Boudier	Professeur émérite (UMII)	(Invitée)

Il faut toujours penser par soi-même. Ne rien apprendre par cœur, mais tout redécouvrir et, en tous cas, ne rien accepter qui ne soit prouvé. Ne rien négliger de ce qui est concevable ou imaginable.
A. Einstein

Si vous trouvez que l'éducation coûte cher, essayez l'ignorance!
Abraham Lincoln

Remerciements / Acknowledgments

Sait-on jamais où les vents nous mènent ?… Moi ils m'ont pas mal baladé pour me faire atterrir à Montpellier pour improbablement faire une thèse de *Casseur de Cailloux*… Donc voici venu le temps des remerciements… Je ne sais pas ce qu'il en est pour les autres mais pour moi c'est quelque chose que j'attends depuis le début de cette dernière étape… Je dis dernière étape car en général les remerciements de thésards présentent l'aboutissement de 3 (4 ou 5 ou…) ans de travail, mais je ne suis pas vraiment d'accord… (comme d'hab. finalement…) c'est plutôt l'aboutissement d'une première phase beaucoup plus large… finalement c'est l'aboutissement de toutes mes études… Donc un moment assez fort… Je me revoie au collège regarder la « pyramide de l'orientation » que vous devez tous connaître, pour moi cette pyramide est un scandale et image l'orientation dans nos écoles… sur cette pyramide ; il y a tout en bas, la primaire, surplombée par les quatre années de collège (je suis alors dans la deuxième), aboutissant au Brevet ! qui me semble assez lointain à ce moment là. Au dessus il y a les 3 années de lycée et LE BAC !! Du haut de mes ~12 ans, ce bac est super loin... mais pourtant il y a encore huit cases au dessus ! Comment motiver un gamin avec une telle représentation !! Même plus tard, au lycée, avec un peu plus de maturité, il est assez difficile de s'imaginer en haut de cette pyramide… beaucoup rêvent plutôt de s'en évader… et pourtant, la fac te permet quand même d'étudier, de t'investir dans quasi toutes les thématiques possibles, il suffit de choisir ! De plus, je pense que la FAC est une école de la vie ; non pas école de la vie au sens apprendre à en chier et à savoir ce que c'est la « vraie vie du travailleur », non mais plutôt la vraie vie dans laquelle tu t'intéresses au monde autour de toi (culture en général, politique, international, actualité, ciné, bouquins, sports…), et surtout la vraie vie dans laquelle tu es ouvert aux autres, et tu découvres tellement de gens de toutes origines, de tous styles, et allant dans des directions aussi multiples que passionnantes… Je ne peux dénombrer le nombre de personnes rencontrées au cours de mes 8 années d'études à la fac qui m'ont tellement apportés ! Finalement tout ça c'est de l'ouverture d'esprit qui te permet d'essayer de comprendre le monde et les gens, et SURTOUT de le et les respecter…

Comprendre le monde, ou plutôt la Terre, est un peu à la croisée des différentes sciences dites « dures ». Finalement en Géosciences, on se sert de maths, de physique, de chimie, pour aboutir à comprendre un processus. C'est cette pluridisciplinarité que j'aime. Même si, comme on me l'a déjà dit, et probablement à juste titre : « si tu veux faire de tout, tu ne seras spécialiste de rien, et finalement tu ne feras rien… », et bien je persiste et m'entête !

Au cours de ce travail de thèse, j'ai du faire du travail de terrain, pétrographique, géochimique, expérimental, tout en ayant à comprendre les précédents travaux, y compris ceux de géophysique ! (un peu dur pour moi !). La force de ce travail, si il y en a une, est, je le crois dans cette pluridisciplinarité qui permet de contraindre un processus en mettant en accord les différentes approches ; plutôt que de rejeter toutes celles qui sont extérieures à notre spécialité. J'espère finalement avoir apporté mon grain de sable pour donner tort aux « détails de l'histoire » qui considèrent que la recherche est peuplée de fainéants…

Bien que passionné dès le début, je dois la continuation de mes études à la fac, à deux personnes qui, grâce à leurs cours passionnants dès la première année de DEUG à Sté, m'ont définitivement passionnés pour la Géologie ; je remercie donc **Henri Gonord** et **Jean-Yves Cottin**.

Gilles (Chazot) tu m'as appris les rudiments de ce qu'est la vrai recherche, et m'a expliqué ses principes ; tu m'a toujours soutenu et si je suis là aujourd'hui c'est bien sûr en partie grâce à toi ; merci.

Jacques Kornprobst m'a permit de baigner dans la vraie pétrologie et de m'éclater à retracer les histoires de cailloux plus bizarres les uns que les autres. Merci à vous !

J'envoie bien évidemment mes plus chaleureux remerciements à « mon chef » **Ben**. Il nous a fallu un petit temps d'adaptation pour pouvoir travailler efficacement ensemble mais une fois le système rodé, ce fut un grand plaisir de bosser ensemble. Je te remercie en particulier pour m'avoir laissé faire évoluer mon projet de thèse comme bon me le semblait, dans des directions qui ne te passionnent pas forcément à la base. Je te remercie aussi pour m'avoir totalement appuyé et soutenu quand il le fallait, sans ton soutient, j'aurai été écrasé et probablement que peu de choses seraient sorties de cette thèse. Au final, ce fut un plaisir de travailler avec toi, j'espère que l'on continuera.

Of course I also thank my "co-director" **Juergen Koepke** for making me discovered experimental petrology, and for his welcome in the Hannover Lab. We had many interesting discussion and it was a pleasure to work with you.

Je remercie ensuite **Françoise Boudier** pour m'avoir fait découvrir l'ophiolite d'Oman, et comment doit se dérouler une mission de terrain. Je te remercie aussi pour les innombrables discussions plus ou moins enflammées que l'on a eues, et pour finalement malgré les désaccords avoir toujours été intéressée pour continuer à débattre. Bien que parfois éprouvant, ce fut passionnant et un bon « jeu ». Je te remercie aussi d'avoir accepté de participer à mon jury.

Je tiens aussi à remercier **Adolphe Nicolas** pour m'avoir fait découvrir l'ophiolite d'Oman, la RZSDC, et le Whisky Perrier...

Christian Nicollet m'a accompagné sur le terrain pendant deux semaines, lors de ma seconde mission. Nous avons de plus sans cesse échangé des observations, des questions, des discussions, des mails de conneries et des pétitions de vieux gauchos... Ce fut passionnant de bosser avec toi, et bien sûr ce n'est pas fini ! Merci à toi.

Je remercie tout particulièrement **Christine Laverne** avec qui j'ai énormément apprécié partager du temps. Dommage que nous n'ayons pas plus bossé ensemble ; ce n'est que partie remise !

Durant ma première mission de terrain, j'ai passé une dizaine de jours seuls avec **Akram Belghoul**, ce fut bien sympa et il m'a bien aidé pour l'échantillonage ; merci bien !

Merci à **Margot Godard** pour des discussions sympa, j'espère que l'on aura l'occasion de retravailler ensemble !

Merci à **Sylvie Demouchy** pour quelques discussions et quelques conseils que j'ai bien appréciés.

I also thank **Catherine Mével**, **Bruno Scaillet**, **Wolfgang Bach**, **Andrea Tommasi**, and **Yves Lagabrielle** who has accepted to evaluate my work and to participate to the Jury.

I thank the friends from Germany for their help for the work and for the life in this strange country ;-), I really enjoyed the life in your country! Many thanks to **Sarah**, **Adrian**, **Swenja**, **Wanja**, **Marieke** and **Mathieu**, **Sara**, **Tatiana**.

Je remercie aussi **François Holtz** pour m'avoir accueilli dans son labo à Hannovre, and **Harald Behrens** for interesting discussions.

A Montpellier, je remercie **Serge Lallemand** qui a sauvé ma seconde mission en Oman en gérant quelques démarches de secours avec le ministère…

Je remercie très chaleureusement mes chers collègues de bureau ! Tout d'abord **Mick** et **Mat** pour les nombreux délires pas forcément compréhensibles par d'autres ! On a quand même bien trippé et sans vous deux l'ambiance de la thèse n'aurait clairement pas été la même ! A nos multiples pauses café-clopes, aux break'it'up & aux break'it down. Désolé de vous avoir imposé toutes mes discussions avec Françoise… Et Mick, désolé de ne pas avoir plus bossé avec Marie !... ;-)

Je remercie donc aussi **Clémence** et **Yoyo** pour les bons moments passés dans ce même bureau. Clémence merci aussi pour m'avoir trouvé mon ATER ! tu m'as sauvé !

En plus de Mat, le reste de la team de ma « promo » :

Tout d'abord **Flo**, j'ai vraiment apprécié de passer ces trois années avec toi, de partager avec toi un nombre incalculable de débats improbables et enflammés, d'aller grimper, pour toutes les soirées et bivouacs… Je te remercie. Et merci de m'avoir laissé la thèse ! ;-)

Ma vie Montpelliéraine aurait été bien différente sans **Bruno** avec qui j'ai partagé la plupart des after jusqu'à n'importe quelle heure n'importe où et n'importe comment !... Bien content de t'avoir rencontré mecton !

J'ai aussi énormément apprécié de partager du temps et les innombrables discussions politiques (et autres) avec **Pierre**. Ce fut sympa de partager ces trois années avec toi !

Karen ! Arrêtes de te plaindre !! Sans tes raleries sur tous les sujets ou tous les moments qui passent, ces trois années auraient aussi été bien différentes ! C'était bien sympa de t'avoir dans le groupe !

Mitch, l'homme de la nuit et l'homme qui répare tout (sauf son appareil photo !). Bien content d'avoir passé du temps avec toi ! Souvent à l'envers mais on a quand même bien trippé… Je suis sur que l'on se recroisera un peu partout pour continuer… ;-)

Notre cher **Nico**, ami des manchos, merci de m'avoir fait découvrir la voile, c'est une expérience géniale pour moi qui suis à la base plus de la montagne… C'était bon de t'avoir dans toutes les sorties et soirées ! Longue route à toi !

Mon petit **Titou**, ton énergie et ton sourire omniprésent m'ont fait cher apprécier de partager un peu de temps (pas assez) avec toi ! Merci pour les quelques sorties grimpes, ballades et bivouacs, soirées plages… Bien content de t'avoir rencontré, et j'espère que l'on gardera le contact ! *[Ya pas d'pinaille mec !]*

La présence des « anciens » a été fort agréable lors des deux premières années ; je suis bien content d'avoir passé un peu de temps avec vous **Nicolas E.**, **Rem**, **Marion**, **Véro**, **Fab**… L'épaulage des plus anciennes (**Ingrid** & **Marianne**) a aussi été bien sympa !

J'ai été bien content de passer du temps avec cette vieille **Mag**, et de refaire le monde anarchiquement avec mon cher **Mot** !

Merci aussi aux autres Montpelliérains avec qui j'ai partagé du temps qui m'a permis de me vider la tête dans la nature ou en ville : **Lara**, **Maelle**, **Tim**, **Anne**, **Tom T**, **Philou**, **Vaness**, **Johanna**, **Charlotte**, **Marie**, **Roco**, **Simon**, **Eugénie**, **Julien**, **Vins** et bien sur **le frère de Flo** ;-)

Les potes de Clermont ont été moralement présents et les rencontres aux *Geologix* ont été importantes pour moi ! Merci à : **El'Gringo**, **Ludo**, **Dédé**, **Julie**, **TomTom**, **Arno**, **Tof**, **Cynthia**, **Flo**, **FloFlo**, **la ptite Aude**, **la vieille Débauche**, **Momo**, **Max**, **Nicopatch** & **Nicotine**, **Lydie**, **Blaise**, bien sûr **Audray** !

Et une petite dédicace à **Simon** et **Audrey** !!

Les potes de Sté ont toujours été présents et ont toujours cru en moi ! Je remercie bien évidement : **Jojo**, **Gros**, **Galette**, **Ludo**, **PJ**, **FX**, **Dioud**, **Julie**, **Soso**, **Van-Y**, **Marion Sr**, **Molduc**, **Lucile**, **Mule**, **Royx**, **TomTom, Dav, Marie, Soso, Etienne.**

Ma famille a aussi toujours cru en moi, et m'a soutenu, merci à vous ! Merci à ma sœur **Ingrid** & à **Guillaume**, **Anne-Marie**, **Marianne**, **Jean-Paul**, les couz. **Jenif** et **Justine**, **Papa**.

Je fais ici une spéciale dédicace à **Sarah** et **Marion** qui déchirent tout et que j'adore ! Ca serait la classe qu'on bosse dans un labo ensemble, un jour...

Merci aussi à **Bertille** pour son soutient moral durant ma première mission en Oman et quelques autres trucs…

Merci aussi bien évidement aux Géologues de l'Extrême et en particulier à mes anciens collègues Stéphanois **Chon** et **Fabien** ! On se sera suivi jusqu'au bout… Pourvu que ça dure !

Un grand merci à **Carole** pour son soutient, de nombreuses discussions, et de bon moments…

Je remercie aussi tout particulièrement ceux qui n'ont jamais cru en moi, ils m'ont permis de d'avoir une motivation encore plus grande pour avancer !

Je dédie finalement ce travail tout d'abord à ma maman qui a toujours tout fait pour que ma vie se déroule au mieux et qui m'a toujours soutenue ; merci.

Je dédie ensuite ce travail à quelques autres personnes sur qui je peux toujours compter et pour qui je serais toujours présent en cas de besoin, Moino, Chloé, Anouk, Polo, Mélanie, Alex, Mag, Ber.




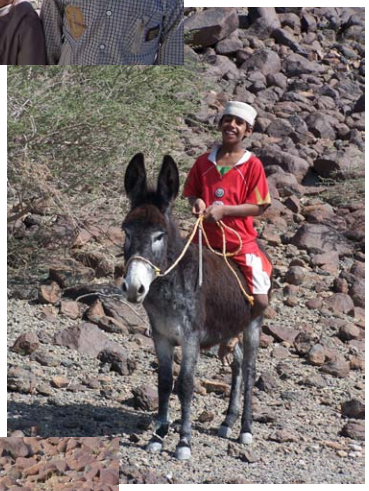






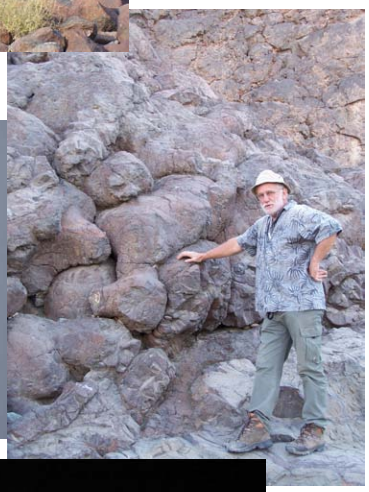


٣٠
30

Abstract

This PhD work is based on field, petrographic, and geochemical observations of rocks originated at the base of the sheeted dike complex, in the Oman ophiolite and at IODP Site 1256, coupled with an experimental study. It provides new constrains on processes that occur at the magma / hydrothermal system transition in oceanic crust formed at fast spreading ridges.

The base of the sheeted dike complex is truncated by intrusive isotropic gabbros, and therefore reheated and recrystallized to the "granoblastic dikes" under temperatures up to 1030°C. Xenoliths of granoblastic microgabbros and microgabbronorites derived from the granoblastic dikes are commonly observed in the about 100 meters thick horizon of isotropic gabbro that underlies the sheeted dike complex. These features can be explained by upward migrations of the melt lens that is present at fast spreading centers. The occurrence of several assimilation features (xenoliths and granoblastic patches) in the isotropic gabbro horizon supports the hypothesis that this horizon represents the fossilization of the upper melt lens. The experimental study was designed to simulate experimentally the effect of partial melting of hydrothermally altered sheeted dikes. The results show that melting starts at 850°C, confirm the residual origin of granoblastic dikes and xenoliths, and attest to the anatectic origin of the oceanic plagiogranites that are commonly present close to the base of the sheeted dike complex. The major and trace element composition of the experimental anatectic melt that represents the main contaminant for primitive MORBs at fast spreading ridges has been determined.

The upper axial melt lens at fast spreading mid-ocean ridges is herein described as a dynamic system that can migrate vertically, and which fossilizes when moving off-axis.

Résumé

Ce travail de thèse est basé sur des observations de terrain, sur une étude pétrographique et géochimique des roches formées à la base du complexe filonien dans l'ophiolite d'Oman et au niveau du Site IODP 1256, ainsi que sur une étude expérimentale. De nouvelles contraintes sont apportées sur les processus se produisant à la transition magma / système hydrothermal dans la croute océanique formée au niveau des dorsales à expansion rapide.

L'intrusion de gabbros isotropes dans la base du complexe filonien a provoqué son réchauffement et sa recrystallization en « dikes granoblastiques » jusqu'à des températures de 1030°C. Des xénolites de microgabbro à orthopyroxene dérivées des dikes granoblastiques sont souvent observées dans le niveau de gabbros isotropes épais de 100 mètres environ qui est présent à la base du complexe filonien. Ces différentes caractéristiques sont à relier à des migrations verticales vers le haut du sommet de la lentille magmatique supérieure qui est observée aux dorsales rapides. Les nombreuses évidences d'assimilation (xénolites et patchs granoblastiques) dans le niveau des gabbros isotropes appuient l'hypothèse que ce niveau représente la fossilisation de la lentille magmatique supérieure. L'étude expérimentale a consisté à tester l'effet de la fusion partielle du complexe filonien préalablement hydrothermalisé. Les résultats montrent que la fusion commence à 850°C, confirment l'origine résiduelle des dikes granoblastiques et des xénolites associées, et attestent de l'origine anatectique des plagiogranites océaniques qui sont couramment observés à proximité de la base du complexe filonien. La composition en éléments majeurs et traces du liquide anatectique a été déterminée. Ce liquide représente le principal contaminant pour les MORBs primitifs émis au niveau des dorsales rapides.

La lentille magmatique supérieure présente au niveau des dorsales médio-océaniques à expansion rapide est ici décrite comme un système dynamique qui peut migrer verticalement, et qui est fossilisée lorsqu'elle se déplace hors axe.

Zusammenfassung

Die vorliegende Dissertation basiert auf geländebezogenen, petrographischen und geochemischen Untersuchungen an Gesteinen vom Gabbro / Dike - Übergang vom Oman-Ophiolith und von der IODP-Bohrung 1256 vom ostpazifischen Rücken, in Verbindung mit einer experimentellen Studie, und soll neue Einblicke in die Geodynamik von schnell-spreizenden ozeanischen Rückensystemen gewinnen.

In beiden Vorkommen wird die Basis der Sheeted Dikes durch Intrusionen von isotropen Gabbros abgeschnitten, die auch eine Rekristallisation der Basalte zu den "Granoblastischen Dikes" bewirkte, wobei Gleichgewichtstemperaturen bis zu 1030°C ermittelt wurden. Alle Natur-Beobachtungen zusammengenommen implizieren, dass die axiale Schmelzlinse eine sehr dynamische Struktur ist, die vertikal zu wandern vermag. Die weite Verbreitung von Assimilationsstrukturen im isotropen Gabbro (Xenolithe und granoblastische Domänen), unterstützen ein Modell, dass der isotrope Gabbro der fossilisierten Schmelzlinse entspricht, nach einer Phase der Entleerung und Bewegung in eine "off-axis" - Position.

Eine experimentelle Studie wurde durchgeführt, um den Prozess des Aufschmelzens von hydrothermal alteriertem Dike-Material am Top der axialen Schmelzlinse zu simulieren. Phasengleichgewichte und Zusammensetzungen der experimentellen Phasen incl. Spurenelemente der Gläser implizieren, dass die an der Basis der Sheeted Dikes verbreiteten ozeanischen Plagiogranite als Aufschmelzprodukte der hydrothermal alterierten Dikes angesehen werden können, während die granoblastischen Lithologien die entsprechenden Residuen darstellen. Die vorliegende Studie charakterisiert die axiale Schmelzlinse als ein sehr dynamisches System, das sich aufwärts- und abwärtsgerichtet bewegen kann, und fossilisiert, wenn es von der "on-axis"- in die "off-axis" - Position wandert.

Table of contents

Introduction

Oceanic crust represents about two thirds of the Earth surface, and nearly half of it formed at fast-spreading mid-ocean ridges. The structure and composition of oceanic crust are constrained by off shore geophysical studies, and in-situ geological mapping and sampling (dredging and drilling), and ophiolitic complexes studies. Geophysical studies of fast-spreading ridges, primarily the East Pacific Rise (e.g., Sinton and Detrick, 1992), have shown that the ridge axis is composed of a magma chamber at depth, which is overlaid by a thin, narrow, and nearly continuous melt lens at its top, and of an upper lid formed by the sheeted dyke complex and the volcanics that seems to be injected from the axial melt lens (Figure 1). The upper melt lens is a key horizon in oceanic crust genesis, as it feeds at least part of the upper and lower crust. Understanding processes acting in and around the melt lens is therefore of major importance to precisely constrain the oceanic crust genesis at fast-spreading ridges. The upper melt lens is also the uppermost known nearly steady-state occurrence of melt at the ridge axis, and it corresponds to the sheeted dike / gabbro transition, where the magmatic system (that builds the crust) and the convecting hydrothermal one (that cools the crust) interact.

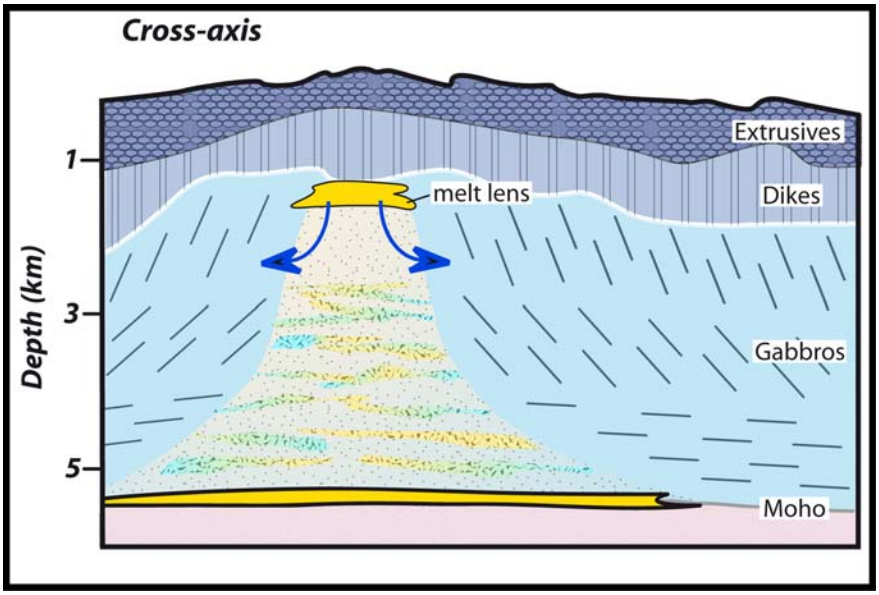

Figure 1: Cross axis view of a ridge accreted at fast spreading centers (Modified from Sinton and Detrick, 1992, Nicolas and Boudier, 1995, Boudier et al., 1996; MacLeod and Yaouancq, 2000; and Nedimovic et al., 2005). A melt lens is present at the bottom of the upper crust and at the moho level. Gabbros are vertically foliated to the top and horizontally layered to the bottom. The mush underneath the upper melt lens is intruded by sills.

Interactions between the magmatic and the hydrothermal systems can modify the composition of the melt lens and therefore influence the whole oceanic crust composition, in particular the mid-ocean ridge basalts (MORB) composition, which are the most accessible,

and therefore most commonly studied oceanic rocks. Several studies have focused on the root zone of the sheeted dike complex and have lead to apparently contrasting models. Some authors have proposed that the melt lens is a steady state horizon (e.g., Nicolas et al., 2008), when others have proposed that it behaves as a dynamic horizon (e.g., Gillis, 2008). The origin of the isotropic gabbro horizon (~100-200m thick) below the sheeted dike complex is either attributed to the melt lens fossilization (e.g., MacLeod and Yaouancq, 2000) or to hydrous partial melting of the root zone of the sheeted dike complex (Nicolas et al., 2008). Hence the fundamental questions I have addressed in this work are: is the interface between the melt lens and the hydrothermal system a steady-state or a dynamic system? Is water incorporated to the melt, and if so through which process(es)? Does the isotropic gabbros represent the fossilization of part (or of all) of the melt lens?

In 2005, the Integrated Ocean Drilling Program (IODP) has drilled Hole 1256D on the Cocos plate, in an oceanic crust formed at the East Pacific Rise at a superfast spreading rate (> 20cm/y). For the first time, IODP Hole 1256D has sampled a complete, intact section of the upper oceanic crust (Wilson et al., 2006). It has reached the upper isotropic gabbros, sampling the contact between the sheeted dike complex and these gabbros. This drillhole gives us the first opportunity to compare this peculiar horizon in an intact portion of present-day oceanic crust with ophiolites and the derived "Penrose" model oceanic lithosphere generated at fast-spreading ridges. This comparison provides further constraints on the dynamic of this complex geological and petrological interface, and allows the elaboration of a common model for its evolution in time.

The main objective of this thesis was to identify processes acting at the gabbro / sheeted dike transition, and to identify the feedbacks between the magmatic and the hydrothermal systems in oceanic crust formed at fast-spreading ridges. Two complementary approaches have been implemented:

- A **compared field work, and petrological study** of IODP Hole 1256D and the Oman ophiolite was carried out. In the Oman ophiolite, two field-work campaigns have been realized (6 weeks during winter 2006-07 and 6 weeks during winter 2007-08). The isotropic gabbro horizon corresponding to the transition from the sheeted dike complex to the foliated gabbros has been studied in details in three areas of the southern massifs in the Oman ophiolite; ~10 other areas have been visited in other massifs to verify the widespread occurrence of the observed relations, hence the proposed model. IODP core 1256D has been

relogged and described in details during a visit in College Station in summer 2007. A petrological study of all samples (from Oman and IODP Hole 1256D) has been conducted, including mineral major element compositions of all lithologies. A comparison between the observations made in Oman and at IODP Site 1256 leads to the elaboration of a common coherent model for the interactions between the magmatic and the hydrothermal systems at fast spreading ridges.

- The approach based on natural rocks was complemented by an **experimental petrology study** that has been performed in the "Institut für Mineralogie" of the Leibniz University Hannover. The objective of this work was to reproduce the melting of the hydrothermally altered base of the sheeted dike complex under pressure, temperature, and redox conditions that match the natural processes. A natural altered dike from the Oman ophiolite has been used as starting material. The composition of the newly formed melt is compared with typical plagiogranitic rocks from oceanic lithosphere, and the coexisting experimental minerals to rocks associated to these oceanic plagiogranites. The trace element composition of the experimental melts is also studied for the first time.

The manuscript is organized in six chapters:

I. A short overview of crustal accretion processes at fast spreading ridges, and a review of what is known to date about processes acting at the gabbro / sheeted dike transition is presented.
II. The main lithologies recovered at the bottom of IODP Hole 1256D are described, and the major element composition of the mineral phases are documented.
III. The sheeted dike / gabbro transition was studied in the Oman ophiolite and results are compared with IODP Hole 1256D. A general model integrating previously published models and new observations is proposed in an article published in *Geochemistry Geophysics Geosystems*.
IV. An experimental study reproducing the melting of hydrothermally altered sheeted dikes is presented. The experimental method is precisely described, and the main results are presented in an article submitted to *Contributions to Mineralogy and Petrology*. A specific and innovative study of the trace element

concentration of the experimental products is also presented in an article that will be submitted to *Geology*.

V. The isotropic gabbro horizon, believed to represent the fossilized melt lens, is then studied to test the model proposed in parts III and IV. Several observations attest to the assimilation of previously hydrothermally altered sheeted dikes within the melt lens.

VI. The conclusion summarizes the main results, and outlines some prospective directions of future research.

The appendix is divided in five parts:

A. Other papers linked to this PhD work and used in the different chapters are presented.

B. The dataset used in Chapters 2 and 4 is given.

C. Abstract of other papers written during this PhD work are presented.

D. Conference abstracts presented during my PhD work are presented.

E. Samples locations and characteristics.

Chapter I.

Magmatic accretion at fast spreading ridges

I.1. Architecture of oceanic crust at fast spreading ridges

I.1.a. General structure

For decades, scientists have explored oceanic crust to understand its structure, the way it is formed, and the processes that are active at the ridge axis. In April 1961, the Mohole project (Bascom, 1961) attempted to drill the whole oceanic crust down to the Moho (this has been reported in the *Life* magazine by John Steinbeck). The drillhole was situated to the west of the Mexico's Baja California and was the first scientific attempt to drill hard rocks. Although limited (only 13 meters of basalts have been recovered below the sediments), the success of drilling hard rocks was promising. The Penrose field conference (Conference Participants, 1972) has led to the elaboration of a consensual model for the oceanic crust structure. During this conference, the oceanic crust seismic models (e.g., Raitt, 1963; Shor et al., 1970) have been put in relation with the ophiolite structures and petrology (Figure I-1). The seismic model displays different layers that correspond to variable P wave velocities (V_P in km/s). The petrological model (ophiolitic model) is composed from the top to the bottom of the basalts (layer 2A), of the sheeted dike complex (layer 2B), of the gabbros (layer 3) and of the peridotites (layer 4).

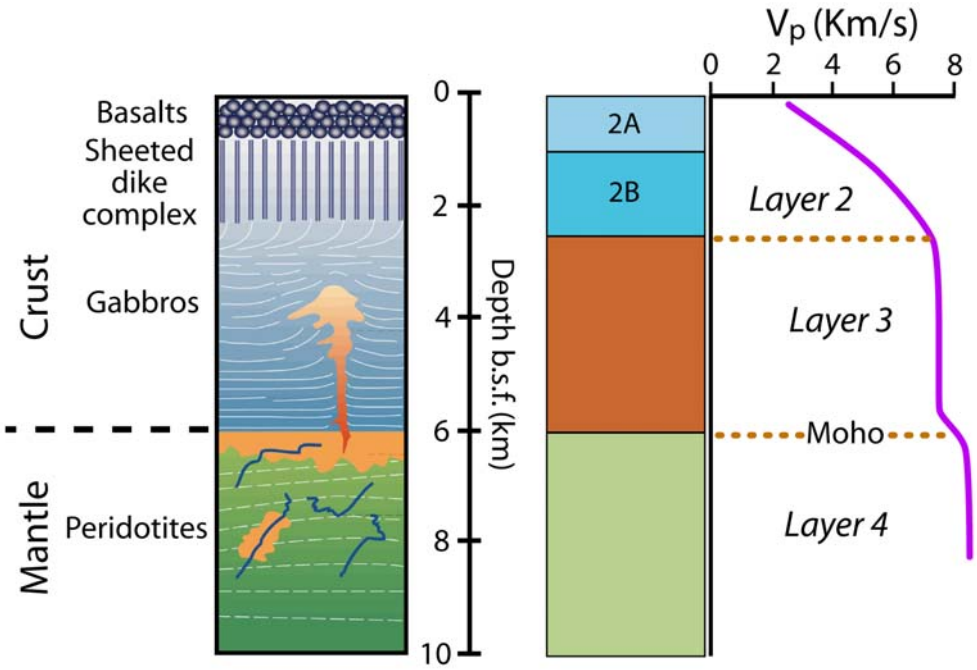

Figure I-1: Petrologic (or ophiolitic; left; after Nicolas et al., 1988) and seismologic (right, Mével, 2003) models for oceanic crust formed at fast spreading centers. Vertical scale shows the depth below the sea floor (b.s.f.) in km. The layer 2A is believed to correspond to the pillow-lavas and lava-flows; the 2B to the sheeted dike complex; the layer 3 to the gabbro pile and the layer 4 to the mantle.

Drilling operations at site 504B (eastern equatorial pacific) have nevertheless reached the layer 3 within the sheeted dike complex horizon (Detrick et al., 1994; Alt et al., 1996) and the recent IODP Hole 1256D (Cocos plate) has reached the gabbros within the layer 2 (Teagle et al., 2006; Wilson et al., 2006). These observations support that parameters such as porosity and alteration are more important than the grain size or the rock type on the control of the location of layer 2 / 3 transition (Wilson et al., 2006).

Porosity is related to fracturing and alteration, and allows hydrothermal circulation, which is mainly concentrated in the upper crust. Recent geochemical and structural studies of the Oman ophiolite show that very high temperature fluids can reach the magma chamber margins in the lower crust (Bosch et al., 2004; Nicolas et al., 2003; Nicolas and Mainprice, 2005). The hydrothermal circulation is classically depicted across-axis, forming cells that are perpendicular to the ridge axis (e.g., Alt et al., 1986). These are believed to be represented by a recharge system with cold sea water injections, away from the ridge axis along off-axis faults, and by a discharge system that rise up to the surface after the reheating occurring close to the magma chamber (e.g., Alt et al., 1986; Lowell et al., 1995; Kelley et al. 2002; Fisher, 2003). At 9°50'N, beneath a well-studied hydrothermal vent field on the East Pacific Rise, microearthquakes hypocenter relocations using the double-difference algorithm (relative location errors are 50 m in average; Waldhauser and Ellsworth, 2000) have been performed (Figure I-2; Tolstoy et al., 2008).

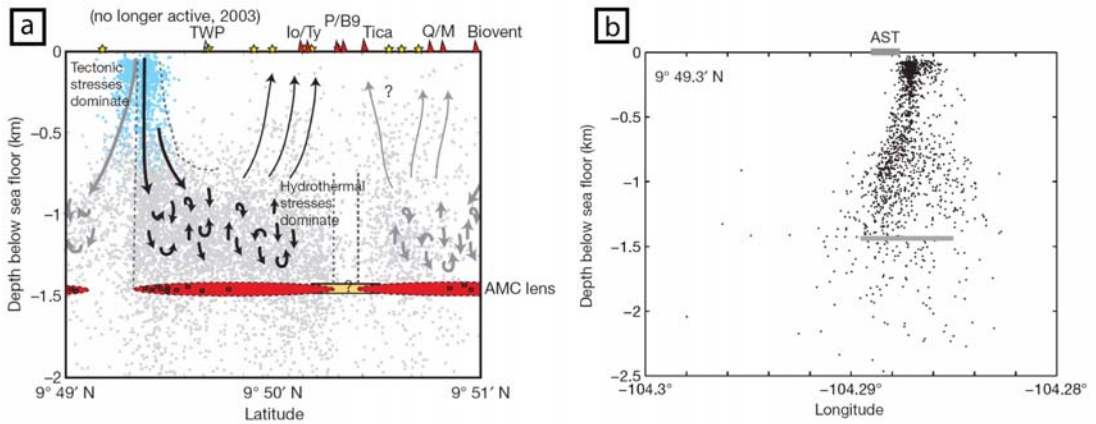

Figure I-2: a) Along axis cross section of the East Pacific Rise between 9°49'N and 9°51'N (Tolstoy et al., 2008). AMC: axial magma chamber or upper melt lens. The features of the best-defined hydrothermal cell are shown with black arrows, and the features inferred in adjacent cells are shown with grey arrows. Light blue dots illustrate the area where tectonic stresses are likely to dominate earthquake generation, creating a zone of permeability. Light grey dots illustrate where hydrothermal stresses probably dominate. Red triangles are high-temperature vents (with their associated names); yellow stars are low temperature vents. b) 200 m wide cross-axis section at 9°49.3'N; AST: axial summit trough; the grey line represents the melt lens reflector.

The hypocenters cluster in a vertical pipe-like zone (Figure I-2b), and in a band that lies directly above the melt lens (Figure I-2a). These data highlight that the convecting hydrothermal system forms along axis cells rather than cross axis ones (Figure I-2).

I.1.b. Magma chamber models

In early models (Figure I-3), the organization of fast-spreading ridge magma chambers was envisioned as a large, mostly molten reservoir (e.g., Cann, 1974; Dewey and Kidd, 1977; Smewing, 1981; Pallister and Hopson, 1981; Casey and Karson, 1981; Nicolas et al., 1988).

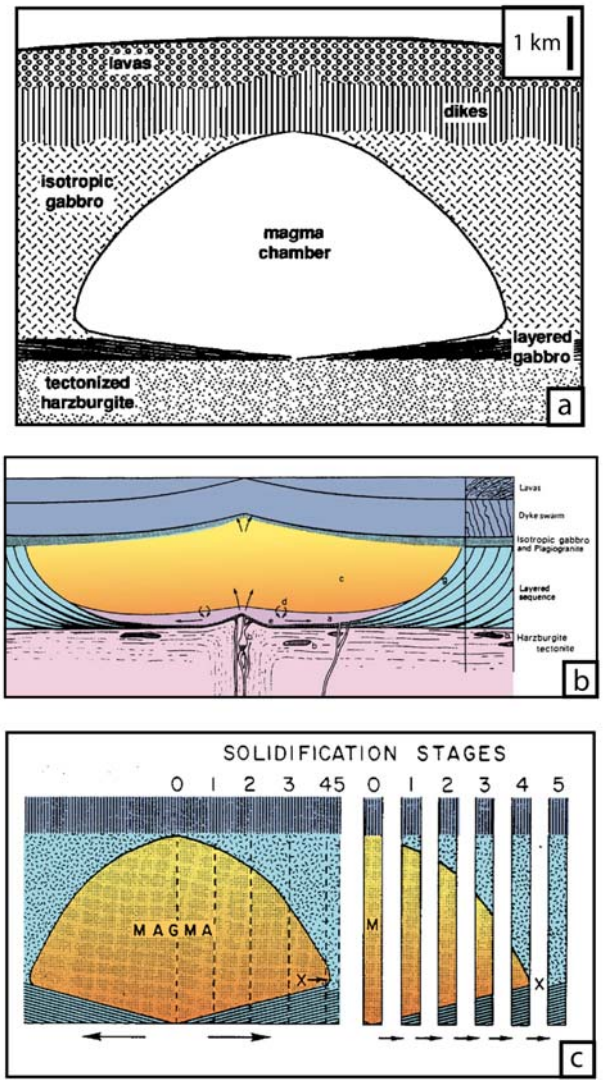

Figure I-3: Early models for the structure of the magma chamber (cross-axis views) that is represented by a large molten domain. a) Cann (1974) model; b) Smewing (1981) model [a]: magma imput; [b]: olivine+spinel fractionation; [c]: main magma body; [d]: limited mixing with primary melts; [e]: olivine-rich cumulates; [g]: cystallization; c) Pallister and Hopson (1981) model: Solidification stages, X= sandwich horizon where downward crystallization from the roof and upward crystal accumulation from the floor converge.

In these models crystal fractionation is expected to produce the evolved composition of most of the mid-ocean ridge basalts (MORB; e.g., Bryan et al., 1976; Stolper, 1980; Grove and Bryan, 1983). Seismic reflection profiles (Morton and Sleep, 1985; Kent et al., 1990), multi-channel seismic imaging (Detrick et al., 1987), and tomographic studies of mid-ocean ridges (Toomey et al., 1989; Caress et al., 1992), and petrological studies of oceanic lithologies (e.g., Smewing, 1981; Browning, 1984; Langmuir et al., 1986; Bloomer et al., 1989; Sinton et al., 1991; Lamoureux et al., 1999) have ruled out the large magma chamber model. The magmatic system is better represented by a thin and narrow, mostly liquid melt lens present at the base of the sheeted dike complex, and that overly a crystal-rich mush (Figure I-4). The size and structure of the melt lens has been further constrained by recent experiments at the East Pacific Rise (Singh et al., 1998; Kent et al., 2000) as outlined in section I.2.a. The presence of melt lenses close to the Moho has also been inferred from ocean bottom seismograph observations (Garmany, 1989), tomographic studies (Dunn et al., 2001), compliance studies (Crawford and Webb, 2002), multi-channel seismic data (Nedimovic et al., 2005), and three dimensional seismic reflection images (Singh et al., 2006). Recently, melt lenses within different levels of the lower crust (~850-900 m above, and at the Moho transition zone) have been observed through seismic reflection images (Figure I-4b; Canales et al., 2009).

These different melt lenses are expected to play a key role in controlling the crustal accretion. The upper melt lens is considered to be the source of the upper crust extrusives (sheeted dike complex and lavas). The different models for the formation of the lower crust which is typically composed of foliated and layered gabbros can be summarized in two end-members: (1) all the crystallization occurs in the shallow melt lens resulting in the subsidence of crystals in a "gabbro-glacier" building the lower crust (Figure I-5a; e.g., Henstock et al., 1993; Phipps Morgan and Chen, 1993; Quick and Denlinger, 1993); and (2) the lower crust crystallized mainly *in-situ* through injection of sills (Figure I-5c; Browning, 1982; Bedard et al., 1988; Gudmundsson, 1990; Kelemen et al., 1997; MacLeod and Yaouancq, 2000). An hybrid model of ductile flow resulting in subsidence from the shallow melt lens (Nicolas et al., 2009; see Appendix A1), with the occurrence of sill injections in the Moho transition zone (Kelemen et al., 1997) is also proposed (Figure I-5b; Boudier et al., 1996).

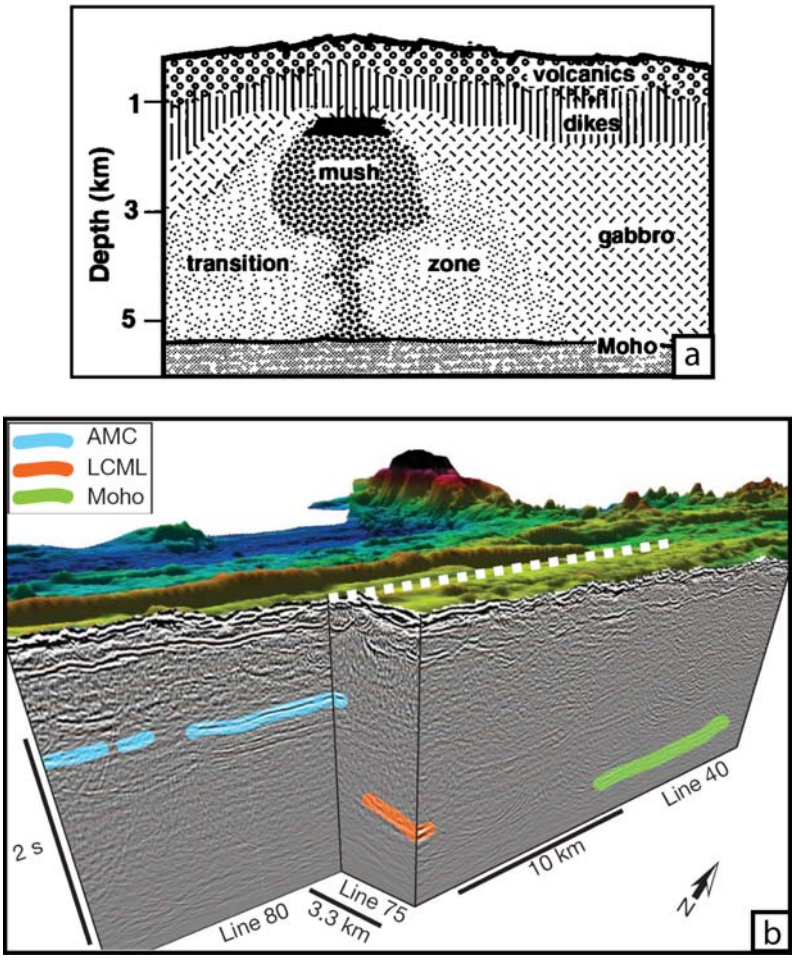

Figure I-4: a) Cross-axis view; the melt lens is restricted to a small domain at or close to, the sheeted dike base, it overlies a mush zone containing less than 20% of melt (Sinton and Detrick, 1992). b) Melt lenses are imaged at different levels of the crust (Canales et al., 2009): AMC=Axial magma chamber, it represents the melt lens depicted in a); LCML=Lower-crustal melt lens, and Moho the Moho melt lens. The section between the AMC and the Moho melt lens is considered to be mostly mushy (<20% melt according Lamoureux et al., 1999). The white dotted line represents the ridge axis.

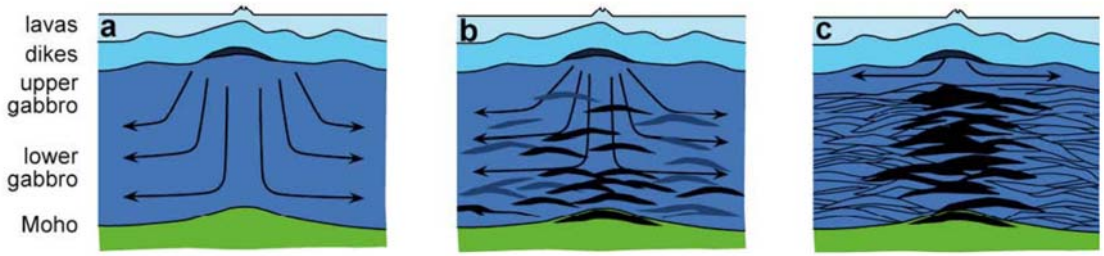

Figure I-5: Oceanic crust accretion models after Korenaga and Kelemen (1998) (B. Ildefonse personal com.). a) The "gabbro glacier" model: all the lower crust is crystallized through subsidence from the upper melt lens (e.g., Henstock et al., 1993; Phipps Morgan and Chen, 1993). b) Mixed model in which the lower crust is fed from the top through subsidence and from the bottom through sill injections (Boudier et al., 1996). c) The "sheeted sill" model in which most of the lower crust crystallize through sill injections (e.g., Kelemen et al., 1997; MacLeod and Yaouancq, 2000).

I.1.c. Ridge segmentation

The ridge present at fast spreading centers is not a continuous feature (e.g., Macdonald et al., 1988); it is segmented at different scales. The largest scale segmentation is represented by the large transform faults that separate ridge segments; the transform offset is tens to hundreds of kilometers. These are believed to be originated from mantle heterogeneities. The second order segmentation is represented by the overlapping of oceanic spreading centers (OSC); these discontinuities offset the ridge by typically 5 to 20 kilometers and are believed to have a significant effect in the mantle. The third order segmentation is defined by changes in the volcanic morphology of the ridge axis and changes in its trend. It is inherited from shallow mantle melt distribution. The finest-scale segmentation is defined by offsets in axial summit trough, and is inferred to be induced by lateral dike intrusions. All these discontinuities are associated to variations in the physical properties and structure of the melt lens (Carbotte, 2008), and should be considered when studying the melt lens evolution.

I.2. The upper melt lens, a key horizon

As discussed in part I.1, the upper melt lens present at the axis of fast spreading ridges feeds most of the upper crust and at least part of the lower one. It is therefore a key horizon for understanding the genesis of the oceanic crust. Several processes or interactions can occur within the melt lens or at its boundaries with surrounding rocks, magmas and hydrothermal fluids. These processes can be fractional crystallization, magma mixing, assimilation of fresh and / or of hydrothermalized rocks, partial melting of the surrounding rocks, and hydration of the magma at different stages of the crystallization. These can occur jointly and at different levels in the melt lens. All these possible processes have the potential to influence the composition of the formed melt, in particular of the MORBs that are the most accessible and therefore most studied oceanic hard rocks for shedding light on the mantle and crustal magmatic processes. All processes operating within and around the upper melt lens have thus important implications on our understanding of the global ridge system, and should be precisely constrained.

I.2.a. Structure

Morton and Sleep (1985) were the firsts to report the presence of a reflector at ~3500 m (below the ridge axis) depth, and interpret it as being related to an upper small melt lens at

the ridge axis at the top of a crystal mush containing a small percentage of melt. This melt lens is located at the bottom of the 2B layer representing the sheeted dike complex. Thermal structure at the axis, inferred from the tomographic study of Dunn et al. (2000), is in agreement with the presence of a small melt lens at the bottom of the sheeted dike complex (Figure I-6). Purdy et al. (1992) and Phipps Morgan and Chen (1993) have shown that the melt lens depth is proportional to the spreading rate; this has been recently confirmed in the Cocos plate where the first gabbros below the sheeted dike (considered as representing the melt lens) have been reached at relatively shallow depth (1157 meters below seafloor basement) by the IODP drilling operations performed at site 1256D (Figure I-7; Wilson et al., 2006). Along axis surveys along the East Pacific Rise show that the range of depth variation of the melt lens is about 1000 m, over tens to hundreds of km (e.g., Hooft et al., 1997; Figure I-8a).

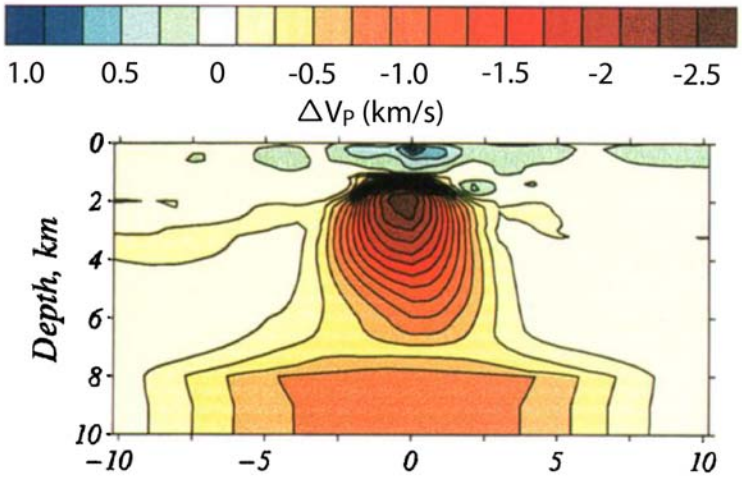

Figure I-6: Cross axis tomographic model of the East Pacific Rise at 9°31.74'N (Dunn et al., 2000). Velocity perturbations are calculated against a one dimensional velocity model.

Canales et al. (2005) have shown at the Juan de Fuca Ridge that the melt lens is present along axis over tens of km (Figure I-8b). The recent study of Canales et al. (2009), using higher resolution seismic reflection data, confirms the along axis continuity over several km of the narrow upper melt lens (Figure I-4b). Preliminary results of a recent multi-streamer 3D seismic reflection study of the 9°50' area of the East Pacific Rise show that the melt lens is divided into a series of discrete magma lens events that are continuous ~5-10 km (Carton et al., 2008; Carbotte, 2008). Cross-axis seismic reflection profiles beneath the East Pacific Rise at 9°30'N (Canales et al;, 2005) show that the width of the melt lens ranges between 600 and 1700 m, which is in good agreement with the first estimates done by Kent et al. (1990). The

width of the melt lens is not correlated to depth variations (Figure I-8c). The erupted melt volume is not correlated to the melt lens depth but well correlated to its width (Bergmanis et al., 2007).

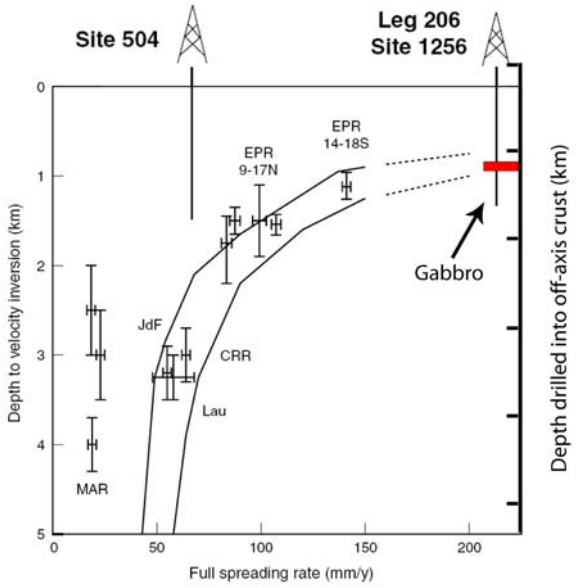

Figure I-7: Depth to the upper axial melt lens reflector against spreading rate (Wilson et al., 2006, after Purdy et al., 1992, and Carbotte et al., 1998). Two models of Phipps Morgan and Chen (1993) are shown (black lines) and extrapolated to higher spreading rates (dashed lines). The penetration of IODP Holes 504B and 1256D are added (black vertical lines) considering ~300 m of off-axis lavas for Hole 1256D (Wilson et al., 2006). The depth of the first gabbros encountered at IODP Hole 1256D fit well the extrapolations of the Phipps Morgan and Chen (1993) model. MAR=Mid Atlantic Ridge; JdF=Juan de Fuca Ridge; Lau=Valu Fa Ridge in Lau Basin; CRR=Costa Rica Rift; EPR=East Pacific Rise.

Collier and Singh (1997) have performed a detailed study of the top of the melt body beneath the East Pacific Rise at 9°40N, and have estimated the thickness of the narrow upper melt lens to be ~30 m. They also show that the melt lens contain less than 30% of crystals. Singh et al. (1998), using single-ship and two-ship multichannel seismic reflection profile near 14°S at the East Pacific Rise, both along- and across-axis, have shown that the melt lens is ~50 m thick, and that its internal properties change rapidly along axis, ranging from nearly pure melt (>90% of melt) to mush containing 40-60% of melt. Over the ~60 km of imaged melt lens, three 2-4 km long zones consist of, nearly pure melt, separated by 15-20 km long mushy zones. Singh et al. (1998) also noted that basaltic samples from the East Pacific Rise contain on average 7-10% of phenocrysts (Batiza and Niu, 1992), which suggest that eruptions originated in nearly pure melt lens segments. Singh et al. (1999) performed a full waveform inversion of the Singh et al. (1998) data, and showed that the ~50 m thick melt lens is underlain by a nearly solid floor (at least 100-150 m thick) and overlain by a 50-60 m thick

solid roof. They also showed that a low velocity zone (150-200 m thick) is present above the melt lens roof and may correspond to the base of the hydrothermal convecting system.

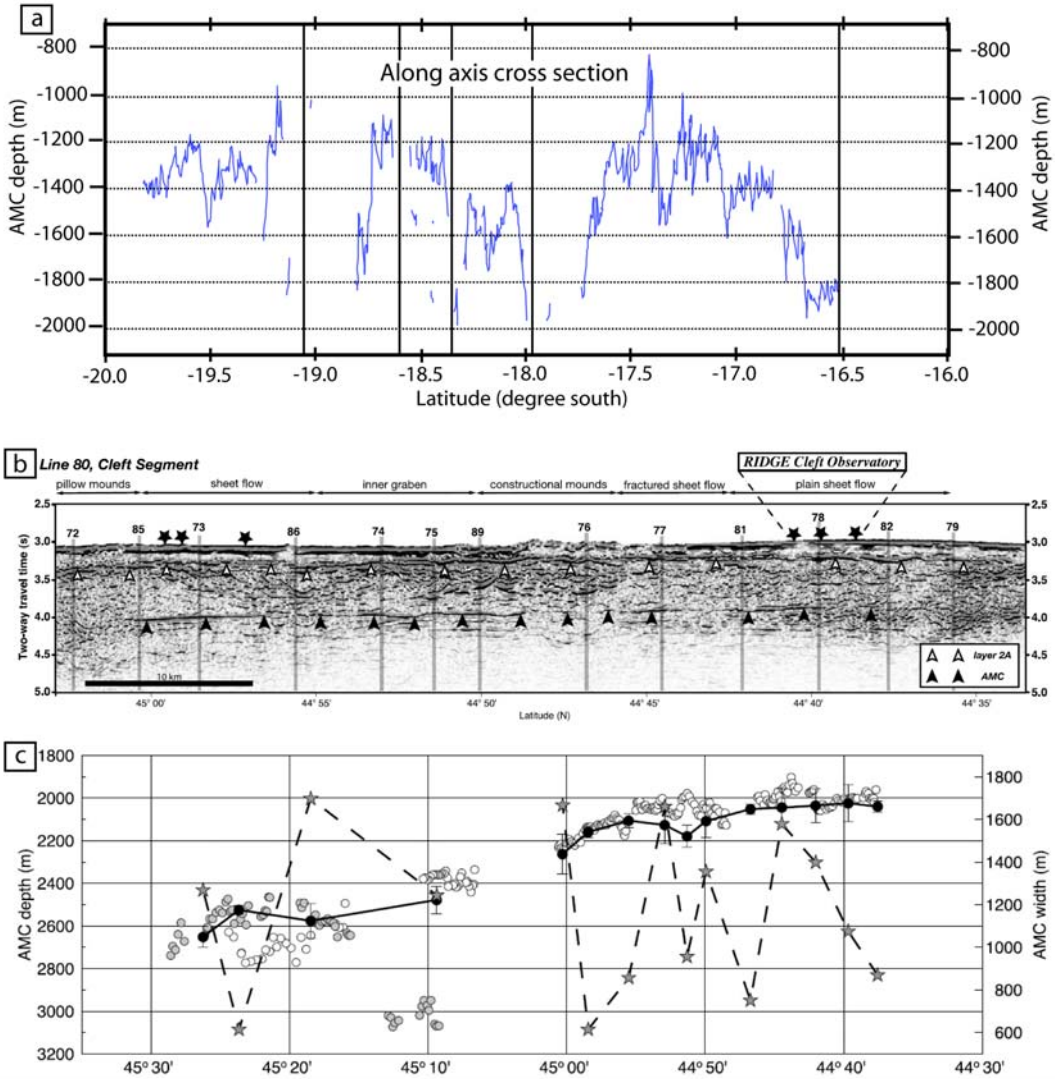

Figure I-8: Along axis imaging of the upper melt lens. a) Depth to the melt lens reflector along the East Pacific Rise between 16° and 20°S (Hooft et al., 1997). Vertical lines indicate the locations of overlapping spreading centers. b) Seismic reflection profile along the Juan de Fuca Ridge between 44°30N and 45°30N (Canales et al., 2005). Black arrows indicate the melt lens position (AMC); white arrows indicate the basement of layer 2A. Vertical black lines and associated numbers show the position of cross axis profiles shown in Canales et al. (2005). c) Melt lens depth (circles; left axis) and width (grey stars; right axis) vs. latitude along the Juan de Fuca Ridge between 44°30N and 45°30N (Canales et al., 2005). Solid line and solid circles correspond to the average melt lens depth estimated from cross-axis profiles. Open and grey circles correspond to two different along axis parallel segments.

Using the hydrothermal plume distribution along the South East Pacific Rise determined by Backer and Urabe (1996), and the mush – melt distribution from the same area proposed by Singh et al. (1998), Singh et al. (1999) proposed that hydrothermal plumes,

which correspond to the discharge part of the system, are associated to melt-rich segments of the axial melt lens. This is also in agreement with the recent study of the hydrothermal system at 9°50'N at the East Pacific Rise (Tolstoy et al., 2008), which shows that the hydrothermal recharge occurs in a location where no reflector is observed, and therefore no melt lens, is present (Figure I-2). These different results are summarized in Figure I-9 (Singh et al., 1999).

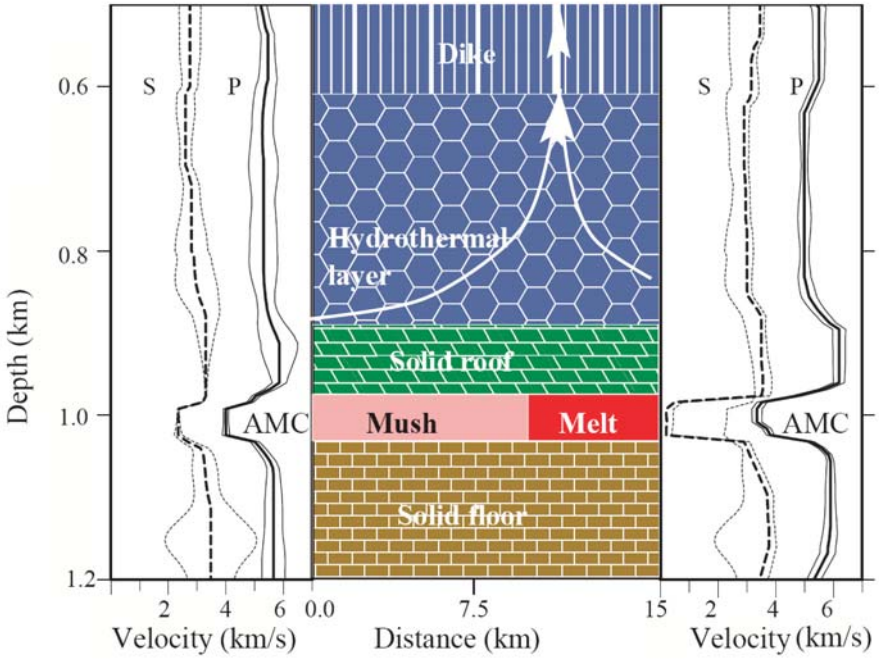

Figure I-9: Schematic along axis model of the melt lens area and associated velocity 1D models (Singh et al., 1999). The left model corresponds to the mush zones and the right one to the melt domains. Note that in melt domains, the S wave velocity is nearly zero at the melt lens depth. Hydrothermal discharge occurs above the melt domains.

I.2.b. Melt storage, composition and delivery

The composition of the melt filling the melt lens is believed to be well represented by the compositions of the sheeted dike complex and the lava erupted on the sea floor (e.g., Sinton and Detrick, 1992), and is therefore similar to typical N-MORB. However, Natland and Dick (1996) proposed that differentiation that is believed to occur in the melt lens can produce iron-rich melts that are too dense to erupt, and that may lie on the melt lens floor. This hypothesis builds on the discovery of ferro-andesitic samples within the isotropic gabbro section below the sheeted dike at Hess Deep. Similar rocks have also been observed in the Oman ophiolite, but structural relationships suggest that they formed by differentiations at the melt lens margins (MacLeod and Yaouancq, 2000). These rocks therefore represent late processes occurring after the dike injections. Dike (and lava) composition is therefore

expected to represent an average composition of the melt lens, and the overall melt lens composition can be considered to be well represented by N-MORB. MacLeod and Yaouancq (2000) proposed that the varytextured gabbro horizon that underlies the sheeted dike complex represent the fossilized melt lens. Using the compositions and the proportions of the different lithologies forming this horizon, they have calculated an average composition that corresponds to typical MORB melts (with Mg#=65 where Mg#=Mg/[Mg+Fe] and TiO_2=1.1wt%).

N-MORB melts represent evolved liquids regarding primitive mantle melts (e.g., Stolper, 1980) and must have fractionated before reaching the upper melt lens. Koga et al. (2001) noted that most of the clinopyroxenes in samples from the Moho transition zone in Oman (>90% of the samples) are equilibrated with MORB melts, and that mixing of various polybaric partial melts of mantle peridotite must have occurred at or below this zone to give the MORB signature. Determining the origin of the MORB composition is beyond the goals of this study. It is just worth noting here that the MORB composition appears to be consistent with channelized, reactive melt transport. For a given degree of partial melting (or a given amount of melt), this results in higher amounts of mineral consumption and higher amounts of newly formed olivine, compared to a melting reaction without channelization / fossilization (e.g., Kelemen et al., 1995; Asimow and Stolper, 1999; Lambart et al., 2009).

The MORB compositions follow the tholeiitic fractionation trend of increasing FeO_{total}, Na_2O, and TiO_2 and decreasing Al_2O_3 and CaO with decreasing MgO (Klein and Langmuir, 1987; Klein et al., 1991). The major variations are attributed to differentiation processes occurring within the melt lens but some variations in composition can also be attributed to physical parameters such as the melt lens morphology and/or depth. For example, the MgO content of the erupted lavas at the East Pacific Rise, 17°30'S, is higher when the melt lens is deeper, and these most primitive lavas are less abundant and derived from narrower melt lens in contrast with more evolved lavas with lower MgO content (Bergmanis et al., 2007). Melt compositions are also correlated to the ridge axis water depth. Klein and Langmuir (1987) have shown that the $Na_{8.0}$ (i.e., the Na_2O calculated value at 8 wt% of MgO, allowing to compare compositions that are not affected by fractional crystallization) increases with increasing water depth at the ridge axis.

Some MORB samples display high chlorine contents that are interpreted as indications of sea water contamination of the melt lens through assimilation of hydrothermally altered crustal rocks (e.g., Michael and Schilling, 1989; Michael and Cornell, 1998). The incorporation of sea water, hence of chlorine into MORB flows during their emplacement on

the seafloor is also possible (Soule et al., 2006). However, Cl incorporation during emplacement cannot account for the higher Cl/K ratio observed in fast spreading ridges MORB vs. slow spreading ridges MORB (Michael and Cornell, 1998), and assimilation effects as proposed by Michael and Cornell (1998) is likely to play a role. Nevertheless partly digested xenocrysts or amphibolite blocks are only rarely observed in MORB, and the Cl assimilation at the melt lens level is not well understood (Michael and Schilling, 1989). More recently, Coogan et al. (2003) have shown that assimilation processes do occur around the melt lens; this will be outlined in chapter I.3.

Significant differentiation is believed to occur occasionally in the melt lens; this is inferred from the occurrence of highly silicic rocks (>60 wt% SiO_2) observed as lavas erupted on the seafloor (Fornari et al., 1983; Haase et al., 2005) and as plutonic rocks (oceanic plagiogranites) present at the sheeted dike base and in the gabbro unit (e.g., Pallister and Hopson, 1981). These silica-rich rocks can alternatively be generated by hydrous partial melting of mafic rocks (variously altered dikes and gabbros; e.g., Koepke et al., 2007). These two processes are not necessarily mutually exclusive, and may operate jointly (e.g., Pedersen and Malpas, 1984). The melt lens crystallization leading to differentiation is believed to be fast if no new magma injection occur (~50 years to crystallize a 50 m thick melt lens according to Singh et al., 1999). Constraining the timescales of magma replenishment and storage in the melt lens, and of magma supply is therefore a critical parameter. These are reviewed in detail together with the timescales for transfers from the mantle and for the melt lens dynamics in France et al. (2009a; section 6.5). Here, only a short overview of the timescale constrains for the replenishment time, residence time and eruptive events associated to the upper melt lens is given.

Using a mathematical model and basalt geochemical data, Rannou et al. (2006) have estimated the replenishment period of the melt lens to be ~750 years. Using the MORB major and trace elements composition, Rubin and Sinton (2007) proposed that this replenishment is achieved in less than 1000 years. Rannou et al. (2006) also proposed that the magma residence time in the melt lens is around 300 years, which is in agreement with the Rubin et al. (2005) study that proposed, using ^{210}Pb-^{226}Ra-^{230}Th radioactive disequilibria in samples from the East Pacific Rise, that the magma resides and mixes in the melt lens over periods of ~200-400 years. The eruptive events (or supply events) are believed to occur over periods of 10 to a few hundreds of years (Hooft et al., 1997; Sinton et al., 2002; Bergmanis et al., 2007).

Do eruptive events have a significant influence on the melt lens structure and volume? Recent studies around 9°50'N at the East Pacific Rise seem to show that eruptions

do have an impact on the melt lens volume and on its melt proportion. Seismic measurements have been done in 1985 and 2008 in this area where two eruptions occur in 1991 and 2005-2006. Preliminary results from the recent multi-streamer reflection imaging experiment (Mutter et al., 2008), suggest that significant variations in the depth of the melt lens reflector have occurred between 1985 and 2008 at 9°50'N, below the location of the 2005-2006 eruption. No significant variation is observed at 9°30'N and 9°40'N, away from the eruption event. The reflectivity strength of the melt lens under the eruption locality is weaker than the one of the melt lens immediately to the North and South (Carton et al., 2008). This may indicate that a lower melt percentage is present in the melt lens that has fed the eruption.

Are the erupted volumes significant comparable to the volume of the melt lens? Soule et al. (2007) have described lava flows over 18 km along axis at the East Pacific Rise, 9°50'N, and estimated the erupted volume of the 2005-2006 eruption to be ~22 x 10^6 m^3. They estimated that the dike feeding this eruption should be on average ~1 m wide (which is the average thickness of sheeted dikes in the Oman ophiolite), 1.4 km high and 18 km long, and should be filled with ~25 x 10^6 m^3 of magma. However, based on the studies of Singh et al. (1998; 1999) at the Southern East Pacific Rise, and on the preliminary results of Carton et al. (2008) at 9°50'N, the melt lens cannot be considered as a continuous melt horizon over 18 km. Singh et al. (1998) proposed that the melt lens containing nearly pure melt and that have the potential to feed eruptions are ~2-4 km long. The eruptible melt lens volume can be estimated by considering an average width of ~1000m (Bergmanis et al., 2007) and an average thickness of 40 m (30 m for Collier and Singh, 1997 and 50 m for Singh et al., 1999), i.e., ~120 x 10^6 m^3. If we consider that the dike feeding the 2005-2006 eruption rooted in a ~2-4 km long melt lens rather than in a 18 km long melt lens, its volume can be considered to be ~4 x 10^6 m^3 resulting in an total supplied volume of ~26 x 10^6 m^3. The supplied volume is therefore roughly one fifth of the eruptible melt lens volume. As the whole melt lens is probably not homogeneously involved in the eruption, some parts may have supplied even more magma; it is therefore expected that significant variations in the seismic properties of the melt lens can locally occur, and the variations in the depth of the axial melt lens observed by Mutter et al. (2008) are possibly linked to the eruption.

Lagabrielle and Cormier (1999), Lagabrielle et al. (2001) and Garel et al. (2002) have shown that periods of waning magma supply and of melt lens replenishment are associated to axial morphological variations. Along axis troughs interpreted as collapsed calderas (40-110m deep) may form when the melt supply of a previously inflated melt lens wanes or ceases. In contrast, the axial morphology is believed to be a broad, smooth dome structure when the

melt supply is higher. Along axis variations of the axial morphology are interpreted by Carbotte (2008) to represent the 4th order of fast spreading ridges segmentation; on each side of this 4th order discontinuity, geochemical compositions are different. This is consistent with Lagabrielle and Cormier (1999) who proposed that axial morphology variations correspond to differences in the magma supply. Hence, variations in basalt composition should be correlated with different axial morphologies. For example, Caroff et al. (1997) have shown that the presence of axial trough is associated to larger geochemical heterogeneities than in zones with dome-shaped axial morphology, and are associated to lavas enriched in rare-earth elements, deriving from melts that have evolved during periods of lesser replenishment.

I.3. The melt lens and the root zone of the sheeted dike complex: relations and evolution

I.3.a. General presentation

In this part, I discuss the available models for the melt lens evolution and for the evolution of the associated root zone of the sheeted dike complex. These zones are spatially associated, and correspond to the interface where the hydrothermal convecting system and the magmatic one are acting together. Several chemical and thermal exchanges can occur during the melts, fluids and rocks transfers. The thermal gradient (~7°/m) is believed to be one of the highest nearly stable thermal gradients on earth (Nicolas et al., 2008; See Appendix A2). Although the foliated gabbros origin is discussed (Boudier et al., 1996; MacLeod and Yaouancq, 2000; Nicolas et al., 2009_Appendix A1), in all models they represent the melt lens floor. I focus here on lithologies occurring above this horizon: *the isotropic gabbro horizon* and on the *base of the sheeted dike complex*.

I.3.b. Interaction processes

Several processes can operate in the melt lens, in the root zone of the sheeted dike complex and at the interface between them (Figure I-10). First of all, eruptions can occur (Figure I-10b), draining out some melt. Consequently, the axial morphology can be modified (Lagabrielle and Cormier, 1999). Crystallization at the melt lens margins (Figure I-10c) may occur when the magma supply decreases or when the thermal regime reaches lower temperatures; such a crystallization stage may lead to magma differentiation (e.g., MacLeod

and Yaouancq, 2000). New melt injections may come from the main, mushy magma chamber below the melt lens (Figure I-10d); this would result in magma mixing and melt lens replenishment. The replenishment can be associated to an inflation of the ridge axis morphology (Lagabrielle and Cormier, 1999) and to assimilation of the melt lens roof (Figure I-10e; e.g., Coogan et al., 2003). The melt lens roof is assumed to be hydrothermalized (see below) and its assimilation may account for the chlorine enrichment observed in some MORBs (Michael and Schilling, 1989; Coogan et al., 2003). As the melt lens feeds at least part of the lower crust through subsidence (Boudier et al., 1996; Nicolas et al., 2009), it may also account for the lower crust contamination documented by Coogan (2003). Some authors consider the melt lens to be a steady state horizon that cannot assimilate its roof (e.g., Nicolas et al., 2008). It this case, the chlorine enrichment / contamination may be explained by the incorporation of Cl-rich brine contained in the roof and / or wall rocks (Figure I-10e; e.g., Michael and Schilling, 1989; Michael and Cornell, 1998).

Even if the contamination mechanism is not fully understood, the incorporation of fluids and especially of water into the melt lens is very obvious. The addition of water to the melt lens, even at low concentrations, has strong implications. It lowers the melt viscosity (Giordano et al., 2008); lowers the solidus and liquidus temperatures (e.g., Berndt et al., 2005); increases the oxygen fugacity for a given hydrogen fugacity (Botcharnikov et al., 2005), and therefore stabilizes the Fe-Ti oxides (Berndt et al., 2005; Feig et al., 2006). The liquid line of descent is consequently modified and a differentiation trend characteristic of calc-alkaline series can be observed (Berndt et al., 2005). The mineral composition of erupted basalts can also be modified by water assimilation; as an example, the olivine and pyroxene Mg# and the An content of plagioclase are expected to increase (Kvassnes et al., 2004; Berndt et al., 2005; Feig et al., 2006; Koepke et al., 2009). High water activities in the melt lens due to assimilation also lowers the solidus temperature of rocks from the roof and the margins of the melt lens, with the potential to trigger hydrous partial melting and to incorporate the newly formed silicic melts into the melt lens. Such a partial melting event can occurs either when fluids are transported into recently crystallized, still hot rocks (Nicolas et al., 2008) or when previously hydrothermally altered rocks are reheated.

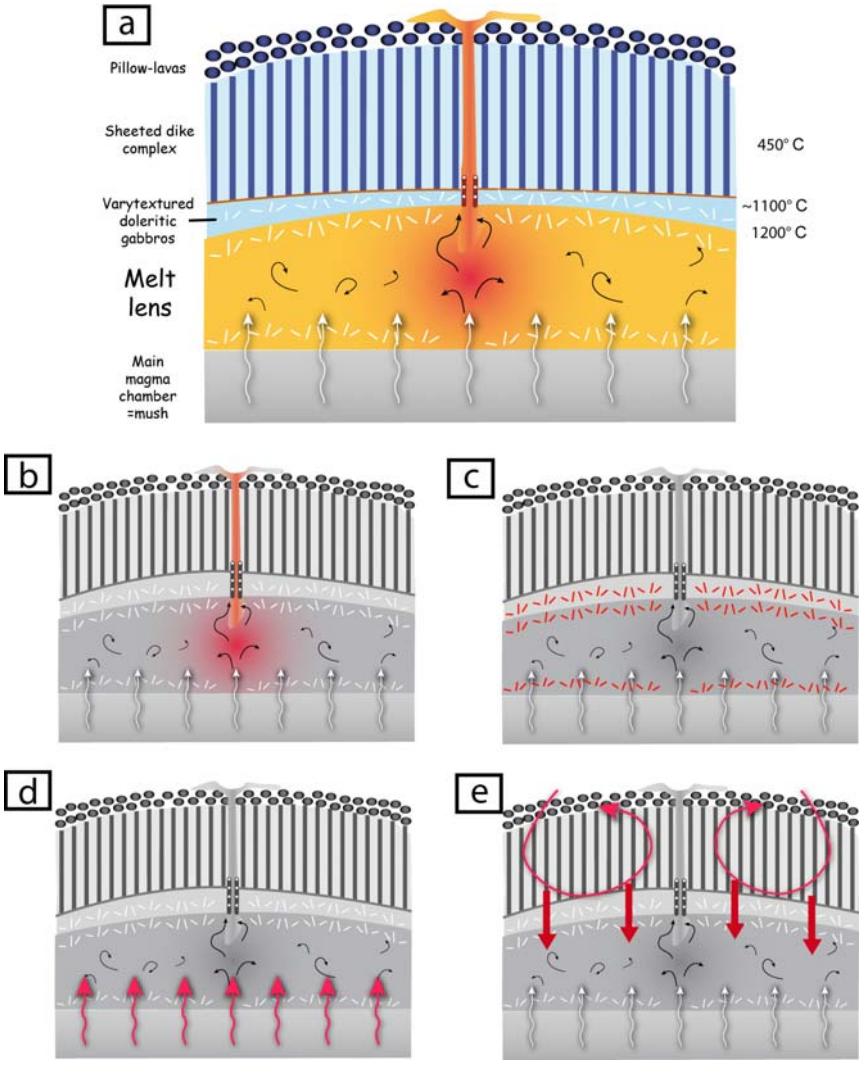

Figure I-10: Schematic cross-axis section showing the melt lens and the root of the sheeted dike complex (not to scale). a) General organization, lithologies and temperatures. After Nicolas et al. (2008). For details see Nicolas et al. (2008). b) Magma drained out during an eruption. c) Melt crystallization at the melt lens margins. d) New magma injection leading to partial or total replenishment of the melt lens. e) Hydrothermal circulation in the crust overlying the melt lens; fluids can be incorporated in the melt lens through assimilation of either hydrothermally altered rocks or brine.

I.3.c. Geological settings

Depending on the geological setting, the melt lens (and associated base of the sheeted dike complex) structure, composition and evolution may vary. As an example, in back-arc systems the higher amount of water present in the melt will influence the crystallization sequence and the solidus and liquidus temperatures. The ridge segmentation can also influence the system, and ridge segments close to transform faults, or close to overlapping segments, may be disturbed by tectonics, allowing deep penetration of water. Boudier et al. (2000) have proposed that the occurrence of gabbronorites in areas of the Oman ophiolite that

are inferred to be located at the tip of propagating segments is related to high oxygen fugacities linked to melt hydration.

I.3.d. Lithostratigraphy

Generally, the basalts forming the sheeted dike complex display intergranular, doleritic textures. The root of the sheeted dike complex has been first described in the Troodos ophiolite (Allen, 1975), and then in the Oman ophiolite (Rothery, 1983; Nicolas and Boudier, 1991; Nicolas et al., 2008). Dikes root into the isotropic upper gabbros (Figure I-11a), the chilled margins progressively disappear in gabbros and the center of dike roots is similar to the surrounding isotropic gabbros (Allen, 1975; Rothery, 1983).

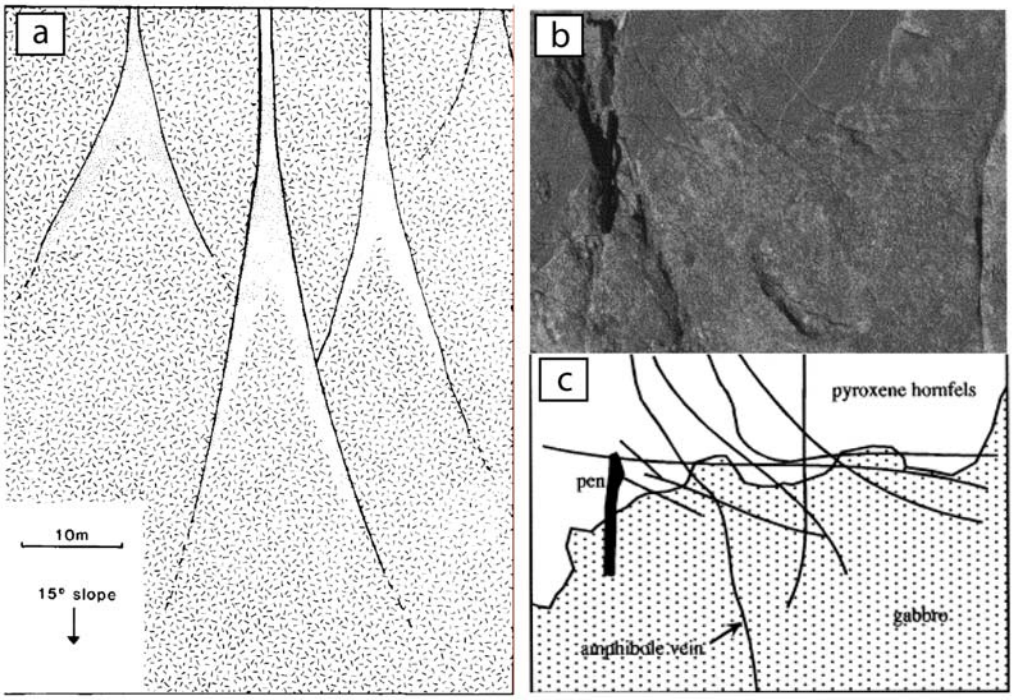

Figure I-11: a) Dikes rooting in the isotropic upper gabbros in the Oman ophiolite, line tone represents high-level gabbro, and dot tone represents doleritic textured microgabbro (Rothery, 1983). The center of the dike roots is similar to the surrounding isotropic gabbros. b-c) Outcrop photograph and sketch of the recrystallized base of the sheeted dike complex truncated by gabbros in the Troodos ophiolite (Gillis and Roberts, 1999).

Nicolas and Boudier (1991) and Nicolas et al. (2008) made similar general observations and describe further the nature of the dike roots. They show that these roots, called "protodikes", display microgranular margins that have a well defined preferred crystallographic orientation, parallel to the dike margin, which records the upward magmatic flow. Dikes are sometimes crosscut by gabbro, diorite or plagiogranites injections (Figure

I-11b-c; Pallister and Hopson, 1981; Gillis and Roberts, 1999). They are then recrystallized and display microgranular textures ("granoblastic" textures in Wilson et al., 2006; Koepke et al., 2008; "hornfelsic" textures in Gillis and Roberts, 1999).

A thin (~100m) and complex horizon mainly composed of varytextured gabbros is present below the base of the sheeted dike complex (e.g., MacLeod and Yaouancq, 2000). The varytextured gabbro horizon is mainly composed of isotropic fine grained gabbros but also isotropic coarse grained gabbros (or pegmatitic gabbros) often with subophitic rock textures, diorites, and plagiogranites. Gabbros may be locally foliated (MacLeod and Yaouancq, 2000), and sometimes crosscut by late dikes.

Below the varytextured gabbro horizon, the gabbros display more equilibrated granular textures with a vertical foliation (Nicolas et al., 2009_Appendix A1), these are believed to result either from subsidence from the floor of the melt lens (Nicolas et al., 2009_Appendix A1) or from the upward moving melt that is believed to orientate crystals (MacLeod and Yaouancq, 2000).

I.3.e. Conceptual models and implications

Since the discovery of the upper melt lens (Morton and Sleep, 1985; Detrick et al., 1987), its role in the oceanic crust accretion has been questioned. The geological setting (mid-ocean ridge, back-arc, propagator tip) is believed to influence the tectonics at or close to the ridge axis, and the water budget and should therefore affect the magmatic processes occurring in the melt lens (Nicolas et al., 2008_Appendix A2).

Nicolas and Boudier (1991) proposed that, as a result of water ingression into the still hot, just crystallized upper gabbros, the latter can undergo hydrous partial melting and the newly formed melts can crystallize to gabbro-diorites. Such a wet anatexis is considered to occur in a steady state system, in which the melt lens is a stable horizon. Hooft et al. (1997) have shown at the Southern East Pacific Rise that the melt lens depth varies along axis, probably in response to variations in the magma supply from below or in response to variable hydrothermal cooling (Figure I-12). This model suggests that during periods of weak hydrothermal cooling, the melt lens migrates upward with the potential to trigger hydrous partial melting to the roof.

In the Troodos ophiolite, the base of the sheeted dike complex is intruded by gabbros and recrystallized to hornfelsic lithologies (Figure I-11b-c; Gillis and Roberts, 1999; Gillis, 2002). At the same structural level, the sheeted dikes can locally melt during the intrusion of

gabbroic mushes (Gillis and Coogan, 2002). Gillis and Coogan (2002) have attributed the gabbro intrusion in the Troodos ophiolite to upward movements of the melt lens, and the recrystallization of the base of the sheeted dike complex to contact metamorphism associated to this upward movement (Figure I-13).

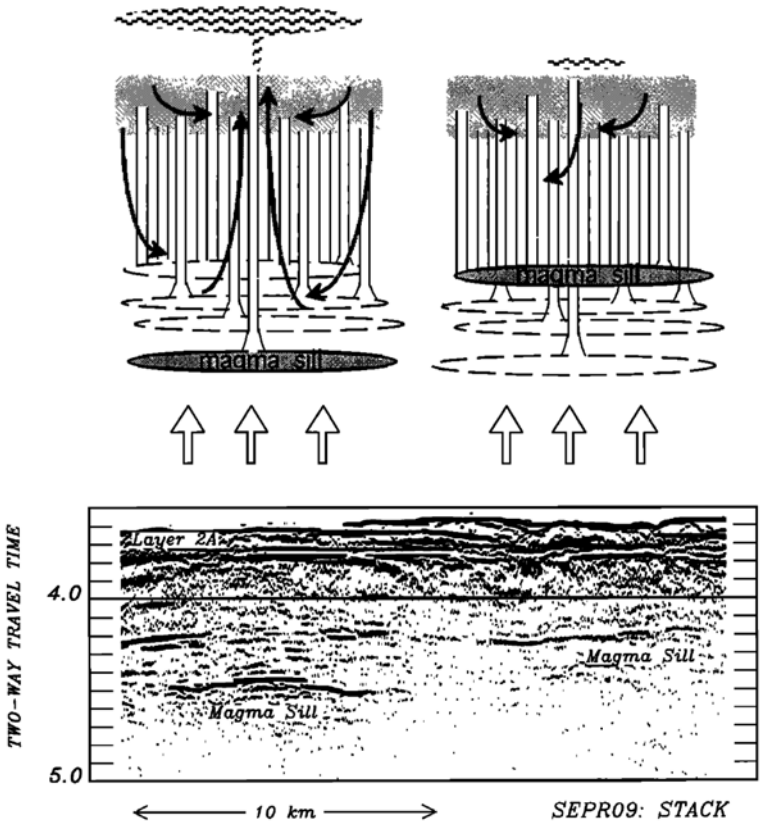

Figure I-12: Top: Cartoon showing two scenarios for the melt lens position depending on the strength of hydrothermal cooling. Bottom: along-axis seismic reflection profile (between 18°13'S and 18°02'S along the East Pacific Rise) illustrating apparent local depth variations of the magma sill (Hooft et al., 1997).

Intrusions of gabbronorites in gabbros and in the sheeted dike complex are known from the Oman ophiolite and according to Boudier et al. (2000) and Nicolas et al. (2000) only in areas of segment propagation. In such areas, a ridge segment is propagating in an older lithosphere (Figure I-14) with the potential to remobilize rocks that have been hydrothermally altered. According to Boudier et al. (2000) gabbronorite injections occur while the main gabbro unit is still deforming as a magmatic mush; the occurrence of orthopyroxene is attributed to the water-rich conditions prevailing in these environments where there is active tectonics at or near the ridge axis (Boudier et al., 2000). Nicolas et al. (2008) postulated that intrusions of gabbronoritic rocks in the base of the sheeted dike base can only occur in these

peculiar areas that correspond to tips of propagating segments (Figure I-14), and cannot be considered as being representative of a "standard" mid-ocean ridge process. According to Yamasaki et al. (2006) gabbronorites are rather related to a late magmatism stage that is probably related to the shallow subduction zone process occurring during the early obduction.

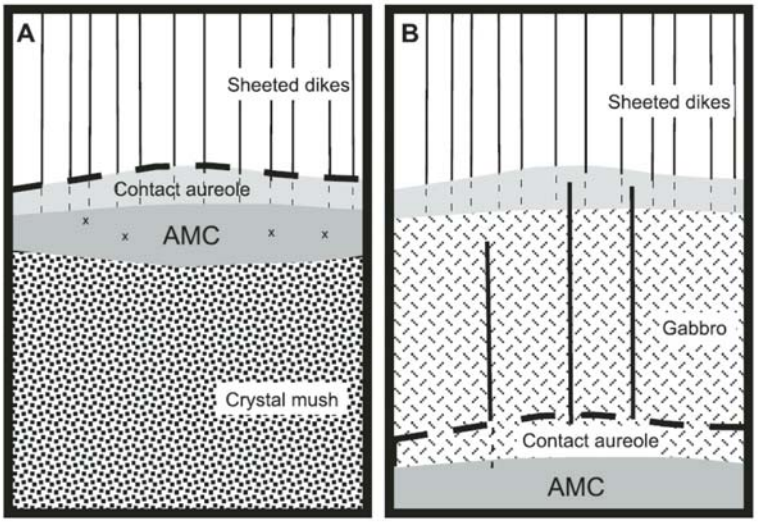

Figure I-13: Migrations of the melt lens can trigger recrystallization at its roof (Gillis (2008), as described in the Troodos ophiolite (Gillis and Roberts, 1999; Gillis, 2002). AMC= Axial Magma Chamber, i.e. the melt lens in this study; x= xenoliths.

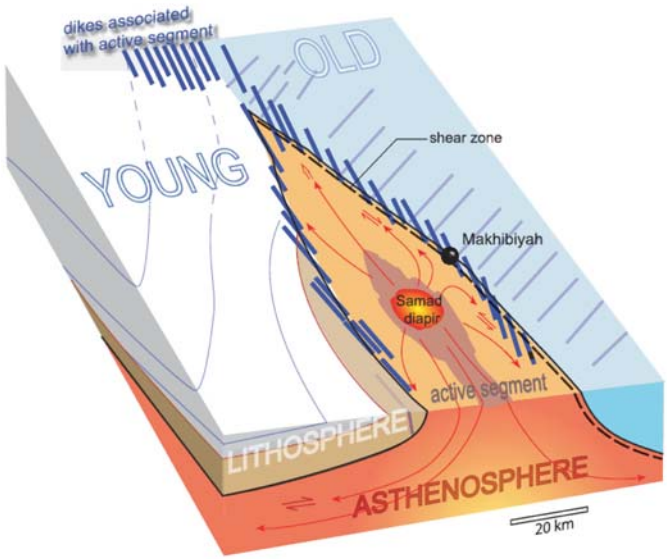

Figure I-14: Tip of a propagating segment that reopens an old domain (Nicolas and Boudier, 2008). Remobilization of hydrothermalized rocks is possible and tectonics at the ridge axis may result in the involvement of water in magmatic processes.

MacLeod and Yaouancq (2000) have studied the Abyad area in the Oman ophiolite, which is considered to be close to the tip of a propagating segment. Despite this peculiar

environment, they have described in this area a steady state system with nearly no gabbro intrusion in base of the sheeted dike.

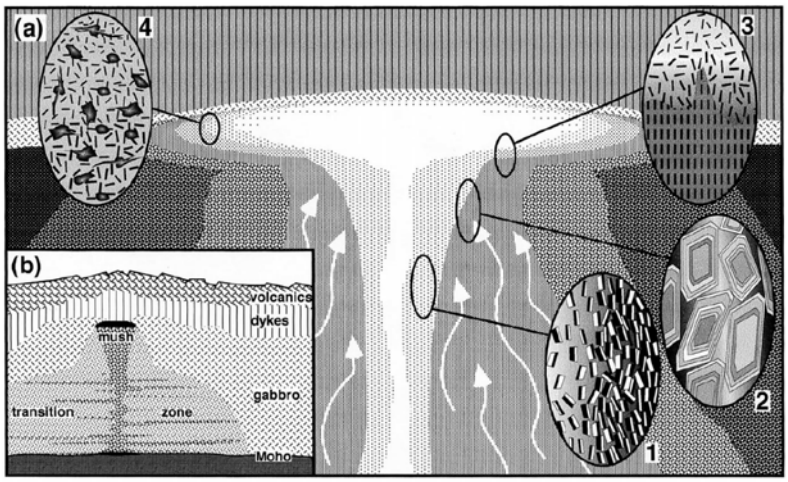

Figure I-15: Melt lens model from MacLeod and Yaouancq (2000). a) Focus on the melt lens and surrounding areas; b) Schematic section across the axis of a fast spreading ridge. In a), 1. shows the foliated gabbros; 2. shows the zoning observed in some plagioclase grains of the sub-melt lens region. 3. shows that some foliated gabbros can also be observed in the varytextured gabbro horizon and 4. proposes that at the melt lens margins some trapped melts can fractionate to form the Fe-Ti pegmatitic gabbro pockets observed in the varytextured gabbro horizon. In this model, MacLeod and Yaouancq (2000) interpret the varytextured gabbro horizon as the crystallized melt lens.

The occurrence of pegmatitic gabbros enriched in Fe-Ti (up to 4.4 wt % of TiO_2) that can only be interpreted as fractionated melts under reducing condition has led MacLeod and Yaouancq (2000) to propose that the varytextured gabbro horizon represent the fossilized melt lens (Figure I-15). They therefore interpret these rocks, present as meter sized pockets in the isotropic gabbros, as trapped melts that have crystallized at the margins of the melt lens.

Coogan et al. (2003) combined geophysical results obtained at the East Pacific Rise with geochemical studies, and with field observations in the Troodos and Oman ophiolites to show that assimilation of roof fragments is common in the melt lens (Figure I-13). They propose that such a process can account for the chlorine enrichment observed in some MORB (Michael and Schilling, 1989). Nevertheless, they do not discuss the possibility of relating this process to tectonics related to segment propagation.

IODP Hole 1256D was drilled in an intact portion of oceanic crust in the Cocos plate formed at the EPR (Teagle et al., 2006), and is assumed to represent a regular ridge segment, away from mid-ocean ridge discontinuities. In this area, Wilson et al. (2006) described, at the base of the sheeted dike complex, truncated dikes with characteristic granoblastic textures

interpreted as reheated, contact-metamorphosed rocks. A detailed study of these granoblastic dikes (Koepke et al., 2008) shows an evolution of the recrystallization downward when approaching the isotropic gabbros, which are believed to intrude the base of the sheeted dike complex. This recrystallization is ascribed to reheating triggered by the melt lens upward migration. Gillis (2008) described similar hornfelsic lithologies present at the base of the sheeted dike complex and as xenoliths in the varytextured gabbro horizon of Pito Deep, Hess Deep, the Troodos ophiolite, and the Him area in the Oman ophiolite. She also ascribed these rocks to recrystallization in an environment of increasing temperature resulting from upward movements of the melt lens (Figure I-13). Gillis (2008) also proposed that the protodikes (Nicolas and Boudier, 1991) microgranular textures do not represent the dike roots but former dikes with chilled margins that have recrystallized during reheating events.

Following the renewed interest in the root zone of the sheeted dike complex triggered by the drilling of IODP Hole 1256D (Teagle et al., 2006), Nicolas et al. (2008) proposed a revised model that build on an older model of Nicolas and Boudier (1991), and is based on about 20 years of structural mapping of the Oman ophiolite, on recent observations, and on recent detailed mappings of selected area, away from discontinuities. It is briefly presented in this chapter, as the corresponding paper is presented in Appendix A2. The studied area is located in the well studied Sumail massif (Nicolas et al., 2000). The bottom-line is the confirmation that protodikes represent the dike roots, and in these areas situated away of ridge tectonics the melt lens is considered as a steady state horizon (Figure I-16). In this model, the steady state melt lens is not fossilized but pinches out at its margins where its roof meets its floor. The varytextured gabbro horizon hence does not represent the melt lens fossilization; most of it is interpreted as resulting from hydrous partial melting triggered by the ingression of hydrothermal fluids into the still hot, crystallized sheeted dike base. The fine grained isotropic gabbros are interpreted as representing protodikes cores and may be the only rocks of the varytextured gabbro horizon that are not originated in the hydrous partial melting of the dikes root zone. Based on these new results they questioned the origin of areas where gabbronorite intrusions in the sheeted dike base has been observed. Considering the presence of gabbronorites as product of ridge tectonic processes (Boudier et al., 2000), Nicolas et al. (2008) propose that nearly half the Oman ophiolite may have formed under the influence of ridge segmentation.

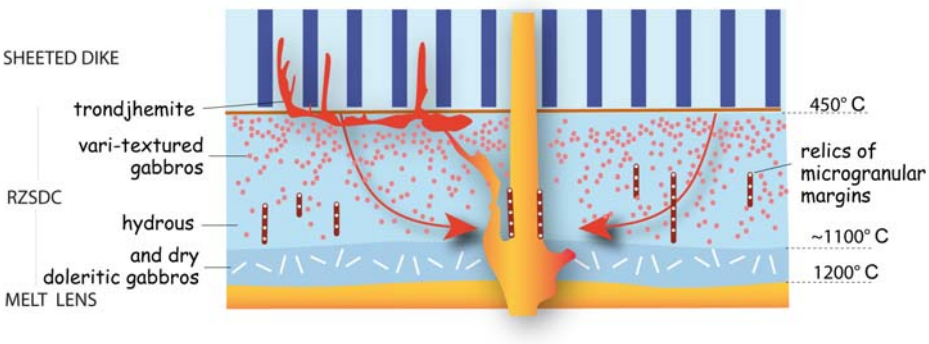

Figure I-16: Conceptual model for the root zone region (varytextured gabbro horizon) from Nicolas et al. (2008) presented in Figure I-10. The bottom of the injected dikes display microgranular margins (protodike) that evolve upward to a dike with chilled margins. The dry ophitic gabbro horizon (thickness <1m) is believed to represent the thermal boundary layer separating the magmatic system from the hydrothermal one. Most of the lithologies present in the root zone of the sheeted dike complex are believed to result from hydrous partial melting (red dots) of protodikes. Microgranular lenses are interpreted as relicts of protodikes after hydrous partial melting.

I.4. Key questions and hypotheses to be tested

In section I.3.e "Conceptual models and implications" I have presented several aspects dealing with the melt lens organization and evolution that are still debated. The key unresolved questions are:

**Is the melt lens fossilized off-axis?*

**Do the varytextured gabbros represent the melt lens fossilization or the product of hydrous partial melting of the root zone lithologies?*

**Is the melt lens a steady-state or a dynamic system?*

**Does the geological context (e.g., tips of propagating segments) influence the processes occurring in and around the melt lens, and how?*

**Does the partial melting of the dikes proposed in most published models results from a temperature increase or from a fluid ingress in still hot, recently crystallized rocks?*

**What are the petrological and geochemical properties of the products of partial melting of hydrothermally altered dikes?*

**How hydrous partial melting of the hydrothermally altered dikes can influence the composition of MORB?*

The main objective of this PhD work was to try answering these questions by using field work, petrology on root zone lithologies, experimental petrology and geochemistry, and by comparing our results with the geophysical data at the mid-ocean ridge axis. Sr and O isotopic systems may be used to infer the effect of HT fluids, however these two isotopic

systems are the ones that are the most affected by low temperature hydrothermal alteration. Therefore the use of isotopes to discuss high temperature (>700°C) processes is hampered. Isotopic in-situ analyses of magmatic mineral cores may help to solve the problem of retrograde metamorphism; nevertheless I did not have access to such techniques.

Chapter II.

“Magmatic / hydrothermal transition in IODP Hole 1256D”

II.1. Geological context

IODP Hole 1256D was recently drilled on the Cocos plate in a 15Ma old crust formed at the East Pacific Rise at superfast (full spreading rate > 20mm/year) spreading rate (Figure II-1; Teagle et al., 2006; Wilson et al., 2006). This drilling hole is of major relevance for this study as it is the first borehole which reached the sheeted dike / gabbro transition in an intact section of fast-spread oceanic crust (Figure II-2). The choice of superfast spread crust was motivated by the correlation between the depth of the melt lens and spreading rate (Figure I-7; Purdy et al., 1992; Phipps Morgan and Chen, 1993), hence the anticipation to reach the base of the sheeted dike at shallower depth (Wilson et al., 2006).

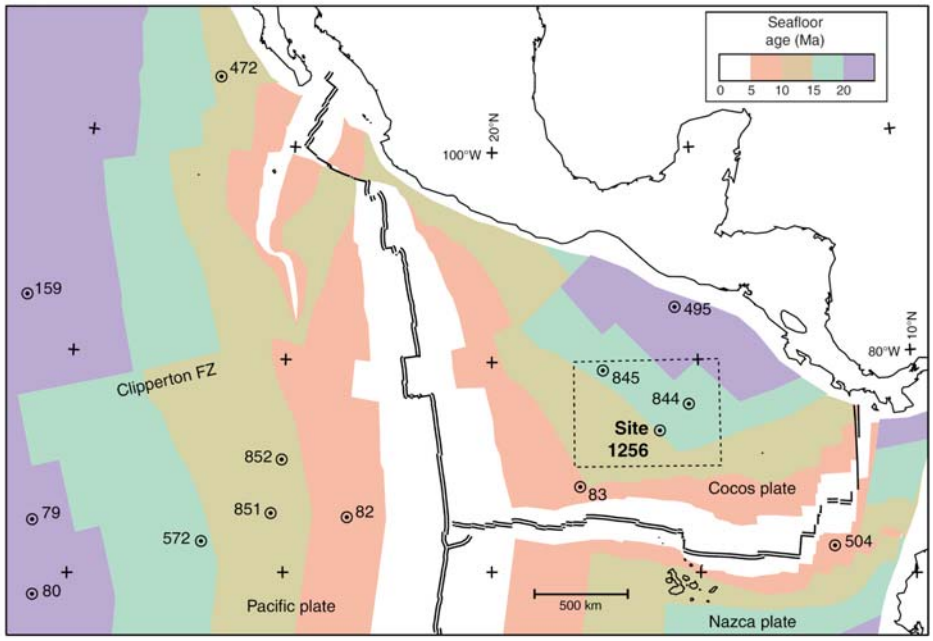

Figure II-1: Age map of the western Pacific seafloor (Teagle et al., 2006). IODP Site 1256 is located on the Cocos plate. Isochrons at 5 m.y. intervals are converted from magnetic anomaly identifications according to the timescale of Cande and Kent (1995). Other numbers correspond to earlier DSDP and ODP sites where the basement was drilled.

The uppermost part of the section recovered at Site 1256 is composed of ~100m lava interval (including a single flow ~75 m thick) that is considered to correspond to an off-axis lava pond (Wilson et al., 2006). In total, 284 m of sheeted and massive flow, and minor pillow flows are interpreted to correspond to off axis eruptions (Wilson et al., 2006). The sheeted and massive flow erupted at the ridge axis are then present from that depth down to 1004 mbsf (meters below sea floor; Figure II-2). 54 meters of mineralized breccias associated to subvertical intrusive contacts mark the transition zone to the relatively thin (~350 m thick) sheeted dike complex.

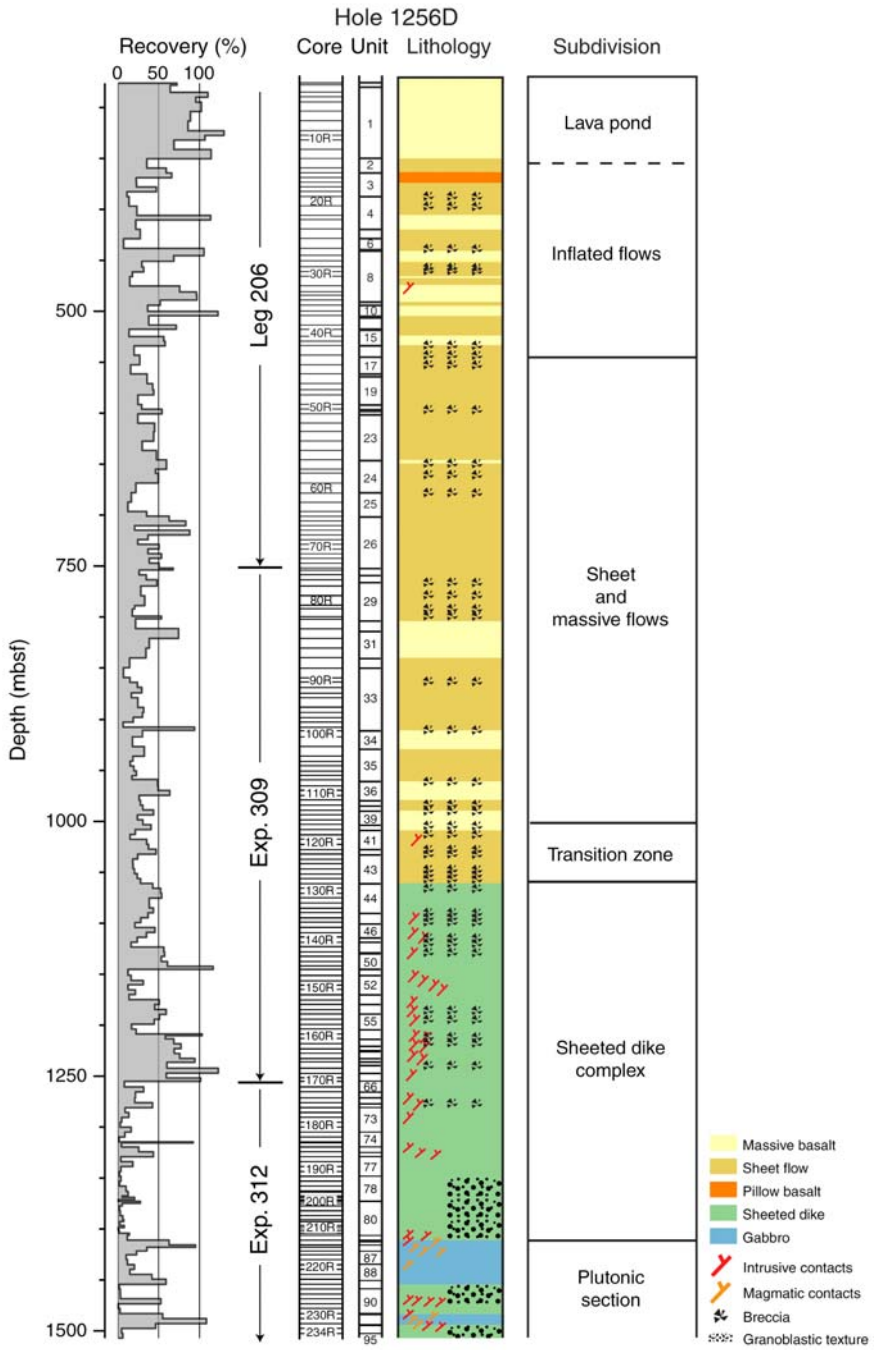

Figure II-2: Simplified igneous lithostratigraphy of IODP Core 1256D recovered during ODP Leg 206 and IODP Expeditions 309 and 312 (Teagle et al., 2006).

The sheeted dike complex is composed of massive basalts/diabases that locally display doleritic textures, and that are crosscut by subvertical dikes with brecciated and mineralized chilled margins. The alteration grade increases downhole from the lavas to the dikes. In lavas, alteration phases are mostly phyllosilicates and iron oxyhydroxides, attesting to temperatures < 150°C, whereas in dikes chlorite and other greenschist phases are observed indicating temperatures > 250°C. Downhole, in the sheeted dikes, the alteration intensity increases. Actinolite is the major alteration phase and is associated with magnesiohornblende, indicating

temperatures close to 400°C. In the lowermost dikes (from 1348 to 1407 mbsf), dikes are partially to pervasively recrystallized to granoblastic textures composed of plagioclase, clinopyroxene, orthopyroxene, oxides, and amphiboles that are interpreted to result from contact metamorphism (Wilson et al., 2006). A detailed petrological study of these granoblastic microgabbronorite dikes is proposed in Koepke et al. (2008). The base of the granoblastic microgabbronorite dikes is crosscut by a trondhjemitic dikelet (20 mm wide), and a quartz oxide diorite is described in the uppermost gabbros. At 1407 msbf, the first gabbros are encountered (=1157 meters sub-basement [msb]=mbsf-sediment thickness); they intrude the granoblastic microgabbronorite dikes (Teagle et al., 2006). The gabbro horizon is complex and contains various gabbros types (gabbro, oxide-gabbros, olivine-gabbro, gabbronorite) of variable grain sizes (fine, medium and coarse grained), some xenoliths of granoblastic microgabbronorite representing recrystallized dikes, and a ~ 24 m thick screen of granoblastic microgabbronorite dikes (Wilson et al., 2006). The lowermost recovered sample is a diabase, presumably a dike, which displays a doleritic texture and contains actinolite and Ti-augite; it is interpreted as a late off axis dike (Wilson et al., 2006).

Below are described the granoblastic microgabbronorite dikes petrology (also described in Koepke et al., 2008), the gabbro horizon petrology, and the mineral compositions of these rocks. These data are compared with observations and data from the Oman ophiolite, and discussed in Chapter III.

II.2. Petrology of the granoblastic microgabbronorite dikes and gabbros

I describe hereafter the IODP Hole 1256D samples studied during this work. The Sheeted dikes / gabbro transition zone, down to the bottom of Hole 1256D, may be subdivided in 8 zones (Figure II-3):

- *zone 1* corresponds to the sheeted dike complex,
- *zone 2* corresponds to the granoblastic microgabbronorite dikes (~60 m thick),
- *zone 3* is the upper part of the gabbros, which display white patches (~5 m thick),
- *zone 4* is an interval that shows a close association of fine and coarse grained gabbros (~45 m thick); zones 3 and 4 correspond to the gabbro 1 interval in Wilson et al. (2006),
- *zone 5* is the granoblastic microgabbronorite horizon (24 m thick) interpreted as a screen of granoblastic microgabbronorite dikes (Wilson et al., 2006),

- *zone 6* is the second gabbro section (~15 m thick),
- *zone 7* correspond to the lower granoblastic microgabbronorites (lower dike screen after Wilson),
- *zone 8* is the lowermost diabase, interpreted as an off-axis dike (Wilson et al., 2006).

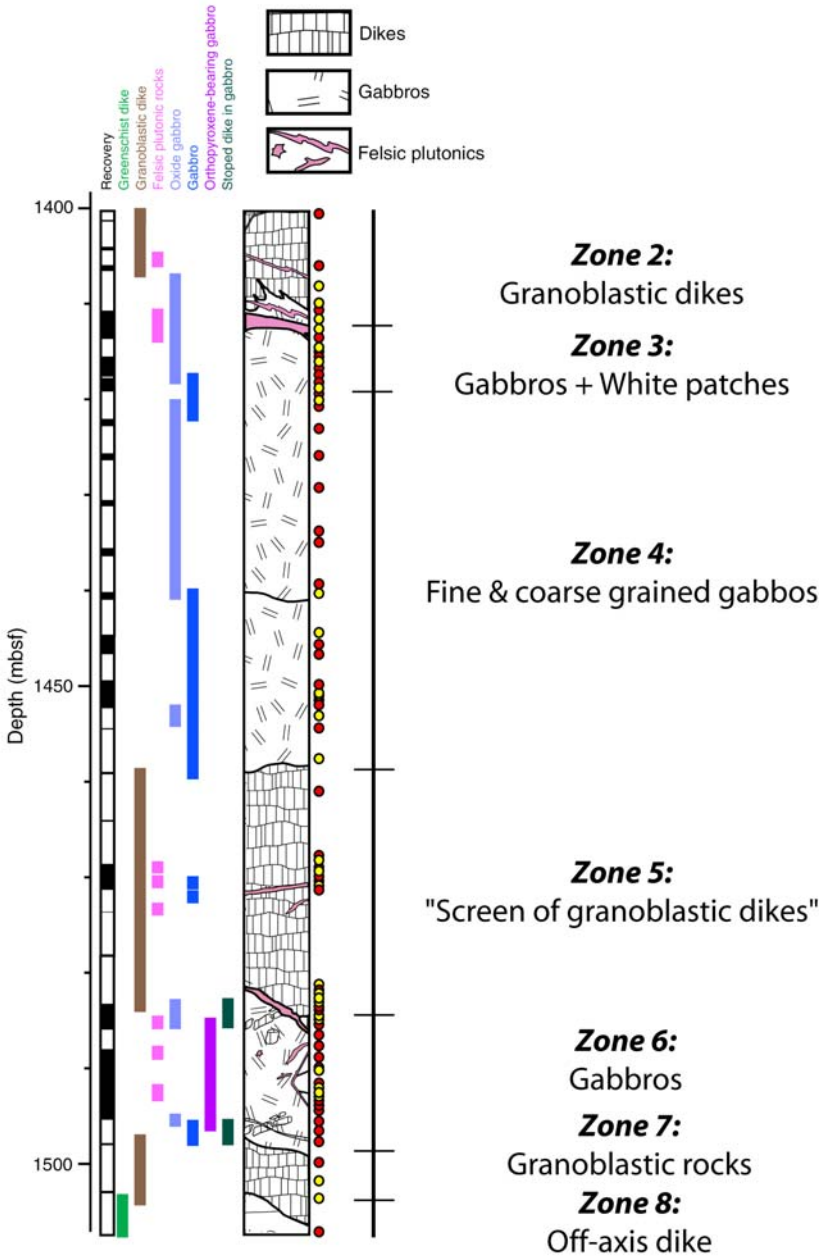

Figure II-3: Schematic lithostratigraphy of the bottom section of IODP Hole 1256D (after Teagle et al., 2006). Yellow and red dots indicate the locations of the studied samples (red: shipboard samples _C. Laverne and B. Ildefonse_; yellow: samples collected in College Station in August 2007).

The sheeted-dike complex displays in general an intergranular, doleritic texture, and contains various alteration phases such as actinolite (Figure II-4a); sub-vertical chilled margins are observed in some samples.

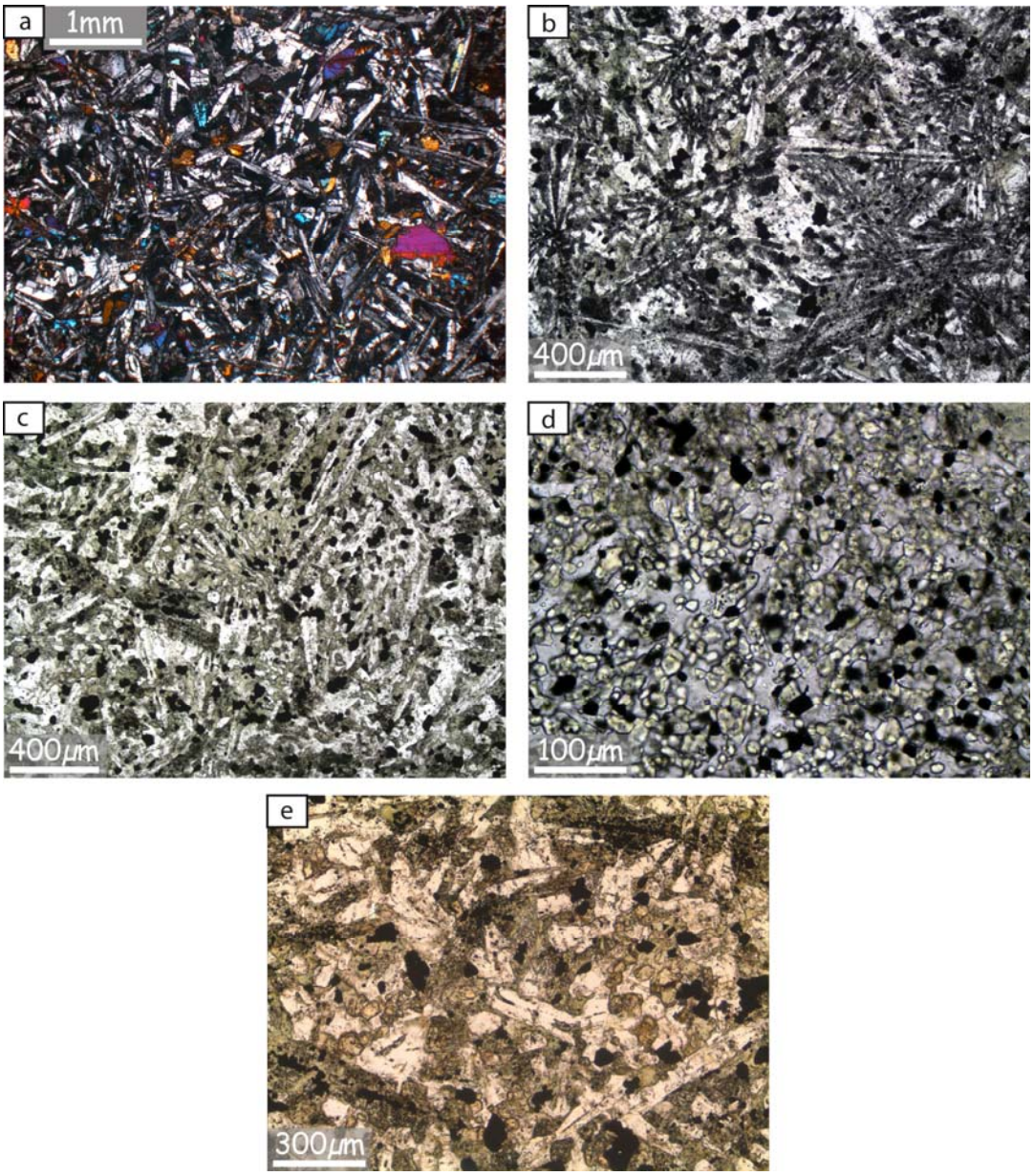

Figure II-4: Microphotographs of IODP Hole 1256D sheeted dike samples. a) diabase (zone 1; sample 176R-2_3-7 (where 176 represents the core number, R2 the section number, 3 the top position in cm and 7 the bottom position in cm); cross-polarized light); b) weakly recrystallization in diabase ~150 m above the contact with gabbros (zone 1; sample 173R-2_6-10; plane-polarized light); c) Stronger granoblastic recrystallization ~38 m above the contact with gabbros (zone 2, sample 198R-1_45-49; plane-polarized light); d) Strong granoblastic recrystallization ~25 m above the contact with gabbros (zone 2, sample 205R-1_10-14; plane-polarized light); e) Coarser grained recrystallized texture close to the contact with gabbro (~10 m above the contact), small pink granular grains are orthopyroxene (zone 2, sample 209R-1_17-19; plane-polarized light). Microphotographs b-d are from IODP database (Teagle et al., 2006).

The granoblastic microgabbronorite dikes display a fine-grained recrystallized texture with increasing recrystallization downsection (Figure II-4b-d; Koepke et al., 2008). However, close to the base of the sheeted dike, some samples display coarser grained texture and seem to be less recrystallized (Figure II-4e). Such less recrystallized meta-dikes, close to the sheeted dike / gabbro transition may be opposed to the model in which the recrystallization is linked to a contact metamorphism event with heat supplied from the bottom (Wilson et al., 2006; Koepke et al., 2008). However, these coarser grained dikes containing orthopyroxene are also recrystallized, and the grain size may instead represent lateral variations in single dikes, the center of dikes being coarser grained than the chilled margins. ~1-2 m above the base of the sheeted dike complex, a small trondhjemitic dikelet (20 mm wide) is observed (Figure II-5a), and may be interpreted as resulting from local anatexis at the base of the sheeted dike complex (Koepke et al., 2008).

Figure II-5: Photographs of cores from IODP Hole 1256D (images are from the data base of Expedition 312 in Teagle et al., 2006). a) Trondhjemitic intrusion in the granoblastic microgabbronorite dikes close to the sheeted dike complex / gabbro transition (sample 212R-1_24-33); b) Gabbroic dikelet (left pieces) in a granoblastic microgabbronorite dike ~4 cm above the contact with the first recovered gabbro (right pieces, sample 213R-1_44-61).

The contact between the sheeted dike complex and gabbro (1407 mbsf) is sharp (Figure II-5b), and the grain size decreases in the gabbro toward the contact (Figure II-6), indicating the intrusive nature of the gabbro. This gabbro is composed of plagioclase (1-2 mm), heterogranular clinopyroxene (1-5 mm), oxides, actinolite, and locally olivine (Figure II-7a). 2-3 cm below the sheeted dike / gabbro contact, a small xenolith of granoblastic microgabbronorite is observed (Figure II-8a). Less than two meters below the contact, a quartz oxide diorite intrusion is observed. It is composed of primary and secondary amphibole (actinolite, and magnesiohornblende), plagioclase, quartz, ilmenite, magnetite and apatite, rutile, and sphene traces (Figure II-7b). Its whole rock composition (Teagle et al., 2006) is characteristic of evolved MORB obtained in differentiation experiments performed in a Fe-Ti MORB system (experiment Fe-21 in Toplis & Carroll, 1995).

Figure II-6: Whole thin section microphotograph (sample 213R-1_52-55; cross-polarized light). The sample displays the contact between granoblastic microgabbronorite dikes and the first encountered gabbro. Note the decreasing grain size in the gabbro toward the contact.

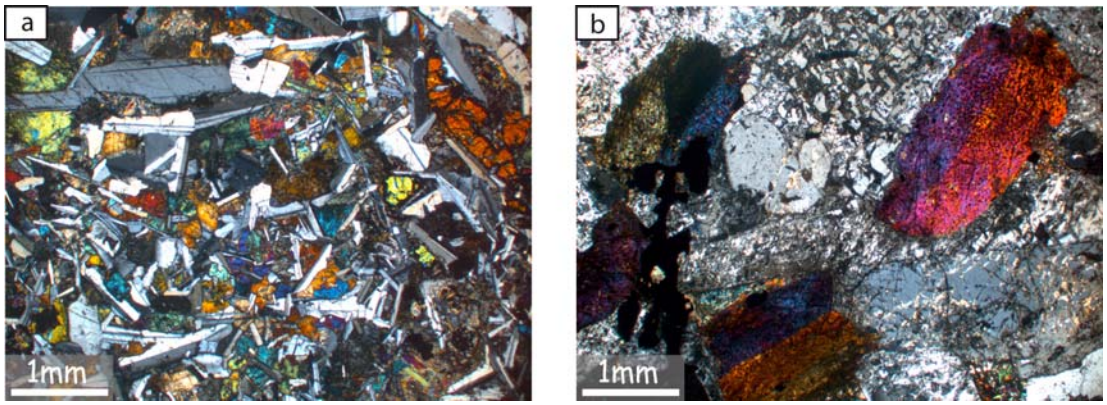

Figure II-7: Microphotographs of the upper plutonic rocks. a) First gabbro encountered below the contact with granoblastic microgabbronorite dikes (zone 3, sample 214R-1_24-26; cross-polarized light). Minerals are plagioclase, clinopyroxene, oxides, olivine, and secondary actinolite. b) Quartz-oxide-diorite present in the plutonic rocks less than two meters below the contact with the recrystallized sheeted dike complex (zone 3, sample 214R-1_43-47; cross-polarized light). Minerals primary and secondary amphibole (actinolite and magnesiohornblende), intergrowths of plagioclase and quartz, ilmenite, magnetite and some traces of apatite.

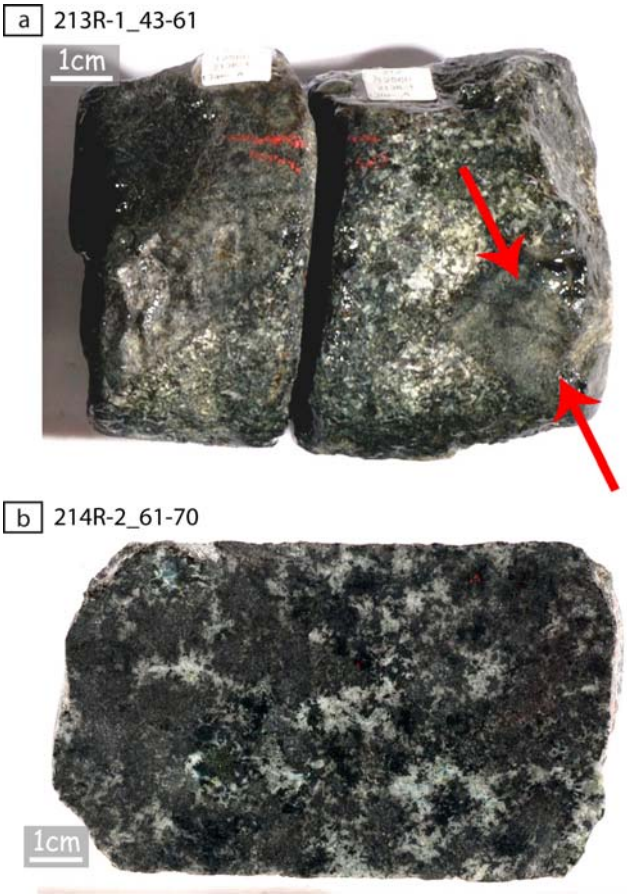

Figure II-8: Photographs of gabbro cores IODP Hole 1256D (images are from the data base of Expedition 312 in Teagle et al., 2006). a) Sharp contact between the granoblastic microgabbronorite dikes and the underlying gabbros; a xenolith with diffuse margins is present in the gabbros (red arrows; sample 213R-1_43-61); b) Typical gabbro with white patches from zone 3. The white domains are highly altered zones (see text for further details; sample 214R-2_61-70).

Below the quartz oxide diorite, gabbros (zone 3) display white patches that can make up to 35 % of the whole rock (Figure II-8b). These white patches are composed of actinolite, plagioclase, prehnite and pumpelleyite and sometimes quartz (Figure II-9a), whereas the dark areas are gabbroic and composed of plagioclase (0.4 to 2 mm), large poikilitic clinopyroxene (up to 1.5 cm), ilmenite, magnetite, and rare olivine (Figure II-9b). Teagle et al. (2006) proposed that the white areas represent a second magmatic episode (an evolved melt composition is required to account for the assemblage plagioclase + quartz). However, these zones do not display sharp contacts with the surrounding gabbro and are more strongly altered at low temperature than the surrounding gabbros (presence of prehnite and pumpellyite; Figure II-9a). In gabbro hand specimens of ophiolites and oceanic crust, white color of plagioclases is usually associated to a high grade of low temperature alteration. A low temperature alteration overprinting the plagioclase rich zones representing a second magmatic episode (Teagle et al., 2006) is therefore expected for the white patches of zone 3. The white patches disappear progressively downward and the transition to zone 4 is not well defined.

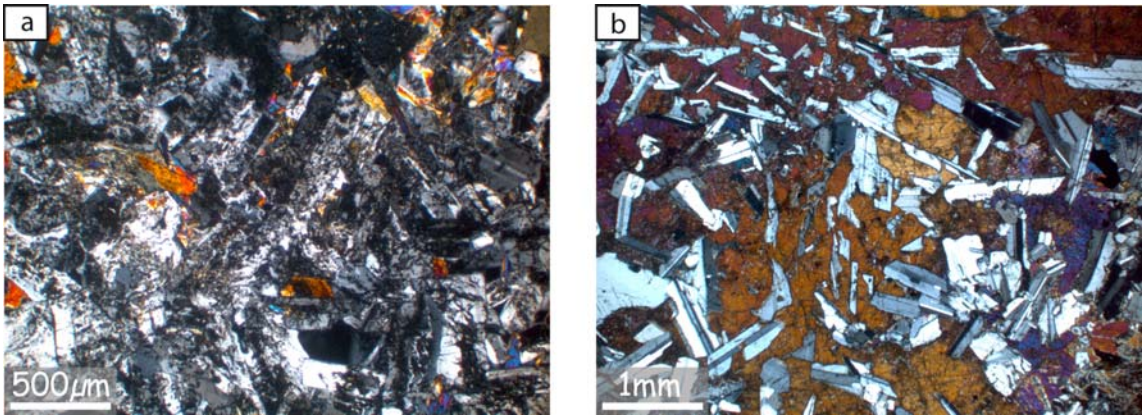

Figure II-9: Microphotographs (cross-polarized light) of sample 215R-1_20-23 from zone 3 (gabbro with white patches). a) White patches domains composed of plagioclase, prehnite, pumpellyite, actinolite and sometimes quartz; b) gabbro is composed of plagioclase, poecilitic-clinopyroxene, ilmenite, magnetite and rare olivine.

Zone 4 is composed of varytextured gabbros (Figure II-10); some are fine grained (1-3 mm) and others coarse grained (0.5-1 cm). The coarse grained gabbros represent less than 30 % of zone 4 and the contact between fine- and coarse-grained gabbros is usually diffuse (Figure II-11).

Figure II-10: Photograph of core 223R-2_43-55 from IODP Hole 1256D (zone 4). Fine and coarse grained gabbroic domains are observed (image is from the data base of Expedition 312 in Teagle et al., 2006).

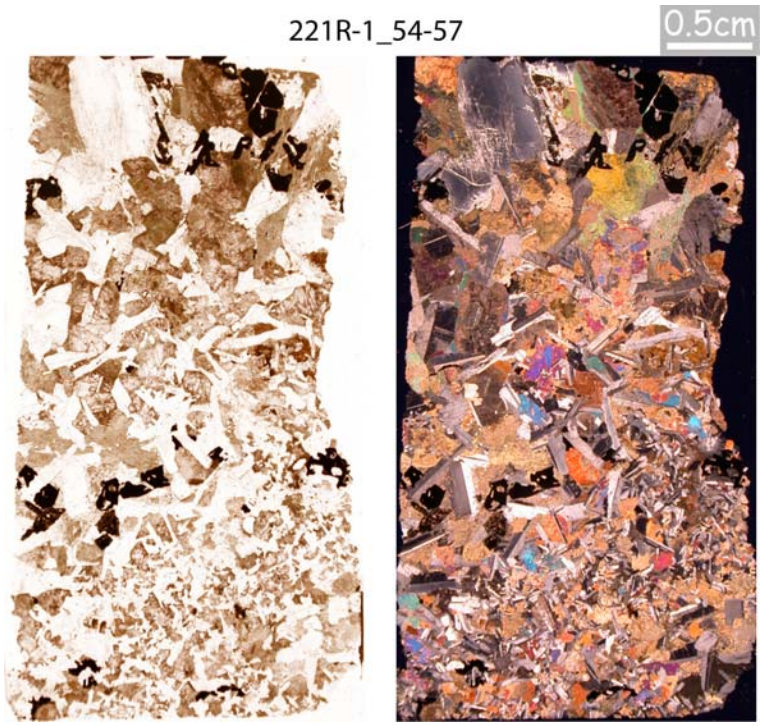

Figure II-11: Whole thin section microphotograph of sample 221R-1_54-57 (zone 4; left: plane-polarized light; right: cross-polarized light). The transition from fine grained gabbro to coarse grained gabbro is continuous.

The fine-grained gabbro is composed of plagioclase, slightly poikilitic clinopyroxene, oxides and rare olivine that can be associated to orthopyroxene close to coarser grained domains (Figure II-12a). Coarse grained areas are composed of plagioclase, orthopyroxene, clinopyroxene and oxides (Figure II-12b). Sparse, centimeter sized xenoliths of granoblastic microgabbronorite are observed in the lowermost few meters of zone 4; these xenoliths are similar to zone 5 (see below) and rimmed by coarse-grained gabbro. The lowermost sample of zone 4 (sample 224R-1_7-9) is composite and contains domains with poikilitic clinopyroxene

associated with plagioclase and secondary amphiboles (actinolite, and magnesiohornblende), and domains with quartz and plagioclases intergrowths associated with oxides and apatite (Figure II-12c-d).

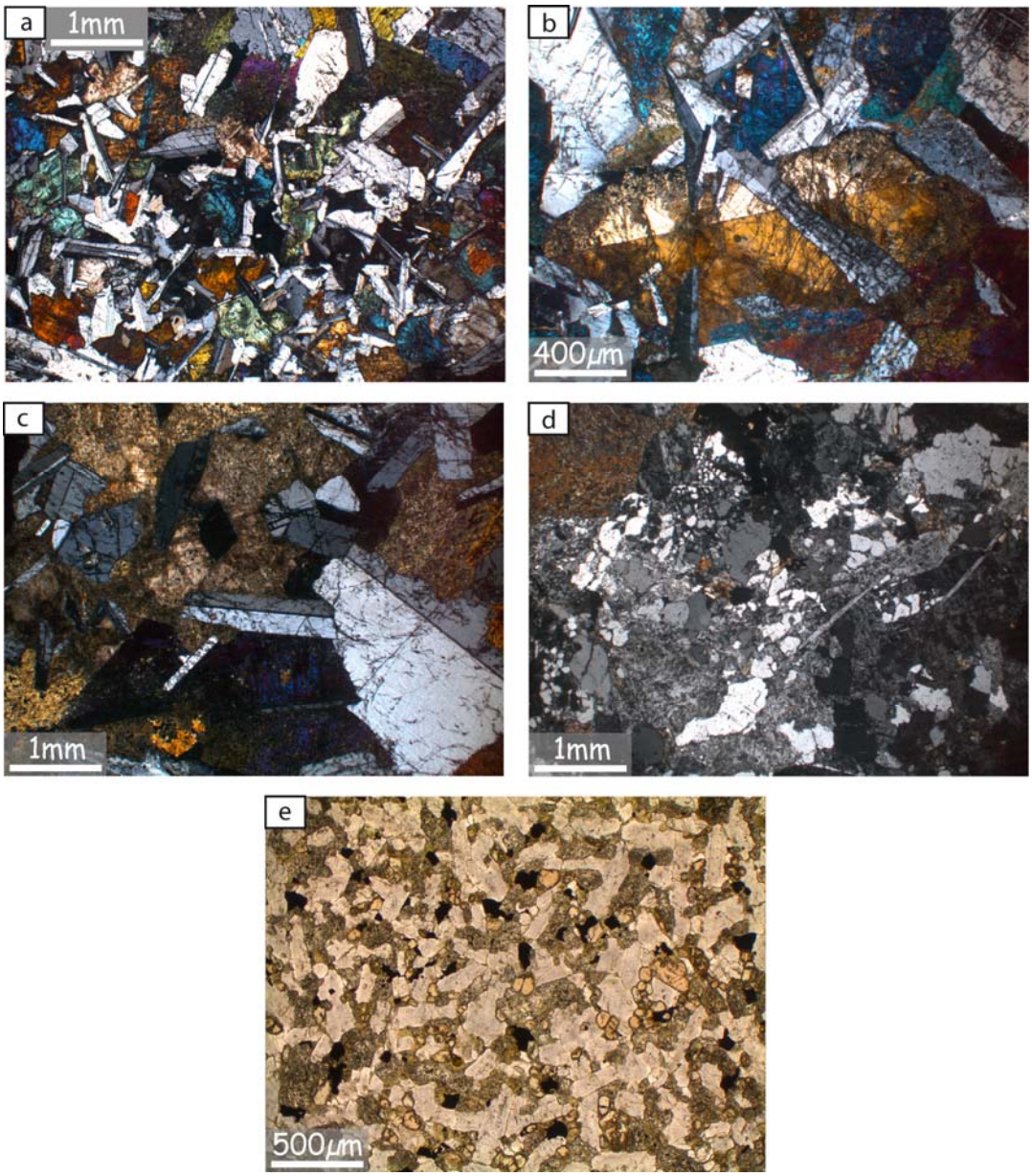

Figure II-12: Microphotographs of IODP Hole 1256D samples. a) Fine-grained gabbro from zone 4 composed of plagioclase, clinopyroxene, oxides, secondary actinolite and rare olivine (not visible on picture; cross-polarized light; sample 218R-1_46-49); b) coarse-grained gabbro from zone 4 composed of plagioclase, clinopyroxene, secondary actinolite and rare orthopyroxene (not visible on picture; cross-polarized light; sample 220R-1_18-18); c) domain with poikilitic clinopyroxene in the lowermost sample of zone 4 (cross-polarized light, sample 224R-1_7-9); d) domain with quartz-plagioclase intergrowths associated to oxide and apatite in the lowermost sample of zone 4 (cross-polarized light, sample 224R-1_7-9); e) granoblastic microgabbronorite sample from zone 5 composed of plagioclase, clinopyroxene, orthopyroxene (pink), oxides, and secondary actinolite (plane-polarized light, sample 227R-1_30-34).

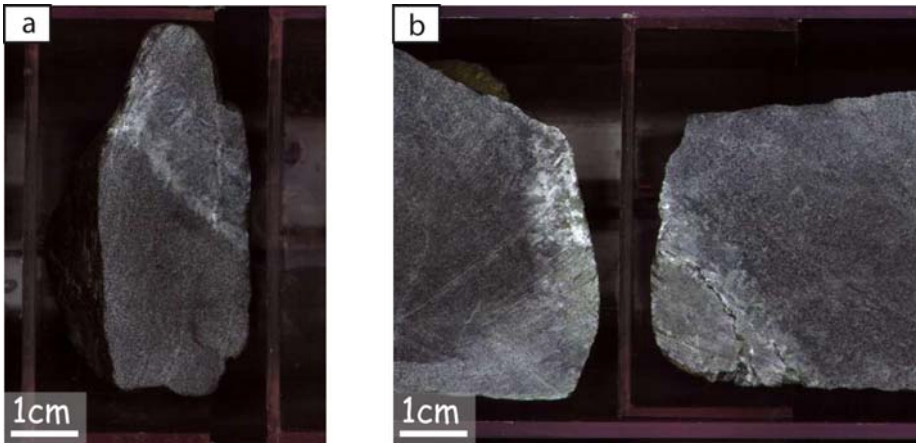

Figure II-13: Photographs of cores from IODP Hole 1256D displaying leucocratic intrusions within the "screen of granoblastic microgabbronorite dikes" (zone 5; images are from the data base of Expedition 312 in Teagle et al., 2006). a) Sharp contact (Sample 227R-1_12-15); b), diffuse contact (sample 227R-2_8-17).

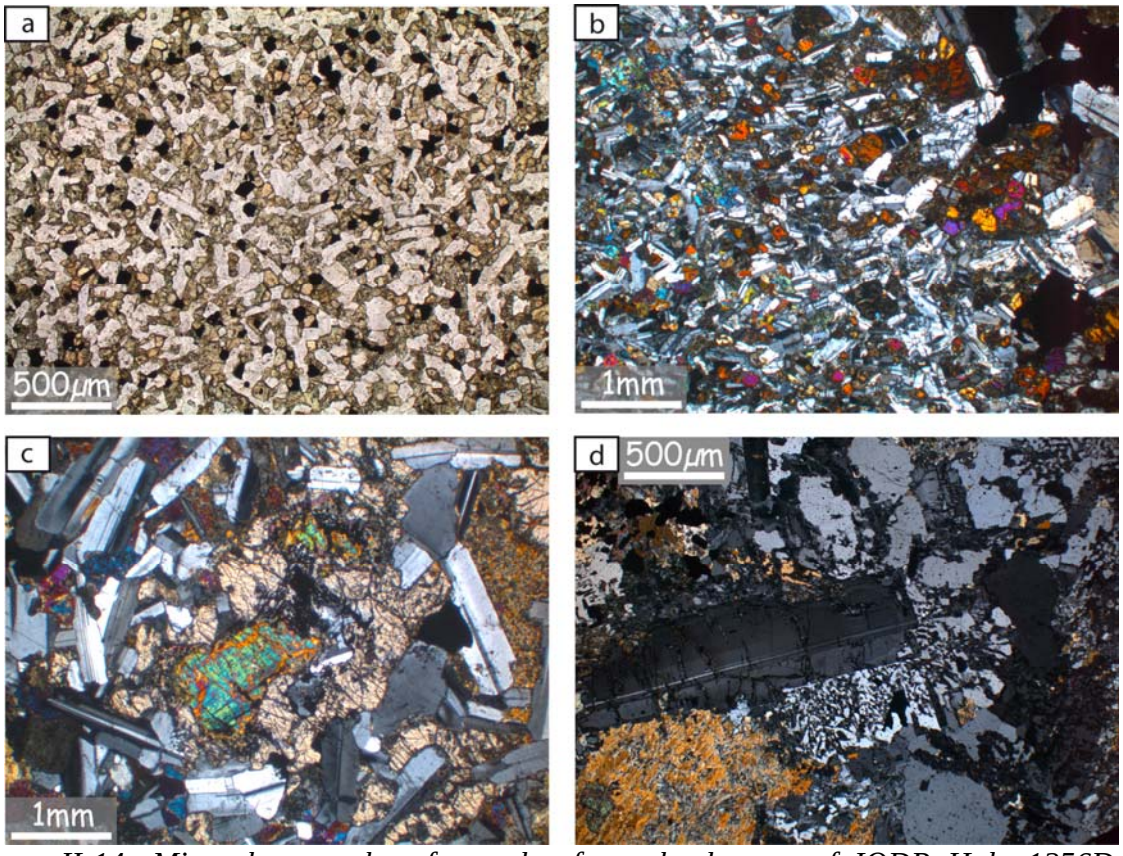

Figure II-14: Microphotographs of samples from the bottom of IODP Hole 1256D. a) Granoblastic texture in a microgabbronorite xenolith from a gabbro in zone 6 (plane-polarized light, sample 230R-1_87-90); b) preferential orientation of plagioclases in a microgabbronorite xenolith from a gabbro in zone 6, the preferential orientation is nearly orthogonal to the contact with the host gabbro (cross-polarized light, sample 230R-1_15-20); c) altered olivine rimed by orthopyroxene in a gabbro in zone 6 (cross-polarized light, sample 232R-1_82-85); d) lowermost sample in zone 6 displaying gabbroic assemblage with plagioclase and clinopyroxene associated to intergrowth of quartz-plagioclase (cross-polarized light, sample 232R-2_98-100).

Zone 5 is composed of granoblastic microgabbronorites with grain size, similar to the coarser granoblastic microgabbronorite dikes in zone 2 (Figure II-12e). The main paragenesis is plagioclase, clinopyroxene, orthopyroxene, ilmenite, magnetite, secondary amphibole (actinolite, and magnesiohornblende), and rare quartz; inclusions of apatite in orthopyroxene have been observed in one sample. Several leucocratic intrusions of coarser grained material are observed (Figure II-13). The granoblastic microgabbronorite / leucocratic intrusion contact is either sharp (Figure II-13a) or diffuse but without any change in grain size (Figure II-13b). The recovery is very low (< 30%) in zone 5.

Zone 6 is composed of gabbro, which contains several xenoliths of granoblastic microgabbronorite that are similar to those in zone 5 (Figure II-14a). Some of the xenolith contain abundant orthopyroxene, one is noritic (plagioclase + orthopyroxene), and one displays a strong shape preferred orientation of plagioclases that forms a large angle with the gabbro contact (Figure II-14b). One xenolith contains olivine that is rimed by orthopyroxene and inverse zoning in plagioclase (Figure II-15); this peculiar sample is discussed in section II.3. The gabbro (grain-size 1-4 mm) is composed of plagioclase, heterogranular to pseudo-poikilitic clinopyroxene, usually orthopyroxene and rare olivine that is mostly decomposed to a phyllosilicate assemblage (Figure II-14c); olivine or its alteration products is locally rimed by orthopyroxene (Figure II-14c). The deepest sample in zone 6 (232R-2_98-100) is composite, with gabbroic domains and domains of quartz-plagioclase intergrowths coexisting with primary amphibole mostly altered to actinolite (Figure II-14d).

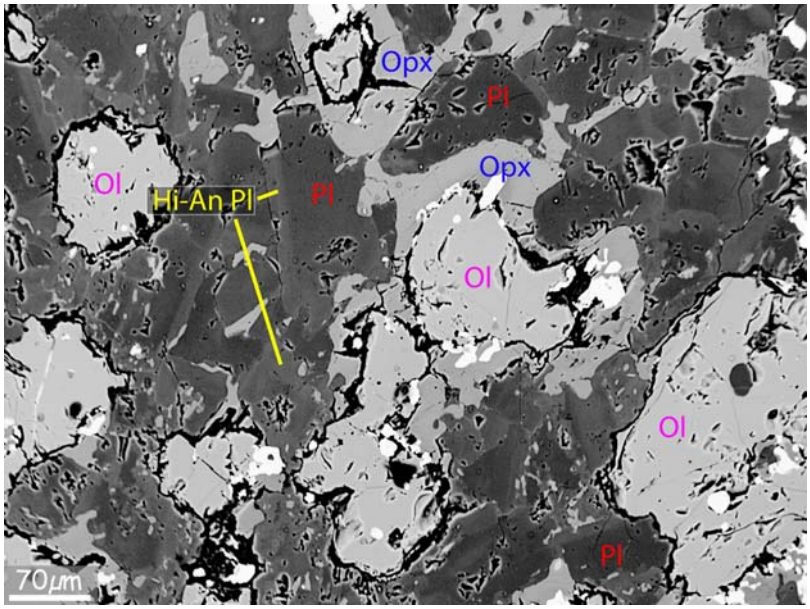

Figure II-15: Backscattered electron image of a xenolith of granoblastic olivine-microgabbronorite of zone 6 (sample 232R-1_82-85). Ol: olivine; Opx: orthopyroxene; Pl: plagioclase; Hi-An Pl: plagioclase rims that are brighter on the BSE image and that correspond to An-rich plagioclase (see section II.3).

The contact between zone 6 and zone 7 is not recovered. Zone 7 is poorly recovered (< 15%) and is composed of granoblastic microgabbronorite that is similar to xenoliths of zone 6. It is composed of plagioclase, clinopyroxene, orthopyroxene, ilmenite and magnetite (Figure II-16a).

The contact between zone 7 and zone 8 is not recovered. Zone 8 is diabase with intergranular texture composed of plagioclase, pink-Ti-augite and some rare oxides (Figure II-16b) not affected by granoblastic overprint.

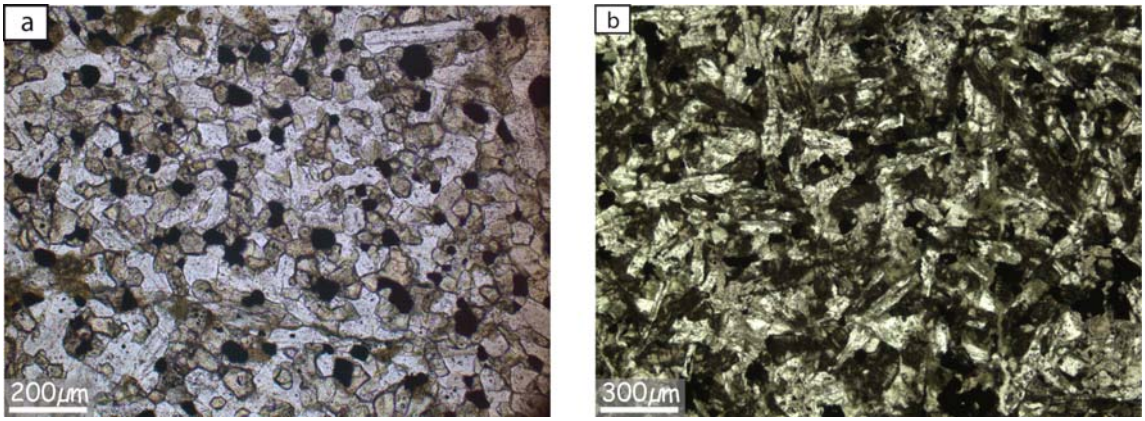

Figure II-16: Microphotographs of IODP Hole 1256D samples from zone 7 (a) and zone 8 (b). a) Granoblastic microgabbronorite composed of plagioclase, clinopyroxene, orthopyroxene and oxides assemblage (sample 234R-1_7-9; plane-polarized light); b) late off-axis diabase composed of intergranular plagioclase, pink-Ti-augite and some rare oxides (sample 234R-1_19-22; plane-polarized light).

II.3. Mineral major element compositions

In-situ mineral major element compositions have been determined for minerals of all the described lithologies (Appendix B1; Figure II-17). Average mineral compositions of the lava pond, lava flows and sheeted dikes (Dziony et al., 2008) are given for comparison. Analyses have been performed at Géosciences Montpellier and at the Institut für Mineralogie, Hannover using a Cameca SX 100 electron microprobe equipped with 5 spectrometers and an operating system "Peak sight". Data were acquired using a 15KV acceleration potential, a static (fixed) beam, Kα emission from all elements, and the "PAP" matrix correction (Pouchou and Pichoir, 1991) in Hannover or a modified matrix correction (Merlet, 1994) in Montpellier. Most element concentrations were obtained with a beam current of 15nA and a counting time of 10 to 120s on peak and background. In all samples, mineral cores have been analyzed, and except in the white patches areas of zone 3, mineral (cores) compositions are homogeneous and averages are used in the text below.

Plagioclase compositions range from An_{41} in diorite (between zone 4 and zone 5) to An_{70} in fine-grained olivine-gabbro (zone 4) (Figure II-17a). Plagioclase An contents in gabbros are in average higher than plagioclase An content in granoblastic microgabbronorites from zones 2, 5, 6, and 7. One gabbro sample from zone 6 has plagioclase An contents similar to the ones of granoblastic microgabbronorites, this gabbro is in contact with a xenolith (sample 230R-1_118-121). In granoblastic microgabbronorite dikes, plagioclase An content is in average slightly lower than the one plagioclases of sheeted dike complex, lava flow and lava pond. No correlation is observed between the plagioclase An content and the plagioclase FeO_t contents (Figure II-17a; and see Appendix A3 for a discussion on the iron content of plagioclases). The large heterogeneity in composition of plagioclases of the white patches areas (with An content ranging from 14 to 59) is attributed, first to initial plagioclases with lower An content than in the surrounding gabbro (cf. the "second magmatic episode" of Teagle et al., 2006), and second to various degrees of plagioclase albitisation during hydrothermal alteration.

Clinopyroxene is Ti-augite in the off-axis dolerite of zone 8 and augite in all other samples. Clinopyroxene Mg# (Mg#=Mg/[Mg+Fe] in molar proportions) ranges from 61 in zone 8 to 83 in coarse-grained gabbros in zone 4, and correlates roughly with the An content of plagioclase (Figure II-17b). In Figure II-17b, dry and wet fractionation trends calculated with MELTS (Ghiorso and Sack, 1995) by Kvassnes et al. (2004) are shown; the studied samples are on average closer to the dry fractionation trends. Al_2O_3 in clinopyroxene range from 0.46 wt% in a granoblastic microgabbronorite sample of zone 5 to 2.86 wt% in the lava flows and is roughly correlated to An content in plagioclase (Figure II-17c). On average, Al_2O_3 in clinopyroxene from granoblastic microgabbronorites in zones 2, 5, 6, and 7 is lower than in clinopyroxene from gabbros in zone 3 and 4 and from basalt and diabase from lava pond, lava flows, sheeted dike, and zone 8 (Figure II-17c). The FeO_t content of clinopyroxene is not correlated to the one of plagioclase (Figure II-17d), it may result from variations in the redox conditions during crystallization or subsequent reequilibration (Appendix A3). TiO_2 and Al_2O_3 in clinopyroxene are correlated in granoblastic microgabbronorites from zones 2, 5, 6, and 7; most of the gabbro, lava pond, lava flow and sheeted dikes samples have clinopyroxenes slightly enriched in Al_2O_3 (Figure II-17e). Clinopyroxene from one gabbro from zone 6 has low Al_2O_3 content similar to the granoblastic microgabbronorites; it corresponds to the gabbro that is in contact with a xenolith (sample 230R-1_118-121).

Orthopyroxene is enstatite in all samples; its Mg# range from 59 in zone 2 to 71 in coarse-grained gabbros in zone 4. It is correlated to the clinopyroxene Mg# (Figure II-17f).

Fo content of olivine present in fine-grained gabbro in zone 4 is 63-64.

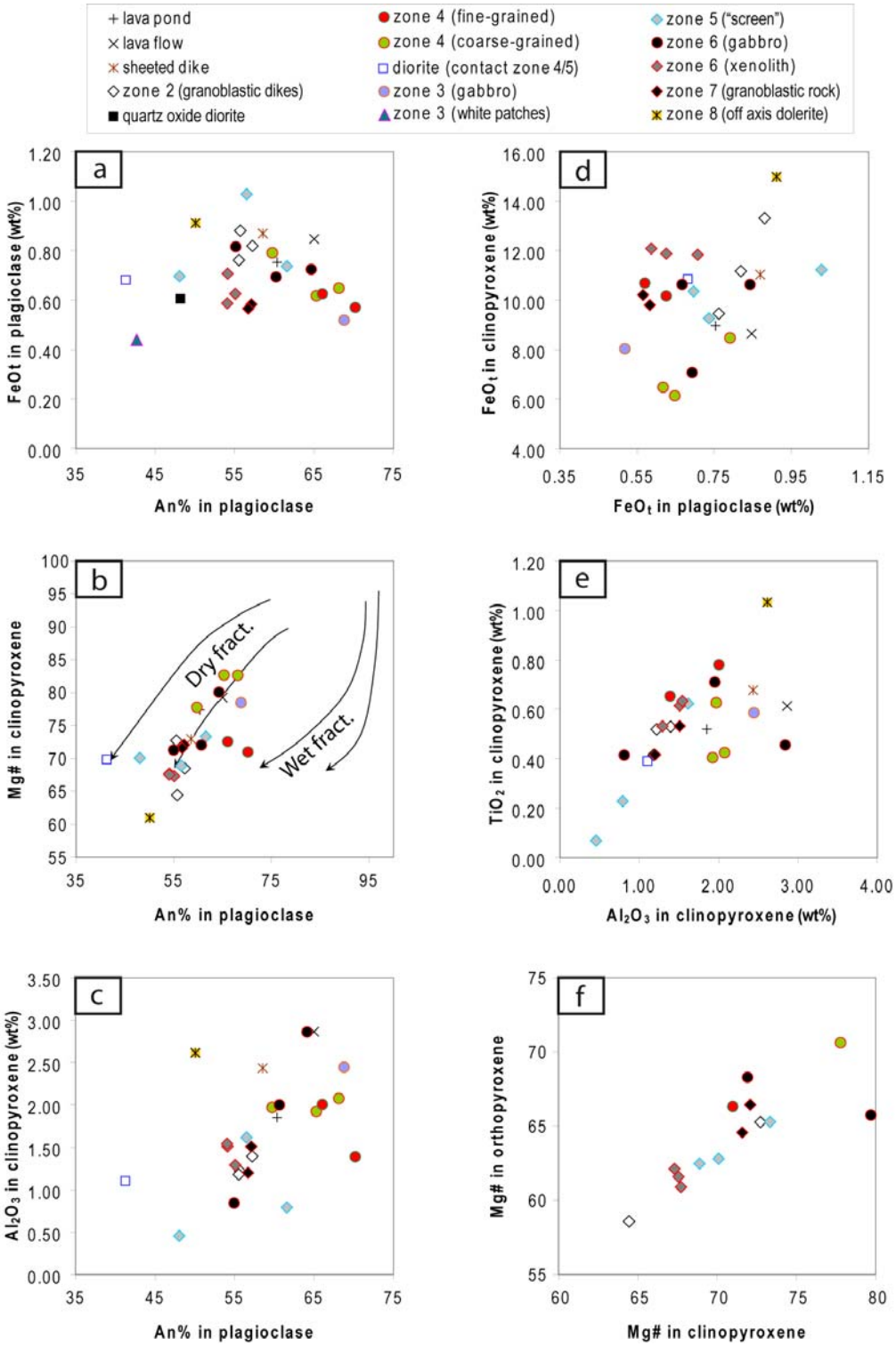

Figure II-17: Mineral compositions of samples from IODP Hole 1256D. a) FeO_t (wt%) in plagioclase vs. An% in plagioclase; b) Mg# in clinopyroxene vs. An% in plagioclase; the dry and wet fractionation trends are from Kvassnes et al. (2004), and calculated using MELTS (Ghiorso and Sack, 1995); the two fractionation trends for the dry and wet case are calculated for two different starting compositions; c) Al_2O_3 (wt%) in clinopyroxene vs. An% in plagioclase; d) FeO_t (wt%) in clinopyroxene vs. FeO_t (wt%) in plagioclase; e) TiO_2 (wt%) in clinopyroxene vs. Al_2O_3 (wt%) in clinopyroxene; f) Mg# in orthopyroxene vs. Mg# in clinopyroxene.

In the xenolith of granoblastic olivine-microgabbronorite from zone 6 that contains olivine rimmed by orthopyroxene and plagioclase with inverse zonations in plagioclases (Figure II-15), olivine Fo content is 70. Plagioclase An content is lower in the grain cores (58) than in the grain margins (75). The association of orthopyroxene rims around olivine together with An-rich plagioclase margins may be interpreted as product of a hydrous partial melting event in this xenolith (Koepke et al., 2005a; 2005b).

Amphiboles are actinolites, and magnesiohornblendes (Figure II-18). Oxides are ilmenite, magnetite and titanomagnetite; the low TiO_2 content of magnetite in most of the samples attests to the low temperature equilibration and prevents the use of the 2-oxides thermo-oxybarometer (Sauerzapf et al., 2008). Calculations with magnetite and ilmenite are possible in the diorite sample close to the zone 4 / zone 5 transition (673°C; ΔNNO=1.34; where NNO is the Ni-NiO solid oxygen buffer equilibrium), in two xenoliths of zone 6 (612°C; ΔNNO=2.66 for sample 230R-1_15-20, and 611°C; ΔNNO=2.52 for sample 230R-1_87-90), and in one gabbro of zone 6 (620°C; ΔNNO=2.46 for sample 230R-2_71-73). Titanomagnetite is present in the lava pond (904°C; ΔNNO=-1.1) and in granoblastic microgabbronorite dikes of zone 2 (851°C; ΔNNO=0.75). Obviously, the highly oxidizing conditions associated to temperatures that are characteristic of greenschist facies conditions constrain the conditions prevailing during the hydrothermal overprint of the samples. Redox conditions prevailing during the high temperature granoblastic overprint are probably closer to the value (ΔNNO=0.75) obtained at 851°C in the granoblastic microgabbronorite dikes from zone 2. Koepke et al. (2008) also show that highly oxidizing conditions (ΔNNO varying from 2.6 to 3.3) are associated to low temperature equilibration (<650°C) in the granoblastic microgabbronorite dikes. In their study, only one granoblastic microgabbronorite is equilibrated at higher temperature (716°C) and as an intermediary redox value (ΔNNO=1.7); it is consistent with an increase of the redox conditions during the cooling.

Thermometry calculations are done using the amphibole-plagioclase thermometer (Holland and Blundy, 1994), the Ti in amphibole semiquantitative thermometer (Ernst and Liu, 1998) and the two-pyroxene thermometer (Andersen et al., 1993). The errors on these temperature estimates are ±35-40°C for the Holland and Blundy (1994) thermometer, are not estimated by Ernst and Liu (1998) for their semi-quantitative thermometer, and are indicated in the Table of Appendix B1 for the two-pyroxene thermometer. Temperature estimations performed with Ti in amphibole, and with the amphibole-plagioclase compositions are relatively coherent (Figure II-19a). They range between ~550°C and 890°C. Temperatures lower than 700°C are associated

to green magnesiohornblende and attest to the retrograde evolution of the rock. Temperatures obtained with the two-pyroxenes thermometer are significantly higher and ranges from ~950°C to ~1065°C (Figure II-19b).

The petrological and geochemical descriptions of IODP Hole 1256D presented herein, together with the article describing the root zone of the sheeted dike complex in the Oman ophiolite (Nicolas et al., 2008; Appendix A2), are used in the following chapters as a background for discussions.

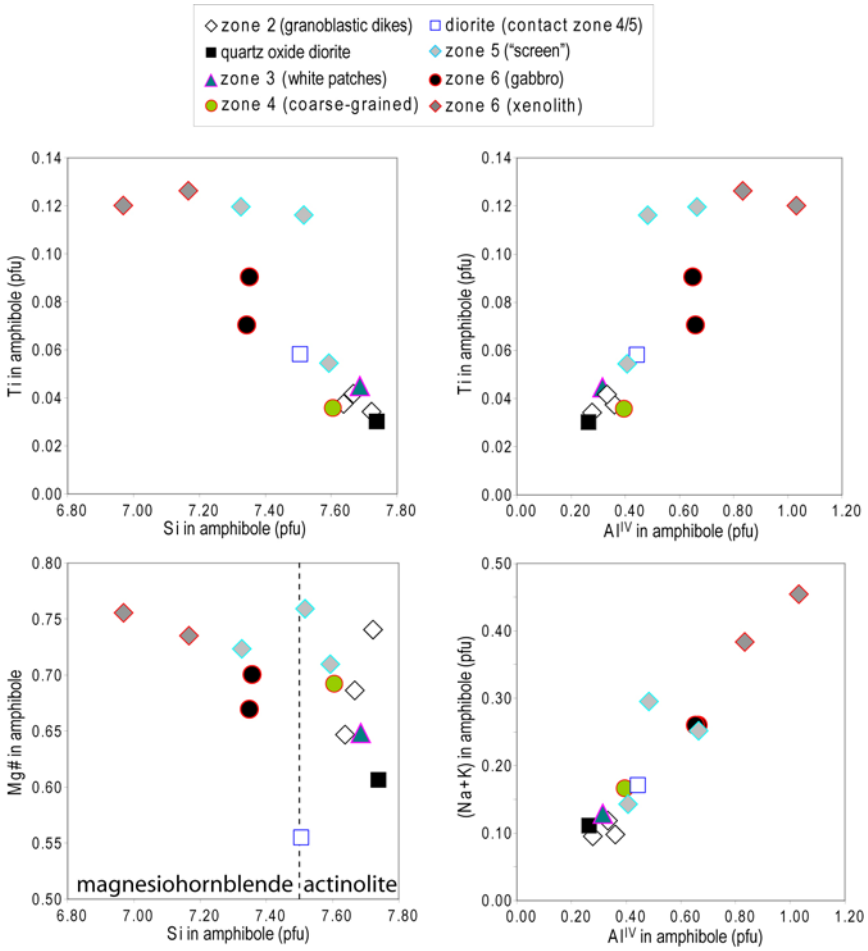

Figure II-18: Amphibole compositions in IODP Hole 1256D samples. pfu=per formula unit, Al^{IV}=tetrahedral Al; same symbols as Figure II-17. No pargasite (amphiboles with [Na+K]>0.5) is observed.

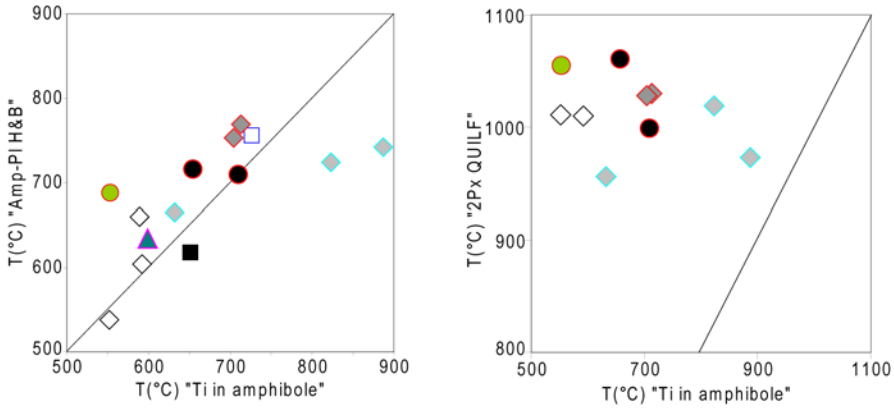

Figure II-19: Comparison of temperature estimations obtained with a) the amphibole-plagioclase thermometer (Holland and Blundy, 1994; "Amp-Pl H&B") and the Ti in amphibole semi-quantitative thermometer (Ernst and Liu, 1998; "Ti in amphibole"), and with b) the two-pyroxene thermometer (Andersen et al., 1993; "2Px QUILF") and the Ti in amphibole semi-quantitative thermometer (Ernst and Liu, 1998; "Ti in amphibole"). Black lines represent the 1:1 correlation.

Chapter III.

“Magmatic / hydrothermal interactions in the Oman ophiolite”

III.1. Visited areas

The Cretaceous Oman ophiolite is regarded to present the best proxy of fast-spreading oceanic crust on land. Nevertheless controversial debates are on-going since decades, and questioned the mid-ocean ridge (MOR) versus supra-subduction zone (SSZ) initial setting (e.g., Warren et al., 2005; Boudier and Nicolas, 2007; Warren et al., 2007). Today, for most scientists at least part of the Oman ophiolite is regarded as subduction zone-related, but the nature of this subduction zone is still under controversial discussion. Many scientists believe that the subduction process is linked to the early stage of obduction (e.g., Boudier et al., 1988; Koepke et al., 2009), and is responsible for a second stage of magmatism ("V2" or "Lassai" lavas) following the major accretion of normal fast-spread crust ("V1" or "Geotimes" lavas). The main difference between lavas is that the "V2" lavas are interpreted as resulting of fluid-enhanced melting of previously depleted mantle, and contrast in composition with the "V1" lavas which resemble modern MORB (for details, and nomenclature of the lavas see Godard et al., 2003). The areas selected in this work are not notably affected by the late- stage magmatism ("V2"), thus the observed field record described here can be exclusively related to the primary magmatic processes of a "normal" fast-spreading ridge.

The Oman ophiolite represents an ideal complement to the detailed studies done on IODP cores related to fast-spread crust, as it provides spatial relationships in three dimensions that a single borehole does not offer. In order to relate the IODP Hole 1256D core in a 3D model, about ten areas along the 500 km long Oman ophiolite have been visited (Figure III-1). Among these, 3 areas where the outcrop continuity is best have been selected for detailed studies. These are located in the southern massifs (Gideah, Al Ahmadi Hills, and Aswad areas). Some peculiar samples from the isotropic gabbro horizon of the Rajmi area located in the northern massif will also be described in Chapter V (Figure III-1).

In all visited areas, the transition between the foliated gabbros and the sheeted dike complex has been examined. The main objective was to understand the structure and the organisation of the isotropic gabbro horizon, and its relations with the underlying foliated gabbros, and with the overlying sheeted dike complex. I present hereafter the different lithologies encountered and the relations observed in the visited areas. An evolutionary model is then presented using detailed mapping descriptions made in the Gideah area, in the Al Ahmadi Hills, and in the core recovered in IODP Hole 1256D; it is the topic of an article published in *Geochemistry, Geophysics, and Geosystems* (France et al., 2009a). The outcome of this paper, a general model on the dynamics of the melt lens system and its key lithologies,

was applied to a third field target, the Aswad area, supporting the validity of the proposed model.

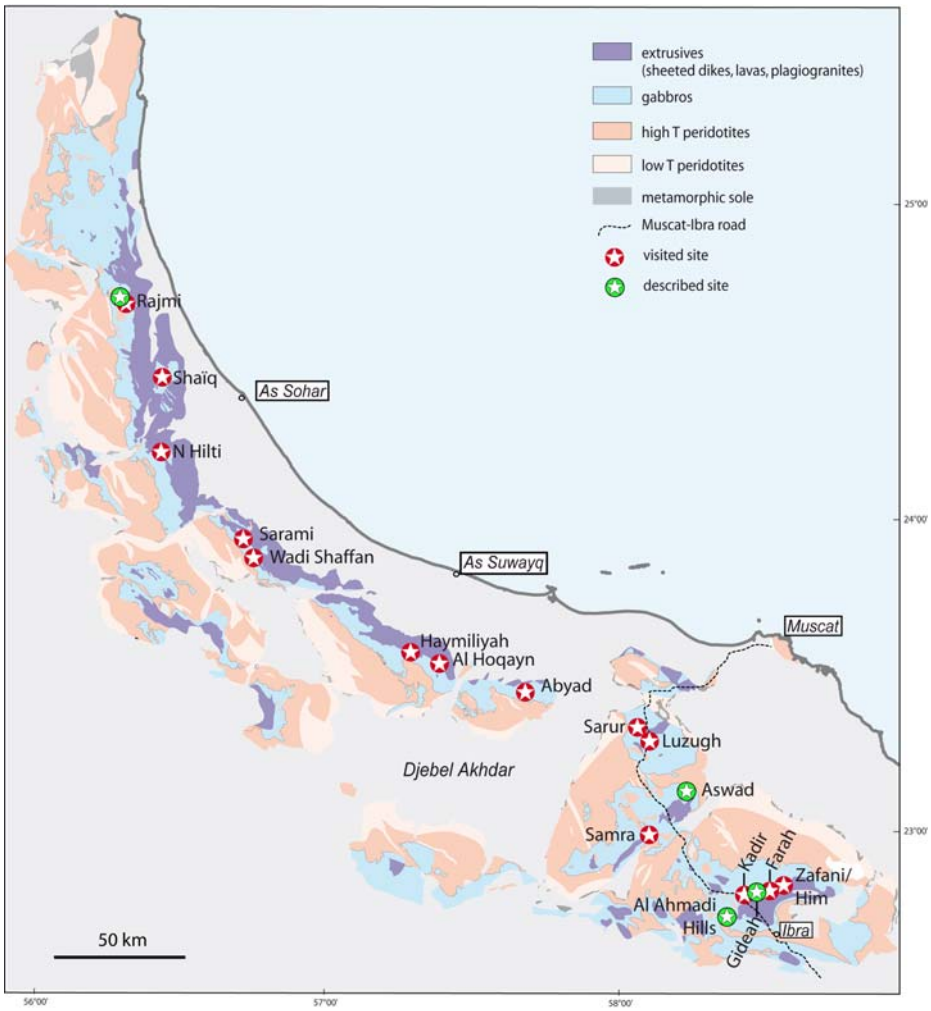

Figure III-1: Simplified geological map of the Oman ophiolite and location of the visited and described sites (after Nicolas et al., 2000).

III.2. Lithostatigraphy

I describe hereafter the main lithologies encountered in various cross-sections, from the sheeted dike complex to the foliated gabbros.

The sheeted dike complex is typically composed of ~1 to 1.5 meters wide dikes intruding each others (Figure III-2), with chilled margins. From the chilled margins toward the dike interior, the texture progressively becomes intergranular, doleritic in the dike centers (Figure III-3). Samples are in general strongly hydrothermally altered, as attested by abundant actinolites and chlorites.

Figure III-2: Classical sheeted dike complex in the Oman ophiolite (Hilti massif).

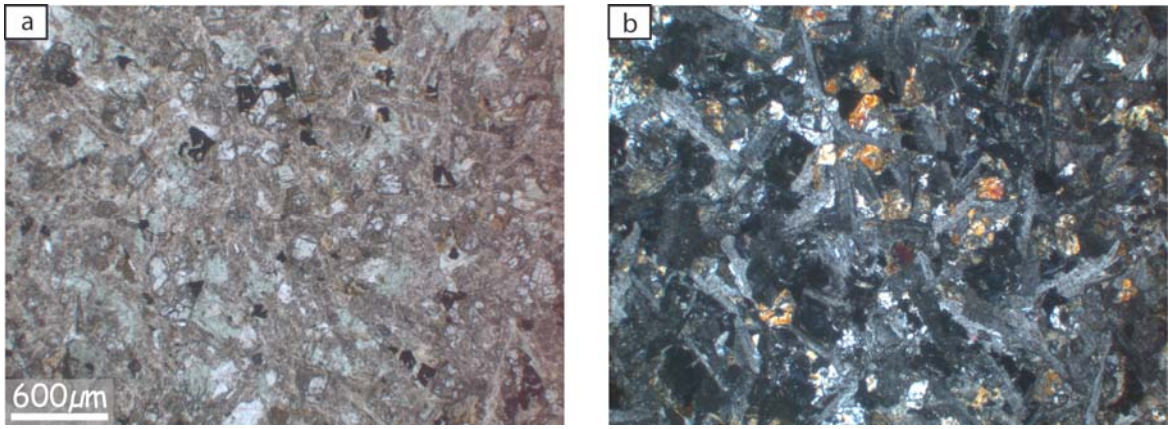

Figure III-3: Microphotographs of an Oman sheeted dike sample (Al Ahmadi Ridge area; sample 07OL01a) composed of plagioclase, clinopyroxene, actinolite, chlorite, and oxides. a) plane-polarized light; b) cross-polarized light.

Below the sheeted dike complex is the isotropic gabbro horizon, also named "varytextured gabbros" (e.g., MacLeod and Yaouancq, 2000). This horizon is approximately 100 meters thick and is mainly composed of isotropic fine-grained ophitic gabbros (Figure III-4a). These are composed of plagioclase, clinopyroxene, and locally amphibole (Figure III-5a-b). Coarser-grained isotropic gabbros are locally present is the varytextured gabbro horizon (Figure III-4b); they are 10 centimeters to a few meters large domains, and can be mingled with fine-grained gabbros (Figure III-4c-d). Coarse-grained gabbros are composed of plagioclase, clinopyroxene, amphibole, and locally orthopyroxene (Figure III-5c-d). They are commonly associated to xenoliths consisting of microgranular gabbros with well equilibrated textures that are frequently observed in the isotropic gabbro horizon (Figure III-6a; Figure III-7). These are composed of plagioclase, clinopyroxene, orthopyroxene, oxide, and secondary amphiboles; Figure III-7)

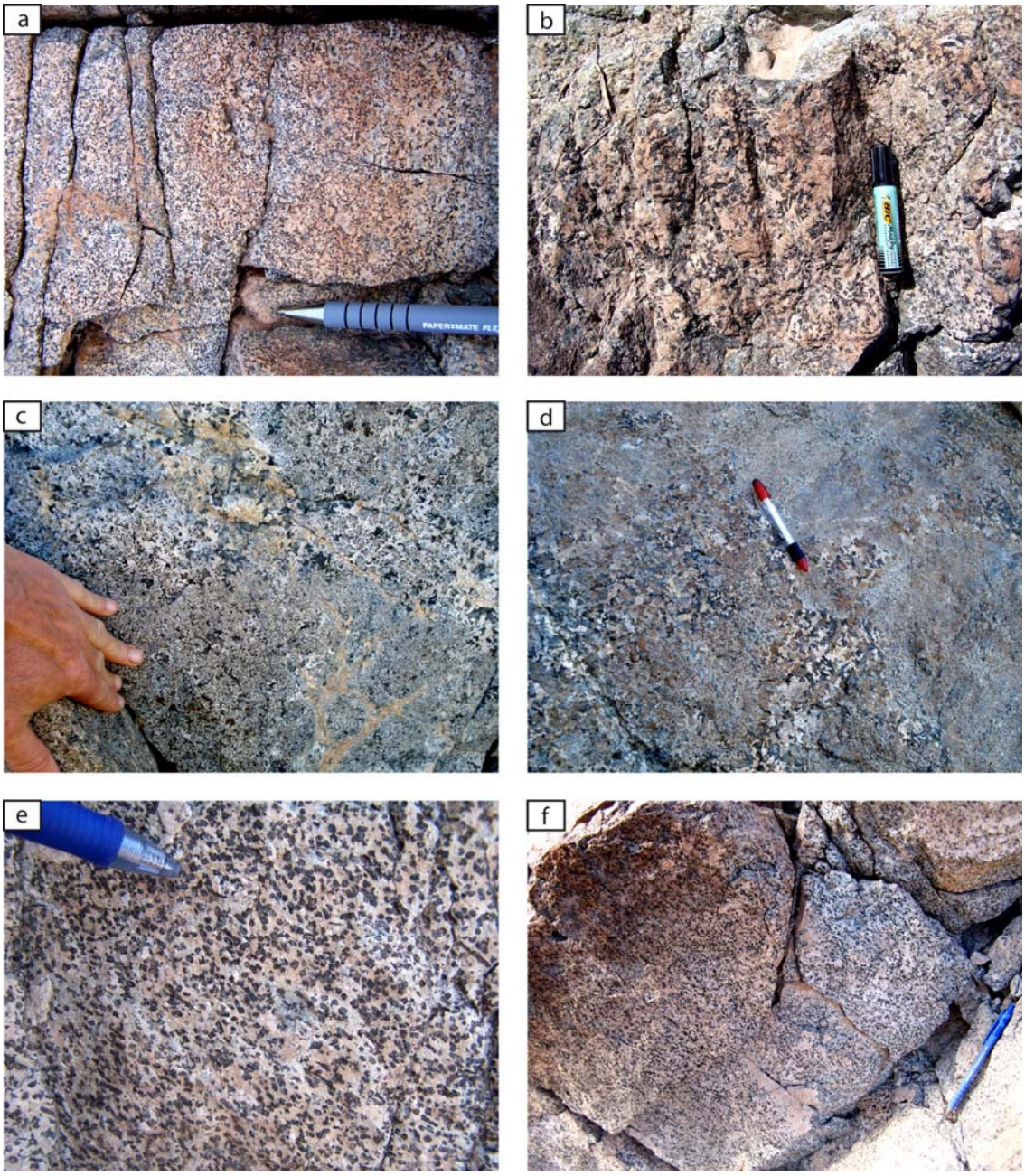

Figure III-4: Various gabbro facies underlying the sheeted dike complex: a) fine-grained isotropic ophitic gabbro (Wadi Gideah area); b) coarse-grained isotropic ophitic gabbro (Al Ahmadi Hills area); c-d) heterogeneous, fine- and coarse-grained isotropic gabbro (Wadi Abyad); e-f) foliated granular gabbro (Aswad area).

Microgabbro xenoliths with well equilibrated textures are observed at all levels in the isotropic gabbro horizon, but are commonly concentrated close to the transition with the sheeted dike complex and close to the transition with the foliated gabbros (Figure III-6). Magmatic breccias with a plagiogranitic, dioritic or gabbroic matrix and microgranular xenoliths of gabbro with well equilibrated textures are locally observed (Figure III-6), and are frequently located close to the sheeted dike complex base.

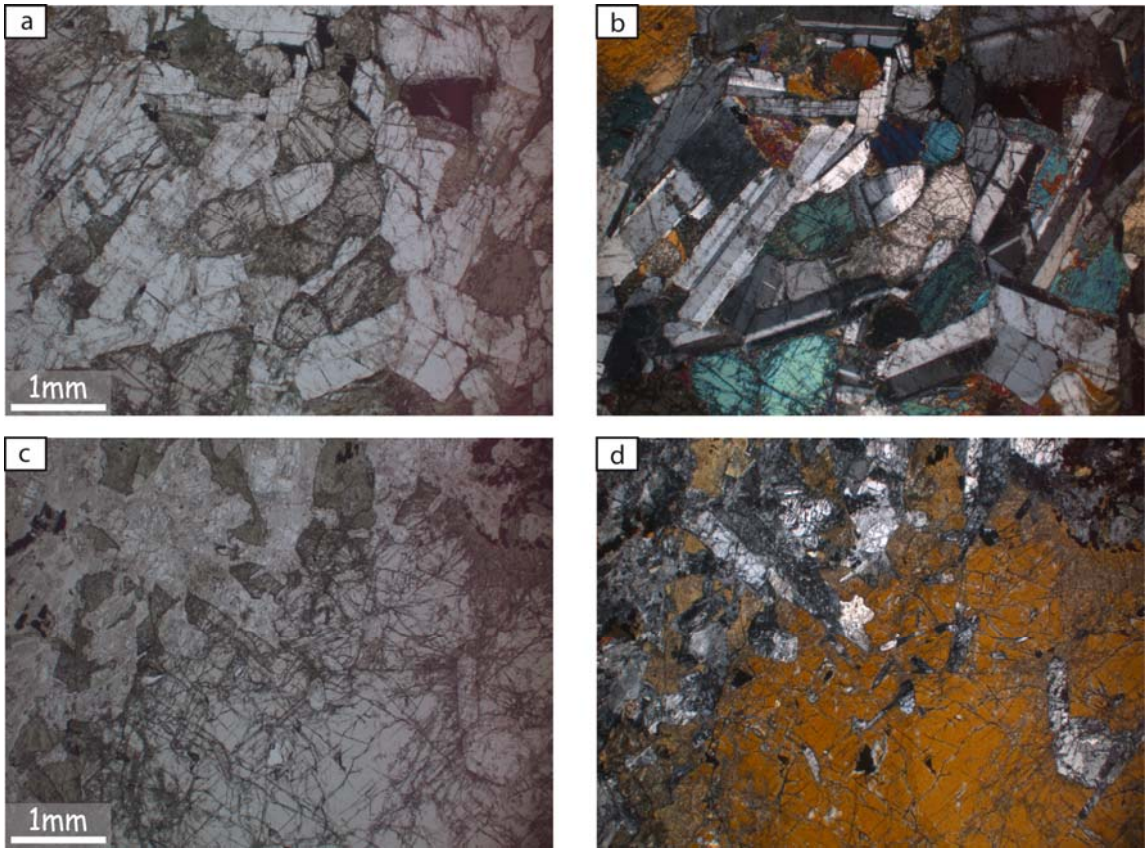

Figure III-5: Microphotographs of Oman fine-grained (a-b), and coarse grained (c-d) isotropic gabbros. a-b) fine-grained isotropic gabbros are composed of plagioclase, clinopyroxene, oxides; this rock also contains locally amphibole and olivine which are not visible in the picture (Sarur area; sample 07OL15); c-d) coarse-grained isotropic gabbros are composed of plagioclase, clinopyroxene; this rock also contains amphibole, and locally orthopyroxene which are not visible in the picture (Sarami area; sample 07OL26a). a, c) plane-polarized light; b, d) cross-polarized light.

About 100-200 meters below the base of the sheeted dike complex, gabbros grade to more granular textures and are foliated (Figure III-4e-f). This magmatic foliation is usually sub-parallel to the overlying sheeted dike and is interpreted as resulting from subsidence at the melt lens floor (Nicolas et al., 2009; see Appendix A1) or from the buoyant ascent of magma through the mush pile (MacLeod and Yaouancq, 2000). Foliated gabbros are composed of plagioclase, clinopyroxene, and locally amphibole, olivine, orthopyroxene (Figure III-8).

In most of the visited areas, the transition from the foliated gabbros to the isotropic gabbros and from the isotropic gabbros to the sheeted dike complex is not observed. These transitions, which occur over a few meters, only, are usually located in river beds (Wadi) that crosscut the outcrops and prevent detailed observation (e.g. Figure III-9, and Figure 1 in MacLeod and Yaouancq, 2000). Three selected zones where the transitions outcrop better are

described in details in sections III.3, III.4, and III.5. I rapidly present hereafter the complex intrusive relationships between isotropic gabbros and microgranular dikes that display well equilibrated textures.

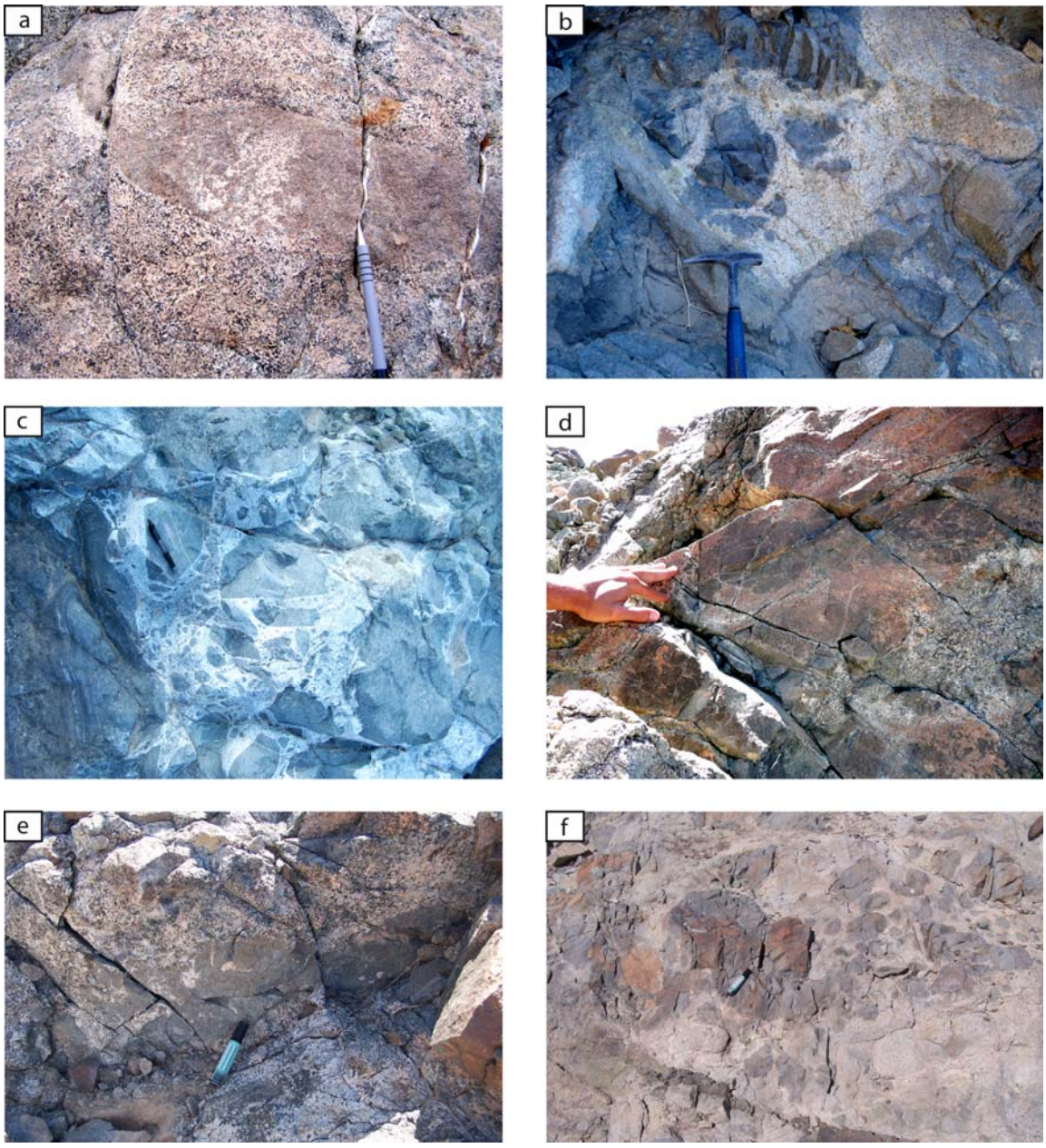

Figure III-6: Magmatic breccias and xenoliths observed in the isotropic gabbro horizon. a) Microgabbro xenoliths with well equilibrated textures in isotropic gabbro (Gideah area); b-c) magmatic breccias observed close to the base of the sheeted dike (plagiogranitic matrix; b: Aswad area; c: Haymiliyah area); d-f) xenolith accumulation in the isotropic gabbros horizon (d: Aswad area; e: Sarur area; f: Haymiliyah area).

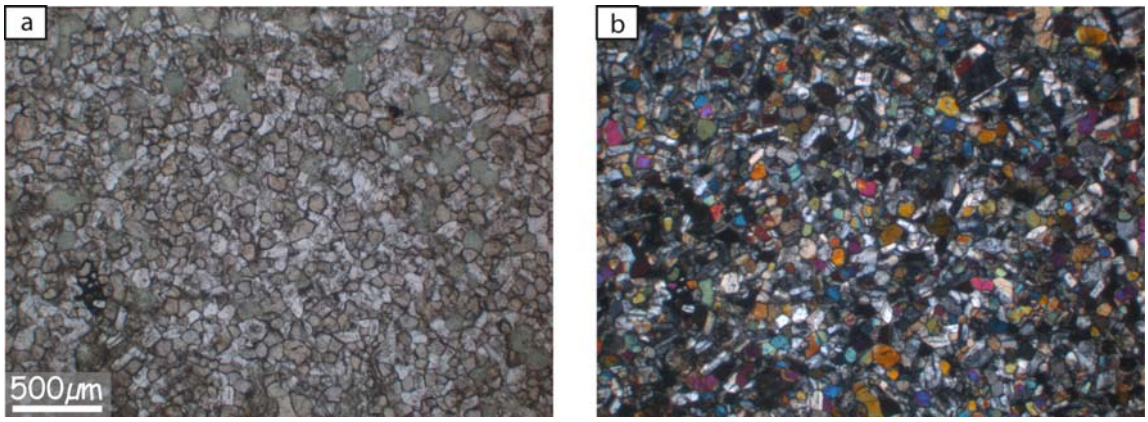

Figure III-7: Microphotographs of a microgranular xenolith with a well equilibrated texture present in the isotropic gabbros of the Aswad area consisting of plagioclase, clinopyroxene, orthopyroxene, and secondary amphibole (Oman ophiolite; sample 07OL54a). a) plane-polarized light; b) cross-polarized light.

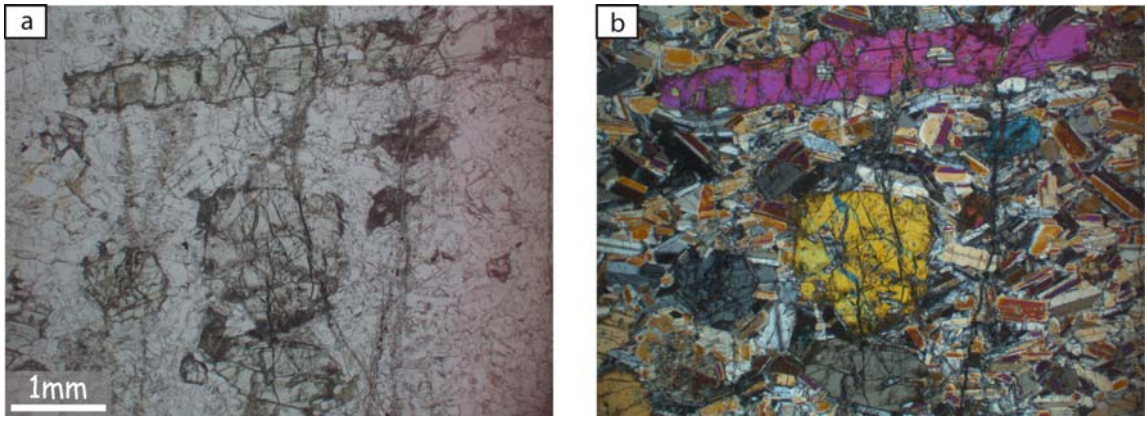

Figure III-8: Microphotographs of a foliated gabbro of the Al Ahmadi Hills area composed of plagioclase and clinopyroxene (Oman ophiolite; sample 08OL29b). a) plane-polarized light; b) cross-polarized light.

Figure III-9: SE-NW view of the area studied by Nicolas et al (2008) in the Aswad area. According Nicolas et al. (2008), the main hill (on the right hand of the picture) is composed of foliated gabbros and the small hills (on the left hand of the picture) are composed of sheeted dikes. The transition between foliated gabbros and the sheeted dike complex is located in the Wadi and outcrops poorly.

Understanding the chronology of intrusions at the base of the sheeted dike complex and in the isotropic gabbro horizon is particularly important to understand processes acting within and around the upper melt lens. Several intrusive relationships observed in this zone

are unclear, and it is difficult to determine which facies is intrusive and which one is intruded (Figure III-10a). The 3 main intrusion types encountered are: *(i)* gabbro intrusion in another gabbro; *(ii)* protodike intrusion in a gabbro; *(iii)* gabbro intrusion in dikes. This late situation is more complex due to the later intrusion of dikes into gabbro and the presence of xenoliths/enclaves in the gabbros. The cross-cutting relationships are sometimes relatively easy to interpret, for example when small intrusions of the intruding material are observed in the intruded one (Figure III-10b).

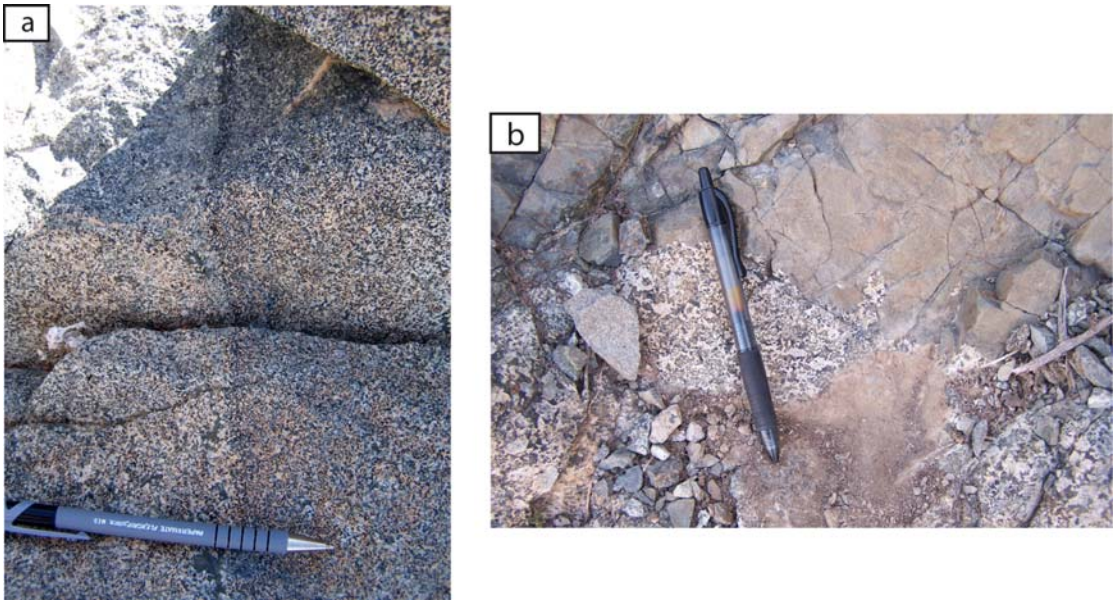

Figure III-10: Igneous contacts observed in the isotropic gabbro horizon: a) intrusion of gabbro in another gabbro, the chronology of intrusion is unclear (Gideah area); b) coarse-grained gabbro intruding microgranular dikes (Aswad area).

The gabbro intruding the base of the sheeted dike complex is either fine or coarse grained. It is composed of plagioclase, clinopyroxene, oxide, amphibole and when fine grained, locally containing olivine (Figure III-11).

In the Aswad area a peculiar outcrop allows discussing the intrusive relationships (Figure III-12). Several contacts between gabbro, diorite, and microgranular gabbro are observed. This outcrop is only ~4 x 5 meters large, and disconnected from neighbouring outcrops; relations with the underlying gabbros and with the overlying sheeted dikes are therefore very hard to identify. On this narrow outcrop, the relative timing of intrusions is locally very hard to identify (Figure III-12b-c). Locally, the gabbro appears clearly intrusive in microgranular gabbros (Figure III-12d). In order to replace these different intrusions in a general evolutionary model for the melt lens region, continuous outcrops are necessary.

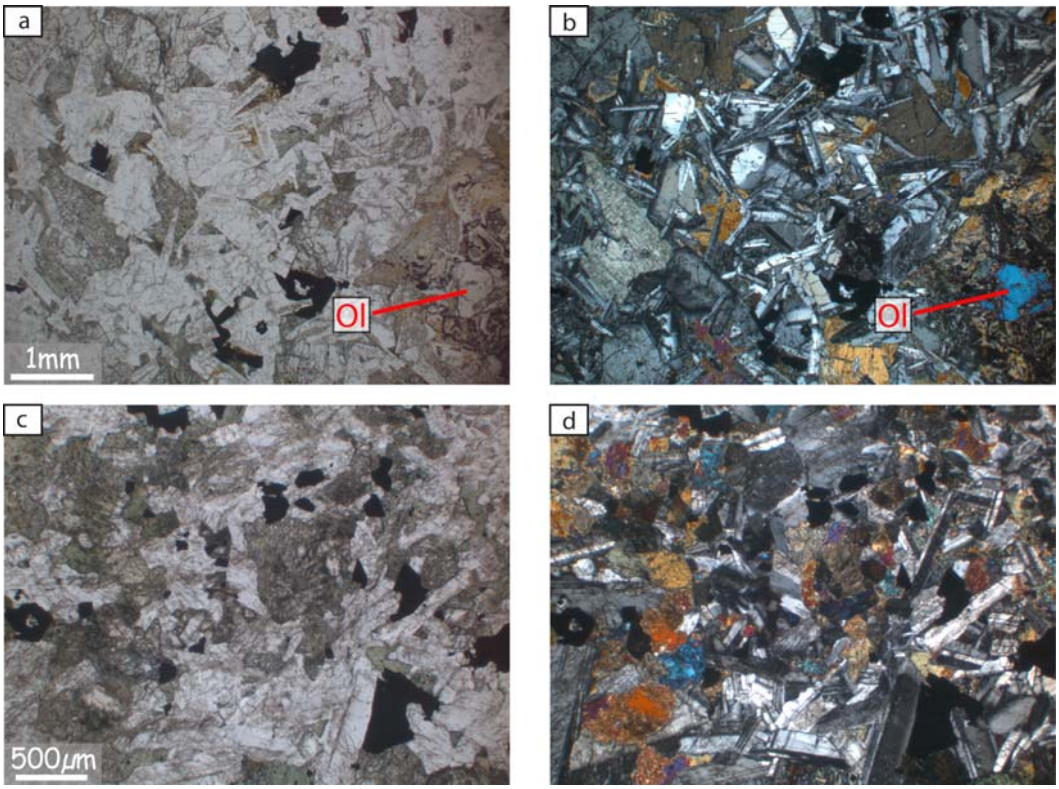

Figure III-11: Microphotographs of fined grained gabbros that intrude the sheeted dike complex. a-b) Al Ahmadi Hills area; sample 07OL01f1; c-d) wadi Gideah area; sample 08OL01c. Isotropic fine-grained gabbros are composed of plagioclase, clinopyroxene, amphibole, oxide, and locally olivine. a, c) plane-polarized light; b, d) cross-polarized light.

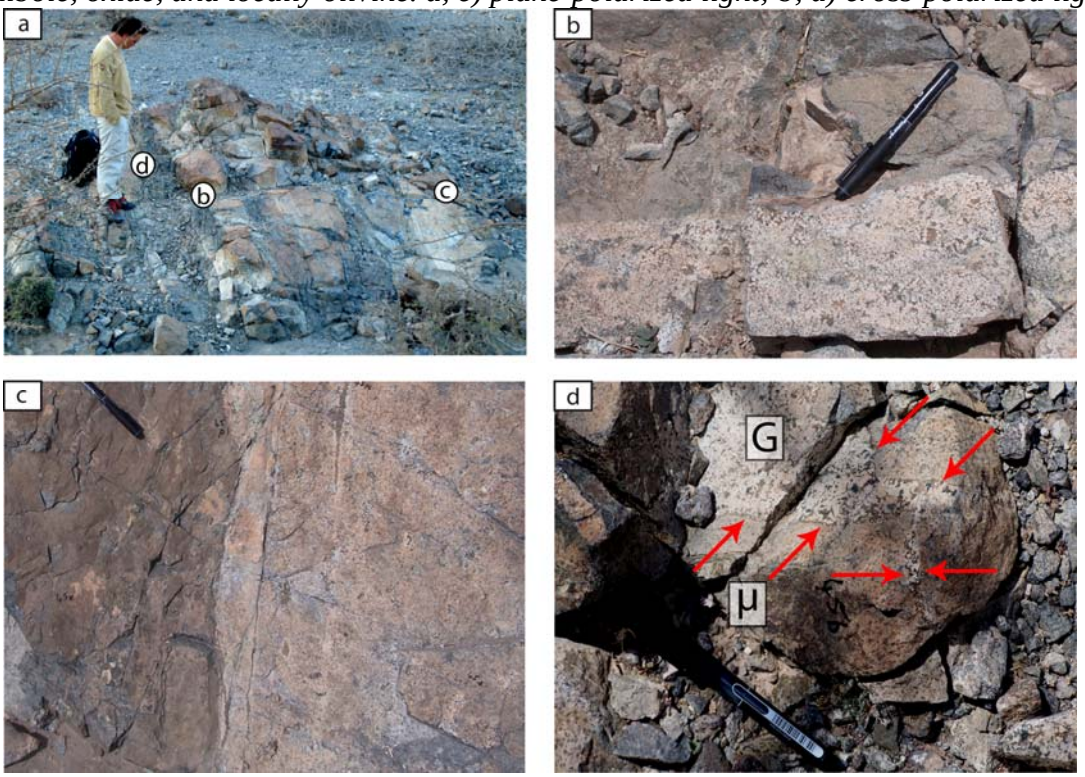

Figure III-12: a) Outcrop displaying multiple intrusive relationships (Aswad area); letters correspond to b), c), and d) pictures. b-c) Contacts between microgranular gabbro and diorite / gabbro, the chronology of intrusion is unclear. d) Microgranular gabbro (µ) intruded by a coarse-grained gabbro (G); contact is pointed by arrows.

III.3. Interactions between magma and hydrothermal system in Oman ophiolite and in IODP Hole 1256D: fossilization of a dynamic melt lens at fast spreading ridges

France, L., Ildefonse, B., and Koepke, J. (2009) Interactions between magma and hydrothermal system in Oman ophiolite and in IODP Hole 1256D: fossilization of a dynamic melt lens at fast spreading ridges. Geochem. Geophys. Geosyst. 10, Q10O19, doi:10.1029/2009GC002652

Geochemistry Geophysics Geosystems G3
AN ELECTRONIC JOURNAL OF THE EARTH SCIENCES
Published by AGU and the Geochemical Society

Article
Volume 10, Number 10
21 October 2009
Q10O19, doi:10.1029/2009GC002652
ISSN: 1525-2027

Click Here for Full Article

Interactions between magma and hydrothermal system in Oman ophiolite and in IODP Hole 1256D: Fossilization of a dynamic melt lens at fast spreading ridges

Lydéric France
Géosciences Montpellier, Université Montpellier 2, CNRS, CC60, F-34095 Montpellier CEDEX 5, France (lfrance@um2.fr)

Also at Institut für Mineralogie, Leibniz Universität Hannover, Callinstrasse 3, D-30167 Hannover, Germany

Benoit Ildefonse
Géosciences Montpellier, Université Montpellier 2, CNRS, CC60, F-34095 Montpellier CEDEX 5, France

Juergen Koepke
Institut für Mineralogie, Leibniz Universität Hannover, Callinstrasse 3, D-30167 Hannover, Germany

[1] The transition between the small melt lens observed on top of fast spreading ridge magma chambers and the overlying sheeted dike complex marks the interface between magma and the hydrothermal convective system. It is therefore critical to our understanding of fast spreading ridge accretion processes. We present maps of two areas of the Oman ophiolite where this transition zone is observed as continuous outcrops. Our observations, which include the base of the sheeted dike being crosscut by gabbros, are consistent with episodic dike injections in a steady state model but also suggest that the root of these dikes is commonly erased by vertical movements of the top of the melt lens. Dike assimilation is a possible mechanism for incorporating hydrated phases, which result from hydrothermal alteration, to the melt lens during upward migrations of its upper boundary. Upward migrations are also responsible for a granoblastic overprint of the root of the dikes that is also observed in the stoped diabase xenoliths. This granoblastic overprint attests to reheating of previously hydrothermally altered lithologies which can even trigger hydrous partial melting due to the lowering of the solidus of mafic lithologies by the presence of a water activity. Clinopyroxenes present in these granoblastic lithologies are typically low in Ti and Al content, thus strongly contrasting with corresponding magmatic clinopyroxene. This may attest to the recrystallization of clinopyroxenes after amphiboles under the peculiar conditions present at the root zone of the sheeted dike complex. Downward migrations of the top of the melt lens result in the crystallization of the isotropic gabbros at its roof, which represent the partly fossilized melt lens. Melt lens fossilization eventually occurs when magma supply is stopped or at the melt lens margins where the thermal conditions become cooler. Melt lens migration, recrystallization of hydrothermally altered sheeted dikes during reheating stages, and assimilation processes observed in the Oman ophiolite are consistent with the observations made in IODP Hole 1256D. We propose a general dynamic model in which the melt lens at fast spreading ridges undergoes upward and downward movements as a result of either eruption/replenishment stages or variations in the hydrothermal/magmatic fluxes.

Components: 34,517 words, 15 figures, 2 tables.

Keywords: fast spreading mid-ocean ridges; Oman ophiolite; hydrothermal system; melt lens; axial magma chamber; ODP.

Geochemistry Geophysics Geosystems G3 FRANCE ET AL.: FOSSILIZATION OF A DYNAMIC MELT LENS 10.1029/2009GC002652

Index Terms: 3614 Mineralogy and Petrology: Mid-oceanic ridge processes (1032, 8416); 3625 Mineralogy and Petrology: Petrography, microstructures, and textures; 3660 Mineralogy and Petrology: Metamorphic petrology.

Received 29 May 2009; **Revised** 25 August 2009; **Accepted** 2 September 2009; **Published** 21 October 2009.

France, L., B. Ildefonse, and J. Koepke (2009), Interactions between magma and hydrothermal system in Oman ophiolite and in IODP Hole 1256D: Fossilization of a dynamic melt lens at fast spreading ridges, *Geochem. Geophys. Geosyst.*, *10*, Q10O19, doi:10.1029/2009GC002652.

Theme: Formation and Evolution of Oceanic Crust Formed at Fast Spreading Rates
Guest Editors: D. A. H. Teagle and D. Wilson

1. Introduction

[2] The structure of fast spreading ridges is inferred from geophysical studies [e.g., *Morton and Sleep*, 1985; *Detrick et al.*, 1987; *Harding et al.*, 1989; *Kent et al.*, 1990] and from structural observations and mapping in ophiolites, in particular the Oman ophiolite [e.g., *Hopson et al.*, 1981; *Pallister and Hopson*, 1981; *Nicolas et al.*, 1988a, 2000; *Umino et al.*, 2003]. Geophysical studies have revealed the presence of a partly to totally molten melt lens (~30 to 100 m thick) at the top of the mostly crystallized magma chamber [e.g., *Sinton and Detrick*, 1992; *Hussenoeder et al.*, 1996; *Collier and Singh*, 1997; *Singh et al.*, 1998; *Dunn et al.*, 2000]. The composition and evolution of this thin melt lens play a key role in oceanic crust genesis as it feeds, at least partly, the upper and lower crust [e.g., *Sinton and Detrick*, 1992; *Boudier et al.*, 1996]. This horizon is also a major exchange interface between seawater and the oceanic crust as it is located at the root of the sheeted dike complex, where the hydrothermal convective system and the melt lens can meet and interact. Several descriptions of the gabbro/sheeted dike transition zone in ophiolites have been published, to attempt understanding the complex structural and petrological relationships within this zone [*Rothery*, 1983; *Nicolas and Boudier*, 1991; *MacLeod and Rothery*, 1992; *Gillis and Roberts*, 1999; *MacLeod and Yaouancq*, 2000; *Coogan et al.*, 2003; *Gillis*, 2008; *Nicolas et al.*, 2008].

[3] The IODP (Integrated Ocean Drilling Program) drilled Hole 1256D into a ~15 Ma crust that formed at the East Pacific Rise at a superfast spreading rate [*Teagle et al.*, 2006]. It is to date the only place in present-day oceanic crust where the uppermost gabbros below the sheeted dike complex has been sampled in situ below a continuous, intact section of upper oceanic crust [*Teagle et al.*, 2006; *Wilson et al.*, 2006; *Alt et al.*, 2007]. Studies in ophiolites or in present-day oceanic crust have led to the elaboration of a variety of models for the evolution of the complex magmatic/hydrothermal interface that constitutes the gabbro/sheeted dike transition zone. It is presented either as a steady state boundary layer [*Rothery*, 1983; *Nicolas and Boudier*, 1991; *MacLeod and Yaouancq*, 2000; *Nicolas et al.*, 2008], or as a dynamic one [*Gillis and Roberts*, 1999; *Coogan et al.*, 2003; *Wilson et al.*, 2006; *Gillis*, 2008; *Koepke et al.*, 2008]. The processes occurring in this transition zone, and the relationships between observed present-day lithologies and the melt lens at the time of accretion are still debated [e.g., *MacLeod and Yaouancq*, 2000; *Gillis*, 2008; *Nicolas et al.*, 2008].

[4] *Nicolas et al.* [2008] postulated that understanding the complex processes acting at the sheeted dike/gabbro transition requires studying undisturbed portions of the ridge, away from domains where accretion was under the influence of discontinuities due to ridge propagation or segmentation. In the present study, we have mapped in details the gabbro/sheeted dike transition zone in two localities of the Oman ophiolite that are, based on large-scale structural mapping [*Nicolas et al.*, 2000], away from major ridge axis tectonic activity. This study bears information on the evolution of the melt lens, and suggests a way to reconcile the apparently contrasting, previously published models.

2. Background

[5] At fast spreading ridges, the upper oceanic crust is composed of, from top to bottom, lavas, sheeted dikes, and isotropic ophitic gabbros (and associated coarse-grained gabbros and "oceanic plagiogranites"). The foliated gabbros, and layered gabbros form the lower crust. Many models, based on thermal modeling and/or ophiolite field data, have

been proposed for the formation of the igneous lower crust [e.g., *Sleep*, 1975; *Nicolas et al.*, 1988b; *Nicolas*, 1989; *Henstock et al.*, 1993; *Phipps Morgan and Chen*, 1993; *Quick and Denlinger*, 1993; *Nicolas and Boudier*, 1995; *Boudier et al.*, 1996; *Kelemen et al.*, 1997; *MacLeod and Yaouancq*, 2000; *Garrido et al.*, 2001]. Most recent models predict that the lower crust is fed from the top, through subsidence of the crystallized material from the melt lens, and/or from the bottom through sill injections [*Boudier et al.*, 1996; *Kelemen et al.*, 1997; *MacLeod and Yaouancq*, 2000; *Nicolas et al.*, 2009]. The balance between these two processes, however, remains poorly constrained and is still debated [e.g., *VanTongeren et al.*, 2008; *Webb*, 2008]. *MacLeod and Yaouancq* [2000] proposed that the lower crust is not fed from the axial melt lens, and that the foliated gabbros in the upper part of the igneous section only preserve the last increment of strain during crystallization in an upwelling melt flow. They observed that plagioclase zoning tends to increase up-section from the layered gabbros to the foliated gabbro, possibly reflecting the evolution of the melt as it migrates toward the top of the crystal mush pile. In contrast, other detailed studies of the high-level gabbros in the Oman ophiolite suggest that the melt lens does play a role in the genesis of the lower crust through subsidence processes [*Coogan et al.*, 2002; *Nicolas et al.*, 2009].

[6] The upper crust (volcanics and sheeted dike) is considered to be injected from the melt lens [e.g., *MacLeod and Yaouancq*, 2000]. However, it may not sample the whole melt lens. Based on observations made at Hess Deep (ODP Site 894), *Natland and Dick* [1996] proposed that the melt lens is partly filled with highly fractionated melts, too dense to erupt. These uneruptable melts are expelled from the underlying crystal mush column and seem to play a minor role in the upper crust accretion as they are expected to lie on the melt lens floor. The detailed structural, petrological, and geochemical study of the Wadi Abyad section, in the Oman ophiolite [*MacLeod and Yaouancq*, 2000] shows that, even if some highly fractionated pegmatitic gabbros may form up to 40% of the outcrops in some parts of the isotropic ophitic gabbro horizon, they are always subordinated to finer-grained and more magnesian gabbro. *MacLeod and Yaouancq* [2000] interpret the Fe-Ti pegmatitic gabbros as melts differentiated under reducing conditions and low water activities, at the border of the melt lens. They also propose that the average composition of the whole isotropic gabbro horizon represents the melt lens composition; their calculations lead to Mg # of 65 and a TiO_2 content of 1.1 wt %, which is relatively similar to the associated sheeted dikes and to typical N-MORB erupted at intermediate to fast spreading ridges [e.g., *Klein*, 2003].

[7] The evolution and stability of the melt lens, as well as its relationships with the overlying hydrothermally altered lithologies are also debated. These points are discussed through detailed studies of the root zone of the sheeted dike complex. This zone is composed of fine-grained isotropic ophitic gabbro, pegmatitic gabbro, some Fe-Ti gabbro and diorite, and oceanic plagiogranites. It has been described in the Oman ophiolite [*Rothery*, 1983; *Nicolas and Boudier*, 1991] and recently revisited in details [*Nicolas et al.*, 2008]. Based on petrological and structural observations, *Nicolas et al.* [2008] present a new steady state model for the evolution of the melt lens. They propose that most of the isotropic gabbro horizon, called "root zone of the sheeted dike complex," is generated by hydrous partial melting triggered by the intrusion of hydrothermal fluids in the recently crystallized, still hot, base of the sheeted dike complex. In this model, the root zone lithologies do not represent the crystallization of the melt lens, which is assumed to pinch out at its tips. *Macleod and Yaouancq* [2000] also describe the root zone of the sheeted dike complex in the Oman ophiolite as a steady state horizon, but in contrast with *Nicolas and Boudier* [1991] and *Nicolas et al.* [2008], they interpret it as the crystallized melt lens under anhydrous and reducing conditions, implying little assimilation of hydrated doleritic roof material. However, they show some assimilation evidences [*MacLeod and Yaouancq*, 2000, Figure 2d]. Reheating and assimilation in the root zone are documented in the Oman ophiolite [*Coogan et al.*, 2003; *Gillis*, 2008], in the Troodos ophiolite [*Gillis and Roberts*, 1999; *Gillis*, 2002; *Gillis and Coogan*, 2002; *Gillis*, 2008], and at Pito Deep and Hess Deep [*Gillis*, 2008]. *Wilson et al.* [2006] and *Koepke et al.* [2008] recently described assimilation and reheating features within the root zone of the sheeted dike complex in the IODP Hole 1256D, the first and so far only borehole in present-day intact ocean crust that reaches the contact between sheeted dikes and gabbro. *Nicolas et al.* [2008] discuss these results by pointing out that reheating and assimilation features are well known in the Oman ophiolite in areas affected by ridge segmentation [*Juteau et al.*, 1988; *MacLeod and Rothery*, 1992; *Nicolas and Boudier*, 1995; *Boudier et al.*, 2000; *Adachi and Miyashita*, 2003; *Miyashita et al.*, 2003; *Umino et al.*, 2003], but have not been

Geochemistry Geophysics Geosystems G3 FRANCE ET AL.: FOSSILIZATION OF A DYNAMIC MELT LENS 10.1029/2009GC002652

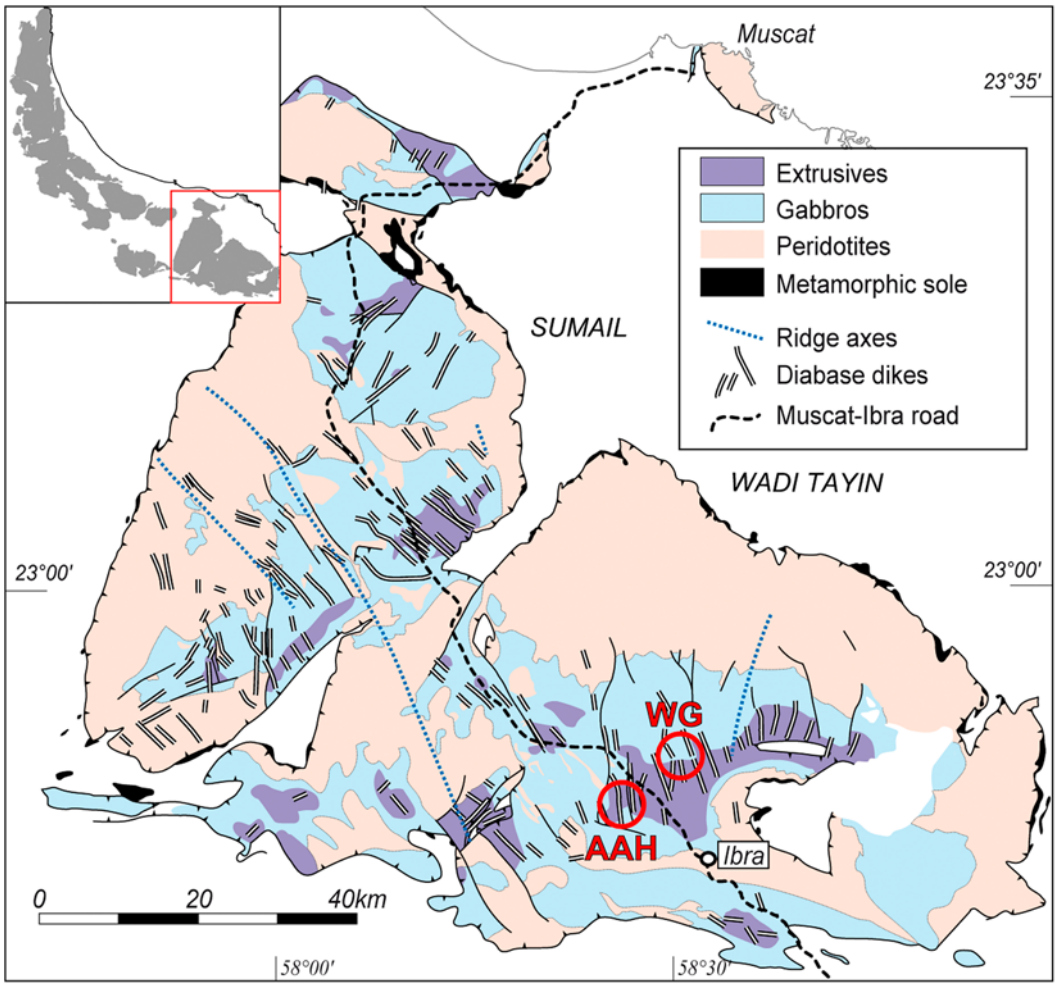

Figure 1. Simplified geological and structural map of the southern massifs and location (red box) in the Oman ophiolite [after *Nicolas et al.*, 2000]. Red circles indicate the locations of the studied zones (WG, Wadi Gideah; AAH, Al Ahamadi Hills).

described in "undisturbed" zones, away from discontinuities, yet. They suggest that reheating and assimilation, in the Oman and Troodos ophiolite, and in the IODP borehole could be related to ridge segmentation.

[8] To further constrain the characteristics of the transition from gabbros to the sheeted dike complex (i.e., the interface between the magmatic and the hydrothermal systems), we have mapped in details this transition in two "undisturbed" areas of the Oman ophiolite (Wadi Gideah area, in the Wadi Tayin Massif, and Al Ahmadi Hills area, in the Ibra plain at the southern end of the Wadi Tayin Massif). Because of its lithological heterogeneity, and of the presence of many igneous contacts and fractures, the root zone of the sheeted dike complex is a zone of preferential meteoric alteration and outcrops very poorly (see, e.g., *MacLeod and Yaouancq* [2000, Figure 1], which shows the outcrops discontinuity). Observations from these two regions are made over continuous outcrops and are consistent with many other visited sites where outcrops are not continuous.

3. Field Observations

[9] The two studied areas are located in the well-exposed Wadi Tayin Massif, one of the southern Massifs in the Oman ophiolite where ridge segmentation effects are minor [*Nicolas et al.*, 2000] (Figure 1). The southern massifs are large and flat-bottomed synclines with the sheeted dike and subvertical gabbro foliation trending ~NW–SE. The NW–SE segments are opened in an older domain where the sheeted dike trends ~NE–SW. The Wadi Gideah area is situated in the Jebel Dimh, 10 km to the north of Ibra and ~10 km to the east of the main road

between Muscat and Ibra. The Al Ahmadi Hills are located in the large Wadi Nam, 6 km to the NW of the Al Ahmadi village and 10 km to the NNW of the town of Ibra.

3.1. Wadi Gideah Area

[10] The mapped area in Wadi Gideah extends from the foliated gabbro in the north to the sheeted dikes in the south, and includes in between the heterogeneous, isotropic ophitic gabbro horizon (Figure 2a). The foliated gabbros present the same characteristics as anywhere else in the Oman ophiolite; they are granular, and display a subvertical foliation trending N–S (Figure 3). Close to the contact with the foliated gabbros, the isotropic ophitic gabbro horizon is very heterogeneous; it is composed of coarse-grained lithologies such as hornblende-olivine-gabbro or hornblende-gabbro, which contain some strongly altered xenoliths of predominantly fine-grained recrystallized diabase, but also gabbro and hornblende-diorite. The relationships between the different lithologies in this particular place are unclear because of the intense weathering. To the south, up-section, isotropic ophitic gabbros become more homogeneous. Some isolated narrow and elongated meter sized zones display a foliation (~N–S, subvertical) that seems to underline the contacts with gabbro injections. Rounded xenoliths of gabbro and diabase, about 10 × 10 cm on average, are accumulated at small hill summits in the whole isotropic gabbro horizon (Figures 2 and 4a). Magmatic breccias with a leucocratic matrix enclosing gabbro or dike xenoliths are also observed (Figures 2 and 4b). Except for one occurrence close to the foliated gabbro (Figure 2), these breccias are located close to, or at the contact between the isotropic ophitic gabbro horizon and the sheeted dikes. Figures 2b and 2c show two hills in the ophitic gabbros topped by sheeted dike. No fault is observed between these two hills. The vertical offset of the contact between gabbros and sheeted dike is consequently assumed to represent initial depth variations of this contact along the ridge axis. To the south, the sheeted dikes present the same characteristics as anywhere else in the Oman ophiolite, and trend N–S, subvertical (Figure 3). Each dike is about 1 to 1.5 m wide and present chilled margins against other dikes. Some later dikes with chilled margins, also 1 to 1.5 m wide, crosscut the isotropic gabbros and the previous sheeted dikes; they are subparallel to the sheeted dike complex (Figure 5).

[11] Isotropic ophitic gabbros intrude the base of the sheeted dikes, and locally assimilate dike fragments (Figure 6). Sparse diabase xenoliths are locally observed. Gabbros clearly crosscut former chilled margins (Figure 6), and locally intrude the sheeted dike base, but do not invade it further than about 1 m above the main contact. Some contact outcrops show a gradation toward the contact from gabbroic rocks to more leucocratic ones (Figures 6c and 6e). Coarse-grained isotropic ophitic gabbros are also common in the root zone and at the contact with xenoliths (Figure 6f).

[12] Dikes truncated by ophitic gabbro show well-equilibrated (with ~120° triple junctions), fine-grained granular textures, called hereafter "granoblastic textures" (Figure 7a). These textures are clearly distinct from the doleritic textures classically observed in Oman ophiolite sheeted dikes. Recrystallized texture is observed on both sides of dike margins; that is, it overprints both last and former dikes (Figures 7a and 7b). The average grain size in the granoblastic margins overprinting the chilled margins is ~10 μm. Ten centimeters away from the margins, the recrystallized textures display coarser granular grains (~50 μm; Figure 7b); plagioclases are largely less recrystallized than pyroxenes. Patches with granoblastic texture (0.5 to 1 mm wide) are also observed in the uppermost isotropic gabbros (Figure 7c). The paragenesis of granoblastic domains includes plagioclase, clinopyroxene, amphibole, magnetite, and ilmenite. Granoblastic texture lithologies are particularly rich in oxides (Figures 7a, 7b, 7e, and 7g). The corresponding mineral assemblages are commonly complex with different generations of clinopyroxenes and amphiboles (Figure 7f) and clinopyroxenes commonly contain numerous tiny oxide inclusions. Oxide inclusion-rich clinopyroxene veins (100 to 200 μm wide) in the base of the sheeted dikes are crosscut by intrusive gabbros (Figures 7g and 7h). The leucocratic lithologies (oceanic plagiogranites) that are sometimes present at the base of the dikes contain tiny clinopyroxenes (20 to 50 μm) associated with oxides, suggesting that these correspond to relics of parageneses from the granoblastic stage. These minerals have rounded shapes and appear to be relics of former larger grains. This observation is critical to constrain the origin (differentiation versus hydrous partial melting) of these oceanic plagiogranites (see discussion below). All samples are moderately to strongly altered in the greenschist facies; actinolite and albitized plagioclases replace magmatic ones, clinopyroxenes and higher-temperature amphibole (hornblende and pargasite). In some samples the granoblastic texture is so strongly altered that it is hardly recognizable (Figure 7d).

Geochemistry Geophysics Geosystems G3 FRANCE ET AL.: FOSSILIZATION OF A DYNAMIC MELT LENS 10.1029/2009GC002652

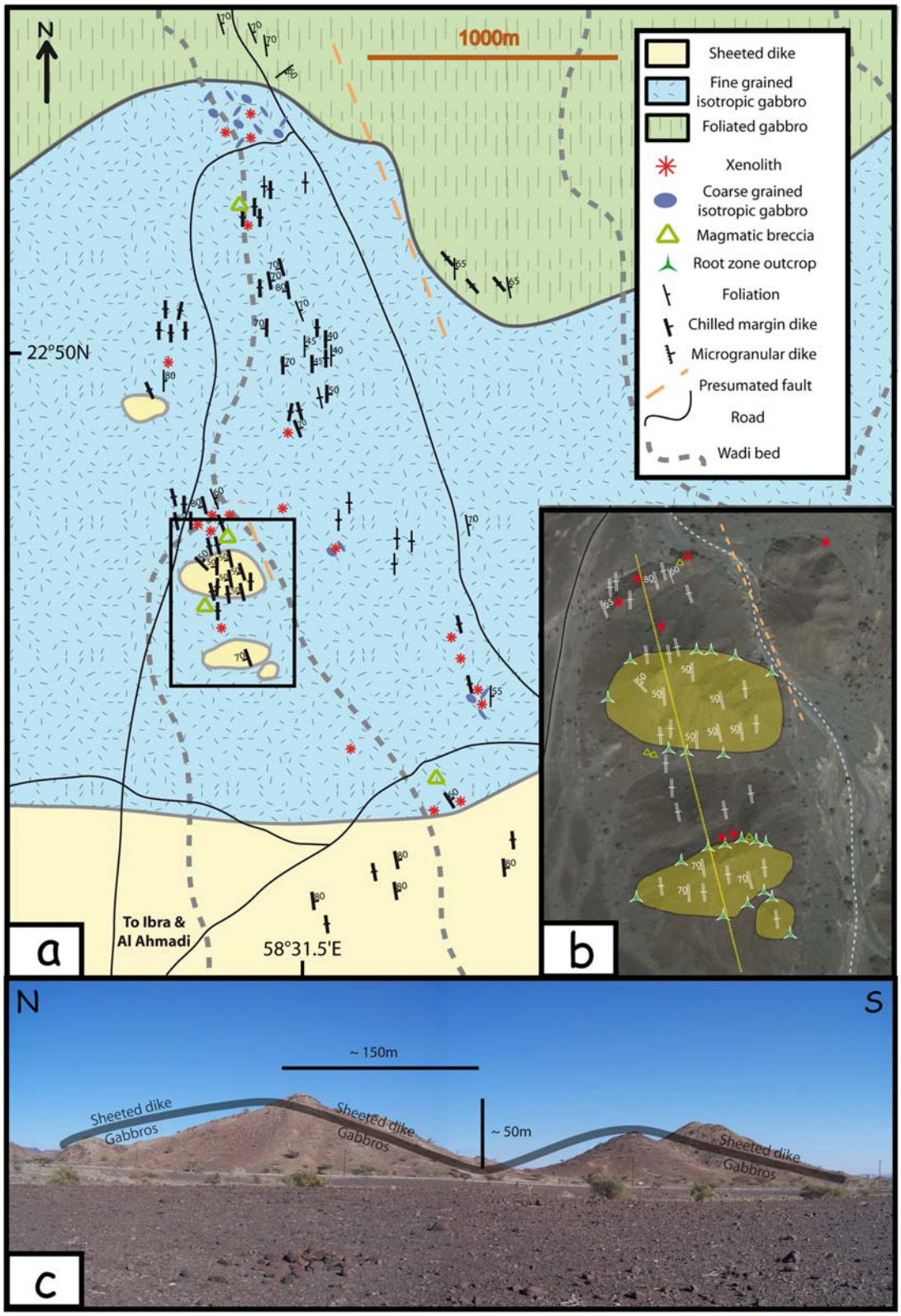

Figure 2. Wadi Gideah area. (a) Geological and structural map. The black rectangle represents the location of Figure 2b. (b) Zoom on the two hills that have their summits and southern flanks composed of sheeted dikes and their northern flanks composed of gabbros. The yellow line indicates the position of the cross section in Figure 2c. (c) Cross section showing the two hills from Figure 2b. The thick gray line indicates the gabbro/sheeted dike transition that is precisely mapped in Figure 2b. No fault has been observed.

Geochemistry Geophysics Geosystems G3 FRANCE ET AL.: FOSSILIZATION OF A DYNAMIC MELT LENS 10.1029/2009GC002652

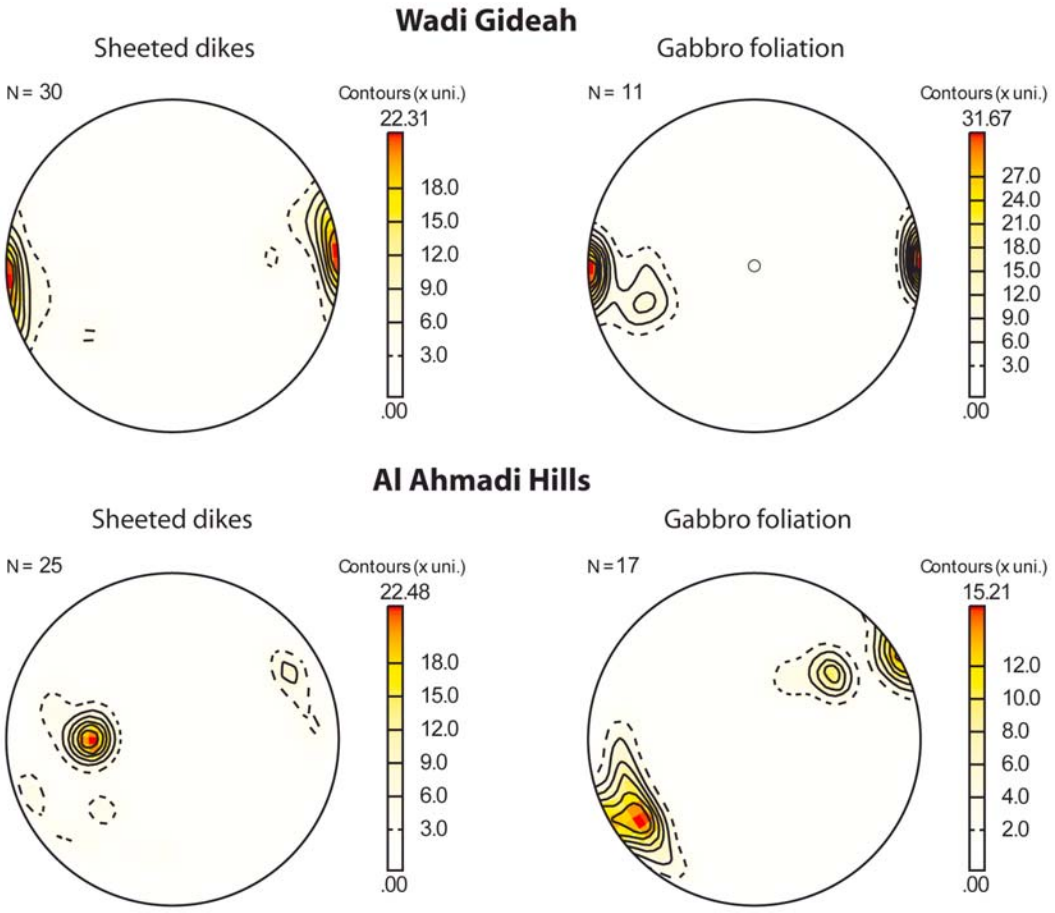

Figure 3. Stereonets (lower hemisphere, nonpolar data, geographical reference system) showing field structural measurements: (left) sheeted dike and (right) magmatic foliations in foliated gabbros (top) in the Wadi Gideah area and (bottom) in the Al Ahmadi Hills area.

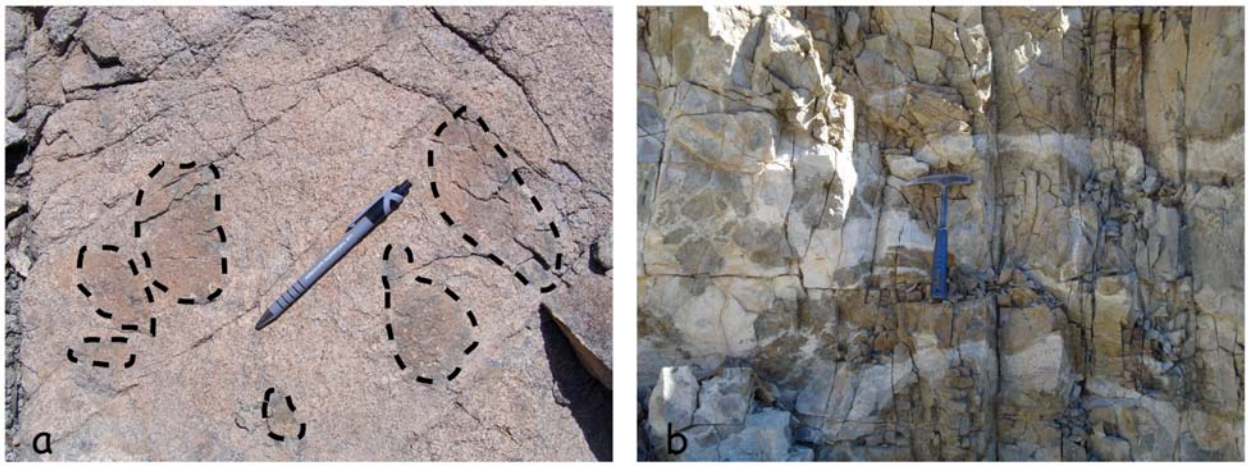

Figure 4. (a) Xenoliths of granoblastic dikes in isotropic ophitic gabbro and (b) magmatic breccia consisting of recrystallized sheeted dike within a silicic (oceanic plagiogranite) matrix. Both outcrops are in the Wadi Gideah area.

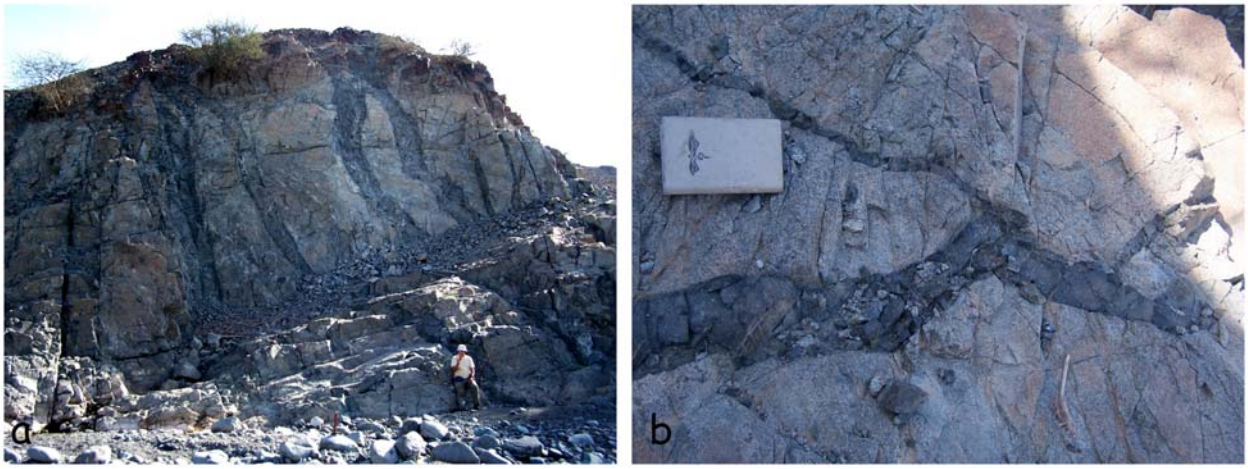

Figure 5. Late diabase dikes crosscutting isotropic ophitic gabbros in the Wadi Gideah area.

3.2. Al Ahmadi Hills

[13] The Al Ahmadi Hills are aligned along a small, 3000 m long and ~50 m high ridge that trends NW–SE (Figure 8a). At the northern tip of this ridge, the first lithology encountered is olivine gabbro, with a steep, strong magmatic foliation oriented 160E75 on average (Figures 3 and 9a). In some rare, about 1 to 5 m large domains, the foliation is hardly identifiable in the field. Microscopic observations show that the foliation is similar to what is observed in the other foliated samples, with olivine mantled by orthopyroxene and pargasite (Figure 9b). This assemblage is described by *Koepke et al.* [2005a, 2005b] and *Nicolas et al.* [2003], and may trace late magmatic processes such as hydrous partial melting reactions or late crystallization in the presence of water.

[14] The transition to the next horizon above, mostly composed of isotropic ophitic gabbros, is sharp. It occurs over less than 10 m. This horizon is strongly altered in the greenschist facies, as shown by the abundance of actinolite. Immediately above this contact, the ophitic gabbros contain numerous large xenoliths (up to 1.5 m large; Figures 8a, 8b, and 8d), which are composed either of oxide-rich granoblastic overprinted dikes (Figure 9c) or of gabbroic rocks. This area is composed of about 60% isotropic ophitic gabbros, 30% xenoliths, and nearly 10% pegmatitic gabbros very similar to those of Wadi Gideah (Figures 6d and 6f), forming the matrix around the xenoliths. In some localized (~10 m) zones, xenoliths represent up to 90% of the outcropping material. Xenolith accumulation appears more abundant in the lower third of the isotropic ophitic gabbro section (Figures 8a and 8d). Xenoliths and pegmatitic gabbros become less abundant, and nearly disappear up-section, to finally reappear close to the contact with the sheeted dikes.

[15] As observed in Wadi Gideah (Figure 6), the contact between the isotropic ophitic gabbros and the overlying sheeted dike complex is very sharp. Gabbros are again intrusive in the sheeted dike and crosscut former dike margins. Close to this contact, dike xenoliths are locally accumulated, generally small (~10 cm, Figure 8c), and form ~1 m wide clusters (Figures 8c and 8d). These xenoliths have granoblastic textures; they are totally metamorphosed in the greenschist facies and the granoblastic texture is commonly blurred. The base of the dikes is also very altered but the recrystallized granular texture, associated to an enrichment in granular oxides, is still recognizable in some samples (Figure 9d); these are interpreted as relics, after subsequent alteration, of the granoblastic overprint. Because of the strong greenschist facies overprint and of the strong weathering, it is not possible to estimate the vertical extent of the granoblastic overprint. These textures are identical to those observed in the same structural position in the Wadi Gideah area.

[16] Up-section, the Al Ahmadi hills continue over ~1000 m with the sheeted dike complex, oriented 0E50 on average (Figure 3). The sheeted dikes are typical of what is observed elsewhere in the Oman ophiolite; it is made of parallel, about 1 to 1.5 m wide, greenschist altered dikes, bounded by dark chilled margins against other dikes.

[17] In the whole section, late dikes crosscut other lithologies. In the lower part of the section, late dikes display microgranular margins that are nearly free of oxides (Figure 9e), and ophitic coarser grained center (Figure 9f). They grade up-section, close to

Geochemistry Geophysics Geosystems G3 FRANCE ET AL.: FOSSILIZATION OF A DYNAMIC MELT LENS 10.1029/2009GC002652

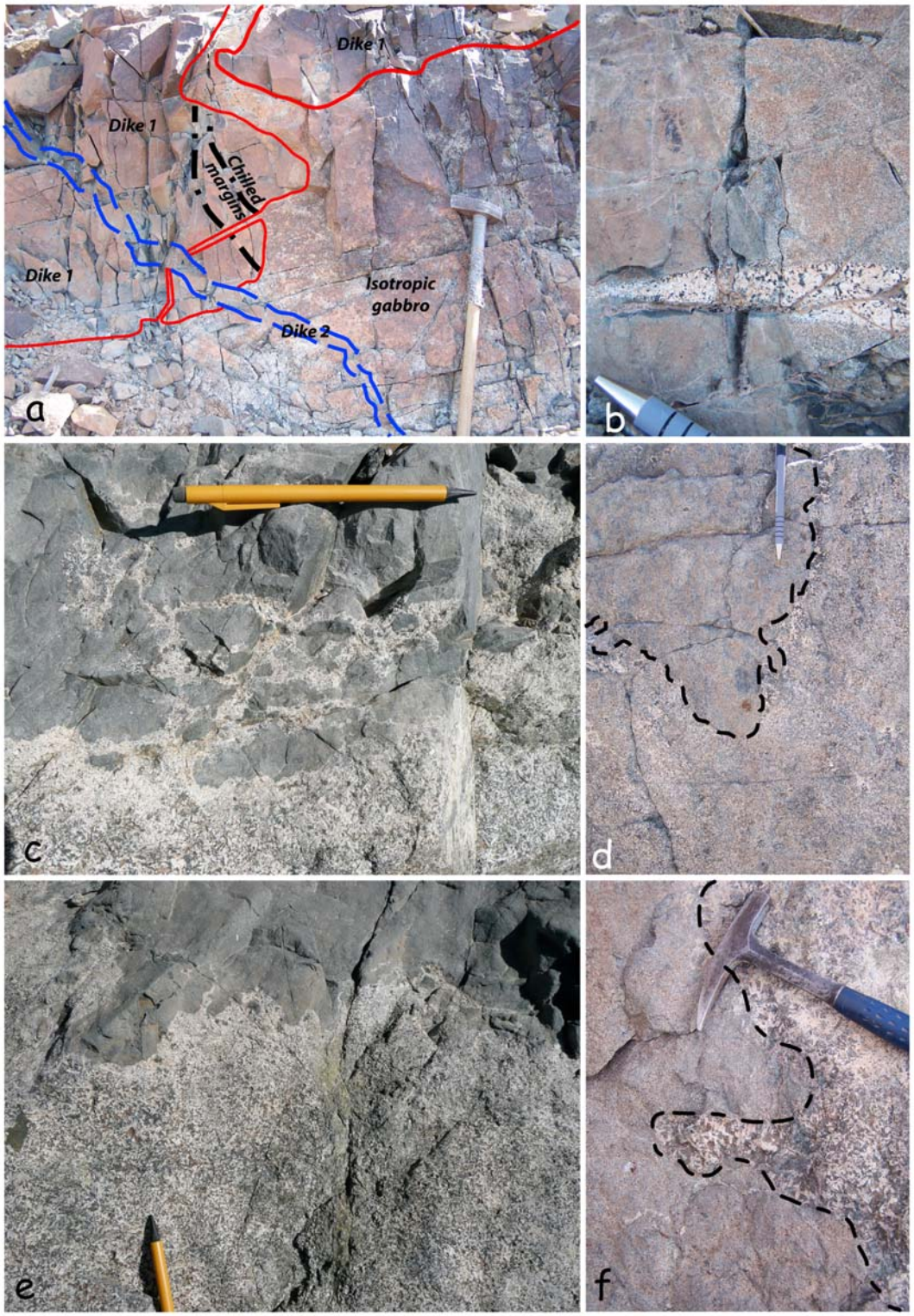

Figure 6. Outcrops in the root zone of the sheeted dikes. (a) Recrystallized sheeted dike (granoblastic dike) intruded by gabbro. Recrystallized chilled margins are crosscut by the intrusive gabbro. A late dike ("dike 2") crosscuts the gabbro and recrystallized dikes ("dike 1"). (b) Dioritic intrusion that crosscuts a recrystallized dike margin with granoblastic texture. (c and e) Gabbro assimilating recrystallized sheeted dike. The gradation to more leucocratic lithology at the contact is visible. A small shear zone affecting the dikes and gabbro is visible on the right side of Figure 106c. (d and f) Xenoliths of recrystallized dikes showing granoblastic texture in isotropic gabbro. Patches of coarser grained gabbro are observed around the xenolith in d), and all surrounding gabbro is pegmatitic in Figure 6f.

Geochemistry Geophysics Geosystems G3 FRANCE ET AL.: FOSSILIZATION OF A DYNAMIC MELT LENS 10.1029/2009GC002652

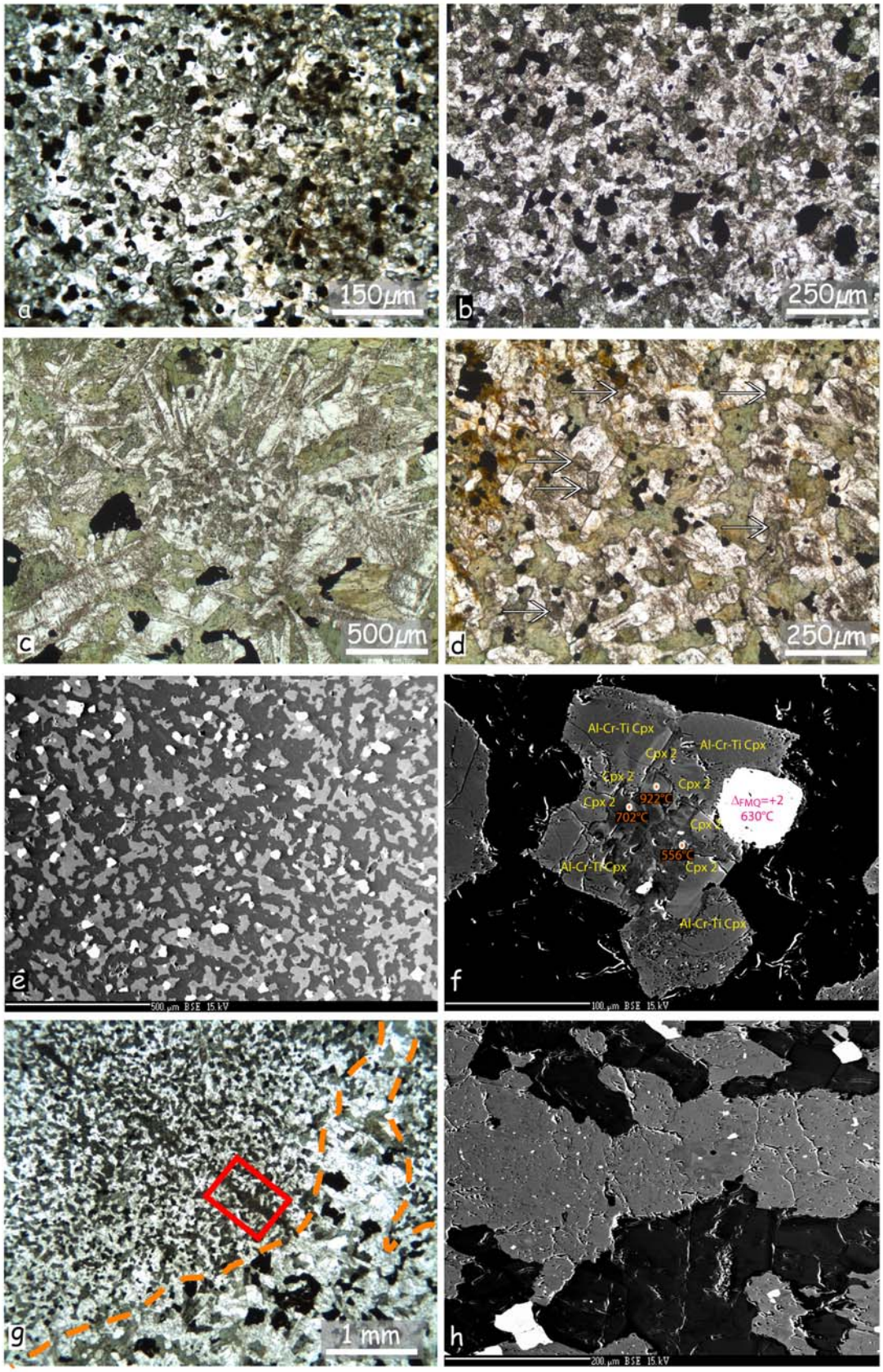

Figure 7

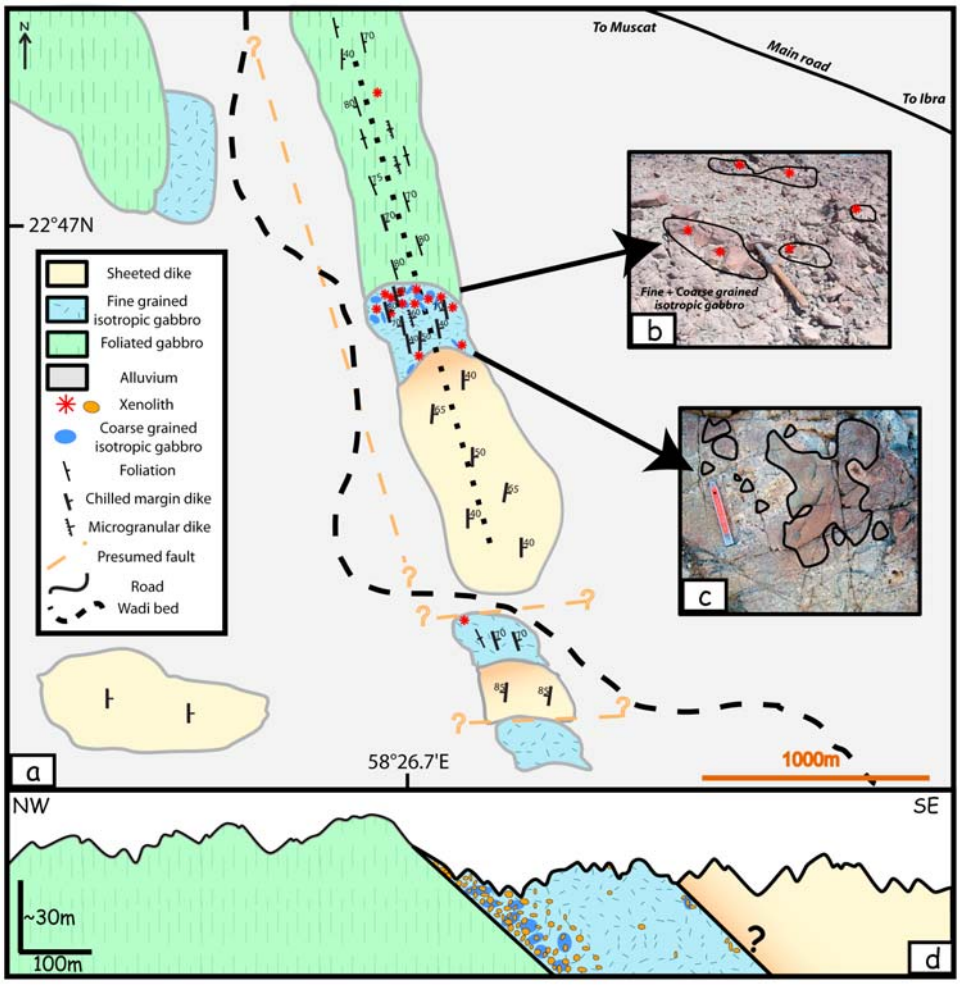

Figure 8. Al Ahmadi Hills area. (a) Geological and structural map. The dotted line indicates the location of the cross section in Figure 8d. (b) Large xenoliths of recrystallized dike fragments close to the foliated gabbro/isotropic gabbro transition. (c) Decimeter-sized xenoliths of recrystallized dikes close to the transition between isotropic gabbro and recrystallized sheeted dikes. (d) NW–SE cross section. Vertical exaggeration is ×3; the isotropic gabbro horizon is ~100 m thick. The base of the sheeted dike is reheated and recrystallized over a distance that is not constrained because of the strong weathering.

Figure 7. Photomicrographs and BSE images of samples from the Wadi Gideah area. (a) Fine-grained granoblastic texture with a high oxide concentration in a recrystallized dike margin (plane-polarized light). (b) Coarser-grained recrystallized texture in the center of a recrystallized dike (plane-polarized light). (c) Granoblastic patch in isotropic gabbro in the center of the picture (plane-polarized light). (d) Coarse-grained recrystallized texture partially erased by a strong greenschist facies alteration in a granoblastic dike (plane-polarized light). Arrows indicate granular grains. (e) BSE image of the granoblastic texture in a recrystallized dike. Dark gray minerals are plagioclases, light gray minerals are clinopyroxene + amphibole, and white minerals are oxides. (f) BSE image focusing on Fe-Mg minerals present in the granoblastic dikes. Different generations of clinopyroxenes (Cpx) and amphiboles are present (orange numbers indicate temperatures estimated with *Ernst and Liu* [1998]). The white phase is a mixture of ilmenite and magnetite. Redox and temperature estimates are calculated using *Sauerzapf et al.* [2008]. (g) Isotropic gabbro cross-cutting a recrystallized granoblastic dike. In the recrystallized dike, the truncated clinopyroxene vein is believed to derivate from a former amphibole bearing hydrothermal vein (cross-polarized light). The red square indicates the position of the BSE in Figure 7h. (h) BSE image of the truncated clinopyroxene vein in Figure 7g. Note the occurrence of numerous tiny oxide inclusions in the clinopyroxenes.

Geochemistry Geophysics Geosystems G3 FRANCE ET AL.: FOSSILIZATION OF A DYNAMIC MELT LENS 10.1029/2009GC002652

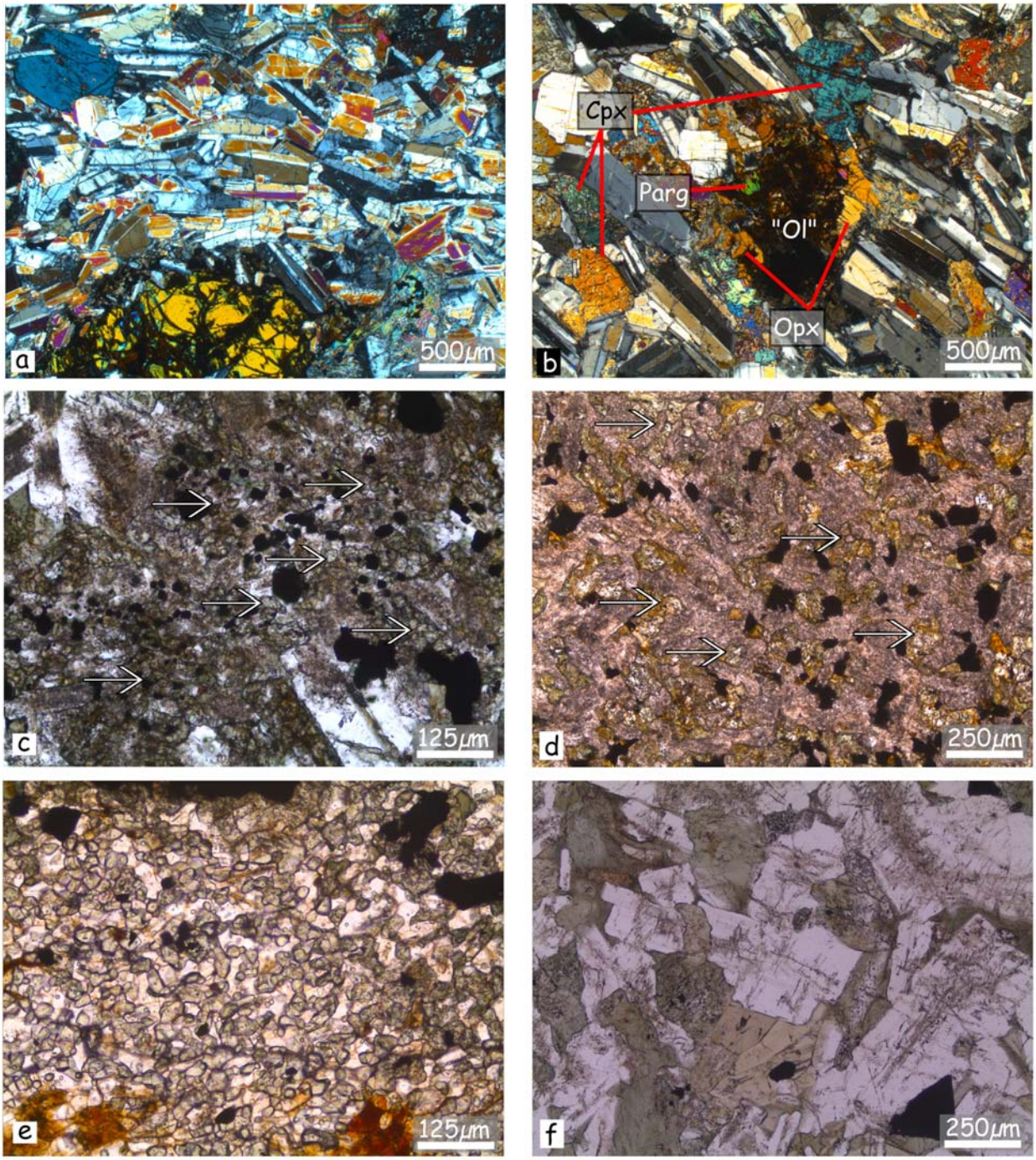

Figure 9. Photomicrographs of samples from the Al Ahmadi Hills area. (a) Foliated olivine-gabbro (cross-polarized light). (b) Altered olivine (Ol) surrounded by orthopyroxene (Opx) and pargasite (Parg) in the foliated gabbro domains where the foliation is hardly identifiable in the field (cross-polarized light). (c) Granoblastic overprint in a diabase xenolith. Arrows indicate the small granoblastic grains (plane-polarized light). (d) Strongly altered coarser-grained recrystallized texture from the base of the sheeted dike complex (center of a recrystallized dike: plane-polarized light). Arrows indicate granular grains. (e) Microgranular texture of a protodike margin (plane-polarized light). (f) Protodike center showing a texture similar to the isotropic ophitic gabbro (plane-polarized light).

the contact with the sheeted dikes, to diabase dikes with chilled margins. *Nicolas and Boudier* [1991] and *Nicolas et al.* [2008] described in the root zone of the sheeted dike complex similar dikes with ophitic texture in the center and microgranular margins, which they name "protodikes," and ascribed to slow cooling in a hot and hydrous environment. The magmatic protodikes depart from the metamorphic granoblastic truncated dikes in that only their margins display microgranular textures (e.g., compare Figure 7a with Figure 9e for the margins and Figure 7b with Figure 9f for the center of dikes). We interpret the late dikes observed in the mapped areas as protodikes that intrude the still hot, recently crystallized gabbros. Because a single protodike cannot be followed in the field over hundreds of meters, the textural transition from protodikes with microgranular margins to dikes with chilled margins up-section is not precisely located.

4. IODP Hole 1256D

[18] IODP Hole 1256D reached for the first time the sheeted dikes/gabbro transition in ultrafast spread oceanic crust [*Teagle et al.*, 2006; *Wilson et al.*, 2006; *Alt et al.*, 2007]. The sheeted dikes/gabbro transition is sharp and represents an intrusive contact similar to those observed in Oman (*Wilson et al.* [2006, Figure 4c] and Figure 6 herein). The base of the sheeted dike complex comprises recrystallized, granoblastic texture domains (granulitic facies) over ~60 m; this texture is identical to the granoblastic one described herein in samples from Oman (see for example the concordance between Figures 7a and 10a for the fine granoblastic lithologies and 7b and 10b for coarser-grained recrystallized ones). The section below the sheeted dike/gabbro contact has been resampled for this study (Table A1).

[19] *Wilson et al.* [2006] describe two granoblastic intervals that are interpreted as "screens of granoblastic dikes," the first one (~15 to 25 m thick) is located between two gabbroic bodies ("gabbro 1" (~45 m) and deeper "gabbro 2" (~15 m)) and the second one (very poorly recovered) at the bottom of the "gabbro 2" interval, close to the bottom of Hole 1256D. The first thick "screen of granoblastic dikes" (Figure 10c) is poorly recovered (<30%; Figure 11). However, even in the most continuous cores of this interval, granoblastic lithologies are crosscut by thin intrusions of gabbros and oceanic plagiogranites, with diffuse to sharp contacts (Figure 11).

[20] We have also observed in the core the presence of sparse, small (cm to ~10 cm) xenoliths in the upper part of the "gabbro 1" interval, at the contact with the base of the granoblastic dikes and, as described by *Wilson et al.* [2006], higher concentrations of xenoliths deeper in the "gabbro 2" interval, close to the bottom of the drilling hole. The sampled xenoliths show recrystallized textures similar to the ones of the base of the granoblastic dikes and to the ones of the thick "screen of granoblastic dikes" located between the "gabbro 1" and "gabbro 2" intervals. Granoblastic patches similar to those observed in Wadi Gideah (Figure 7c) are also observed in the "gabbro 1" and "gabbro 2" intervals (Figure 10d).

5. Mineral Compositions and Thermometry

[21] Mineral electron microprobe analyses were performed at Géosciences Montpellier and at the Institut für Mineralogie, Hannover using a Cameca SX 100 electron microprobe equipped with 5 spectrometers and an operating system "Peak sight." Data were obtained using a 15 KV acceleration potential, a static (fixed) beam, Kα emission from all elements, and the "PAP" matrix correction [*Pouchou and Pichoir*, 1991] in Hannover and its modification [*Merlet*, 1994] in Montpellier. Most element concentrations were obtained with a beam current of 15 nA and a counting time of 10 to 120 s on peak and background.

[22] Analyses presented herein (Table A1) were acquired on samples from the base of the Oman sheeted dike (granoblastic domains), from diabase xenoliths that are present in the isotropic ophitic gabbros, from coarse-grained gabbros that surround these xenoliths, from oceanic plagiogranites sampled at the base of the sheeted dikes, from a protodike, and from foliated gabbros. All Oman samples come from the Al Ahmadi Hills and Wadi Gideah areas. We also present for comparison analyses of IODP Hole 1256D samples. These samples come from the lowermost granoblastic dikes (just above the first recovered gabbro), from the "screen of granoblastic dikes" located between the "gabbro 1" and "gabbro 2" intervals, and from granoblastic xenoliths in gabbros.

5.1. Root Zone Lithologies and Protodikes

[23] In Oman samples, plagioclase compositions are very variable; they range from An_{10} to An_{57} in

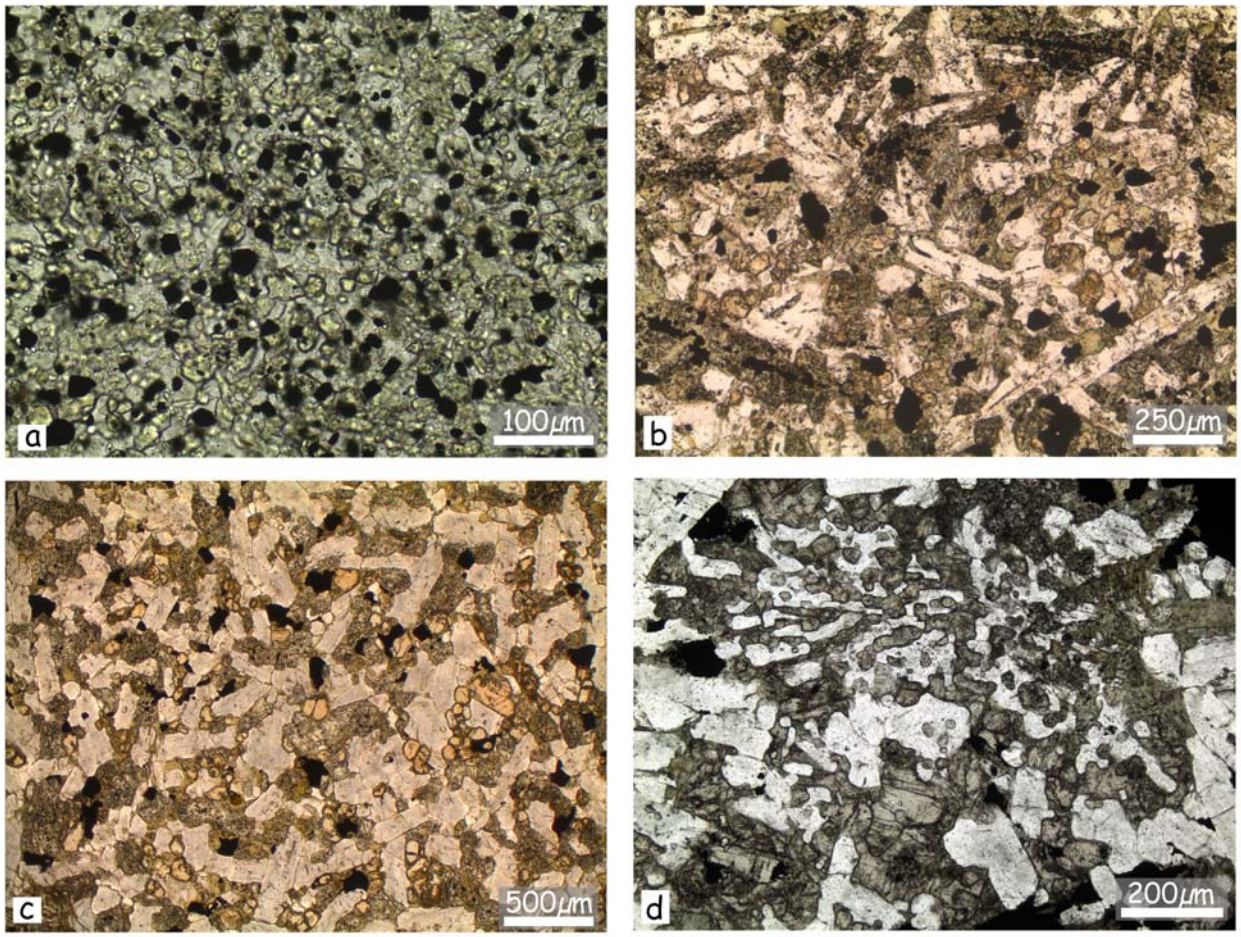

Figure 10. Photomicrographs of samples from IODP Hole 1256D (plane-polarized light). Photographs in Figures 10a and 10d are from the IODP database (Expedition 312; http://iodp.tamu.edu/janusweb/imaging/tsmicro.shtml). (a) High oxide concentration in a fine-grained granoblastic dike (recrystallized base of the sheeted dike complex; sample 312_1256D_205R1_10-14). (b) Coarser-grained, partially recrystallized texture (pyroxenes are granular and recrystallized) in diabase at the base of the granoblastic dike interval (sample 312_1256D_209R1_170-19). (c) Coarser-grained, partially recrystallized texture in the "granoblastic screen" located between gabbro 1 and gabbro 2 (interpreted as xenoliths of recrystallized dikes in the present study (see section 6.3 for further discussion); sample 312_1256D_227R1_30-34). Pyroxenes are granular, and oxide-bearing clinopyroxenes are inferred to crystallize after former amphiboles. (d) Patch with structure interpreted as a former granoblastic domain in isotropic gabbro (sample 312_1256D_223R3_1-6).

granoblastic lithologies and xenoliths, and reach An_{74} in the protodike (Figure 12). Clinopyroxene Mg # ranges from 59 to 72 in granoblastic lithologies and reaches 75 in the protodike (Figure 12). Al_2O_3 and TiO_2 are significantly low compared to typically magmatic clinopyroxenes from oceanic mafic rocks and to those obtained experimentally in corresponding tholeiitic systems (Figure 13). TiO_2 is strongly correlated with Al_2O_3 (with $Al_2O_3/TiO_2 \approx 3$) and shows an apparent linear trend pronounced at low concentrations (Figure 13). CaO contents are high, and Cr_2O_3 is nearly always under detection limits. Orthopyroxenes are present only in protodikes and have an Mg # of 68. Amphibole compositions are variables, including actinolite, hornblende, edenite, and pargasite. One granoblastic dike sample from the Wadi Gideah area contains zoned plagioclases, with An_{22} cores and An_{38} rims. Granoblastic patches observed in the isotropic ophitic gabbros (Figure 7c) are similar in compositions to other granoblastic lithologies, with An_{48} plagioclases and Mg # = 69 for clinopyroxenes. Oxide bearing clinopyroxene from the truncated veins observed at the sheeted dike/gabbro transition (Figures 7g and 7h) plot in the TiO_2 versus Al_2O_3 linear trend (Figure 13).

[24] In oceanic plagiogranites, plagioclases are albite to oligoclase with An ranging from 7 to 27.

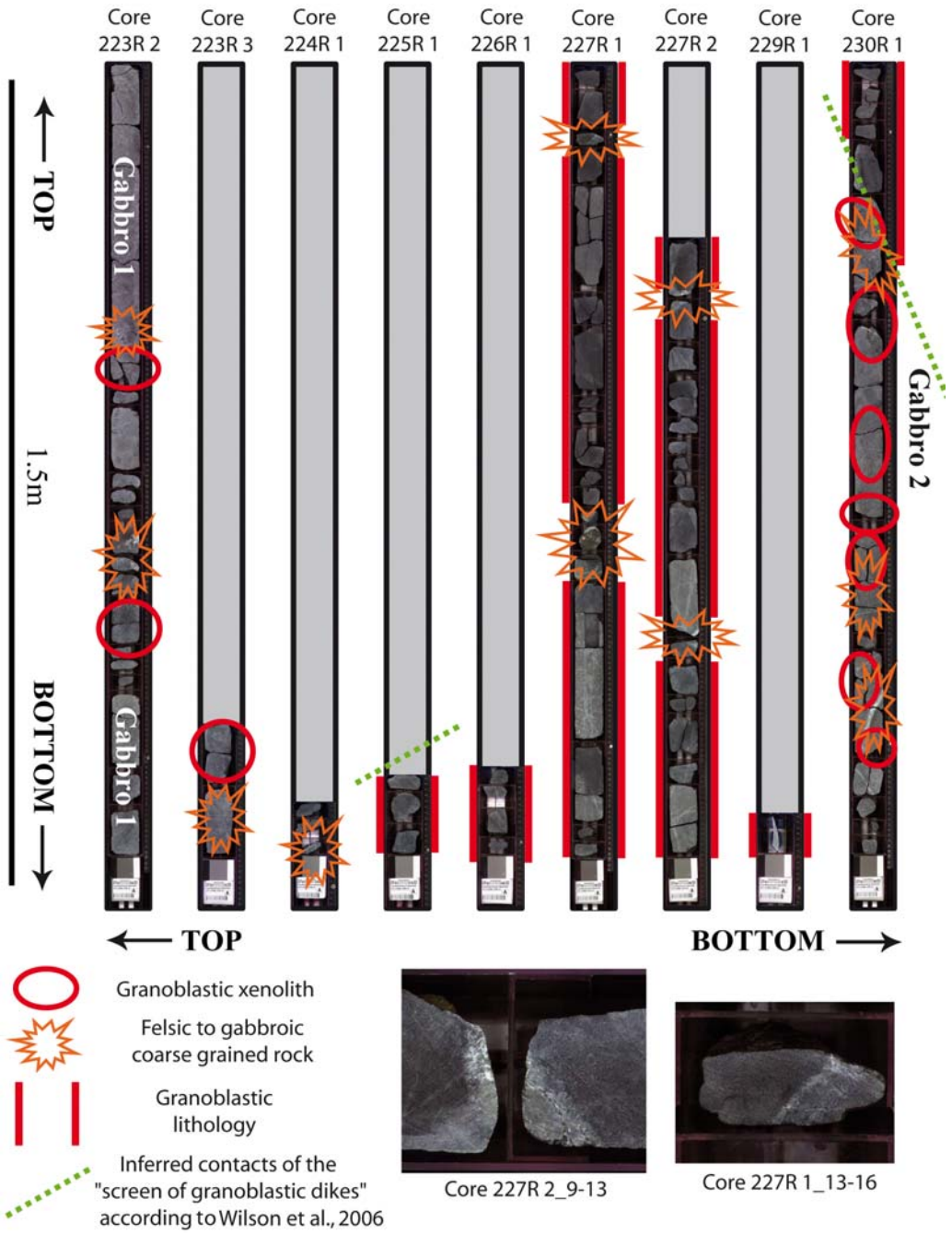

Figure 11. IODP 1256D drilled cores between 1450.8 and 1484.4 mbsf. From top to bottom, encountered lithologies are xenolith-bearing gabbro 1, granoblastic lithologies described as a ''screen of granoblastic dikes'' by *Wilson et al.* [2006], and xenolith-bearing gabbro 2. The two photographs show some of the felsic to mafic ''melts'' that crosscut the recrystallized granoblastic lithologies. Red circles highlight the xenoliths of granoblastic lithologies, and orange stars highlight the occurrence of felsic to gabbroic coarse-grained material. Intervals with recrystallized granoblastic texture are highlighted by thick red lines along the core margins. The dotted green lines represent the upper and lower limits of the ''screen of granoblastic dikes'' described by *Wilson et al.* [2006]. The continuous granoblastic domains are less than 1 m thick.

Small clinopyroxenes, which show petrographic features similar to those from granoblastic lithologies are characteristically low in Al, Ti, and Cr, and plot on the TiO_2 versus Al_2O_3 linear trend (Figure 13).

[25] Mineral compositions from the IODP Hole 1256D granoblastic lithologies are similar to those from the same lithologies in Oman (Table A1 and Figure 12). Plagioclase composition ranges from

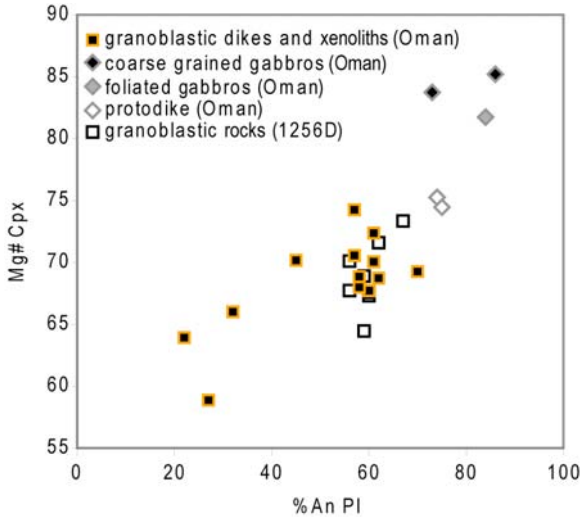

Figure 12. Mg # of clinopyroxene versus An content of plagioclases for recrystallized granoblastic dikes and xenoliths from Oman and from IODP Hole 1256D (average values for each sample). Protodike, foliated gabbro, and coarse-grained gabbro compositions are given for comparison. As low-temperature alteration has led to a late albitisation of some samples, the maximum values of the An content are used.

andesine (An_{41}) to labradorite (An_{67}). Clinopyroxenes range from augite to diopside, with Mg # between 63 and 74, low Al_2O_3 and low TiO_2 contents, high CaO content, and Cr_2O_3 always under the detection limit (Figure 13). These clinopyroxenes plot in the TiO_2 versus Al_2O_3 linear trend (Figure 13). Orthopyroxenes are enstatite, with Mg # between 58 and 66. Amphiboles are hornblende and pargasite with late actinolite.

5.2. Isotropic/Foliated Gabbro Transition in Wadi Gideah

[26] Xenolith samples contain plagioclase ranging from An_{31} to An_{57}. Clinopyroxenes are either augite or diopside, and have Mg # between 61 and 77. They are depleted in Al_2O_3 and TiO_2, and enriched in CaO; Cr_2O_3 is always under detection limits; they plot in the TiO_2 versus Al_2O_3 linear trend (Figure 13). Amphiboles are hornblende.

[27] Gabbroic samples contain olivine with Mg # of 78; plagioclases range from An_{57} to An_{86} and clinopyroxenes are mostly diopside with Mg # of 86. Clinopyroxenes have high Al_2O_3 contents and high Cr_2O_3 contents (up to ~1 wt %) and plot out of the TiO_2 versus Al_2O_3 linear trend defined by clinopyroxenes from granoblastic lithologies at the base of the sheeted dikes. Amphiboles are pargasite.

5.3. Foliated Gabbros

[28] In foliated gabbros olivine is Fo_{73}, and plagioclase is bytownite with An_{84}. Clinopyroxenes range from augite to diopside, with Mg # of 88 on average, and plot out of the TiO_2 versus Al_2O_3 linear trend defined by clinopyroxenes from the granoblastic samples. Cr_2O_3 content is 0.55 wt %, clearly above the detection limit. Amphiboles are hornblende, edenite and pargasite. In the domains of foliated gabbros that contain late orthopyroxene and pargasite rims around olivine, plagioclase is bytownite with An_{83}, clinopyroxenes are augite to diopside with Mg # of 82 in average and also plot out of the TiO_2 versus Al_2O_3 linear trend defined by granoblastic clinopyroxenes. Cr_2O_3 contents are also above the detection limit (0.17 wt %). Orthopyroxene that rims olivine is enstatite with an average Mg # of 73.

5.4. Thermometry

[29] Calculated temperatures obtained from amphibole compositions with the *Ernst and Liu* [1998] semiquantitative thermometer, from coexisting amphibole and plagioclase with the *Holland and Blundy* [1994] thermometer, and from coexisting clinopyroxenes and orthopyroxenes with the *Andersen et al.* [1993] thermometer, are summarized in Table 1. The errors on these temperature estimates are indicated in Table 1 for the two-pyroxene thermometer, are ±35–40°C for the *Holland and Blundy* [1994] thermometer, and are not estimated by *Ernst and Liu* [1998] for their semiquantitative thermometer. Temperatures obtained from amphiboles compositions reach ~1020°C with the *Ernst and Liu* [1998] thermometer, ~820°C with the *Holland and Blundy* [1994] thermometer, and are consistent with granulite facies conditions. Temperatures obtained with the *Andersen et al.* [1993] thermometer reach 1030°C in granoblastic lithologies (xenoliths and truncated dikes) and 950°C in protodikes.

6. Discussion

6.1. A Dynamic Melt Lens

[30] The occurrence of a sharp contact between sheeted dikes and underlying gabbro, with abruptly truncated sheeted dikes, and of gabbroic to oceanic plagiogranitic dikelets intruding the sheeted dike, together with the evidence that gabbroic and oceanic plagiogranitic bodies crosscut former dike margins, imply a magmatic contact that is not disturbed by

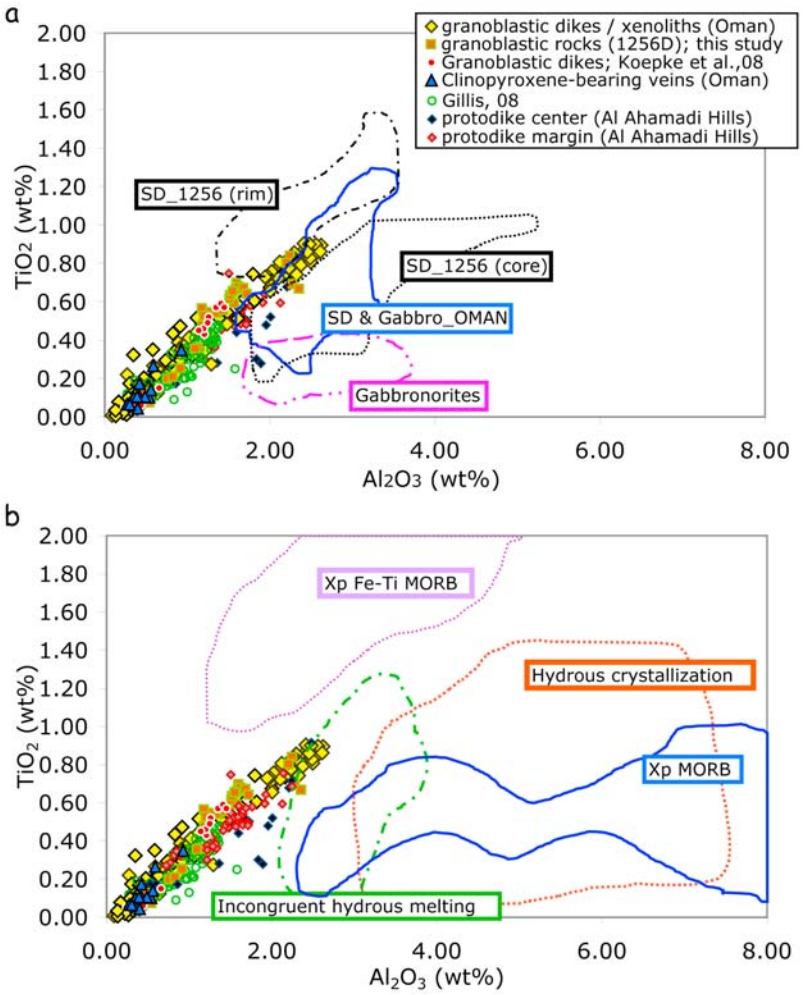

Figure 13. TiO_2 versus Al_2O_3 in clinopyroxene for recrystallized granoblastic dikes and xenoliths from Oman and from IODP Hole 1256D. Fields represent data from literature for comparison: (a) natural samples and (b) experimental samples. Natural sample data are from *Dziony et al.* [2008] for the IODP Hole 1256D sheeted dikes not affected by granoblastic imprint (SD), from *Miyashita et al.* [2003] and *Pallister and Hopson* [1981] for the Oman ophiolite sheeted dikes and gabbros, and from *Boudier et al.* [2000] and *Gerbert-Gaillard* [2002] for the Oman gabbronorites. Experimental data are from *Snyder et al.* [1993], *Toplis and Carroll* [1995], and *Toplis et al.* [1994] for Fe-Ti MORB crystallization experiments (Xp Fe-Ti MORB); from *Berndt et al.* [2005] and *Feig et al.* [2006] for hydrous crystallization experiments in primitive MORB-type system; from *Grove and Bryan* [1983] and *Kinzler and Grove* [1992] for MORB crystallization experiments (Xp MORB); and from *Koepke et al.* [2004] for clinopyroxenes formed during hydrous partial melting of gabbros. Note that the clinopyroxene in the granoblastic lithologies form a characteristic linear trend at low concentrations, which is not shown by data for typical MORB magmatic processes, neither from natural occurrences nor from experiments.

tectonics (Figure 6). This magmatic contact could be the consequence of either the upwelling of a magma body which intrudes the dikes, or hydrous partial melting of the dikes. The latter could be induced either by an injection of hydrous fluids in a still hot (>850°C) environment [*Nicolas et al.*, 2008], or by the upwelling of the magma body which reheats some previously hydrothermally altered lithologies above their hydrous solidus [e.g., *Coogan et al.*, 2003; *Wilson et al.*, 2006]. Both hydrous melting processes lead to the generation of felsic to mafic melts, depending on temperature [*Beard and Lofgren*, 1991; *Koepke et al.*, 2005b]. Observations made in Oman and in IODP Hole 1256D allow the identification of active processes in the root zone of the sheeted dike complex.

[31] The granoblastic textures at the base of the sheeted dikes could be ascribed to contact metamorphism, as proposed for IODP Hole 1256D [*Wilson et al.*, 2006; *Koepke et al.*, 2008], the Troodos ophiolite [*Gillis and Roberts*, 1999], or Wadi Him in

Geochemistry Geophysics Geosystems G3 FRANCE ET AL.: FOSSILIZATION OF A DYNAMIC MELT LENS 10.1029/2009GC002652

Table 1. Maximum An Content of Plagioclase and Temperature Estimates[a]

Lithology	Location	Sample	%An Max	T_{max} Amp (°C)	T Amp H&B (°C)	T Opx-Cpx (°C)
RZ_dike	Gideah	08OL15b-leuco	60	660	692	–
RZ_dike	Gideah	08OL15b	61	922	728	–
RZ_dike	Gideah	08OL01e	60	571	615	–
RZ_dike	Gideah	08OL04a	58	885	731	–
RZ_dike	Gideah	08OL05a	62	633	680	–
RZ_dike	Gideah	07OL51b	22	562	739	–
RZ_dike	Gideah	08OL06i	47	754	640	–
RZ_Cpx vein	Gideah	08OL15i1	70	853	711	–
RZ_dike	Al Ahmadi	08OL07b	32	650	820	–
RZ_Plagiogranite	Gideah	07OL48d	27	–		–
Granoblastic patch in isotropic gabbro	Gideah	08OL01d	58	726	784	–
Xenolith in isotropic gabbro	Gideah	08OL06f	61	998	727	–
Xenolith close to isotropic/foliated gabbro transition	Al Ahmadi	08OL29e	45	665	729	–
Xenolith close to isotropic/foliated gabbro transition	Gideah	07OL49c1	57	758	803	–
Xenolith close to isotropic/foliated gabbro transition	Gideah	07OL49b1	57	788	772	–
Coarse-grained gabbro	Gideah	07OL49d1	73	1023	811	–
Coarse-grained gabbro	Gideah	07OL49d2	86	953	683	–
Protodike border	Al Ahmadi	08OL29c	75	831	672	949 ± 40
Protodike center	Al Ahmadi	08OL29d	74	868	676	–
Foliated gabbro A	Al Ahmadi	08OL29b	87	750	701	–
Foliated gabbro B	Al Ahmadi	08OL29a	84	999	731	773 ± 18
Granoblastic dikes	1256D	312_1256D_D202R1_8-10	59	592	604	1010 ± 24
Granoblastic screen	1256D	312_1256D_D225R1_4-8	67	887	699	965 ± 77
Granoblastic screen	1256D	312_1256D_D226-R1-4-6	59	823	724	1019 ± 34
Granoblastic screen	1256D	312_1256D_D227R1_30-34	56	632	665	956 ± 77
Granoblastic xenolith in isotropic gabbro	1256D	312_1256D_D230R1_15-20	56	–		1017 ± 30
Granoblastic xenolith in isotropic gabbro	1256D	312_1256D_D230R1_73-80	60	713	769	1030 ± 35
Granoblastic xenolith in isotropic gabbro	1256D	312_1256D_D230R1_87-90	60	704	753	1028 ± 21
Lower granoblastic interval	1256D	312_1256D_D233R1_14-18	62	–		1003 ± 50

[a] Amphibole thermometer (*Ernst and Liu* [1998] (T_{max}) and *Holland and Blundy* [1994] (H&B)) and two-pyroxene thermometer [*Andersen et al.*, 1993]. Pl_c, plagioclase core; Pl_b, plagioclase rim; Amp, amphibole; ilm, ilmenite; magt, magnetite; Cpx, clinopyroxene; Chlo, chlorite; Ol, olivine; Opx, orthopyroxene; Qz, quartz.

Oman [*Gillis*, 2008]. However, in contrast to what is postulated by *Gillis* [2008], contact metamorphism is not the only process producing well-equilibrated fine-grained textures. Alternatively, *Rothery* [1983], *Nicolas and Boudier* [1991], and *Nicolas et al.* [2008] argue that microgranular textures of "protodike" margins are magmatic and represent, in a steady state system, the roots of the sheeted dikes. We propose that the late dikes described herein correspond to such protodikes. However, several features described in the dikes truncated by gabbro and in granoblastic xenoliths depart from the protodike description:

[32] 1. The core of truncated dikes is also granoblastic (Figures 7b and 9d) while the core of protodikes is described as texturally close to isotropic ophitic gabbro [*Nicolas et al.*, 2008] (Figure 9f).

[33] 2. All granoblastic xenoliths and truncated dikes described in this study contain either high oxide concentrations (up to 10% of ilmenite + magnetite), or numerous oxide inclusions in pyroxenes, or both (Figures 7, 9c, and 9d). The observed oxide concentrations depart from the published protodike descriptions [see, e.g., *Nicolas et al.*, 2008, Figure 6a], and the occurrence of numerous tiny oxides inclusions in the clinopyroxenes of granoblastic lithologies is interpreted as a consequence of the granulitic overprint of previously hydrothermally altered dike rocks. *Koepke et al.* [2008] described the evolution of the granoblastic metamorphism in the drilled core from site 1256D and show that similar clinopyroxenes with oxide inclusions, present in the granoblastic dikes from IODP Hole 1256D, recrystallized from former amphiboles. In Oman, the occurrence of veins composed of oxide-bearing clinopyroxenes at the base of the truncated granoblastic sheeted dikes (Figures 7g and 7h) also points to a metamorphic origin. Amphibole-bearing hydrothermal veins are common at the base of the sheeted dike complex, but magmatic clinopyroxenite veins have not been described. We postulate here that these peculiar veins result from the recrystallization of amphibole-bearing hydrothermal veins through dehydration reactions during a reheating episode.

[34] 3. Clinopyroxenes from the prograde veins have compositions similar to those in the granoblastic dikes and xenoliths (Table A1 and Figure 13). They are poor in Al_2O_3, rich in CaO and plot in the TiO_2 versus Al_2O_3 linear trend defined by granoblastic clinopyroxenes (Figure 13). These compositions clearly differ from published ones for magmatic natural and experimental clinopyroxenes in oceanic lithologies (Figure 13). Such compositions with uncommon low Al_2O_3 contents may indicate, as shown by *Spear and Markussen* [1997], inframagmatic temperature equilibration (<1000°C), and are consistent with granulite facies conditions. The correlation of Al_2O_3 with TiO_2 could be explained by the fact that Ti stability in clinopyroxene is linked to its Al content [*Lundstrom et al.*, 1998]. The very low Cr_2O_3 content (always under detection limits) also supports the metamorphic origin of these minerals, as magmatic oceanic pyroxenes contain higher amounts of Cr [*Koepke et al.*, 2008]. An incongruent origin linked to low degrees of hydrous partial melting of previously hydrothermally altered dikes may also be proposed as it would also result in the destabilization and dehydration of amphibole-bearing lithologies.

[35] All granoblastic xenoliths and truncated dikes have similar petrological and geochemical characteristics, which are clearly different from protodikes. Their occurrence attests to a reheating stage that we relate to the upwelling of the top of the melt lens. The presence of granoblastic xenoliths and patches in the isotropic ophitic gabbros, which are believed to represent some reheated pieces of previously hydrothermally altered sheeted dike, attests to assimilation processes, and is consistent with an upwelling stage. Upward migration of the melt lens summit can be triggered either by an upward migration of the whole melt lens, or by an inflation of its volume. Alternatively, the intrusive contact of gabbro with sheeted dikes, and associated reheating could be related to the off-axis injection of a new melt lens, as recently imaged at the East Pacific Rise by *Canales et al.* [2008].

[36] The common occurrence of leucocratic rocks (oceanic plagiogranites) at the contact between the sheeted dikes and the underlying gabbros may be related either to differentiation at the top of the melt lens or to hydrous partial melting of the sheeted dikes [*Pedersen and Malpas*, 1984; *Beard and Lofgren*, 1991]. In the present case, because reheating and magma upwelling are documented, and temperatures up to 920°C and 1000°C are calculated for the granoblastic dikes and the xenoliths, respectively, leucocratic rocks are likely generated by hydrous partial melting induced by reheating of hydrothermally altered dikes. This hypothesis is also supported by the occurrence, in the oceanic plagiogranites, of relic pyroxenes that are chemically identical to those of the reheated granoblastic dikes (Table A1). The reverse zoning observed in

plagioclases at the base of one granoblastic dike in Wadi Gideah may result from an early hydrothermal alteration stage leading to the albitisation of plagioclases (An_{22}), followed by hydrous partial melting that leads to the generation of wet dioritic melts percolating through the base of dikes and crystallizing An_{38} plagioclase rims.

[37] The late dikes (hereafter "dike 2," Figure 5) that crosscut the isotropic ophitic gabbros postdate the contact between the gabbro and the sheeted dikes, and imply the crystallization of the isotropic ophitic gabbros subsequently to a downward migration of the melt lens. Dikes 2 could either be injected from the remaining melt lens, or be injected laterally along axis, or be related to an off-axis magmatic episode. Because dikes 2 grade downward to protodikes, they must be emplaced in a still hot environment (~950°C according to the two-pyroxene thermometer), hence not far off axis. The low Al content of the clinopyroxenes present in protodikes also attests to a relatively low temperature equilibration that can correspond to subsolidus conditions. The equilibration of pyroxenes at these temperatures may result from slow cooling of the isotropic gabbro body. We interpret dikes 2 intrusion in ophitic gabbro as illustrating the downward migration of the top of the melt lens. This downward movement results in the crystallization of the isotropic ophitic gabbros, and allows injection of new dikes in this still hot environment from the underlying melt lens or laterally, along axis. The downward movement could be triggered either by downward migration of the whole melt lens or by a deflation of its volume.

[38] In Wadi Gideah, the sheeted dikes/gabbro transition is a well-defined contact that can be mapped in the field (Figure 2). We interpret the mapped contact (Figure 2c) as reflecting a ~50 m depth variation of the melt lens roof over a distance of ~150 m. However, one cannot exclude that this offset is related to a thin fault or shear zone, which is not visible due to the poor outcropping conditions between the two hills. Larger amplitude (one to several kilometers) variations of the melt lens summit depth have been documented by seismic imaging at the East Pacific Rise [*Cormier*, 1997; *Hussenoeder et al.*, 1996; *Solomon and Toomey*, 1992; *Singh et al.*, 1998]. An along-axis "fine-scale segmentation" of the melt lens reflector has been recently imaged in the 9°50N region of the East Pacific Rise [*Carbotte et al.*, 2008], and reveals comparable depth variations of tens of meters.

6.2. Stoping, Assimilation, and Coarse-Grained Gabbros

[39] In the context of magma upwelling at the root of the sheeted dikes, the occurrence of oxide-rich, granoblastic xenoliths in the isotropic ophitic gabbros is significant. Some xenoliths are located near the contact with sheeted dikes, but most of them appear to be accumulated at the base of the isotropic ophitic gabbro horizon, as seen in Al Ahmadi Hills, above the contact with foliated gabbros (Figure 8). The density of granoblastic xenoliths is ~3.02 g cm^{-3} (by considering the modal proportions from our petrological observations and crystal densities at 1000°C [*Fei*, 1995]: ~60% plagioclase, d ≈ 2.6 g cm^{-3}; ~30% clinopyroxene, d ≈ 3.3 g cm^{-3}; ~5% magnetite, d ≈ 4.9 g cm^{-3} and ~5% ilmenite, d ≈ 4.5 g cm^{-3}). Because plagioclase is the only mineral of the granoblastic assemblage that has a density lower than the estimated whole rock, and samples with plagioclase contents >60% are rare, this estimated density is a lower bound. It is significantly higher than the density of a dry basaltic melt that is thought to fill the melt lens, which is ~2.7 g cm^{-3}, (calculated with a pressure of 1 kbar and a temperature of 1100°C [e.g., *Lange and Carmichael*, 1990]). The melt density can be slightly higher if more evolved, and slightly lower if hydrous, but such melts are not expected to be dominant in the melt lens. Stoping is also controlled by the rheology of the host magma. It requires that the crystal content in the melt lens is low enough that it does not change significantly the density and viscosity of the magma. Geophysical and petrophysical studies show that underneath the melt lens is the main magma chamber, which contains on average a minimum of 80% of crystals [e.g., *Caress et al.*, 1992; *Collier and Singh*, 1997; *Singh et al.*, 1998; *Lamoureux et al.*, 1999; *Dunn et al.*, 2000; *Crawford and Webb*, 2002]. Xenoliths have therefore sunk through the mostly liquid melt lens to accumulate at its floor. These xenoliths are now observed in the lower part of the isotropic ophitic gabbros, which we must then interpret as representing the melt lens fossilized once away from the axis. As the floor of the melt lens is believed to continuously subside [e.g., *Nicolas et al.*, 2009], we speculate that the xenolith accumulation that we observe occurred close to the off-axis margin of the melt lens. Presumably, dike fragments are also stoped on axis, but they cannot be preserved as they are either fully assimilated or entrained and transposed downward within the foliated gabbros [*Boudier et al.*, 1996; *Nicolas et al.*, 2009] in which they are observed as

recrystallized microgabbronorite centimeter to decimeter thick lenses [*Boudier et al.*, 2000]. *Singh et al.* [1998] have shown that the melt lens is not continuous along the ridge axis but that it ranges from pure melt to mush. The partly crystallized zones may represent the first step toward the fossilization of the melt lens occurring when a decrease in the magmatic activity happens in a given section of the ridge.

[40] We also interpret the granoblastic patches (0.5 to 1 mm wide) in the ophitic gabbros as relics resulting from the partial assimilation of sheeted dike fragments (Figure 7c). The oxide-rich granoblastic texture of xenoliths is consistent, as described above, with a granulitic overprint, and related dehydration of previously hydrothermally altered lithologies. Enclosing gabbros contain amphiboles that record temperatures (~1020°C) higher than the hydrous solidus of gabbro, which points to the hydrated nature of the magma surrounding the xenoliths [*Koepke et al.*, 2005b; *Feig et al.*, 2006]. The concentration of coarse-grained gabbro around xenoliths (Figure 6f) is also consistent with magma hydration, as water is known to enhance crystal growth. In natural settings, high water pressure generally leads to more oxidizing conditions [e.g., *Botcharnikov et al.*, 2005]. However, the hydrated nature of magmas that produced coarse-grained gabbros is not consistent with differentiation under reducing conditions as proposed by *MacLeod and Yaouancq* [2000]. *Nicolas et al.* [2008] have proposed that coarse-grained gabbros could also be generated by the arrival of hydrothermal fluids in the root zone at high temperature (~1100–1200°C), leading to local, nearly total melting of gabbroic rocks. The coarse-grained gabbros described herein are spatially associated to granoblastic xenoliths that come from the base of the sheeted dike (~100 m above in the section), and sunk through the melt lens. Therefore, we propose an alternative process for the genesis of coarse-grained gabbro present in the studied areas that involves fluids brought by the dehydration of stoped and assimilated hydrothermally altered diabases in the melt lens. A way to test the role of recycled water in the genesis of coarse-grained gabbro would be to analyze the fluorine and chlorine contents of amphiboles [*Coogan et al.*, 2001]. Amphiboles with high chlorine contents and low fluorine contents attest to a hydrothermal origin, and the ones with low chlorine contents and high fluorine contents attest to a magmatic origin. We postulate that amphibole crystallizing from melts that are hydrated through recycling of previously hydrothermally altered dikes may have high fluorine and high chlorine contents. *Coogan* [2003] proposed that the fluids leading to the crystallization of many of the magmatic amphiboles that are present in the Oman ophiolite gabbros are brought by such recycling processes. A review of the amphibole compositions presented by *Coogan* [2003] shows that many of them are fluorine and chlorine rich (>1000 ppm), which is consistent with our hypothesis. *Gillis et al.* [2003] show that magmatic amphiboles from fast spreading ridges are chlorine enriched regarding the ones from slow spreading ridges; it also argues for important recycling of hydrothermally altered lithologies at fast spreading centers.

[41] Another consequence of stoping and assimilation of hydrothermally altered diabases is the geochemical contamination of the melt lens. Assimilation processes in the melt lens should have a significant effect on the composition of the melts, in particular for volatile elements [*Gillis et al.*, 2003]. Our results are consistent with the model [*Coogan et al.*, 2003], which states, from the chlorine content of EPR basalts [e.g., *Michael and Schilling*, 1989; *Michael and Cornell*, 1998], that ~20% of the oceanic crust may go through a cycle of crystallization, alteration, and assimilation.

6.3. Comparison With IODP Hole 1256D

[42] Many features in IODP Hole 1256D match the observations made in the Oman ophiolite. In particular, the root of the sheeted dike complex is recrystallized to granoblastic textures, oceanic plagiogranites are present close to the dike root zone, the isotropic ophitic gabbro horizon contains granoblastic xenoliths and patches, and the compositions of minerals that form the granoblastic textures are similar to Oman ones (Table A1 and Figures 10–13). IODP Hole 1256D can therefore be included in the same general model for the melt lens dynamics and for the relationships between the hydrothermal and magmatic systems.

[43] In the Al Ahmadi Hills section, large xenoliths (up to 1.5 m) displaying granoblastic textures are observed close to the isotropic ophitic gabbros/foliated gabbros transition, and are highly concentrated in some areas. These xenoliths can be partly assimilated by enclosing gabbro, and be associated to felsic melts at their border. In IODP Hole 1256D, the ~20 m thick "screen of granoblastic dikes" located ~50 m below the sheeted dike/gabbro contact [*Wilson et al.*, 2006] is poorly recovered (<30%), and several thin horizons of gabbros and oceanic plagiogranites isolate larger (<1 m) granoblastic zones (Figure 11). In the light of the obser-

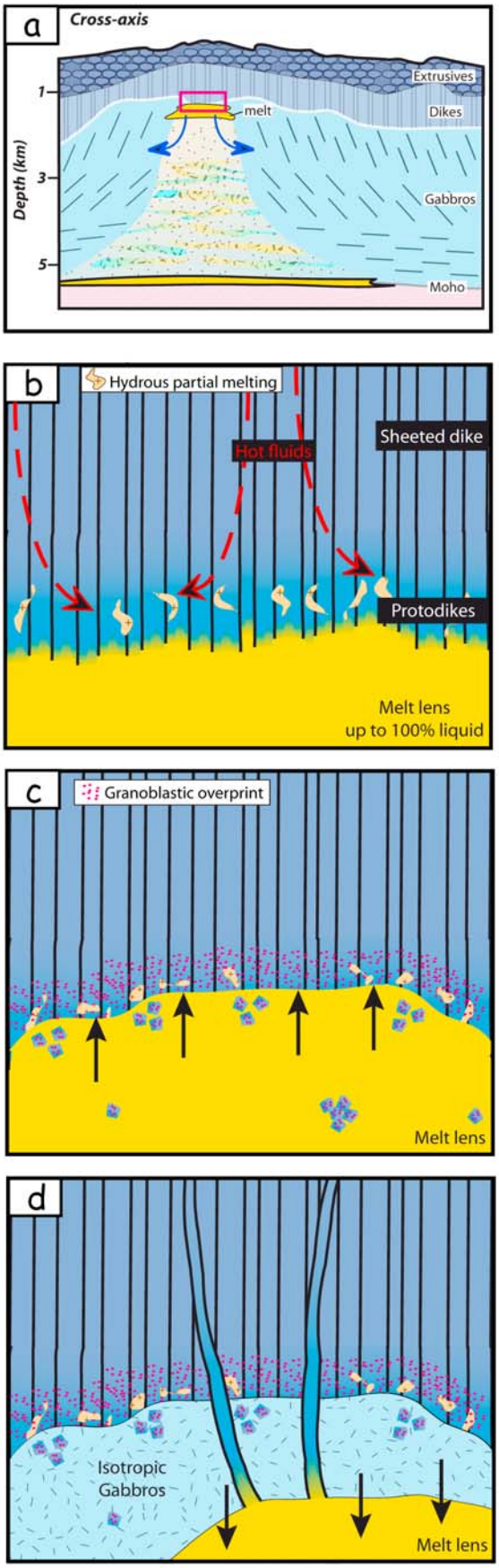

vations made in Oman, we propose that this zone may correspond to granoblastic xenoliths, surrounded by silicic to gabbroic melts, which are accumulated in the isotropic gabbro horizon about 50 m below the sheeted dike/gabbro contact. It also suggests that the bottom of Hole 1256D is close to the transition with the foliated gabbros and so to the bottom of the fossilized melt lens that would be ~100 m thick. This interpretation is in contrast with the model presented by *Koepke et al.* [2008, Figure 14c]; they interpreted the two gabbro screens as two separate intrusions into the lowermost part of the granoblastic dikes, shortly above the top of the fossilized magma chamber, which was hence not yet reached in Hole 1256D.

6.4. A general Model

[44] The model presented here elaborates on detailed mapping, sampling and descriptions made in the Wadi Gideah and Al Ahmadi Hills areas, and on subsequent petrological and geochemical study. We visited ~10 other areas in the Oman ophiolite, which are consistent with our model. As described above, observations and analyses made on samples from the sheeted dikes/gabbro transition zone in IODP Hole 1256D, are also consistent with what is observed in Oman, and with our model.

[45] The evolution of a melt lens can be tracked through the observed geological and petrological features (Figure 14). We first assume an episodic, steady state melt lens that injects dikes in the upper crust (Figure 14b). The base of these dikes is made of protodikes with microgranular margins and grade

Figure 14. General schematic model for the dynamics of the melt lens. (a) Schematic cross section at the axis of a fast spreading ridge (modified after *Sinton and Detrick* [1992]). The red rectangle indicates the location of the axial melt lens. (b) Steady state stage with injection of dikes that have at their base microgranular margins (protodikes). Hydrous partial melting is proposed to occur in the root zone of the sheeted dike complex as a result of hydrothermal fluid intrusion [*Nicolas et al.*, 2008]. (c) Upward migration of the top of the melt lens resulting in reheating and recrystallization of the base of the dikes (red dots) to granoblastic dikes and in assimilation of xenoliths in the melt lens. Hydrous partial melting of the hydrothermally altered base of the dikes can also occur. (d) Downward migration of the top of the melt lens resulting in the crystallization of the isotropic ophitic gabbros. New dikes can be injected laterally or from below; their root is typical of protodikes, with microgranular margins, and they grade upward to "classical" dikes with chilled margins (see section 6.4 for further discussion).

upward to "normal" dikes with chilled margins [*Rothery*, 1983; *Nicolas and Boudier*, 1991; *Nicolas et al.*, 2008]. In this steady state system, the injection of hydrothermal fluids in the dike root zone may trigger, locally, hydrous partial melting [*Nicolas et al.*, 2008]. This steady state system can evolve as a dynamic one with upward and downward migrations of the top of the melt lens (Figures 14c and 14d) as proposed by *Hooft et al.* [1997], *Gillis* [2002, 2008], *Gillis and Roberts* [1999], *Gillis and Coogan* [2002], *Coogan et al.* [2003], and *Koepke et al.* [2008]. These migrations can represent either vertical movements of the melt lens itself or inflation and deflation of its volume. Lateral migrations or injections may also be proposed as near-axis melt lenses have recently been observed at the East Pacific Rise [*Canales et al.*, 2008].

[46] Upward migrations or lateral intrusions can be for example triggered by magma replenishment and result in the assimilation of the hydrothermally altered dikes, with the formation of xenoliths (Figure 14c). The roof is reheated by magma upwelling, and hydrothermally altered sheeted dikes recrystallize in a granulitic granoblastic assemblage; they may locally undergo hydrous melting. Granoblastic lithologies also develop in xenoliths, which are partly to totally assimilated while sinking through the melt lens. If not totally assimilated, xenoliths sink down to the melt lens floor where they accumulate. They can then either be entrained downward in the igneous lower crust and be transposed in foliated gabbros, or be fossilized with the isotropic ophitic gabbros.

[47] Downward or lateral migrations can be triggered by a waning magmatic activity of the melt lens and/or by an eruption-related draining stage, and result in the crystallization of the isotropic gabbros at the roof and/or at the sides of the melt lens (Figure 14d). This crystallization corresponds to a partial fossilization of the melt lens which would become complete if melt supply to the melt lens was stopped.

[48] Numerous scenarios can be elaborated combining the three stages described above: steady state, upward migration of the top of the melt lens, and downward migration of the top of the melt lens. Several episodes of upward and downward migrations may alternate, and only the highest level reached by the top of the melt lens will be eventually recorded at the contact with the sheeted dike. In the case of an upward migration following a downward one, the melt lens would assimilate the recently crystallized gabbros, and the overlying recrystallized sheeted dike if the upward migration is large enough. The presence of gabbroic xenoliths in the isotropic ophitic gabbro horizon attests to this process.

6.5. Time Scale Constraints

[49] At fast spreading ridges, the time scales associated with magma migration, its residence within the main magma chamber and within the melt lens, and depth variations of the melt lens represent major parameters of the dynamics of oceanic crust formation. Unfortunately these time scales remain poorly constrained. We compile here published data dealing with these different time scales in order to replace our model on the evolution of a dynamic melt lens into a possible time frame.

[50] Seismic reflection profiles of the East Pacific Rise (EPR) at 19°S (spreading rate: ~15 cm/y [*Hooft et al.*, 1997]) suggest variations in the magma supply on a time scale of ~100,000 years. *Hooft et al.* [1997] also propose that spreading events like dike intrusions and eruptions occur on much shorter time scales (tens to hundred years). *Lagabrielle and Cormier* [1999] propose that elongated summit troughs present at the EPR (17–18°S, spreading rate: ~15 cm/y) represent elongated collapsed calderas that form every ~100,000 years when a given ridge section deflates as a result of waning magma supply. *Pollock et al.* [2009] propose, based on spatial and temporal variations of basalt MgO contents at the EPR (Pito Deep, spreading rate: ~14 cm/y), that the magmatic temperatures, hence the magma supply, remain constant over time scales of tens of thousands of years, suggesting a nearly continuous magma recharge of the system at that time scale. It is in agreement with the observations of *Sinton et al.* [2002] on the south EPR that suggest, based on the MgO content of successive units, that magmatic temperatures can remain constant over hundreds to tens of thousands of years.

[51] *Rannou et al.* [2006] use a mathematic model based on geochemical data to infer that the magmatic system of the EPR at 17–19°S has a replenishment period of ~750 years for a magma residence time of ~300 years. This residence time is in good agreement with the estimate of *Rubin et al.* [2005] who propose, based on ^{210}Pb-^{226}Ra-^{230}Th radioactive disequilibria on samples from the EPR at 9°N (spreading rate: ~11 cm/y) and 17°S, and from the Juan de Fuca Ridge (spreading rate: ~5.6 cm/y), that melt can be transferred within decades from the mantle to melt lens where it mixes and resides during ~200–400 years. *Rubin and Sinton* [2007]

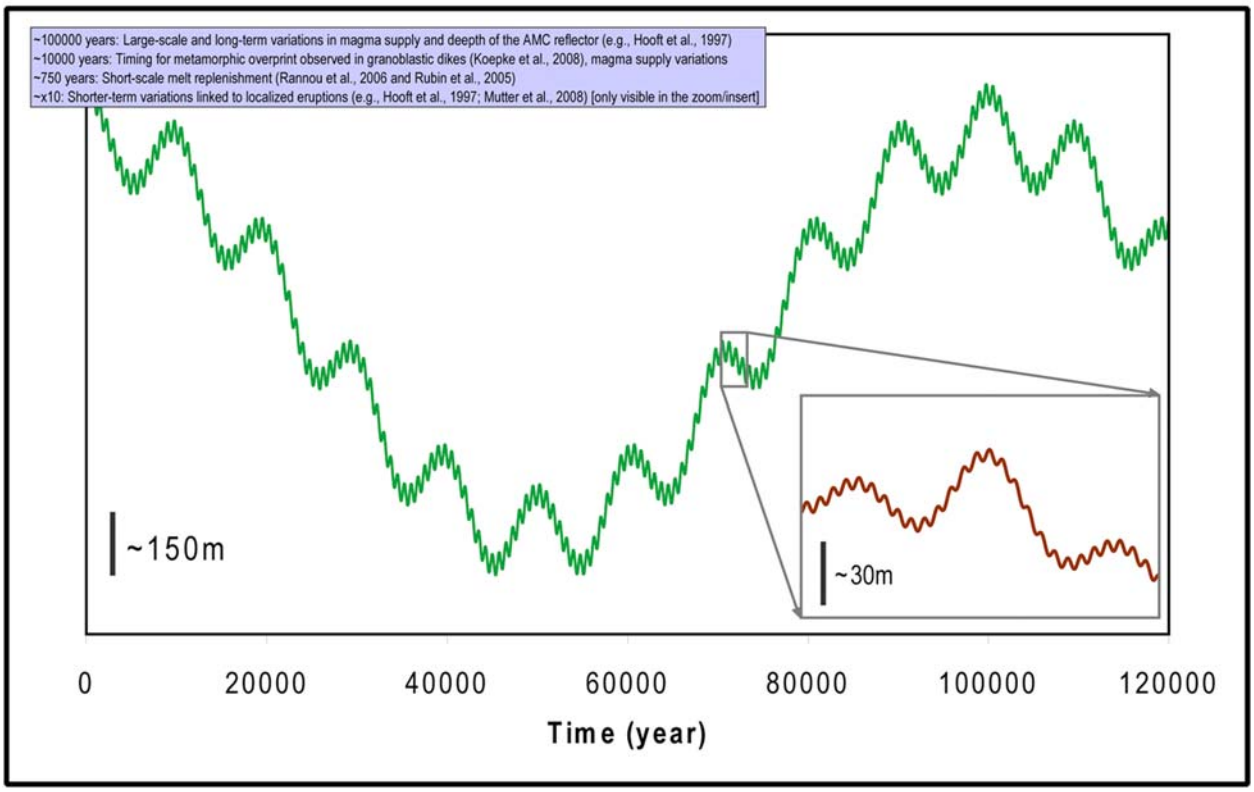

Figure 15. Compilation of estimated time scales for the dynamics of the melt lens in a depth versus time schematic graph. Four periods of depth variation are displayed (100,000, 10,000, 750, ×10 years). The insert on a portion of the curve allows the visualization of the shortest time period (×10 years). See section 6.5 for further discussion.

also propose a magma replenishment time <1000 years at fast spreading ridges. Using the chemical zonations of olivine crystals present in four samples from the EPR (9°30′N and 10°30′N), *Pan and Batiza* [2002] have proposed that magma mixing events and eruptions may be in some cases separated by times as short as a few months.

[52] Preliminary results of the recent multistreamer reflection imaging experiment in the 9°50′N region of the EPR [*Mutter et al.*, 2008] show significant variation in the depth of the melt lens reflector between 1985 and 2008 at 9°50′N, possibly as a result of the 1991 and/or 2005–2006 eruptions in that area, while there is no significant variation observed at 9°30′N and 9°40′N. *Carton et al.* [2008] report a variation in the reflectivity strength of the melt lens that they interpret as indicating a lower melt percentage between 9°45.2′N and 9°51.9′N, consistent with melt drainage during 1991 and 2005–2006 eruptions. These observations suggest that if replenishment has occurred or started since the last eruption, it is either incomplete or reduced (compared to the erupted melt volume). The timing between these events is in agreement with the time scale of ten to tens of years proposed for spreading events by *Hooft et al.* [1997]. *Sinton et al.* [2002] and *Bergmanis et al.* [2007] also propose that eruptions along intermediate to superfast spreading centers are highly episodic and have repose times of ten years to a few hundred years.

[53] *Gillis* [2008] and *Koepke et al.* [2008] have tried to estimate the duration of the thermal overprint, which we link to upward movements of the melt lens summit, by studying plagioclase zoning in granoblastic domains. *Gillis* [2008] estimates a minimum duration of 50 years for Hess Deep sample (spreading rate: ~13.5 cm/year). *Koepke et al.* [2008] propose an overprint duration of ~10,000 years for a sample from IODP Hole 1256D.

[54] In summary, multidisciplinary results provide indirect constraints on time scales for the vertical fluctuations of the melt lens ranging from a few tens of years to ~100,000 years. In Figure 15, we propose a way to take into account these apparently contrasting results and to interpret them in a single schematic model. Four different time scales, consistent with published estimates, are used to describe the evolution of the summit of the melt lens: 100,000, 10,000, 750 and tens of years (Figure 15).

These different time scales correspond to different processes and/or to different spatial scales. The long period (~100,000 years) proposed by *Hooft et al.* [1997] may represent variations in the magma supply from the mantle and correspond to variations of the depth of the melt lens in the scale of several hundreds of meters. The higher the spreading rate (hence the magma supply), the shallower the depth of the melt lens [*Purdy et al.*, 1992; *Phipps Morgan and Chen*, 1993; *Wilson et al.*, 2006]. The ~10,000 year period is identified by *Koepke et al.* [2008] and *Pollock et al.* [2009] and may correspond to temporary high positions of the melt lens related to shorter-term variations in the magma supply. The ~750 years period is the one identified by *Rannou et al.* [2006], *Rubin et al.* [2005], and *Rubin and Sinton* [2007] for the melt lens replenishment. The shortest period corresponds to local, individual eruptions [e.g., *Hooft et al.*, 1997; *Mutter et al.*, 2008]. The oscillatory evolution proposed in Figure 15 is an attempt to integrate published time scales constraints that are currently available. However, it remains schematic and probably too simplistic to illustrate natural processes. The regular oscillatory evolution is probably too simple and irregularities are likely to occur at each time scale. The very short time between magma mixing and eruptions documented by *Pan and Batiza* [2002] may be an example of such episodic irregularities. The insert in Figure 15 proposes, as an example, an irregular evolution of the 750 year period for a portion of the curve. The depth variations of the summit of the melt lens identified in the present study range from meters to several tens of meters and match the short and middle time scales (≤10,000 years).

7. Conclusions

[55] New detailed mapping and petrological studies of the gabbro/sheeted dikes transition zone performed in "undisturbed" zones of the Oman ophiolite provide information about the evolution of the melt lens at fast spreading ridges. It further constrains the interactions between the magmatic system and the convective hydrothermal system at the ridge axis. The comparison of the Oman ophiolite with IODP Hole 1256D results in a global coherent model, which reconciles the apparently contrasting previous published ones (Figure 14).

[56] We assume that sheeted dikes can be injected from an episodically steady state melt lens as described by *Nicolas et al.* [2008]. However, this steady state behavior is overprinted by upward migrations of the melt lens that are documented in the Oman ophiolite and at the East Pacific Rise. These upward migrations induce reheating, dehydration, and hydrous partial melting at the roof of the melt lens, leading to the occurrence of oceanic plagiogranites and assimilation of hydrothermally altered rocks in the melt lens. These processes imply a contamination of the melt lens by silicic melts formed during hydrous partial melting and by hydrothermal fluids recycled through assimilation. Downward migrations of the top of the melt lens can also occur and result in the crystallization of the isotropic ophitic gabbros that represent a fossilized melt lens. Melt lens crystallization eventually occurs at the melt lens margins where the thermal regime is cooler.

[57] We also show that the well-equilibrated, fine-grained diabase textures observed in numerous oceanic or ophiolitic sites can have either a magmatic origin (protodikes) or a metamorphic origin (granoblastic dikes). Composition (e.g., Ti, Al, Cr in clinopyroxene), mineralogy (abundance of oxides), detailed petrographic observations (e.g., presence of clinopyroxenes with characteristic oxide inclusions), and description of associated lithologies (e.g., texture in the dike cores) are required to distinguish these two origins.

[58] At fast spreading ridges, the top of the melt lens, which corresponds to the magmatic/hydrothermal interface, should be considered as a dynamic interface. On the first order, the melt supply from the underlying main magma chamber, the occurrence of eruptions, and the vigor of the hydrothermal convecting system regulate its position. Short wavelength variations of the depth of the summit of the melt lens are observed (50 m of variation for distance of 150 m along axis).

Appendix A

[59] Mineral compositions of samples from the Oman ophiolite and from IODP Hole 1256D are presented in Table A1. FeO is the FeO total, Mg # = MgO/(MgO + FeOt) in molar proportions, and An % = CaO/(CaO + Na2O + K2O) in molar proportions; in the lithology names, RZ means root zone of the sheeted dikes. Foliated gabbro A is the "normal" foliated gabbro, and foliated gabbro B represents the foliated gabbro domains where the foliation is hardly identifiable in the field and that contain orthopyroxene and pargasite. The asterisks identifies samples analyzed in Montpellier; other samples were analyzed in Hannover. Plc means

Geochemistry Geophysics Geosystems G3 FRANCE ET AL.: FOSSILIZATION OF A DYNAMIC MELT LENS 10.1029/2009GC002652

Table A1 (Sample). Mineral Compositions of Samples From the Oman Ophiolite and From IODP Hole 1256D[a] [The full Table A1 is available in the HTML version of this article]

Sample	Zone	Lithology	Mineral	SiO_2	Al_2O_3	TiO_2	CaO	Na_2O	K_2O	MnO	MgO	FeO	Cr_2O_3	Total	Mg #	An %
08OL15b-leuco	Gideah	RZ_dike	Pumpellyite	36.07	22.70	0.30	22.36	0.06	0.01	0.08	1.51	8.89	–	91.97	–	–
08OL15b-leuco	Gideah	RZ_dike	Pumpellyite	35.94	21.81	0.19	22.75	0.07	0.00	–	1.49	9.33	0.02	91.59	–	–
08OL15b-leuco	Gideah	RZ_dike	Pumpellyite	35.93	20.15	0.10	21.96	0.06	0.01	–	1.63	10.68	0.06	90.57	–	–
08OL15b-leuco	Gideah	RZ_dike	Plc	55.22	27.73	0.08	11.06	5.51	0.07	0.06	0.03	0.51	–	100.28	–	52.60
08OL15b-leuco	Gideah	RZ_dike	Plc	54.72	28.22	0.06	11.23	5.30	0.05	0.02	0.01	0.40	–	100.02	–	53.93
08OL15b-leuco	Gideah	RZ_dike	Plc	54.40	28.12	0.06	11.38	5.26	0.07	–	0.03	0.53	0.04	99.88	–	54.46
08OL15b-leuco	Gideah	RZ_dike	Plc	54.21	28.54	0.06	11.31	5.24	0.05	–	0.00	0.43	0.06	99.89	–	54.42
08OL15b-leuco	Gideah	RZ_dike	Plc	53.84	28.81	0.06	11.42	5.04	0.12	0.03	0.06	0.54	0.04	99.94	–	55.61
08OL15b-leuco	Gideah	RZ_dike	Plc	53.18	29.33	0.04	12.26	4.57	0.07	–	0.05	0.52	0.03	100.05	–	59.71
08OL15b-leuco	Gideah	RZ_dike	Plc	53.96	28.64	0.05	11.56	5.09	0.03	–	0.03	0.44	0.00	99.80	–	55.65
08OL15b-leuco	Gideah	RZ_dike	Plc	53.85	28.37	0.06	11.40	5.49	0.06	0.05	0.02	0.51	0.00	99.81	–	53.45
08OL15b-leuco	Gideah	RZ_dike	Plc	55.56	27.79	0.06	10.08	5.98	0.09	–	0.01	0.39	0.00	99.96	–	48.21
08OL15b-leuco	Gideah	RZ_dike	Plc	53.48	28.95	0.06	11.53	5.25	0.06	0.01	0.00	0.40	0.04	99.78	–	54.84
08OL15b-leuco	Gideah	RZ_dike	Plc	52.55	29.25	0.08	12.29	4.70	0.08	0.00	0.03	0.59	0.01	99.58	–	59.10
08OL15b-leuco	Gideah	RZ_dike	Plb	64.12	22.55	0.03	3.95	9.41	0.11	0.04	0.03	0.24	0.03	100.50	–	18.82
08OL15b-leuco	Gideah	RZ_dike	Plb	63.33	22.77	0.02	4.26	9.45	0.17	0.00	0.01	0.26	0.04	100.30	–	19.92
08OL15b-leuco	Gideah	RZ_dike	Plb	63.84	22.64	0.02	4.15	9.41	0.08	–	0.01	0.38	0.06	100.58	–	19.60
08OL15b-leuco	Gideah	RZ_dike	Plb	62.82	23.62	0.02	4.95	9.11	0.09	–	0.01	0.35	0.01	100.96	–	23.09
08OL15b-leuco	Gideah	RZ_dike	Plb	62.83	23.15	0.04	4.84	8.72	0.09	0.01	0.00	0.34	0.01	100.04	–	23.49
08OL15b-leuco	Gideah	RZ_dike	Plb	63.79	23.21	0.02	4.46	9.34	0.12	0.01	0.01	0.35	0.03	101.32	–	20.86
08OL15b-leuco	Gideah	RZ_dike	Plb	64.66	22.40	0.02	3.50	10.08	0.10	–	0.00	0.32	–	101.09	–	16.10
08OL15b-leuco	Gideah	RZ_dike	Plb	61.70	24.28	0.02	5.91	8.47	0.08	–	0.01	0.36	0.02	100.86	–	27.84
08OL15b-leuco	Gideah	RZ_dike	magt	0.00	0.40	1.23	0.04	0.00	0.00	–	0.03	90.92	0.18	92.79	–	–
08OL15b-leuco	Gideah	RZ_dike	magt	0.05	0.34	1.03	0.10	–	–	0.04	–	90.53	0.25	92.33	–	–
08OL15b-leuco	Gideah	RZ_dike	magt	0.12	0.43	1.04	0.03	–	0.01	0.07	0.01	91.23	0.15	93.08	–	–
08OL15b-leuco	Gideah	RZ_dike	magt	0.07	0.40	1.02	0.06	0.02	0.01	0.07	0.02	90.22	0.09	91.99	–	–
08OL15b-leuco	Gideah	RZ_dike	ilm	0.04	0.12	40.55	0.03	0.04	0.00	1.48	0.06	51.99	0.04	94.37	–	–
08OL15b-leuco	Gideah	RZ_dike	ilm	0.10	0.08	44.13	0.03	0.00	–	1.77	0.08	48.78	0.02	94.98	–	–
08OL15b-leuco	Gideah	RZ_dike	ilm	0.02	0.04	46.43	0.05	–	0.00	1.28	0.01	49.73	0.05	97.61	–	–
08OL15b-leuco	Gideah	RZ_dike	ilm	–	0.05	46.75	0.03	0.00	0.01	1.33	0.10	49.56	0.00	97.83	–	–
08OL15b-leuco	Gideah	RZ_dike	ilm	0.02	0.06	47.13	–	0.03	–	1.57	0.08	48.39	0.00	97.28	–	–
08OL15b-leuco	Gideah	RZ_dike	Apatite	0.18	0.02	–	54.52	0.03	0.00	0.06	–	0.08	0.03	54.92	–	–
08OL15b-leuco	Gideah	RZ_dike	Amp	51.79	2.70	0.30	9.50	0.38	0.04	0.46	14.72	17.21	–	97.11	62.99	–
08OL15b-leuco	Gideah	RZ_dike	Amp	51.02	3.94	0.35	11.94	0.59	0.04	0.28	13.85	16.16	–	98.17	65.04	–
08OL15b-leuco	Gideah	RZ_dike	Amp	52.55	3.72	0.28	10.67	0.29	0.06	0.40	13.89	15.39	0.05	97.29	62.12	–
08OL15b-leuco	Gideah	RZ_dike	Amp	50.86	3.91	0.32	11.42	0.66	0.07	0.31	13.47	17.10	0.07	98.18	62.87	–
08OL15b-leuco	Gideah	RZ_dike	Amp	49.98	4.82	0.32	11.00	0.76	0.07	0.32	12.47	17.66	–	97.40	59.89	–
08OL15b-leuco	Gideah	RZ_dike	Amp	51.44	2.65	0.28	7.95	0.43	0.06	0.61	14.03	20.17	0.04	97.66	57.60	–
08OL15b-leuco	Gideah	RZ_dike	Amp	51.39	3.36	0.43	11.08	0.56	0.10	0.45	13.53	16.85	0.04	97.79	62.05	–

[a] FeO is the FeO total, Mg # = MgO/(MgO + FeOt) in molar proportions, An % = CaO/(CaO + Na_2O + K_2O) in molar proportions. In the lithology names, RZ means root zone of the sheeted dikes. Foliated gabbro A is the "normal" foliated gabbro, and foliated gabbro B represents the foliated gabbro domains where the foliation is hardly identifiable in the field and that contain orthopyroxene and pargasite. The asterisks identify samples analyzed in Montpellier; other samples were analyzed in Hannover. Pl_c, plagioclase core; Pl_b, plagioclase rim; Amp, amphibole; ilm, ilmenite; magt, magnetite; Cpx, clinopyroxene; Chlo, chlorite; Ol, olivine; Opx, orthopyroxene; Qz, quartz.

plagioclase core, Plb means plagioclase rim, Amp means amphibole, ilm means ilmenite, magt means magnetite, Cpx means clinopyroxene, Chlo means chlorite, Ol means olivine, Opx means orthopyroxene, and Qz means quartz.

Acknowledgments

[60] We wish to thank Adolphe Nicolas and Françoise Boudier for their dedicated assistance in the field during the first field season spent by Lydéric France in Oman and for many discussions in the lab. Christian Nicollet is also thanked for his help in the field and for discussions. Many thanks to Christine Laverne for allowing us to examine her thin sections from IODP Hole 1256D and for her unique expertise in low-temperature alteration mineralogy. We express our warm thanks to the various people involved at different technical stages of this work: Christophe Nevado, Dorianne Delmas, and Otto Diedrich for their beautiful thin sections and Claude Merlet and Wanja Dziony for their assistance during the microprobe analyses. The manuscript benefited from thorough reviews by Laurence Coogan, John MacLennan. This research used samples and data provided by the Integrated Ocean Drilling Program (IODP). Funding for this research was provided by CNRS-INSU program 3F and by the Université Franco-Allemande/Deutsch-Französische Hochchule. We thank Salim Al Busaidi, Director General of Minerals, Ministry of Commerce and Industry of the Sultanate of Oman, for allowing us to conduct this research work in the Oman ophiolite.

References

Adachi, Y., and S. Miyashita (2003), Geology and petrology of the plutonic complexes in the Wadi Fizh area: Multiple magmatic events and segment structure in the northern Oman ophiolite, *Geochem. Geophys. Geosyst.*, *4*(9), 8619, doi:10.1029/2001GC000272.

Alt, J. C., D. A. H. Teagle, S. Umino, S. Miyashita, N. R. Banerjee, D. S. Wilson, the IODP Expeditions 309 and 312 Scientists, and the ODP Leg 206 Scientific Party (2007), IODP Expeditions 309 and 312 drill an intact upper oceanic basement into gabbros, *Sci. Drill.*, *4*, 4–10, doi:10.2204/iodp.sd.4.01.2007.

Andersen, D. J., D. H. Lindsley, and P. M. Davidson (1993), QUILF: A Pascal program to assess equilibria among Fe-Mg-Mn-Ti oxides, pyroxenes, olivine, and quartz, *Comput. Geosci.*, *19*, 1333–1350, doi:10.1016/0098-3004(93)90033-2.

Beard, J. S., and G. E. Lofgren (1991), Dehydration melting and water-saturated melting of basaltic and andesitic greenstones and amphibolites at 1, 3, and 6.9 kb, *J. Petrol.*, *32*, 365–401, doi:10.1093/petrology/32.2.365.

Bergmanis, E. C., J. Sinton, and K. H. Rubin (2007), Recent eruptive history and magma reservoir dynamics on the southern East Pacific Rise at 17°30′S, *Geochem. Geophys. Geosyst.*, *8*, Q12O06, doi:10.1029/2007GC001742.

Berndt, J., J. Koepke, and F. Holtz (2005), An experimental investigation of the influence of water and oxygen fugacity on differentiation of MORB at 200 MPa, *J. Petrol.*, *46*, 135–167, doi:10.1093/petrology/egh066.

Botcharnikov, R. E., J. Koepke, F. Holtz, C. McCammon, and M. Wilke (2005), The effect of water activity on the oxidation and structural state of Fe in a ferro-basaltic melt, *Geochim. Cosmochim. Acta*, *69*, 5071–5085, doi:10.1016/j.gca.2005.04.023.

Boudier, F., A. Nicolas, and B. Ildefonse (1996), Magma chambers in the Oman ophiolite: Fed from the top and the bottom, *Earth Planet. Sci. Lett.*, *144*, 239–250, doi:10.1016/0012-821X(96)00167-7.

Boudier, F., M. Godard, and C. Armbruster (2000), Significance of gabbronorite occurrence in the crustal section of the Semail ophiolite, *Mar. Geophys. Res.*, *21*, 307–326, doi:10.1023/A:1026726232402.

Canales, J. P., S. M. Carbotte, J. C. Mutter, M. R. Nedimovic, H. Carton, M. Xu, K. Newman, O. Aghaei, M. Marjanovic, and L. C. Stowe (2008), Discovery of off-axis melt lenses at the RIDGE-2000 East Pacific Rise integrated studies site, *Eos Trans. AGU*, *89*(53), Fall Meet. Suppl., Abstract B21A-0319.

Carbotte, S. M., J. C. Mutter, J. P. Canales, M. R. Nedimovic, H. Carton, M. Xu, K. Newman, M. Marjanovic, O. Aghaei, and L. Stowe (2008), New observations of the magmatic segmentation of the East Pacific Rise from Siquieros to Clipperton from a multi-streamer seismic reflection imaging study, *Eos Trans. AGU*, *89*(53), Fall Meet. Suppl., Abstract B21A-0320.

Caress, D. W., M. S. Burnett, and J. A. Orcutt (1992), Tomographic image of the axial low-velocity zone at 12°50′N on the East Pacific Rise, *J. Geophys. Res.*, *97*(B6), 9243–9263, doi:10.1029/92JB00287.

Carton, H., S. M. Carbotte, J. C. Mutter, J. P. Canales, M. R. Nedimovic, K. Newman, M. Marjanovic, M. Xu, O. Aghaei, and L. Stowe (2008), Characteristics of the crustal magma body in the 2005–06 eruption area at 9°50′N on the East Pacific Rise from a 3D multi-channel seismic investigation, *Eos Trans. AGU*, *89*(53), Fall Meet. Suppl., Abstract B23F-03.

Collier, J. S., and S. C. Singh (1997), Detailed structure of the top of the melt body beneath the East Pacific Rise at 9°40′N from waveform inversion of seismic reflection data, *J. Geophys. Res.*, *102*(B9), 20,287–20,304, doi:10.1029/97JB01514.

Coogan, L. A. (2003), Contaminating the lower crust in the Oman ophiolite, *Geology*, *31*(12), 1065–1068, doi:10.1130/G20129.1.

Coogan, L. A., R. N. Wilson, K. M. Gillis, and C. J. MacLeod (2001), Near-solidus evolution of oceanic gabbros: Insights from amphibole geochemistry, *Geochim. Cosmochim. Acta*, *65*(23), 4339–4357, doi:10.1016/S0016-7037(01)00714-1.

Coogan, L. A., G. Thompson, and C. J. MacLeod (2002), A textural and geochemical investigation of high level gabbros from the Oman ophiolite: Implications for the role of the axial magma chamber at fast-spreading ridges, *Lithos*, *63*, 67–82, doi:10.1016/S0024-4937(02)00114-7.

Coogan, L. A., N. C. Mitchell, and M. J. O'Hara (2003), Roof assimilation at fast spreading ridges: An investigation combining geophysical, geochemical, and field evidence, *J. Geophys. Res.*, *108*(B1), 2002, doi:10.1029/2001JB001171.

Cormier, M. H. (1997), The ultrafast East Pacific Rise: Instability of the plate boundary and implications for accretionary processes, in *Mid-Ocean Ridges. Dynamics of Processes Associated With Creation of New Ocean Crust*, edited by J. R. Cann, H. Elderfield, and A. Laughton, *Philos. Trans. R. Soc. London, Ser. A*, *355*(1723), 341–367, doi:10.1098/rsta.1997.0012.

Crawford, W. C., and S. C. Webb (2002), Variations in the distribution of magma in the lower crust and at the Moho beneath the East Pacific Rise at 9°–10°N, *Earth Planet. Sci. Lett.*, *203*(1), 117–130, doi:10.1016/S0012-821X(02)00831-2.

Detrick, R. S., P. Buhl, E. Vera, J. Mutter, J. Orcutt, J. Madsen, and T. Brocher (1987), Multi-channel seismic imaging of a crustal magma chamber along the East Pacific Rise, *Nature*, *326*, 35–41, doi:10.1038/326035a0.

Dunn, R., D. Toomey, and S. Solomon (2000), Three-dimensional seismic structure and physical properties of the crust and shallow mantle beneath the East Pacific Rise at 9°30′N, *J. Geophys. Res.*, *105*(B10), 23,537–23,555, doi:10.1029/2000JB900210.

Dziony, W., J. Koepke, and F. Holtz (2008), Data report: Petrography and phase analyses in lavas and dikes from the hole 1256D (ODP Leg 206 and IODP Expedition 309, East Pacific Rise) [online], *Proc. Integrated Ocean Drill. Program*, *309/312*, 22 pp., doi:10.2204/iodp.proc.309312.201.2008. (Available at http://publications.iodp.org/proceedings/309_312/201/201_.htm)

Ernst, W. G., and J. Liu (1998), Experimental phase-equilibrium study of Al- and Ti-contents of calcic amphibole in MORB—A semiquantitative thermobarometer, *Am. Mineral.*, *83*, 952–969.

Fei, Y. (1995), Thermal expansion, in *Mineral Physics and Crystallography: A Handbook of Physical Constants*, *AGU Ref. Shelf*, vol. 2, edited by T. J. Ahrens, pp. 29–44, AGU, Washington, D. C.

Feig, S. T., J. Koepke, and J. E. Snow (2006), Effect of water on tholeiitic basalt phase equilibria: An experimental study under oxidizing conditions, *Contrib. Mineral. Petrol.*, *152*(5), 611–638, doi:10.1007/s00410-006-0123-2.

Garrido, C. J., P. B. Kelemen, and G. Hirth (2001), Variation of cooling rate with depth in lower crust formed at an oceanic spreading ridge: Plagioclase crystal size distributions in gabbros from the Oman ophiolite, *Geochem. Geophys. Geosyst.*, *2*(10), 1041, doi:10.1029/2000GC000136.

Gerbert-Gaillard, L. (2002), Caractérisation géochimique des péridotites de l'ophiolite d'Oman: Processus magmatiques aux limites lithosphère-asthénosphère, Ph.D. memoir, 241 pp., Géosci. Montpellier, Univ. Montpellier 2, Montpellier, France.

Gillis, K. M. (2002), The root zone of an ancient hydrothermal system exposed in the Troodos ophiolite, Cyprus, *J. Geol.*, *110*, 57–74, doi:10.1086/324205.

Gillis, K. M. (2008), The roof of an axial magma chamber: A hornfelsic heat exchanger, *Geology*, *36*(4), 299–302, doi:10.1130/G24590A.1.

Gillis, K. M., and L. A. Coogan (2002), Anatectic migmatites from the roof of an ocean ridge magma chamber, *J. Petrol.*, *43*(11), 2075–2095, doi:10.1093/petrology/43.11.2075.

Gillis, K. M., and M. D. Roberts (1999), Cracking at the magma-hydrothermal transition: Evidence from the Troodos ophiolite, Cyprus, *Earth Planet. Sci. Lett.*, *169*, 227–244, doi:10.1016/S0012-821X(99)00087-4.

Gillis, K. M., L. A. Coogan, and M. Chaussidon (2003), Volatile element (B, Cl, F) behaviour in the roof of an axial magma chamber from the East Pacific Rise, *Earth Planet. Sci. Lett.*, *213*, 447–462, doi:10.1016/S0012-821X(03)00346-7.

Grove, T. L., and W. B. Bryan (1983), Fractionation of pyroxene-phyric MORB at low pressure: An experimental study, *Contrib. Mineral. Petrol.*, *84*, 293–309, doi:10.1007/BF01160283.

Harding, A. J., J. A. Orcutt, M. E. Kappus, E. E. Vera, J. C. Mutter, P. Buhl, R. S. Detrick, and T. M. Brocher (1989), Structure of young oceanic crust at 13°N on the East Pacific Rise from expanding spread profiles, *J. Geophys. Res.*, *94*(B9), 12,163–12,196, doi:10.1029/JB094iB09p12163.

Henstock, T. J., A. W. Woods, and R. S. White (1993), The accretion of oceanic crust by episodic sill intrusion, *J. Geophys. Res.*, *98*, 4143–4161, doi:10.1029/92JB02661.

Holland, T., and J. Blundy (1994), Non-ideal interactions in calcic amphiboles and their bearing on amphibole-plagioclase thermometry, *Contrib. Mineral. Petrol.*, *116*, 433–447, doi:10.1007/BF00310910.

Hooft, E. E. E., R. S. Detrick, and G. M. Kent (1997), Seismic structure and indicators of magma budget along the southern East Pacific Rise, *J. Geophys. Res.*, *102*(B12), 27,319–27,340, doi:10.1029/97JB02349.

Hopson, C. A., R. G. Coleman, R. T. Gregory, J. S. Pallister, and E. H. Bailey (1981), Geologic section through the Samail ophiolite and associated rocks along a Muscat-Ibra transect, southeastern Oman mountains, *J. Geophys. Res.*, *86*, 2527–2544, doi:10.1029/JB086iB04p02527.

Hussenoeder, S. A., J. A. Collins, G. M. Kent, R. S. Detrick, A. J. Harding, J. A. Orcutt, J. C. Mutter, and P. Buhl (1996), Seismic analysis of the axial magma chamber reflector along the southern East Pacific Rise from conventional reflection profiling, *J. Geophys. Res.*, *101*(B10), 22,087–22,105, doi:10.1029/96JB01907.

Juteau, T., M. Beurrier, R. Dahl, and P. Nehlig (1988), Segmentation at a fossil spreading center: The plutonic sequence of the Wadi Haymiliyah area (Haylayn block, Sumail nappe, Oman), *Tectonophysics*, *151*, 167–197, doi:10.1016/0040-1951(88)90245-4.

Kelemen, P. B., K. Koga, and N. Shimizu (1997), Geochemistry of gabbro sills in the crust/mantle transition zone of the Oman ophiolite: Implications for the origin of the lower oceanic crust, *Earth Planet. Sci. Lett.*, *146*, 475–488, doi:10.1016/S0012-821X(96)00235-X.

Kent, G. M., A. J. Harding, and J. A. Orcutt (1990), Evidence for a smaller magma chamber beneath the East Pacific Rise at 9°30′N, *Nature*, *344*(6267), 650–653, doi:10.1038/344650a0.

Kinzler, R. J., and T. L. Grove (1992), Primary magmas of mid-ocean ridge basalts: 1. Experiments and methods, *J. Geophys. Res.*, *97*(B5), 6885–6906, doi:10.1029/91JB02840.

Klein, E. M. (2003), Geochemistry of the igneous ocean crust, in *Treatise on Geochemistry*, vol. 3, *The Crust*, edited by R. Rudnick, pp. 433–463, doi:10.1016/B0-08-043751-6/03030-9, Elsevier, Amsterdam.

Koepke, J., S. T. Feig, J. Snow, and M. Freise (2004), Petrogenesis of oceanic plagiogranites by partial melting of gabbros: An experimental study, *Contrib. Mineral. Petrol.*, *146*, 414–432, doi:10.1007/s00410-003-0511-9.

Koepke, J., S. Feig, and J. Snow (2005a), Late stage magmatic evolution of oceanic gabbros as a result of hydrous partial melting: Evidence from the Ocean Drilling Program (ODP) Leg 153 drilling at the Mid-Atlantic Ridge, *Geochem. Geophys. Geosyst.*, *6*, Q02001, doi:10.1029/2004GC000805.

Koepke, J., S. T. Feig, and J. Snow (2005b), Hydrous partial melting within the lower oceanic crust, *Terra Nova*, *17*, 286–291, doi:10.1111/j.1365-3121.2005.00613.x.

Koepke, J., D. M. Christie, W. Dziony, F. Holtz, D. Lattard, J. Maclennan, S. Park, B. Scheibner, T. Yamasaki, and S. Yamazaki (2008), Petrography of the Dike/Gabbro Transition at IODP Site 1256 (Equatorial Pacific): The evolution of the Granoblastic Dikes, *Geochem. Geophys. Geosyst.*, *9*, Q07O09, doi:10.1029/2008GC001939.

Lagabrielle, Y., and M. H. Cormier (1999), Formation of large summit troughs along the East Pacific Rise as collapse calderas: An evolutionary model, *J. Geophys. Res.*, *104*(B6), 12,971–12,988, doi:10.1029/1999JB900015.

Lamoureux, G., B. Ildefonse, and D. Mainprice (1999), Modelling the seismic properties of fast-spreading ridge crustal low-velocity zones: Insights from Oman gabbro textures, *Tectonophysics*, *312*(2–4), 283–301, doi:10.1016/S0040-1951(99)00183-3.

Lange, R. L., and I. S. E. Carmichael (1990), Thermodynamic properties of silicate liquids with emphasis on density, thermal expansion and compressibility, *Rev. Mineral. Geochem.*, *24*(1), 25–64.

Lundstrom, C. C., H. F. Shaw, F. J. Ryerson, Q. Williams, and J. Gill (1998), Crystal chemical control of clinopyroxene-melt partitionning in the Di-Ab-An system: Implications for elemental fractionations in the depleted mantle, *Geochim. Cosmochim. Acta*, *62*(16), 2849–2862, doi:10.1016/S0016-7037(98)00197-5.

MacLeod, C. J., and D. A. Rothery (1992), Ridge axial segmentation in the Oman ophiolite: Evidence from along-strike variations in the sheeted dyke complex, in *Ophiolites and Their Modern Analogues*, edited by L. M. Parson, B. J. Murton, and P. Browning, *Geol. Soc. Spec. Publ.*, *60*, 39–63, doi:10.1144/GSL.SP.1992.060.01.03.

MacLeod, C. J., and G. Yaouancq (2000), A fossil melt lens in the Oman ophiolite: Implications for magma chamber processes at fast spreading ridges, *Earth Planet. Sci. Lett.*, *176*, 357–373, doi:10.1016/S0012-821X(00)00020-0.

Merlet, C. (1994), An accurate computer correction program for quantitative electron probe microanalysis, *Mikrochim. Acta*, *114–115*, 363–376, doi:10.1007/BF01244563.

Michael, P. J., and W. C. Cornell (1998), Influence of spreading rate and magma supply on crystallization and assimilation beneath mid-ocean ridges: Evidence from chlorine and major element chemistry of mid-ocean ridge basalts, *J. Geophys. Res.*, *103*, 18,325–18,356, doi:10.1029/98JB00791.

Michael, P. J., and J. G. Schilling (1989), Chlorine in mid-ocean ridge magmas: Evidence for assimilation of seawater-influenced components, *Geochim. Cosmochim. Acta*, *53*, 3131–3143, doi:10.1016/0016-7037(89)90094-X.

Miyashita, S., Y. Adachi, and S. Umino (2003), Along-axis magmatic system in the northern Oman ophiolite: Implications of compositional variation of the sheeted dike complex, *Geochem. Geophys. Geosyst.*, *4*(9), 8617, doi:10.1029/2001GC000235.

Morton, J. L., and N. H. Sleep (1985), Seismic reflections from a Lau basin magma chamber, in *Geology and Offshore Resources of Pacific Island Arcs—Tonga Region*, edited by D. W. Scholl and T. L. Vallier, pp. 441–453, Circum-Pac. Counc. for Energy and Miner. Resour., Houston, Tex.

Mutter, J. C., H. Carton, S. M. Carbotte, J. P. Canales, M. R. Nedimovic, K. R. Newman, M. Marjanovic, M. Xu, O. Aghaei, and L. C. Stowe (2008), Searching for changes in AMC characteristics on the EPR using comparisons of reflection images obtained in 1985 and 2008, *Eos Trans. AGU*, *89*(53), Fall Meet. Suppl., Abstract B21A-0319.

Natland, J. H., and H. J. B. Dick (1996), Melt migration through high-level gabbroic cumulates of the East Pacific Rise at Hess Deep: The origin of magma lenses and the deep crustal structure of fast-spreading ridges, *Proc. Ocean Drill Program Sci. Results*, *147*, 21–58, doi:10.2973/odp.proc.sr.147.002.1996.

Nicolas, A. (1989), *Structures of Ophiolites and Dynamics of Oceanic Lithosphere*, 367 pp., Kluwer, Boston, Mass.

Nicolas, A., and F. Boudier (1991), Rooting of the sheeted dike complex in the Oman ophiolite, in *Ophiolite Genesis and Evolution of the Oceanic Lithosphere*, edited by T. Peters, A. Nicolas, and R. G. Coleman, pp. 39–54, Kluwer Acad., Dordrecht, Netherlands.

Nicolas, A., and F. Boudier (1995), Mapping oceanic ridge segments in Oman ophiolites, *J. Geophys. Res.*, *100*(B4), 6179–6197, doi:10.1029/94JB01188.

Nicolas, A., G. Ceuleneer, F. Boudier, and M. Misseri (1988a), Structural mapping in the Oman ophiolites: Mantle diapirism along an oceanic ridge, *Tectonophysics*, *151*, 27–56, doi:10.1016/0040-1951(88)90239-9.

Nicolas, A., I. Reuber, and K. Benn (1988b), A new magma chamber model based on structural studies in the Oman ophiolite, *Tectonophysics*, *151*, 87–105, doi:10.1016/0040-1951(88)90242-9.

Nicolas, A., F. Boudier, B. Ildefonse, and E. Ball (2000), Accretion of Oman and United Arab Emirates ophiolite: Discussion of a new structural map, *Mar. Geophys. Res.*, *21*, 147–179, doi:10.1023/A:1026769727917.

Nicolas, A., D. Mainprice, and F. Boudier (2003), High-temperature seawater circulation throughout crust of oceanic ridges: A model derived from the Oman ophiolites, *J. Geophys. Res.*, *108*(B8), 2371, doi:10.1029/2002JB002094.

Nicolas, A., F. Boudier, J. Koepke, L. France, B. Ildefonse, and C. Mevel (2008), Root zone of the sheeted dike complex in the Oman ophiolite, *Geochem. Geophys. Geosyst.*, *9*, Q05001, doi:10.1029/2007GC001918.

Nicolas, A., F. Boudier, and L. France (2009), Subsidence in magma chamber and the development of magmatic foliation in Oman ophiolite gabbros, *Earth Planet. Sci. Lett.*, *284*, 76–87, doi:10.1016/j.epsl.2009.04.012.

Pallister, J. S., and C. A. Hopson (1981), Samail Ophiolite Plutonic Suite: Field relations, phase variation, cryptic variation and layering, and a model of a spreading ridge magma chamber, *J. Geophys. Res.*, *86*(B4), 2593–2644, doi:10.1029/JB086iB04p02593.

Pan, Y., and R. Batiza (2002), Mid-ocean ridge magma chamber processes: Constraints from olivine zonation in lavas from the East Pacific Rise at 9°30′N and 10°30′N, *J. Geophys. Res.*, *107*(B1), 2022, doi:10.1029/2001JB000435.

Pedersen, R. B., and J. Malpas (1984), The origin of oceanic plagiogranites from the Karmoy ophiolite, western Norway, *Contrib. Mineral. Petrol.*, *88*, 36–52, doi:10.1007/BF00371410.

Phipps Morgan, J., and Y. J. Chen (1993), The genesis of oceanic crust: Magma injection, hydrothermal circulation, and crustal flow, *J. Geophys. Res.*, *98*(B4), 6283–6297, doi:10.1029/92JB02650.

Pollock, M. E., E. M. Klein, J. A. Karson, and D. S. Coleman (2009), Compositions of dikes and lavas from the Pito Deep Rift: Implications for crustal accretion at superfast spreading centers, *J. Geophys. Res.*, *114*, B03207, doi:10.1029/2007JB005436.

Pouchou, J. L., and F. Pichoir (1991), Quantitative analysis of homogeneous or stratified microvolumes applying the model "PAP," in *Electron Probe Quantification*, edited by K. F. J. Heinrich and D. E. Newbury, pp. 31–75, Plenum, New York.

Purdy, G. M., L. S. L. Kong, G. L. Christeson, and S. C. Salomon (1992), Relationship between spreading rate and the seismic structure of mid-ocean ridges, *Nature*, *355*, 815–817, doi:10.1038/355815a0.

Quick, J. E., and R. P. Denlinger (1993), Ductile deformation and the origin of layered gabbro in ophiolites, *J. Geophys. Res.*, *98*, 14,015–14,027, doi:10.1029/93JB00698.

Rannou, E., M. Caroff, and C. Cordier (2006), A geochemical approach to model periodically replenished magma chambers: Does oscillatory supply account for the magmatic evolution of EPR 17–19°S?, *Geochim. Cosmochim. Acta*, *70*, 4783–4796, doi:10.1016/j.gca.2006.07.007.

Rothery, D. A. (1983), The base of a sheeted dyke complex, Oman ophiolite: Implications for magma chambers at oceanic spreading axes, *J. Geol. Soc.*, *140*, 287–296, doi:10.1144/gsjgs.140.2.0287.

Rubin, K. H., and J. M. Sinton (2007), Inferences on mid-ocean ridge thermal and magmatic structure from MORB compositions, *Earth Planet. Sci. Lett.*, *260*, 257–276, doi:10.1016/j.epsl.2007.05.035.

Rubin, K. H., I. Van des Zander, M. C. Smith, and E. C. Bergmanis (2005), Minimum speed limit for ocean ridge magmatism from ^{210}Pb–^{226}Ra–^{230}Th disequilibria, *Nature*, *437*, 534–538, doi:10.1038/nature03993.

Sauerzapf, U., D. Lattard, M. Burchard, and R. Engelmann (2008), The titanomagnetite-ilmenite equilibrium: New experimental data and thermo-oxybarometric application to the crystallization of basic to intermediate rocks, *J. Petrol.*, *49*, 1161–1185, doi:10.1093/petrology/egn021.

Singh, S. C., G. M. Kent, J. S. Collier, A. J. Harding, and J. A. Orcutt (1998), Melt to mush variations in crustal magma properties along the ridge crest at the southern East Pacific Rise, *Nature*, *394*(6696), 874–878, doi:10.1038/29740.

Sinton, J. M., and R. S. Detrick (1992), Mid-ocean ridge magma chambers, *J. Geophys. Res.*, *97*, 197–216, doi:10.1029/91JB02508.

Sinton, J., E. Bergmanis, K. Rubin, R. Batiza, T. K. P. Gregg, K. Grönvold, K. C. Macdonald, and S. M. White (2002), Volcanic eruptions on midocean ridges: New evidence from the superfast spreading East Pacific Rise, 17°–19°S, *J. Geophys. Res.*, *107*(B6), 2115, doi:10.1029/2000JB000090.

Sleep, N. H. (1975), Formation of oceanic crust: Some thermal constraints, *J. Geophys. Res.*, *80*(B29), 4037–4042, doi:10.1029/JB080i029p04037.

Snyder, D., I. S. E. Carmichael, and R. A. Wiebe (1993), Experimental study of liquid evolution in an Fe-rich, layered mafic intrusion: Constraints of Fe-Ti oxide precipitation on the T-fO_2 and T-ρ paths of tholeiitic magmas, *Contrib. Mineral. Petrol.*, *113*, 73–86, doi:10.1007/BF00320832.

Solomon, S. C., and D. R. Toomey (1992), The structure of mid-ocean ridges, *Annu. Rev. Earth Planet. Sci.*, *20*, 329–364, doi:10.1146/annurev.ea.20.050192.001553.

Spear, F. S., and J. C. Markussen (1997), Mineral zoning, P-T-X-M phase relations, and metamorphic evolution of some Adirondack granulites, New York, *J. Petrol.*, *38*(6), 757–783, doi:10.1093/petroj/38.6.757.

Teagle, D. A. H., J. C. Alt, S. Umino, S. Miyashita, N. R. Banerjee, D. S. Wilson, and the Expedition 309/312 Scientists (2006), Superfast spreading rate crust 2 and 3, *Proc. Integrated Ocean Drill. Program*, *309/312*, 50 pp., doi:10.2204/iodp.proc.309312.2006. (Available at http://publications.iodp.org/scientific_prospectus/309_312/index.html)

Toplis, M. J., and M. R. Carroll (1995), An experimental study of the influence of oxygen fugacity on Fe-Ti oxide stability, phase relations, and mineral-melt equilibria in ferro-basaltic systems*J. Petrol.*, *36*(5), 1137–1170.

Toplis, M. J., G. Libourel, and M. R. Carroll (1994), The role of phosphorus in crystallisation processes of basalt: An experimental study, *Geochim. Cosmochim. Acta*, *58*(2), 797–810, doi:10.1016/0016-7037(94)90506-1.

Umino, S., S. Miyashita, F. Hotta, and Y. Adachi (2003), Along-strike variation of the sheeted dike complex in the Oman Ophiolite: Insights into subaxial ridge segment structures and the magma plumbing system, *Geochem. Geophys. Geosyst.*, *4*(9), 8618, doi:10.1029/2001GC000233.

VanTongeren, J. A., P. B. Kelemen, and K. Hanghoj (2008), Cooling rates in the lower crust of the Oman ophiolite: Ca in olivine, revisited, *Earth Planet. Sci. Lett.*, *267*(1–2), 69–82, doi:10.1016/j.epsl.2007.11.034.

Webb, S. C. (2008), Is there a deep hydrothermal circulation at the EPR?, *Eos Trans. AGU*, *89*(53), Fall Meet. Suppl., Abstract B21A-0327.

Wilson, D. S., et al. (2006), Drilling to gabbro in intact ocean crust, *Science*, *312*, 1016–1020, doi:10.1126/science.1126090.

III.4. Aswad area: further constrains on the model

In order to test and constrain further the model proposed in France et al. (2009a), I have done detailed mapping in the Aswad area (Sumail massif, Oman ophiolite; Figure III-13). The studied area includes the zone mapped and described by Nicolas et al. (2008) (Figure III-14).

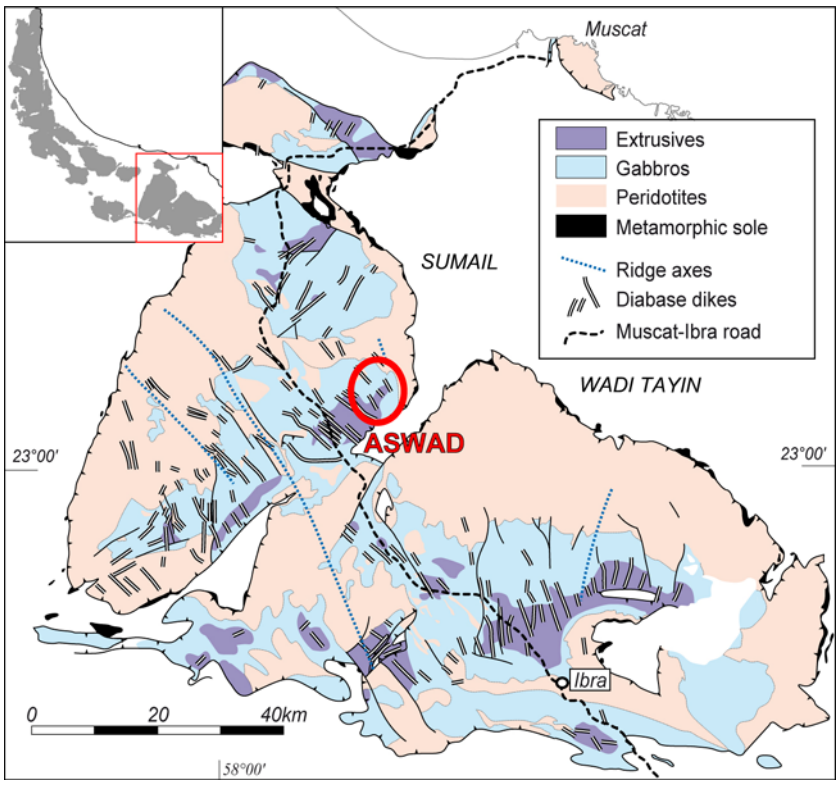

Figure III-13: Simplified geological and structural map of the southern massifs and location (Red box) in the Oman ophiolite (after Nicolas et al., 2000). The red circle indicates the location of the Aswad area.

The studied area is ~2.5 x 2.5 km large, and extends from the foliated gabbros to the sheeted dike complex. A preliminary petrological study of the collected samples has been done and is presented in section III.5. The mapping work consisted in precisely located field observations (lithology identification, structure measurements, and sampling) that are reported on the geological map (Figure III-14; Figure III-15). The foliation in the foliated gabbros is generally parallel to the sub-vertical sheeted dike orientation (trending ~140°N). As in the sections studied in France et al. (2009a), isolated foliated gabbro domains (a few meters large) are observed within the isotropic gabbro horizon; the foliation is parallel to the general direction defined by the foliated gabbros and by the sheeted dike complex. The contact between the isotropic gabbros and the sheeted dike complex is observed in several places ("SD/gabbro contact" in Figure III-15), and is always sharp (Figure III-16) and intrusive

(Figure III-17; Figure III-11). Coarse-grained isotropic gabbros are abundant along the contact (Figure III-15). Consistent with observations of France et al. (2009a), coarse-grained gabbros are commonly concentrated around the microgranular gabbro xenoliths (Figure III-18). Microgranular xenoliths are present at nearly all the SD/gabbro contact outcrops (Figure III-15), but are also observed sparsely in the isotropic gabbros (Figure III-15). The sharp contact between the microgranular base of the sheeted dike complex and the isotropic gabbros, together with the abundance of microgranular xenoliths (Figure III-15), attest to upward migrations of the top of the melt lens associated to important assimilation processes (France et al., 2009a). The microgranular base of the sheeted dike complex, and the microgranular gabbro xenoliths are therefore recrystallized after a reheating event and can be called granoblastic.

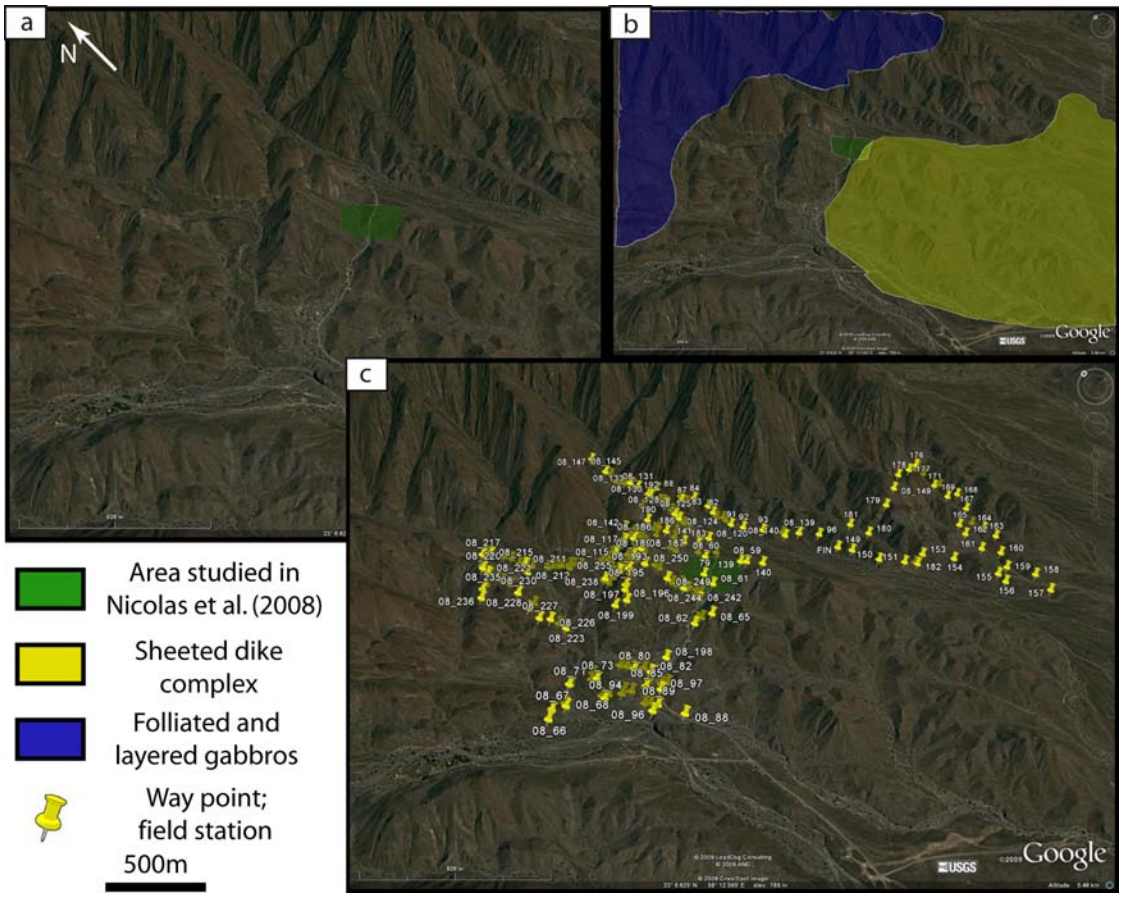

Figure III-14: Google Earth ® view of the Aswad area. a) studied area; the green box indicates the area mapped and described in Nicolas et al. (2008). b) The studied area is located between the sheeted dike complex (yellow) and the foliated gabbros (blue). c) Measurement and sampling stations (~250 stations).

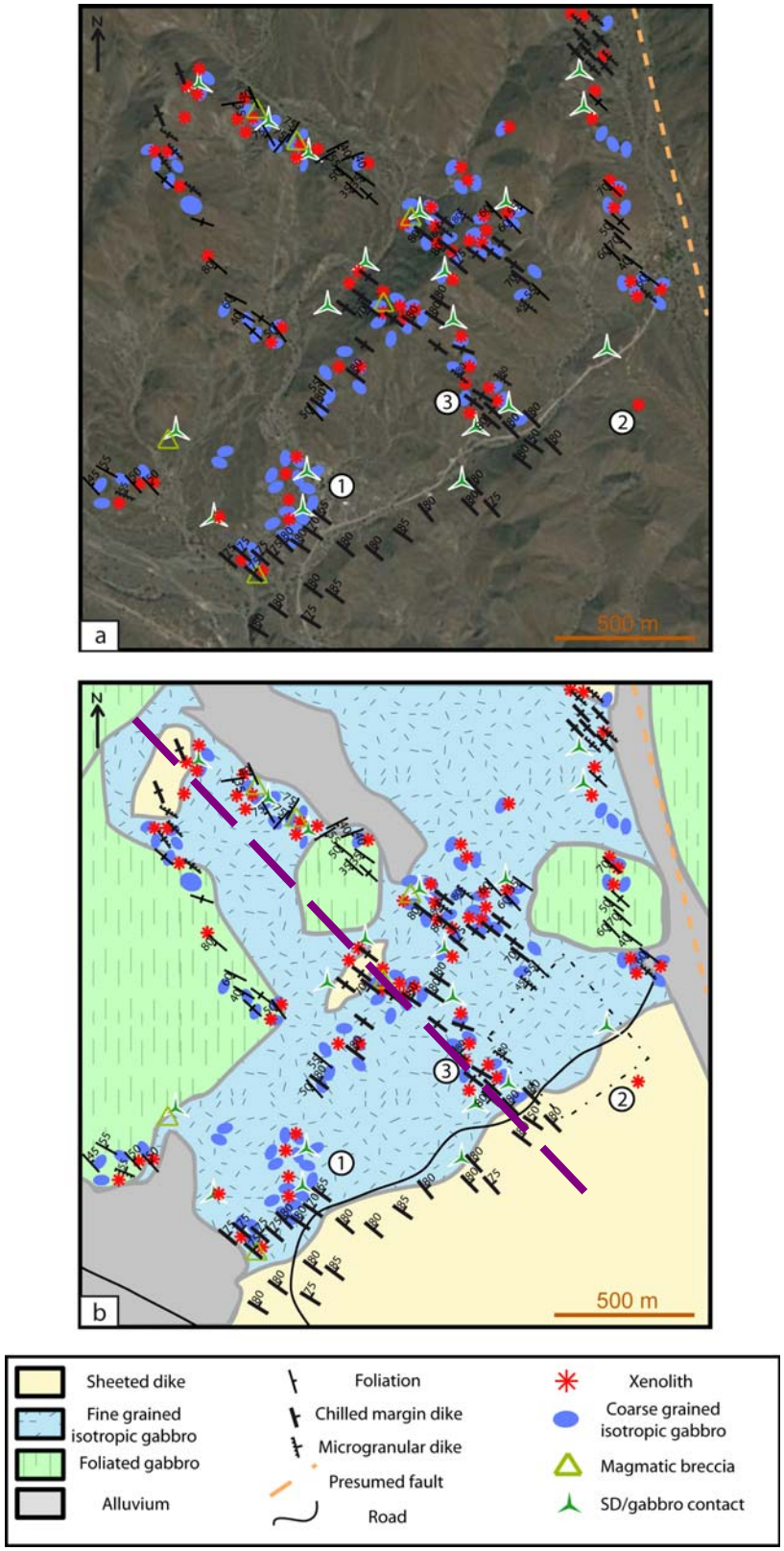

Figure III-15: Aswad area structural and lithological information on a Google Earth ® view (a) and on a geological map (b). The root zone outcrops represent zones of contact between the sheeted dike complex base and the isotropic gabbros. Purple dashed line: cross-section of Figure III-19. 1: location of photographs in Figure III-16; 2 is discussed in text at the end of this section and indicates the location of the outcrop presented in Figure III-20; 3: location of samples presented in section III.5. The dashed box indicates the area mapped and described in Nicolas et al. (2008).

The main difference with the areas studied in France et al. (2009a) is that several sheeted dike complex bodies (some meters wide) are observed within the isotropic gabbros (see "SD/gabbro contact" in Figure III-15). These bodies correspond to outcrops where gabbros intrude the base of the sheeted dike complex (recrystallized to granoblastic microgabbro), and represent the fossilized roof of the melt lens. The widespread occurrence of these "SD/gabbro contact" outcrops lead to propose the schematic and interpretative cross section of Figure III-19. As no fault has been identified in these areas, the depth variation of the sheeted dike / gabbro contact is interpreted as initial depth variations of the melt lens roof.

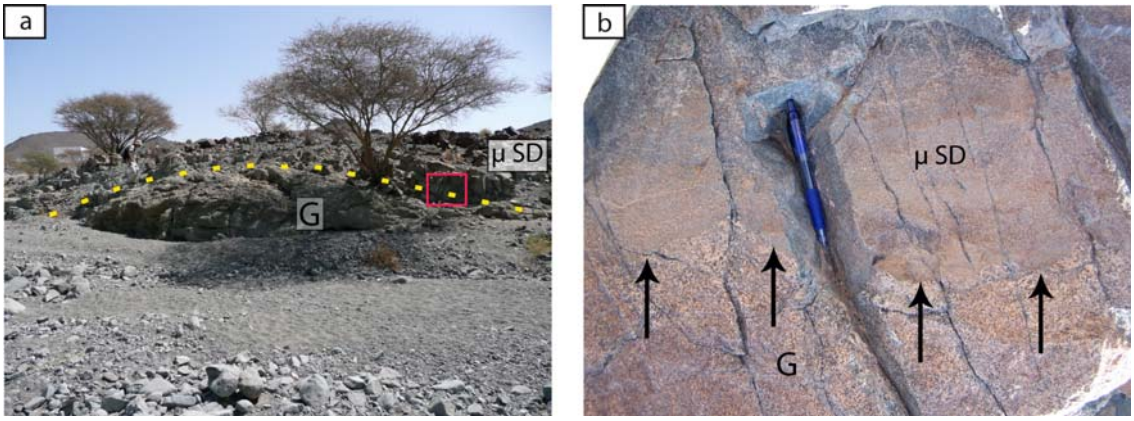

Figure III-16: Sharp contact between intrusive isotropic gabbro (G) and the recrystallized sheeted dike complex / granoblastic microgabbro dikes (µ SD). This outcrop corresponds to station 1 on Figure III-15. The red box indicates the location of the photograph in b) and arrows point the contact.

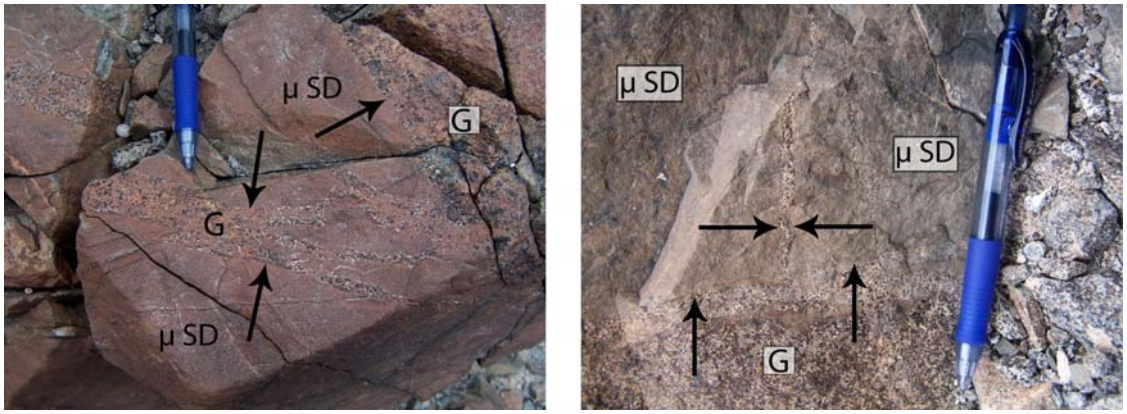

Figure III-17: Recrystallized sheeted dike complex (µ SD) / isotropic gabbro (G) contact. The contact (pointed by arrows) is sharp and fine-grained isotropic gabbro intrudes the granoblastic microgabbro dikes.

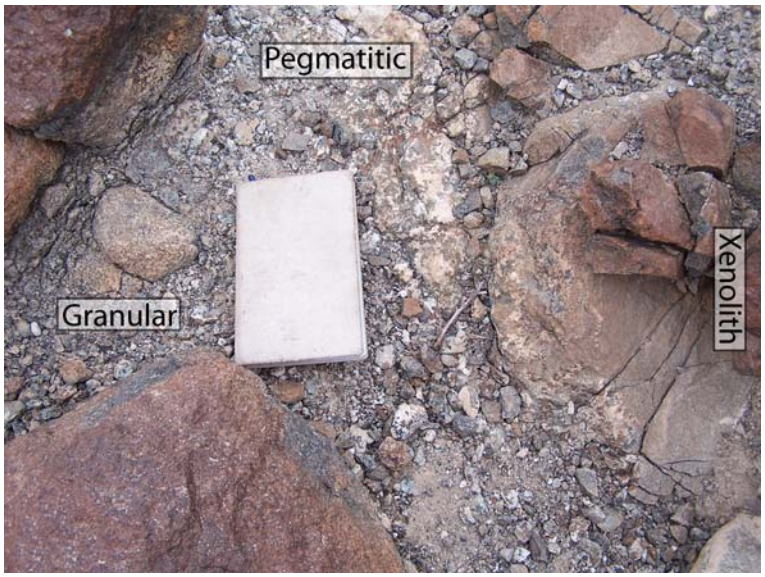

Figure III-18: Coarse-grained (pegmatitic) gabbros are preferentially located at the margins of a granoblastic microgabbro xenolith within granular gabbros. The occurrence of coarse-grained gabbro around xenoliths representing previously hydrothermally altered sheeted dikes is attributed to dehydration of xenoliths (France et al., 2009a).

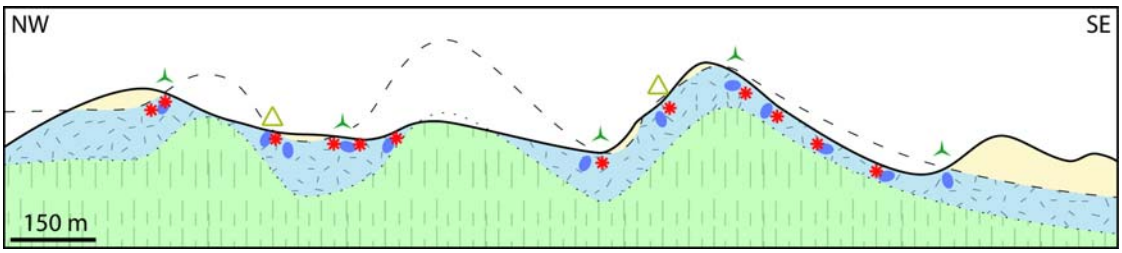

Figure III-19: Schematic and interpretative NW-SE cross-section from the Aswad area (see location in Figure III-15). The dashed line represents the contact between the sheeted dike complex and the isotropic gabbro horizon (inferred melt lens roof), and the dotted line represents the foliated gabbros / isotropic gabbros transition (inferred melt lens bottom). Symbols are the same as in Figure III-15.

Upward migrations are supported by the truncated base of the sheeted dike complex that are recrystallized to granoblastic microgabbro, and by granoblastic microgabbro xenoliths present in the isotropic gabbro horizon, but large downward migrations are also suggested by precise inspection of the sheeted dike complex. Within the sheeted dike complex, ~50-100m above the contact with the isotropic gabbros, some rare isotropic gabbro screens, ≤1 meter large, are observed (e.g., station 2 on Figure III-15; Figure III-20). These may be relicts of a former higher level of the melt lens that has migrated downward and crystallized these isotropic gabbros. Following this downward migration, new dikes have been injected and compose the new sheeted dike complex. One of these gabbro screens contains a granoblastic microgabbro xenolith (Figure III-20). The presence of xenoliths in these gabbro screens highlights former upward migrations of the melt lens that have resulted in assimilation.

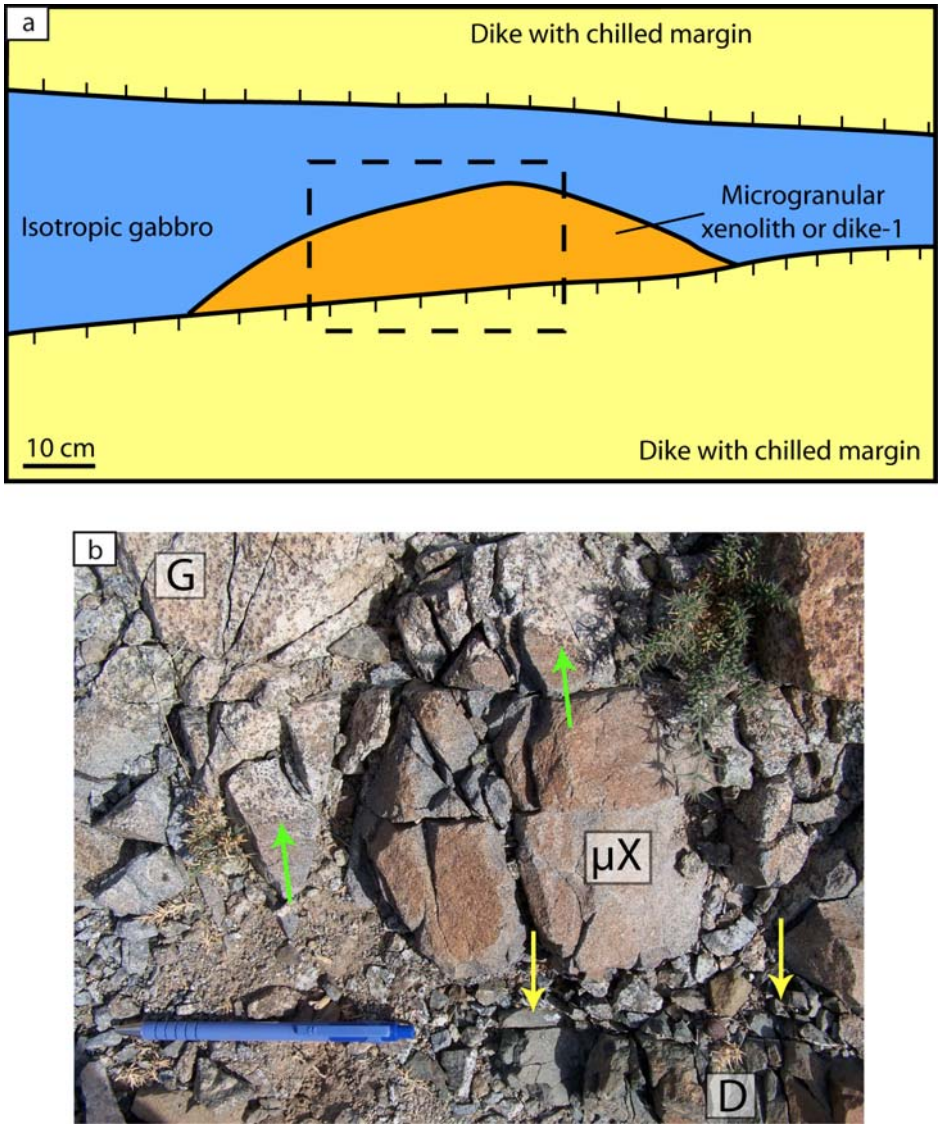

Figure III-20: Zone 2 on map of Figure III-15; gabbro screen containing a microgranular xenolith (or former granoblastic microgabbro dike ["dike-1]) within the sheeted dike complex. The dashed box in a) corresponds to the phototograph in b). In b) green arrows point the isotropic gabbro (G) / microgranular xenolith (µX) contact, and yellow arrows point the dike chilled margin (D).

Observations made in the Aswad area support upward and downward migrations of the melt lens, its fossilization, and assimilation processes, as proposed in France et al. (2009a). However in the Aswad area xenoliths are more abundant and assimilation of hydrothermally altered dikes and therefore upward migrations of the melt lens seems to be more abundant.

III.5. Reheating of the Aswad sheeted dikes

Samples from the Aswad area have been studied in collaboration with Christian Nicollet during the research practice of Baptiste Debret (first Master year) at the Laboratory "Magmas & Volcans" of Clermont-Ferrand (France). An article that will be submitted to *Lithos* is in preparation. I present hereafter the purpose of this study and the main results that are relevant to my PhD work.

The objective of this study was to determine the metamorphic evolution of Oman samples that have been exposed to high temperature after their crystallization. Samples from different depths of the ophiolitic complex are used (the sheeted dike base; the upper isotropic gabbros; the lower layered gabbros; meta-gabbro dikes from the Moho transition zone). Samples are studied through petrographic observations, in-situ microanalyses, and thermometry. Results highlight two different metamorphic evolutions, corresponding to the upper and lower gabbroic complex, that are mainly controlled by temperature, presence and quantity of fluids, cooling rate, deformation, and initial texture and mineralogy.

I present here petrological descriptions and mineral in-situ analyses of a sample (08OLC6) from the center of a dike close to the sheeted dike / gabbro transition; the sample location is station 3 in Figure III-15. In this area and similarly to other visited areas, the isotropic gabbros intrude the base of the sheeted dike complex base (Figure III-12d; Figure III-16; Figure III-17) and contain several microgranular enclaves (Figure III-15).

The studied sample is composed of plagioclase, clinopyroxene, different generations of amphibole, magnetite, and ilmenite. Microprobe in-situ analyses are given in Table III.1.

Isotropic gabbros and dikes show a similar retrograde evolution from the magmatic stage (plagioclase + clinopyroxene), through amphibolite facies conditions (brown amphibole crystallization [edenite and pargasite]), to green schist / low amphibolite facies conditions (green amphibole crystallization [edenite and hornblende]). Under green schist facies conditions, amphibole can also recrystallize as actinolites. The retrograde evolution can be observed in single amphibole grains that display zonations (Figure III-21).

mineral	SiO_2	Al_2O_3	TiO_2	CaO	Na_2O	K_2O	MnO	MgO	FeO	Cr_2O_3	NiO	Total	*X*	Pl/Hb (°C)	Ti in Amp (°C)
Hbb	44.94	8.96	3.36	10.66	2.18	0.23	0.24	13.74	13.33	0.01	0.02	97.66	*64.76*	812	973
Hbb	44.24	8.77	3.40	10.90	2.16	0.25	0.17	13.39	13.71	0.05	0.00	97.04	*63.50*	820	976
Hbb	44.88	9.02	3.11	11.32	1.89	0.29	0.17	13.19	12.87	0.00	0.04	96.78	*64.62*	843	953
Hbb	43.76	9.44	3.76	10.81	2.21	0.22	0.21	13.36	12.89	0.03	0.00	96.70	*64.87*	885	998
Hbb	43.91	9.57	3.45	11.44	2.12	0.27	0.15	12.01	14.12	0.03	0.02	97.11	*60.26*	828	979
Hbb	44.28	8.95	3.51	10.71	2.09	0.21	0.25	13.25	13.56	0.00	0.03	96.85	*63.54*	819	983
Hbb-g	46.11	9.07	0.61	11.78	1.75	0.34	0.15	14.44	13.06	0.03	0.03	97.39	*66.34*	808	608
Hbg	46.47	8.35	0.48	11.37	1.59	0.18	0.18	14.37	12.78	0.00	0.02	95.80	*66.71*	771	582
Hbg	46.22	8.80	0.71	11.65	1.69	0.42	0.23	13.48	13.89	0.02	0.05	97.16	*63.37*	792	627
Hbg	44.23	11.05	0.45	11.50	1.98	0.38	0.19	13.27	13.17	0.07	0.04	96.32	*64.24*	860	576
Hbg	49.94	5.28	1.29	11.56	0.91	0.18	0.15	14.68	12.33	0.05	0.05	96.41	*67.97*	647	729
Hbg	51.54	4.81	1.05	11.50	0.80	0.21	0.13	15.50	12.30	0.17	0.02	98.04	*69.21*	624	687
Hbb (2)	51.16	4.66	0.59	11.65	0.80	0.20	0.20	15.06	12.23	0.05	0.04	96.64	*68.70*	608	604
Hbb (2)	47.15	7.26	1.89	11.60	1.45	0.41	0.22	13.41	14.50	0.00	0.00	97.89	*59.38*	470	818
Hbb (2)	45.87	7.91	2.16	11.37	1.54	0.45	0.20	12.76	14.30	0.08	0.04	96.68	*61.39*	761	855
Hbg (2)	48.48	4.26	0.76	11.52	1.54	0.27	0.21	15.93	13.61	0.02	0.02	96.63	*67.59*	678	636
Hbg (2)	43.03	10.19	0.33	11.42	1.62	0.37	0.19	13.60	12.59	0.00	0.06	93.41	*65.80*	857	551
Actinolite (2)	52.95	2.99	0.46	11.45	0.54	0.08	0.26	16.34	11.57	0.08	0.01	96.73	*71.57*	544	577
Pl	58.82	25.49	0.05	8.14	6.92	0.27	0.00	0.03	0.41	0.00	0.00	100.13	*38.8*		
Pl	58.52	25.67	0.08	8.20	6.94	0.22	0.04	0.02	0.46	0.00	0.00	100.14	*39.0*		
Pl	49.31	32.33	0.10	15.59	2.89	0.06	0.00	0.03	0.64	0.00	0.00	100.94	*74.6*		
Pl	48.59	32.02	0.05	15.49	2.73	0.11	0.04	0.01	0.65	0.00	0.00	99.69	*75.3*		
Pl	51.44	28.73	0.01	13.93	3.18	0.15	0.00	0.32	2.64	0.00	0.00	100.39	*70.1*		
Cpx	53.76	0.39	0.07	24.03	0.12	0.04	0.19	14.34	7.25	0.00	0.01	100.22	*77.9*		
magnetite	3.22	0.49	3.62	2.99	0.00	0.03	0.00	0.10	81.89	1.91	0.00	94.27			
Ilmenite	0.03	0.04	47.48	0.06	0.00	0.01	1.30	0.07	53.19	0.04	0.00	102.22			

Table III.1: Microprobe data for sample 08OLC6 from the Aswad area of the Oman ophiolite. X: compositional parameter (mol %): plagioclase- An %; clinopyroxene and amphibole-Mg# (where Mg#=Mg/[Mg+Fe_t]); Pl/Hb: temperature calculated with the plagioclase-amphibole thermometer (Holland and Blundy, 1994); Ti in Amp: temperature calculated with the Ti in amphibole semiquantitative thermometer (Ernst and Liu, 1998), which is valid if Ti-oxides (e.g., ilmenite or titanomagnetite) coexist with amphibole; Hbb: brown hornblende; Hbg: green hornblende; (2): second generation (granoblastic); Pl: plagioclase; Cpx: clinopyroxene.

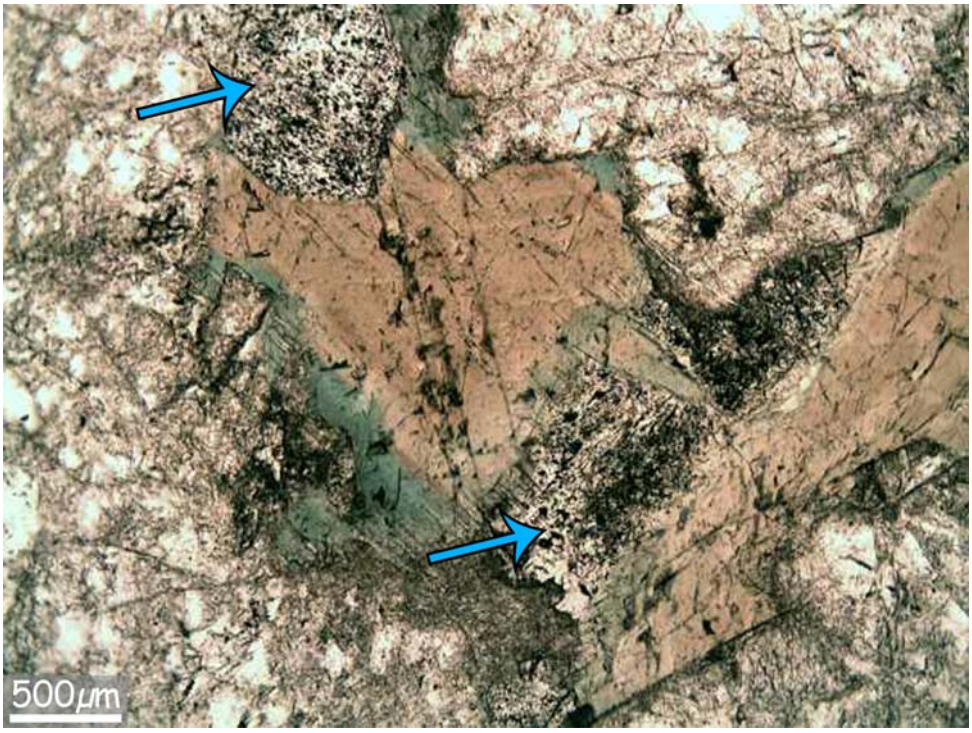

Figure III-21: Microphotograph of an isotropic gabbro sample (sample 08OLC3b) showing the retrograde evolution from the magmatic stage to the green schist facies conditions (plane-polarized light). Altered clinopyroxenes (blue arrows) attest to the magmatic conditions, brown amphibole attests to the amphibolite facies conditions and green amphibole attests to the green schist / amphibolite facies conditions.

Temperature estimations have been performed for retrograde amphiboles using the amphibole-plagioclase thermometer (Holland and Blundy, 1994) and the Ti in amphibole semiquantitative thermometer as Ti-bearing oxides are present (Ernst and Liu, 1998), and range from 885°C to 624°C and from 998°C to 582°C, respectively. For both thermometers, the higher estimated temperatures correspond to brown amphiboles, and the lower to green amphiboles. Another amphibole generation (brown/green amphiboles [hornblende and edenite] and actinolites) is observed in granoblastic assemblages (Figure III-22). Some areas are totally recrystallized to granoblastic assemblages and mimic the magmatic ophitic texture (Figure III-22c-d). These assemblages are present in the whole sample and can develop after former large amphibole grains (Figure III-23).

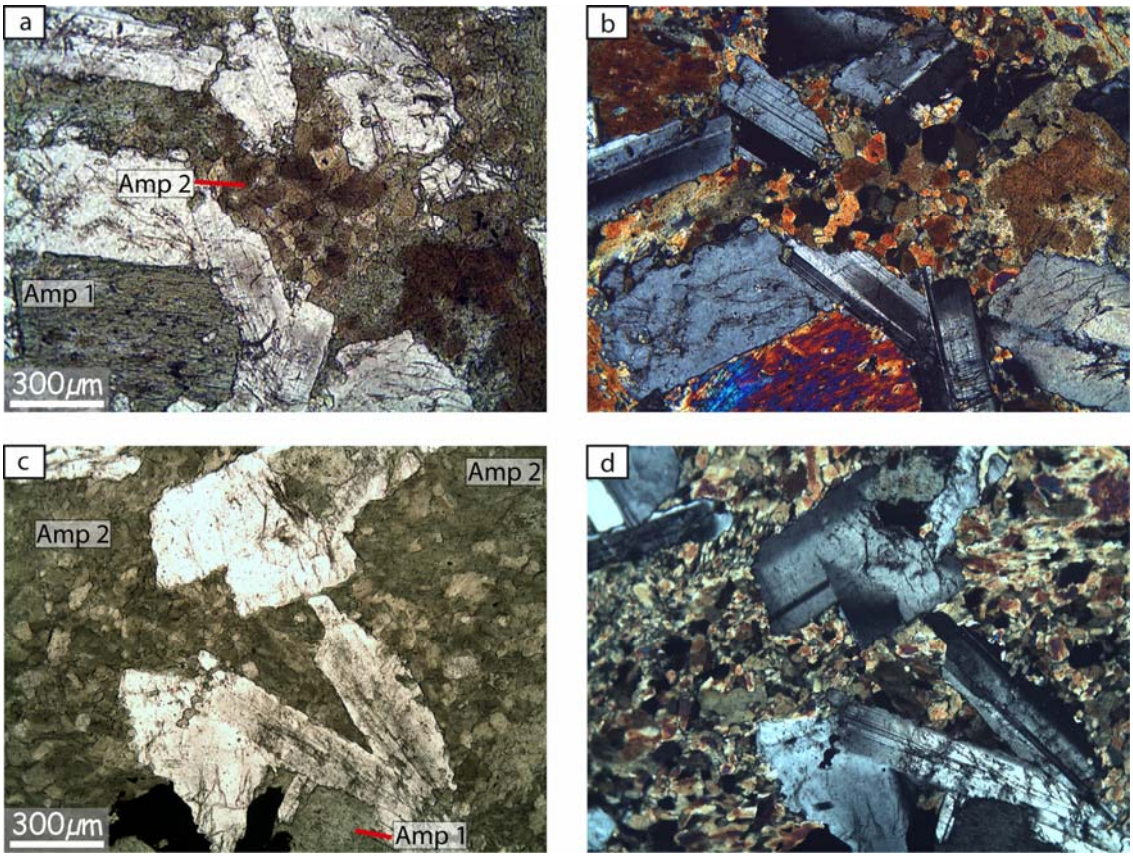

Figure III-22: Microphotographs of granoblastic amphibole assemblages (Amp 2) (a, c: plane-polarized light; b, d: cross-polarized light). Former large amphibole grains are also observed (Amp 1). Amp 1 seems to mimic former clinopyroxenes, and granoblastic assemblages of Amp 2 overprint former Amp 1 grains. The granoblastic assemblages of Amp 2 mimic the magmatic ophitic texture. Sample 08OLC6.

Temperature estimations for the granoblastic assemblages range from 857°C to 470°C using the amphibole-plagioclase thermometer (Holland and Blundy, 1994), and from 855°C to 551°C using the Ti in amphibole semiquantitative thermometer (Ernst and Liu, 1998). In contrast with the large amphibole grains, the granoblastic domains do not crystallize after clinopyroxenes in a purely retrograde system. It should either overprint the larger grains during a deformation stage or under increasing temperatures (prograde evolution). In the present case, no deformation is evidenced (e.g., plagioclase grains display magmatic textures; Figure III-21; Figure III-22; Figure III-23), and the overgrowths relations show that brown-amphibole granoblastic assemblages recrystallize after large green-amphibole grains (Figure III-23). The green-amphibole granoblastic assemblages are equilibrated at lower temperatures than the brown-amphibole granoblastic assemblages. It shows that the green-amphibole granoblastic assemblages overprint the brown-amphibole granoblastic assemblage during a second retrograde evolution.

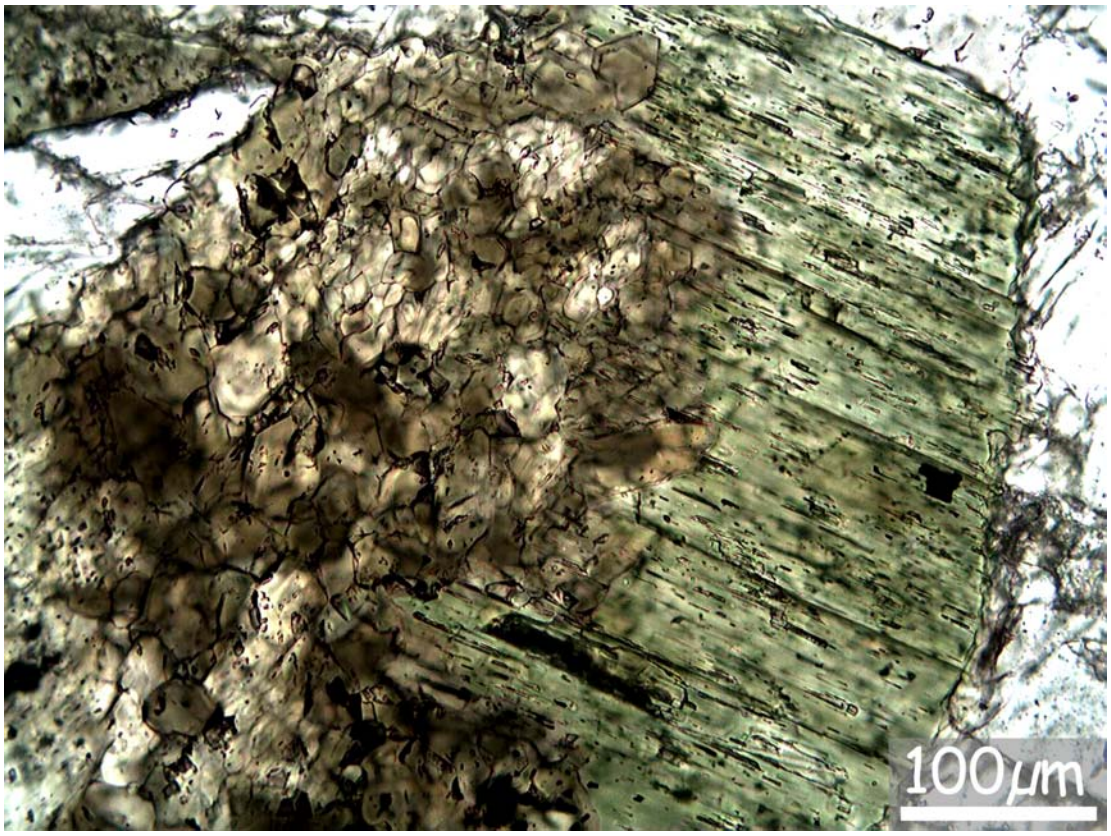

Figure III-23: Microphotograph of sample 08OLC6 from the base of the sheeted dike complex (plane-polarized light). The large green amphibole is overgrown by aggregates of granoblastic brown amphibole. The granoblastic brown amphibole assemblage has crystallized at higher temperature than the large green amphibole grain.

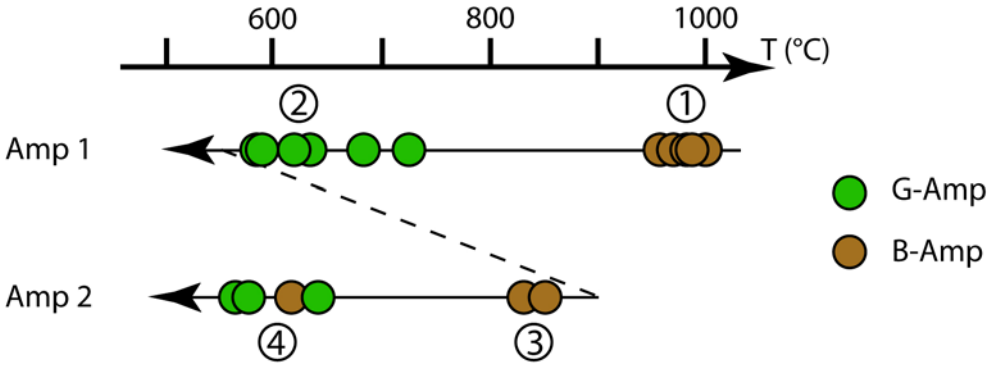

Figure III-24: Temperature evolution for different generations of amphiboles in sample 08OLC6: 1) large brown amphibole grains (B-Amp) crystallize, 2) following a retrograde evolution (Amp 1), large green amphibole (G-Amp) grains form. 3) Following a prograde event (reheating), granoblastic brown amphibole assemblages crystallize before 4) a second retrograde evolution (Amp 2) that leads to the crystallization of the granoblastic green assemblages (replacing the brown ones).

The succession of different amphibole types is: 1) large brown-amphibole grains, 2) large green-amphibole grains, 3) small granoblastic assemblages of brown-amphibole, 4) small granoblastic assemblages of green-amphibole, and 5) the lower temperature alteration to

actinolites. This evolution is summarized in Figure III-24 and is characterized by a reheating event (between stages 2 and 3).

Similar brown-amphibole granoblastic domains (as in stage 3) are observed in isotropic gabbro samples, and also attest to prograde metamorphism of these rocks (Figure III-25).

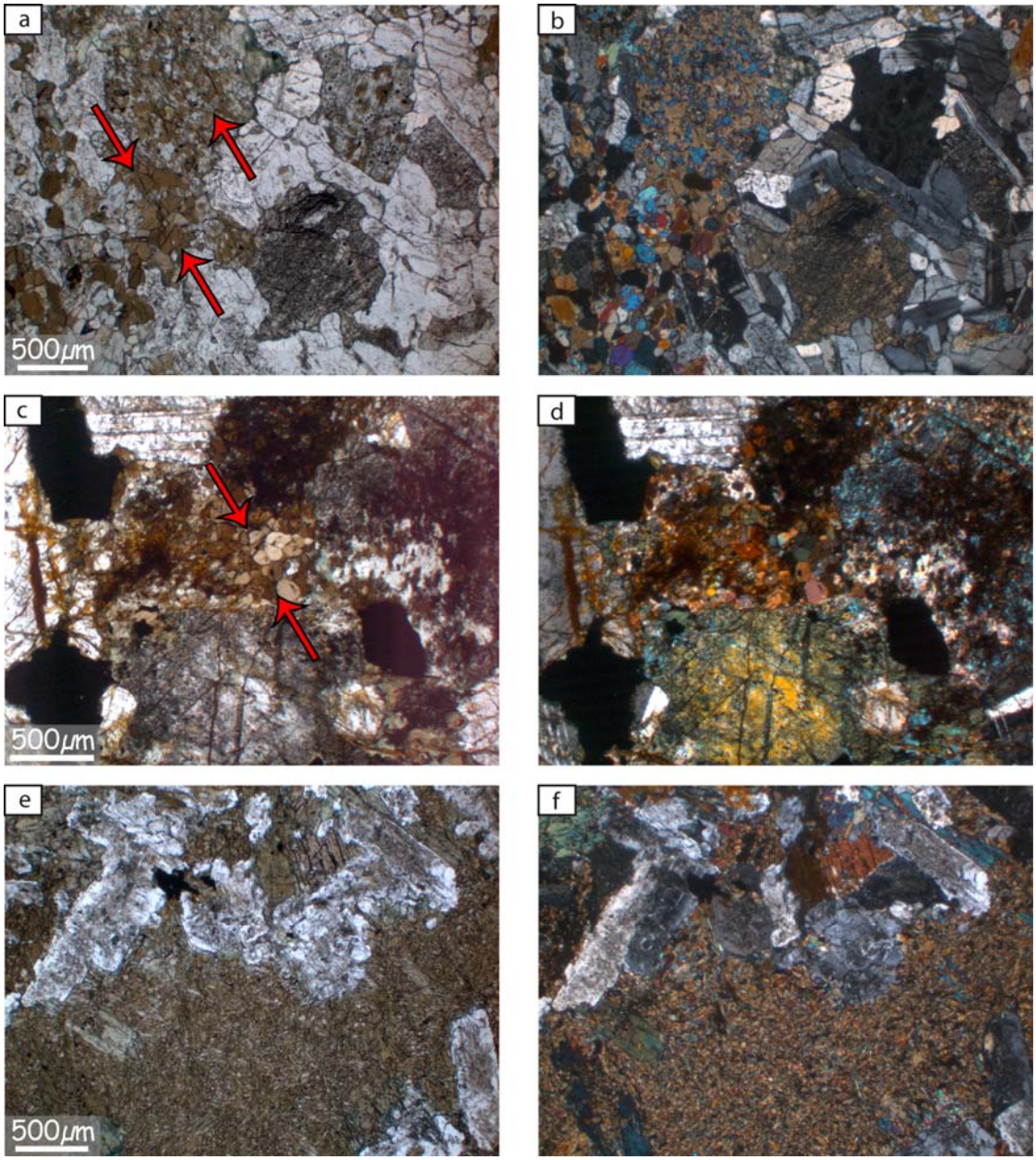

Figure III-25: Microphotographs of amphibole granoblastic assemblages is fine-grained isotropic gabbros (a-b: sample 07OL47b; c-d: sample 07OL57a; e-f: sample 07OL53a). a, c, e) plane-polarized light; b, d, f) cross-polarized light. In a-d amphibole granoblastic assemblages are pointed by arrows; in e-f the large brow-amphibole assemblage is overprinted and recrystallized to a brown-amphibole granoblastic assemblage.

The petrographic and micro-analytical characteristics observed in lithologies at the base of the sheeted dike complex from the Aswad area show that it has been reheated, which is consistent with the field observations (gabbro intrusion in the base of the sheeted dike complex, and occurrence of granoblastic microgabbro xenoliths in gabbros). The petrological characteristics observed in the Aswad area are consistent with the general model proposed in France et al. (2009a), in which the top of the melt lens is a dynamic horizon that can move up and down with the potential to reheat the previously hydrothermally altered lithologies.

III.6. Conclusion

Coupled structural, petrological, and geochemical studies of different areas of the Oman ophiolite, and a comparison with the IODP Hole 1256D support a common general model (France et al., 2009a) reconciling previous, apparently contrasting models for the interactions between the base of the sheeted dike complex and the upper melt lens present at fast spreading ridges. The results of this study are consistent with the hypothesis that the melt lens is a dynamic horizon that can migrate upward and downward, and that becomes fossilized off axis. Upward migrations results in prograde metamorphic reactions in the base of the sheeted dikes, which recrystallize to granoblastic dikes. Depending on the temperature increase occurring during upward migrations and on the extent of previous hydrothermal alteration, the granoblastic dikes represent either dehydrated previously altered dike rocks or hydrous partial melting residues. Assimilation is evidenced by the occurrence of granoblastic xenoliths in the isotropic gabbro horizon, and by the microgranular lenses observed in the foliated gabbros. The assimilation process can be responsible for the high chlorine content measured in the MORB melts of fast spreading ridges. Downward migrations of the melt lens result in the crystallization of isotropic gabbros at its roof and margins. Some gabbro screens present within the sheeted dike complex (50-100 m above their truncated base) attest to former higher levels of the melt lens.

The precise recrystallization processes, and the detailed evolution of the mineral assemblages in the granoblastic dikes have been described by Koepke et al. (2008). However the origin of the peculiar composition of the granoblastic dikes minerals remain poorly constrained. The melt formed during the hydrous partial melting of the base of the sheeted dike complex can mix with the melt lens magma and contaminate it. Constraining the composition of the formed melt is therefore of major importance to discuss the composition of MORB present at fast spreading ridges. In order to test the evolution of the mineral assemblages, to precise the recrystallization processes, and to better understand the melting

processes occurring at the base of the sheeted dike complex, we present in Chapter IV an experimental study reproducing the melting of hydrothermally altered dikes at the base of the sheeted dike complex.

Chapter IV.

“Melting the hydrothermally altered sheeted dike complex: experimental study”

IV.1. Introduction

In Chapter III, I have shown, through a study of the root zone of the sheeted dike complex in the Oman ophiolite and a comparison with rocks recovered in IODP Hole 1256D, that the upper melt lens present at fast spreading ridges is a dynamic system, which can migrate vertically (Gillis, 2008; France et al., 2009a). Upward migrations are associated to reheating of the previously hydrothermally altered roof (sheeted dikes and isotropic gabbros), and hydrous partial melting can proceed as a result of lowering the solidus temperature in the presence of water (Gillis and Coogan, 2002; Coogan et al., 2003; France et al., 2009a). The granoblastic dikes present at the base of the sheeted dike complex, and the granoblastic xenoliths that are observed in isotropic gabbros in association with plagiogranitic rocks result from recrystallization under amphibolite to granulite facies conditions, and may have undergone hydrous partial melting (France et al., 2009a). The melt formed during partial melting of hydrothermally altered dikes is believed to be compositionally close to typical oceanic plagiogranites (for low degrees of partial melting; Beard and Lofgren, 1991); for definition of the term "ocean plagiogranites" see Koepke et al., (2008). The associated residue may be similar to granulites, and may contain amphiboles depending on the temperature, and on the water activity. The hydrous solidus temperature is around 900°C (Beard and Lofgren, 1991). Redox conditions have a strong influence on the composition of the newly formed melt, on the composition of the residual phases, and on their liquidus temperatures (e.g., Appendix A3). Gillis and Coogan (2002), Coogan et al. (2003), and France et al. (2009a) have shown that hydrous partial melting of altered dikes at the base of the sheeted dike complex, has the potential of mixing the newly generated melt with primitive MORB in the melt lens, thus playing a significant role in MORB contamination at fast spreading ridges. This is potentially an effective crustal contamination process, as attested by the chlorine content of MORBs (Michael and Schilling, 1989; Michael and Cornell, 1998). Determining the precise composition (major, trace and volatile elements) of the melt formed during partial melting of previously hydrothermally altered dikes is therefore of major importance to evaluate the MORB components (primary melt, assimilated melt, and fractionated melt), and to constrain the composition of anatectic plagiogranites and discuss the origin of oceanic plagiogranites. Determining the mode and the mineral compositions of the residual assemblage and comparing these with the granoblastic rocks will help to test the dynamic model proposed by France et al. (2009a).

I have performed partial melting experiments using a hydrothermally altered sheeted dike sample as starting material. The starting material sample comes from the Oman ophiolite, and matches the average sheeted dike complex composition; it is highly hydrothermally altered, and no relics of magmatic phases are present. Experimental conditions have been selected to match the ones present at the base of the sheeted dike complex: a pressure of 100MPa, a temperature ranging from 750°C to 1030°C, water saturated conditions, and precisely constrained redox conditions (~NNO where NNO is the Ni-NiO solid buffer equilibrium). Experiments have been performed at the Institut für Mineralogie of the Leibniz Univeristy Hannover (Germany) using a cold-seal pressure vessel (CSPV; below 850°C), and at higher temperature, an internally heated pressure vessel (IHPV) equipped with a Shaw membrane (for details see below). Details on starting material, experimental conditions and results are presented in a paper submitted to *Contributions to Mineralogy and Petrology* (section IV.3); I present hereafter details on the experimental procedure.

IV.2. Detailed experimental techniques

IV.2.a. Sample preparation

The starting material (sample 08OL30) has been crushed to a powder, and then sieved in order to obtain a powder homogeneous in grain size. Precious metal tubes were used as capsule containers; in the present case I have used gold that prevent iron loss toward the capsule wall. 15-20 mm long tubes (diameter=2.8 mm) were used (N°1 in Figure IV-1). First, tubes were cleaned using an acetone bath plunged in an ultrasonic cleaner (~15 min); then gold tubes were placed at 800°C in a one atmosphere oven for ~20 min. Then, one tube end was pinched (N°2 in Figure IV-1) and welded (N°3 in Figure IV-1). Subsequently the capsule was filled; for water added experiments (see details in section IV.3), ~5 mg of distilled water was first added into the capsule, then ~50 mg of rock powder was added, and the whole assemblage was compressed in the capsule. The other tube end was then pinched and welded (N°4 in Figure IV-1). Because the welding heat could trigger water loss, a special cooling procedure using liquid nitrogen was required. After the welding, the capsule was weighed and placed in a 110°C furnace for 5 min, and then weighed again to verify that no water loss occurred during the welding process. Capsule is weighed after each preparation step, and if the weight remains stable during the different stages, the capsule is considered closed and can be used for experiments.

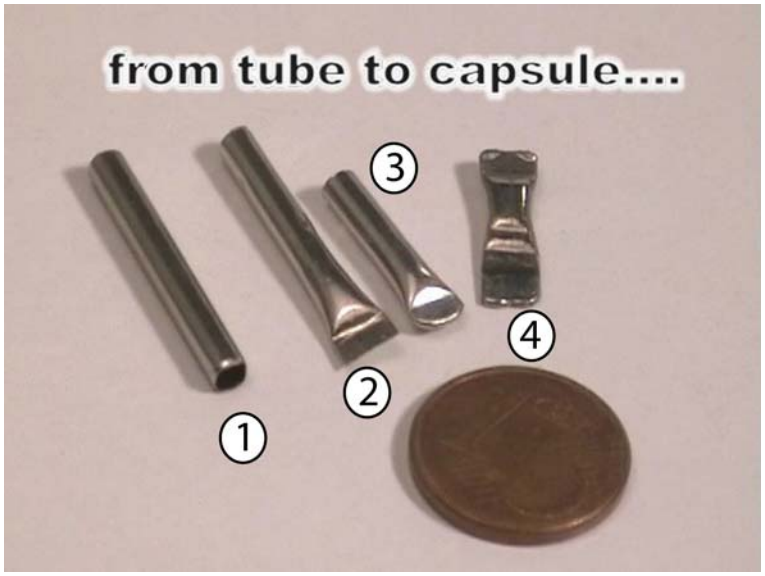

Figure IV-1: Steps in the capsule making (1 cent coin for scale). 1) 1.5 cm long tube; 2) one tube end has been pinched, and 3) welded; 4) after the filling, the second capsule end has been pinched and welded.

IV.2.b. Cold-seal pressure vessel

The used CSPV are horizontal externally heated vessels (Figure IV-2) that are pressurized with water. Pressure was controlled with a pressure transducer calibrated against a strain gauge manometer, and temperature was controlled using an external Ni-CrNi thermocouple. Before this study, ovens were calibrated to identify the hottest zone. The capsules were centered in this zone. In CSPV, the redox conditions were controlled using a solid buffer (a Ni-NiO assemblage in the present case). However, Scaillet et al. (1992) have shown that the maximum buffer lifetime is in the order of a few days, which is much less than the time spanned by our experiments. The redox conditions are nevertheless considered to be close to the NNO buffer because of the vessel composition (Ni), and of the use of water for pressurization (Klimm et al., 2003).

To run an experiment, the oven was first pre-heated to the desired temperature in order to shorten the heating time for samples. The vessel that contains the sample was then pressurized to the desired pressure (~100 MPa) before being introduced in the oven. The heating results in a pressure increase; pressure was therefore decreased during the heating stage to maintain ~100 MPa. When pressure and temperature were stable (after 30-60 min), the experiment was started, and pressure and temperature were controlled twice a day. At the end of the experiment, the vessel was removed from the oven and immediately exposed to a

flux of compressed air (initial cooling rate ~200°/min). In order to ensure isobaric quenching, pressure was increased during the cooling.

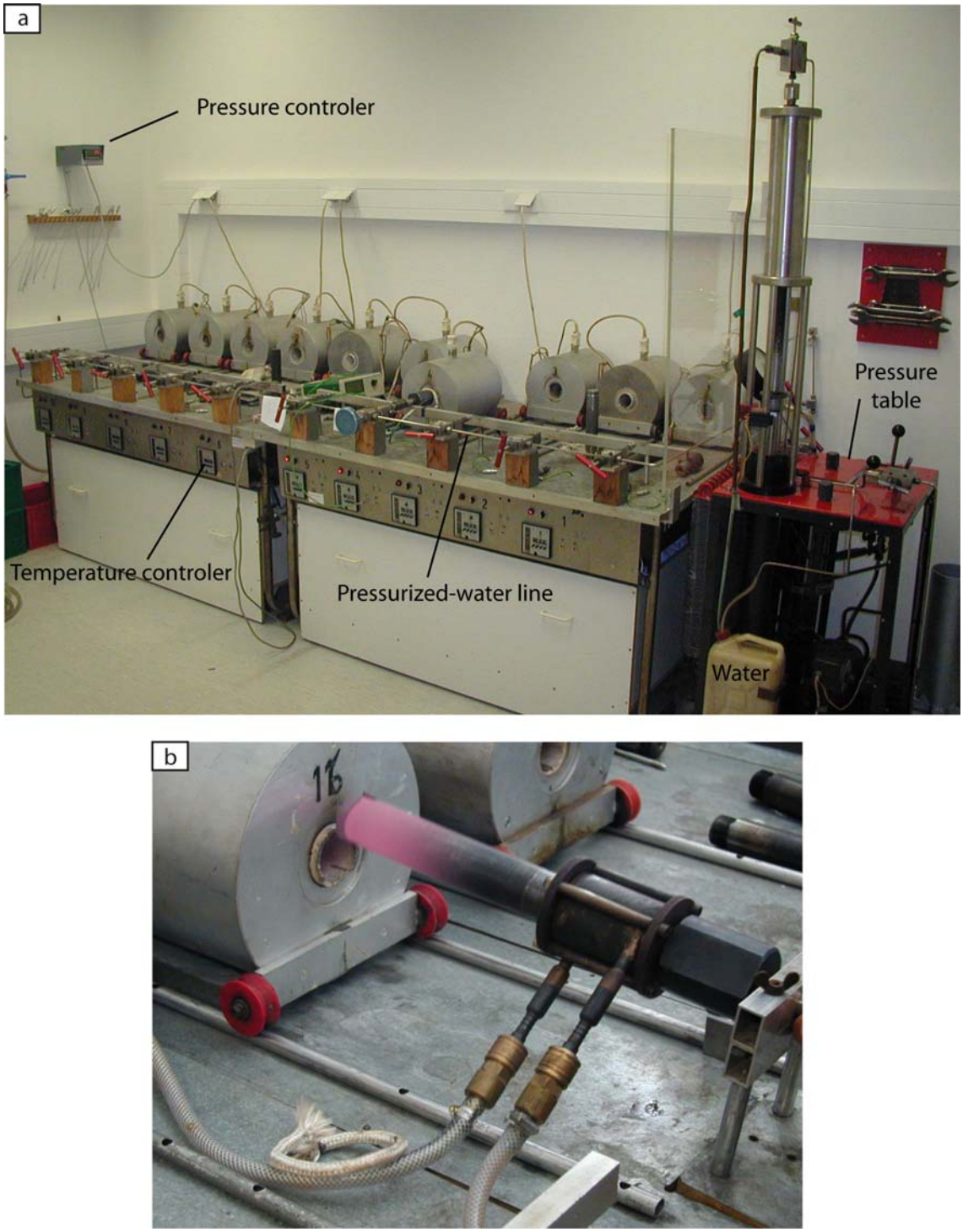

Figure IV-2: Water pressurized CSPV ramp of the experimental lab of the Institut für Mineralogie of the Leibniz Univeristy Hannover. a) ovens, and b) hot vessel just removed from the oven.

IV.2.c. Internally heated pressure vessel

The used IHPV are vertical internally heated vessels (Figure IV-3) that are pressurized with argon. Pressure was controlled with a strain gauge manometer, and temperature was controlled using four S-type thermocouples. Details are given in Berndt et al. (2002).

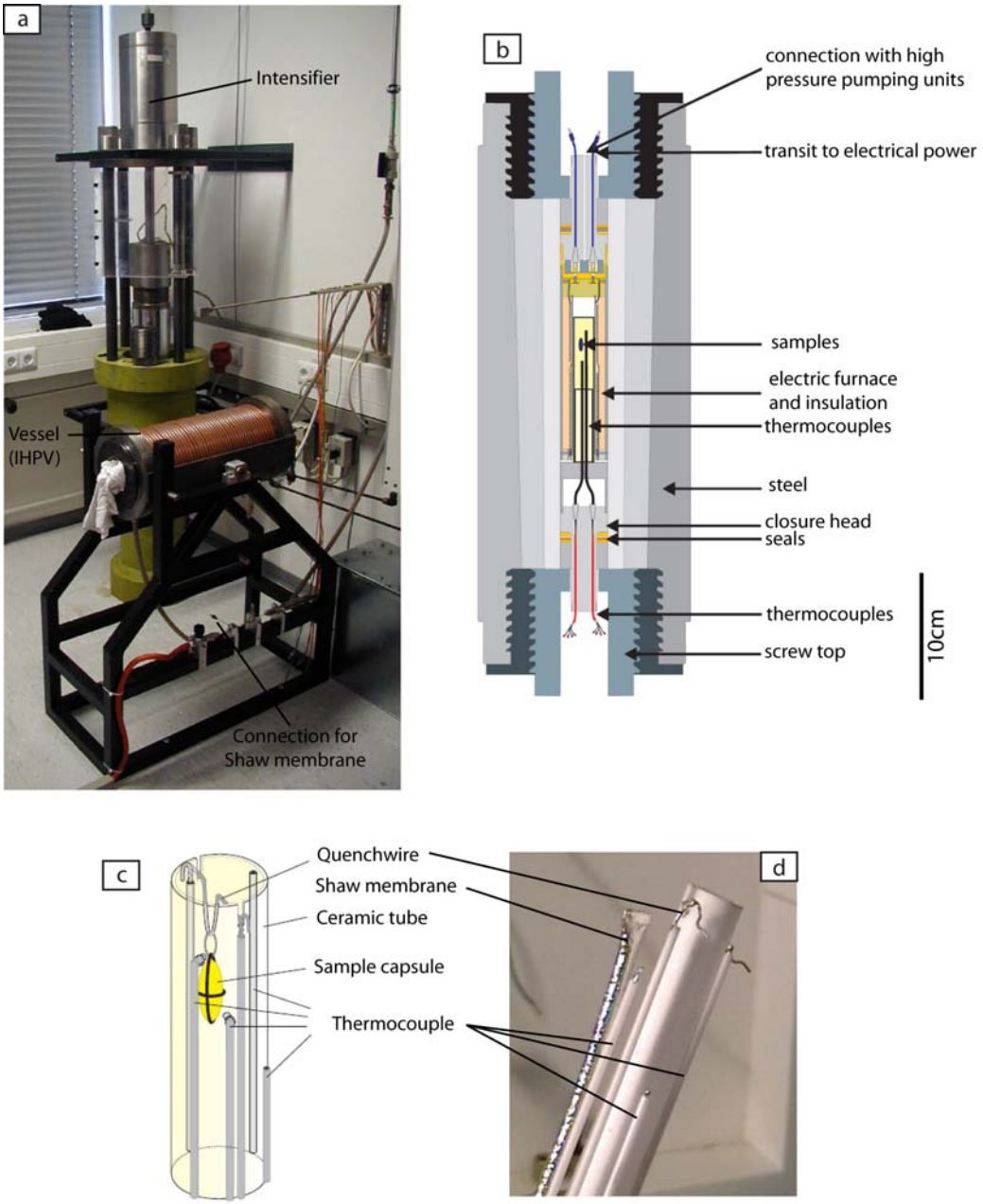

Figure IV-3: Argon pressurized IHPV equipped with a Shaw membrane as used in the experimental lab of the Institut für Mineralogie of the Leibniz Univeristy Hannover. a) IHPV before the sample loading; b) vessel internal structure; c-d) focus on the sample area, capsules are hanged using a thin platinum wire, which is fused electrically at the end of the experiment to allow rapid quenching (see text for further description); 4 S-type thermocouples are used to control the temperature gradient present around the sample, and a Shaw membrane is present to control the redox conditions.

In the IHPV, redox conditions were fixed by the given H_2 pressure which was measured using a Shaw membrane (e.g., Scaillet et al., 1992; Berndt et al., 2002; Figure IV-3d). Berndt et al. (2002) have shown that H_2 pressure in the used pressure vessel is constant during experiment duration, after an initial phase of equilibration. They have also shown that osmotic hydrogen equilibrium between membrane and vessel is obtained in less than 48 hours at 1000°C and 207 MPa. As the experiments presented herein were longer, it is expected that the final H_2 pressure measured within the membrane corresponds to the vessel one.

Capsules were hanged into the sample holder using a thin platinum wire (the "quench" wire; Figure IV-3c-d) and introduced horizontally in the vessel (Figure IV-3a). The whole IHPV was then toppled over vertically and thermocouples, Shaw membrane, and high pressure tubes were connected. Then, the vessel was first evacuated and then flushed with hydrogen. Then, the initial H_2 pressure of the run was applied, and the vessel was isolated from the H_2-reservoir. Afterwards, about 50% of the final Argon pressure was applied from the intensifier (Figure IV-3a) and the vessel was isolated from the Argon-pressure line. Temperature was then continuously rose (~30°/min), up to the desired temperature reached after ~30 min. Temperature, pressure and H_2 pressure were continuously recorded, and controlled after experiment to check the experiment conditions stability. At the end of the experiment, the quench wire was fused electrically and the capsules dropped isobarically into the cold quench area (~20°C); the cooling rate was ~150°/s. Effective quenching is evidenced by the absence of "quench minerals" (Figure IV-4).

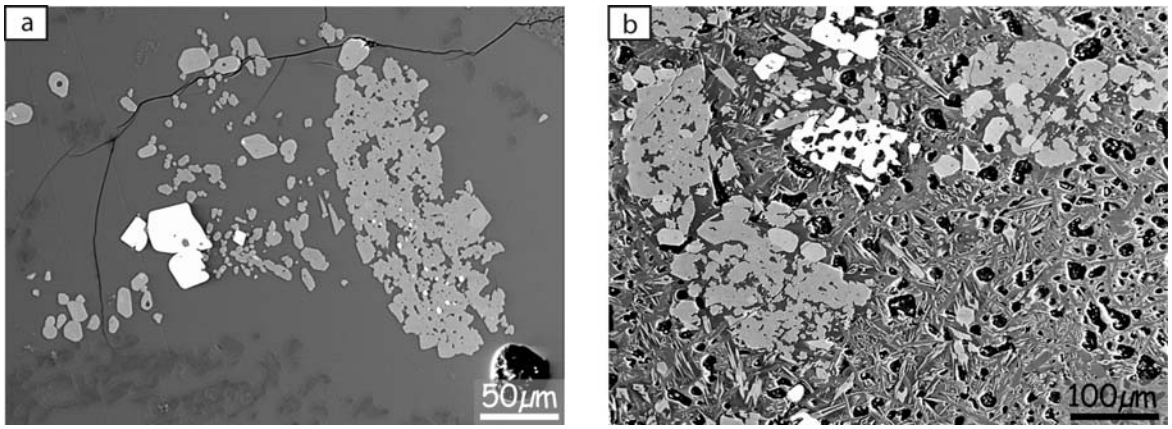

Figure IV-4: The quenching quality is evidenced by the absence of "quench minerals" (a). When quenching fails, melt is partially to totally recrystallized to "quench minerals" (b) (experiments at 1000°C).

IV.3. Hydrous partial melting in the sheeted dike complex at fast spreading ridges: Experiments and nature

Article submitted to *Contributions to Mineralogy and Petrology* (August 6, 2009).

Lydéric France[1,2,*], Juergen Koepke[2], Benoit Ildefonse[1], Sarah B. Cichy[2], Fabien Deschamps[3]

1: Géosciences Montpellier, CNRS, Université Montpellier 2, CC60, F-34095 Montpellier Cedex 05, France
2: Institut für Mineralogie, Leibniz Universität Hannover, Callinstrasse 3, D-30167 Hannover, Germany
3: LGCA UMR CNRS 5025, université Joseph-Fourier, BP 53, 38041 Grenoble cedex, France

IV.3.a. Abstract

In ophiolites and in present day oceanic crust formed at fast spreading ridges, oceanic plagiogranites are commonly observed at, or close to the base of the sheeted dike complex. They can be produced either by differentiation of mafic melts, or by hydrous partial melting of the hydrothermalized sheeted dikes. In addition, the hydrothermalized base of the sheeted dike complex, which is often infiltrated by plagiogranitic veins, is locally recrystallized into granoblastic dikes that are commonly interpreted as a result of prograde granulitic metamorphism. To test the anatectic origin of oceanic plagiogranites, we performed melting experiments on a natural hydrothermalized dike, under conditions that match those prevailing at the base of the sheeted dike complex.

All generated melts are water saturated, transitional between tholeiitic and calc-alkaline, and match the compositions of oceanic plagiogranites observed close to the base of the sheeted dike complex. Newly crystallized clinopyroxene and plagioclase have compositions that are characteristic of the same minerals in granoblastic dikes. Published silicic melt compositions obtained in classical MORB fractionation experiments also broadly match the compositions of oceanic plagiogranites; however, the compositions of the coexisting experimental minerals significantly deviate from those of the granoblastic dikes.

Our results demonstrate that hydrous partial melting is a likely common process in the root zone of the sheeted dike complex, starting at temperatures exceeding 850°C. The newly formed melt can either crystallize to form oceanic plagiogranites, or may be recycled within the melt lens resulting in hybridized and contaminated MORB melts. The residue after the partial melting event is represented by the granoblastic dikes. Our results support a model with a dynamic melt lens that has the potential to trigger hydrous partial melting reactions in the previously hydrothermalized sheeted dikes.

Keywords: mid-ocean ridge, axial magma chamber, hydrothermal system, sheeted dike complex, partial melting, experimental petrology, oceanic plagiogranite, granoblastic dikes

IV.3.b. Introduction

At fast spreading ridges, the root zone of the sheeted dike complex is a peculiar geological horizon where the thermal gradient can be as high as 7°C/m, one of the highest, nearly stable gradient observed on earth (Nicolas et al., 2008). Moreover, the contact of the sheeted dike with the underlying melt lens can be regarded as an interface between two convecting systems, the magmatic and the hydrothermal one. Highly hydrothermalized basaltic rocks from the base of the sheeted dike complex are therefore in the vicinity of a relatively constant heat source, which has the potential to trigger dehydration and/or melting reactions. Nicolas et al. (2008) have studied in the Oman ophiolite the varytextured gabbro horizon located directly below the sheeted dike complex, and have interpreted most of the observed lithologies as hydrous partial melting products. Gillis and Coogan (2002), Wilson et al. (2006), Gillis (2008) and Koepke et al. (2008) investigated the base of the sheeted dike complex in the Troodos ophiolite, in the Oman ophiolite, and in IODP (Integrated Ocean Drilling Program) Hole 1256D. They described typical granoblastic, hornfelsic lithologies in amphibolite- to granulite-facies, and relate them to reheated, dehydrated sheeted dike ("granoblastic dikes"). To further understand the active processes at the sheeted dike / gabbro transition, France et al. (2009a) have compared this zone in the Oman ophiolite with the recent IODP Hole 1256D, and propose a dynamic model with up- and downward migrations of the gabbro/sheeted dike interface that is consistent with published models and descriptions of Gillis and Coogan (2002), Wilson et al. (2006), Gillis (2008) and Koepke et al. (2008). The mobility of the melt lens is supported by the observed reheating of the base of the sheeted dike, and recycling of the previously hydrothermalized sheeted dike in the underlying varytextured gabbros. The occurrence of partly assimilated sheeted dike fragments within the uppermost gabbros suggests that the lowermost sheeted dikes underwent hydrous partial melting.

Oceanic plagiogranites, as defined in Koepke et al. (2007), are common in the oceanic crust, in particular at the base of the sheeted dike complex (e.g., Pallister and Hopson, 1981), where they are generally found as relatively small bodies (Koepke et al., 2004; 2007). These oceanic plagiogranites are believed to represent products of either differentiated MORB, liquid immiscibility between a mafic and a felsic melt, or hydrous partial melting of gabbros

or sheeted dikes. Formation from MORB differentiation has been proposed in natural settings (e.g., Beccaluva et al., 1977; Coleman and Donato, 1979; Dubois, 1983; Lippard et al., 1986; Amri et al., 1996; Floyd et al., 1998; Selbekk et al., 1998; Beccaluva et al., 1999; Niu et al., 2002; Rao et al., 2004; Bonev and Stampfli, 2009; Rollinson, 2009) and has also been verified in experimental studies (Dixon-Spulber and Rutherford, 1983; Berndt et al., 2005, Feig et al., 2006). Liquid immiscibility has been observed in rapidly quenched basaltic flows from the upper oceanic crust (e.g., Sato, 1978; Philpotts, 1982), inferred from ophiolites (Ménot, 1987; Ulrich and Borsien, 1996; Shastry et al., 2001) and described experimentally (Dixon and Rutherford, 1979).

IV.3.c. Natural occurrences and previous experiments on hydrous partial melting of mafic rocks

Hydrous partial melting of mafic rocks has been proposed or described in several studies (e.g., Malpas 1979; Gerlach et al., 1981; Pedersen and Malpas, 1984; Flagler and Spray, 1991; Spray and Dunning, 1991; Twinning, 1996; Floyd et al., 1998; Selbekk et al., 1998; Gillis and Coogan, 2002; Coogan et al., 2003; Stakes and Taylor, 2003; Koepke et al., 2004, 2005a; Luchitskaya et al., 2005; Koepke et al., 2007; Nicolas et al., 2008; Rollinson, 2009). Most of these studies deal with ophiolites and attempt to determine the origin of plagiogranitic rocks. The interpretation of an anatectic origin is based on structural evidences, and/or on trace element geochemical modeling. Evidences of hydrous partial melting of mafic lithologies have also been reported from young oceanic crust at both slow spreading (e.g., Mével, 1988) and fast spreading (e.g., Koepke et al., 2005b; 2008) centers. The partial to complete assimilation of previously hydrothermalized sheeted dike, in magma chambers at fast spreading ridges, implies that the assimilated hydrothermalized rocks undergo hydrous partial melting. This recycling process is described in ophiolites (Coogan et al., 2003; Gillis, 2008; France et al., 2009a), and in present day oceanic crust (Wilson et al., 2006; Koepke et al., 2008; France et al., 2009a), or inferred from chlorine contents in amphiboles (Coogan, 2003; Coogan et al., 2003) and MORB (e.g., Michael & Schilling, 1989).

Experimental work that precisely matches the conditions (low pressure, high temperature, hydrous and highly oxidizing conditions, basaltic composition, hydrothermal alteration) prevailing at the base of the sheeted dike is lacking. Several experimental studies (e.g., Beard and Lofgren, 1989; Hacker 1990; Beard and Lofgren, 1991; Rapp et al., 1991; Rushmer 1991, 1993; Sen and Dunn, 1994; Wolf and Wyllie, 1994; Rapp and Watson, 1995;

Patino Douce and Beard, 1995; Prouteau et al., 1999; Johannes and Koepke, 2001) have focused on the melting of mafic lithologies to investigate the origin of Archean tonalites, trondhjemites and granodiorites (TTG rocks; Barker 1979), which are believed to result from dehydration melting of amphibolites. Other authors have studied the melting of basalts in hydrous environment (Holloway and Burnham, 1972; Helz 1973; Beard and Lofgren, 1991; Kawamoto, 1996). Although some of these works approach the appropriate natural conditions (e.g., Beard and Lofgren, 1991), they are not fully relevant to the study of hydrous melting at the base of the sheeted dikes. These studies deal with subduction processes and most of them are conducted at pressures (in general ≥500 MPa) that are much higher than those (~100 MPa) prevailing at the base of the upper, basaltic oceanic crust. Moreover, most of these studies use dehydration melting experiments which are valid for the subduction environment but not for the base of the sheeted dikes where a lot of water is available at low pressure, resulting in water saturated conditions. The study of Beard and Lofgren (1991) approaches those conditions relevant to partial melting/assimilation of hydrothermalized sheeted dike at the gabbro/dike transition. Unfortunately, they don't provide the mineral compositions, and the redox conditions are not fixed but roughly estimated. The redox conditions, which are influenced by the presence of a high temperature hydrothermal system at the base of the sheeted dike (Nicolas et al., 2008), must be precisely controlled to understand and follow the evolution of melt and minerals with temperature. Koepke et al. (2004) have performed hydrous partial melting experiments on gabbroic lithologies from the lower oceanic crust with controlled redox conditions, but these experiments are not applicable to hydrous partial melting at the base of the sheeted dike complex. Hydrous partial melting of sheeted dike and gabbro may produce different melts and different residual phases because of different composition and mineralogy of the used starting material. While typical oceanic gabbros show a marked refractory character (e.g., extremely depleted in incompatible elements like Ti and K; mostly high in Mg#, with Mg#=Mg/[Mg+Fe]), most sheeted dikes are more evolved with compositions of evolved MORB. Another characteristic feature of the dikes at the gabbro/dike transition is related to significant hydrothermal alteration responsible for the formation of considerable amounts of hydrous minerals, which affects the melting behavior of a rock, in particular at lower temperatures, where the completion of a global equilibrium is often hampered.

IV.3.d. Experimental and analytical techniques

IV.3.d.1. Starting material

In order to closely match natural processes, we have selected a representative sample (08OL30) of typically altered sheeted dikes from the Oman ophiolite. It has been sampled in the Aswad area located in the southern Sumail massif, which is inferred to correspond to typical oceanic crust away from ridge discontinuities, and not affected by ridge tectonics or obduction-related deformation (Nicolas et al., 2000; Nicolas et al., 2008). Its whole rock composition is representative of typical sheeted dike from the Oman ophiolite (Fig. 1; Table 1). Compared to the average sheeted dike rocks sampled at ODP/IODP Hole 1256D and ODP Hole 504B, at Hess Deep, and at the Blanco Depression (Table 1), the chosen starting material is slightly more evolved. It is strongly altered due to a static hydrothermal overprint, which is a common feature of the sheeted dike complex in the studied area. The selected sample is composed of albitized plagioclase (An_{03}), actinolite, prehnite, pumpellyite, titanite, and some magnetite (Fig. 2), an assemblage typical of greenschist-facies conditions (see section "phase compositions in the partly molten system" for mineral compositions). Primary magmatic phases are not observed.

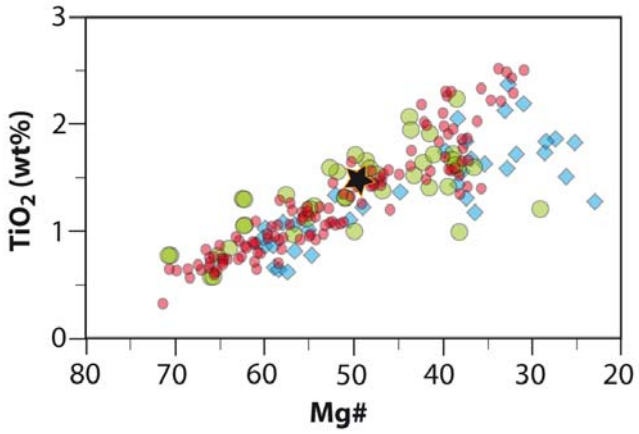

Figure 1: *Comparison of the bulk rock composition of the starting material (08OL30) with those of sheeted dike complex and extrusives of the Oman ophiolite in a TiO_2 vs Mg# diagram (with Mg#=Mg/[Mg+Fe_{total}]); after Miyashita et al. (2003). Symbols are black star: starting material, red small circle: sheeted dike complex by Miyashita et al. (2003), green large circle: sheeted dike complex by Lippard et al. (1986), and Type 1 dikes by Rochette et al. (1991), blue diamonds: Geotimes volcanics by Lippard et al. (1986) and V1 lava by Einaudi et al. (2000).*

After crushing the starting rock, three grain size fractions were obtained by sieving (30-100 µm, 100-150 µm, and 150-250 µm) and were used for preliminary experiments. These experiments were performed at a temperature of 1000°C to study the effect of grain

size of the starting material on the kinetics of the melting reaction (Table 2). In the three experimental products, minerals and melts have identical compositions within the analytical errors. Moreover, the phases are homogeneous, crystals display no zonation, and compositions are identical within the whole capsule volume, independent of the grain size of the starting material (Fig. 3a). No relict phases of the starting material were observed. As experiments performed with coarser grain size produce larger experimental crystals and melt pools, which are more suitable for electron microprobe measurements, we chose the 150-250 µm fraction as starting material (Table 1).

	SiO_2	TiO_2	Al_2O_3	Fe_2O_3(t)	MnO	MgO	CaO	Na_2O	K_2O	P_2O_5	LOI	total	Mg #
080L30	50.38	1.40	15.04	10.29	0.06	4.99	7.19	4.44	0.19	0.11	4.74	98.8	-
080L30_recalculated	53.55	1.48	15.98	10.94	0.07	5.30	7.64	4.72	0.20	0.12	-	100	*49.0*
Oman, Umino et al., 2003	52.51 ± 2.09	1.17 ± 0.45	16.06 ± 0.92	10.41 ± 1.83	0.15 ± 0.05	6.68 ± 1.28	8.51 ± 2.81	4.21 ± 1.34	0.18 ± 0.15	0.11 ± 0.03	-	100	*56.0*
Oman, Miyashita et al., 2003	52.59 ± 1.72	1.33 ± 0.50	15.64 ± 0.76	10.89 ± 2.16	0.16 ± 0.05	6.03 ± 1.55	8.86 ± 2.68	4.24 ± 1.39	0.16 ± 0.12	0.11 ± 0.05	-	100	*52.3*
1256D, Teagle et al., 2006	50.56	1.55	13.75	13.57	0.23	6.88	10.75	2.53	0.05	0.13	-	100	*50.1*
Hess Deep, Pollock et al., 2009	50.57	1.37	14.31	11.58	0.20	8.02	10.82	2.78	0.05	0.31	-	100	*57.8*
504B, Bach et al., 1996	49.36	0.80	16.12	9.60	0.15	8.93	13.11	1.86	0.01	0.06	-	100	*64.8*
Blanco Depression, Cordier et al., 2007; Juteau et al., 1995	50.08	1.99	13.97	13.15	0.21	6.79	10.60	2.82	0.22	0.16	-	100	*50.5*

Table 1: Whole rock compositions of the starting material and of sheeted dike complex from different oceanic localities. Composition of the sheeted dike complex from Oman (Umino et al., 2003; Miyashita et al., 2003), from IODP Hole 1256D in the Cocos plate (Teagle et al., 2006), from Hess Deep (East Pacific Rise [EPR]; Pollock et al., 2009), from ODP Hole 504B (Bach et al., 1996), and from the Blanco Fracture Zone on the Juan de Fuca ridge (average of data from Juteau et al., 1995 and Cordier et al., 2007). For comparison, compositions of sample 08OL30 (starting material) are recalculated at 100%. Standard deviations are given for the Oman sheeted dike. Mg#=Mg/(Mg+Fe_{total}); LOI=loss on ignition.

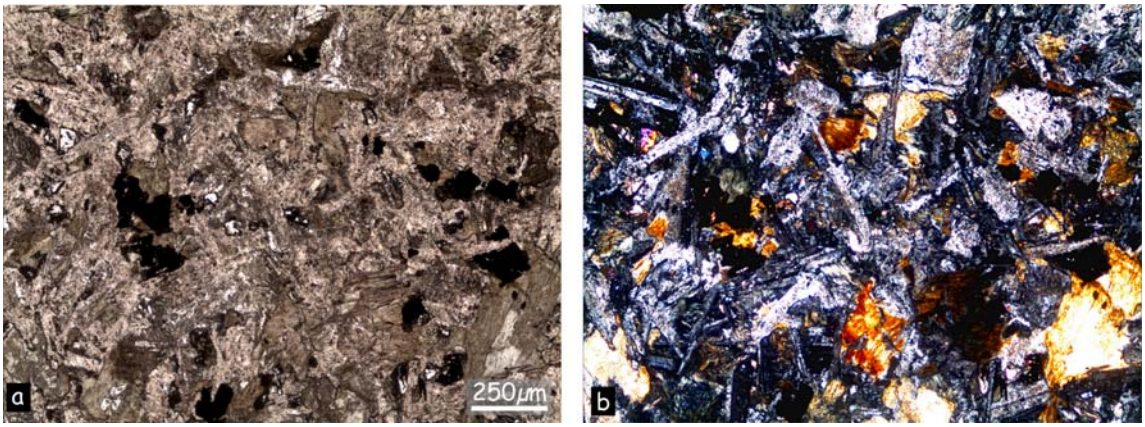

Figure 2: *Microphotographs of the starting material (08OL30).* ***a)*** *plane-polarized light;* ***b)*** *cross-polarized light.*

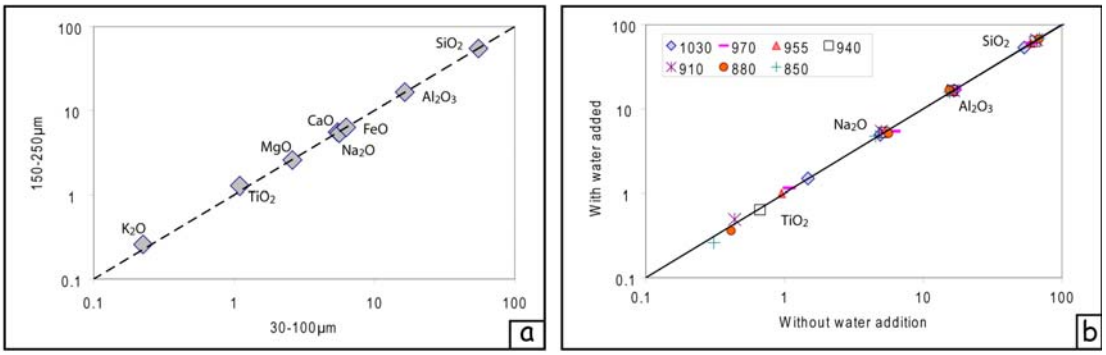

Figure 3: *Comparison of melt compositions from experiments performed with identical starting compositions (wt%) for different grain sizes of the starting material (a). Each data point represents the average for one oxide (as indicated). The corresponding experiments were performed at 1000°C. b) Comparison of melt compositions from experiments performed with identical starting compositions (wt%) for experiments with and without water added shown for the TiO_2, Na_2O, Al_2O_3 and SiO_2 at different temperatures. In both logarithmic plots, the line represents the 1:1 correlation. Grain size (a), and the addition of water to the starting material (b) have no influence on the melt composition.*

IV.3.d.2. Experimental method

Melting experiments (≥850°C) have been performed in an internally heated pressure vessel (IHPV) at the experimental lab of the Institut für Mineralogie (Hannover, Germany), equipped with a Shaw membrane and a rapid quench device. Details of the IHPV are presented in Berndt et al. (2002). The vessel was pressurized with argon at 100 MPa, a pressure relevant to the level of the axial melt lens within the ocean crust. The pressure was controlled with a strain gauge manometer (uncertainty of ±5 MPa). Previous calibrations on the vessel show that temperature is homogeneous over the sample with less than 10° of variation and a measurement accuracy better than ±10°. This is also indicated by the regular evolution of the melt and mineral compositions with temperature (see below). Experimental conditions are summarized in Table 2. In all experiments, the prevailing fO_2 corresponds to FMQ+1 – FMQ+2, where FMQ is the fayalite-magnetite-quartz oxygen buffer equilibrium (for values see Table 2). At the beginning of the experiment, the temperature rises continuously (30°C/min) to reach the final experimental temperature after ~30 min. At the end of experiments, the samples were quenched isobarically using a rapid quench facility to prevent crystallization during cooling (~150°/s). Effective quenching is evidenced by the absence of "quench minerals" in melts in spite of the presence of low viscous basaltic melts with high water content.

RUN N°	Capsule	Temp. (°C)	f(H_2)	Δ_{FMQ}	Phases	duration	grain size
#3	#10[D] #12[W]	***1030***	2.18	1.38	melt, Ol, Cpx	72h	150-250µm
#1	#2c[W] #3b[W] #4a[W]	***1000***	2.77	1.56	melt, Ol, Cpx, Pl, TiMagt, Pl_m	72h	150-250µm 100-150µm 30-100µm
#4	#13[D] #14[W]	***970***	1.89	1.51	melt, Ol, Cpx, Pl, TiMagt, Pl_m	96h	150-250µm
#7	#23 [D] #25[W]	***955***	2.63	1.24	melt, Ol, Cpx, Pl, TiMagt, Ilm, Pl_m	96h	150-250µm
#6	#17[D] #18[W]	***940***	2.02	1.45	melt, Ol, Cpx, Pl, Amp, Opx, TiMagt, Ilm, Pl_m, Titanite, Apatite	96h	150-250µm
#2	#5[D] #8[W]	***910***	2.24	1.36	melt, Cpx, Pl, Amp, Opx, TiMagt, Ilm, Pl_m, Titanite	120h	150-250µm
#5	#15[D] #16[W]	***880***	0.97	2.09	melt, Cpx, Pl, Amp, Opx, TiMagt, Ilm, Pl_m, Titanite, Act	120h	150-250µm
#8	#24[D] #26[W]	***850***	2.53	1.13	melt, Cpx, Pl, Amp, Opx, TiMagt, Ilm, Pl_m, Titanite, Act	144h	150-250µm
#metam 1	#9[D] #11[W]	***800***	-	0.79	Pl, Amp, Opx, TiMagt, Ilm, Titanite, Act, Ab (+Pl_m+Cpx)	504h	150-250µm
#metam 2	#21[D] #22[W]	***750***	-	0.80	Pl, Amp, Opx, TiMagt, Ilm, Titanite, Act, Ab (+Pl_m+Cpx)	624h	150-250µm

Table 2: Experimental conditions. Temp.=temperature; D = experiment without water addition, W = experiment with water addition. The oxygen fugacity is given in log units relative to the FMQ oxygen buffer. Minerals in parentheses (+Pl_m+Cpx) are localized in the prehnite reaction zones (see "prehnite break-down reaction" part for further details). Ol=olivine, Cpx=clinopyroxene, Pl=plagioclase, TiMagt=titanomagnetite, Pl_m=metastable plagioclase, Ilm= ilmenite, Amp=amphibole, Opx=orthopyroxene, Act=actinolite, Ab=albite, Magt=magnetite.

In addition to the high temperature runs in the partially molten regime, subsolidus experiments (750°C and 800°C) have been performed in an externally heated cold-seal pressure vessel (CSPV). This vessel was pressurized with water at 100 MPa and controlled with a pressure transducer calibrated against a strain gauge manometer. The accuracy of pressure measurements was 1 MPa and pressure variations during the experiments were less than ±5 MPa. The temperature was controlled with an external Ni-CrNi thermocouple (vessels were calibrated for temperature). The temperature variations were less than 5°C, while the accuracy was estimated to be ±10°C. Experiment conditions are summarized in Table 2. In all experimental runs, fO_2 corresponds to the NNO oxygen buffer (≈FMQ+1), established by adding a solid buffer composed of a Ni-NiO assemblage around the gold capsule. After experiments, samples were quenched isobarically by using a flux of compressed air (initial

cooling rate ~200°/min). For all the experiments gold was used as capsule material. Thus, iron diffusion into the capsule material can be neglected.

Since the natural samples from the root zone of the sheeted dike complex contain high amounts of hydroxyl-bearing minerals (actinolite, prehnite, pumpellyite), it was expected that water would be released in the partial melting experiments (dehydration melting). Due to the relatively low water solubility in basaltic melts at the given shallow pressure of 100 MPa (~ 3%; Berndt et al., 2002), water-saturating in the experiments was expected. We performed one experimental series under water-saturated conditions by adding distilled water (5 mg) to the starting material (50 mg) and another series without adding water, corresponding to typical dehydration experiments. The two capsules (with and without water addition) were run simultaneously at each temperature. For each temperature, results from both capsules are identical for the phase relations and phase compositions (Fig. 3b), suggesting that in both experimental series, water saturation was reached, and that the dehydration melting produces enough water for reaching water-saturated condition. In all experiments bubbles are present, attesting fluid (mainly composed of water) saturation (Fig. 4). The similarity between the two series show that experiments are reproducible.

IV.3.d.3. Analytical method

Experimental results were analyzed using a Cameca SX100 electron microprobe (Institut für Mineralogie, Hannover, Germany) equipped with 5 spectrometers, "Peak sight" software is used. All analyses were performed using a 15 kV acceleration potential, a static (fixed) beam, Kα emission from all elements. The matrix correction is based on Pouchou and Pichoir (1991). Analyses of crystals were performed with a beam current of 15 nA using a focused beam and a counting time of 10 to 30 s on peak and background. Analyses of glass were performed with a beam current, which was set to 6 nA to minimize migration and volatilization of the alkali elements. Counting time was from 2 to 5 s for Na and K and from 5 to 10 for other elements (Si, Ti, Al, Mg, Fe, Ca, Mn, Cr). In the experiments where melt pools are large enough, the beam was defocused to a spot size of 5 to 20 μm. Backscattered electron (BSE) images were also obtained on the Cameca SX100 electron microprobe.

IV.3.e. Experimental results

IV.3.e.1. Attainment of equilibrium

The use of fine grained starting material (≤1 μm) in partial melting experiments enhances the achievement of global equilibrium. Unfortunately, it prevents suitable

microprobe analyses due to very small newly formed experimental phases. The advantage of using coarser grained starting material is the formation of relatively large crystals in the experimental products, which enables easy microprobe analyses of the experimental phases. However, too coarse-grained starting material may prevent the achievement of global equilibrium, since cores of unreacted starting material may be still present after the experiment, as observed in many typical dehydration melting experiments of mafic protoliths (e.g., Hacker, 1990; Beard and Lofgren, 1991; Patino Douce and Beard, 1995; Johannes and Koepke, 2001). This effect is most pronounced concerning plagioclase, which is the rate-controlling phase in many basaltic systems (Johannes and Koepke, 2001). These authors show that reaction kinetics can be significantly enhanced in water-saturated systems, as it was the case in our experiments. Moreover, the starting material in our experiments shows a pervasive alteration overprint (plagioclase with An<03, actinolite, titanite, prehnite, pumpellyite, magnetite), and no typical primary magmatic phases (e.g., olivine, pyroxene, An-rich plagioclase, or magmatic amphibole) were present. Hence, the phase assemblage had to change completely during the melting reaction, thus minimizing the risk of formation of typical core/rim complexes of the reacting minerals. Due to the favorable conditions in our melting experiments, no relics of the starting material are present in most of the melting experiments, in particular those experiments performed at temperatures > 910°C.

Several lines of evidence are listed below, which suggest that a state close to equilibrium has been attained in our "magmatic" experiments (i.e., temperatures > 910°C): (1) No zonations in newly formed crystals are observed (Fig. 4) and crystal compositions are homogeneous within each experiment and between the two series (with and without addition of water). (2) Newly formed crystals are euhedral (e.g., Ol) or mimic previous minerals that are not present anymore (e.g., Cpx and Pl; Fig. 4). (3) No relictic phases from the starting materials are observed (for temperature > 910°C). (4) All phase compositions vary systematically with temperature, and compositional trends are consistent with the ones expected from literature (e.g., rise of the plagioclase An content; see “phase compositions in the partly molten system” section). (5) Glass compositions also vary systematically with temperature (see “phase compositions in the partly molten system” section), and are homogeneous within each experiment and between the two series (with and without addition of water).

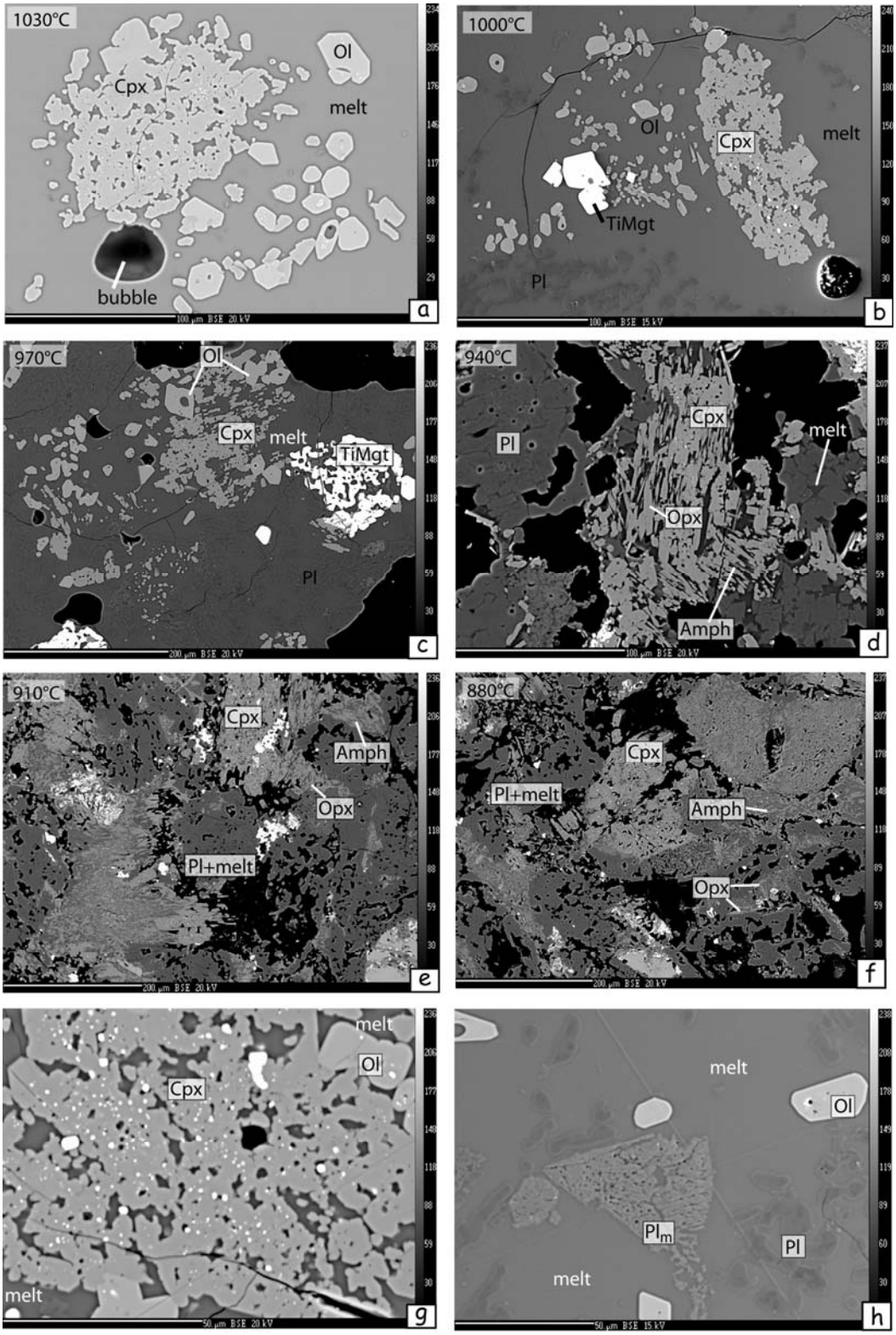

Figure 4: *Backscattered electron images of the experimental results in the partly molten system for different temperatures* ***a)*** *1030°C with water added (melt proportion is not representative for the whole sample which shows >90% melt);* ***b)*** *1000°C with water added;* ***c)*** *970°C with water added;* ***d)*** *940°C without water addition;* ***e)*** *910°C without water addition;* ***f)*** *880°C without water addition;* ***g)*** *numerous tiny oxide-inclusions in clinopyroxene and olivine in the experiment performed at 970°C without water addition;* ***h)*** *"metastable plagioclase" in the experiment performed at 1000°C with water added. Minerals abbreviations are the same as in Table 2.*

Nevertheless, a second type of plagioclase was observed in all experiments at temperatures ≤ 1000°C. Compared to the equilibrium plagioclase which shows an idiomorphic habit, these are spongy with very irregular grain boundaries (Fig. 4h) and highly enriched in An component (Table in Appendix B2). These crystals are interpreted to represent metastable phases which were recrystallized after prehnite (for further details see section "Prehnite break-down reaction"). Since these crystals occur only very rarely, we consider that the approaching of global equilibrium in these experiments is not hampered.

In subsolidus experiments, reactions are not complete and new phases are only observed as coronitic assemblages. Therefore, these experiments will only be used to understand the metastable assemblages present in the partly molten system (see section "prehnite break-down reaction").

IV.3.e.2. Phase relations in the partial molten system

The evolution of the phase relations (Fig. 5) was established with the help of backscattered electron images (BSE) images (e.g., Fig. 4).

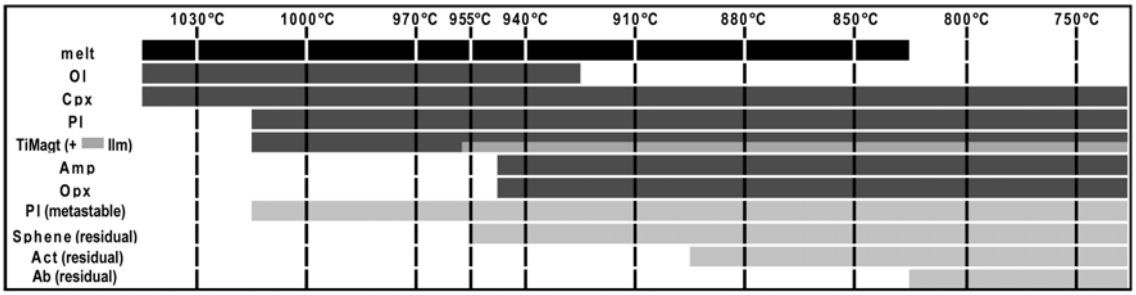

Figure 5: *Phases present in the products of partial melting and subsolidus experiments as a function of temperature. Minerals abbreviations are the same as in Table 2.*

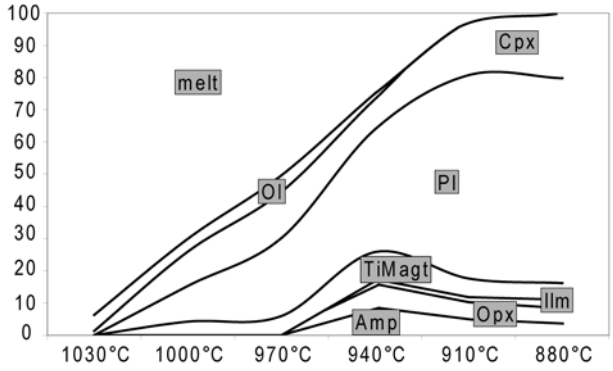

Figure 6: *Phase proportions in the partly molten system calculated with a least square model according Albarède and Provost (1977). Standard deviation < 1 for all values. Values obtained for experiments at temperatures < 950°C are less accurate. Incoherent values are obtained at 850°C. Minerals abbreviations are the same as in Table 2.*

Figure 6 gives a rough estimate of the phase proportions which were obtained via least square calculations (Albarède and Provost, 1977). The first melt was observed at temperatures as low as 850°C, and the liquidus temperature is slightly higher than 1030°C. While in the low-temperature experiment performed at 850°C melt pools seem to remain isolated, at temperatures > 910°C the melt phase forms a connected framework. Melt proportion is low (<10%) for temperatures < 910°C, and a large increase is observed between 940°C and 970°C (Fig. 4); above 970°C the melt proportion continues to increase linearly until the liquidus is reached. The liquidus phases are olivine and clinopyroxene; plagioclase and titanomagnetite are present below 1000°C. The saturation of olivine and clinopyroxene at near liquidus condition in tholeiitic systems is somewhat uncommon, but can be ascribed to the high water activities as experiments are water saturated (e.g., Gaetani et al. 1993, Feig et al., 2006). First olivine appears at 940°C. Amphibole is stable in experiments up to 940°C. At this temperature, when applying the TiO_2 contents of amphibole to the semi-quantitative TiO_2-in-amphibole thermometer of Ernst and Liu (1998), the estimated temperature is 950°C and matches very well the run temperature, implying the achievement of equilibrium condition. The application of this thermometer is justified, since the amphibole in our experiments is coexisting with a Ti-rich oxide phase (Ernst and Liu, 1998).

Orthopyroxene is stable up to 940°C. Application of the 2-pyroxene thermometer (Andersen et al., 1993) reveals equilibrium temperatures which are largely overestimated: 1092±31°C for the 940°C run; 1039±30°C for the 910°C run; 1041±36°C for the 880°C run, and 1056±14°C for the 850°C run (data of Table in Appendix B2 are used, these are averages of experiments with and without water addition). This large discrepancy can be explained by the presence of a high water activity, as the presence of water shifts the Mg# of clinopyroxene and orthopyroxene to higher values and consequently to higher calculated temperatures (Feig et al., 2006). Ilmenite is present up to temperatures of 955°C; at higher temperatures, only titanomagnetite is stable. Application of the 2-oxide thermo-oxybarometer (Sauerzapf et al., 2008) reveals an equilibrium temperature of 929°C and ΔNNO=+0.58 for the 955°C experiment, 901°C and ΔNNO=+1.01 for the 940°C experiment, 872°C and ΔNNO=+0.83 for the 910°C experiment, 814°C and ΔNNO=1.35 for the 880°C experiment, 779°C and ΔNNO=+0.82 for the 850°C experiment, and 719°C and ΔNNO=+0.89 for the 750°C subsolidus experiment (data of Table in Appendix B2 are used, these are averages of experiments with and without water addition). The accuracy of the 2-oxide thermo-oxybarometer is ±70° for the temperature and ±0.4 log units for the oxygen fugacity (Sauerzapf et al., 2008). Hence, these estimations are consistent with the conditions of the

experiments (Table 2). Numerous tiny oxides with grain sizes < 5 µm were observed as inclusions in nearly all olivine and clinopyroxene grains (Fig. 4g). This observation is of significance, since similar features are observed in clinopyroxenes from the granulite-facies granoblastic dikes in natural settings (e.g., Koepke et al., 2008; France et al., 2009a), providing a tool for identifying such clinopyroxenes as residual phases after hydrous partial melting. Titanite is stable from low temperature experiments to 940°C. In experiments from 910°C to 1000°C, some rare grains of a metastable plagioclase (Pl_m) are observed (Fig. 4h).

IV.3.e.3. Prehnite break-down reaction

In the subsolidus experiments, some sparse, complex mineral assemblages with an apparent coronitic structure are locally present (Fig. 7).

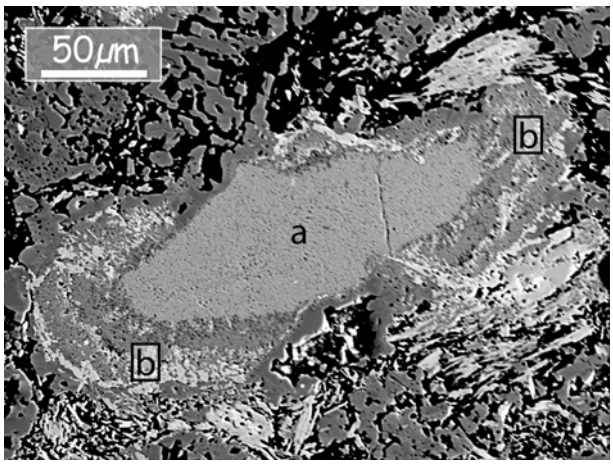

Figure 7: *Backscattered electron image of a coronitic assemblage (750°C with water added experiment) that displays in the center (a) a mineral assemblage compositionally similar to "dry prehnite"; it is interpreted as an anorthite+wollastonite assemblage. At the rim (b) of this assemblage, an assemblage of metastable plagioclase (Pl_m) and Ca-Al-rich clinopyroxene is observed (brighter). This assemblage is interpreted to be derived from the prehnite break-down reaction (see the part "Prehnite break-down reaction" for more details).*

In the center of these assemblages, the composition is similar to that of a "dry prehnite". The margins consist of a close intergrowth of plagioclase, which is slightly enriched in An compared to the equilibrium plagioclase, and clinopyroxene. Clinopyroxene is not present elsewhere in the subsolidus experiments, but these ones present in the coronitic assemblages are enriched in CaO and Al_2O_3 compared to the ones of partial melting experiments. According to Liou (1971), prehnite, which is present in our starting material, should react to an assemblage of anorthite + wollastonite when temperature increases (1 prehnite ⇔ 2 anorthite + 1 wollastonite + H_2O). The composition of the assemblage "2 anorthite + 1 wollastonite" corresponds exactly to that of the "dry prehnite" which was analyzed in the corresponding run (Table in Appendix B2). Since the compositions of the phases forming the

close intergrowth network of the rim also deviate slightly from the corresponding equilibrium compositions of plagioclase and clinopyroxene, we interpret the whole coronitic assemblage as a metastable product of the prehnite breakdown reaction. We speculate that the sparse plagioclases with an apparent spongy structure as presented in Figure 4h, which are much richer in An compared to the equilibrium plagioclases, correspond to metastable relics of such prehnite breakdown reactions. It should be noted that in experimental dehydration melting of mafic systems relics of An-rich plagioclases may persist metastably for a very long time, even at high water activities (more than 36 days in experiments of Johannes and Koepke, 2001).

IV.3.e.4. Phase compositions in the partial molten system

The phase compositions of the starting material and of the experimental products are listed in Table in Appendix B2; indicated compositions are averages of mineral compositions in experiments with and without water addition (Fig. 3b). Detailed compositions for each series (with and without water addition) are provided as supplementary material. The dependence of olivine composition on temperature is shown in Figure 8a. The forsterite content (Fo) is nearly identical between the 1000°C and the 1030°C experiments; it may reflect the identical Mg# of the melt in these two runs. The partitioning of Fe and Mg between olivine and melt ($K_{D_{Fe-Mg}}^{Ol-melt} = \frac{X_{Liq}^{Mg} / X_{Ol}^{Mg}}{X_{Liq}^{Fe^{2+}} / X_{Ol}^{Fe^{2+}}}$) is classically considered to be 0.30±0.02 (Roeder and Emslie, 1970). Toplis (2005) has reviewed this partitioning coefficient, and has proposed a new equation to calculate $K_{D_{Fe-Mg}}^{Ol-melt}$ that can vary as a function of temperature, alkalis, and water. Using this equation for the conditions of our experiments leads to a predicted value of 0.30±0.02. $K_{D_{Fe-Mg}}^{Ol-melt}$ measured in our experiments is ~0.25 by using the FeO^{tot} of the melt, which is not in the accepted error range. However, as the oxygen fugacity is known in our experiments, the real FeO value (including only the Fe^{2+}) in the melt can be calculated using the Kress and Carmichael (1991) model; the resulting average $K_{D_{Fe-Mg}}^{Ol-melt}$ is 0.28 which is in the accepted range of error according to Toplis (2005), which support the assumption that equilibrium is nearly attained in our experiments.

In the melting experiments, typical clinopyroxene is augite. As expected, its composition varies systematically with temperature. With rising temperature, the wollastonite component and the Mg# increase (from 38 to 44, and from 66 to 78, respectively), as well as the concentration of TiO_2 and Al_2O_3. Clinopyroxene Al_2O_3 content decreases with temperature from 3 to 1.26 wt% (Fig. 8b) whereas the melt Al_2O_3 content is nearly stable.

This demonstrates the dependence of the partition coefficient $D_{Al_2O_3}^{Cpx-melt}$ on temperature. It decreases by a factor of ~2 (from ~0.2 to ~0.1) with temperature. Orthopyroxene is clinoenstatite; the wollastonite component and Mg# are, for all temperatures, between 3 and 4, and between 63 and 72, respectively.

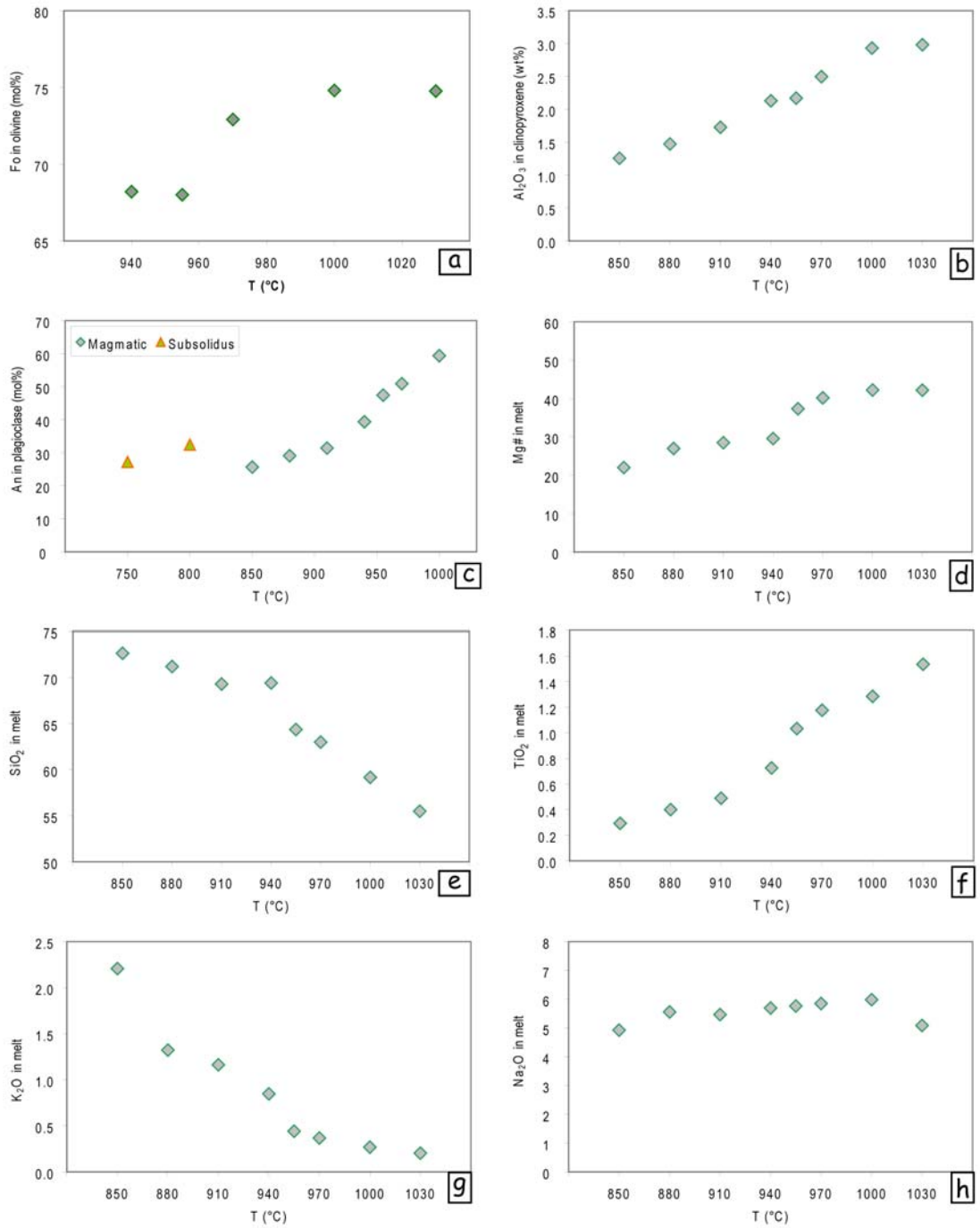

Figure 8: *Compositional features of the experimental phases as a function of temperature.* ***a)*** *Forsterite content in olivine;* ***b)*** *Al_2O_3 content of clinopyroxene in the partly molten system;* ***c)*** *Anorthite content of plagioclase in the partly molten and subsolidus systems;* ***d)*** *Mg# in melt;* ***e)*** *SiO_2 in melt;* ***f)*** *TiO_2 in melt;* ***g)*** *K_2O in melt;* ***h)*** *Na_2O in melt.*

The anorthite (An) content of plagioclase increases with temperature from 26 to 59. For comparison, subsolidus plagioclase compositions are indicated in Figure 8c; the An content increases with temperature from 27 to 31.5. In the partly molten system the FeO_t content of plagioclase increases with temperature, reaching 0.94 wt% in the 1000°C run. This increase is correlated with increasing FeO_t content in the melt. In contrast, the partition coefficient $D_{FeO_t}^{Pl-melt}$ increases with decreasing temperature. Lundgaard and Tegner (2004) have shown that $D_{FeO_t}^{Pl-melt}$ depends on the redox conditions and on the silica content of the melt ($D_{FeO_t}^{Pl-melt}$ is higher for more oxidizing conditions and for higher silica contents). As our experiments are performed at very similar redox conditions, we attribute this increase of $D_{FeO_t}^{Pl-melt}$ to the increase in silica content of the melt with decreasing temperature.

Titanomagnetite is present from 850°C to 1000°C; it contains between 8 and 14 wt% of TiO_2 while the Al_2O_3 and MgO contents increase with temperature (from 1.55% to 4.21%, and from 1.26% to 4.39%, respectively). Ilmenite is present from 850°C to 955°C; minor components as SiO_2, Al_2O_3, and MgO globally increase with temperature. The amount of Cr_2O_3 in both oxides is below detection limit.

Amphiboles in the experiments with melt present are edenite and pargasite. As expected, their TiO_2, Al_2O_3, and Na_2O contents increase with temperature. For comparison, they vary from actinolite to hornblende in subsolidus experiments.

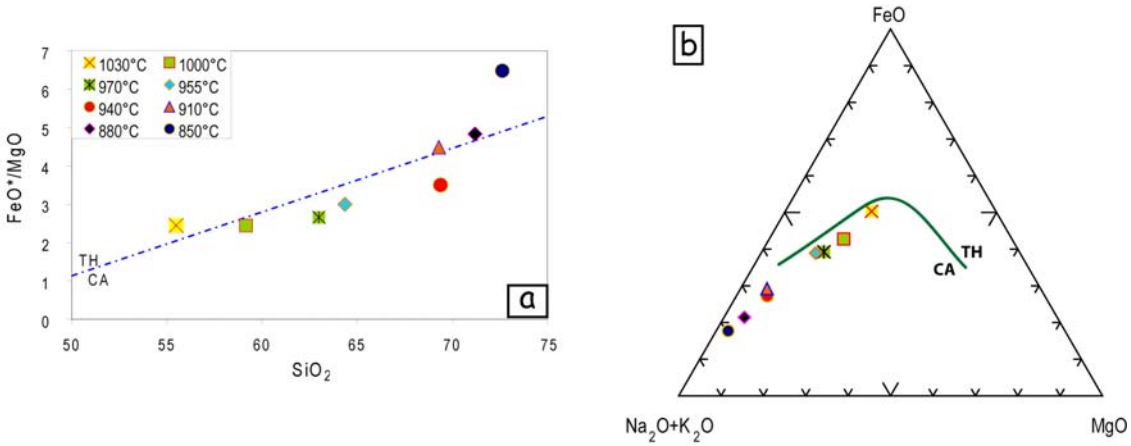

Figure 9: a) *FeO*/MgO versus SiO_2 diagram from Miyashiro (1974). FeO*=FeO_{total}; TH=tholeiitic field, CA=Calc-alkaline field* ***b)*** *Alkaline (Na_2O+K_2O)-FeO_{total}-MgO discriminating diagram from Irvine and Baragar (1971).*

Melt is saturated with water in all experiments (presence of bubbles). In the experimental melt obtained with the highest temperature (1030°C), which displays the largest

melt pools, a water content of 4.8 wt% has been determined by FTIR (Fourier Transformed InfraRed spectroscopy). The Mg# of the melt increases with temperature from 22 to 42.2 (Fig. 8d). The SiO_2 and K_2O contents decrease with increasing temperature, whereas the TiO_2, MgO, FeO and CaO contents increase (Fig. 8). Those melts formed at the lowermost temperature (~850°C) reach SiO_2 contents of 72.6 wt%. In a FeO_{total}/MgO versus SiO_2 discriminating diagram (Miyashiro, 1974), and in an Alkaline (Na_2O+K_2O)-FeO_{total}-MgO discriminating diagram (Irvine and Baragar, 1971), the experimental melts plot close to the transition between the calc-alkaline and tholeiitic series (Fig. 9).

IV.3.f. Discussion

IV.3.f.1. Melt evolution: Origin of oceanic plagiogranites at the base of the Sheeted Dikes

Our experimental melts are compared with other experimental results and with natural data in Figure 10. For comparison with experimental data, we used MORB fractionation experiments (Dixon-Spulber and Rutherford, 1983; Berndt et al., 2005), Fe-Ti MORB fractionation experiments (Juster et al., 1989; Toplis and Carroll, 1995), immiscible melt compositions (Dixon and Rutherford, 1979), and gabbro, amphibolite and basalt anatexis experiments (Koepke et al., 2004, Beard and Lofgren, 1991, and Thy et al., 1999, respectively). Our experiments are relatively similar to those of Beard and Lofgren (1991), and the melt compositions are therefore similar. Nevertheless, our experiments reach lower silica contents despite lower temperature equilibration (850°C in our experiments and 900°C in the Beard and Lofgren ones). The K_2O contents of our experimental melts are similar to most of the Beard and Lofgren (1991) experiments, except for one of their series that display lower contents, and which corresponds to a highly K_2O depleted starting composition. Fe-Ti MORB fractionation melts and immiscible liquids are depleted in Al_2O_3 and enriched in TiO_2 regarding other experiments. Interestingly, in our lower temperature experiments, the composition of the melt is below the line of saturation for TiO_2 in basaltic melts defined by Koepke et al. (2007) (Fig. 10). This allows us to discriminate between gabbro melting (Koepke et al., 2004) and hydrothermalized dikes melting (Beard and Lofgren, 1991, and this study) as only hydrothermalized dikes melts reach silica contents higher than 68 wt% for TiO_2 concentrations <0.5wt% (Fig. 10). Our experimental melts are relatively similar with those formed in MORB fractionation experiments, except for the lower temperatures (i.e., with the higher silica content), which are slightly depleted in MgO and CaO and slightly enriched in K_2O (Fig. 10).

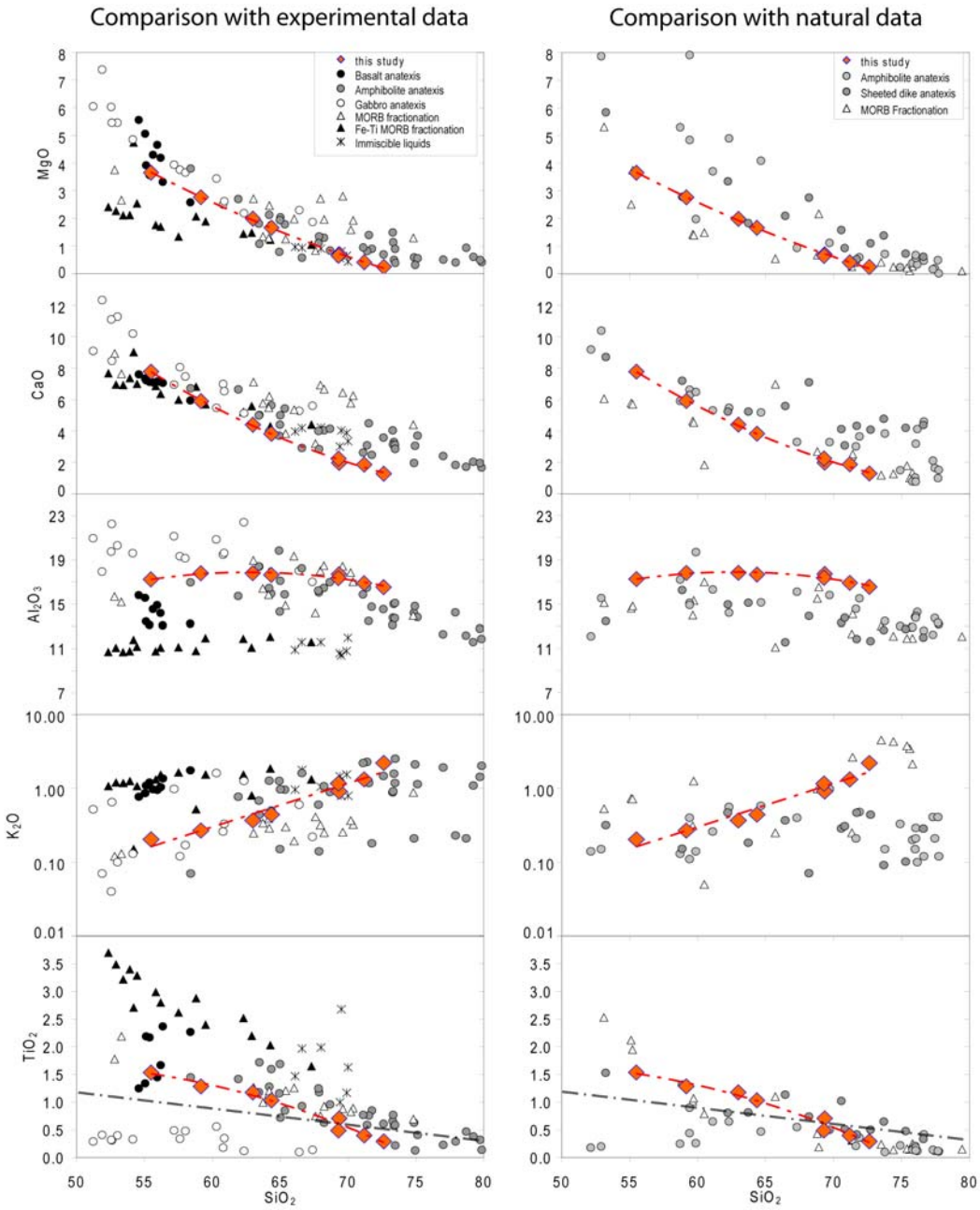

Figure 10: *Harker diagrams (Oxide versus SiO_2). Comparison of melts from this study with other experimental melts (left column) and with natural rocks (right column). Experimental data are from Dixon-Spulber and Rutherford (1983) and Berndt et al. (2005) for MORB fractionation experiments, from Juster et al. (1989) and Toplis and Carroll (1995) for Fe-Ti MORB fractionation experiments, from Dixon and Rutherford (1979) for immiscible liquid compositions and from Koepke et al. (2004), Beard and Lofgren (1991), and Thy et al. (1999) for gabbro, amphibolite and basalt anatexis, respectively. Natural data are from Gillis and Coogan (2002) for rocks interpreted as sheeted dikes partial melts, from Gerlach et al. (1981), Pedersen and Malpas (1984) and Flagler and Spray (1991) for rocks interpreted as amphibolite partial melts and from Beccaluva et al. (1977), Beccaluva et al. (1999) and Ghazi et al. (2004) for rocks interpreted as MORB fractionation. The dashed line corresponds to the regression line for the experimental melt compositions of this study. The dashed-dotted line in TiO_2 vs. SiO_2 diagrams represent the saturation of TiO_2 in basaltic melts defined by Koepke et al. (2007).*

To compare our experimental results with natural data, we used published analyses of oceanic plagiogranites interpreted as sheeted dikes partial melts (Gillis & Coogan, 2002), as amphibolite partial melts (Gerlach et al., 1981; Pedersen and Malpas, 1984; Flagler and Spray, 1991), and as differentiated MORB (Beccaluva et al., 1977; Beccaluva et al., 1999; Ghazi et al., 2004). In these studies, the oceanic plagiogranite origin has been inferred from trace element concentrations and structural relationships. These natural rocks have relatively homogeneous compositions, and globally match our experimental melts. Nevertheless, the melts formed in our lower temperature experiments and oceanic plagiogranites interpreted as differentiated MORB are slightly enriched in K_2O compared to other natural oceanic plagiogranites (Fig. 10). Our experimental melts are also slightly enriched in Al_2O_3 compared to all natural plagiogranites (Fig. 10).

To summarize, despite small differences, the melts produced during the experimental hydrous partial melting of hydrothermalized sheeted dike have major element compositions that are similar to other experimental works testing the partial melting of oceanic lithologies, and to natural plagiogranites interpreted as products of oceanic lithologies anatexis (Fig. 10). However, the observed major element trends are also very similar to those obtained by experiments simulating MORB fractionation and to oceanic plagiogranites interpreted as resulting from MORB fractionation (Fig. 10). Thus, whole rock major element compositions of our experimental melts cannot be used as a tool for discriminating different processes of oceanic plagiogranite genesis. Field studies and major element compositions have been combined with trace element compositions (especially rare earth elements) to better constrain their origin (e.g., Gerlach et al., 1981; Flagler and Spray, 1991; Floyd et al., 1998; Luchitskaya et al., 2005; Bonev and Stampfli, 2009; Brophy, 2008, 2009; Rollinson, 2009). At fast spreading ridges, the granoblastic dikes that are spatially associated to oceanic plagiogranites present at or close to the base of the sheeted dike complex, and as xenoliths in plagiogranites, may help to further constrain the plagiogranites origin. If these granoblastic dikes represent the residue after a hydrous partial melting event (Coogan et al., 2003; Gillis, 2008; France et al., 2009a), then their forming mineral compositions should match the ones of our experimental residual minerals.

IV.3.f.2. Evolution of the residual minerals: formation of "granoblastic dikes"

Detailed petrological descriptions of the granoblastic dike horizon from the Oman ophiolite and from IODP Hole 1256D are given in France et al. (2009a), and Koepke et al. (2008). Gillis (2008) also describe granoblastic dikes (called hornfelsic lithologies) from Pito

Deep, Hess Deep, and the Troodos ophiolite. A typical granoblastic assemblage is composed of clinopyroxene, plagioclase and two oxides (ilmenite and magnetite to titanomagnetite). In IODP Hole 1256D, orthopyroxene is also present. This paragenesis matches well the residual mineral assemblage observed in our partial melting experiments coexisting with a plagiogranitic melt. Olivine, which is a stable residual phase in experiments performed at temperatures > 940°C, is absent from the described natural granoblastic dikes. This implies relatively low temperatures associated to their formation.

In natural granoblastic dikes, plagioclase compositions range from An_{20} to An_{60}, and clinopyroxene is augite with Mg# varying from 60 to 75. These compositions are similar to our experimental results, in which plagioclases vary from An_{26} to An_{59} (Fig. 8c) and clinopyroxene showing Mg# varying from 66 to 78. Magnetite from granoblastic dikes have lower TiO_2 contents than residual magnetite in our experiments, but as shown by Koepke et al., (2008), they were probably re-equilibrated at lower temperature (~600°C) during a later, retrograde step ("second" hydrothermal alteration; see Koepke et al., 2008). In contrast, the composition of plagioclase and pyroxene obtained in MORB differentiation experiments (Berndt et al., 2005) does not match the composition of those from granoblastic assemblages. In differentiation experiments, plagioclase compositions range from An_{55} to An_{88} and clinopyroxene is mostly augites with Mg# varying from 72 to 86.

Gillis (2008), Koepke et al. (2008), and France et al. (2009a) have shown that clinopyroxene from granoblastic dikes are particularly low in Al_2O_3 and TiO_2 (Fig. 11). France et al. (2009a) propose that such compositions are characteristic of granoblastic lithologies (Fig. 11a). Residual clinopyroxene in the present study displays also very low, correlated Al_2O_3 and TiO_2 contents that follow a trend similar to that for granoblastic dike clinopyroxene (Fig. 11b). For comparison, clinopyroxene in MORB differentiation experiments from Berndt et al. (2005) has higher Al_2O_3 contents (between 3.3 and 6.8 wt% instead of 1.2 to 3 wt% in the present study). This difference may be related to the much higher temperature in differentiation experiments. The peculiar TiO_2 *vs.* Al_2O_3 trend obtained for clinopyroxene in the present study seems to be characteristic of hydrous partial melting of previously hydrothermalized basaltic lithologies, and may be linked to the low temperature conditions coupled to water saturated conditions at high oxygen fugacities in our experiments. These peculiar conditions prevail in the root zone of the sheeted dike complex. A critical parameter controlling this trend is the oxygen fugacity, which controls the stability of Fe-Ti oxides; the latter in turn controls the Ti budget for Ti partioning between clinopyroxene and melt.

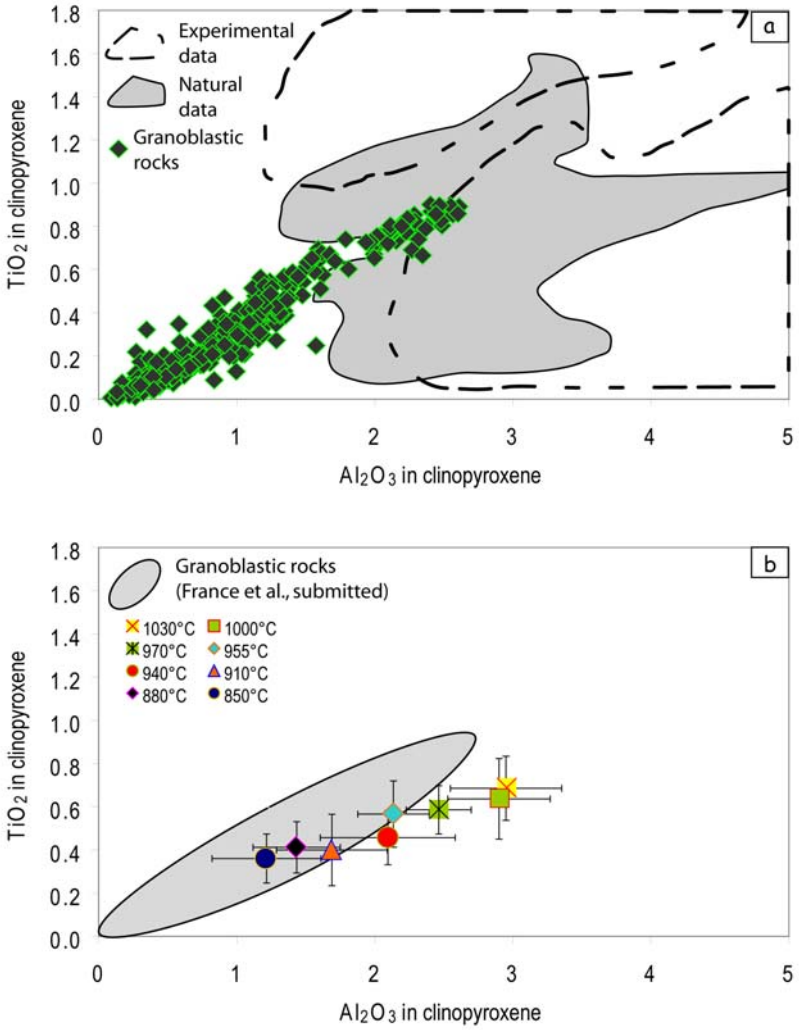

Figure 11: *Correlation between TiO_2 and Al_2O_3 in clinopyroxene.* ***a)*** *Comparison between clinopyroxenes in granoblastic dikes (diamonds; compositions from France et al., 2009a) and experimental and natural data from oceanic crust lithologies; after France et al. (2009a). Experimental data (dashed field) are from Snyder et al. (1993), Toplis and Carroll (1995) and Toplis et al. (1994) for Fe-Ti MORB crystallization experiments, from Berndt et al. (2005) and Feig et al. (2006) for hydrous crystallization experiments in primitive MORB-type system; from Grove and Bryan (1983) and Kinzler and Grove (1992) for MORB crystallization experiments, and from Koepke et al. (2004) for clinopyroxenes formed during hydrous partial melting of gabbros. Natural data (grey field) for oceanic crust lithologies are from Dziony et al. (2008) for IODP Hole 1256D sheeted dikes not affected by granoblastic imprint, from Miyashita et al. (2003) and Pallister and Hopson (1981) for Oman ophiolite sheeted dikes and gabbros, and from Boudier et al. (2000) and Gerbert-Gaillard (2002) for Oman gabbronorites.* ***b)*** *Comparison between clinopyroxenes of granoblastic rocks (dikes and xenoliths; grey field) and clinopyroxenes in the partly molten system of the present study equilibrated at different temperatures. Note that the grey field corresponds to the diamonds of a).*

The experimental trend in the present study has a slightly lower slope than in natural granoblastic dikes; the correspondence between the two trends is best at low TiO_2 and Al_2O_3 contents of clinopyroxene (Fig. 11b). For the strongly oxidizing conditions of our

experiments, the stability field of Fe-Ti oxides is larger, and TiO_2 is consequently incorporated in lesser amount into silicates, resulting in a lower TiO_2/Al_2O_3 ratio for clinopyroxene. The observed difference suggests that dehydration and melting reactions at the base of the sheeted dike complex in natural settings proceed at slightly less oxidizing conditions than in our experiments, which were performed at redox conditions corresponding to an oxygen fugacity between QFM+1 and QFM+2.

Figures 11 and 12 show that TiO_2 and Al_2O_3 contents in clinopyroxene strongly depend on temperature. The relation between Al_2O_3 and temperature can be fitted by a regression curve (R^2=0.98) with:

$$T = 93.145\ Al_2O_3 + 742$$

Where T is temperature in °C and Al_2O_3 the Al_2O_3 content in clinopyroxene in wt%. The result can be considered accurate with an uncertainty of ±40°C. This thermometer seems appropriate for estimating equilibration temperatures of the granoblastic dikes and related lithologies at the base of the sheeted dike complex in the oceanic crust. Since pressure and composition also strongly influence the Al_2O_3 content in clinopyroxene, the use of this thermometer is restricted to shallow pressure (100 MPa in this study).

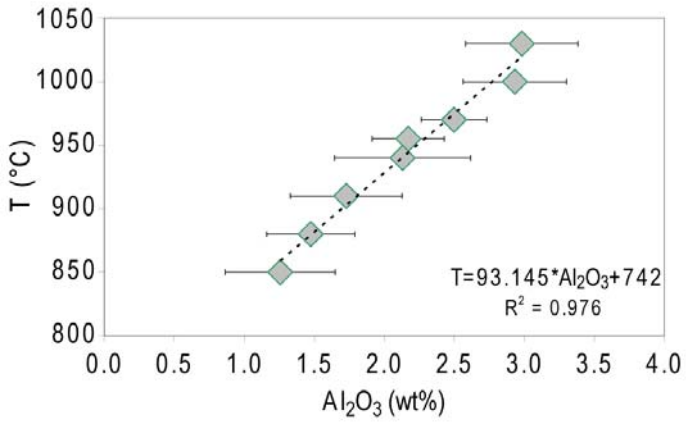

Figure 12: *Al_2O_3 content (wt%) in clinopyroxene from our experiments as a function of temperature. Standard deviations of analyses are shown. The dashed line is the linear regression with the equation y=93.145x+742 (R^2=0.976).*

One interesting feature of typical granoblastic dikes is reproduced by our experiments. Granoblastic dikes usually contain clinopyroxenes with countless inclusions of tiny oxide with grain sizes from <1 µm to some tens of µm (Koepke et al., 2008; France et al., 2009a). Oxides associated to clinopyroxene have also been observed in hydrothermalized altered gabbros but in close association with amphibole (Manning and MacLeod, 1996). In granoblastic dikes, oxide represents inclusions in pure clinopyroxene, and amphibole is not

associated to the inclusions. The oxide inclusions present in granoblastic dikes have been ascribed to the prograde evolution of secondary clinopyroxenes developing from complex alteration assemblages originating from primary clinopyroxenes which include fibrous actinolitic amphibole and extremely fine-grained (<5 μm) coexisting ilmenite and magnetite oxide phases (for details see Koepke et al., 2008, and France et al., 2009a). In our experiments, primary material does not contain clinopyroxene and new clinopyroxene crystallizes mostly after amphibole. However, we observe similar features, i.e., newly crystallized clinopyroxenes that contain numerous tiny oxide inclusions (Fig. 4g). The presence of these oxide inclusions can be explained by the Mg/Fe budget of the minerals involved in the reaction. Amphibole from the starting material has a lower Mg# (~61) than that of the newly crystallized clinopyroxene (e.g., 78 at 1000°C). An iron excess is therefore available during clinopyroxene crystallisation, resulting in the concentration of iron in the tiny oxides. Since our experiments were performed under highly oxidizing conditions, the stability of Fe-Ti oxides is possible.

The results of our experiments (phase relations, mineral and melt compositions, and other petrographic characteristics such as tiny oxide inclusion in clinopyroxene) support the working models in which granoblastic dikes and associated oceanic plagiogranites at the base of the sheeted dike complex at fast-spreading ridges are formed by dehydration and partial melting of previously hydrothermalized sheeted dikes. Temperatures as high as 1000°C has been recorded in the granoblastic dikes from several natural settings (Gillis, 2008; Koepke et al., 2008; France et al., 2009a), this is clearly above the hydrous solidus temperature determined in this study (~850°C), and implies that hydrous partial melting locally proceeded. Koepke et al. (2008) observed in the granoblastic dikes from IODP Hole 1256D the presence of domains of both "dry" and "hydrous" parageneses. Such "dry" domains, for which significantly higher equilibration temperatures were recorded, probably represent zones which were not, or less hydrothermalized, preventing the triggering of hydrous partial melting, since the temperature did not exceed the corresponding dry solidus. These similarities between our experimental results and the corresponding natural settings strongly support an anatectic origin of those plagiogranites that are commonly observed at the base of the sheeted dike complex and that are associated with granoblastic lithologies.

IV.3.f.3. MORB contamination at the base of the sheeted dikes

Our experimental study supports models in which, at fast-spreading ridges, the magmatic / hydrothermal interface is a dynamic horizon with magma that can reheat

previously hydrothermalized sheeted dikes during upward migrations of the top of the melt lens. The absence of olivine in granoblastic dikes of all studied natural settings implies that the temperatures for the partial melting process did not exceed 940 °C (Figs. 5, 6), corresponding to a melt fraction ≤ 30 %. In our experiments, such melts are highly silicic (SiO_2 of ≥ 68.5 %; Fig. 8). Hence, they are expected to be highly viscous (for the 850°C experimental melt, and using a theoretical water content of 5wt%, $\eta=10^{4.4}$ Pa.s, when calculated using Giordano et al., 2008). Due to the very strong thermal gradient at the interface between the melt lens and the sheeted dikes, melt formation is restricted to a relatively narrow zone at the base of the sheeted dikes, and the amount of such silicic melts is probably relatively low. As the formed melts are of relative low temperature and highly viscous, they probably do not have the potential to erupt, and can therefore get trapped as small intrusive veins near the location of generation. Such a scenario is described in the core recovered in IODP Hole 1256D; a 20 mm-wide vein of trondhjemitic composition intrudes the granoblastic dikes at 1404 meters below sea-floor (mbsf), ~ two meters above the first appearance of gabbro marking the top of the fossil melt lens (Teagle et al., 2006). Felsic igneous rocks are also relatively abundant in the coarse-grained material recovered in junk baskets during hole clearing operations at 1373 mbsf (Teagle et al., 2006). These leucocratic rock fragments, which consist of plagioclase, quartz, and altered green hornblende, are probably derived from leucocratic intrusions that were not recovered in the core. These felsic lithologies most likely represent products of hydrous partial melting of previously hydrothermalized sheeted dikes. As hydrous partial melting is believed to occur during upward migrations of the melt lens, the newly formed, highly viscous, silica-rich melt can also be assimilated into the MORB melt within the melt lens. This melt is transitional between tholeiitic and calc-alkaline (Fig. 9) and represents a source of contamination for primary tholeiitic MORB. It will in particular increase the SiO_2 content of the MORB melt, but also the amount of K_2O, rare earth elements and chlorine. This assimilation process may be responsible for the formation of andesitic extrusives which are locally observed in recent oceanic crust (e.g., Haase et al., 2005) and for the chlorine contamination of MORB (e.g., Michael and Schilling, 1989). On the other hand, the residual phases of the hydrous partial melting reaction behave rather refractory, resulting in the occurrence of residual enclaves in the corresponding melts, which display granulite facies granoblastic parageneses consisting of clinopyroxene + plagioclase + Fe-Ti oxides ± orthopyroxene. These enclaves are described in IODP Hole 1256D (Teagle et al., 2006; Koepke et al., 2008; France et al., 2009a), at Pito Deep and Hess Deep (Gillis, 2008), and in the Troodos and Oman ophiolites (Gillis, 2008;

Nicolas et al., 2009; France et al., 2009a). All of these geological settings are portions of present-day or fossil mid-ocean ridges where a dynamic dike / gabbro transition has been proposed.

IV.3.g. Conclusion

Partial melting experiments of a sample of the hydrothermalized sheeted dike complex from the Oman ophiolite have been performed to test the origin of oceanic plagiogranites present at the base of the sheeted dike complex at fast spreading centers. These oceanic plagiogranites are associated to granoblastic lithologies that form the base of the sheeted dike complex and xenoliths in plagiogranites and gabbros. Our experimental results show that:

- Melts produced during partial melting of hydrothermalized sheeted dikes are highly silicic (up to 72.6 wt%) and match the composition of oceanic plagiogranites.
- The residue of the partial melting experiments matches the modal and peculiar chemical compositions of granoblastic lithologies. Granoblastic lithologies are therefore interpreted to represent the residue after the partial melting event that produce the oceanic plagiogranites.
- The heat source necessary to trigger the partial melting event is believed to be provided by the underlying melt lens. This study therefore supports a model in which the sheeted dike complex / gabbro transition is a dynamic horizon that migrates vertically, with the potential to locally reheat the base of the sheeted dike complex during upward movements.
- Partial melting of hydrothermalized sheeted dikes, and partial assimilation of newly formed melts in the axial melt lens are potential candidates for the contamination (e.g., the chlorine enrichment) observed in some MORB.

IV.4. Mineral recrystallization during experiments: a preliminary study

In France et al. (2010a), we have studied the evolution of mineral mode, and mineral and melt compositions with increasing temperature. The evolution of mineral shapes, fabrics and associations can also bring information on the recrystallization processes, and on incongruent reactions. Using the electron back-scattered diffraction (EBSD) technique, I present hereafter a preliminary study of the mineral orientations in the experimental results, and compare these results to natural samples.

EBSD measurements are performed using a CamScan X500FE “crystal probe” at the Geosciences Montpellier laboratory. For each measurement point, EBSD result is a diffraction diagram displaying Kikuchi bands that are characteristic of one crystal orientation for one given mineral. A software (Channel 5, HKL technology) is then used to convert Kikuchi bands to crystallographic orientation maps (e.g., Figure IV-5) and pole figures. EBSD results can be used to build modal maps (Figure IV-5a) and crystal orientation maps (Figure IV-5b-d).

France et al. (2010a) show that in experimental results, assemblages (100-250 μm large) of several small grains (~10 μm) mimic starting material mineral shapes. For example, clinopyroxene assemblages mimic previous large actinolite assemblages (e.g., Figure 4b-d in section IV.3.e.1, and Figure IV-5a herein), and newly formed plagioclase assemblages mimic previous large albite grains. Nevertheless, clinopyroxenes crystallized after actinolite aggregates formed of millions of fine needles that are either parallel or randomly oriented, and it is therefore expected that in a single clinopyroxene assemblage, the small apparently individual newly formed grains have different crystal orientations.

For this preliminary study, I have mapped the crystallographic orientations of a portion of the 970°C experimental product (with water added). At this temperature all minerals are newly formed and no relic of starting material is observed. Crystal orientation maps show that clinopyroxene assemblages are composed of small grains that have uniform crystal orientation in a single assemblage (Figure IV-5). This suggests that each “assemblage” represent one single, sponge-like grain with coherent orientation, rather than an aggregate of small, individual, randomly orientated grains. In plagioclase assemblages, small grains mostly show uniform crystal orientation, and some are organized along narrow sub-parallel bands with coherent crystal orientation in an individual band (Figure IV-5b). The observed structures imply that crystallization was not a random process starting from individually orientated nuclei in the melt, as it would be expected for typical crystallization experiments using a homogeneous glass as starting material. Here, it is indicated that the characteristic properties of the starting material (hydrothermally altered dolerite) with its characteristic textural and structural mineral features represent special precursor leading to the observed crystal orientation in plagioclase and clinopyroxene aggregates. Olivine grains have grown from the melt through the melting reactions, and display random crystallographic orientations.

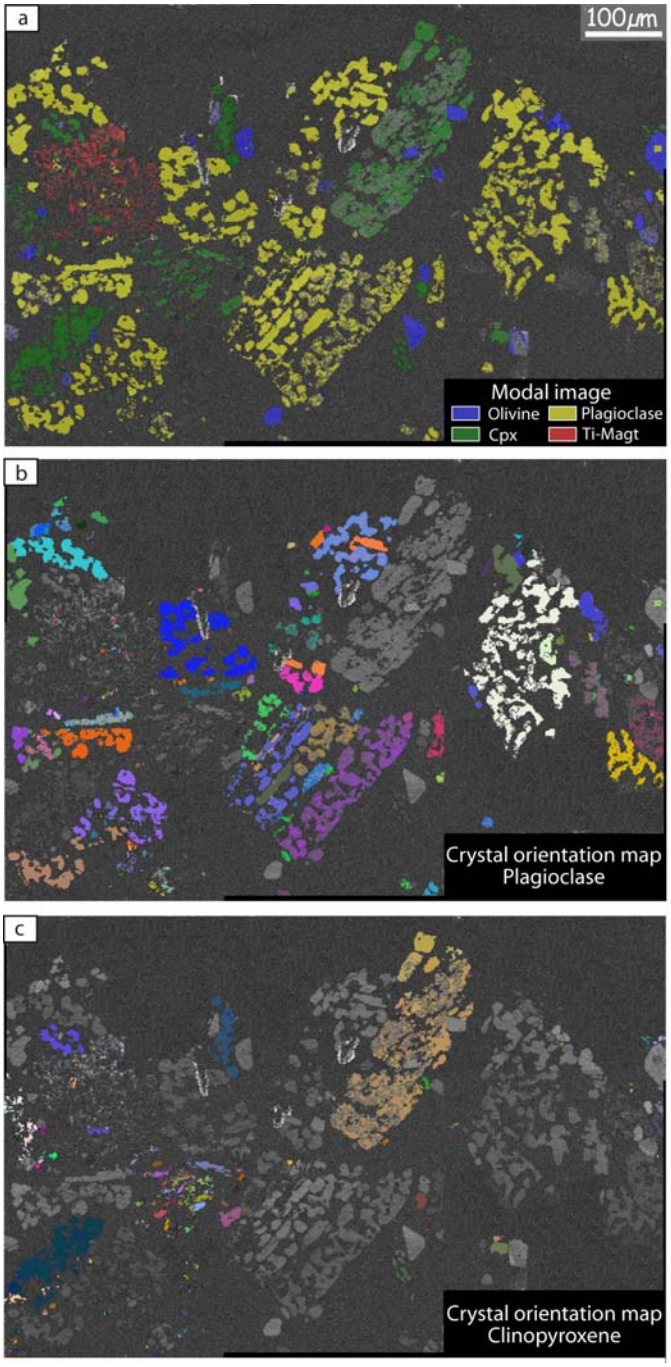

Figure IV-5: EBSD maps; in b) and c) the color is a function of crystal orientation generated using the "all euler" function in HKL software. a) modal map; b) plagioclase crystals orientations, the grain in the central bottom part is composed of narrow sub-parallel bands that display uniform crystal orientation in a single band, other grain assemblages as the white one, have uniform crystal orientation; c) clinopyroxene crystals orientations, the grain assemblages have uniform crystal orientations.

The observed orientation effect in the experiments can be related to the drilled natural rocks from the EPR: In strongly recrystallized microgabbronorite xenoliths present in the isotropic gabbro horizon of IODP Hole 1256D, and described by France et al. (2009a), clinopyroxenes showing a characteristic poikilitic to poikiloblastic feature, are locally

observed (Figure IV-6), suggesting that recrystallization processes are similar in nature and experiments. In natural recrystallized samples similar poikiloblastic plagioclases are not observed. However, clinopyroxene and orthopyroxene inclusions are observed in some plagioclase grains (Figure IV-7). These inclusions are localized in a given plagioclase grain, along domains that display different optical properties and different chemical compositions (lower An content) than the main plagioclase grain, attesting to distinct plagioclase generations (Figure IV-7). The occurrence of such inclusions is not well understood but may attest to former poikilitic plagioclases similar to the ones observed in experimental results. These poikilitic plagioclases would have then recrystallized in the presence of melt. This process would result in the occurrence of the second generation of plagioclase associated to pyroxenes inclusions.

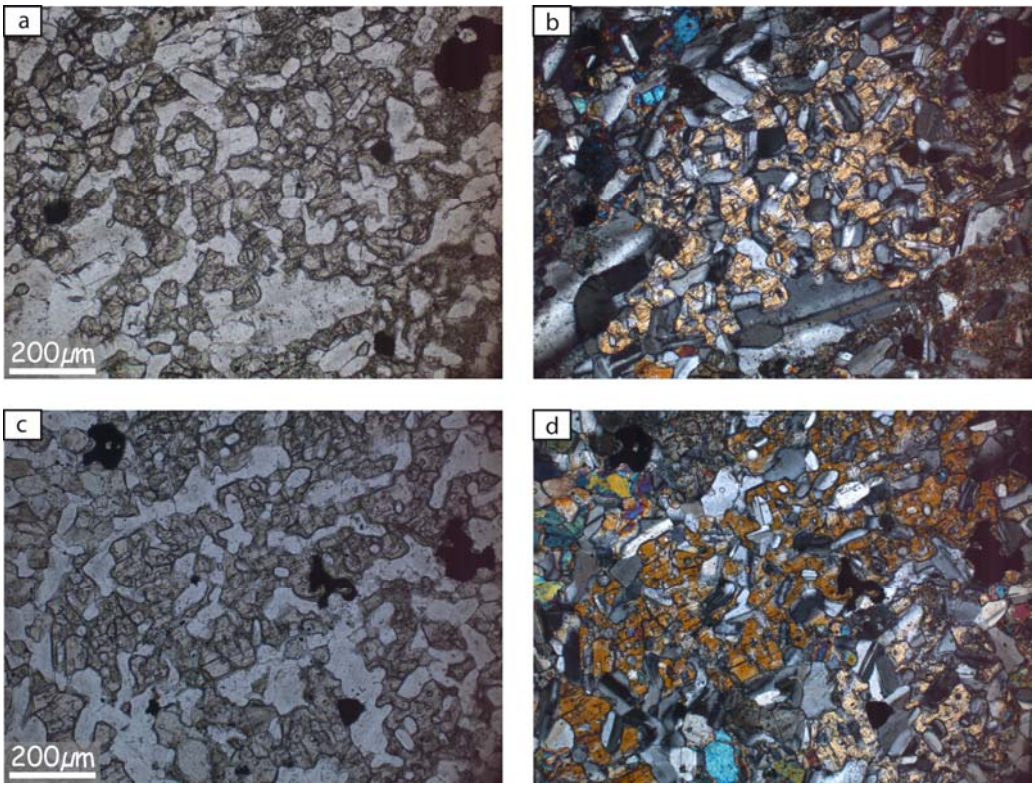

Figure IV-6: Sponge-like clinopyroxenes in xenolith with granoblastic features in zone 6 gabbros from the bottom of IODP Hole 1256D (see Chapter II, sample 232R-2_37-41). The two domains (a-b and c-d) display sponge-like poikiloblastic clinopyroxene grains containing plagioclase inclusions. These textures are similar to those observed in experimental results (Figure IV-5). Note that both clinopyroxenes show homogeneous interference colors implying that these represent single crystals with a sponge-like structure. a and c: plane-polarized light microphotographs, b and d : cross-polarized light microphotographs.

To summarize, EBSD measurements in the experimental products can help to explain specific structures observed in the natural rocks from the dike / gabbro transition, as steps of

complex crystallization events using specific components of granoblastic lithologies as precursors (e.g., clinopyroxenes with poikiloblastic features). They also show that, despite a randomly orientated starting material, newly formed minerals in a given assemblage can show a unique crystallographic orientation, suggesting that they form one single grain. The detailed processes occurring during recrystallization and their evolution with temperature are not well understood and further studies are needed. A systematic EBSD survey using products of experiments performed at different temperatures (from 750°C to 1030°C in a subsolidus and partly molten regime) by France et al. (2010a) would help to shed light on the details and mechanisms of the recrystallization processes occurring during the melting of hydrothermally altered dikes.

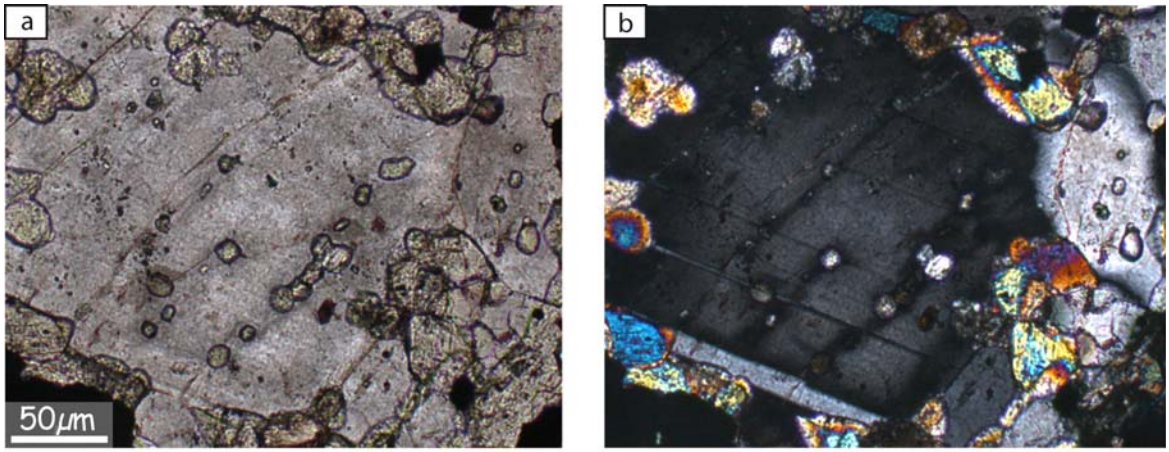

Figure IV-7: Plane- (a) and cross- (b) polarized light microphotographs of a plagioclase grain containing clinopyroxene and orthopyroxene inclusions (IODP Hole 1256D, sample 233R-1_8-12).

IV.5. Melting the hydrothermally altered sheeted dike complex: an experimental / trace elements study

Preliminary version of an article that will be submitted to *Geology*.

Lydéric France[1,2], Benoit Ildefonse[1], Juergen Koepke[2], Chris J. MacLeod[3], Marguerite Godard[1]

1: Géosciences Montpellier, CNRS, Université Montpellier 2, CC60, F-34095 Montpellier Cedex 05, France
2: Institut für Mineralogie, Leibniz Universität Hannover, Callinstrasse 3, D-30167 Hannover, Germany
3: School of Earth, Ocean and Planetary Sciences, Cardiff University, Main Building, Park Place, Cardiff CF10 3YE, UK

IV.5.a. Abstract

Oceanic plagiogranites are ubiquitously sampled in oceanic crust. At fast spreading ridges, they are preferentially located close to the gabbro / sheeted dike transition. The origin of oceanic plagiogranites is still debated; the favored formation processes are late-stage fractionation of tholeiitic melt, and hydrous partial melting of mafic rocks. Experimental studies have shown that major element compositions alone are not sufficient to discriminate between these two processes. Geochemical modeling is needed, but because melting and crystallization are complex processes, models need experimental verifications. Here we present the first in-situ trace element measurements of partial melts generated in partial melting experiments of hydrothermally altered sheeted dikes. The experiments were performed at those conditions prevailing at the base of the sheeted dike complex overlying active axial magma chambers. We also present for comparison trace element analyses of natural samples from the Oman ophiolite. An anatectic origin for the oceanic plagiogranites that are observed close to the root of the sheeted dike complex is supported by similar trace element patterns of experimental and natural melts. Experiment residue have the same composition as the so-called "granoblastic microgabbro dikes" sampled at the base of the sheeted dike complex, which is consistent with their interpretation as reheated and partially molten hydrothermally altered dikes. These results finally support a model in which the top of the melt lens representing the interface between magmatic and hydrothermal system is a dynamic horizon that can migrates vertically and interact with the overlying sheeted dikes. Our results imply that anatectic plagiogranitic melt formed during upward melt lens migrations represent the main crustal contaminant for the MORB-type melts filling the melt lens. The trace element compositions of anatectic silicic melts presented in this study is therefore of major importance to understand and simulate real MORB compositions under fast-spreading ridges.

Key words: *oceanic plagiogranites, fast spreading mid-ocean ridge, hydrous partial melting, trace element, experimental petrology, granoblastic dikes.*

IV.5.b. Introduction

Oceanic crust commonly contains relatively small intrusions of leucocratic, evolved material generally called oceanic plagiogranites (e.g., Koepke et al., 2004, 2007). These are most commonly believed to be generated either by differentiation of MORB melts (e.g., Coleman and Peterman, 1975; Pallister and Knight, 1981; Bonev and Stampfli, 2009), or by hydrous partial melting of mafic rocks (e.g., Pedersen and Malpas, 1984; Amri et al., 1996; Koepke et al., 2004). At slow spreading ridges, hydrous partial melting of mafic rocks is commonly described associated to shear zones that allow hydrothermal influx (e.g., Flagler and Spray, 1991; Koepke et al., 2007). In oceanic crust formed at fast spreading centers away from ridge segmentation and tectonic discontinuities, the origin of oceanic plagiogranites, commonly present at the base of the sheeted dike complex (SDC; Fig. 1a) remains debated. In these zones, the thermal regime and the magma supply are believed to remain stable over periods of tens of thousand of years (Pollock et al., 2009) preventing differentiation; only gaps in the magma supply would result in strongly differentiated igneous rocks. Large shear-zones in fast-spread crust are spatially associated to ridge segmentation zones (Nicolas et al., 2000; Nicolas and Boudier, 2008), and cannot provide hydrous fluids, with the potential to trigger hydrous partial melting, away from these zones. In segment centers, away from discontinuities, only the hydrothermal convecting system has the potential to bring fluids close to the magma chamber (Manning et al., 1996). Nicolas et al. (2008) propose that the intrusion of hydrothermal fluids in the recently crystallized, still hot, root zone of the SDC can trigger hydrous partial melting without any reheating event. Gillis and Coogan (2002), Coogan et al. (2003) and France et al. (2009a) propose that the melt lens underneath the SDC is a dynamic horizon that migrates vertically, with the potential of locally triggering hydrous partial melting in the reheated base of the hydrothermally altered SDC. In this dynamic model, the new melts formed during upward migrations of the melt lens can subsequently be incorporated into the melt lens, thus providing a source of contamination of MORB melts (e.g., Haase et al. 2005).

Figure 1: a) Outcrop in the Aswad area of the Oman ophiolite (coordinates: 23°07'23N 58°12'06E) showing oceanic plagiogranites (felsic rocks) at the base of the sheeted dike complex (dark rocks). The microgabbro xenoliths and the sheeted dike complex base are recrystallized to granoblastic textures.

Discriminating between fractionation and hydrous partial melting is not trivial and both processes may operate jointly in modern ocean crust (e.g., Brophy, 2008, 2009). Experimental studies have shown that major element compositions of oceanic plagiogranites are similar for the two processes (e.g., Koepke et al., 2004; France et al., 2010a). Several authors have proposed to model the trace element evolution of melts during both MORB fractionation and hydrous partial melting in order to reproduce natural trace element trends (e.g., Gerlach et al., 1981; Pedersen and Malpas, 1984; Flagler and Spray, 1995; Floyd et al., 1995; Luchitskaya et al., 2005; Bonev and Stampfli, 2009). One weakness of these models is that hydrous partial melting of hydrothermally altered lithologies results in the simultaneous destabilization and stabilization of different mineral phases (incongruent melting), which complicate the models. However, the modal evolution is known from some relevant experimental studies (e.g., Beard and Lofgren; 1991, Berndt et al., 2005; France et al., 2010a) and can be used to improve the models (e.g., Haase et al., 2005; Brophy, 2008). Direct measurement of trace elements in experimental products matching the base of the SDC conditions is lacking for crystallization experiments simulating crystal fractionation, and only Fisk et al. (1995) have analyzed trace element contents of melt formed during partial melting experiments. However, these experiments were performed at one atmosphere and under dry conditions, thus, at conditions which are not relevant to those anatectic processes ongoing at the base of the hydrothermally altered SDC. In order to shed light on the origin of oceanic plagiogranites at the base of the SDC, to provide new constraints for the associated modeling, and to constrain the composition of the main crustal MORB contaminant, we have analyzed

for the first time the trace element contents of melts formed by the experimental melting of hydrothermally altered sheeted dikes from experiments performed by France et al. (2010a). These results are compared to natural samples from the Oman ophiolite, which is the best analogue for a fast-spreading ridge on land.

IV.5.c. Experimental and analytical techniques

Hydrous partial melting experiments have been performed using a representative sample of hydrothermally altered SDC from the Oman ophiolite as starting material (08OL30, details on experiments and starting material in France et al., 2010a). After crushing, two fractions (100-150µm and 150-250µm) have been used in a preliminary experiment to control the effect of grain size on the experimental results; the 150-250µm fraction has been used as it allowed us to obtain larger melt pools. Conditions were selected to match those prevailing at the base of the SDC; pressure was 100MPa, oxygen fugacity corresponded to FMQ+1.2 to +1.6 (where FMQ is the fayalite-magnetite-quartz oxygen buffer equilibrium) and temperature ranged from 850 to 1030°C. Two capsules containing 50mg of rock powder were run simultaneously at each temperature, one of them containing 5mg of additional distilled water.

Major elements were measured using a Cameca SX 100 electron microprobe (Institut für Mineralogie, Hannover, Germany) and trace elements in experimental melts using a Cameca IMS4f ion probe (Géosciences Montpellier, France). Natural sample trace element contents have been measured using an ICP-MS (Department of Earth Sciences, Cardiff, UK). Details on analytical methods can be found in the Data Repository DR1. Analytical results can be found in the Data Repository DR2 and DR3.

IV.5.d. Trace element contents

The chondrite normalized rare earth element (REE) concentrations of the starting material show convex shape from the light REE to the middle REE, a slight Eu positive anomaly and slightly decreasing values from the middle REE to the heavy REE (Fig. 2a).

Trace element contents of the experimental melts have been measured for experimental runs from 1030°C to 955°C (Figs. 2a and 2d). At lower temperatures (i.e., higher silica content and lower degree of partial melting) melt-pools are too small (<20µm) to be analyzed. REE and other trace elements continuously evolve with temperature. For

example, light REE continuously increase, to more than 30 times the chondrite, by progressively decreasing the temperature to 955°C (Fig. 2a).

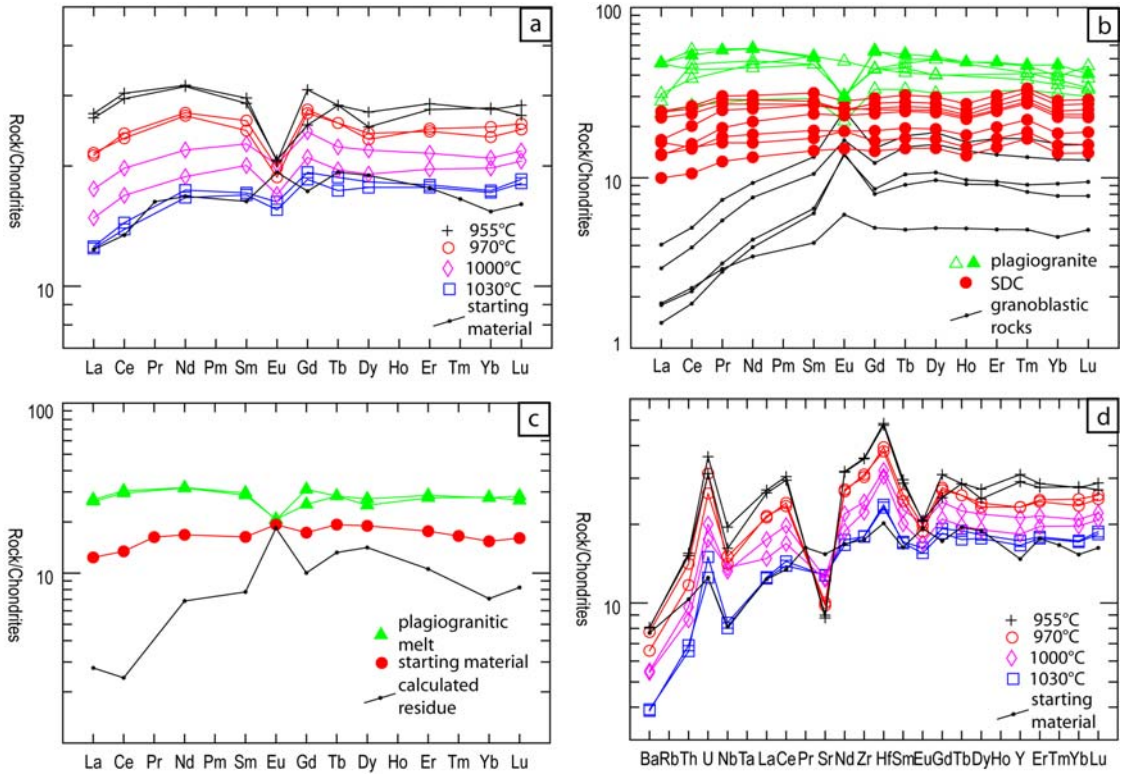

Figure 2: Chondrite normalized REE and trace elements contents (normalization after Anders and Grevesse, 1989). a) Experimental melts: black crosses: 955°C (40% of melt); red circles: 970°C (50% of melt); pink diamonds: 1000°C (70% of melt); blue boxes: 1030°C (93% of melt), and starting material (08OL30): black dots. b): Oman samples: green triangles: oceanic plagiogranites (this study + Pallister and Knight, 1981); red circles: sheeted dike complex; black dots: granoblastic microgabbro dikes and xenoliths. c) Green triangles: newly formed plagiogranitic melt (955°C); red circles: starting material (highly hydrothermally altered sheeted dike); black dots: calculated residue (with a melt proportion of 40% estimated by France et al., 2010a from experiments). d) Trace element concentrations of experimental melts and starting material (08OL30); same symbols as a).

Experiments performed to test the grain size effect (France et al., 2010a) show that concentrations are slightly higher when using the coarser grain size. Nevertheless, trace element concentrations are similar and fractionations of REE are of the same order (e.g., $(La/Sm)_N$=1.18 in the finer grained experiment and 1.23 in the coarser one). The small differences in concentration may be linked to a slight difference in the mode of the starting material probably related to a sieving artifact. For each temperature, experiments containing only the starting material and those containing additional water have similar REE and other trace element contents. Light REE normalized concentrations (Fig. 2a) show convex shapes from La to Sm with a depletion of the lighter elements. A negative europium anomaly is

observed, which increases with decreasing temperature. From Gd to Lu, spectrums are mostly flat or slightly decrease (Fig. 2a). Normalized trace element contents (Fig. 2d) show U, and Zr-Hf positive anomalies, low Ba and Th values and a Sr negative anomaly; these anomalies are more pronounced when temperature decreases. V also strongly decreases with temperature. Ti/V ratio increases from ~20 at 1030°C to more than 50 at 955°C.

Natural samples from the SDC / gabbro transition of the Oman ophiolite (Wadi Abyad; for map and details on the locality see MacLeod and Yaouancq, 2000) show interesting similarities with our experimental results (Fig. 2b). Sheeted dike complex samples display nearly flat REE spectrums with normalized concentrations ranging from 10 to 30 times the chondrite. Plagiogranites are enriched in REE compared to the SDC; chondrite normalized spectrums show a convex shape from La to Sm and a negative Eu anomaly. Normalized contents slightly decrease from Gd to Lu. Enrichments reach 50 times the chondrite. The granoblastic microgabbro dikes, intruded by gabbros at the base of the SDC and the associated granoblastic microgabbro xenoliths present in the isotropic gabbros are largely depleted in light REE, display a positive Eu anomaly, and show slightly decreasing contents from middle REE to heavy REE (Fig. 2b).

IV.5.e. Discussion

France et al. (2010a) have shown that in the corresponding sheeted dike melting experiments, that the modal content of plagioclase increases with decreasing temperature. This is the rationale for the low Ba_N contents and the negative Eu, and Sr anomalies present in the partial melts, since theses elements are strongly incorporated in plagioclase. In experimental melts Sr shows a compatible behavior, whereas Eu is slightly incompatible. The incompatible behavior of Eu probably reflects the highly oxidizing conditions prevailing during the experimental runs, as the oxidized species (Eu^{3+}) is more incompatible in a plagioclase / melt system, than the reduced one (Eu^{2+}; Wilke and Behrens, 1999). The evolution of Ti/V ratio in natural compositions is classically used to determine the tectonic settings of ophiolitic rocks (Shervais, 1982). However, the presence of titanomagnetite in experimental results (France et al., 2010a) and the large increase of the Ti/V ratio in the experimental melts (from 20 to more than 50) with decreasing temperature clearly attests to the incorporation of V in titanomagnetite ($D_V^{TiMgt-melt} >> 1$), and prevents the use of the Ti/V ratio as a discrimination tool. As experimental conditions (pressure, temperature, redox

conditions and composition) closely match those external parameter controlling the natural process, the discriminating use of such a ratio should be carefully evaluated.

Experimental melts formed during partial melting of hydrothermally altered dikes reproduce the REE contents of most of the analyzed Oman plagiogranites samples (Fig. 2a-b). However, some natural plagiogranites show REE concentrations which are notably higher than those of the experimental runs (Fig. 2b). Figure 2a shows that the REE content of experimental melts increase by decreasing the temperature (from 1030 to 955°C). It is therefore to expect that in those runs performed at lower temperature, where the melt pools are too small to be analyzed by SIMS, the REE contents continuously increase, probably matching values of those natural plagiogranites with higher REE contents. Pallister and Knight (1981) have shown that the REE contents of Oman plagiogranites (Fig. 2c) can also be reproduced by MORB fractionation modeling. Thus, the mineral associations left back after melt extraction for both processes (incongruent mineral assemblage or residue for partial melting and fractionated cumulate minerals for fractional crystallization) may have similar REE compositions, but correspond to distinct lithologies. The residue of partial melting of the base of the SDC would be represented by the recrystallized base of the SDC, and by the associated granoblastic microgabbro xenoliths observed in underlying gabbros. The cumulate after the fractionation of a basaltic melt within the melt lens would be represented by plutonic rocks as gabbros, troctolites or werhlites. France et al. (2009a, 2010a) have shown that the granoblastic microgabbro dikes and xenoliths represent reheated parts of the SDC that may have suffered hydrous partial melting. To test this hypothesis, we have calculated the trace element composition of the residue present in our experiments, using the relation:

$$[concentration]_{starting\ material} = x\,[concentration]_{melt} + (1-x)\,[concentration]_{residue},$$

with x the melt fraction. The melt fraction present in our experiments has been determined by France et al. (2010a) via least square calculations using major element compositions of the starting material (corresponding to the composition of the system), the melt, and the residual minerals (93% of melt at 1030°C; 70% at 1000°C; 50% at 970°C and 40% at 955°C). Since the starting material and the melt compositions are known, the composition of the residue in equilibrium with the plagiogranitic melt can be calculated (Fig. 2c). Experimental melts have been analyzed in experiments performed between 1030°C and 955°C; as the melt formed at the lower temperature is the closest of plagiogranitic compositions, this experiment is used to calculate the residue composition. The calculated residue REE pattern is largely depleted in light REE, displays a positive Eu anomaly and has a convex shape from the middle REE to

the heavy REE, thus matching the corresponding patterns of natural granoblastic dikes and xenoliths from the Oman ophiolite (Fig. 2b), implying a residual origin for these rocks.

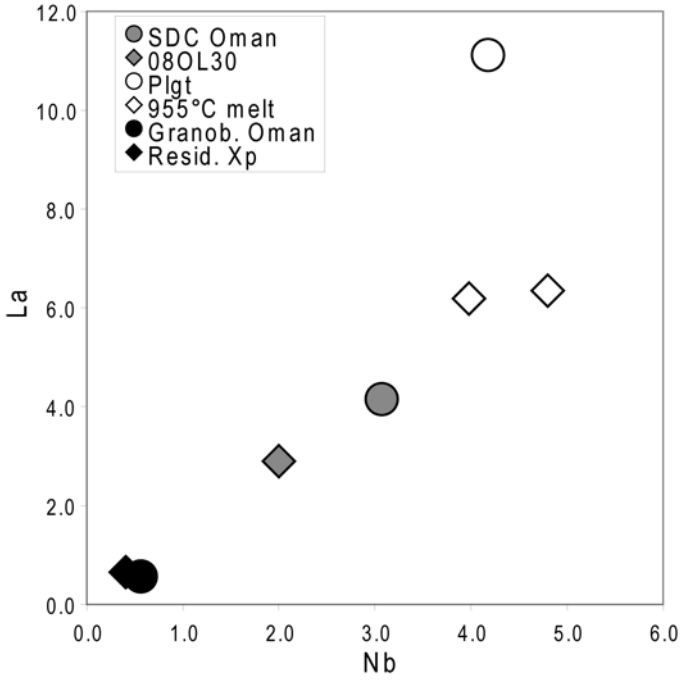

Figure 3: La vs. Nb plot ruling out a pure dehydration origin for granoblastic dikes and xenoliths: average of Oman ophiolite sheeted dike (SDC Oman); starting material from the Oman ophiolite (08OL30); Oman ophiolite plagiogranites (Plgt); experimental melts formed at 955°C (955°C melt); average of Oman ophiolite granoblastic microgabbro dikes and xenoliths (Granob. Oman); calculated residue in equilibrium with the experimental plagiogranitic melt formed at 955°C (Resid. Xp). During pure dehydration, Nb is not mobilized by fluids and its concentration in the dehydrated rock should be similar to the concentration in the altered SDC. La can be mobilized by fluids and would be depleted in the dehydrated rock. During partial melting, both La and Th are incompatible elements and are enriched in the newly formed melt and depleted in the residue.

Alternatively, the granoblastic lithologies may represent previously hydrothermally altered lithologies that have been reheated very slowly allowing dehydration without any partial melting. Figure 3 compares the evolution of incompatible elements that have different behavior during hydrous fluid percolation; La has a mobile behavior when Nb is an immobile element. In comparison to the sheeted dike average composition, the granoblastic microgabbro dikes and xenoliths are depleted in both La and Nb, whereas oceanic plagiogranites are enriched (Fig. 3). Similar observation can be done with experimental results (Fig. 3). In the case of an origin through SDC dehydration, the granoblastic microgabbro dikes would have Nb contents similar to the SDC ones. Figure 3 clearly attests of the incompatible behavior of La and Nb during partial melting process and rules out a pure dehydration origin. The composition similarities between experimental melts and oceanic

plagiogranites, between the experimental residue and granoblastic microgabbros and the close association of plagiogranitic rocks with granoblastic microgabbros in natural settings clearly attest of the anatectic origin of oceanic plagiogranites present at the sheeted dike gabbro transition. Granoblastic microgabbro dikes and xenoliths are therefore interpreted as residue of partial melting of previously hydrothermally altered dikes.

The anatectic origin of oceanic plagiogranites present at the base of the SDC, and the prograde origin of granoblastic microgabbros support recent models proposing that the upper melt lens imaged at the base of the SDC of fast spreading centers is a dynamic horizon (e.g., Gillis and Coogan, 2002; Coogan et al., 2003; Koepke et al., 2008; France et al., 2009a). Upward migrations of this melt lens should therefore be responsible for the reheating stage triggering partial melting of the previously hydrothermally altered SDC base. During the melt lens upward migrations, the formed plagiogranitic liquid can be mixed into the melt lens and contribute to MORB composition. Melt lens migrations are inferred from several oceanic settings as the EPR (e.g., Hooft et al., 1997; Koepke et al., 2008; France et al., 2009a), the Troodos ophiolite (e.g., Gillis and Coogan, 2002), and the Oman ophiolite (e.g., Gillis, 2008; France et al., 2009a), and 20% of the oceanic crust are considered to go through a cycle of crystallization, alteration, and then assimilation (Coogan et al., 2003). The melt formed during melting of hydrothermally altered dikes is hence the main contaminant component at the melt lens level, and the knowledge of its composition determined herein is therefore of major interest.

IV.5.f. DR 1: Analytical methods:

Experimental results were analyzed using a Cameca SX100 electron microprobe (Institüt für Mineralogie, Hannover) equipped with 5 spectrometers, "Peak sight" software is used. All analyses were performed using a 15kV acceleration potential, a static (fixed) beam, Kα emission from all elements. The matrix correction is based on Pouchou and Pichoir (1991). Analyses of glass were performed with a beam current which was set to 6nA to minimize migration and volatilization of the alkali elements. Counting time was from 2 to 5 s for Na and K and from 5 to 10 for other elements (Si, Ti, Al, Mg, Fe, Ca, Mn, Cr). In the experiments where melt pools are large enough, the beam was defocused to a spot size of 5 to 20μm. Backscattered electron (BSE) images were also obtained on the Cameca SX100 electron microprobe.

Trace element analyses on experimental results were carried out at the Géosciences Montpellier lab (Montpellier, France) using a Cameca IMS4f ion probe. Polished sections of the experimental results were carbon-coated. We used a 15 kV accelerating voltage of O^- primary beam with a 10 nA intensity. To reduce mass interference by molecular ion species, the energy filtering method was used where secondary ions were subjected a 4500 V accelerating voltage with a -80 V offset with ±30 eV energy window (Shimizu and Hart, 1982). A mass resolving power of 500, and a projected beam size between 20 and 30 μm were used. Each analysis consists of 10 cycles starting from 25.7 mass (used as background and for magnet adjustment), then ^{30}Si (2 s), ^{45}Sc (2 s), ^{47}Ti (2 s), ^{51}V (2 s), ^{88}Sr (2 s), ^{89}Y (2 s), ^{90}Zr (2 s), ^{93}Nb (10 s), ^{137}Ba (10 s), ^{180}Hf (20 s), ^{232}Th (30 s), ^{238}U (30 s) and almost all the rare earth isotopes (10 s) (counting time in bracket). The counting time is 30 s for Eu and 20 s for Lu. The data were corrected for oxide interferences (e.g., Fahey et al., 1987). Concentrations recalculated using ^{30}Si as the reference mass showed no systematic offset induced by the choice of the reference element. The calibration factor was determined from the measurement of NIST 610 (Reed, 1992; Pearce et al., 1997) at the beginning and the end of each analytical session. Typical error on the samples (1 sigma error of mean: s/pn, n = number of cycles) is less than 15% for all trace elements, except for Tb, Er, Lu, Hf (<17.5%), Th (23%) and U (32%). Signal stability was also carefully monitored for every analysis.

Trace element contents of Oman samples have been performed at the Department of Earth Sciences at the Cardiff University by using an ICP-MS.

IV.5.g. DR 2: Major element compositions

Sample	Phase	SiO_2	Al_2O_3	TiO_2	CaO	Na_2O	K_2O	MnO	MgO	FeO	Cr_2O_3	NiO	P_2O_5	Total	*n*	Mg#
08OL30	whole rock	53.55	15.98	1.48	7.64	4.72	0.20	0.07	5.30	9.84	-	-	0.12	98.90	*1*	*49.0*
1030	melt_recalc.	55.48	17.25	1.54	7.77	5.09	0.20	0.05	3.66	8.94	0.00	0.00	0.00	100.00	*58*	42.2
1000	melt_recalc.	59.16	17.80	1.29	5.90	5.98	0.27	0.07	2.77	6.76	0.00	0.00	0.00	100.00	*33*	42.2
970	melt_recalc.	62.99	17.81	1.18	4.40	5.85	0.37	0.05	1.99	5.29	0.00	0.00	0.09	100.00	*38*	40.2
955	melt_recalc.	64.36	17.66	1.03	3.83	5.76	0.44	0.04	1.67	4.99	0.02	0.00	0.11	100.00	*22*	37.3
940	melt_recalc.	69.34	17.72	0.71	1.98	5.66	0.91	0.02	0.71	2.70	0.08	-	0.13	100.00	*35*	28.0
910	melt_recalc.	69.29	17.35	0.49	2.25	5.46	1.16	0.02	0.65	2.93	0.13	0.00	0.06	100.00	*27*	28.5
880	melt_recalc.	71.19	16.90	0.40	1.88	5.56	1.32	0.02	0.42	2.01	0.06	0.00	0.04	100.00	*27*	27.0
850	melt_recalc.	72.63	16.54	0.29	1.30	4.92	2.21	0.00	0.25	1.62	0.08	0.00	0.02	100.00	*12*	22.0

The sample name is 08OL30 for the starting material; for experiments, it corresponds to the experimental temperature (in °C); "melt_recalc.": melt composition recalculated at 100%; n: number of analyses; Mg#=Mg/[Mg+Fe] in molar proportions.

IV.5.h. DR 3: Trace element compositions

These are presented in Appendix B3.

IV.6. Conclusion

The experimental study and associated geochemical investigations presented in this chapter, coupled with the field and petrological studies presented in Chapter III, support the interpretation of oceanic plagiogranites that are present close to the base of the sheeted dike complex at fast spreading ridges, as anatectic rocks formed during the reheating of altered sheeted dikes. Such a reheating stage is consistent with the models presented by Gillis (2008), Koepke et al. (2008), and France et al. (2009a), which describe the melt lens present at fast spreading ridges as a dynamic system that can migrate vertically. The chemical composition (major and trace elements) of the experimentally formed melt, which can mix within the melt lens, is also determined for the first time, well-suited for the quantification of MORB contamination at fast-spreading ridges.

The performed experiments also provide new constraints on the origin of granoblastic microgabbros occurring at the base of the SDC, and as xenoliths in the isotropic gabbro horizon below the SDC. The granoblastic microgabbronorite dikes and xenoliths have lower incompatible element contents (e.g., light REE) than the regular diabases from the sheeted dike complex, resulting from dehydration and / or partial melting. Granoblastic microgabbronorite dikes and xenoliths therefore should be distinguished from those

microgabbros which are regarded as the roots of late basaltic dikes emplaced in the very hot environment at base of the SDC and slowly cooled to typical protodikes (e.g., Nicolas et al., 2008). A partial melting event, locally triggered by a fluid ingression in recently crystallized rocks as proposed by Nicolas et al. (2008) is also ruled out. In that model, the fluids migrate downward along localized pathways (cracks and/or faults); hence one should expect to see gradients of recrystallization from fully recrystallized rocks close to fluid pathways to doleritic rocks away of these pathways. This is in contrast with the base of the sheeted dike complex that is pervasively recrystallized to granoblastic microgabbronorites.

The occurrence of numerous tiny oxide inclusions in newly formed clinopyroxenes, interpreted as results from prograde metamorphism (Chapter II), is reproduced experimentally, and results from recrystallization after amphibole. Manning and MacLeod (1996) have described metamorphic retrograde clinopyroxenes that are associated to oxides. However, these oxides occur in association with granular clinopyroxene grains at the contact with amphibole, close to amphibole bearing veins, and not as inclusions in clinopyroxenes as in granoblastic microgabbro dikes. These retrograde oxide-clinopyroxene assemblages may recall the petrology of granoblastic microgabbro dikes that contain several granular oxides; nevertheless in the case of retrograde evolution, it only occurs in normal gabbros close to late hydrothermal veins in contrast with granoblastic microgabbro dikes where the oxides occurs pervasively and associated to fully recrystallized textures.

The peculiar characteristics of granoblastic microgabbro dikes presented herein (mineral major element compositions, whole-rock trace element composition, occurrence of oxide inclusions in clinopyroxenes, and occurrence of granoblastic microgabbro xenoliths in the isotropic gabbro and foliated gabbro) clearly show that their formation is related to prograde metamorphism, i.e. reheating. Trace elements also support a residual origin after partial melting rather than a metamorphic one in the sub-solidus regime (where rocks are reheated and dehydrated without any partial melting). Nevertheless, both processes may co-exist. Samples with the lowest TiO_2 and Al_2O_3 contents in clinopyroxenes are expected to be equilibrated under temperatures that are below the hydrous solidus, and may represent dehydrated rocks that have not undergone any hydrous partial melting. Koepke et al. (2008) have shown that in a single sample, “dry” and “wet” domains coexist. Hence, it is expected that both pure dehydration and anatexis can occur in a single sample, depending on the previous hydrothermal alteration extent and heterogeneity.

The experimental results also provide the basis for a new thermometer, which can be applied to tholeiitic to calc-alkaline rocks crystallized at shallow pressure (~100 MPa) at the

transition between magmatic and metamorphic processes, under water-saturated conditions and relatively oxidizing conditions (slightly higher than the FMQ equilibrium). It is based on the temperature dependence of Al incorporation in clinopyroxene under these conditions.

Chapter V. "Further discussion: Recrystallization in gabbros"

In Chapters 3 and 4, I have shown that the melt lens is a dynamic horizon that can migrates upward with the potential to reheat and assimilate the base of the hydrothermally altered sheeted dike. I have also shown that the isotropic ophitic gabbros that are found below the sheeted dike complex represent the fossilization of this melt lens. Several successive upward and downward migrations of the melt lens roof can also result in the reheating and assimilation of some isotropic gabbros (Chapter 3).

A detailed study of the isotropic gabbro horizon is required to highlight the assimilation processes and should help to constrain the fossilization processes.

A detailed study of the isotropic gabbros recovered at IODP Site 1256 is presented in a paper submitted to *Geochemistry Geophysics Geosystems* (Koepke et al.; Appendix A4). It shows that assimilation of previously hydrothermally altered dikes is a widely developed process and confirms the model presented in France et al. (2009a). This study also shows that the isotropic gabbros are highly heterogeneous with different generations of melts crystallizing in close association, and that the isotropic gabbros have in average more evolved compositions than the overlying sheeted dike complex and lavas.

A similar study of the Oman ophiolite isotropic gabbro horizon would help to further constrain the fossilization process. I present hereafter a preliminary study of two peculiar coarse-grained gabbros sampled in the Wadi Rajmi area, in the northern massifs of the Oman ophiolite (Figure III-1). This preliminary study shows that high water activities can locally occur in the melt lens, in association with recycled lithologies. The Wadi Rajmi area is located close to a segment boundary and large shear zones are observed in the mantle section, hence results presented here cannot be generalized for sure to a single model of evolution of a dynamic melt lens. The objective of this preliminary study is to highlight petrological processes occurring when hydrothermally altered lithologies are reheated and recycled.

Two peculiar coarse grained gabbros have been studied (07OL34 and 07OL36). Figure V-1 presents the outcrop of sample 07OL36. A spotty, coarse-grained gabbro containing orthopyroxene megacrysts intrudes a fine-grained isotropic gabbro that is characteristic of the isotropic gabbro horizon (Figure V-1). Some thin leucocratic dikelets are observed in the fine-grained isotropic gabbro; these probably represent products of anatexis. The coarse-grained gabbro either represents the anatectic product of the fine-grained gabbro, or the crystallization of a melt originated deeper in the section.

Figure V-1: Outcrop showing the sampling area of sample 07OL36. Two main facies are observed: a fine-grained gabbro and a spotty coarse-grained one containing orthopyroxene megacrysts.

Sample 07OL36 contains two domains; the first one is composed of large poikilitic plagioclase grains, which contain smaller granular clinopyroxene chadacrysts (Figure V-2a-b, Figure V-3, Figure V-4). Some poikilitic orthopyroxene and amphibole grains containing granular clinopyroxene chadacrysts are also observed (Figure V-4). The second domain is mainly composed of clinopyroxene grains containing tiny oxide inclusions and subordinated amphibole (Figure V-3b). The two domains are organized as patches and are homogeneously distributed in the sample (Figure V-4). Close to the contact between the two domains, some clinopyroxene grains containing tiny oxide inclusions are included in the poikilitic plagioclases. Some quartz is locally observed.

Sample 07OL34 is composed of large clinopyroxene and plagioclase grains. Plagioclase grains contain numerous small individual clinopyroxene inclusions (Figure V-2c-f). Back-scattered electron (BSE) images show that clinopyroxene grains are compositionally heterogeneous. The inclusions display a zonation with a relatively sharp contact between the core and the margin (Figure V-5a-b). Large clinopyroxene grains display heterogeneous cores and homogeneous thin margin (<100µm; Figure V-5c-d).

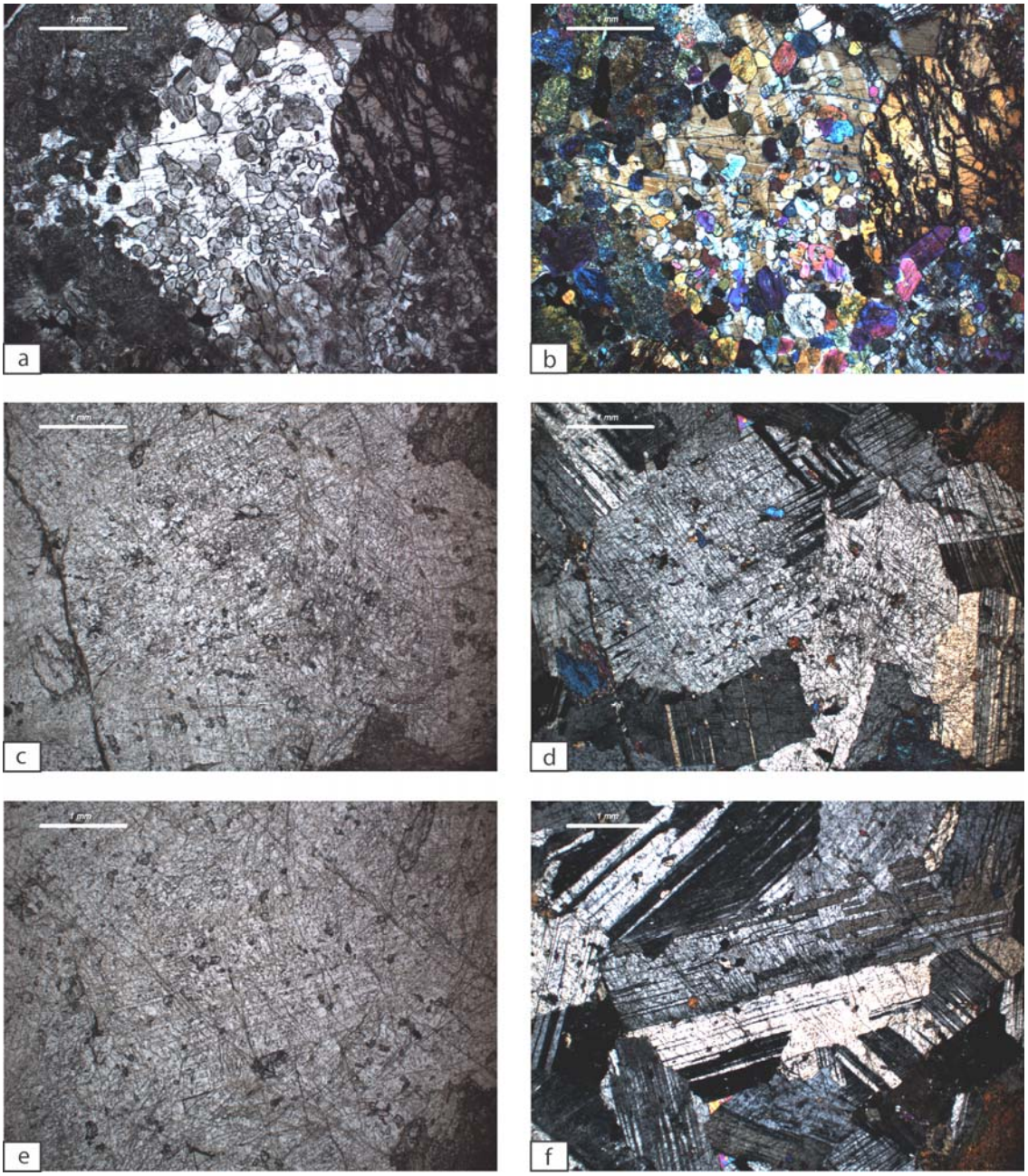

Figure V-2: Microphotographs of samples 07OL36 (a-b), and 07OL34 (c-f); plane-polarized light for a, c, e, and cross-polarized light for b, d, f. a-b) poikilitic plagioclase grains contain several individual granular clinopyroxene grains that are devoid of oxide. On the left side of the picture, a dark domain exclusively composed of clinopyroxenes containing tiny oxide inclusions is observed. c-f) Large plagioclase grains containing numerous individual clinopyroxene inclusions.

In-situ mineral compositions have been analysed using a CAMECA SX-100 microprobe (Montpellier) and are presented in Appendix B4. In sample 07OL36, minerals from different domains display different compositions. The granular clinopyroxenes included in the poikilitic plagioclases have higher Al_2O_3, TiO_2 and Cr_2O_3, and lower CaO contents than

the clinopyroxenes containing numerous tiny oxide inclusions in the clinopyroxene rich domains. Close to the poikilitic plagioclase domains, clinopyroxenes containing tiny oxide inclusions have margins with compositions similar to the granular clinopyroxenes contained in plagioclases.

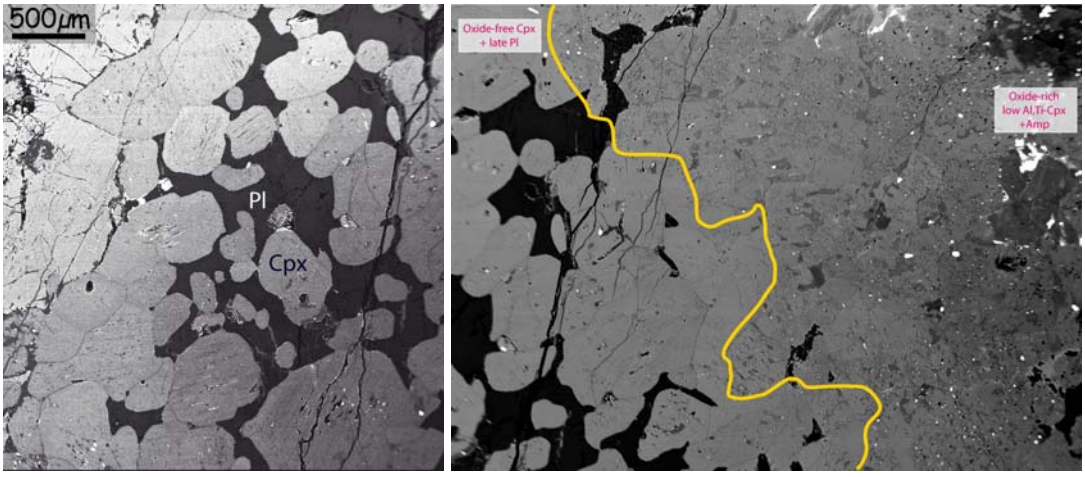

Figure V-3: Back-scattered images of sample 07OL36. left image: poikilitic plagioclase containing free of oxide granular clinopyroxene grains; right image: two zones are present in sample 07OL36 and separated by the yellow line: the left domain is composed of poikilitic plagioclase containing granular clinopyroxene grains that are devoid of oxide, and the right domain is nearly exclusively composed of oxide-bearing clinopyroxenes and subordinated amphiboles.

In 07OL36 the Mg# of clinopyroxenes is 77 on average; plagioclases have An contents up to 93 (88 on average). Amphiboles are actinolite, hornblende and edenite. Temperature estimations using the semi-quantitative thermometer of Ernst and Liu (1998) are up to 780°C. Temperature estimations using the two-pyroxene thermometer of Andersen et al. (1993) give 895±45°C using the granular clinopyroxenes contained in poikilitic plagioclases and 862±67°C using the clinopyroxenes containing tiny oxide inclusions. Temperature estimations using the Al in clinopyroxene thermometer of France et al. (2010a) give 922°C for the granular clinopyroxenes contained in poikilitic plagioclases and 822°C using the clinopyroxenes that contain tiny oxide inclusions. In 07OL34, plagioclases have An contents up to 99 (96 on average). Two different types of clinopyroxene, bright and dark, are observed on the BSE images (Figure V-5). The bright ones, which compose the core of clinopyroxene inclusions observed in large plagioclase grains, are enriched in iron (Mg#=83) compared to the dark ones (Mg#=92). The core of large clinopyroxene grains is heterogeneous and composed of both clinopyroxene species (bright and dark in the BSE images; Figure V-5c-d), and the margin is homogeneous and composed of the dark species. Temperature estimation

using the Al in clinopyroxene thermometer of France et al. (2010a) gives on average 816°C (811°C for the "bright" clinopyroxenes and 821°C for the "dark" ones). Amphiboles are actinolites and hornblendes; temperature estimations using the semiquantitative thermometer of Ernst and Liu (1998) are up to 841°C.

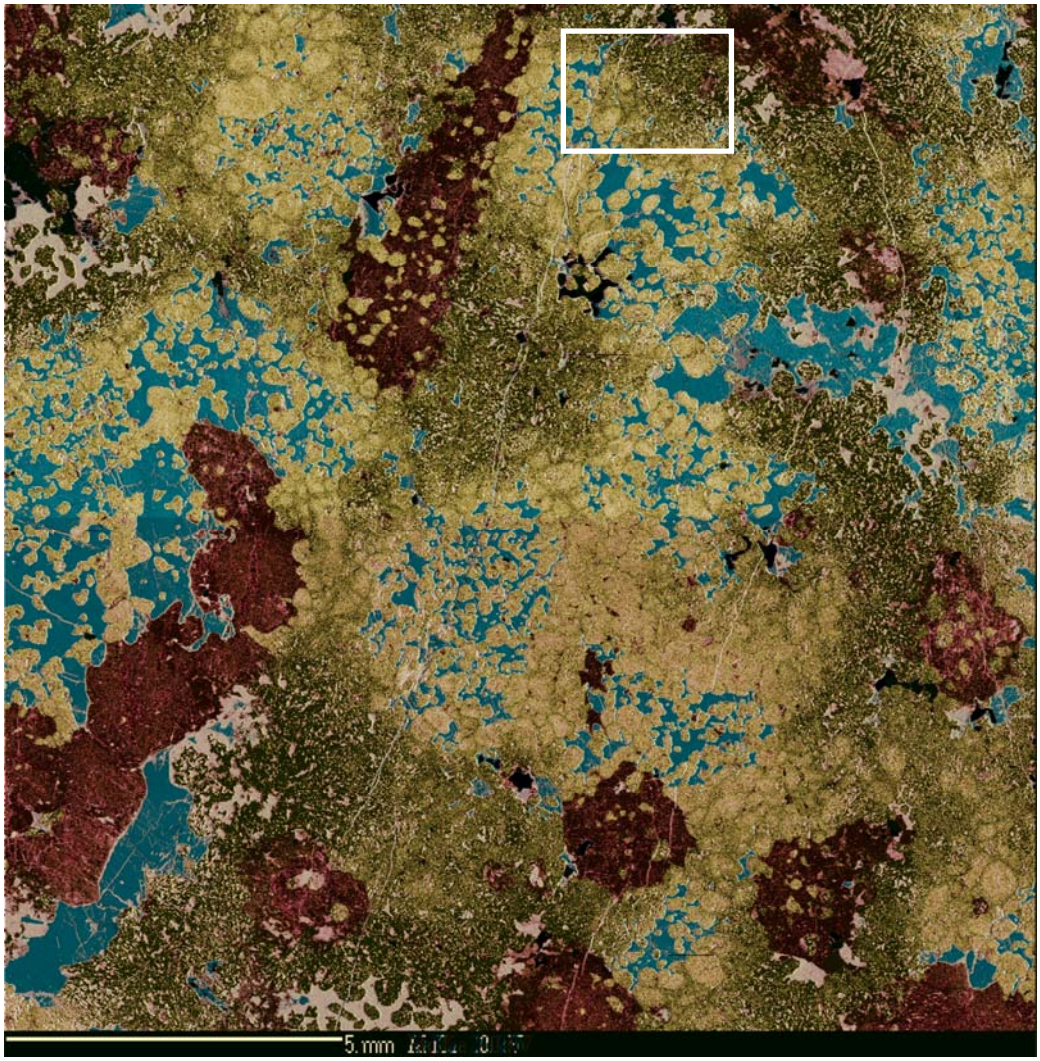

Figure V-4: Compositional image (Al+Ca+Mg) of sample 07OL36 (image width: 1.5cm). Blue: plagioclase; yellow: granular clinopyroxene devoid of oxide; green: clinopyroxene containing tiny oxide inclusions; red: orthopyroxene; purple: amphibole. Note the patchy texture of the sample with zones composed exclusively of clinopyroxene containing tiny oxide inclusions and subordinated amphibole and zones composed of poikilitic plagioclase containing granular and clinopyroxene grains that are devoid of oxide. A poikilitic amphibole grain is observed in the central-left lower part of the image and poikilitic orthopyroxenes are observed in the central upper part and in the lower right part of the image. The white box indicates the location of the picture in Figure V-3b.

Although they represent only minor amounts of the recovered lithologies in present day oceanic crust and in ophiolites, samples containing high-An content plagioclases, high-Mg# clinopyroxenes, and / or clinopyroxene crystallizing before plagioclase are commonly

described (e.g., Ridley et al., 2006; Cordier et al., 2007; Koepke et al., 2009). Such peculiar samples should bring important information on processes occurring at least locally within the oceanic crust.

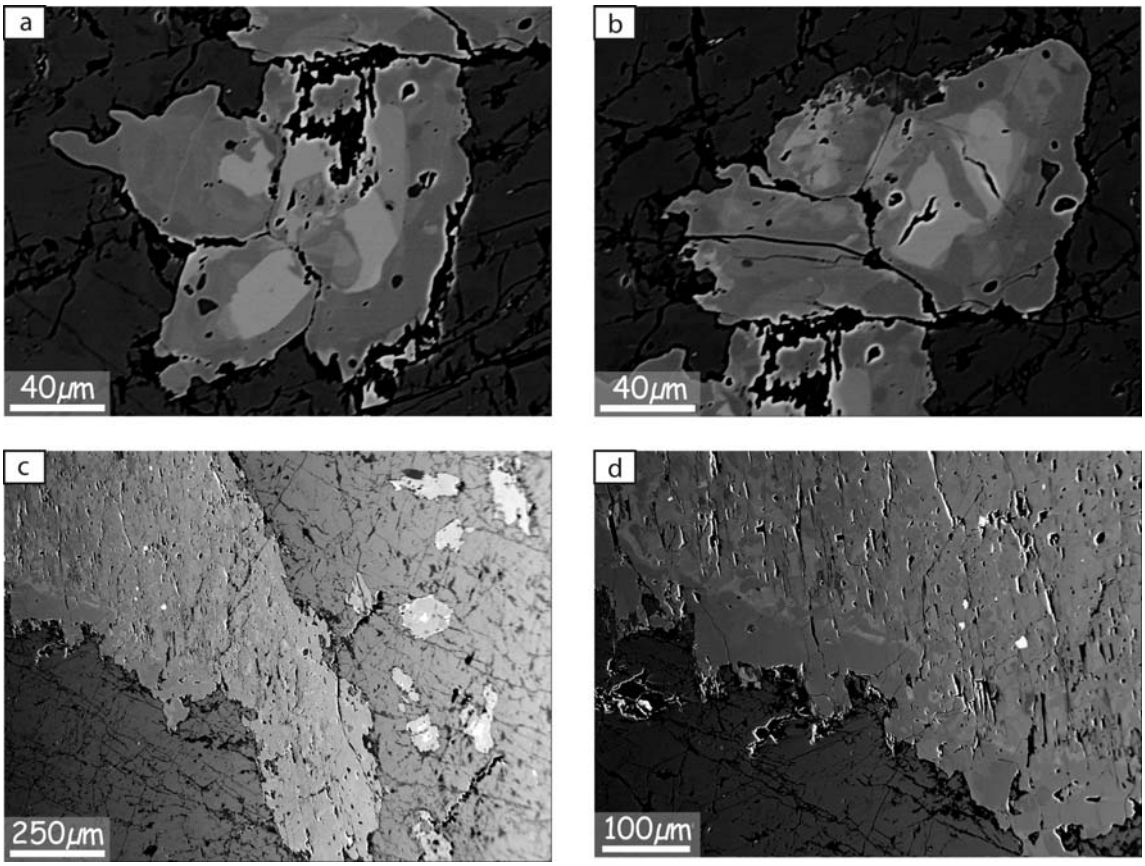

Figure V-5: Back-scattered images of sample 07OL34. a-b) zoned clinopyroxene inclusions in a plagioclase grain; the contact between the core (iron enriched) and the margin (magnesium enriched) is sharp. c-d) Large clinopyroxene grain displaying a heterogeneous core and a homogeneous margin (magnesium enriched).

The occurrence of clinopyroxene inclusions in plagioclase of sample 07OL34, and of poikilitic plagioclases containing granular clinopyroxenes in sample 07OL36 (Figure V-2, Figure V-3, Figure V-4, Figure V-5), highlights the late crystallization of plagioclase with respect to clinopyroxene. This feature is not characteristic of typical dry MORB melts that crystallize plagioclase first (e.g., Grove and Bryan, 1983). Alternatively, it is described in subduction settings where water activities are high (e.g., Gaetani et al., 1993). The early crystallization of clinopyroxene is also observed in the crystallization of evolved MORB melts in water-rich environments corresponding to highly oxidizing conditions (Berndt et al., 2005), and in the crystallization of primitive tholeiitic basalts under high water activities and oxidizing conditions (Feig et al., 2006; Figure V-6). The early crystallization of clinopyroxene

with respect to plagioclase is therefore always associated to high water activities. Hence in both studied samples (07OL34 and 07OL36), the early crystallization of clinopyroxene is attributed to a water rich environment.

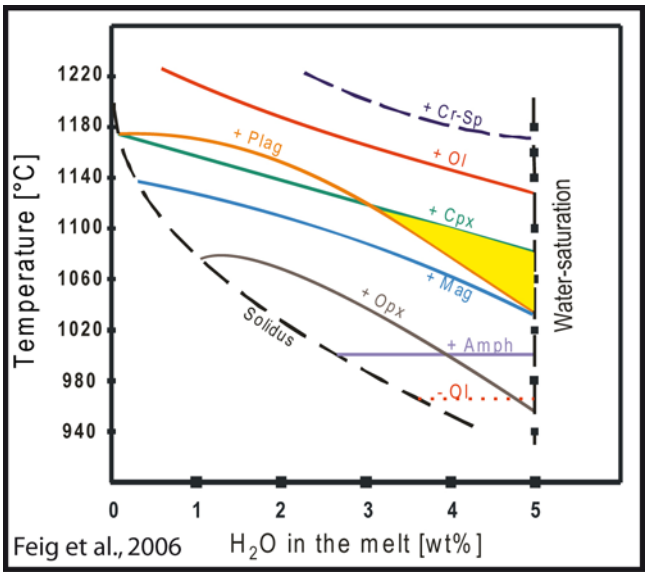

Figure V-6: Temperature vs. water content phase relations diagram for hydrous tholeiitic basalt at 200MPa (after Feig et al., 2006). Curves with "+" represent the stability curves of minerals and curve with "-" show the end of the stability field. Yellow field highlight the field where clinopyroxene crystallizes before plagioclase.

Hydrous conditions are usually not expected at mid-ocean ridges (e.g., Michael and Chase, 1987) but as shown in Chapters 3 and 4 and in recent studies (e.g., Coogan, 2003; Bosh et al., 2004; Cordier et al., 2007; Nicolas et al., 2008; Koepke et al., submitted_Appendix A4) high temperature hydrothermalism and / or melt lens dynamics may result, at least locally, in melt hydration. The poikilitic texture of some amphiboles, containing granular clinopyroxenes, points to their magmatic origin and also support the crystallization after a hydrous melt. However, maximum temperature estimations performed on these amphiboles are up to 780°C and point to a subsolidus equilibration, probably indicating a re-equilibration at lower temperature during the retrograde evolution. The occurrence of orthopyroxene in sample 07OL36 is also consistent with the crystallization of a hydrous melt (Boudier et al., 2000; Feig et al., 2006).

Mineral major element compositions, especially those of clinopyroxene and plagioclase, are peculiar and also uncommon for MORB systems. Clinopyroxene Mg# is up to 96 in sample 07OL34 and up to 82 in sample 07OL36, and plagioclase An contents are up to 99 in sample 07OL34 and up to 93 in sample 07OL36. These values are clearly higher than classical minerals in typical dry MORB systems. They can be attributed either to Mg-Ca rich

melts nearly free of Fe-Na (Panjasawatong et al., 1995; Kohut and Nielsen, 2003; Ridley et al., 2006), or to the crystallization under high water activities (e.g., Hattori and Sato, 1996; Kuritani, 1998; Ginibre et al., 2002; Landi et al., 2004; Feig et al., 2006; Cordier et al., 2007; Koepke et al., 2009). The occurrence of a gabbro xenolith recovered in basalts at the East Pacific Rise (Ridley et al., 2006), which contain high-An plagioclase, has been attributed to the crystallization of a Ca-supra rich melt principally because water-rich magmas are unexpected at oceanic spreading centers. Nevertheless such Ca-rich melt (or Ca-Mg-rich melts) have never been sampled and alternatively, we have shown in Chapters 3 and 4 and in Koepke et al. (submitted; Appendix A4) that hydrous melts can occur at the melt lens level. Using the melt fractionation trend calculations performed by Kvassnes et al. (2004) using MELTS (Ghiorso and Sack, 1995), mineral compositions of the studied samples (07OL34 and 07OL36) are consistent with a wet fractionation trend (Figure V-7). Taking into account the uncommon crystallization sequence and mineral compositions, the studied samples (07OL34 and 07OL36) are interpreted as resulting from the crystallization of a hydrous melt. Although the hydrated nature of the melt is established, the hydration origin remains unclear and has yet to been constrained.

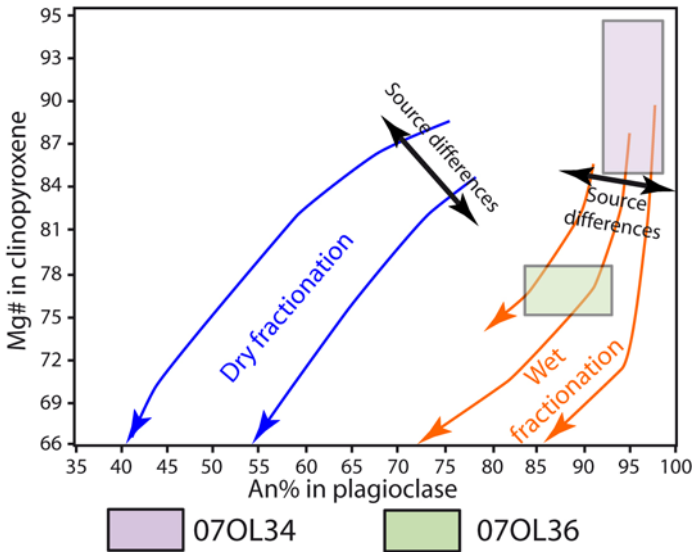

Figure V-7: Mg# in clinopyroxene vs. An content of plagioclase (after Kvassnes et al., 2004. The dry and wet fractionation trends are from Kvassnes et al. (2004), and calculated using MELTS (Ghiorso and Sack, 1995); both fractionation trends are calculated for different initial compositions. The studied samples (07OL34 and 07OL36) overlap the wet fractionation trend.

In sample 07OL36, the origin of oxide-bearing clinopyroxene domains is unclear. The origin of oxide inclusions can be attributed either to low-temperature alteration occurring

during the retrograde evolution (Manning and MacLeod, 1996), or to recrystallization after amphibole of previously hydrothermally altered lithologies occurring during a reheating stage (France et al., 2009a, 2010a). The mineralogical distribution in the sample, with two different domains (domains with poikilitic plagioclases containing granular clinopyroxenes that are devoid of oxide, and domains with oxide-bearing clinopyroxenes) can be used to discuss further the origin of oxide inclusions. The absence of oxide in granular clinopyroxene chadacrysts hosted by poikilitic plagioclase may be explained by the fact that they are isolated from percolating hydrothermal fluids, and therefore not altered. However, the local occurrence of oxide-bearing clinopyroxenes in unaltered poikilitic plagioclases rules out this hypothesis, and attests to the earlier origin of oxide-bearing clinopyroxenes with respect to the poikilitic plagioclases. This early crystallization of oxide-bearing clinopyroxenes is also supported by the occurrence at the borders of domains composed of oxide-bearing clinopyroxenes, of some oxide-bearing clinopyroxenes that display margins with compositions similar to oxide-free granular clinopyroxenes hosted by poikilitic plagioclases (Figure V-8). A secondary origin of the free of oxide granular clinopyroxenes and associated to poikilitic plagioclases with respect to the oxide-bearing clinopyroxenes is therefore attested.

The absence of plagioclase in the oxide-bearing clinopyroxene domains is also unclear (Figure V-4). The hydrous partial melting of previously hydrothermally altered dikes leads to the stabilisation of clinopyroxene at higher temperature than plagioclase, and have therefore the potential to stabilize clinopyroxenitic residue (France et al., 2010a). During such a hydrous partial melting stage, the recrystallization of clinopyroxene after amphibole leads to the occurrence of oxide-bearing clinopyroxene similar to those observed here (France et al., 2010a). The oxide-bearing clinopyroxene domains are therefore interpreted as representing a residue after the hydrous partial melting of a previously hydrothermally altered protolith. This hydrous partial melting event produces a hydrous melt that may mix with classical MORB melts contained within the melt lens and results in the crystallization of the surrounding domains where clinopyroxene crystallize before plagioclase and where mineral compositions attest to a water rich environment. Clinopyroxene from the two domains have different compositions, which is consistent with this scenario (Figure V-8). Oxide-bearing clinopyroxenes interpreted as residues have lower Cr_2O_3 and Al_2O_3 contents than the oxide-free clinopyroxenes interpreted as magmatic, and hence are equilibrated at lower temperature (France et al., 2010a). Furthermore, oxide-bearing clinopyroxenes plot well within the field of residual clinopyroxenes from granoblastic dikes and of residual clinopyroxenes formed after

the melting of hydrothermally altered dikes (France et al., 2009a, 2010a), whereas the oxide-free granular clinopyroxenes plot on average off that trend (Figure V-8), pointing to a likely magmatic origin. Temperature estimations performed using the two-pyroxene thermometer (Andersen et al., 1993) and using the Al in clinopyroxene thermometer (France et al., 2010a) also give higher temperature for the oxide-free granular clinopyroxene, consistent with a magmatic origin (the solidus temperature of hydrothermally altered dikes is 850°C according France et al., 2010a).

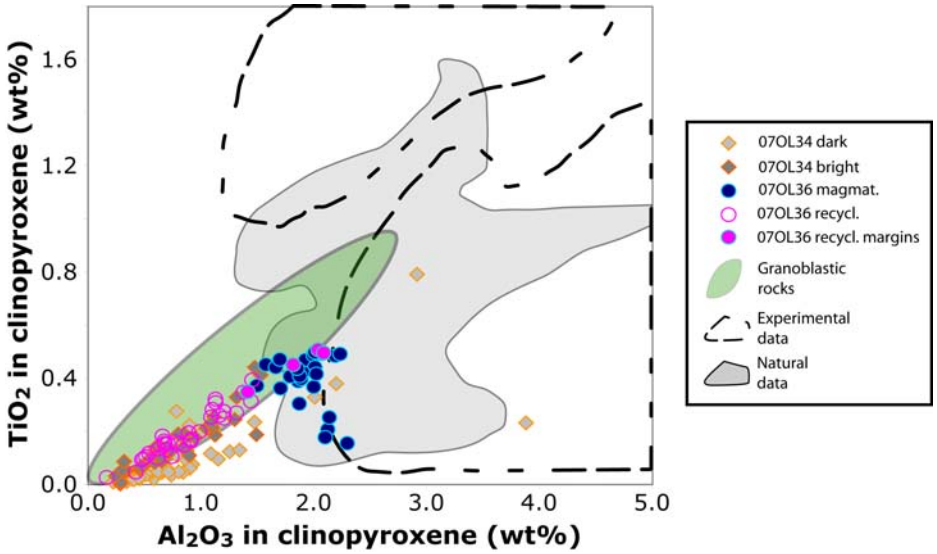

Figure V-8: Correlation between TiO_2 and Al_2O_3 in clinopyroxene. The studied samples (07OL34 and 07OL36) are compared to clinopyroxenes in granoblastic dikes (green field; compositions from France et al., 2009a), and to experimental and natural data from oceanic crust lithologies. Experimental data (dashed field) are from Snyder et al. (1993), Toplis and Carroll (1995) and Toplis et al. (1994) for Fe-Ti MORB crystallization experiments, from Berndt et al. (2005) and Feig et al. (2006) for hydrous crystallization experiments in primitive MORB-type system, from Grove and Bryan (1983) and Kinzler and Grove (1992) for MORB crystallization experiments, and from Koepke et al. (2004) for clinopyroxenes formed during hydrous partial melting of gabbros. Natural data (grey field) for oceanic crust lithologies are from Dziony et al. (2008) for IODP Hole 1256D sheeted dikes not affected by granoblastic imprint, from Miyashita et al. (2003) and Pallister and Hopson (1981) for Oman ophiolite sheeted dikes and gabbros, and from Boudier et al. (2000) and Gerbert-Gaillard (2002) for Oman gabbronorites. "07OL34 dark" corresponds to the dark parts of clinopyroxenes on BSE images; "07OL34 bright" corresponds to the bright parts of clinopyroxenes on BSE images; "07OL36 magmat." corresponds to free of oxide granular clinopyroxenes hosted by poikilitic plagioclases; "07OL36 recycl." corresponds to the oxide-bearing clinopyroxenes; "07OL36 recycl. margins" corresponds to the margins of the oxide-bearing clinopyroxenes.

In sample 07OL34 the hydrated nature of the originated melt is supported by the crystallization sequence and the mineral compositions. The high water activity of the crystallizing melt can't be related to magmatic fluids as only minor amounts are present in

normal MORBs. The water origin can be either attributed to the tectonic setting of the studied area (segment end; Boudier et al., 2000), or to the shallow subduction occurring during the early obduction (see discussion in section III.1; e.g., Koepke et al., 2009), or to recycling of previously hydrothermally altered rocks (e.g., France et al., 2009a).

The occurrence of clinopyroxene zoned inclusions in plagioclase is meaningful: this zonation is reverse with cores enriched in iron in comparison with the margins, and the contact between cores and margins is sharp. The margins are therefore equilibrated with a more primitive melt (containing at least the same water content to account for the high An content of plagioclases) and / or with a melt with higher water activities. The sharp contact between inclusions cores and margins can be attributed either to a sudden magma recharge (with a more primitive composition and / or higher water activities) or to an inherited origin of the cores. The Al_2O_3 contents are similar in cores and margins, and suggest a similar equilibration temperature (~815°C according France et al., 2010a). The low Al content, and so the low temperature recorded in inclusion cores can't be attributed to re-equilibration with surrounding minerals as a sharp contact is observed with inclusion margins. Furthermore only the crystallization of a highly primitive melt or of a hydrous melt can account for the Mg# (83) of the inclusion cores. Temperature (~810°C) obtained for inclusion cores is incoherent with highly primitive melts; these cores have therefore probably crystallized after a water rich melt similarly to the inclusion margins. The origin of water (linked to the tectonic setting, to the early obduction, or to recycling) can't be determined without doubt, but the sharp contact between inclusion cores and margins point to a recycled origin. Hydrous magmas are indeed expected at segment ends and during the shallow subduction process but sudden change in the magma composition is not expected while it does during recycling. Sample 07OL34 has therefore crystallized under high water activities, probably consequently to the recycling of hydrothermally altered lithologies.

The recycling event proposed in the genesis of both studied samples can be attributed either to vertical movements of the upper melt lens present at fast spreading ridges (e.g., France et al., 2009), or to a magma intrusion close to previously hydrothermalized lithologies (e.g., Koepke et al., 2007). Such intrusions are observed in the Oman ophiolite and attributed to a second magmatic stage triggered by the early obduction (e.g., Boudier et al., 1988; Koepke et al., 2009). Finally, the cause of the recycling stage can't be determined, and this preliminary study can't be used to further constrain the general dynamic model highlighted by France et al. (2009). Nevertheless, it highlights processes occurring when recycling of hydrothermally altered lithologies occurs.

Conclusion

At least part of the upper and lower oceanic crust formed at fast spreading ridges is fed by the upper melt lens that is imaged at the base of the sheeted dike complex. Hence the role of the melt lens in oceanic crust genesis is critical. Interactions between the melt lens and the overlying, hydrothermally altered sheeted dike complex may have first-order consequences on the melt composition, and therefore on the whole oceanic crust composition. The objective of this study was to identify the different processes occurring within the melt lens and at the interface between this melt lens and the overlying sheeted dikes. To study these processes, I carried out comparison between the Oman ophiolite and IODP Hole 1256D, the first drilling hole that has reached the sheeted dikes / gabbro transition. Detailed field studies have been performed in the Oman ophiolite, and the Oman samples have been petrologically and geochemically studied, and compared to samples from IODP Hole 1256D. An experimental study that reproduces partial melting of hydrothermally altered dikes at the top of the melt lens has also been carried out.

The main results are:

- In the Oman ophiolite and at IODP Site 1256, the base of the sheeted dike complex is truncated by isotropic gabbros. These gabbros locally contain olivine and can be either fine or coarse grained.
- The base of the truncated dikes is recrystallized to a well equilibrated (granoblastic texture) granulitic assemblage. The granoblastic dikes are composed of plagioclase, clinopyroxene, oxides, and orthopyroxene. The clinopyroxenes contain numerous tiny oxide inclusions.
- Numerous xenoliths of either gabbro or granoblastic microgabbro and granoblastic microgabbronorite are observed within the isotropic gabbro horizon. A xenolith accumulation is also observed close to the isotropic / foliated gabbro transition.
- Numerous granoblastic patches and other evidences of assimilation are observed within the isotropic gabbro horizon.
- Experimental melts formed during partial melting of hydrothermally altered dikes are highly silicic and similar to the oceanic plagiogranites observed close to the sheeted dikes / gabbro transition.
- Patterns of trace element analysed with SIMS in the experimental melts are similar to those of typical oceanic plagiogranites observed close to the sheeted dikes / gabbro transition.

- The residual assemblage after the experimental partial melting of hydrothermally altered sheeted dikes is petrographically and geochemically similar to the granoblastic dikes and xenoliths.

These different observations support the following conclusions:

- The sheeted dikes / gabbro transition (hydrothermal / magma transition) in the Oman ophiolite and at IODP Site 1256 can be described in a single coherent model, which reconciles apparently contrasting previous models. This model proposes that the melt lens underlying the sheeted dike complex is a dynamic horizon that can inflate and deflate and / or migrate upward and downward. A review of the associated time-scales is presented in the article that describes this model (France et al., 2009a); it shows that the identified melt lens migrations are associated to time scales ≤10,000 years.
- Upward migrations of the top of the melt lens result in the reheating of the base of the sheeted dike complex, and in the assimilation of hydrothermally altered diabases (France et al., 2009a; Koepke et al., submitted_Appendix A4).
- The origin of microgranular dikes and xenoliths present at the base of the sheeted dike complex is bimodal. Some have crystallized in a still hot, hydrous environment and have a pure magmatic origin (protodikes; Nicolas et al., 1991, 2008), and some are recrystallized in the amphibolite to granulite facies during the reheating event associated to upward migrations, and can therefore be regarded as metamorphic products (granoblastic dikes). Both processes result in very similar textures, and a multi-disciplinary study (field observations, petrological characterization, and geochemical characterization) is necessary to decipher the origin of a given sample.
- The partial melting of hydrothermally altered diabase start at temperatures as low as 850°C.
- The chemical composition (major and trace elements) of the melt formed experimentally during hydrous partial melting of the base of the sheeted dikes, and the associated phase relations have been determined (France et al., 2010a, 2010b). The obtained trace element composition is a useful reference for future detailed geochemical MORB investigations.

- Hydrous partial melting of the base of the hydrothermally altered sheeted dike complex produces a plagiogranitic hydrous melt, and a residue that is compositionally similar to granoblastic dikes (France et al., 2010a, 2010b).
- Assimilation of hydrothermally altered diabases in the melt lens is a common process and results in contamination processes in the melt lens (France et al., 2009a; 2010b).
- Downward migrations of the top of the melt lens result in the crystallization of isotropic gabbros. The isotropic gabbro horizon represents the fossilized melt lens (France et al., 2009a).
- At IODP Site 1256, the bottom of the hole is expected to be very close to the melt lens / magma chamber transition, which is assumed to be the isotropic / foliated gabbro transition (France et al., 2009a).
- A new thermometer relevant for rocks crystallized at the melt lens level has been elaborated (France et al., 2010a). It is based on the Al content of clinopyroxenes:

$$T = 93.145\ Al_2O_3 + 742$$

The proposed model could be further tested by complementary studies, which include the following:

- As proposed in France et al. (2009a), analyzing the Cl and F content of amphiboles present in the isotropic gabbros should attest of the recycled origin of the fluid crystallizing the magmatic amphiboles.
- A detailed petrological and geochemical study of the isotropic gabbro horizon in the Oman ophiolite, compared with the precise study of this horizon at IODP Site 1256 (Koepke et al., submitted; Appendix A4), and an in-situ trace element study of the different minerals from the isotropic gabbro horizon, in both the Oman ophiolite and IODP Hole 1256D, should bring further constraints to our understanding of the processes occurring within the melt lens, and of the processes that result in the melt lens fossilization.
- An experimental study of the melting of partially hydrothermally altered sheeted dikes containing magmatic minerals relics may precise the melting reactions occurring during the upward migrations of the top of the melt lens.

Results presented in by France et al. (2010a) are obtained using a fully altered starting material which may be to simplistic to reproduce natural processes.

- An in-situ measurement of the Fe^{3+}/Fe^{2+} ratio in minerals of the different oceanic lithologies will help to further constrain the available models for the accretion of ocean crust, of lower crustal rocks, down to the base of the crust. It will also help to constrain the influence of water during the crystallization of the different oceanic lithologies. Such analyses should be performed with the help of synchrotron radiation tools. A corresponding proposal was submitted to ESRF (European Synchrotron Radiation Facility) in September 2009 (L. France: "*A Redox log of the oceanic crust from plagioclases Fe^{3+}/Fe^{2+} micro-XANES in-situ measurements*"). The results are expected to provide the first redox log of an oceanic crust section and will also help to further constrain the new oxybarometer proposed in France et al. (2009b; Appendix A3). This oxybarometer is based on microprobe analyses of two of the most common minerals present is basaltic series (clinopyroxene + plagioclase). It will be useful for all petrological and geochemical studies of oxidizing magmatic systems.

References

Albarède F, Provost A (1977) Petrological and geochemical mass balance equations: an algorithm for least-square fitting and general error analysis. *Computers and Geosciences* **3**:309-326. doi:10.1016/0098-3004(77)90007-3

Allen CR (1975) The petrology of a portion of the Troodos Plutonic Complex, Cyprus. *Thesis, PhD, Univ. of Cambridge (unpubl.)*

Alt JC, Honnorez J, Laverne C, Emmermann R (1986) Hydrothermal alteration of a 1km section through the upper oceanic crust, deep sea drilling project Hole 504b_Mineralogy, chemistry, and evolution of seawater-basalt interactions. *J. Geophys. Research* **91-B10**: 10,309-10,335

Alt JC, Laverne C, Vanko DA, Tartarotti P, Teagle DAH, Bach W, Zuleger E, Erzinger J, Honnorez J, Pezard PA, Becker K, Salisbury MH, Wilkens RH (1996) Hydrothermal alteration of a section of upper oceanic crust in the eastern equatorial Pacific: a synthesis of results from Site 504 (DSDP Legs 69, 70, and 83, and ODP Legs 111, 137, 140, and 148.). *In Alt, J.C., Kinoshita, H., Stokking, L.B., and Michael, P.J. (Eds.), Proc. ODP, Sci. Results, College Station, TX (Ocean Drilling Program)* **148**: 417-434

Amri I, Benoit M, Ceuleneer G (1996) Tectonic setting for the genesis of oceanic plagiogranites: evidence from a paleospreading structure in the Oman ophiolite. *Earth and Planetary Science Letters* **139**: 177-194

Anders E, Grevesse N (1989) Abundances of the elements: meteoritic and solar. *Geochimica et Cosmochimica Acta* **53**: 197-214.

Andersen DJ, Lindsley DH, Davidson PM (1993) QUILF: A Pascal program to assess equilibria among Fe-Mg-Mn-Ti oxides, pyroxenes, olivine, and quartz. *Computers and Geosciences* **19**: 1,333-1,350. doi:10.1016/0098-3004(93)90033-2

Asimow PD, Stolper EM (1999) Steady-state mantle-melt interactions in one dimension: equilibrium, transport and melt focusing. *Journal of Petrology* **40-3**: 475-494. doi:10.1093/petrology/40.3.475

Bach W, Erzinger J, Alt JC, Teagle DAH (1996) Chemistry of the lower sheeted dike complex, Hole 504B (Leg 148): influence of magmatic differentiation and hydrothermal alteration. *In Alt JC, Kinoshita H, Stokking LB, Michael PJ (Eds.), Proc. ODP, Sci. Results, College Station, TX (Ocean Drilling Program)* **148**: 39-55. doi:10.2973/odp.proc.sr.148.114.1996

Backer ET, Urabe T (1996) Extensive distribution of hydrothermal plumes along the superfast spreading East Pacific Rise, 13°30'-18°40'S. *Journal of Geophysical Research* **101-B4**:8,685-8,695

Barker F (1979) Trondhjemites, dacites and related rocks. *Elsevier, Amsterdam* 659 pp.

Bascom WN (1961) A Hole in the Bottom of the Sea: The Story of the Mohole Project. *Doubleday and Company, Inc., Garden City, New York,* 352 pp.

Batiza R, Niu Y (1992) Petrology and magma chamber processes at the East Pacific Rise. *Journal of Geophysical Research* **97**:6,779-6,797

Beard JS, Lofgren GE (1989) Effect of Water on the Composition of Partial Melts of Greenstone and Amphibolite. *Science* **244**: 195-197

Beard JS, Lofgren GE (1991) Dehydration melting and water saturated melting of basaltic and andesitic greenstones and amphibolites at 1, 3, and 6.9 kb. *Journal of Petrology* **32**: 365-401

Beccaluva L, Ohnenstetter D, Ohnenstetter M, Venturelli G (1977) The trace element geochemistry of Corsican ophiolites. *Contributions to Mineralogy and Petrology 64*: 11-31

Beccaluva L, Chinchilla-Chaves AL, Coltorti M, Giunta G, Siena F, Vaccaro C (1999) Petrological and structural significance of the Santa Elena-Nicoya ophiolitic complex in Costa Rica and geodynamic implications. *European Journal of Mineralogy* **11**: 1,091-1,107

Bedard JH, Sparks RSJ, Renner R, Cheadle MJ, Hallworth MA (1988) Peridotite sills and metasomatic gabbros in the eastern layered series of the Rhum complex. *J. Geol. Sot. London* **145**: 207-224

Bergmanis EC, Sinton J, Rubin KH (2007) Recent eruptive history and magma reservoir dynamics on the southern East Pacific Rise at 17°30'S. *Geochemistry Geophysics Geosystems* **8-12**: Q12O06. doi:10.1029/2007GC001742

Berndt J, Liebske C, Holtz F, Freise M, Nowak M, Ziegenbein D, Hurkuck D, Koepke J (2002) A combined rapid-quench and H2-membrane setup for internally heated pressure vessels: Description and application for water solubility in basaltic melts. *American Mineralogist* **87**: 1,717-1,726

Berndt J, Koepke J, Holtz F (2005) An experimental investigation of the influence of water and oxygen fugacity on differentiation of MORB at 200 MPa. *Journal of Petrology* **46**: 135-167

Bloomer SH, Natland JH, Fisher RL (1989) Mineral relationships in gabbroic rocks from fracture zones of Indian Ocean ridges: evidence for extensive fractionation, parental diversity and boundary-layer recrystallization. *In Magmatism in the Ocean Basins, edited by Saunders AD and Norry MJ, Geol. Soc. London Spec. Publ.* **42**: 107-124

Bonev N, Stampfli G (2009) Gabbro, plagiogranite and associated dykes in the supra-subduction zone Evros Ophiolites, NE Greece. *Geological Magazine* **146-1**: 72-91. doi:10.1017/S0016756808005396

Bosch D, Jamais M, Boudier F, Nicolas A, Dautria JM, Agrinier P (2004) Deep and high temperature hydrothermal circulation in the Oman ophiolite: Petrological and isotopic evidence. *Journal of Petrology* **45(6)**: 1,181-1,208. doi:10.1093/petrology/egh010

Botcharnikov RE, Koepke J, Holtz F, McCammon C, Wilke M. (2005) The effect of water activity on the oxidation and structural state of Fe in a ferro-basaltic melt. *Geochimica et Cosmochimica Acta* **69**: 5,071-5,085. doi:10.1016/j.gca.2005.04.023

Boudier F, Nicolas A (2007) Comment on "dating the geologic history of Oman's Semail ophiolite: insights from U-Pb geochronology" by C.J. Warren, R.R. Parrish, D.J. Waters and M.P. Searle. *Contributions to Mineralogy and Petrology* **154**: 111-113

Boudier F, Ceuleneer G, Nicolas A (1988) Shear zones, thrusts and related magmatism in the Oman ophiolite: initiation of thrusting at an ocean ridge. *Tectonophysics* **151**: 275–296

Boudier F, Nicolas A, Ildefonse B (1996) Magma chambers in the Oman ophiolite: fed from the top and the bottom. *Earth and Planetary Science Letters* **144**: 239-250. doi:10.1016/0012-821X(96)00167-7

Boudier F, Godard M, Armbruster C (2000) Significance of gabbronorite occurrence in the crustal section of the Semail ophiolite. *Marine Geophysical Research* **21**: 307-326. doi:10.1023/A:1026726232402

Brophy JG (2008) A study of rare earth element (REE)-SiO2 variations in felsic liquids generated by basalt fractionation and amphibolite melting: a potential test for discriminating. *Contributions to Mineralogy and Petrology* **156**: 337-357. doi: 10.1007/s00410-008-0289-x

Brophy JG (2009) La-SiO_2 and Yb-SiO_2 systematics in mid-ocean ridge magmas: implications for the origin of oceanic plagiogranite. *Contributions to Mineralogy and Petrology* **158**: 99-111. doi: 10.1007/s00410-008-0372-3

Browning P (1982) The petrology, geochemistry and structure of the plutonic rocks of the Oman Ophiolite. *PhD Thesis, The Open University, Milton Keynes,* 405 pp.

Browning P (1984) Cryptic variation within the cumulate sequence of the Oman ophiolite: magma chamber depth and petrological implications. *In: Gass I, Lippard SJ, Shelton AW (Eds.), Ophiolites and Oceanic Lithosphere. Special Publication-Geological Society of London,* **13**: 71-82

Bryan W, Frey BFA, Dickey JS (1976) Inferred geologic settings and differentiation in basalts from the Deep Sea Drilling Project. *Journal of Geophysical Research* **81**: 4,285-4,304

Canales JP, Detrick RS, Carbotte SM, Kent GM, Diebold JB, Harding A, Babcock J, Nedimovic MR, Van Ark E (2005) Upper crustal structure and axial topography at intermediate spreading ridges: Seismic constraints from the southern Juan de Fuca Ridge. *Journal of Geophysical Research* **110**: B12,104. doi: 10.1029/2005JB003630

Canales JP, Nedimovic MR, Kent GM, Carbotte SM, Detrick RS (2009) Seismic reflection images of a near-axis melt sill within the lower crust at the Juan de Fuca ridge. *Nature* **460**: 89-94. doi:10.1038/nature08095

Cande SC, Kent DV (1995) Revised calibration of the geomagnetic polarity timescale for the Late Cretaceous and Cenozoic. *Journal of Geophysical Research* **100**: 6,093–6,095. doi:10.1029/94JB03098

Cann JR (1974) A model for oceanic crustal structure developed. *Geophysical Journal of the Royal Astronomical Society* **39**: 169-187

Carbotte SM (2008) Focusing in on Mid-Ocean Ridge Segmentation. *Eos Trans. AGU Fall Meet. Suppl.* **89-53**: T34B-01

Carbotte SM, Mutter C, Mutter J, Ponce-Correa G (1998) Influence of magma supply and spreading rate on crustal magma bodies and emplacement of the extrusive layer: Insights from the East Pacific Rise at lat 16°N. *Geology* **26-5**: 455-458

Carbotte SM, Mutter JC, Canales JP, Nedimovic MR, Carton H, Xu M, Newman K, Marjanovic M, Aghaei O, Stowe L (2008) New observations of the magmatic segmentation of the East Pacific Rise from Siquieros to Clipperton from a multi-streamer seismic reflection imaging study. *Eos Trans. AGU Fall Meet. Suppl.* **89-53**: B21A-0320

Caress DW, Burnett MS, Orcutt JA (1992) Tomographic image of the axial low velocity zone at 12°50'N on the East Pacific Rise. *Journal of Geophysical Research* **97-B6**: 9,243-9,263

Caroff M, Lagabrielle Y, Spadea P, Auzende JM (1997) Geochemical modeling of nonsteady-state magma chambers: A case study from an ultrafast spreading ridge, East Pacific Rise, 17-19°S. *Geochimica et Cosmochimica Acta* **61-20**: 4,367-4,374

Carton H, Carbotte SM, Mutter JC, Canales JP, Nedimovic MR, Newman K, Marjanovic M, Xu M, Aghaei O, Stowe L (2008) Characteristics of the crustal magma body in the 2005-06 eruption area at 9°50'N on the East Pacific Rise from a 3D multi-channel seismic investigation. *Eos Trans. AGU Fall Meet. Suppl.* **89-53**: B23F-03

Casey JF, Karson JA (1981) Magma chamber profiles from the Bay of Islands ophiolite complex. *Nature* **298**: 295-301

Collier JS, Singh SC (1997) Detailed structure of the top of the melt body beneath the East Pacific Rise at 9°40'N from waveform inversion of seismic reflection data. *Journal of Geophysical Research* **102-B9**: 20,287-20,304. doi:10.1029/97JB01514

Coleman RG, Donato MM (1979) Oceanic plagiogranite revisited. *In: Barker F (eds) Trondhjemites, dacites, and related rocks. Elsevier, Amsterdam* 149-167

Coleman RG, Peterman ZE (1975) Oceanic plagiogranite. *Journal of Geophysical Research* **80-8**: 1,099-1,108

Conference Participants (1972) Penrose field conference on ophiolites. *Geotimes* **17**: 24-25

Coogan LA (2003) Contaminating the lower crust in the Oman ophiolite. *Geology* **31-12**: 1,065-1,068. doi:10.1130/G20129.1

Coogan LA, Mitchell NC, O'Hara MJ (2003) Roof assimilation at fast spreading ridges: An investigation combining geophysical, geochemical, and field evidence. *Journal of Geophysical Research* **108-B1**: 2002 doi:10.1029/2001JB001171

Cordier C, Caroff M, Juteau T, Fleutelot C, Hémond C, Drouin M, Cotton J, Bollinger C (2007) Bulk-rock geochemistry and plagioclase zoning in lavas exposed along the northern flank of the Western Blanco Depression (Northeast Pacific): Insight into open-system magma chamber processes. *Lithos* **99**: 289-311

Crawford WC, Webb SC (2002) Variations in the distribution of magma in the lower crust and the Moho beneath the East Pacific Rise at 9°-10° N. *Earth and Planetary Science Letters* **203**: 117-130

Detrick RS, Buhl P, Vera E, Mutter J, Orcutt J, Madsen J, Brocher T (1987) Multi-channel seismic imaging of a crustal magma chamber along the East Pacific Rise. *Nature* **326**: 35-41

Detrick R, Collins J, Stephen R, Swift S (1994) In situ evidence for the nature of the seismic Layer 2/3 boundary in oceanic crust. *Nature* **370**: 288-290. doi:10.1038/370288a0

Dewey JF, Kidd SF (1977) Geometry of plate accretion. *Geological Society of America Bulletin* **88**: 960-968

Dixon S, Rutherford MJ (1979) Plagiogranites as late-stage immiscible liquids in ophiolite and mid-oceanic ridge suites: an experimental study. *Earth and Planetary Science Letters* **45**: 45-60

Dixon-Spulber S, Rutherford MJ (1983) The origin of rhyolite and plagiogranite in oceanic crust: an experimental study. *Journal of Petrology* **24**: 1-25

Dubois M (1983) Plagiogranite and hydrothermalism: an approach from Cyprus and Oman ophiolitic complexes. *PhD dissertation, University of Nancy 1, France*

Dunn RA, Toomey DR, Solomon SC (2000) Three-dimensional seismic structure and physical properties of the crust and shallow mantle beneath the East Pacific Rise at 9°30'N. *Journal of Geophysical Research* **105-B10**: 23,537-23,555

Dunn RA, Toomey DR, Detrick RS, Wilcock WSD (2001) Continuous mantle melt supply beneath an overlapping spreading centre on the East Pacific Rise. *Science* **291**: 1,955-1,958

Dziony W, Koepke J, Holtz F (2008) Data report: Petrography and phase analyses in lavas and dikes from the hole 1256D (ODP Leg 206 and IODP Expedition 309, East Pacific Rise). *In Teagle DAH, Alt JC, Umino S, Miyashita S, Banerjee NR, Wilson DS, and the Expedition 309/312 Scientists. Proc. IODP, 309/312: Washington, DC (Integrated Ocean Drilling Program Management International, Inc.).* doi:10.2204/iodp.proc.309312.201.2008

Einaudi F, Pezard P, Cocheme JJ, Coulon C, Laverne C, Godard M (2000) Petrography, geochemistry and physical properties of continuous extrusive section from the Sarami Massif, Semail ophiolite. *Marine Geophysical Research* **21**: 387-407

Ernst WG, Liu J (1998) Experimental phase-equilibrium study of Al- and Ti-contents of calcic amphibole in MORB - A semiquantitative thermobarometer. *American Mineralogist* **83**: 952-969

Fahey AJ, Zinner EK, Crozaz G, Kornacki AS (1987) Microdistributions of Mg isotopes and REE abundances in a Type A calcium-aluminum-rich inclusion from Efremovka. *Geochimica et Cosmochimica Acta* **51**: 3,215-3,229. doi: 10.1016/0016-7037(87)90130-X

Feig ST, Koepke J, Snow JE (2006) Effect of water on tholeiitic basalt phase equilibria: An experimental study under oxidizing conditions. *Contributions to Mineralogy and Petrology* **152-5**: 611–638. doi:10.1007/s00410-006-0123-2

Fisher AT (2003) Geophysical constraints on hydrothermal circulation: Observations and models. *In Energy and Mass Transfer in Marine Hydrothermal Systems (eds. Halbach PE, Tunnicliffe V, Hein JR)*, Dahlem Univ. Press, Berlin **Vol. 3**: 29–52

Fisk MR, Johnson KTM, Alt JC (1995) Effect of assimilation of altered oceanic crust on magma chemistry: an experimental study. *In Erzinger J, Becker K, Dick HJB, Stokking LB, Proceedings of the Ocean Drilling Program, Scientific Results* **137-140**: 43-51

Flagler PA, Spray JG (1991) Generation of plagiogranite by amphibolite anatexis in oceanic shear zones. *Geology* **19**: 70-73

Floyd PA, Yaliniz MK, Goncuoglu MC (1998) Geochemistry and petrogenesis of intrusive and extrusive ophiolitic plagiogranites, central Anatolian Crystalline Complex, Turkey. *Lithos* **42**: 225-241

France L, Ildefonse B, Koepke J (2009a) Interactions between magma and hydrothermal system in Oman ophiolite and in IODP Hole 1256D: fossilization of a dynamic melt lens at fast spreading ridges. *Geochemistry Geophysics Geosystems* **10**: Q10O19. doi: 10.1029/2009GC002652 (Chapter III)

France L, Koepke J, Ildefonse B, Bech F (2009b) A new method to estimate the oxidation state of basaltic series from microprobe analyses. *Journal of Volcanology and Geothermal Research* Accepted for publication after moderate revision (Appendix A3)

France L, Koepke J, Ildefonse B, Cichy S, Deschamps F (2010a) Hydrous partial melting in the sheeted dike complex at fast spreading ridges: Experiments and nature. *Submitted to Contributions to Mineralogy and Petrology* (Chapter IV)

France L, Ildefonse B, Koepke J, MacLeod CJ, Godard M (2010b) Melting the hydrothermally altered sheeted dike complex: an experimental / trace element study. *In prep. for Geology* (Chapter IV)

Gaetani GA, Grove TL, Bryan WB (1993) The influence of water on the petrogenesis of subduction-related igeneous rocks. *Nature* **365**: 332-334

Garel E, Dauteuil O, Lagabrielle Y (2002) Deformation processes at fast to ultra-fast oceanic spreading axes_mechanical approach. *Tectonophysics* **346**: 223-246

Garmany J (1989) Accumulations of melt at the base of young oceanic crust. *Nature* **340**: 628-632

Gerbert-Gaillard L (2002) Caractérisation géochimique des péridotites de l'ophiolite d'Oman: processus magmatiques aux limites lithosphère-asthénosphère. *PhD memoir from Géosciences Montpellier, France* 241pp.

Gerlach DC, Leeman WP, Avé Lallemant HG (1981) Petrology and geochemistry of plagiogranite in the Canyon Mountain ophiolite, Oregon. *Contribution to Mineralogy and Petrology* **72**: 82-92

Ghazi AM, Hassanipak AA, Mahoney JJ, Duncan RA (2004) Geochemical characteristics, ^{40}Ar-^{39}Ar ages and original tectonic setting of the Band-e-Zeyarat-Dar Anar ophiolite, Makran accretionary prism, S.E. Iran. *Tectonophysics* **393**: 175-196

Ghiorso MS, Sack RO (1995) Chemical mass transfer in magmatic processes IV. A Revised and internally consistent thermodynamic model for the interpolation of liquid-solid equilibria in magmatic systems at elevated temperatures and pressures. *Contribution to Mineralogy and Petrology* **119**: 197–212

Gillis KM (2002) The root zone of an ancient hydrothermal system exposed in the Troodos ophiolite, Cyprus. *The Journal of Geology* **110**: 57-74. doi:10.1086/324205

Gillis KM (2008) The roof of an axial magma chamber: A hornfelsic heat exchanger. *Geology* **36-4**: 299-302. doi: 10.1130/G24590A.1

Gillis KM, Coogan LA (2002) Anatectic migmatites from the roof of an ocean ridge magma chamber. *Journal of Petrology* **43-11**: 2,075-2,095. doi:10.1093/petrology/43.11.2075

Gillis KM, Roberts MD (1999) Cracking at the magma-hydrothermal transition: Evidence from the Troodos ophiolite, Cyprus. *Earth and Planetary Science Letters* **169**: 227-244. doi:10.1016/S0012-821X(99)00087-4

Ginibre C, Wörner G, Kronz A (2002) Minor- and trace-element zoning in plagioclase: implications for magma chamber processes at Parinacota volcano, northern Chile. *Contributions to Mineralogy and Petrology* **143**: 300-315

Giordano D, Russell JK, Dingwell DB (2008) Viscosity of magmatic liquids: A model. *Earth and Planetary Science Letters* **271**: 123-134

Godard M, Dautria JM, Perrin M (2003) Geochemical variability of the Oman ophiolite lavas: relationship with spatial distribution and paleomagnetic directions. *Geochemistry Geophysics Geosystems* **4-6**: 1-15

Grove TL, Bryan WB (1983) Fractionation of pyroxene-phyric MORB at low pressure: an experimental study. *Contributions to Mineralogy and Petrology* **84**: 293-309

Gudmundsson A (1990) Emplacement of dikes, sills and crustal magma chambers at divergent plate boundaries. *Tectonophysics* **176**: 257-275

Haase KM, Stroncik NA, Hékinian R, Stoffers P (2005) Nb-depleted andesites from the Pacific-Antarctic Rise as analogs for early continental crust. *Geology* **33-12**: 921-924. doi: 10.1130/G21899.1

Hacker BR (1990) Amphibolite-facies to granulite-facies reactions in experimentally deformed, unpowdered amphibolite. *American Mineralogist* **75**: 1,349-1,361

Hattori K, Sato H (1996) Magma evolution recorded in plagioclase zoning in 1991 Pinatubo eruption products. *American Mineralogist* **81**: 982-994

Helz RT (1973) Phase relations of basalt in their melting ranges at PH_2O=5 kb as a function of oxygen fugacity. *Journal of Petrology* **14**: 249-302

Henstock TJ, Woods AW, White RS (1993) The accretion of oceanic crust by episodic sill intrusion. *Journal of Geophysical Research* **98-B3**: 4,143-4,161

Holland T, Blundy J. (1994) Non-ideal interactions in calcic amphiboles and their bearing on amphibole-plagioclase thermometry. *Contributions to Mineralogy and Petrology* **116**: 433-447

Holloway JR, Burnham CW (1972) Melting relations of basalt with equilibrium water pressure less than total pressure. *Journal of Petrology* **13**: 1-29

Hooft EEE, Detrick RS, Kent GM (1997) Seismic structure and indicators of magma budget along the southern East Pacific Rise. *Journal of Geophysical Research* **102-B12**: 27,319-27,340. doi:10.1029/97JB02349

Irvine TN, Baragar WRA (1971) A guide to the chemical classification of the common volcanic rocks. *Canadian Journal of Earth Sciences* **8**: 532-548

Johannes W, Koepke J (2001) Uncomplete reaction of plagioclase in experimental dehydration melting of amphibolite. *Australian Journal of Earth Sciences* **48**: 581-590

Juster TC, Grove TL, Perfit MR (1989) Experimental Constraints on the Generation of FeTi Basalts, Andesites, and Rhyodacites at the Galapagos Spreading Center, 85W and 95W. *Journal of Geophysical Research* **94-B7**: 9,251-9,274

Juteau T, Beurrier M, Dahl R, Nehlig P (1988) Segmentation at a fossil spreading center: The plutonic sequence of the Wadi Haymiliyah area (Haylayn block, Sumail nappe, Oman). *Tectonophysics* **151**: 167-197. doi: 10.1016/0040- 1951(88)90245-4

Juteau T, Bideau D, Dauteuil O, Manac'h G, Naidoo DD, Nehlig P, Ondreas H, Tivey MA, Whipple KX, Delaney JR (1995) A Submersible Study in the Western Blanco Fracture Zone, N.E. Pacific: Structure and Evolution during the Last 1.6 Ma. *Marine Geophysical Researches* **17**: 399-430

Kawamoto T (1996) Experimental constraints on differentiation and H2O abundance of calc-alkaline magmas. *Earth and Planetary Science Letters* **144**: 577-589

Kelemen PB, Shimizu N, Salters VJM (1995) Extraction of midocean-ridge basalt from the upwelling mantle by focused flow of melt in dunite channels. *Nature* **375**: 747-753. doi:10.1038/375747a0

Kelemen P, Koga K, Shimizu N (1997) Geochemistry of gabbro sills in the crust-mantle transition zone of the Oman ophiolite: implications for the origin of the oceanic lower crust. *Earth and Planetary Science Letters* **146**: 475-488

Kelley DS, Baross JA, Delaney JR (2002) Volcanoes, fluids and life at mid-ocean ridge spreading centers. *Annual Reviews in Earth and Planetary Sciences* **30**: 385-491.

Kent GM, Harding AJ, and Orcutt JA (1990) Evidence for a smaller magma chamber beneath the East Pacific Rise at 9°30'N. *Nature* **344**: 650-653

Kent GM, Singh SC, Harding AJ, Sinha MC, Orcutt JA, Barton PJ, White RS, Bazin S, Hobbs RW, Tong CH, Pye JW (2000) Evidence from three-dimensional seismic reflectivity images for enhanced melt supply beneath mid-ocean-ridge discontinuities. *Nature* **406-6,796**: 614-618

Kinzler RJ, Grove TL (1992) Primary Magmas of Mid-Ocean Ridge Basalts 1. Experiments and Methods. *Journal of Geophysical Research* **97-B5**: 6,885-6,906. doi: 10.1029/91JB02840

Klein EM, Langmuir CH (1987) Global correlations of ocean ridge basalt chemistry with axial depth and crustal thickness, *Journal of Geophysical Research* **92**, 8,089-8,115

Klein EM, Langmuir CH, Staudigel H (1991) Geochemistry of basalts from the Southeast Indian Ridge, 115°E-138°E. *Journal of Geophysical Research* **96**: 2,089-2,107

Klimm K, Holtz F, Johannes W, King PL (2003) Fractionation of metaluminous A-type granites: an experimental study of the Wangrah Suite, Lachlan Fold Belt, Australia. *Precambrian Research* **124**: 327-341

Koepke J, Feig ST, Snow J, Freise M (2004) Petrogenesis of oceanic plagiogranites by partial melting of gabbros: an experimental study. *Contributions to Mineralogy and Petrology* **146**: 414-432

Koepke J, Feig S, Snow J (2005a) Late stage magmatic evolution of oceanic gabbros as a result of hydrous partial melting: Evidence from the Ocean Drilling Program (ODP) Leg 153 drilling at the Mid-Atlantic Ridge. *Geochemistry Geophysics Geosystems* **6**:Q02001. doi:10.1029/2004GC000805

Koepke J, Feig ST, Snow J (2005b) Hydrous partial melting within the lower oceanic crust. *Terra Nova* **17**: 286-91. doi: 10.1111/j.1365-3121.2005.00613.x

Koepke J, Berndt J, Feig ST, Holtz F (2007) The formation of SiO_2-rich melts within the deep oceanic crust by hydrous partial melting of gabbros. *Contributions to Mineralogy and Petrology* **153**: 7-84. doi: 10.1007/s00410-006-0135-y

Koepke J, Christie DM, Dziony W, Holtz F, Lattard D, Maclennan J, Park S, Scheibner B, Yamasaki T, Yamazaki S (2008) Petrography of the Dike/Gabbro Transition at IODP Site 1256 (Equatorial Pacific): The evolution of the Granoblastic Dikes. *Geochemistry Geophysics Geosystems* **9-7**: Q07O09. doi: 10.1029/2008GC001939

Koepke J, Schoenborn S, Oelze M, Wittmann H, Feig ST, Hellebrand E, Boudier F, Schoenberg R (2009) Petrogenesis of crustal wehrlites in the Oman ophiolite: Experiments and natural rocks. *Geochemistry Geophysics Geosystems* **10-10**: Q10002. doi: 10.1029/2009GC002488

Koepke J, Dziony W, France L, Gabbros from IODP Site 1256 (Equatorial Pacific): Insight into axial magma chamber processes at fast-spreading ocean ridges. *Submitted to Geochemistry Geophysics Geosystems* (Appendix A4)

Koga KT, Kelemen PB, Shimizu N (2001) Petrogenesis of the crust-mantle transition zone and the origin of lower crustal wehrlite in the Oman ophiolite. *Geochemistry Geophysics Geosystems* **vol. 2**: 2000GC000132

Kohut EJ, Nielsen RL (2003) Low-pressure phase equilibria of anhydrous anorthite-bearing mafic magmas. *Geochemistry Geophysics Geosystems* **4**: 1,057. doi: 10.1029/2002GC000451

Korenaga J, Kelemen PB (1997) Origin of gabbro sills in the Moho transition zone of the Oman ophiolite: Implications for magma transport in the oceanic lower crust. *Journal of Geophysical Research* **102-B12**: 27,729-27,749

Kress VC, Carmichael ISE (1991) The compressibility of silicate liquids containing Fe_20_3 and the effect of composition, temperature, oxygen fugacity and pressure on their redox states. *Contributions to Mineralogy and Petrology* **108**: 82-92

Kuritani T (1998) Boundary layer crystallization in a basaltic magma chamber: evidence from Rishiri volcano, northern Japan. *Journal of Petrology* **39**: 1,619-1,640

Kvassnes AJS, Strand AH, Moen-Eikeland H, Pedersen RB (2004) The Lyngen Gabbro: the lower crust of an Ordovician Incipient Arc. *Contributions to Mineralogy and Petrology* **148**: 358-379

Lagabrielle Y, Cormier MH (1999) Formation of large summit troughs along the East Pacific Rise as collapse calderas: An evolutionary model. *Journal of Geophysical Research* **104-B6**: 12,971-12,988. doi:10.1029/1999JB900015

Lagabrielle Y, Garel E, Dauteuil O, Cormier MH (2001) Extensional faulting and caldera collapse in the axial region of fast spreading ridges: Analog modeling. *Journal of Geophysical Research* **106-B2**: 2,005-2,015

Lambart S, Laporte D, Schiano P (2009) An experimental study of focused magma transport and basalt-peridotite interactions beneath mid-ocean ridges: implications for the generation of primitive MORB compositions. *Contributions to Mineralogy and Petrology* **157**: 429-451

Lamoureux G, Ildefonse B, Mainprice D (1999) Modelling the seismic properties of fast-spreading ridge crustal Low-Velocity Zones: insights from Oman gabbro textures. *Tectonophysics* **312**: 283-301

Landi P, Métrich N, Bertagnini A, Rosi M (2004) Dynamics of magma mixing and degassing recorded in plagioclase at Stromboli (Aeolian Archipelago, Italy). *Contributions to Mineralogy and Petrology* **147**: 213-227

Langmuir CH, Bender JF, Batiza R (1986) Petrologic and tectonic segmentation of the East Pacific Rise, 5°30'-14°30'N. *Nature* **322**: 422-426

Liou JG (1971) Synthesis and stability relations of prehnite, $Ca_2Al_2Si_3O_{10}(OH)_2$. *American Mineralogist* **56**: 507-531

Lippard SJ, Shelton AW, Gass IG (1986) The ophiolite of Northern Oman. *In: Geological Society Memoir, 11. Blackwell, Oxford* 178pp.

Lowell RP, Rona PA, Von Herzen RP (1995) Seafloor hydrothermal systems. *Journal of Geophysical Research* **100**: 327-352

Luchitskaya MV, Morozov OL, Palandzhyan SA (2005) Plagiogranite magmatism in the Mesozoic island-arc structure of the Pekulney Ridge, Chukotka Peninsula, NE Russia. *Lithos* **79**: 251-269. doi: 10.1016/j.lithos.2004.04.056

Lundgaard KL, Tegner C (2004) Partitioning of ferric and ferrous iron between plagioclase and silicate melt. *Contributions to Mineralogy and Petrology* **147**: 470-483

Macdonald KC, Fox PJ, Perram LJ, Eisen MF, Haymon RM, Miller SP, Carbotte SM, Cormier MH, Shor AN, (1988) A new view of the mid-ocean ridge from the behaviour of ridge-axis discontinuities. *Nature* **335-6,187**: 217-225

MacLeod CJ, Yaouancq G (2000) A fossil melt lens in the Oman ophiolite: Implications for magma chamber processes at fast spreading ridges. *Earth and Planetary Science Letters* **176**: 357-373. doi: 10.1016/S0012-821X(00)00020-0

Malpas J (1979) Two contrasting trondhjemite associations from transported ophiolites in Western Newfoundland: Initial report. *In: Barker F (ed) Trondhjemites, dacites, and related rocks. Elsevier, Amsterdam* 465-487

Manning CE, MacLeod CJ (1996) Fracture-controlled metamorphism of Hess Deep gabbros, Site 894: Constraints on the roots of mid-ocean-ridge hydrothermal systems at fast-spreading centers. *In Mével C, Gillis KM, Allan JF, Meyer PS (eds.), Proceedings of the Ocean Drilling Program, Scientific Results* **147**: 189-212

Manning CE, Weston PE, Mahon KI (1996) Rapid high-temperature metamorphism of East Pacific Rise gabbros from Hess Deep. *Earth and Planetary Science Letters* **144**: 123-132

Ménot RP (1987) Magmatismes paléozoïques et structuration carbonifère du massif de Belledonne, Alpes françaises. Contraintes nouvelles pour les schémas d'évolution de la chaîne varisque ouest-européenne. *PhD dissertation, University Lyon 1, France*

Mével C (1987) Evolution of oceanic gabbros from DSDP Leg 82: influence of the fluid phase on metamorphic crystallizations. *Earth and Planetary Science Letters* **83**: 67-79

Mével C (1988) Metamorphism in ocean layer 3, Gorringe Bank, Eastern Atlantic. *Contributions to Mineralogy and Petrology* **100**: 496-509

Mével C (2003) Serpentinization of abyssal peridotites at mid-ocean ridges. *C.R. Geosciences* **335**: 825-852

Michael PJ, Chase RL (1987) The influence of primary magma composition, H2O and pressure on Mid-Ocean Ridge Basalt differentiation. *Contributions to Mineralogy and Petrology* **96**: 245-263

Michael PJ, Cornell WC (1998) Influence of spreading rate and magma supply on crystallization and assimilation beneath mid-ocean ridges: Evidence from chlorine and major element chemistry of mid-ocean ridge basalts. *Journal of Geophysical Research* **103**: 18,325-18,356

Michael PJ, Schilling JG (1989) Chlorine in mid-ocean ridge magmas: evidence for assimilation of seawater-influenced components. *Geochimica et Cosmochimica Acta* **53**: 3,131-3,143

Miyashiro A (1974) Volcanic rock series in island arcs and active continental margins. *American Journal of Science* **274**: 321-355

Miyashita S, Adachi Y, Umino S (2003) Along-axis magmatic system in the northern Oman ophiolite: Implications of compositional variation of the sheeted dike complex. *Geochemistry Geophysics Geosystems* **4-9**: 8,617. doi: 10.1029/ 2001GC000235

Morton JL, Sleep NH (1985) Seismic reflections from a Lau basin magma chamber. *In: Scholl DW, Vallier TL (Editors), Geology and offshore resources of pacific island arcs-Tonga region. Circum-Pacific Council for Energy and Mineral Resources, Earth Science Series, Houston, Texas* 441-453

Mutter JC, Carton H, Carbotte SM, Canales JP, Nedimovic MR, Newman KR, Marjanovic M, Xu M, Aghaei O, Stowe LC (2008) Searching for Changes in AMC Characteristics on the EPR Using Comparisons of Reflection Images Obtained in 1985 and 2008. *Eos Trans. AGU, Fall Meet. Suppl.* **89-53**: B21A-0319

Natland JH, Dick HJB (1996) Melt migration through high-level gabbroic cumulates of the East Pacific Rise at Hess Deep: The origin of magma lenses and the deep crustal structure of fast-spreading ridges. *In Mével C, Gillis KM, Allan JF, Meyer PS (Eds.), Proc. ODP, Sci. Results, College Station, TX (Ocean Drilling Program)* **147**: 21-58. doi: 10.2973/odp.proc.sr.147.002.1996

Nedimovic MR, Carbotte SM, Harding AJ, Detrick RS, Canales JP, Diebold JB, Kent GM, Tischer M, Babcock JM (2005) Frozen magma lenses below the oceanic crust. *Nature* **436**: 1,149-1,152

Nicolas A, Boudier F (1991) Rooting of the sheeted dike complex in the Oman ophiolite. *In Ophiolite Genesis and Evolution of the Oceanic Lithosphere, edited by Peters T, Nicolas A, Coleman RG, Kluwer Acad., Dordrecht, Netherlands* 39-54

Nicolas A, Boudier F (1995) Mapping oceanic ridge segments in the Oman ophiolite. *Journal of Geophysical Research* **100-B4**: 6,179-6,197

Nicolas A, Boudier F (2008) Large shear zones with no relative displacement. *Terra Nova* **20**: 200-205. doi: 10.1111/j.1365-3121.2008.00806.x

Nicolas A, Mainprice D (2005) Burst of high-temperature seawater injection throughout accreting oceanic crust: A case study in Oman ophiolite. *Terra Nova* **17**: 326-330. doi:10.1111/j.1365-3121.2005.00617.x

Nicolas A, Reuber I, Benn K (1988) A new magma chamber model based on structural studies in the Oman ophiolite. *Tectonophysics* **151**: 87-105. doi:10.1016/0040-1951(88)90242-9

Nicolas A, Boudier F, Ildefonse B, Ball E (2000) Accretion of Oman and United Arab Emirates ophiolite: Discussion of a new structural map. *Marine Geophysical Research* **21**: 147-179. doi: 10.1023/A:1026769727917

Nicolas A, Mainprice D, Boudier F (2003) High-temperature seawater circulation throughout crust of oceanic ridges: A model derived from the Oman ophiolites. *Journal of Geophysical Research* **108-B8**: 2,371. doi: 10.1029/2002JB002094

Nicolas A, Boudier F, Koepke J, France L, Ildefonse B, Mevel C (2008) Root zone of the sheeted dike complex in the Oman ophiolite. *Geochemistry Geophysics Geosystems* **9:Q05001**. doi:10.1029/2007GC001918

Nicolas A, Boudier F, France L (2009) Subsidence in magma chamber and the development of magmatic foliation in Oman ophiolite gabbros. *Earth and Planetary Science Letters* **284**: 76-87. doi: 10.1016/j.epsl.2009.04.012

Niu Y, Gilmore T, Mackie S, Greig A, Bach W (2002) Mineral chemistry, whole-rock compositions, and petrogenesis of Leg 176 gabbros: data and discussion. *In: Natland JH, Dick HJB, Miller DJ, Von Herzen RP (eds) Proc ODP, Sci Results, Ocean Drilling Program, College Station, TX,* **176**: 1-60, [Online] http://www-odp.tamu.edu/publications/176_SR/VOLUME/CHAPTERS/SR176_08.PDF [Cited 23-08-2003]

Pallister JS, Hopson CA (1981) Samail Ophiolite Plutonic Suite: Field relations, phase variation, cryptic variation and layering, and a model of a spreading ridge magma chamber. *Journal of Geophysical Research* **86-B4**: 2,593-2,644. doi:10.1029/ JB086iB04p02593

Pallister JS, Knight RJ (1981) Rare-Earth Element Geochemistry of the Samail Ophiolite near Ibra, Oman. *Journal of Geophysical Research* **86-B4**: 2,673-2,697

Panjasawatong Y, Danyushevsky LV, Crawford AJ, Harris KL (1995) An experimental study of the effects of melt composition on plagioclase-melt equilibria at 5 and 10 kbar: implications for the origin of high An plagioclase in arc and MORB magmas. *Contributions to Mineralogy and Petrology* **118**: 420-435

Patino Douce AE, Beard JS (1995) Dehydration-melting of biotite gneiss and quartz amphibolite from 3 to 15 kbar. *Journal of Petrology* **36**: 707-738

Pearce JA, Lippard SJ, Roberts S (1984) Characteristics and tectonic significance of supra-subduction zone ophiolites. *In Kokelaar BP, Howeels MF, eds. Marginal basin geology: volcanic and associated sedimentary and tectonic processes in modern and ancient marginal basins. Geol. Soc. Lond. Spec. Publ.* **16**: 77-94

Pearce NJG, Perkins WT, Westgate JA, Gorton MP, Jackson SE, Neal CR, Chenery SP (1997) A compilation of new and published major and trace element data for NIST SRM 610 and NIST SRM 612 glass reference materials. *Geostandard Newsletter* **21**: 115-144

Pedersen RB, Malpas J (1984) The origin of oceanic plagiogranites from the Karmoy ophiolite, Western Norway. *Contributions to Mineralogy and Petrology* **88**: 36-52

Philpotts AR (1982) Compositions of immiscible liquids in volcanic rocks. *Contributions to Mineralogy and Petrology* **80**: 201-218

Phipps Morgan J, Chen YJ (1993) The genesis of oceanic crust: Magma injection, hydrothermal circulation, and crustal flow. *Journal of Geophysical Research* **98**: 6,283-6,297

Pollock ME, Klein EM, Karson JA, Coleman DS (2009) Compositions of dikes and lavas from the Pito Deep Rift: Implications for crustal accretion at superfast spreading centers. *Journal of Geophysical Research* **114**: B03,207. doi: 10.1029/2007JB005436

Pouchou JL, Pichoir F (1991) Quantitative analysis of homogeneous or stratified microvolumes applying the model ‘‘PAP’’. *In: Heinrich KFJ, Newbury DE (eds) Electron probe quantification. Plenum Press, New York* 31-75

Prouteau G, Scaillet B, Pichavant M, Maury RC (1999) Fluid-present melting of ocean crust in subduction zones. *Geology* **27-12**: 1,111-1,114

Purdy GM, Kong LSL, Christeson GL, Salomon SC (1992) Relationship between spreading rate and the seismic structure of mid-ocean ridges. *Nature* **355**: 815-817. doi: 10.1038/355815a0

Quick JE, Denlinger RP (1993) Ductile deformation and the origin of layered gabbro in ophiolites. *Journal of Geophysical Research* **98**: 14,015-14,027

Raitt RW (1963) The crystal rocks. *In The Sea, edited by Hill MN, Wiley Interscience, New York* **3**: 85-102

Rannou E, Caroff M, Cordier C (2006) A geochemical approach to model periodically replenished magma chambers: Does oscillatory supply account for the magmatic evolution of EPR 17-19°S? *Geochimica et Cosmochimica Acta* **70**: 4,783-4,796. doi: 10.1016/j.gca.2006.07.007

Rao DR, Rai H, Kumar JS (2004) Origin of oceanic plagiogranite in the Nidar ophiolitic sequence of eastern Ladakh, India. *Current Science* **87-7**: 999-1,005

Rapp RP, Watson EB (1995) Dehydration melting of metabasalt at 8–32 kbar: implications for continental growth and crust-mantle recycling. *Journal of Petrology* **36**: 891-931

Rapp RP, Watson EB, Miller CF (1991) Partial melting of amphibolite/eclogite and the origin of Archean trondhjemites and tonalites. *Precambrian Research* **51**: 1-25

Reed WP (1992) Certificate of analysis, standard reference materials 610 611. *(National Institute of Standard and Technology)*

Ridley WI, Perfit MR, Smith MC, Fornari DJ (2006) Magmatic processes in developing oceanic crust revealed in a cumulate xenolith collected at the East Pacific Rise, 9°50'N. *Geochemistry Geophysics Geosystems* **7**: Q12O04. doi: 10.1029/2006GC001316

Rochette P, Jenatton L, Dupuy C, Boudier F, Reuber I (1991) Diabase dikes emplacement in the Oman ophiolite: A magnetic fabric study with reference to geochemistry. *In: Ophiolite Genesis and Evolution of the Oceanic Lithosphere, edited by Peters T, Nicolas A, Coleman RG, Kluwer Acad., Dordrecht, Netherlands* 39-54

Roeder PL, Emslie RF (1970) Olivine–liquid equilibrium. *Contributions to Mineralogy and Petrology* **29**: 275-289

Rollinson H (2009) New models for the genesis of plagiogranites in the Oman Ophiolite. *Lithos* **112**: 603-614. doi: 10.1016/j.lithos.2009.06.006

Rothery DA (1983) The base of a sheeted dyke complex, Oman ophiolite: Implications for magma chambers at oceanic spreading axes. *J. Geol. Soc. London* **140**: 287-296. doi:10.1144/gsjgs.140.2.0287

Rubin KH, Sinton JM (2007) Inferences on mid-ocean ridge thermal and magmatic structure from MORB compositions. *Earth and Planetary Science Letters* **260**: 257-276. doi: 10.1016/j.epsl.2007.05.035

Rubin KH, Van des Zander I, Smith MC, Bergmanis EC (2005) Minimum speed limit for ocean ridge magmatism from ^{210}Pb-^{226}Ra-^{230}Th disequilibria. *Nature* **437**. doi: 10.1038/nature03993

Rushmer T (1991) Partial melting of two amphibolites: contrasting experimental results under fluid-absent conditions. *Contributions to Mineralogy and Petrology* **107**: 41-59

Rushmer T (1993) Experimental high-pressure granulites: some applications to natural mafic xenolith suites and Archean granulite terranes. *Geology* **21**: 411-414

Sato H (1978) Segregation vesicles and immiscible liquid droplets in ocean-floor basalt of Hole 396B, IPOD/DSDP Leg 46. *In: Dimitriev L, Heirtzler J, et al (eds) Initial reports of the Deep Sea Drilling Project, U.S. Government Printing Office, Washington* **46**: 283-291

Sauerzapf U, Lattard D, Burchard M, Engelmann R (2008) The titanomagnetite-ilmenite equilibrium: New experimental data and thermo-oxybarometric application to the crystallization of basic to intermediate rocks. *Journal of Petrology* **49-6**: 1,161-1,185. doi:10.1093/petrology/egn021

Scaillet B, Pichavant M, Roux J, Humbert G, Lefèvre A (1992) Improvements of the Shaw membrane technique for measurement and control of fH_2 at high temperatures and pressures. *American Mineralogist* **77**: 647-655

Selbekk RS, Furnes H, Pedersen RB, Skjerlie KP (1998) Contrasting tonalite genesis in the Lyngen magmatic complex, north Norwegian Caledonides. *Lithos* **42**: 243-268

Sen C, Dunn T (1994) Dehydration melting of a basaltic composition amphibolite at 1.5 and 2.0 GPa: implications for the origin of adakites. *Contributions to Mineralogy and Petrology* **117**: 394-409

Shastry A, Srivastava RK, Chandra R, Jenner GA (2001) Fe-Ti enriched mafic rocks from South Andaman ophioite suite: implications of late stage liquid immiscibility. *Current Science* **80**: 453-454

Shervais JW (1982) Ti-V plots and the petrogenesis of modern and ophiolitic lavas. *Earth and Planetary Science Letters* **59**: 101-118

Shimizu N, Hart SR (1982) Application of the ion microprobe to geochemistry and cosmochemistry. *Annual Review of Earth and Planetary Sciences* **10**: 483-526

Shor GG, Menard HW, Raitt RW (1970) Structure of the Pacific Basin. *In The Sea, edited by Maxwell AE, Wiley Interscience, New York* **4**: 3-27

Singh SC, Kent GM, Collier JS, Harding AJ, Orcutt JA (1998) Melt to mush variations in crustal magma properties along the ridge crest at the southern East Pacific Rise. *Nature* **394-6696**: 874-878

Singh SC, Harding AJ, Kent GM, Sinha MC, Combier V, Bazin S, Tong CH, Barton PJ, Hobbs RW, White RS, Orcutt JA (2006) Seismic reflection images of the Moho underlying melt sills at the East Pacific Rise. *Nature* **442**: 287-290

Sinton JM, Detrick RS (1992) Mid-ocean ridge magma chambers. *Journal of Geophysical Research* **97**: 197-216. doi:10.1029/91JB02508

Sinton JM, Smaglik SM, Mahoney JJ, Macdonald KC (1991) Magmatic processes at superfast spreading oceanic ridges: Glass compositional variations along the East Pacific Rise, 13°-23°S. *Journal of Geophysical Research* **96**: 6,133-6,155

Sinton JM, Bergmanis E, Rubin KH, Batiza R, Gregg TKP, Grönvold K, Macdonald KC, White SM (2002) Volcanic eruptions on mid-ocean ridges: New evidence from the superfast spreading East Pacific Rise, 17°-19°S. *Journal of Geophysical Research* **107-B6**: 2,115. doi: 10.1029/2000JB000090

Smewing JD (1981) Mixing Characteristics and Compositional Differences in Mantle-Derived Melts Beneath Spreading Axes: Evidence From Cyclically Layered Rocks in the Ophiolite of North Oman. *Journal of Geophysical Research* **86-B4**: 2,645-2,659

Snyder D, Carmichael ISE, Wiebe RA (1993) Experimental study of liquid evolution in an Fe-rich, layered mafic intrusion: constraints of Fe-Ti oxide precipitation on the T-fO_2 and T-ρ paths of tholeiitic magmas. *Contributions to Mineralogy and Petrology* **113**: 73-86. doi: 10.1007/BF00320832

Soule SA, Fornari DJ, Perfit MR, Ridley WI, Reed MH, Cann JR (2006) Incorporation of seawater into mid-ocean ridge lava flows during emplacement. *Earth and Planetary Science Letters* **252**: 289-307

Soule SA, Fornari DJ, Perfit MR, Rubin KH (2007) New insights into mid-ocean ridge volcanic processes from the 2005–2006 eruption of the East Pacific Rise, 9°46'N-9°56'N. *Geology* **35-12**: 1,079-1,082

Spray JG, Dunning GR (1991) A U/Pb age for the Shetland Islands oceanic fragment, Scottish Caledonides: evidence from anatectic plagiogranites in 'layer 3' shear zones. Geological Magazine **128**: 667-671

Stakes DS, Taylor HP (2003) Magmatic, Metamorphic and Tectonic Processes in Ophiolite Genesis: Oxygen isotope and chemical studies on the origin of large plagiogranite bodies in northern Oman, and their relationship to the overlying massive sulphide deposits. *Geological Society, London, Special Publications* **218**: 315-351. doi: 10.1144/GSL.SP.2003.218.01.17

Steinbeck J (1961) High Drama to Bold Thrust through Ocean Floor. Earth second layer is tapped in prelude to Mohole. *Life* **April**: 111-122

Stolper E (1980) A phase diagram for mid-ocean ridge basalts: preliminary results and implications for petrogenesis. *Contributions to Mineralogy and Petrology* **74**, 13-27

Teagle DAH, Alt JC, Umino S, Miyashita S, Banerjee NR, Wilson DS, and the Expedition 309/312 Scientists (2006) Superfast Spreading Rate Crust 2 and 3. *Proceedings of the Integrated Ocean Drilling Program* **309/312.** doi:10.2204/iodp. proc.309312.2006

Thy P, Lesher CE, Mayfield JD (1999) Low-pressure melting studies of basalt and basaltic andesite from the southeast Greenland continental margin and the origin of dacites at site 917. *In: Larsen HC, Duncan RA, Allan JF, Brooks K (eds) Proceedings of the ODP, Science Research, Ocean Drilling Program, College Station* **163**: 95-112

Tolstoy M, Waldhauser F, Bohnenstiehl DR, Weekly RT, Kim WY (2008) Seismic identification of along-axis hydrothermal flow on the East Pacific Rise. *Nature* **451**: 191-184. doi: 10.1038/nature06424

Toomey DR, Purdy GM, Solomon SC (1989) Three-dimensional structure of the East Pacific Rise at 9°30'N. *Eos Trans. AGU* **70**: 1,317

Toplis MJ (2005) The thermodynamics of iron and magnesium partitioning between olivine and liquid: criteria for assessing and predicting equilibrium in natural and experimental systems. *Contributions to Mineralogy and Petrology* **149**: 22-39

Toplis MJ, Carrol MR (1995) An Experimental Study of the Influence of Oxygen Fugacity on Fe-Ti Oxide Stability, Phase Relations, and Mineral-Melt Equilibria in Ferro-Basaltic Systems. *Journal of Petrology* **36-5**: 1,137-1,170

Toplis MJ, Libourel G, Carroll MR (1994) The role of phosphorus in crystallisation processes of basalt: An experimental study. *Geochimica et Cosmochimica Acta* **58-2**: 797-810. doi: 10.1016/0016-7037(94)90506-1

Twinning K (1996) Origin of plagiogranites in the Troodos ophiolite, Cyprus. *The Ninth Keck Research Symposium in Geology* 245-248

Ulrich T, Borsien GR (1996) Fedoz metagabbros and Forno metabasalt (Val Malenco, N Italy): comparative petrographic and geochemical investigations. *Schweiz Miner Petrogr Mitt* **76**: 521-535

Umino S, Miyashita S, Hotta F, Adachi Y (2003) Along-strike variation of the sheeted dike complex in the Oman Ophiolite: Insights into subaxial ridge segment structures and the magma plumbing system. *Geochemistry Geophysics Geosystems* **4-9**: 8,618. doi: 10.1029/2001GC000233

Waldhauser F, Ellsworth WL (2000) A double-difference earthquake location algorithm: Method and application to the Northern Hayward Fault, California. *Bull.Seism. Soc. Am.* **90**: 1,353-1,368

Warren CJ, Parrish RR, Waters DJ, Searle MP (2005) Dating the geologic history of Oman's Semail Ophiolite: insights from U–Pb geochronology. *Contributions to Mineralogy and Petrology* **150**: 403-422

Warren CJ, Searle MP, Parrish RR, Waters DJ (2007) Reply to Comment by F. Boudier and A. Nicolas on ''Dating the geologic history of Oman's Semail Ophiolite: insights from U–Pb geochronology'' by C.J. Warren, R.R. Parrish, M.P. Searle and D.J. Waters. *Contributions to Mineralogy and Petrology* **154**: 115-118

Wilke M, Behrens H (1999) The dependence of the partitioning of iron and europium between plagioclase and hydrous tonalitic melt on oxygen fugacity. *Contributions to Mineralogy and Petrology* **137**: 102-114

Wilson DS, Teagle DAH, Alt JC, Banerjee NR, Umino S, Miyashita S, Acton GD, Anma R, Barr SR, Belghoul A, Carlut J, Christie DM, Coggon RM, Cooper KM, Cordier C, Crispini L, Durand SR, Einaudi F, Galli L, Gao Y, Geldmacher J, Gilbert LA, Hayman NW, Herrero-Bervera E, Hirano N, Holter S, Ingle S, Jiang S, Kalberkamp U, Kerneklian M, Koepke J, Laverne C, Vasquez HLL, Maclennan J, Morgan S, Neo N, Nichols HJ, Park SH, Reichow MK, Sakuyama T, Sano T, Sandwell R, Scheibner B, Smith-Duque CE, Swift SA, Tartarotti P, Tikku AA, Tominaga M, Veloso EA, Yamasaki T, Yamazaki S, Ziegler C (2006) Drilling to gabbro in intact ocean crust. *Science* **312**: 1,016-1,020. doi: 10.1126/science.1126090

Wolf MB, Wyllie PJ (1994) Dehydration-melting of amphibolite at 10 kbar: the effects of temperature and time. *Contributions to Mineralogy and Petrology* **115**: 369-383

Yamasaki T, Maeda J, Mizuta T (2006) Geochemical evidence in clinopyroxenes from gabbroic sequence for two distinct magmatisms in the Oman ophiolite. *Earth and Planetary Science Letters* **251**: 52-65. doi:10.1016/j.epsl.2006.08.027

Interactions entre processus magmatiques et hydrothermaux aux dorsales océaniques à expansion rapide: implications pour la dynamique de la lentille magmatique axiale

Résumé : Ce travail de thèse est basé sur des observations de terrain, sur une étude pétrographique et géochimique des roches formées à la base du complexe filonien dans l'ophiolite d'Oman et au niveau du Site IODP 1256, ainsi que sur une étude expérimentale. De nouvelles contraintes sont apportées sur les processus se produisant à la transition magma / système hydrothermal dans la croute océanique formée au niveau des dorsales à expansion rapide.

L'intrusion de gabbros isotropes dans la base du complexe filonien a provoqué son réchauffement et sa recrystallization en « dikes granoblastiques » jusqu'à des températures de 1030°C. Des xénolites de microgabbro à orthopyroxene dérivées des dikes granoblastiques sont souvent observées dans le niveau de gabbros isotropes épais de 100 mètres environ qui est présent à la base du complexe filonien. Ces différentes caractéristiques sont à relier à des migrations verticales vers le haut du sommet de la lentille magmatique supérieure qui est observée aux dorsales rapides. Les nombreuses évidences d'assimilation (xénolites et patchs granoblastiques) dans le niveau des gabbros isotropes appuient l'hypothèse que ce niveau représente la fossilisation de la lentille magmatique supérieure. L'étude expérimentale a consisté à tester l'effet de la fusion partielle du complexe filonien préalablement hydrothermalisé. Les résultats montrent que la fusion commence à 850°C, confirment l'origine résiduelle des dikes granoblastiques et des xénolites associées, et attestent de l'origine anatectique des plagiogranites océaniques qui sont couramment observés à proximité de la base du complexe filonien. La composition en éléments majeurs et traces du liquide anatectique a été déterminée. Ce liquide représente le principal contaminant pour les MORBs primitifs émis au niveau des dorsales rapides.

La lentille magmatique supérieure présente au niveau des dorsales médio-océaniques à expansion rapide est ici décrite comme un système dynamique qui peut migrer verticalement, et qui est fossilisée lorsqu'elle se déplace hors axe.

Mots-clés : Coute océanique, lentille magmatique supérieure, base du complexe filonien, ophiolite d'Oman, Integrated Ocean Drilling Program, Puits IODP 1256D, fusion partielle hydratée, dikes granoblastiques, assimilation, contamination des MORBs, pétrologie expérimentale, gabbros isotropes, plagiogranite océanique

Magmatic / Hydrothermal Interactions at Fast Spreading Mid-Ocean Ridges: Implications on the Dynamics of the Axial Melt Lens

Abstract: This PhD work is based on field, petrographic, and geochemical observations of rocks originated at the base of the sheeted dike complex, in the Oman ophiolite and at IODP Site 1256, coupled with an experimental study. It provides new constrains on processes that occur at the magma / hydrothermal system transition in oceanic crust formed at fast spreading ridges.

The base of the sheeted dike complex is truncated by intrusive isotropic gabbros, and therefore reheated and recrystallized to the "granoblastic dikes" under temperatures up to 1030°C. Xenoliths of granoblastic microgabbros and microgabbronorites derived from the granoblastic dikes are commonly observed in the about 100 meters thick horizon of isotropic gabbro that underlies the sheeted dike complex. These features can be explained by upward migrations of the melt lens that is present at fast spreading centers. The occurrence of several assimilation features (xenoliths and granoblastic patches) in the isotropic gabbro horizon supports the hypothesis that this horizon represents the fossilization of the upper melt lens. The experimental study was designed to simulate experimentally the effect of partial melting of hydrothermally altered sheeted dikes. The results show that melting starts at 850°C, confirm the residual origin of granoblastic dikes and xenoliths, and attest to the anatectic origin of the oceanic plagiogranites that are commonly present close to the base of the sheeted dike complex. The major and trace element composition of the experimental anatectic melt that represents the main contaminant for primitive MORBs at fast spreading ridges has been determined.

The upper axial melt lens at fast spreading mid-ocean ridges is herein described as a dynamic system that can migrate vertically, and which fossilizes when moving off-axis.

Keywords: Oceanic crust, upper melt lens, base of the sheeted dike complex, Oman ophiolite, Integrated Ocean Drilling Program, IODP Hole 1256D, hydrous partial melting, granoblastic dikes, assimilation, MORBs contamination, experimental petrology, isotropic gabbros, oceanic plagiogranite

Discipline : Structure et évolution de la Terre et des autres planètes
Laboratoire : Géosciences Montpellier, UMR 5243, université Montpellier 2, CC 60, 34095 Montpellier Cedex 5, France

ANNEX

Annex A.

Other papers linked to the PhD work

Annex A1.

“Subsidence in magma chamber and the development of magmatic foliation in Oman ophiolite gabbros”

Earth and Planetary Science Letters 284 (2009) 76–87

Contents lists available at ScienceDirect

Earth and Planetary Science Letters

journal homepage: www.elsevier.com/locate/epsl

Subsidence in magma chamber and the development of magmatic foliation in Oman ophiolite gabbros

Adolphe Nicolas, Françoise Boudier *, Lydéric France

Géosciences, Université de Montpellier 2-CNRS, 34095 Montpellier, France

ARTICLE INFO

Article history:
Received 12 December 2008
Received in revised form 8 April 2009
Accepted 12 April 2009
Available online 22 May 2009
Editor: R.D. van der Hilst

Keywords:
Oman ophiolite
fast spreading ridges
magma chamber
gabbro subsidence

ABSTRACT

In the Oman ophiolite, the horizon where the melt lens pinched during drifting away from the ocean ridge axis has been identified. Starting in the Root Zone of the Sheeted Dike Complex (RZSDC) located above this horizon, 18 sections down to the upper gabbros unit have been mapped in great detail, in selected areas of the southern massifs of this ophiolite. They are complemented by 133 sites, located throughout the entire ophiolite, where the transition from the RZSDC to the uppermost foliated gabbros is well exposed. Altogether, half the sites and 11 cross sections display, within a few tens of meters beneath the RZSDC, a magmatic foliation which is parallel to the overlying sheeted dikes. In the other sites and cross sections, the gabbro foliation is either flat-lying or steep but not parallel to the sheeted dikes. Compared to the RZSDC isotropic ophitic gabbros where clinopyroxene is interstitial between plagioclase laths, in the topmost steeply foliated gabbros, clinopyroxene is idiomorphic, becoming rapidly granular and tabular down section by recrystallization and peripheral alteration to hornblende. Moving down from these uppermost gabbros and over one hundred meters, the steep foliation becomes stronger and the poorly recovered top gabbros grade into the recrystallized, granular gabbros of the gabbro unit. These repeated observations indicate to ascribe these gabbros to subsidence of a compacting mush from the floor of the melt lens into the underlying, main magma chamber. The topmost gabbros beneath RZSDC, which were expelled from the melt lens by drifting very soon after settling on the melt lens floor, display in plagioclase a spectacular zoning pointing to a fast cooling. Moving downwards, stronger foliation, increased compaction and recovery–recrystallization are explained by the time spent by the subsiding mush inside the magma chamber increasing by one order of magnitude (~50 to 500 yr) over this vertical distance. This field-based study brings compelling field evidence supporting the former models of subsidence which were based on the assumption that the mush that settled onto the floor of the melt lens is sucked downwards during drifting of the crust away from the ridge axis.

1. Introduction

The Oman ophiolite is regarded as being issued from a fast, possibly super fast, spreading ridge (review in Nicolas et al., 2000). By reference to such oceanic ridges, it is legitimate to look in this ophiolite for the traces of a melt lens at the top of an axial magma chamber (Morton and Sleep, 1985; Detrick et al., 1987; Kent et al., 1993; Collier and Singh, 1997). Melt lenses are located between 1 and 3 km below seafloor. They extend ~1 km on each side of the ridge (Kent et al., 1993) and they are only about 50 m thick (Collier and Singh, 1997), though a recent 3D study imaging both top and bottom of the melt lens shows that it could be 200–300 m thick (Singh and Arnulf, personal communication). The roof of a melt lens is the Root Zone of the Sheeted Dike Complex (RZSDC). The RZSDC has been recently revisited in Oman in order to achieve an updated comparison with the section crossed by the IODP hole 1256D (Nicolas et al., 2008). This study made it possible to identify where, in a vertical cross section through the gabbro unit, was located the level of the active melt lens at the oceanic ridge axis of origin. Structural studies conducted around this critical level at a very high resolution now give some hints on the transition from RZSDC gabbros to gabbros generated on the floor of this lens and subsiding from there to generate the main gabbro unit (Quick and Denlinger, 1993; Henstock et al., 1993; Phipps Morgan and Chen, 1993; Chenevez et al., 1998). In contrast with the melt lens which is filled by a high melt/crystal basaltic magma, thus with a low viscosity, the accreting gabbro unit below, down to the Moho, is a low melt/crystal mush fraction near that of a solid (Nicolas and Ildefonse, 1996; Lamoureux et al., 1999).

We wish here to study the mechanism of gabbro subsidence from the floor of the melt lens down into the main gabbro unit and, in particular, to understand the sharp transition between the RZSD gabbros, to the uppermost part of the gabbro unit. In our first model of a magma chamber (Nicolas et al., 1988), it was recognized that a magmatic mush had been flowing down parallel to the steep magma chamber walls but, even after the concept of subsidence had became explicit, 5 to 10 yr later, we never investigated further the subsidence mechanism. Here we address how the magmatic foliation in gabbros is

* Corresponding author.
E-mail address: francoise.boudier@gm.univ-montp2.fr (F. Boudier).

0012-821X/$ – see front matter © 2009 Elsevier B.V. All rights reserved.
doi:10.1016/j.epsl.2009.04.012

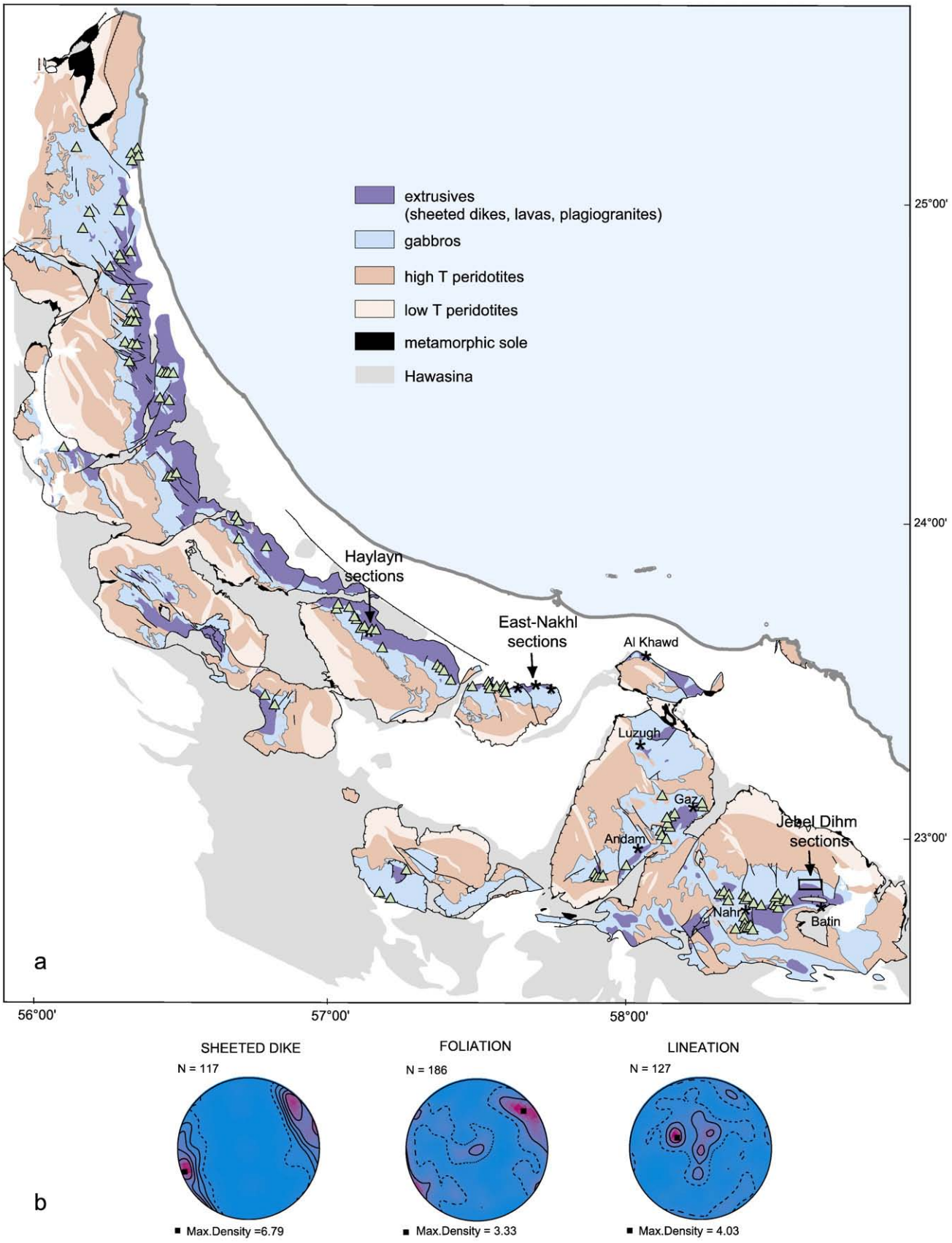

Fig. 1. (a) Location in the Oman ophiolite of the stations where uppermost gabbros display a good contact with the RZSDC (triangles), and of the new detailed cross sections (stars) (see Table 1). In a box, the small mapped area of Jabal Dihm (Fig. 3). (b) Field orientations of the magmatic foliations and lineations with reference to the averaged local sheeted dike complex attitude, for all the indexed sites in (a). Lower hemisphere of projection, geographical reference system, contours at 1, 2, *x* times uniform distribution; *N*, number of measurements.

generated and how, over a surprisingly short distance, it rotates to steep attitudes.

2. Floor of the melt lens

In Oman, it is only possible to observe the end-product of the RZSDC, once the system has drifted away from the melt lens. At ~1 km away from the ridge axis the melt lens pinches out (according to marine seismic images) and its roof comes in contact with its floor. Locating, in a vertical section through the ophiolite, the horizon of this vanished lens has been a major result of our study of the RZSDC (Nicolas et al., 2008). We maintain here that the lower RZSDC gabbros are amphibole-bearing isotropic gabbros with a comparatively even and fine-grained (~1 mm) ophitic texture. They locally grade downward into dry, isotropic and coarser-grained ophitic gabbros. This horizon, a few meters thick, is regarded as the very roof of the melt lens, representing the thermal boundary layer between the magmatic system of the melt lens, and the high temperature (HT) hydrothermal system cleansing the RZSDC. Where the melt lens closes, this level should come in contact with the gabbros issued from the floor of this lens. In sharp contrast with the RZSDC gabbros, gabbros from the floor have a magmatic foliation, also displaying distinct textures as shown below. There is another piece of evidence allowing us to locate this critical level, which is the occurrence of anorthosite lenses which are under study. They are commonly observed within the foliated gabbros beneath the melt lens level, but never above in the RZSDC.

3. Systematic measurements

3.1. Local measurements from the entire ophiolite belt

During the course of the systematic structural mapping of the Oman ophiolite which was based on 6000 field stations (Nicolas et al., 2000), the transition from RZSDC to uppermost gabbros had been commonly observed and 133 stations have been selected here. The total number of sites studied is 183 because the cross sections which are specifically considered below contribute 50 new individual sites (location in Fig. 1).

The stereographic projection of Fig. 1b shows a dominant orientation of the foliations close to that of the sheeted dikes with, however, a minor fraction of foliations which are horizontal. Lineations are steeply plunging to the NW. Few lineations are horizontal, mostly parallel to the sheeted dikes trend. Histograms of Fig. 2 provide a more detailed analysis of these structural relations. They present the angular relations measured in each site between foliation–lineation in gabbros and the attitude of the local sheeted dikes.

As histograms cannot convey the complete structural information which is derived from a given site, three orientation cases are defined, referring to the sheeted dikes attitude (Fig. 2c). Assuming that the sheeted dikes attitude defines the vertical ridge plane, the cases are the three orthogonal orientations in the ridge system: 1) vertical plane parallel to ridge axis, 2) horizontal plane and 3) vertical plane normal to ridge axis (Fig. 2c). Their respective orientations can be approximately retrieved on the histograms (Fig. 2a and b). In the first case, the foliation plane is within 30° in azimuth and no more than 35° in dip to the sheeted dikes. The scattering is explained by many uncertainties, including the difficulty to measure the nascent foliation in the field. This case corresponds to 47% of the 183 sites studied. The lineation plunges on average 50° (Figs. 1b and 2c). In the two next cases, foliations are at variable azimuths to the sheeted dikes. The case of flat-lying foliations typically has dips relative to the sheeted dikes larger than 45°. It is present in 22% of the sites, and its average lineation trend relative to that of the sheeted dikes is 25° (Fig. 2b). The third case, with steep foliations at high angles to the sheeted dikes, is present in 31% of the sites. Lineations have an average plunge of 50° (Fig. 2c).

3.2. New cross sections

The present and the preceding study on the RZSDC are based on very detailed field mapping at the scale of a few tens of meters, drastically contrasting with previous, low resolution mapping at scales from the kilometer to a few hundreds meters (Nicolas et al., 2000). However, thanks to this general knowledge of the entire ophiolite belt, it has been possible to select the proper areas for these new studies. As explained in the high resolution study on RZSDC, areas of detailed mapping have been selected inside massifs which are clear from local tectonic and magmatic complexities related to ridge segmentation. This is why the field work was conducted in the SE massifs of the Oman ophiolite (Fig. 1). The field data are based on 18 short cross sections. They are located mainly in the southern Wadi Tayin and Semail massifs, with a few sections in the Nakhl and Haylayn massifs, all sections being located away from segmented areas (stars in Fig. 1).

The cross sections cover several hundred meters starting from the RZSDC down to the upper gabbros of the main gabbro unit. In 11 sections out of the 18, foliations and lineations immediately below the melt lens horizon are steep. These sections which are described here (Table 1) contrast with the 7 other sections, where foliations in the uppermost foliated gabbros are parallel or at a small angle to the floor of the former melt lens and to RZSDC horizon, before steepening down section. Because they unveil the floor of the melt lens and its magmatic settling, these 7 sections deserve a further study. However, foliation and lineation attitudes from all the 18 sections, referred to the local attitude of the sheeted dike complex, are incorporated in the stereonets of Fig. 1.

Half of the 11 cross sections described here are located in a Jabal Dihm area of Wadi Tayin massif (box in Fig. 1a and map in Fig. 3a). They are the main reference, but cross sections in other areas totally support the results obtained in Jabal Dihm. Cross sections in Jabal Dihm start from the base of the sheeted dikes and extend, over a average distance of 1500 m in a NNW to N direction to within the homogeneous, granular upper gabbros of the gabbro unit (Fig. 3a). The distance between structural measurements and rock specimens sampling in view of lab studies varies between ~20 m and ~200 m. The main features of these cross sections are presented in Table 1 and only two typical cross sections from Jabal Dihm are presented here (Fig. 3b and c). Stereographic projection of foliations and lineations in the mapped area of Jebel Dihm (Fig. 3d) exhibits the close parallelism of foliations with sheeted dike trends in this area, and the steep NW plunge of lineations. There is a clear similarity of foliations and lineations attitudes with those from field stations scattered throughout the ophiolite (Fig. 1).

The Farah crustal section is comparatively thin, with a gabbro unit some 3 km thick and the Him section somewhat thicker (~4 km). These estimates rely, at depth to the north, on dips in mantle foliations and lower gabbros layering which are generally parallel on each side of the Moho and, above to the south in the lid of the Ibra synform, on the steep attitude of the sheeted dikes feeding flat-lying lava flows

Fig. 2. Histograms and classes of orientation of foliated gabbros measured within the first tens of meters beneath RZSDC (sites Fig. 1a). a) Histogram of angular difference, in azimuth and dip, between foliation and local sheeted dikes. In a sheeted dike referential restored to vertical, the histograms show azimuth and dip of the foliation. b) Classes of gabbro attitudes considered separately. c) visualization of dominant structural relations between sheeted dikes attitude and gabbro foliations and lineations; case(1), corresponds to gabbros with foliations parallel or close to the SD attitude and case (2), to those which have a trend at high angle to the SD and a flat-lying dip; case (3) corresponds to steep foliations at a high azimuthal angle to the SD. Lineatiosn (L) show a steep plunge in steep foliations (case (1) and (3)), and a dominant parallelism with SD in flat-lying foliations (case (2)).

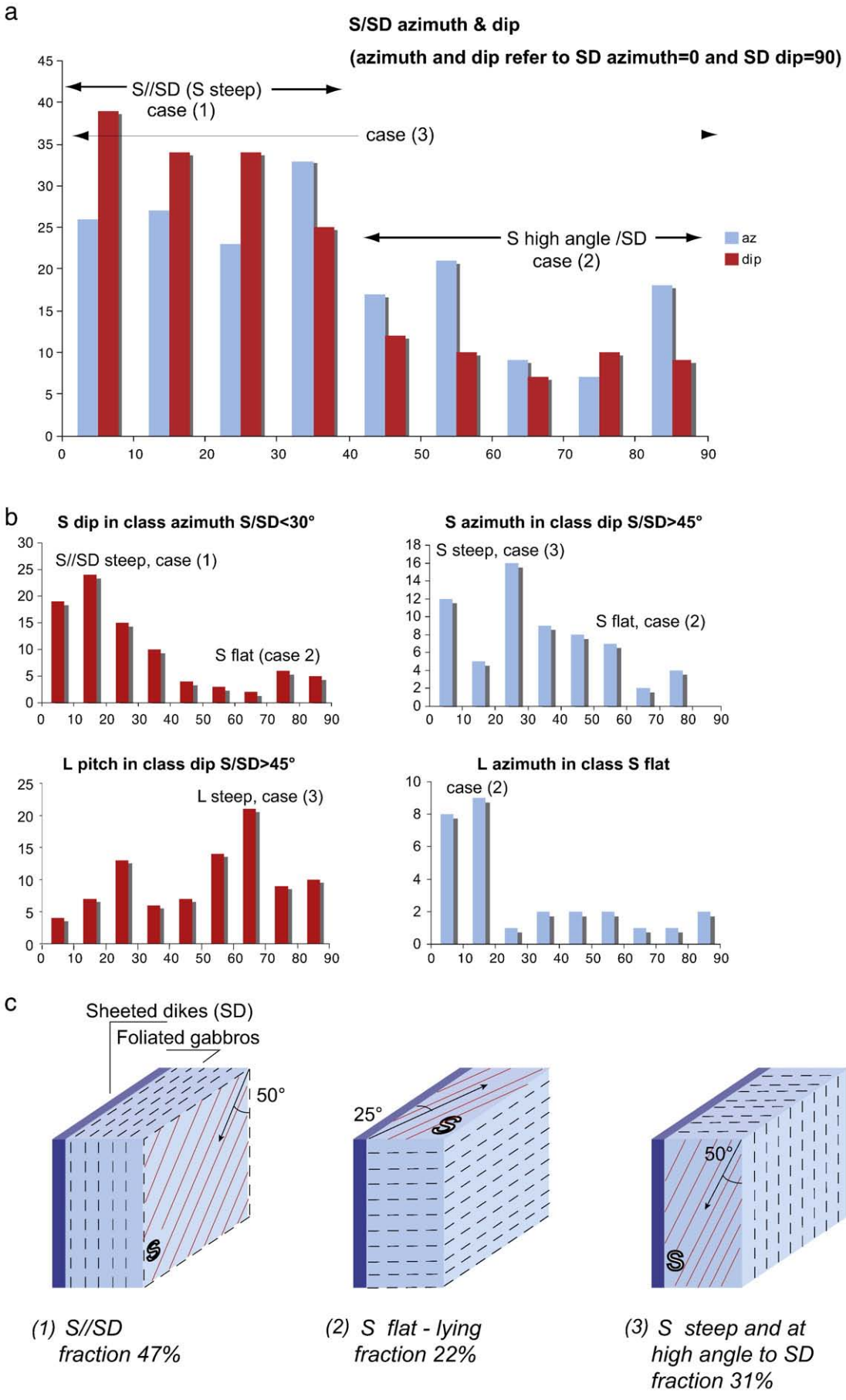
a
S/SD azimuth & dip
(azimuth and dip refer to SD azimuth=0 and SD dip=90)
S//SD (S steep)
case (1)
case (3)
S high angle /SD
case (2)
az
dip
b
S dip in class azimuth S/SD<30°
S//SD steep, case (1)
S flat (case 2)
S azimuth in class dip S/SD>45°
S steep, case (3)
S flat, case (2)
L pitch in class dip S/SD>45°
L steep, case (3)
L azimuth in class S flat
case (2)
c
Sheeted dikes (SD)
Foliated gabbros
50°
25°
50°
(1) S//SD
fraction 47%
(2) S flat - lying
fraction 22%
(3) S steep and at
high angle to SD
fraction 31%

(box in Fig. 1). In both sections, exposures are excellent and very similar, except a tectonic discontinuity due to a small north-directed thrust in Him (Fig. 3c). This thrust is underlined by trondhjemite and diabase breccias, showing that the thrust was active very close to the ridge axis. The Farah section which is continuous is briefly described now (Fig. 3b).

The detailed mapping starts in basal isotropic gabbros from the RZSDC, only a few tens of meters above the presumed level of the melt lens. This level is marked by coarser-grained and rusty, isotropic gabbros. Immediately below, slightly foliated gabbros, rich in stocky clinopyroxenes, are regarded as issued from the melt lens floor. Within less than 30 m to the NW, the foliation, parallel to a poor layering defined by plagioclase enrichment with respect to pyroxene and olivine, is measured in the field, with a steep dip and a plunging lineation. At 150 m NW from the lens floor, the foliation becomes quite obvious and the plagioclase segregation evolves into anorthosite lenses, from 3 to 30 cm thick; at 250 m from the start, some anorthosites are nearly pure plagioclase. Northward and down section, the mapping has been stopped where the first outcrops of foliated, granular gabbros, clearly belonging to the main gabbro unit were reached. The NNW–SSE trend of the first granular, foliated gabbros records the progressive rotation toward the E–W trending lower gabbros (Fig. 3a).

4. Transition from RZSDC to gabbro unit

From the base of the RZSDC, down into the gabbro unit, the uppermost foliated gabbros evolve mainly in the first 100–150 m, developing within ~20 m vertically beneath the RZSDC, steep foliations and lineations as shown in Figs. 1b and 3d. These foliations are remarkably parallel to the overlying sheeted dike complex attitude, except locally where foliation is contorted in response to local hydrous melting and recrystallization of the foliated gabbros (Nicolas et al., 2008). This plastic softening has been described in an environment of large hydrous melting (Bosch et al., 2004). These foliations are quite conspicuous at 50 m beneath the RZSDC and well recovered, as typical upper granular gabbros at 100–150 m beneath this limit. Moving 1–2 km down section from the upper gabbros into the layered gabbros, the foliations progressively depart from their attitude concordant with that of sheeted dikes and their average dip decreases. The thick and contrasted layers are thought to derive from sill injections which are interlayered with the tight, laminar layering prevailing in the upper gabbros (Boudier et al., 1996). Despite the difficulty to discriminate the contribution of subsidence versus sills intrusion in the lower gabbros, constraints are provided by Coogan (2003) tracing lower crust contamination by seawater-derived chlorine. Transitions in gabbro textures are described now, focusing on the first tens of meters beneath the RZSDC where they mostly evolve.

4.1. Transition in thin sections

4.1.1. Isotropic, ophitic gabbros from the base of the RZSDC

Ophitic gabbros from the RZSDC are isotropic, fine-grained and hydrated as evoked in Fig. 4a. Locally, they grade down section at the very roof of the lens into coarser-grained and dry gabbros, where temperature was in excess of 1000 °C, due to proximity with the melt lens, itself at 1200 °C (Nicolas et al., 2008). In both facies, the clinopyroxene is interstitial and poikilitic between plagioclase laths. It is largely replaced by hornblende in the first one and essentially fresh in the second one. Similarly, olivine is totally altered in the first one and much less in the second, to HT hydrothermal assemblages (Bosch et al., 2004). In the "dry" gabbros, the limited HT alteration is assumed to have originated when the gabbros drifted outside the protective environment of the melt lens.

4.1.2. Lens floor gabbros

This new gabbro facies is observed right beneath the contact with the preceding RZSDC ophitic gabbros (Fig. 4b). In the field, these gabbros are identified by their incipient foliation, their association with anorthosite lenses, never observed above and the habitus of clinopyroxene. The incipient foliation is moderately dipping, before getting steeper downward. In thin section, differences with the overlying gabbros are striking (Fig. 4a and b). Plagioclase is elongated in thin, heavily twinned laths, usually 0.5–2 mm long, locally up to 4 mm. A striking feature is an spectacular zoning, with altered plagioclase cores (first enlarged thin section of Fig. 4b). In tiny voids between the last plagioclase outgrowth, quartz has been identified. Plagioclase analyses on three samples from the same level in Wadi Gaz and Nahr (Nicolas et al., 2008) show normal zoning with An_{77-80} core and An_{65-70} rim. In the same level of Jebel Dihm area, Pallister and Hopson (1981) measured in their hypidiomorphic textured gabbros, a similar normal zoning of plagioclase with An_{77-84} core and An_{37-55} rim. Such features reflect conditions of crystallization out of equilibrium which we tend to ascribe to fast cooling. Melt compaction being reduced at the top of the section, magma pockets crystallize in gabbros and anorthosites as poikilitic clinopyroxene, brown hornblende or opaque phases as illustrated on the second enlarged thin section of Fig. 4b. Whereas in the isotropic gabbro, clinopyroxene is interstitial between plagioclase laths, it is here idiomorphic (enlarged thin section in Fig. 4b), grading down section into tabular grains with plagioclase either in laths molded around or in tiny tablets inside clinopyroxene. Olivine which is present in all gabbros throughout the main gabbro unit is here nearly always altered by HT hydrothermal fluids (Bosch et al., 2004). As clinopyroxene, it contains tiny plagioclase inclusions, pointing to an early nucleation of plagioclase compared to the other phases.

4.1.3. Foliated uppermost gabbros

Below the RZSDC base, a foliation develops in gabbros (Fig. 4c), becoming more conspicuous and steeper down section over a vertical distance of around one hundred meters. Within this distance, the extreme zoning of plagioclase has vanished and the poikilitic assemblage of clinopyroxene are reduced. Beyond 100 m depth, foliation is very strong, grading into the granular gabbros.

4.1.4. Foliated, granular, upper gabbros

In these gabbros, plagioclase laths and twins tend to thicken, zoning is absent, grain boundaries are curvilinear with 120° triple junctions and the overall grain size increases, mainly by thickening of plagioclase laths, all signs indicating that recrystallization is progressing (Fig. 4d). Clinopyroxene becomes more tabular, defining a strong magmatic foliation together with elongated olivine aggregates. Also contrasting with the overlying gabbros where the clinopyroxene is largely replaced by hornblende and the olivine, totally altered, the granular gabbros are only moderately affected by the same HT to VHT (up to 1000 °C) hydrothermal metamorphism (Bosch et al., 2004). A highly significant feature is the observation of mutual impingements in plagioclase tablets, indicative of stress-induced dissolution at grain contact. This has been ascribed to suspension flow occurring in a very thick mush during its subsidence within the magma chamber. Flow would be controlled by dissolution–recrystallization processes (Nicolas and Ildefonse, 1996). The attenuated layering locally developed in these gabbros is defined by anorthosite lenses and stretched microgabbronorites lenses parallel to the foliation. Such occurrences have been described by Boudier et al. (2000) and are ascribed to roof pendants stoped in the melt lens.

4.2. Transition in crystallographic fabrics and strain measurements

Increasing strain moving down section deduced from strength of foliation in these upper gabbros can be quantified by measurements of

Table 1
Description of the 18 sections (see locations on Fig. 1a) crossing from the RZSDC lower limit, through the uppermost foliated gabbros and down to the upper granular gabbros belonging to the gabbro unit.

Section	Haylayn	Gaz	Narh	Farah W	Farah center	Farah E
UTM coordinates	51582E/261383N	62310E/255626N	64705E/25210N	66551E/25292N	66631E/252963N	66651E/252959N
Length, trend	750 m, NE–SW	800 m SE–NW	1000 m SE–NW	1200 m, S–N	800 m S–N	2000 m
Sheeted dikes	NW–SE	NW–SE vertical	NW–SE	N–S vertical	N–S vertical	SE–NW
Tilt		20°SE	Vertical	20°S	20°S	NNW–SSE
Field conditions	Fair	Excellent	Excellent	Excellent	Good	Vert.
						20°S
						Excellent
Lens horizon	Exposed	Exposed	Exposed	Exposed	Exposed	Exposed
RZSDC thickness		100 m		75 m	100 m	60 m
Top gabbro	Fine grain	Coarse grain	Fine grain	Fine grain	Fine grain	Fine grain
Plag	Strongly zoned	Weakly zoned	Strongly zoned	Weakly zoned	No	Strongly
Cpx	Euhedral stocky	Euhedral stocky	Stocky, tabular	Stocky, tabular	Stocky	Zoned
Interstitial opaque	Yes	Yes	Yes	Yes	Abundant	Euhedral
Opx				Abundant	Yes	Stocky
						Yes
						Abundant
Top foliation	NW–SE vertical	NW–SE vertical	NW–SE	N–S vertical	N–S vertical	N–S W dip
Lineation	SW steep	SE steep	Vertical	N steep	NE steep	N steep
Shear sense		4, SW down	NW steep N	1, W down	3, W down	1, W down
Lower foliation	SW steep	NW–SE vertical	N–S vertical	N–S W dip	N–S vertical	N–S W dip
Lineation	SW steep	N plunge	N steep plunge		N steep	NW plunge
Transition to main gabbro unit	No	~200 m	~400 m	400 m	170 m	350 m
		70 m	Complex	~130 m thick	60 m thick	100 m thick
Intrusions	Trondjhemite	Sheeted dike	HT dikes	HT dikes	HT dikes	HT dikes
		Trondjhemite	Breccias		Microgabbros	Microgabbros
Anorthosite lens	Common thin	Common	Abundant	Abundant	Abundant	Abundant
Thickest	20 cm	40 cm	80 cm	100 cm	40 cm, folded	30 cm
HT hydro.alter.	No	No	Important	Present	Very important	Important
LT tectonics	Locally	No	No	No	No	No
HT tectonics		NW–SE graben	Small grabens?	No	Yes	Shear bands
Foliated gabbro/sheeted dikes	Parallel	Parallel	Top, parallel	Parallel	Parallel	Top, parallel
			Below 30°N			Below 30°W

Section	Him W	Him center	Him E	Batin	Andam
UTM coordinates	66828E/252937N	66931E/252888N	67327E/25272N	67116E/25210N	60743E/254012N
Length, trend	2200 m N–S	2000 m NW–SE	2000 m S–N	300 m N–S	2500 m SE–NW
Sheeted dikes	NNE–SSW steep	N–S vertical	N–S vertical	NW–SE 45°W	NW–SE vertical
Tilt	20°S	20°S	20°S		
Field conditions	Good	Excellent	Good	Excellent	Good
Lens horizon	Exposed	Exposed	Exposed	Exposed	Not exposed
RZSDC thickness	100 m	130 m	100 m		
Top gabbro	Fine grain	Fine grain	Coarse grain	Fine grain	Fine grain
Plag	Strongly zoned		Weakly zoned	Weakly zoned	No
Cpx	Euhedral		Stocky, tabular	Stocky tabular	Stocky
Interstitial opaque	Yes		Yes	Yes	
Opx	Yes		Yes	Abundant	
Top foliation	N–S W dip	N–S vertical	NW–SE	N–S vertical	NW–SE SE dip
lineation	N steep	N steep	Vertical	N very steep	NW plunge
Shear sense			NW steep		
Lower foliation	NW–SE W dip	NW–SE vertical	N–S vertical	NW–SE steep	NE–SW E dip
Lineation	NW plunge	NW plunge	N plunge	N plunge	NE plunge
Transition to main gabbro unit	300 m		600 m		~400 m
	100 m thick		200 m thick		
Intrusions	HT dikes	HT dikes	HT dikes		HT dikes
	Microgabbros	Trondjhemite	Trondjhemites		Wherlites
Anorthosite lens	Common	Uncommon	No	Abundant	Common
Thickest	20 cm			80 cm	15 cm
HT hydro.alter.	Very important	Important	Very important	Important	Common
LT tectonics	No	No	No	Major thrusts	
HT tectonics	N thrust	large N thrust	No		
Foliated gabbro/sheeted dikes	Top, parallel	Top, parallel	Parallel		Top parallel
	Below 30°W	Below 20°W			Below45°NE

Coordinates are those of the starting point in RZSDC (Ttransverse Mercator, WGS, zone 40). First line deals with general features of the section; starting from RZSDC and pointing down section;"trend", as all other orientations in the table, are averaged; "field conditions" refer to quality of outcrops and their continuity. Third line emphasizes critical paragenetic features in uppermost gabbros. Grain size is normally "fine grain" (plagioclase laths, 1–2 mm on average); it is "coarse grain" when a few grains or more are in the range of 2–4 mm; similarly, orthopyroxene ("opx") is noted even if very scarce. In sixth line, distance horizontally along the section, from lens horizon to granular gabbros belonging to the main gabbro unit, is estimated with its thickness, when possible. "Intrusions" line points to unusual abundance of mainly trondjhemites and werhlites. HT dikes refer to diabase dikes emplaced in country rocks still at high temperature (HT~800 °C) which are exposed as dikes, sills and breccias and correspond, in RZSDC, to protodikes and, beneath in foliated gabbros, to microgabbros lenses. "HT hydrothermal alteration" line refers to the occurrence of hydrous anatexis and hydrous gabbro diking (Bosch et al., 2004) which alter the foliated gabbros. "LT tectonics" refers to emplacement related events and "HT tectonics", to ridge related events.

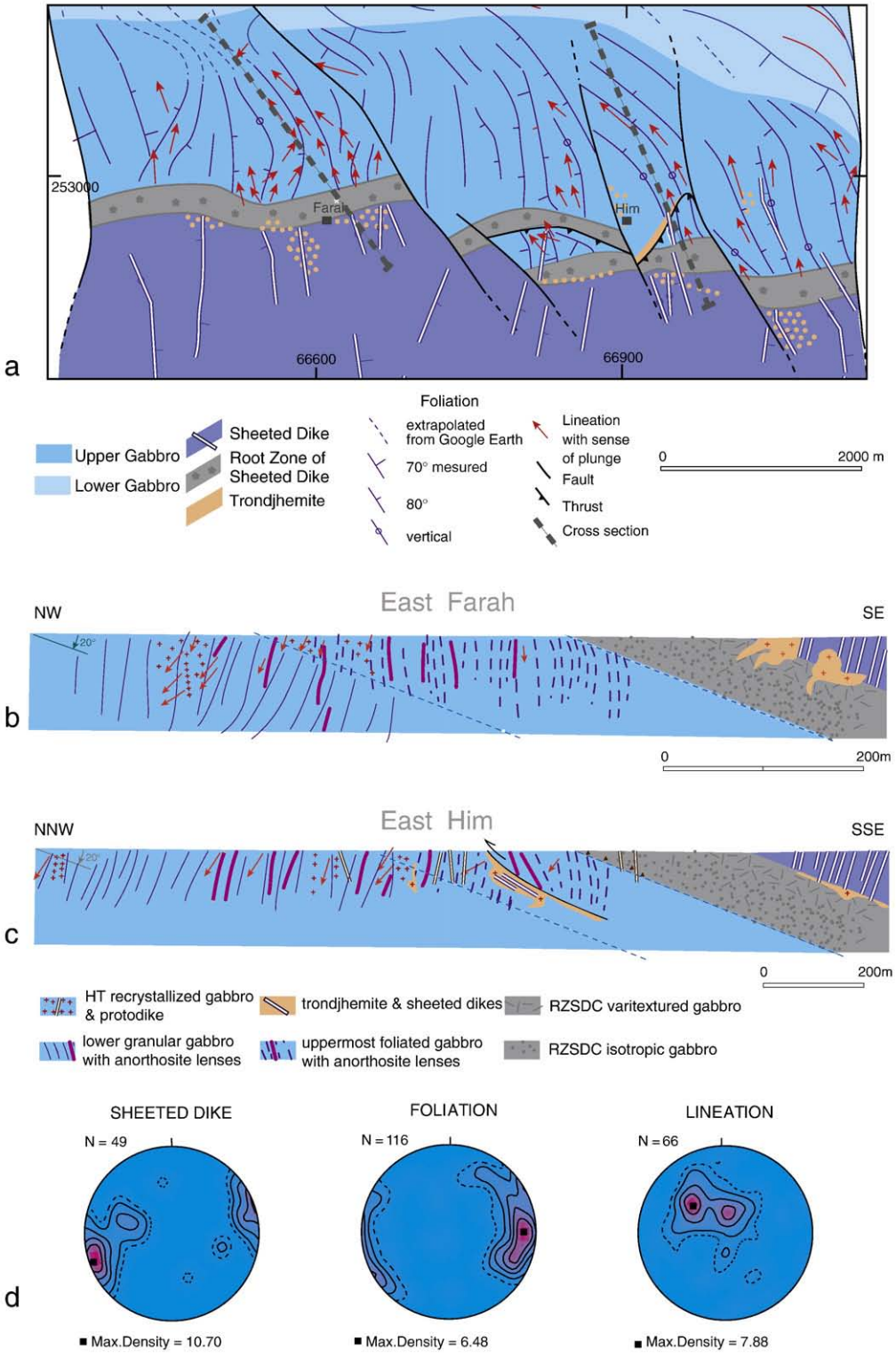

Fig. 3. Map and sections in the Dihm area of Wadi Tayin massif. (a) Detailed map from the sheeted dikes (south) to the lower gabbros (north) (box in Fig. 1). (b) and (c) East Farah and East Him cross sections from the RZSDC (simplified) and transition from uppermost, foliated gabbros to foliated, granular gabbros, with location in map (a). (d) Field orientations of the magmatic foliations and lineations with reference to the local sheeted dike complex attitude, in the mapped area. Lower hemisphere of projection, geographical reference system, contours at 1, 2, *x* times uniform distribution, *N*, number of measurements.

plagioclase crystallographic fabrics (Fig. 5). The fabric strength is measured by the pfJ index, as described by (Mainprice and Silver, 1993) and derived of the Orientation Distribution Function (ODF) (Bunge, 1982). The pfJ index provides a comparative measurement of the fabric strength, thus of the strain. Samples have been chosen along Wadi Farah, at increasing depth from ~10 m below the RZSDC to 80 m and finally down to 365 m, into the upper gabbro unit. We notice in Fig. 5 that the plagioclase preferred orientation; with [010] maximum perpendicular to the gabbro foliation (see Lamoureux et al. (1999); Yaouancq and MacLeod (2000)), increases drastically between 10 and

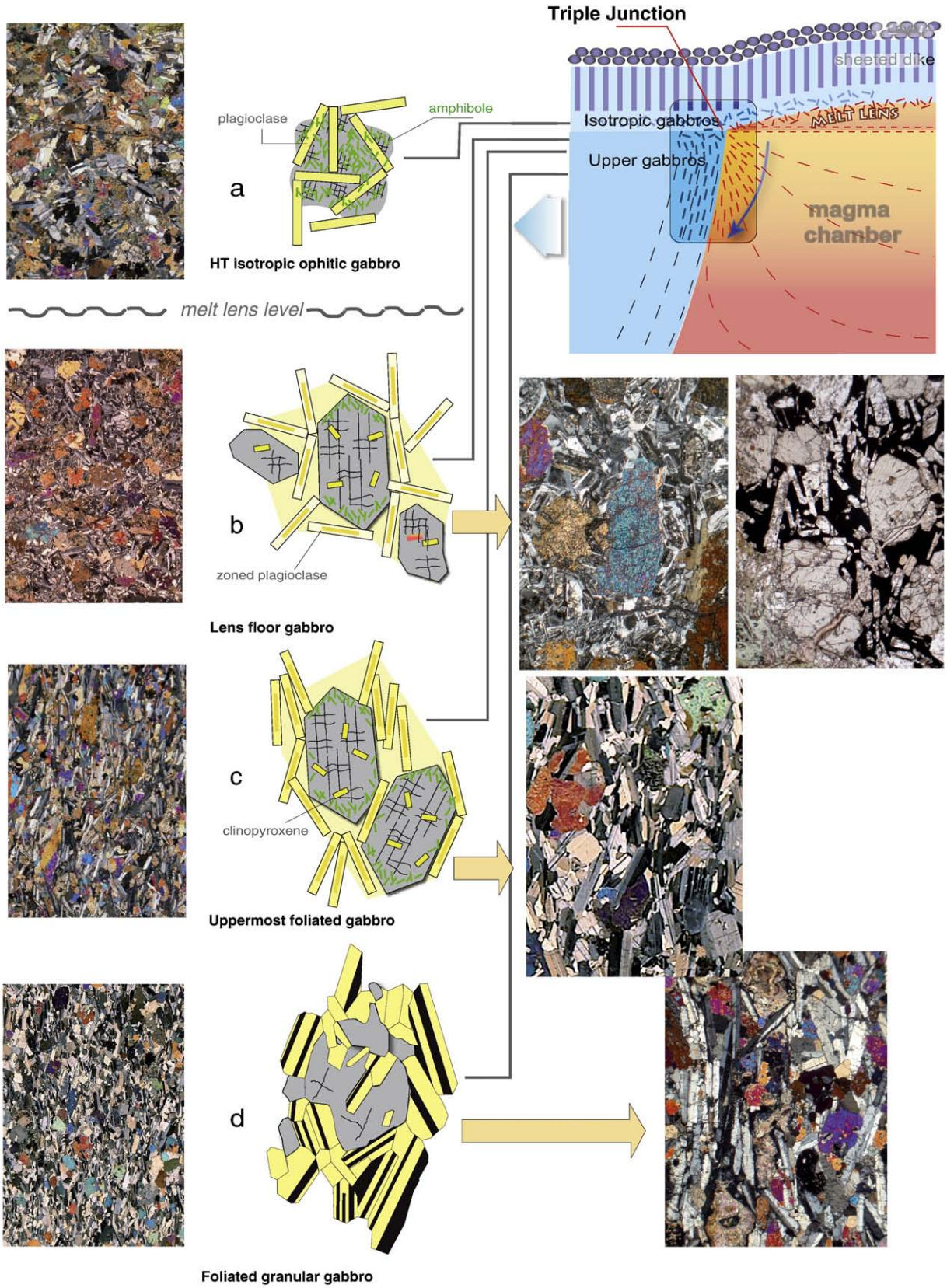

Fig. 4. Progressive evolution of gabbro textures from the RZSDC to the top of the main gabbro unit. When foliation is present, thin sections are presented in their original attitude. (a) Isotropic ophitic gabbro from the RZSDC. (b) Gabbro from the floor of the melt with idiomorphic clinopyroxene and extreme zoning in plagioclase thin laths, also illustrating the development of a steep foliation; (c) Uppermost foliated gabbro with a good foliation, thicker and less zoned plagioclase, and recrystallized clinopyroxene in large tabular grains. (d) Foliated granular gabbro, 100 m below floor of melt lens, recording a strong foliation and recrystallization. Width field of view is 12 mm for low magnification, 3 mm for high magnification. Samples (a) 89OA12b; (b) 06OA20i and 890A34; (c) 90OA97; (d) 06OA3.

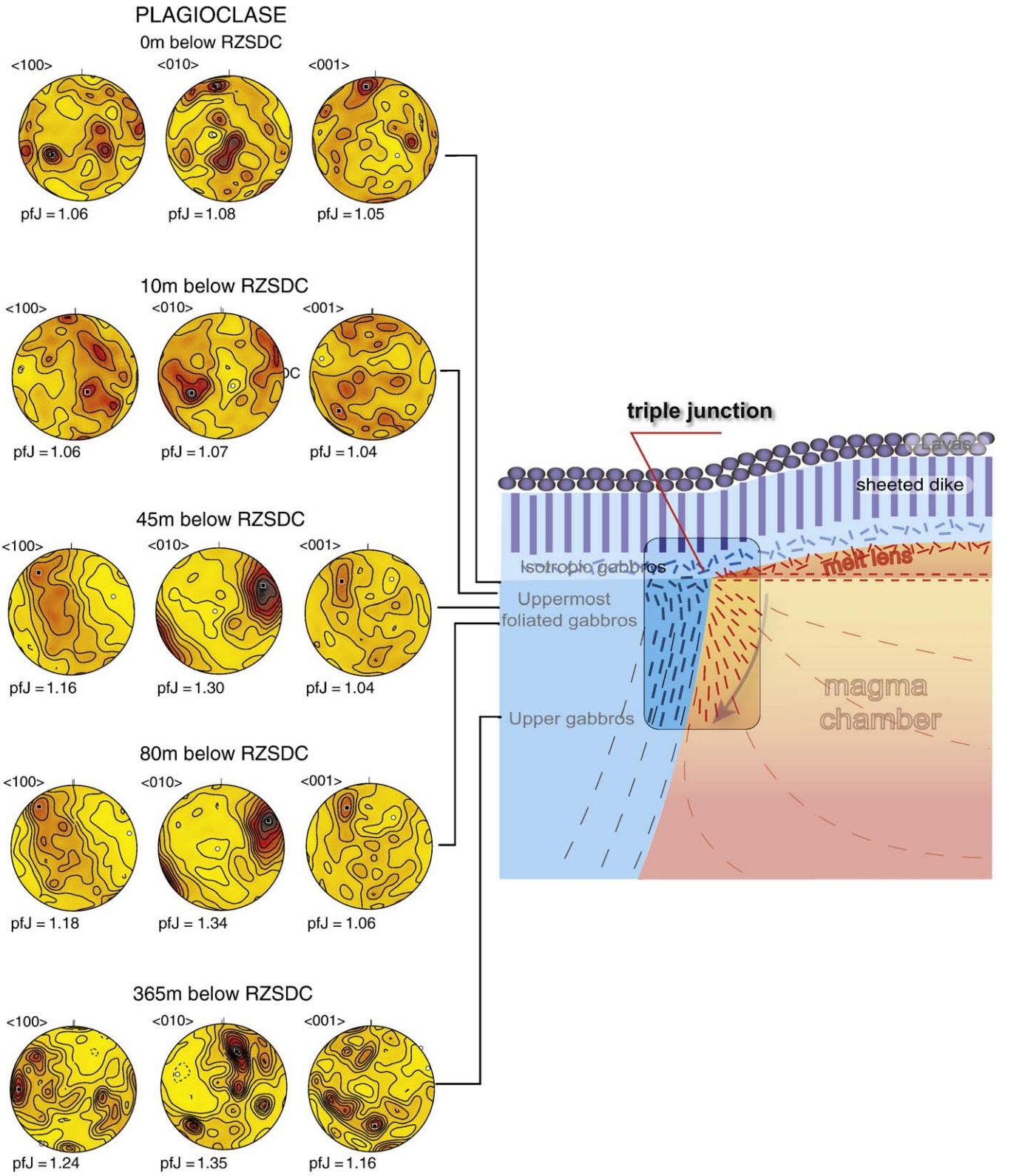

Fig. 5. Crystallographic orientations of plagioclase in samples selected along Wadi Farah, at depths between ~10 and 365 m below the RZSDC, represented with their position in the upper gabbro section. Crystallographic preferred orientations are Electron BackScattering Diffraction (EBSD) measurements; lower hemisphere, non polar data, stereoplot in the geographical reference frame with north marked; contours at 1, 1.5, 2, 2.5…times uniform distribution. pfJ indexes of Mainprice and Silver (1993) measure strengths of crystallographic axes preferred orientation. Samples: 07OA20a, c_1, d, e and 07_2OA13.

45 m, and then evolves only slightly. The <100> axes, form a girdle in the foliation plane for the shallower samples, then tend to concentrate in a maximum parallel to the flat-lying lineation for the deepest sample. The plagioclase fabrics record the rapid strain increase related with rotation of individual markedly anisometric crystals, defining the steeply dipping foliation.

5. Discussion

5.1. General model of subsidence through the magma chamber

Near Moho, gabbro layering and foliation show a flat attitude parallel to this limit. Upsection, these structures rotate progressively to the steep attitude of uppermost gabbros, generally parallel to the average orientation of the sheeted dike complex. Based on their mapping in Jebel Dihm and in Nakhl massif respectively, Pallister and Hopson (1981) and Browning (1984) suggested that the inclined walls of the magma chamber were oriented towards the ridge axis. Our systematic mapping confirmed the steepening up section of foliations but, under the control of structural and kinematic data in the underlying mantle, it was concluded that facing was away from the ridge axis (Nicolas et al., 1988). In this model, the foliation is not developed by magmatic settling but by plating along the magma chamber walls and eventually cooling along these walls, of a highly viscous suspension, down flowing parallel to the walls (Nicolas and Ildefonse, 1996). In the upper gabbros, the flow results essentially from the downwards subsidence of the mush crystallizing on the melt lens floor. In contrast with this, MacLeod and Yaouancq (2000) have explained the steep foliations in Oman upper gabbros as recording ascent of a mush through the magma chamber towards the melt lens. This view is not supported by petrological results favoring in Oman the subsidence model (Coogan et al., 2002) and by the new data presented here. At shallow depth in the gabbro unit, subsidence is induced by the drift of the crust away from the ridge axis which sucks downwards the material settling onto the floor of the melt lens (see the glacier model of Quick and Denlinger (1993), and the physical modelling of Chenevez et al. (1998)). In the latter paper, a new horizontal magmatic flow component is added to this vertical subsidence flow, in the gabbro unit near Moho. It is due to coupling with the forced mantle flow drifting away from the ridge axis. A last evidence for the subsiding process from the melt lens is the presence of microgabbronorites lenses aligned in the foliation. These are ascribed to roof pendants stopping in the melt lens and subsiding below its floor (Nicolas et al., 2008).

Based on the new data presented here an updated interpretation of subsidence is sketched in Fig. 6. The foliation attitude of uppermost gabbros below the RZSDC is close to that of the sheeted dikes (Figs. 1b and 2). Thus, the foliation plane of gabbros is parallel to the ridge symmetry plane, which also controls the shape of the magma chamber (Chenevez et al., 1998). While it is subsiding from the melt lens floor into the magma chamber, the highly viscous gabbroic mush progressively develops a magmatic foliation which rotates to become parallel to the magma chamber walls (Fig. 6b). Lineations which are, on average, steeply plunging (Figs. 1b and 2), register the downward particle motion.

5.2. Deformation analysis in the subsiding gabbros

The physical analysis of the subsidence process at the scale of a spreading ridge, as envisaged here, is described by Chenevez et al. (1998). Near the top of the magma chamber where the walls are vertical, Fig. 7 illustrates qualitatively the three contributions to the deformation during subsidence of a layer which had settled on the floor of the melt lens.

As the strain illustrated in Figs. 5 and 6 is time-dependent, one caveat is that strain is significantly reduced near the surface where the transit time through the chamber is shorter, resulting in a foliation which is less steep and less pronounced there than in gabbros deeper down. This is illustrated in Figs. 6 and 7 showing that gabbros issued more internally on the floor of the lens reach the magma chamber wall at greater depths and are more affected by magmatic flow and crystal/melt interactions.

5.3. Subsidence initiation on melt lens floor

When the crust issued from a stable melt lens drifts away from the ridge axis, only the points issued from the pinching limit of the lens and drifting through the triple junction carry information on the nature and structure of the lens floor, because they have subsided and rotated only over meters before crossing and being frozen at the magma chamber wall. This opens a window on the active processes

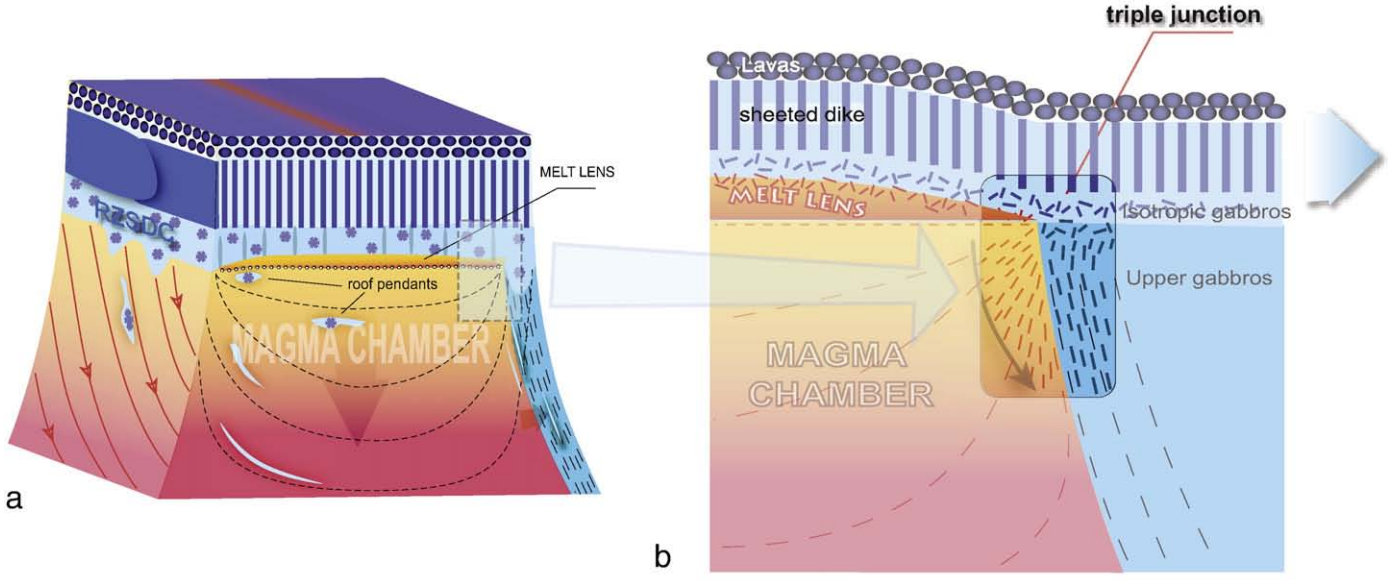

Fig. 6. Models of subsidence, (a) sketch of lid and top kilometer in gabbro unit and (b) detailed view on the triple junction at the closure of melt lens. (a) Origin of layered and foliated gabbros by subsidence of the mush crystallized on the floor of the lens. Left side: magmatic flow surface, internal to the magma chamber wall, with imprint of the plunging flow lineations. Right side: frozen foliations in gabbros outside the magma chamber (bright blue). Roof pendants (light blue), falling from the RZSDC into the melt lens, recrystallize during subsidence, in micronorites which are stretched in lenses parallel to the gabbro foliation. (b) Closure of the melt lens at a triple junction which is stationary in a drifting crust. At the triple junction, the RZSDC isotropic gabbros from the roof of the melt lens join the gabbros from its floor. Just below, the steep foliated gabbros were deposited near the triple junction, the top gabbros subsiding on a shorter distance than deeper gabbros which are issued from the floor further away from the triple junction. Inside the magma chamber, dotted lines in (a) are isochrons tracing the subsidence of a layer from the lens. Dashes in (b) trace the nascent magmatic foliation. (For interpretation of the references to colour in this figure legend, the reader is referred to the web version of this article.)

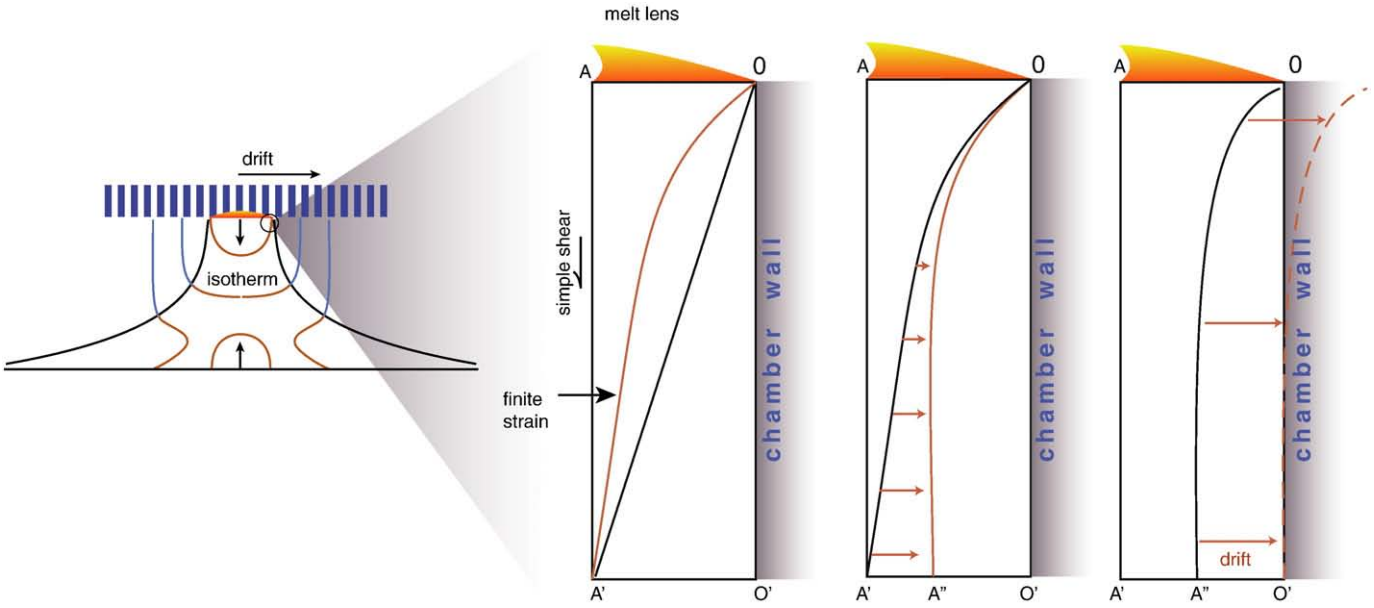

Fig. 7. Deformation in the gabbro mush of the magma chamber with subsidence from the melt lens floor. The small model on the left illustrates the subsidence of layers or isochrons (red lines) within the gabbro mush filling the magma chamber below the melt lens (yellow) and the lid (blue bars) (section in the vertical plane parallel to the spreading direction, simplified from Chenevez et al., 1998). The boxes on the right represent the three contributions to the deformation of a subsiding layer, before it reaches the magma chamber wall and freezes. This wall (on the right of the boxes) is taken as vertical in the uppermost levels which are here considered. a) Simple shear with O, the triple junction, as a fixed origin. The segment OA, belonging to a layer deposited on the lens floor, is transformed by simple shear along the AA′ direction into O′. The red line is the trajectory of finite strain (orientation of foliation), showing how the long axis of the strain ellipse rotates with successive strain increments. It illustrates the layering-foliation rotation with depth. Finite shear strain ($\gamma = 3$) is derived from assumption that a 1 km half length for the lens subsides to the Moho, over the 3 km height of the magma chamber. Near the melt lens, strain is smaller because interrupted by drifting. b) Qualitative effects of compaction by expelling intergranular melt and by magmatic flow assisted by dissolution–recrystallization (Nicolas and Ildefonse, 1996). Being time-dependent, flattening increases with depth and transforms O′A′ in O′A″. c) Spreading-related translation. With a drift of O′A″ and the point A″ transposed into O′, the initial layer OA has entirely crossed the magma chamber wall (red dashed line). It is now nearly vertical and stretched nearly 3 times. (For interpretation of the references to colour in this figure legend, the reader is referred to the web version of this article.)

taking place in the melt lens. The texture acquired during settling on the floor of the melt lens is slightly altered by initiation of foliation. Compaction is reduced, as shown by the presence of oikocrysts, crystallized from the residual melt which was trapped within the solid frame and which rapidly disappears down section by compaction of the melt. Clinopyroxene is idiomorphic and strikingly different from its interstitial habit in the immediately overlying isotropic ophitic gabbros. Down section, it rapidly recrystallizes in stocky and tabular grains. Finally in plagioclase, disequilibrium growth is indicated by the elongated laths with very thin growth twins and by their extreme zoning. Final crystallization and this zoning occur during cooling in these gabbros while crossing the magma chamber wall. At the shallow RZSDC depth, gabbros are efficiently cooled by seawater convection (Nicolas et al., 2008) and the cooling is very fast.

From the vertical distances of subsiding gabbros beneath the lens floor, it is possible to estimate the time which they spent in the magma chamber. Accounting for vertical stretching and the estimated dip of RZSDC base in the field, the depth beneath the melt lens where gabbros have recrystallized and developed the strong foliation of the granular gabbros is in the range of 100 m. The required time lapse is estimated between 500 and 1000 yr, based on this distance and the half spreading of 5–10 cm/y accepted above. The spectacular textural changes illustrated in Fig. 4 are also possible because, during subsidence, gabbros are still a sponge soaked by a basaltic liquid.

6. Conclusion

Shifting from mapping at the scale of Oman ophiolite belt (Nicolas et al., 2000) to that of a few tens of meters makes it possible to study fine-scale structures, specifically the paleo-melt lens of a fast spreading ridge. A first study at this scale dealt with the RZSDC (Nicolas et al., 2008), a side result of which was to identify in the field the horizon of the pinched melt lens, between the RZSDC and the main gabbro unit. Based on 183 stations throughout the belt where this horizon was exposed and 18 detailed sections crossing from this horizon downwards, a comprehensive study brings field evidence for subsidence of a gabbro mush from the floor of the melt lens, through the magma chamber, during accretion of the gabbro unit. So far, subsidence was only a model based on the assumption that drifting of the crust away from the ridge axis sucked downwards the gabbro mush settling onto the floor of the melt lens. Subsidence is demonstrated here by the field data displaying in half the stations in the gabbros beneath the pinched melt lens floor, a discordant and steep magmatic foliation parallel to the sheeted dike complex and to the ridge plane. One quarter of the stations have foliations parallel or close to the floor of the RZSDC. They reveal information on the melt lens floor and will be studied in a next contribution. Steep foliations appear within ten to a few tens of meters below this floor. The top gabbros which settled on the melt lens floor near its closure, slightly subsided before being expelled by drifting through the cold wall of the magma chamber. As a result, their texture suggest a very fast cooling. The time spent by the immediately underlying gabbros inside the magma chamber, before drifting outside, being in the range of only 100 yr, the textures are still poorly compacted and recovered, in contrast with well recrystallized gabbros derived from 100 m below the lens floor which subsided for 500–1000 yr. The steep foliation induced by subsidence is traced downward in the upper gabbros over 1 to 1.5 km, before progressively rotating into the flat-lying lower gabbros.

Acknowledgements

We acknowledge the support of the University of Montpellier as well as the friendly cooperation established in Oman with the Director of Minerals of the MCI, Dr Salim Al-Busaidi. Benoit Ildefonse is thanked for his help in the software treatment of EBSD data. The manuscript has been improved thanks to constructive remarks by Rob van der Hilst, the editor, and by two anonymous reviewers.

References

Bosch, D., Jamais, M., Boudier, F., Nicolas, A., Dautria, J.M., Agrinier, P., 2004. Deep and high temperature hydrothermal circulation in the Oman ophiolite: petrological and isotopic evidence. J. Petrol. 45 (6), 1181–1208.

Boudier, F., Nicolas, A., Ildefonse, B., 1996. Magma chambers in the Oman ophiolite: fed from the top or from the bottom? Earth Planet. Sci. Lett. 144, 239–250.

Boudier, F., Godard, M., Armbruster, C., 2000. Significance of noritic gabbros in the gabbro section of the Oman ophiolite. Mar. Geophys. Res. 21-3/4, 307–326.

Browning, P., 1984. Cryptic variation within the cumulate sequence of the Oman ophiolite: magma chamber depth and petrological implications. In: Gass, I., Lippard, S.J., Shelton, A.W. (Eds.), Ophiolites and Oceanic Lithosphere. Special Publication — Geological Society of London, vol. 13, pp. 71–82.

Bunge, H.J., 1982. Texture analysis in Materials Science. 593 pp.

Chenevez, J., Machetel, P., Nicolas, A., 1998. Numerical models of magma chamber in the Oman ophiolite. J. Geophys. Res. 103, 15,443–15,455.

Collier, J.S., Singh, S.C., 1997. Detailed structure of the top of the melt body beneath the East Pacific Rise at 9°40′ from waveform inversion of seismic reflection data. J. Geophys. Res. 102 (B9), 20,287–20,304.

Coogan, L.A., 2003. Contaminating the lower crust in the Oman ophiolite. Geology 31, 1065–1068.

Coogan, L.A., Thompson, G., MacLeod, C.J., 2002. A textural and geochemical investigation of high level gabbros from the Oman ophiolite: implications for the role of the axial magma chamber at fast-spreading ridges. Lithos 63, 67–82.

Detrick, R.S., Buhl, P., Vera, E., Mutter, J., Orcutt, J., Madsen, J., Trocher, T., 1987. Multi-channel seismic imaging of a crustal magma chamber along the East Pacific Rise. Nature 326, 35–41.

Henstock, T.J., Woods, A.W., White, R.S., 1993. The accretion of oceanic crust by episodic sill intrusion. J. Geophys. Res. 98 (B3), 4143–4161.

Kent, G.M., Harding, A.J., Orcutt, J.A., 1993. Distribution of magma beneath the East Pacific Rise between the Clipperton transform and the 9°17′N Deval from forward modeling of common depth point data. J. Geophys. Res. 98, 13,945–13,969.

Lamoureux, G., Ildefonse, D., Mainprice, D., 1999. Modelling the seismic properties of fast-spreading ridge crustal LVZ: insights from Oman gabbro textures. Tectonophysics 312, 283–301.

MacLeod, C.J., Yaouancq, G., 2000. A fossil melt lens in the Oman ophiolite: implications for magma chamber processess at fast spreading ridges. Earth Planet. Sci. Lett. 176, 357–373.

Mainprice, D., Silver, P.G., 1993. Interpretation of SKS-waves using samples from the subcontinental lithosphere. Phys. Earth Planet. Inter. 78, 257–280.

Morton, J.L., Sleep, N.H., 1985. A mid-ocean ridge thermal model: constraints on the volume of axial hydrothermal heat flux. J. Geophys. Res. 90, 11,345–11,353.

Nicolas, A., Ildefonse, B., 1996. Flow mechanism and viscosity in basaltic magma chambers. Geophys. Res. Lett. 23 (16), 2013–2016.

Nicolas, A., Reuber, I., Benn, K., 1988. A new magma chamber model based on structural studies in the Oman ophiolite. Tectonophysics 151, 87–105.

Nicolas, A., Boudier, F., Ildefonse, B., Ball, E., 2000. Accretion of Oman and United Arab Emirates ophiolite — discussion of a new structural map. Mar. Geophys. Res. 21-3/4, 147–179.

Nicolas, A., Boudier, F., Koepke, J., Lydéric, F., Ildefonse, B., Mével, C., 2008. Root zone of the sheeted dike complex in the Oman ophiolite. Geochem. Geophys. Geosys 9 (5). doi:10.1029/2007GC001918.

Pallister, J.S., Hopson, C.A., 1981. Samail ophiolite plutonic suite: field relations, phase variation, cryptic variation and layering, and a model of a spreading ridge magma chamber. J. Geophys. Res. 86, 2593–2644.

Phipps Morgan, J., Chen, Y.J., 1993. The genesis of oceanic crust: magma injection, hydrothermal circulation and crustal flow. J. Geophys. Res. 98, 6283–6297.

Quick, J.E., Denlinger, R.P., 1993. Ductile deformation and the origin of layered gabbro in ophiolites. J. Geophys. Res. 98 (B8), 14,015–14,027.

Yaouancq, G., MacLeod, C.J., 2000. Petrofabric investigation of gabbros from the Oman ophiolite: comparison between AMS and rock fabric. Mar. Geophys. Res. 21, 289–305.

Annex A2.

“Root zone of the sheeted dike complex in the Oman ophiolite”

Geochemistry Geophysics Geosystems G3
AN ELECTRONIC JOURNAL OF THE EARTH SCIENCES
Published by AGU and the Geochemical Society

Article
Volume 9, Number 5
2 May 2008
Q05001, doi:10.1029/2007GC001918
ISSN: 1525-2027

Root zone of the sheeted dike complex in the Oman ophiolite

Adolphe Nicolas and Françoise Boudier
Géosciences Montpellier, CNRS, Université Montpellier 2, CC60, F-34095 Montpellier Cédex 05, France (francoise.boudier@gm.univ-montp2.fr)

Jurgen Koepke
Institut für Mineralogie, Leibniz Universität Hannover, Callinstrasse 3, D-30167 Hannover, Germany

Lydéric France and Benoît Ildefonse
Géosciences Montpellier, CNRS, Université Montpellier 2, CC60, F-34095 Montpellier Cédex 05, France

Catherine Mevel
Géosciences Marines, IPG, CNRS, 4 Place Jussieu, F-75252 Paris Cédex 05, France

[1] In the Oman ophiolite crustal section, a contact zone between the gabbro unit and the volcanics and diabase sheeted dikes, called the root zone of the sheeted dike complex, has been recently mapped at a fine scale in a selected area. The Oman ophiolite is derived from a fast spreading ridge which had a melt lens located between the main gabbro unit and the root zone of the sheeted dike complex. With a few exceptions accounted for, this horizon has a fairly constant thickness, ~100 m, and a crude internal pseudo-stratigraphy. At the base of the root zone are isotropic ophitic gabbros interpreted as a thermal boundary layer. This layer is transitional between the magmatic system of the melt lens, convecting at 1200°C, and a high-temperature (<1100°C) hydrothermal system, convecting within the root zone. Above this level, the isotropic gabbros have been, locally, largely molten due to an influx of seawater, at ~1100°C, thus generating varitextured ophitic and pegmatitic gabbros. These latter gabbros constitute the upper part of the root zone and are associated with trondjhemitic intrusions as screens in the lower sheeted dikes. Diorites and trondjhemites were also generated by hydrous melting, at temperatures below 1000°C. The whole root zone is a domain of very sharp average thermal gradient (~7°C/m). At the top of the root zone, a new thermal boundary layer, with diabase dikes hydrated in amphibolite facies conditions, separates the preceding high-temperature convective system from the well-known greenschist facies (<450°C) hydrothermal system operating throughout the sheeted dike complex, up to the seafloor. The isotropic gabbros near the base of the root zone are intruded by protodikes with distinctive microgranular margins and an ophitic center. Protodike swarms are exceptional because, intruding a medium at ~1100°C, they are largely destroyed by dike-in-dike intrusions and by hydrous melting. However, they demonstrate that this zone was generated by melt conduits issued from the underlying melt lens. Each dike of the sheeted dike complex is thus fed by one protodike. As this zone has been recently drilled by IODP in the eastern Pacific Ocean, a brief comparison is proposed.

Components: 13,629 words, 15 figures, 2 tables.

Keywords: fast spreading ridges; lid/gabbros transition; Oman ophiolite; HT hydrothermalism.

Index Terms: 8140 Tectonophysics: Ophiolites (3042); 8135 Tectonophysics: Hydrothermal systems (0450, 1034, 3017, 3616, 4832, 8424); 3614 Mineralogy and Petrology: Mid-oceanic ridge processes (1032, 8416).

Received 1 December 2007; **Revised** 13 February 2008; **Accepted** 12 March 2008; **Published** 2 May 2008.

Nicolas, A., F. Boudier, J. Koepke, L. France, B. Ildefonse, and C. Mevel (2008), Root zone of the sheeted dike complex in the Oman ophiolite, *Geochem. Geophys. Geosyst.*, *9*, Q05001, doi:10.1029/2007GC001918.

1. Introduction

[2] A small melt lens has been imaged by multichannel seismic profiles in the late 1980s below fast spreading centers, extending <1 to 4 km on each side of the ridge axis and locally as thin as 30 m [e.g., *Detrick et al.*, 1987; *Harding et al.*, 1989; *Collier and Singh*, 1997; *Singh et al.*, 1998, 2006; *Kent et al.*, 2000]. This discovery has raised the question of how this lens relates to the overlying sheeted dike complex, as previously described from oceanic drilling [e.g., *Alt et al.*, 1993, 1996; *Bach et al.*, 2003] and in tectonic windows such as Hess Deep [*Karson et al.*, 1992, 2002b] and fracture zones [e.g., *Juteau et al.*, 1995; *Karson et al.*, 2002a]. The recent IODP hole in the eastern Pacific Ocean in Hole 1256D [*Wilson et al.*, 2006], has penetrated, at 1400 m below seafloor, 100 m of gabbros at the base of the sheeted dike complex. It is not certain that the last cored gabbros have attained the level of the former melt lens and represent the top of the gabbro unit. On the basis of field studies in Oman, we will propose criteria to distinguish gabbros which have settled on the floor of the former melt lens from gabbros crystallized at and above its roof. This zone between the base of the sheeted dikes and the top of the gabbro unit is called herein the root zone of the sheeted dike complex (RZSDC).

[3] The RZSDC has recently raised interest with petrological studies in Cyprus [*Gillis and Roberts*, 1999; *Gillis*, 2002; *Gillis and Coogan*, 2002] and in Oman [*MacLeod and Yaouancq*, 2000], following earlier descriptions of the RZSCD by *Pallister and Hopson* [1981] and *Rothery* [1983]. More general studies have been conducted by *Coogan et al.* [2003] and in Oman ophiolite, by *MacLeod and Rothery* [1992] and by *Nicolas and Boudier* [1991], whose comprehensive structural study is expanded here. General descriptions regard the RZSDC as a thin and complex assemblage of hydrous gabbros and more acidic, plutonic bodies, increasingly intruded upsection by diabase dikes, thus grading into the sheeted dike complex. In some studies, this zone has been ascribed to the final stage of the magmatic differentiation of the gabbro unit. This differentiation would occur at the top of a magma chamber, in the presence of residual water of deep origin. The RZSCD has also been regarded as originating at and above the melt lens roof as a thermal boundary layer between two main convective systems: below, the melt lens filled with a basaltic magma at ~1200°C, and above, the diabase sheeted dike complex and associated volcanics which are cooled by seawater hydrothermal cells [*Nicolas and Boudier*, 1991; *Chenevez and Nicolas*, 1997; *Gillis and Roberts*, 1999]. We depart here from our former interpretation, by introducing a new hydrothermal convection system, operating at very high temperature between the two systems mentioned above.

[4] We regard the well-known hydrothermal system [e.g., *Nehlig et al.*, 1994; *Alt et al.*, 1996] as low temperature (LT, up to 400–450°C), because it is shown below that the RZSDC, when it was active above the melt lens, was altered by a high temperature (HT > 400–450°C) hydrothermal system, just as the gabbro unit located below [*Manning et al.*, 1996; *Nicolas et al.*, 2003; *Bosch et al.*, 2004]. The LT hydrothermal cells close at a depth of ~1–2 km, at the base of the sheeted dike complex.

[5] Considering the renewed interest in this zone arising from the recent drilling of IODP Hole 1256D [*Wilson et al.*, 2006], it seemed appropriate to revisit our 1991 study in Oman ophiolite, incorporating it in a new detailed map. This ophiolite is both very large with magnificent outcrops, and inferred to be derived from a fast spreading oceanic ridge [*Nicolas et al.*, 2000], where melt lenses are actually inferred from seismic-velocity inversions. This study is focused on a limited area in the Sumail Massif, which is located in the southern part of the belt where our mapping is more detailed. In this area, all units from the lavas to the Moho are parallel and gently tilted, in contrast with domains affected by ridge segmentation, as briefly recalled below. Petrostructural descriptions from a few tens of sites from other massifs studied during the structural mapping of the Oman ophiolite show that RZSCD in this ophiolite generally have many common features throughout the belt [*Nicolas et al.*, 2000]. However, significant differences are noted depending on

whether the RZSDC belong to a domain affected by ridge segmentation or not. The results presented here on RZSDC should apply to ocean ridges spreading in steady state conditions, but we will briefly envisage how RZSDC would be modified in situations affected by ridge segmentation.

[6] Finally, as a word of caution, it should be stressed that RZSCD are complex interface zones where several processes have been active at different times. In particular, field observations are the end product of superimposed processes initiated above the melt lens and continued off-axis on a few tens of kilometers.

2. Choice of the Studied Area

[7] Magmatic intrusions are observed in a number of RZSDC in the Oman ophiolite. They were mapped as "late intrusive" [*Lippard et al.*, 1986; *Ministry of Petroleum and Minerals*, 1986], encompassing, wehrlites and gabbronorites, uralitic gabbros, diorites and tronjhemites, the last one making up magmatic breccias with diabase dikes. Olivine gabbros have not been reported among these intrusions These "late intrusive" have been related to domains where accretion was under the influence of major tectonic and magmatic activity related to ridge propagation [*Juteau et al.*, 1988; *MacLeod and Rothery*, 1992; *Nicolas and Boudier*, 1995; *Boudier et al.*, 2000; *Adachi and Miyashita*, 2003; *Miyashita et al.*, 2003; *Umino et al.*, 2003]. Here, they are referred to as domains of "ridge segmentation" and opposed to domains where the accretion should have been steady state, called here "normal" domains, considering their continuity and homogeneity. To better identify and estimate the fraction of the Oman ophiolite affected by ridge segmentation we used, as first criterion, the occurrence of gabbronorite and large diorite-trondjhemite bodies; both are, without ambiguity, late intrusions in RZSDC and they have been attributed to hydrated magmas [*Boudier et al.*, 2000]. However, trondjhemites are also present, as small bodies, in domains away from segmented areas. Consequently, only the bodies larger than 1 km in extension were considered to define the domains of ridge segmentation. With these criteria, we have estimated, from the geological map of northern Oman at a scale of 1/250,000 [*Ministry of Petroleum and Minerals*, 1992], that the total surface fraction of gabbro areas affected in Oman ophiolite by these large intrusions is 47% versus 53% of "normal" gabbro areas.

[8] Our field study is located in the Sumail massif, one of the southern massifs in the Oman ophiolite where the effects of ridge segmentation are minor (Figure 1). This very large and flat-bottomed synform has been mapped with the highest density of field stations during the systematic structural mapping in this ophiolite, over the last 25 years. The general structure of the ophiolite is dominated by a central, NW-SE trending system which was opened inside a NE-SW trending external domain [*Nicolas and Boudier*, 1995; *Nicolas et al.*, 2000]. The large NW-SE ridge segment extends in the Nakhl and Haylayn massifs to the NW, and in the Wadi Tayin massif to the SE. It is subdivided in individual segments which are centered on a few mantle diapirs.

[9] The area considered here is located between Samrah oasis and Wadi Abda (Figures 1 and 2). This oceanic crust was generated by the NW-SE trending spreading center of Maqsad [e.g., *Jousselin et al.*, 1998].

3. Main Petrostructural Units in the Mapped Area

[10] The map in Figure 2 is based on ~100 main field stations, each one generally covering small cross sections or a few sites of individual measurements. The map also integrates a few geological limits from the geological map of Oman at the 1:100,000 scale [*Ministry of Petroleum and Minerals*, 1986]. For mapping purposes, the following operational units, from top to bottom of the ophiolitic sequence, are retained (see cross section in Figure 2): 1, lavas; 2, sheeted dike complex; 3, RZSDC; and 4, main gabbro unit represented at this level by the uppermost foliated gabbros. The RZSDC lower limit with these foliated gabbros is remarkably sharp, generally marked by a discordance (Figure 2). Its upper boundary is traced where the diabase dikes fraction attains ~90%. These unit boundaries depart only marginally from those of *Nicolas and Boudier* [1991].

3.1. Lavas

[11] Lavas crop out close to Wadi Abda (Figure 2a) and in a small area. In Wadi Abda, lava flows have an orientation of 95S25°, with some dispersion; they are conformable with the underlying sheeted dike unit. As this locality is close to the eastern limit of the Sumail synform, next to an extrusion of the underlying Hawasina sedimentary units, the

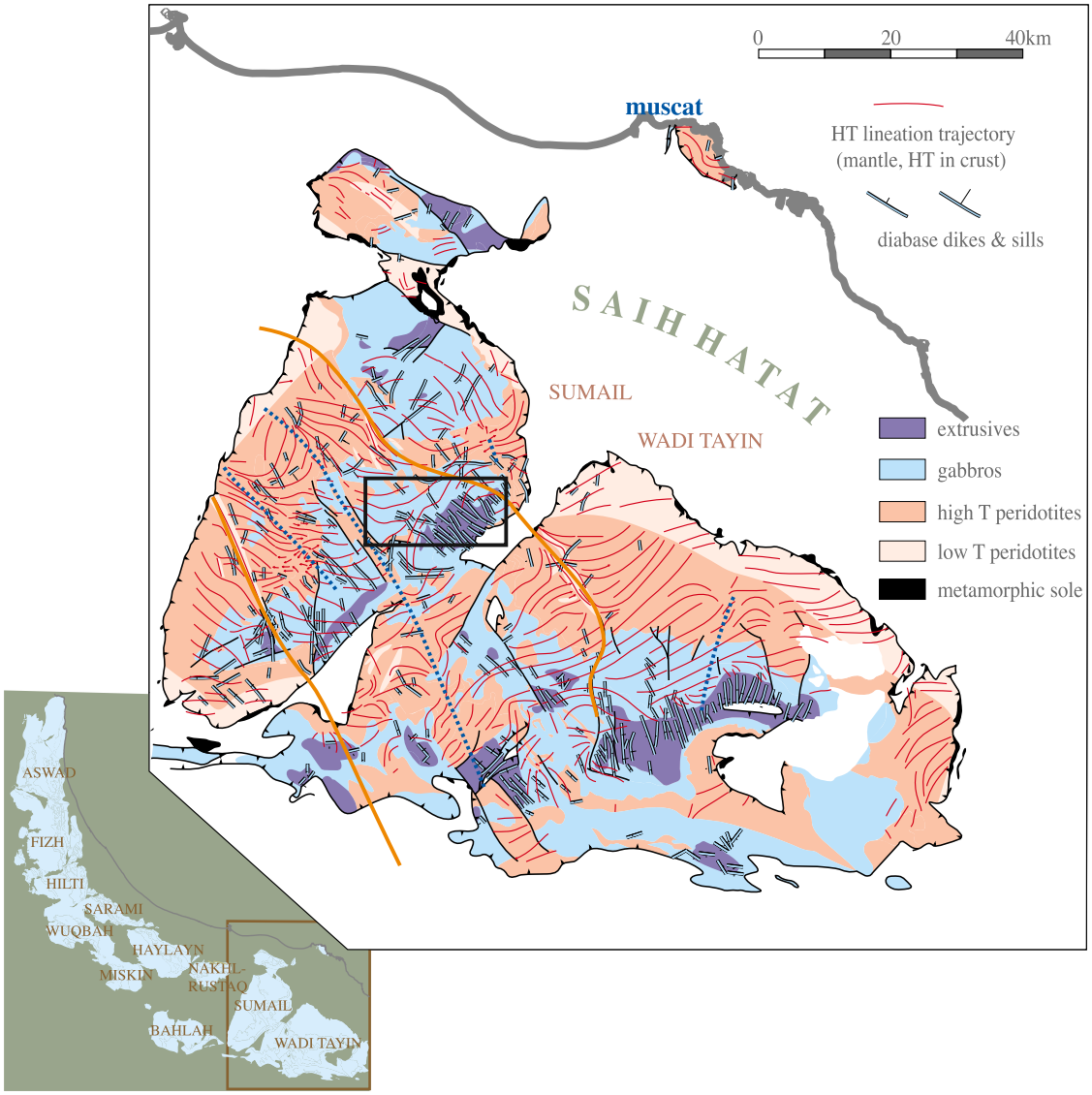

Figure 1. Simplified geological and structural map of Sumail and Wadi Tayin massifs, and location in the Oman ophiolite [after *Nicolas et al.*, 2000]. The black rectangle shows the location of the map in Figure 2. Blue dotted lines are inferred ridge axes, and yellow lines are limits of the large NW-SE segment opened in a NE-SW ridge system.

lava flows may have been locally tilted with respect to more internal units.

3.2. Sheeted Dikes

[12] This unit is composed of parallel, ~1 m thick, diabase dikes, bounded by dark and very fine-grained chilled margins. Older dikes are commonly larger, and seem to be more altered by hydrothermal fluids, grading into epidosites and bounded by epidote-rich veins. Younger dikes are thinner, black and less altered. Average field orientations at each measurement station are based on 10 to 50 individual chilled margins measurements.

[13] In the deepest diabase dikes (2b in cross section, Figure 2), chilled margins are less conspicuous and internal texture is coarser (0.1–0.2 mm) than in the dikes above (2a, Figure 2). They are little affected by greenschist facies, LT, hydrothermal alteration and display, with a brown hornblende an amphibolite, HT, metamorphism (Figure 3a).

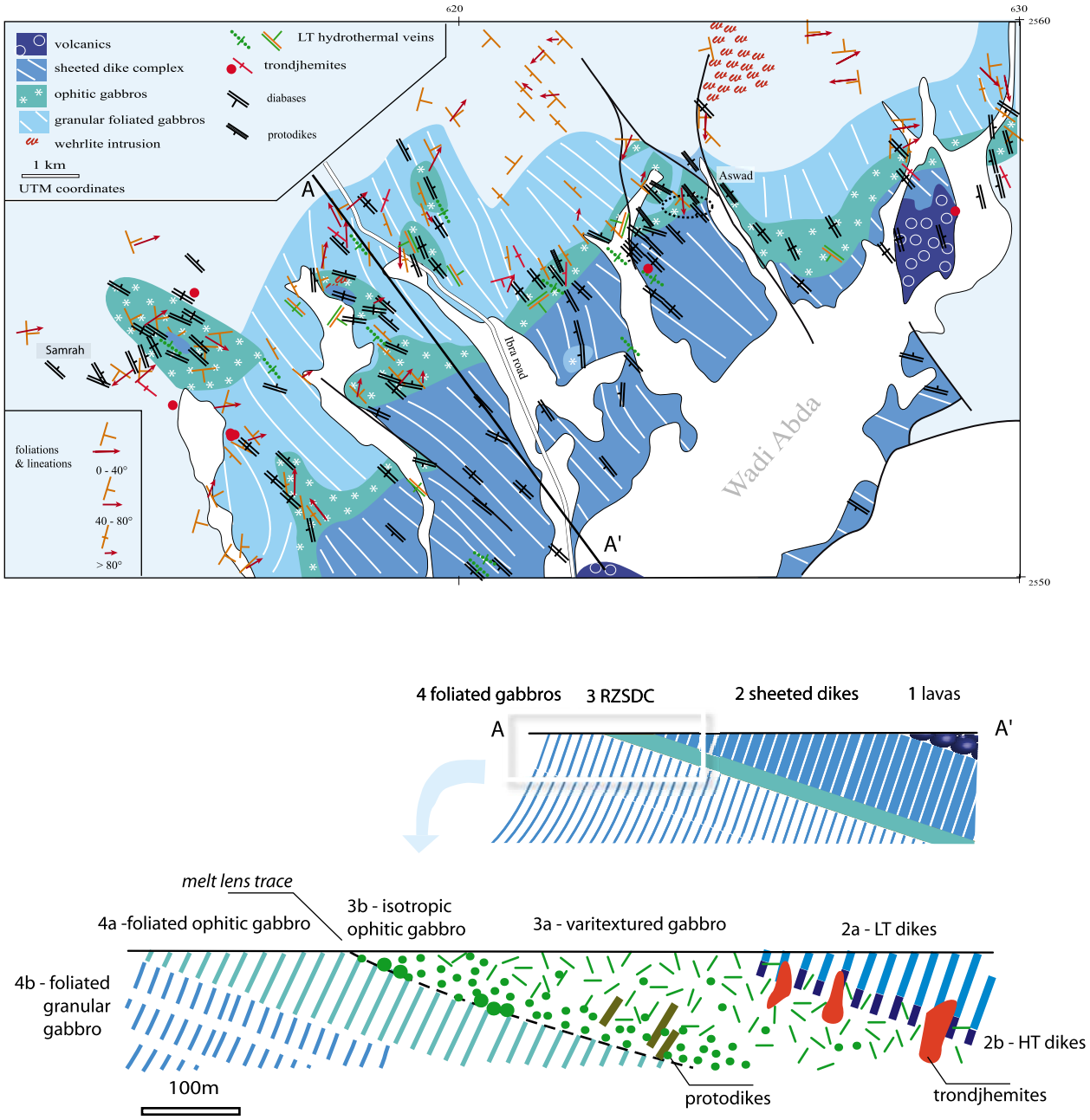

Figure 2. Map and cross section in the upper ophiolite units, from Samrah to Wadi Abda (Sumail massif) (location in Figure 1). Dotted ellipse is Wadi Gaz location. The upper cross section, along the A-A′ profile in map, locates the main units, and the lower cross section (box in the upper section) illustrates the RZSDC structure and petrology.

3.3. Root Zone of the Sheeted Dike Complex

[14] Gabbroic rocks in this critical zone are isotropic (3b in cross section, Figure 2) and varitextured gabbros (3a, Figure 2), characterized by an ophitic texture, where the meshes between the network of plagioclase laths are filled by clinopyroxene oikocrysts, usually altered to hornblende, and olivine grains which usually are totally altered (Figures 3b and 3c). Collectively, we refer to these rocks as "ophitic gabbros."

[15] A crude order of superimposition and relative chronology within the RZSDC can be established from the relations between different ophitic gabbros and other related facies described below, pointing to a decrease of temperature with time. In

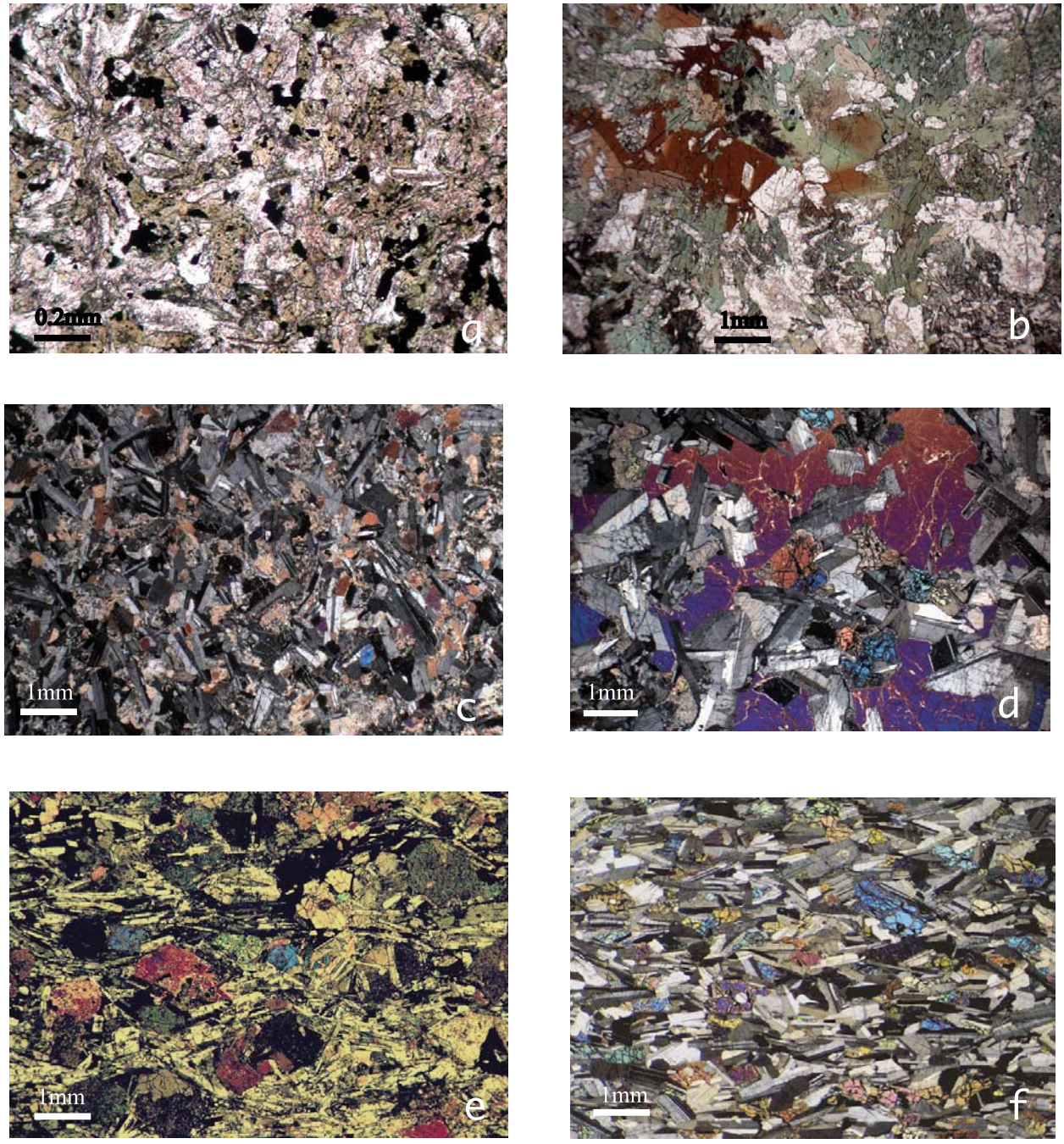

Figure 3. Microphotographs of (a) lowermost HT diabase dike from the sheeted dike complex, characterized by a medium-grained texture and brown hornblende (06OA-31k), (b) varitextured ophitic gabbro where clinopyroxene has been totally replaced by brown and green amphibole (06OA-20a), (c) fine-grained isotropic ophitic gabbro with interstitial brown hornblende and clinopyroxenes altered in green hornblende (OM06-25), (e) dry to nearly dry coarse-grained isotropic ophitic gabbro from the base of the RZSDC in which olivine presents a thin rim of HT hydrous alteration (06OA-2), (e) foliated, ophitic gabbro with plagioclase laths molded around subhedral clinopyroxene, from a few meters below the RZSDC, and (f) foliated granular upper gabbro from the gabbro unit (OM06-17).

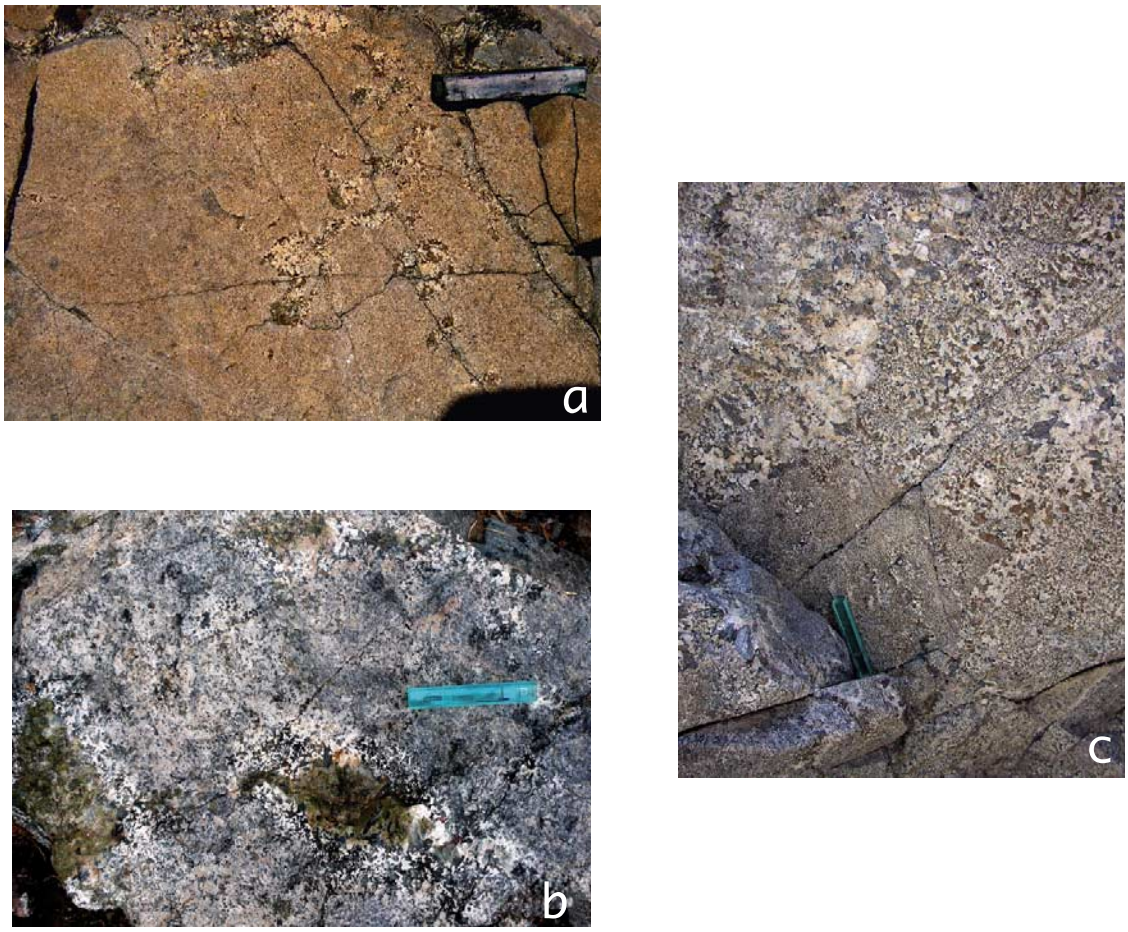

Figure 4. Facies of varitextured gabbros (scale bar is 10 cm). (a) Isotropic ophitic gabbro evolving in varitextured gabbro within nests of pegmatitic recrystallization (06OA20). (b) Varitextured ophitic gabbro with nests of LT (greenschist facies) crystallization with epidote-rich cores, indicative of an evolution ending with an episode of "autometamorphism" (06OA23). (c) Varitextured and pegmatitic ophitic gabbro with rooting of a pegmatitic dike (05OA17).

this respect, it is critical to integrate the results on a HT seawater alteration, ubiquitously present in the main gabbro unit [*Gregory and Taylor*, 1981; *Stakes and Taylor*, 1992; *Manning et al.*, 2000; *Nicolas et al.*, 2003; *Bosch et al.*, 2004]. Mineral assemblages resulting from HT ($\leq$1000°C) reactions described in the gabbro unit are also recorded in the RZSDC, with generally a complete HT alteration of olivine in a mixture of pale hornblende and chlorite, and of clinopyroxene in brown hornblende. The $\geq$1000°C hydrous reactions that develop orthopyroxene are not common in the RZSDC described here, in contrast with areas related to ridge segmentation [*Boudier et al.*, 2000].

[16] At the base of the RZSDC, just above the foliated gabbros described below, locally, restricted gabbro outcrops present a coarser isotropic ophitic texture, where olivine is still present in stocky crystals together with disordered plagioclase laths (plagioclase is also present in olivine as minute inclusions)(larger green dots in cross section, Figure 2). The meshes within the plagioclase framework are occupied by poikilitic clinopyroxene and opaque minerals (Figure 3d). Such gabbros have only a limited HT hydrous alteration, following the terminology defined by *Bosch et al.* [2004] in the main gabbro unit. In order to distinguish them from the overlying ophitic gabbros, we call them the dry ophitic gabbros. The transition from this thin horizon of mildly or no hydrated gabbros to the largely hydrated, overlying ophitic gabbros can be traced in the field. Small hills with reddish, weathered blocks of dry ophitic gabbros and underlying granular gabbros contrast with more grayish low lands formed by hydrated ophitic gabbros.

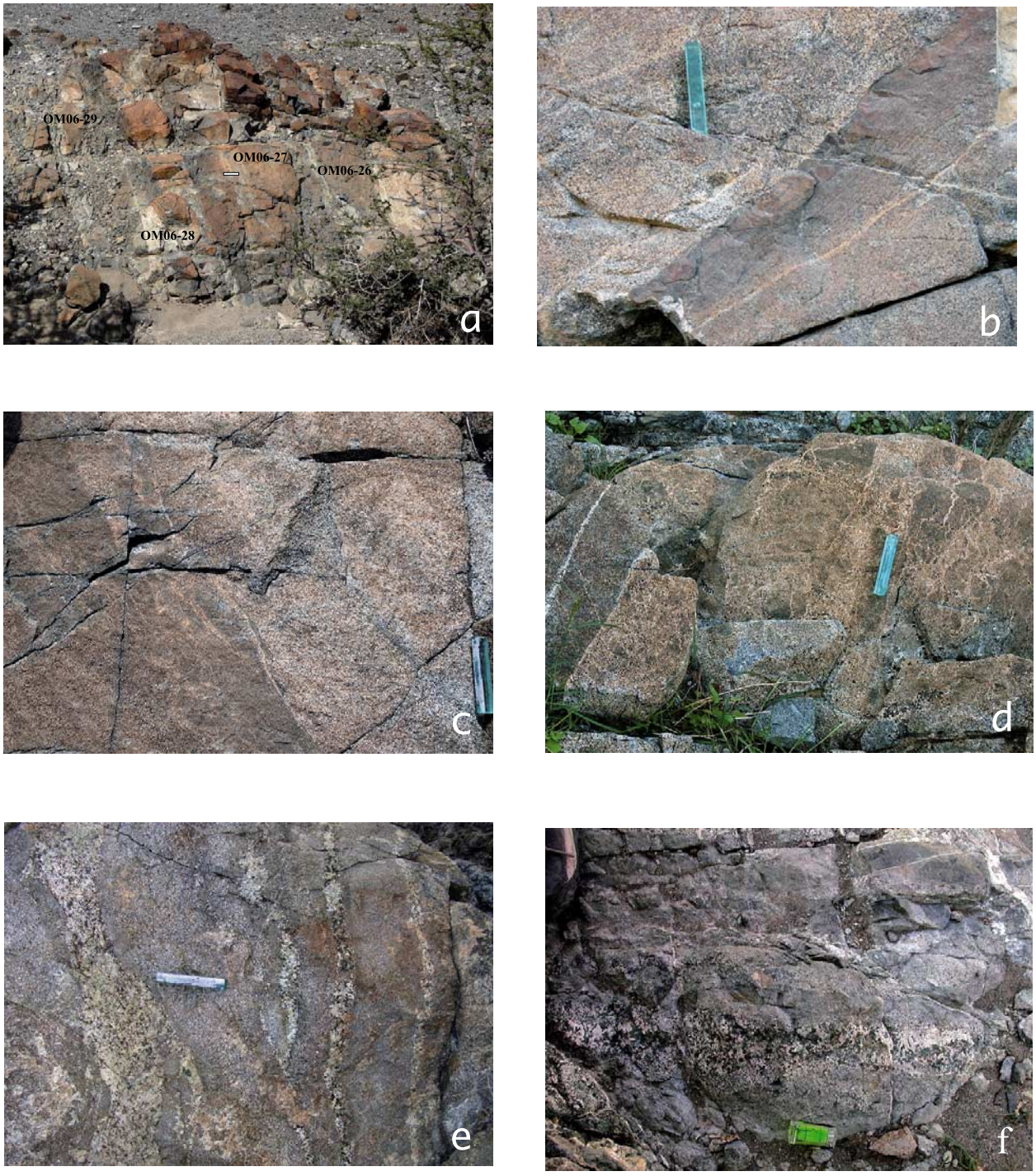

Figure 5. Diabase protodikes (scale bar is 10 cm). (a) Swarm of protodikes and dioritic intrusions (outcrop 06OA31, with reference to microprobe analysis sampling). (b) Sliver of a protodike with its microgranular margin intruding an ophitic gabbro (top, left) and grading internally into an ophitic gabbro (89OA101). (c and d) Same outcrop as Figure 5b, showing in Figure 5c a dark and fine-grained protodike margins and in Figure 5d a brecciated protodike, both being dismembered and assimilated by a gabbroic matrix. (e and f) HT pegmatitic gabbro dikes crosscutting protodikes (06OA2) (scale bar in Figure 5f is 3 cm).

[17] Isotropic ophitic gabbros may recrystallize in varitextured, locally, pegmatitic gabbros (Figure 4). In the varitextured gabbros, olivine is totally altered; clinopyroxene oikocrysts are largely or totally replaced by a brown hornblende grading into greenish hornblende (Figure 3b). In the field, pegmatitic varitextured gabbros are found as veins and inside circular patches, some 10 cm across, with dark green amphibole at the margin, whitish plagioclase in between and, commonly, epidote in the center (Figure 4b). Pegmatitic gabbros intrusions are either parallel to the sheeted dikes or flat-lying sills (Figure 4c).

[18] Diorites and trondjhemites occur as later intrusions of restricted size in the studied area, but can be hundreds of meters in segmentation-related areas. Trondjhemites are located close to, or within, the sheeted dike complex, commonly making up the dominant screen in the transition zone to the 100% sheeted dike unit. Trondjhemites are also observed in magmatic, brecciated dikes and sills in which they constitute the matrix surrounding corroded diabase fragments.

3.4. Protodikes With Microgranular Margins

[19] *Nicolas and Boudier* [1991] described "diabase protodikes" in the Oman RZSDC. They differ from other diabase dikes by their microgranular versus chilled margins and by a coarser and occasionally fluidal, ophitic texture, slightly different in this respect from their ophitic gabbros country rocks. When the protodikes are not brecciated, their orientations are within 10–20° to those of sheeted dikes (Figure 8). They can be isolated or mutually intrusive as in any dike swarm (Figure 5a), but most commonly, they are dispersed in an ophitic gabbro matrix. Protodike margin texture is microgranular and mosaic-shaped, with stocky plagioclase (Figure 6a). An anomalous concentration in opaque phases is locally noted in these fine-grained margins. Although hardly visible in thin section, protodikes contain a good preferred crystallographic orientation parallel to that of the dike, thus recording upward magmatic flow (Figures 6a and 6b). This fabric concerns mainly plagioclase, and is stronger in the microgranular margins (Figure 6a) than in the center (Figure 6b). In contrast with protodike cores which vanish into their ophitic gabbro matrix, the microgranular margins are very symptomatic because they survive to dike-in-dike intrusions, either as thin lenses inducing a fluidal aspect to (Figures 5b and 5c), or as blocks in magmatic breccias (Figure 5d). Orthopyroxene occurrence in the microgranular margins of protodikes is uncommon and restricted to some localities.

[20] Protodikes are usually emplaced in isotropic ophitic gabbros. They are, in turn, intruded by varitextured pegmatitic gabbros (Figures 5e and 5f). This demonstrates that their intrusion commonly occurred in the RZSDC after crystallization of the isotropic gabbros but before that of the varitextured gabbros. However, there is a continuum between protodikes and the LT diabase dikes with typical chilled margins. Some basaltic dikes are devoid of chilled margins and are coarser-grained in their center. The presence of diabase protodikes with their typical microgranular margins can be considered as a specific attribute of RZSDC. Finally, it should be mentioned that the microgranular texture is similar to that observed in microgabbronorites in the granular gabbros where they form lenses parallel to the gabbro layering (see below).

3.5. Foliated, Ophitic, and Granular Gabbros

[21] The base of the RZSDC is locally difficult to identify, despite the fact that it is a sharp discordance between overlying isotropic, ophitic gabbros and underneath foliated, ophitic gabbros (4a in cross section, Figure 2). Their foliation is magmatic (Figure 3e) commonly underlined by anorthosite layers. Foliation and layering are parallel to the general trend of the overlying sheeted complex and the associated lineation is steep. In the field, foliation and layering are commonly obliterated by large and irregular zones of recrystallized gabbros which had been ascribed to hydrous partial melting triggered by seawater intrusion at the wall of the magma chamber below the melt lens [*Nicolas et al.*, 2003; *Bosch et al.*, 2004] (Figure 4).

[22] Downward, the foliated, ophitic gabbros grade into the gabbro unit, through the foliated, granular gabbros (4b, Figure 2). Their texture is dominated by preferentially oriented tabular plagioclase laths, defining a strong magmatic foliation, together with elongated olivine aggregates and more stocky clinopyroxene grains (Figure 3f).

[23] In both the foliated, ophitic and granular gabbros, the layering is generally absent, or defined by anorthosite and microgabbro lenses, usu-

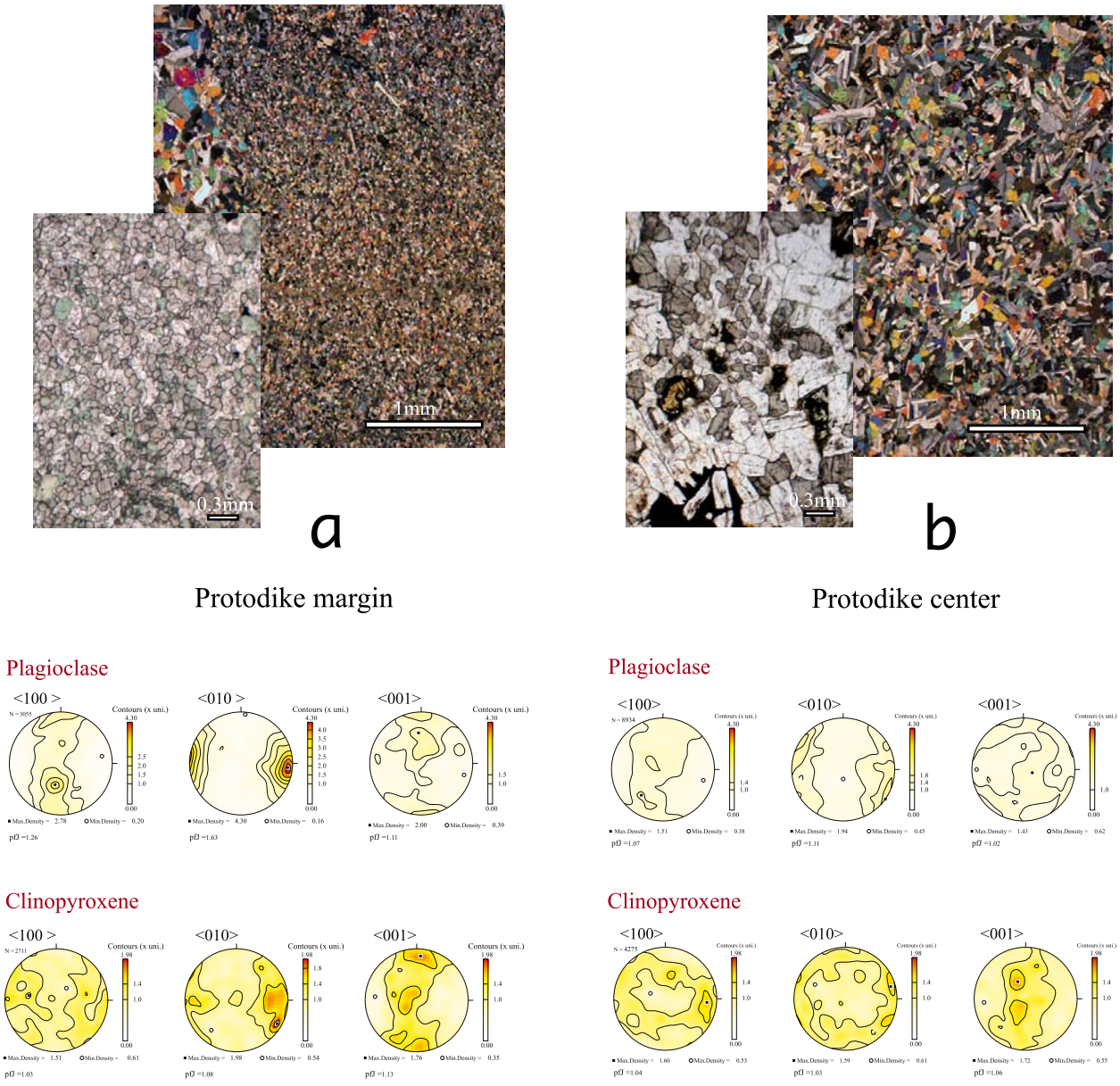

Figure 6. (a) (top) Plane polarized light microphotograph across the margin of a vertical protodike (06OA31) with, superimposed, enlarged and plain light view of the microgranular texture and (below) related crystallographic preferred orientation. (b) (top) Plane polarized light microphotograph of the ophitic protodike center (same sample as Figure 6a), with, superimposed, enlarged and plain light view of the ophitic texture and (bottom) related crystallographic preferred orientation. Crystallographic preferred orientations are Electron BackScattering Diffraction (EBSD) measurements (lower hemisphere, nonpolar data, stereoplot in the structural reference frame with dike margin NS vertical).

ally no more than 10 cm thick. Textures in microgabbro and microgabbronorite lenses compare with the microgranular margins of protodikes, though generally more foliated. They are thought to derive from diabase dikes stopping into the melt lens, and recrystallizing in the water which they introduced [*MacLeod and Rothery*, 1992; *Nicolas et al.*, 2000; *Coogan et al.*, 2003].

[24] In the Aswad area (Figure 2), within the upper granular gabbros about 100 m below the transition to the RZSDC doleritic gabbros, the steep magmatic foliation is locally sharply crosscut by a ~50 m thick sill complex of pegmatitic doleritic

Figure 7. (a) Sill with multiple intrusions of varitextured ophitic gabbros and one protosill, emplaced in the uppermost foliated gabbros (06OA2). (b) Contact between the steeply foliated gabbro (bottom) and the base of the sill (top). Scale bar is 10 cm.

gabbro and protosills (similar to a protodike, but in a sill orientation) (Figure 7).

4. Structural Relationships in Map

[25] The orientation of diabase dikes in the sheeted dike complex is fairly homogeneous (Figure 8), on average 135°E, vertical (Figure 8) which remains unchanged within the RZSDC. The LT hydrothermal veins and the protodikes are oriented 135°E, vertical too and, more loosely, the pegmatitic gabbros and trondjhemite intrusions, which are either close to the sheeted dikes or flat-lying. Foliations in the uppermost foliated gabbros are also, on average, parallel to the sheeted dikes.

[26] Another striking feature of the RZSDC is its limited thickness. Its horizontal extension in the field varies from less than 500 m, which is an upper limit, to less than 200 m in a few places. The average lava flow orientation, 95S25°, may exceed the general dip of the paleohorizontal, because they are located close to the thrust limit of the Sumail massif. We rather rely on the many measurements indicating that in the northern area, between Wadi Abda and north of Ibra road, the crust/mantle boundary is on average oriented 90S15°. An average ESE dip of ~20° seems to be a good estimate for the RZSDC in the considered domain. Bracketing the RZSDC lateral extension between 200 and 500 m, with a 20° dip, its thickness ranges from 70 to 170 m. We retain an average thickness of 100 m which is consistent with previous estimates in Oman [*Rothery*, 1983; *Nicolas and Boudier*, 1991; *MacLeod and Yaouancq*, 2000]. There are, however, minor local variations in thickness, in addition to the major ones described below. A vertical variation of the upper limit of 30 m, over a distance of 100 m has been locally measured in northern Oman.

5. Wadi Gaz Section: Microprobe Analysis

[27] A detailed petrographic and microprobe analysis has been carried on a sampling of Wadi Gaz (Figure 2), in an area covering a complete section from the upper level foliated ophitic gabbros to the sheeted dike complex (Figure 9). The RZSDC extends over ~70 m in thickness, on the eastern slope of the wadi, but continuous exposure is

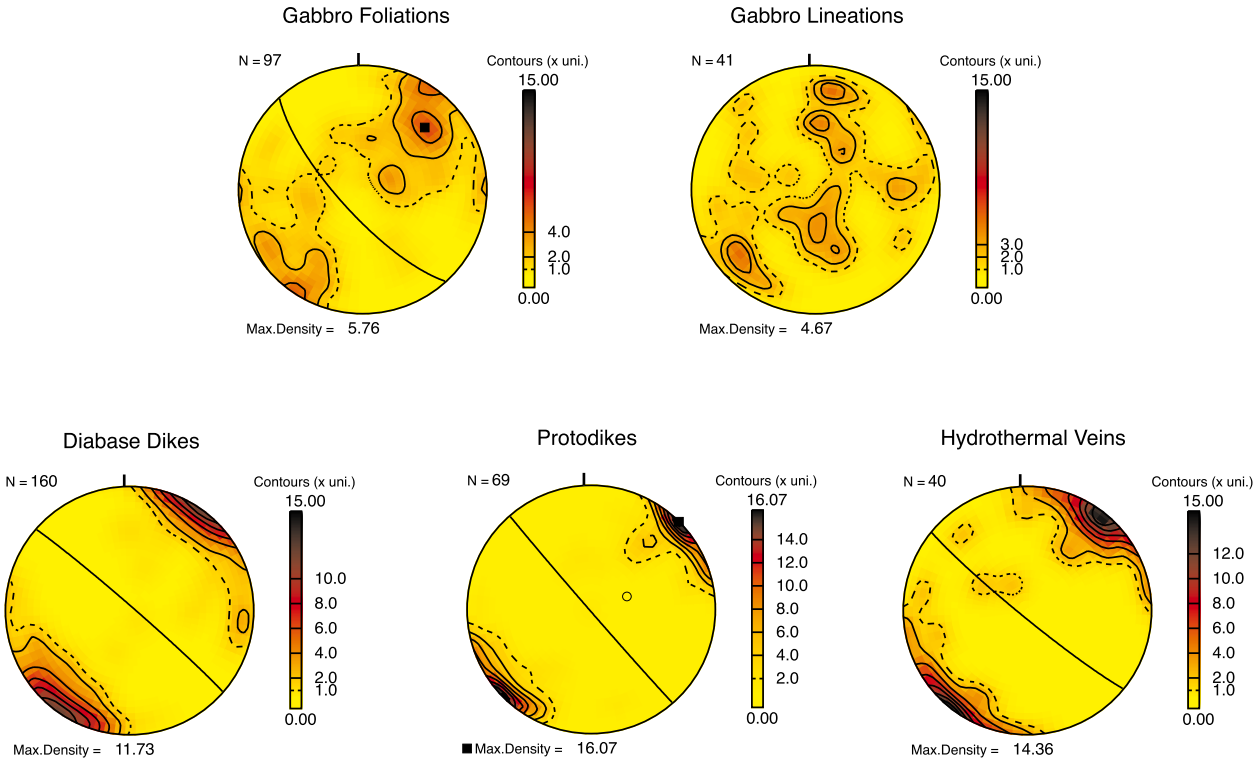

Figure 8. Stereonets of field structures (geographical reference frame, lower hemisphere of projection, nonpolar data). Thirty percent of the measurements come from small areas near Aswad.

Figure 9. Photograph of the Wadi Gaz area sampled for detailed textural and petrographical study. Analyzed samples (Tables 1 and 2) are plotted; see also Figure 2.

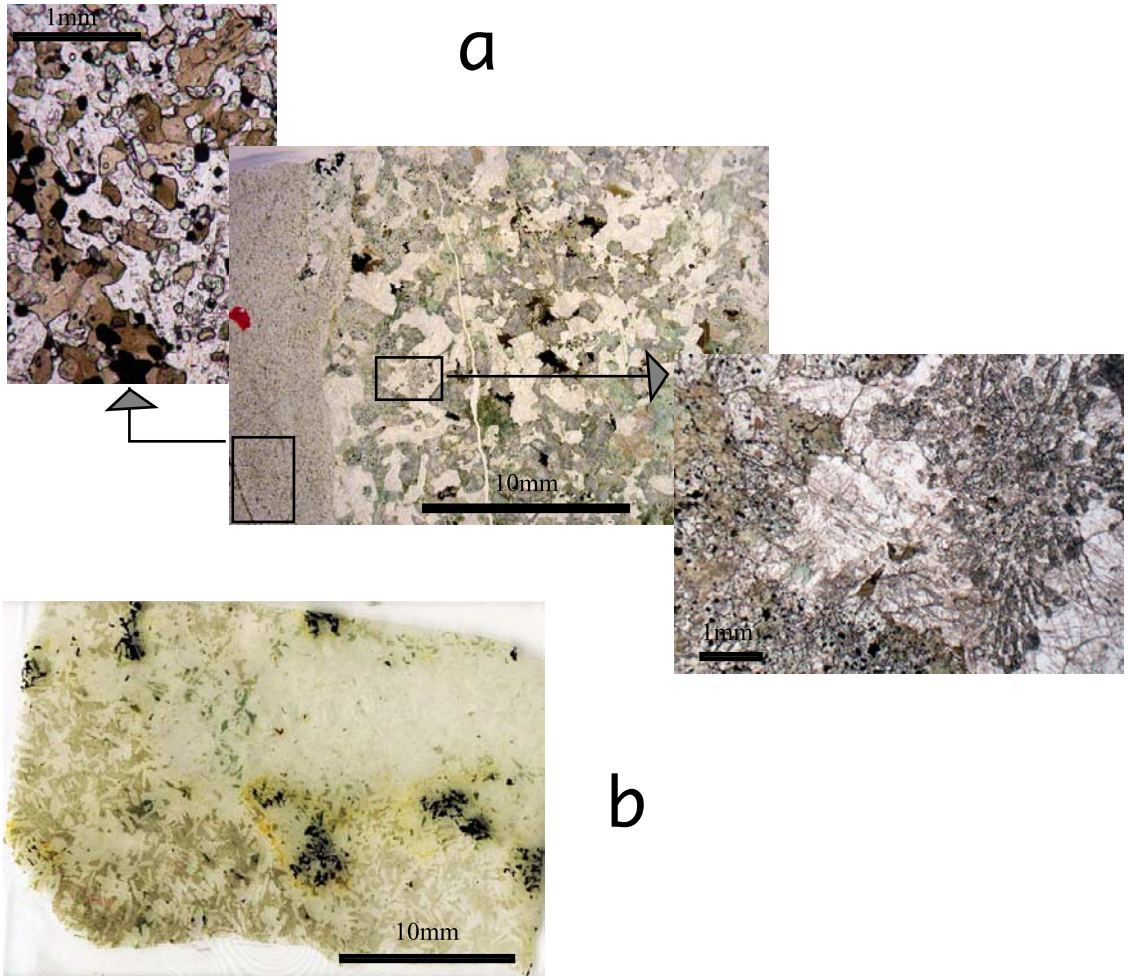

Figure 10. Microphopographs of critical zones studied. (a) Development of granoblastic texture in ophitic gabbro at contact of a microgranular protodike (sample OM06-22). Both ophitic gabbro and protodike contain pargasitic amphibole, specially developed along a microcrack in the protodike. (b) Subophitic domain in contact with intergranular domain at scale of the thin section, in varitextured gabbros (sample OM06-30). The subophitic domain is remarkably fresh and contains poikilitic Ti-rich pargasite associated with poikilitic ilmenite; the intergranular domain is weathered and devoid of oxides.

limited between the wadi bed and the terrace where the upper road circulates (Figure 9). The terrace level is some 10 m below the sheeted dike complex. The base of the RZDSC is well marked by a sharp contact between foliated and isotropic ophitic gabbro. Above this horizon, there is a zone of isotropic gabbros, locally intruded by a sheeted protodike complex, cropping out horizontally and vertically over 10 to 20 m (Figure 5a), a feature which is uncommon and specially well exposed in Wadi Gaz. Protodikes are associated with dioritic intrusions. The center of these dikes is composed of ophitic gabbros, locally displaying a fluidal texture with a crystallographic fabric (Figure 6b), grading outward into microgranular margins (Figure 6a). Microgranular margins are also isolated in the ophitic gabbro matrix, either as slivers or as brecciated blocks. The upper level of the RZSDC is marked by a rapidly increasing abundance of diabase dikes, reaching 50% diabase dikes at the terrace level. Varitextured gabbros, together with trondjhemitic intrusions, are the predominant screens between diabase dikes. The first diabase dikes are metamorphosed in amphibolite facies conditions, containing a brown-green hornblende (Figure 3a), in contrast with the overlying dikes which are in the greenschist facies.

[28] The studied samples are located on Figure 9, their textures are imaged in Figures 3 and 10, they are described in Table 1, and their major elements analyses are presented in Table 2.

Table 1. Description of Analyzed Samples

Sample	Description	Texture	Grain Size	Photograph
OM06-17	foliated granular olivine-gabbro located 900 m beneath the RZSDC, 2 km west of Aswad farm, foliation marked by plagioclase tablets elongation and by alignment of tabular clinopyroxene fresh olivine except oxidation in microcracks, small amount of brown amphibole.	foliated granular	1–2 mm	Figure 3f
OM06-18	foliated equigranular microgabbro lens in OM06-17 gabbro plagioclase, clinopyroxene, no oxides; alteration microveins including mylonite.	microgranular	0.5 mm	
OM06-22	microgranular margin of a protodike including larger (0.1 mm) pargasitic amphiboles and its contact with ophitic gabbro, with pargasitic amphibole.	microgranular (margin)	0.02 mm	Figure 10a
		ophitic (gabbro)	1 mm	
OM06-24 and 25	ophitic gabbro, variable grain size, clinopyroxene interstitial and locally replaced by brown and green hornblende.	ophitic	1–5 mm	Figure 3c
OM06-26	microgabbro, margin of a protodike, rich in oxides (magnetite and ilmenite); except for their rim clinopyroxene phenocrysts have a composition significantly different from clinopyroxene in the matrix.	microgranular	0.1 mm	Figure 5a
OM06-27	ophitic gabbro with HT pargasitic amphibole largely replaced by magnesio-hornblende, both interstitial around clinopyroxene and reactional inside them.	ophitic	3–5 mm	Figure 5a
OM06-28	diorite with plagioclase, interstitial clinopyroxene replaced by magnesio-hornblende rare high-T amphiboles, magnetite, ilmenite.	ophitic	1 mm	Figure 5a
OM06-29	ophitic gabbro with poikilitic clinopyroxene replaced by medium-T magnesiohornblende, totally altered olivine, rare oxides.	ophitic	1 mm	Figure 5a
OM06-30	varitextured ophitic gabbro with 10 mm poikilitic clinopyroxene including plagioclase laths, poikilitic iron oxide, in contact with an intergranular finer-grained domain devoid of iron oxides.	ophitic		Figure 10b
06OA-31b and c	respectively margin and center of a protodike intruding and brecciating ophitic gabbro center and margin of the dike have similar minerals composition.			Figures 6a and 6b
	•margin fine-grained (Figure 6a) with polygonal plagioclase, clinopyroxene with 1% titanium value, totally altered olivine and ~10% interstitial iron oxides.	microgranular	0.1 mm	
	•center ophitic gabbro with prismatic pl and granular clinopyroxene evolving locally in clots of polygonal grains, oxidized olivine.	ophitic	1 mm	

Table 1. (continued)

Sample	Description	Texture	Grain Size	Photograph
06OA-2b	coarse-grained "dry" ophitic gabbro, located at contact with a foliated ophitic gabbro, with plagioclase laths randomly oriented, locally included in 5 to 10 mm sized poikilitic clinopyroxene. hydrous alteration limited to fibrous rims of chlorite and actinolite surrounding olivine interstitial amphiboles (<1%) zoned from brown to blue-green.	coarse ophitic	3–5 mm	Figure 3d
06OA-20a	varitextured ophitic gabbro, pl (∼1 mm) zoned and altered, interstitial clinopyroxene (5 to 10 mm), grading into brown, then green amphibole.	ophitic	1 mm 5–10 mm	Figure 3b

[29] On the basis of plagioclase-clinopyroxene compositions, most rocks are highly primitive, with plagioclase, 86% An and clinopyroxene, Mg# 86 (Figure 11). They grade into moderately differentiated gabbroic rocks. The most differentiated rock is dioritic with plagioclase 43% An and clinopyroxene, Mg# 73. No orthopyroxene has been observed in the samples analyzed. The composition of amphiboles is shown in Figure 12, where the estimated thermometry is derived from *Koepke et al.* [2005a], on the basis of reliability of the TiO_2-in-amphibole thermometry, and coexisting amphibole-plagioclase thermometer of *Holland and Blundy* [1994], applied to oceanic gabbros (see detail in Figure 12a). Thus the amphibole compositions constrain the crystallization path of these gabbros. One typical protodike microgranular margin (OM06-22) (see Figure 10a) contains a pargasitic amphibole grown at very high temperature (∼1000°C). All sampled gabbros contain, as interstitial or overgrowth phases, pargasites formed at >900°C, down to edenites and magnesiohornblendes, formed at 800–700°C. TiO_2 content of amphiboles is highly variable. We notice that amphiboles with high TiO_2 content (2.55 to 5.07) are high-T pargasitic amphibole that coexist with ilmenite (see Figure 10b), as outlined in the composition of oceanic gabbros [*Koepke et al.*, 2005a]. We notice the wide range in values of TiO_2 (0 to 5% for whole rock) coupled with variable An content in plagioclase that also characterize the varitextured gabbro and dike root zone in the best documented gabbro section of Wadi Abyad in Oman [*MacLeod and Yaouancq*, 2000]. The pargasitic amphiboles in the present study are also rich in fluor (Figure 12b) and, by comparison with compilation of oceanic gabbros by *Coogan et al.* [2001], pargasites from Wadi Gaz area exhibit high chlorine content (1000–2000 ppm), in the same order as amphiboles from the Oman gabbro section compiled by *Coogan* [2003].

6. Discussion

6.1. Structure of the RZSDC in the Mapped Area

[30] A remarkable feature of RZSDC is the common, dominant orientation of all structures parallel to diabase dikes in the sheeted complex (Figure 8): LT hydrothermal veins, tonalite-trondjhemite intrusions, diabase protodikes and foliated gabbros below the RZSDC. As the sheeted dike complex is generally assumed to be parallel to the ridge symmetry plane, most structures in the RZSDC and below should be parallel to the ridge symmetry plane, which also controls the shape of the magma chamber [*Nicolas et al.*, 1988; *Chenevez et al.*, 1998].

[31] This simple RZSDC model is locally modified in different ways, some of which being illustrated in the studied area (Figure 2). West of the Aswad farm, RZSDC formations constitute a sill, 10 m thick, which transects steeply dipping foliated gabbros from the gabbro unit (Figure 7). This may relate to lateral or downward migration of the melt lens position with time. Near the Luzugh oasis (Sumail massif), the RZSDC overlies a flat-lying foliated ophitic gabbros. This is possibly due to rapid lateral migration or subsidence of the melt lens. Subsidence of melt lens has been documented at the East Pacific Rise

Table 2. Minerals Composition

Samples	Lithology	Phase	SiO_2	TiO_2	Al_2O_3	Cr_2O_3	FeO	MnO	NiO	MgO	CaO	Na_2O	K_2O	F	Cl	Total	XMg	Xan
OM06-17	ol-gabbro	ol	38.69	0.02	0.02	0.01	21.97	0.36	0.09	39.70	0.11	0.01	0.01			100.99	76.31	
OM06-17	ol-gabbro	cpx	52.61	0.50	2.26	0.15	6.31	0.20		16.66	21.15	0.28	0.00			100.11	82.48	
OM06-17	ol-gabbro	pl core	48.87	0.04	32.16	0.02	0.48	0.01		0.04	15.96	2.69	0.03			100.29		76.62
OM06-17	ol-gabbro	pl rim	50.06	0.07	31.11	0.01	0.50	0.01		0.07	14.66	3.39	0.07			99.96		70.51
OM06-18	mocrogabbro	cpx	52.14	0.66	2.70	0.16	6.57	0.15		16.18	21.36	0.32	0.00			100.24	81.44	
OM06-18	microgabbro	pl	49.33	0.05	31.89	0.00	0.53	0.02		0.04	15.68	2.92	0.03			100.50		74.78
OM06-22	dike	pl relict	45.42	0.02	34.09		0.49	0.06		0.00	18.46	1.21	0.03			99.79		89.42
OM06-22	dike	pl	56.76	0.04	27.29		0.49	0.01		0.02	9.37	6.37	0.25			100.60		44.83
OM06-22	dike	mt	0.09	5.54	1.29		87.69	0.05		0.00	0.14	0.05	0.00			94.86	0.00	
OM06-22	dike	il	0.08	49.68	0.01	0.02	49.35	2.48		0.05	0.27	0.00	0.00			101.95		
OM06-22	dike	cpx	52.91	0.20	0.81	0.04	9.04	0.29		15.10	22.12	0.31	0.01			100.83	74.86	
OM06-22	dike	am	43.28	3.31	9.49	0.02	13.94	0.19	0.02	13.32	11.36	2.31	0.55	0.07	0.26	98.11	63.01	
OM06-22	granoblastic in gabbro	cpx	51.76	0.59	2.42	0.40	7.85	0.22		15.01	22.12	0.39	0.00			100.76	77.32	
OM06-22	granoblastic in gabbro	am	43.06	2.06	11.06	0.33	12.15	0.17		14.17	11.64	2.33	0.71			97.68	67.52	
OM06-22	granoblastic in gabbro	pl	46.65	0.02	33.79		0.41	0.01		0.00	17.66	1.74	0.04			100.34		84.86
OM06-22	gabbro	cpx	51.67	0.43	2.93	0.46	5.79	0.18		16.41	22.41	0.29	0.01			100.56	83.48	
OM06-22	gabbro	cpx rim	49.70	0.56	2.15	0.66	10.91	0.25		15.12	21.03	0.36	0.01			100.75	71.19	
OM06-22	gabbro	pl	46.41	0.02	33.99		0.44	0.01		0.00	17.70	1.68	0.05			100.30		85.37
OM06-22	gabbro	am	41.95	3.67	10.33	0.09	12.99	0.17	0.03	13.67	11.31	2.80	0.22	0.05	0.15	97.44	65.25	
OM06-22	gabbro	mt	0.07	8.71	1.61	0.81	82.09	0.55		0.21	0.01	0.01	0.01			94.06		
OM06-24	microgabbro	cpx	51.20	0.60	2.32	0.11	6.75	0.19		16.78	20.80	0.31	0.00			99.07	81.58	
OM06-24	microgabbro	am	51.65	0.78	3.06	0.01	14.22	0.26	0.03	16.13	10.43	0.94	0.17	0.05	0.09	97.83	66.91	
OM06-24	microgabbro	pl	50.78	0.05	29.77		0.63	0.04		0.06	13.50	4.07	0.05			98.95		64.71
OM06-25	microgabbro	am	51.27	0.93	4.77	0.40	9.25	0.14	0.02	18.16	11.57	1.23	0.13	0.01	0.10	97.99	77.78	
OM06-25	microgabbro	am	46.48	0.52	9.98	0.02	9.60	0.15	0.03	16.90	11.68	2.21	0.31	0.01	0.13	98.03	75.83	
OM06-25	microgabbro	cpx	51.69	0.76	2.71	0.34	6.64	0.17		16.43	21.26	0.36	0.01			100.36	81.52	
OM06-25	microgabbro	pl	48.55	0.04	32.34		0.31	0.00		0.01	16.06	2.66	0.03			100.01		76.92
OM06-26	microgabbro	il	0.05	50.09	0.01	0.11	44.68	4.99		0.05	0.27	0.01	0.00			100.26		
OM06-26	microgabbro	mt	0.10	9.80	3.65	0.53	77.38	0.48		0.04	0.13	0.01	0.00			92.12		
OM06-26	microgabbro	pl	53.55	0.07	29.14	0.01	0.58	0.01		0.05	12.19	4.87	0.05			100.52		58.04
OM06-26	microgabbro	pl relict	46.32	0.02	33.93		0.49	0.01		0.01	17.86	1.56	0.02			100.20		86.38
OM06-26	microgabbro	pl matrix	52.81	0.07	29.28		0.61	0.02		0.07	12.25	4.80	0.06			99.96		58.49
OM06-26	microgabbro	cpx matrix	50.95	0.96	2.49	0.03	9.29	0.27		14.78	20.86	0.38	0.01			100.01	73.93	
OM06-26	microgabbro	cpx relict	51.76	0.39	3.60	0.95	4.62	0.13		16.58	22.14	0.24	0.01			100.42	86.49	
OM06-26	microgabbro	cpx rim	51.17	0.85	2.57	0.08	9.03	0.26		14.97	20.86	0.37	0.01			100.17	74.73	
OM06-27	gabbro	am core	45.44	2.42	7.89	0.02	15.50	0.22	0.04	13.13	10.78	2.29	0.21	0.18	0.23	98.35	60.16	
OM06-27	gabbro	am rim	51.27	0.53	3.41	0.00	14.48	0.23	0.01	15.69	11.10	1.07	0.09	0.05	0.16	98.09	65.89	
OM06-27	gabbro	am interst	41.27	5.07	11.08	0.03	14.93	0.23		11.45	11.06	2.98	0.08			98.19	57.75	
OM06-27	gabbro	cpx	52.64	0.27	0.71	0.00	9.65	0.35		14.41	21.88	0.24	0.00			100.15	72.69	
OM06-27	gabbro	mt	0.07	9.97	1.46	0.11	82.00	0.47		0.06	0.00	0.01	0.01			94.16		
OM06-27	gabbro	il	0.00	48.05	0.09	0.02	50.26	1.19		0.15	0.03	0.01	0.01			99.81		
OM06-27	gabbro	pl	55.57	0.06	27.74	0.01	0.54	0.01		0.04	10.22	5.68	0.06			99.94		49.85
OM06-27	gabbro	cpx	52.02	0.69	1.76	0.01	9.72	0.28		15.06	20.50	0.38	0.02			100.42	73.42	

Table 2. (continued)

Samples	Lithology	Phase	SiO_2	TiO_2	Al_2O_3	Cr_2O_3	FeO	MnO	NiO	MgO	CaO	Na_2O	K_2O	F	Cl	Total	XMg	Xan
OM06-28	gabbro	cpx	51.20	1.04	1.99	0.01	9.71	0.28		14.92	20.35	0.45	0.01			99.96	73.26	
OM06-28	gabbro	il	0.01	49.45	0.02	0.00	51.00	1.33		0.17	0.06	0.00	0.00			102.04		
OM06-28	gabbro	mt	5.39	12.05	2.52	0.10	68.89	0.60		1.38	2.48	0.01	0.02			93.44		
OM06-28	gabbro	pl	56.69	0.07	26.27		0.50	0.01		0.04	9.19	6.71	0.07			99.56		43.10
OM06-29	ol-gabbro	ol	38.66	0.03	0.01	0.00	24.06	0.44	0.09	37.83	0.06	0.03	0.02			101.23	73.70	
OM06-29	ol-gabbro	pl	47.48	0.04	33.43		0.50	0.02		0.03	16.64	2.11	0.03			100.29		81.34
OM06-29	ol-gabbro	cpx	51.59	0.39	2.69	0.44	4.36	0.13		17.18	21.54	0.25	0.01			98.59	87.54	
OM06-29	ol-gabbro	am	49.82	0.97	5.32	0.02	11.30	0.16	0.03	16.32	11.59	1.20	0.23	0.01	0.24	97.21	72.02	
OM06-30	sub-ophitic gabbro	am	45.88	2.55	7.54	0.01	14.69	0.32	0.01	13.77	10.35	2.74	0.22	0.54	0.13	98.74	62.56	
OM06-30	sub-ophitic gabbro	am	42.60	3.75	11.62	0.02	12.53	0.21	0.00	13.35	11.67	3.06	0.03	0.40	0.03	99.27	65.52	
OM06-30	sub-ophitic gabbro	mt	0.36	8.98	2.14	0.09	82.21	0.17		0.12	0.01	0.04	0.01			94.13		
OM06-30	sub-ophitic gabbro	cpx	52.42	0.93	2.74	0.14	7.07	0.21		16.31	20.59	0.35	0.01			100.75	80.45	
OM06-30	sub-ophitic gabbro	pl core	53.06	0.07	30.13		0.57	0.02		0.07	12.35	4.59	0.05			100.90		59.78
OM06-30	sub-ophitic gabbro	pl rim	65.54	0.00	22.41	0.00	0.26	0.02	0.00	0.00	2.74	10.26	0.11			101.34		12.84
OM06-30	intergranular	pl relict	65.31	0.00	22.50	0.00	0.03	0.01	0.00	0.02	2.89	10.13	0.18			101.06		13.61
06 OA 31c	protodike center	cpx	50.93	0.87	2.63	0.04	8.74	0.19		14.60	20.25	0.39	0.01		0.02	98.78	74.86	
06 OA 31c	protodike center	pl	53.75	0.08	29.35	0.02	0.52	0.02		0.07	11.67	4.96	0.05		0.01	100.56		56.50
06 OA 31c	protodike center	ol	43.17	0.01	10.99	0.03	7.97	0.07		22.79	2.09	0.41	0.04		0.01	87.67	83.59	
06 OA 31b	protodike margin	cpx	50.95	0.92	2.66	0.06	8.79	0.21		14.78	20.48	0.37	0.01			99.26	74.98	
06 OA 31b	protodike margin	pl	53.18	0.09	29.09	0.02	0.60	0.02		0.09	12.10	4.70	0.05			99.95		58.74
06 OA 2b	dry ophitic gabbro	ol	39.01	0.01	0.03	0.03	19.53	0.34		40.80	0.20	0.01	0.01		0.00	99.97	78.83	
06 OA 2b	dry ophitic gabbro	pl core	48.25	0.04	32.35	0.03	0.48	0.02		0.05	16.06	2.39	0.03		0.01	99.73		78.79
06 OA 2b	dry ophitic gabbro	pl rim	52.41	0.08	29.56	0.03	0.47	0.02		0.07	12.98	4.22	0.06		0.00	99.91		62.95
06 OA 2b	dry ophitic gabbro	cpx	50.94	1.42	3.09	0.08	6.09	0.19		15.40	21.49	0.46	0.01		0.01	99.29	81.85	
06 OA 2b	dry ophitic gabbro	br-am	44.53	3.49	9.02	0.01	10.14	0.18		15.28	10.63	3.22	0.31		0.03	97.16	72.87	
06 OA 2b	dry ophitic gabbro	am	57.54	0.04	0.46	0.01	3.78	0.11		22.37	12.46	0.23	0.00		0.00	97.21	91.35	
06 OA 2b	dry ophitic gabbro	am	43.36	0.47	10.59	0.01	19.63	0.40		8.68	11.58	1.92	0.16		0.06	96.92	44.06	
06 OA 2b	dry ophitic gabbro	am II	47.14	0.44	8.85	0.02	8.19	0.13		17.90	11.32	2.65	0.25		0.10	97.28	79.58	
06 OA 2b	dry ophitic gabbro	chl	29.58	0.02	18.25	0.02	15.12	0.21		22.24	0.08	0.07	0.16		0.01	85.86	72.38	
06 OA 20	ophitic gabbro	br-am	43.92	3.00	10.24	0.04	12.74	0.17		13.61	10.89	2.59	0.41		0.23	97.92	65.57	
06 OA 20	ophitic gabbro	gr-am	47.26	0.61	8.38	0.03	13.44	0.16		14.09	11.30	1.96	0.20		0.19	97.73	65.14	
06 OA 20	gabbro	pl	47.24	0.05	34.25	0.00	0.60	0.01		0.01	16.80	2.23	0.03		0.02	101.32		80.65
06 OA 20	gabbro	pl rim	51.79	0.11	30.85	0.03	0.58	0.03		0.05	12.99	4.11	0.13		0.01	100.80		63.60

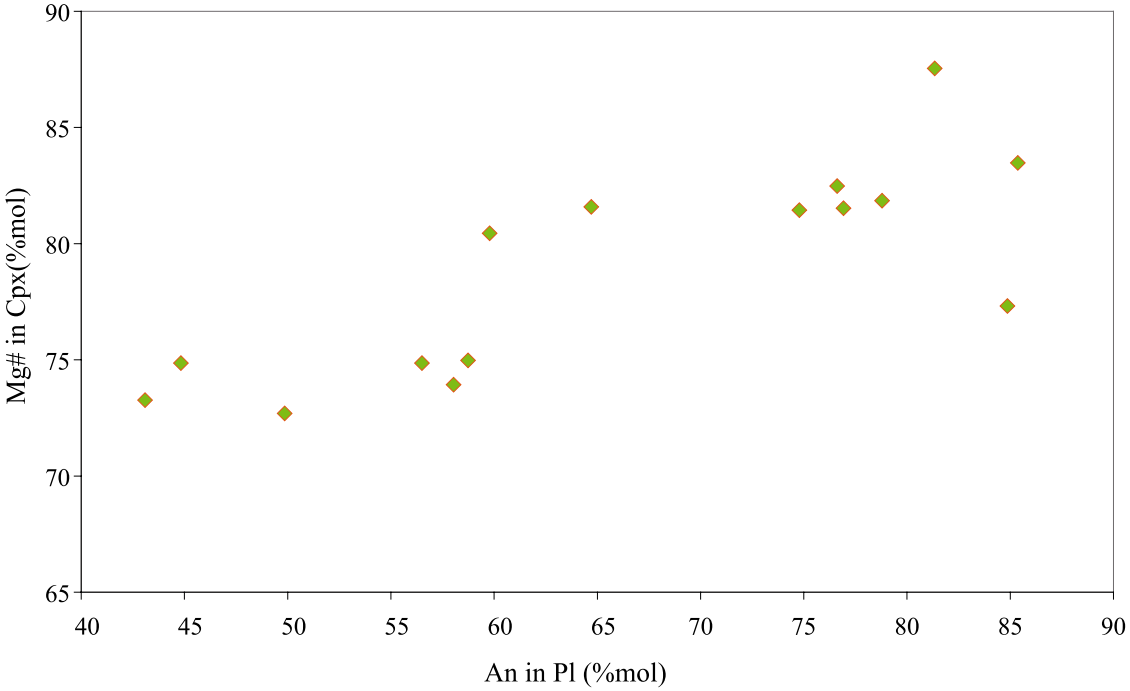

Figure 11. Composition of plagioclases and clinopyroxenes of the Wadi Gaz dike rocks (see analyses in Table 1).

[*Hooft et al.*, 1997; *Lagabrielle and Cormier*, 1999; *Garel et al.*, 2002]. Conversely, a rise of the melt lens would result in an assimilation of its roof, as also envisaged by *Coogan et al.* [2003]. This could explain the local abundance of micro-gabbro-norite lenses locally interlayered within the foliated and layered gabbros.

6.2. Wadi Gaz as a Typical Section Through the RZDSC

[32] We have defined the base of the RZDSC in the Wadi Gaz section (location in Figure 2) as coinciding with both the floor and the roof of a melt lens (cross section in Figure 2). This important boundary has been traced in the field on the western side of the Wadi Gaz (Figure 9). It is where the floor and the roof of the melt lens were squeezed together when the melt lens closed, due to drifting away from the ridge axis. After settling on the floor of the lens, the gabbro mush subsided within the magma chamber and rotated, developing a steep foliation which was frozen when this mush solidified as a gabbro and drifted out of the magma chamber [*Quick and Denlinger*, 1993; *Chenevez et al.*, 1998] (Figure 13a). The uppermost, crude and steep foliation taken as the top of the RZSDC has been developed right at the limit of the melt lens. The roof of the melt lens has crystallized at <1200°C in dry conditions as a coarse and dry ophitic gabbro, representing the base of the RZSDC and locally preserved (Figure 13c). Above, we interpret the RZSDC isotropic ophitic gabbros as related to successive stages of protodike intrusions. The protodikes were injected near the roof of the melt lens where temperature was in the range of 1100°C–1000°C (Figure 13c). The center of the dikes crystallizes as isotropic ophitic gabbros with microgranular margins resulting from a rapid cooling at the contact with the hot and hydrated ophitic gabbros. Protodikes would be split by subsequent dike-in-dike intrusions in a medium also submitted to hydrous recrystallization and anatexis. As a result, protodikes would be mostly destroyed and, usually, only recalled by slivers or breccias of their microgranular margins within an ophitic gabbro matrix. This is typically seen in Wadi Gaz where, exceptionally, a small sheeted protodike complex has been preserved. A few tens of meters above this complex, the isotropic ophitic gabbros partly recrystallize and melt by hydrous anatexis. Pegmatitic veins in varitextured gabbros and minor trondjhemite intrusions are generated by this anatexis. Finally, we have described at the base of the greenschist facies sheeted dike complex a limited horizon of amphibolite facies diabase dikes. They would represent a thermal boundary layer between the HT RZSDC and the overlying LT sheeted dike complex.

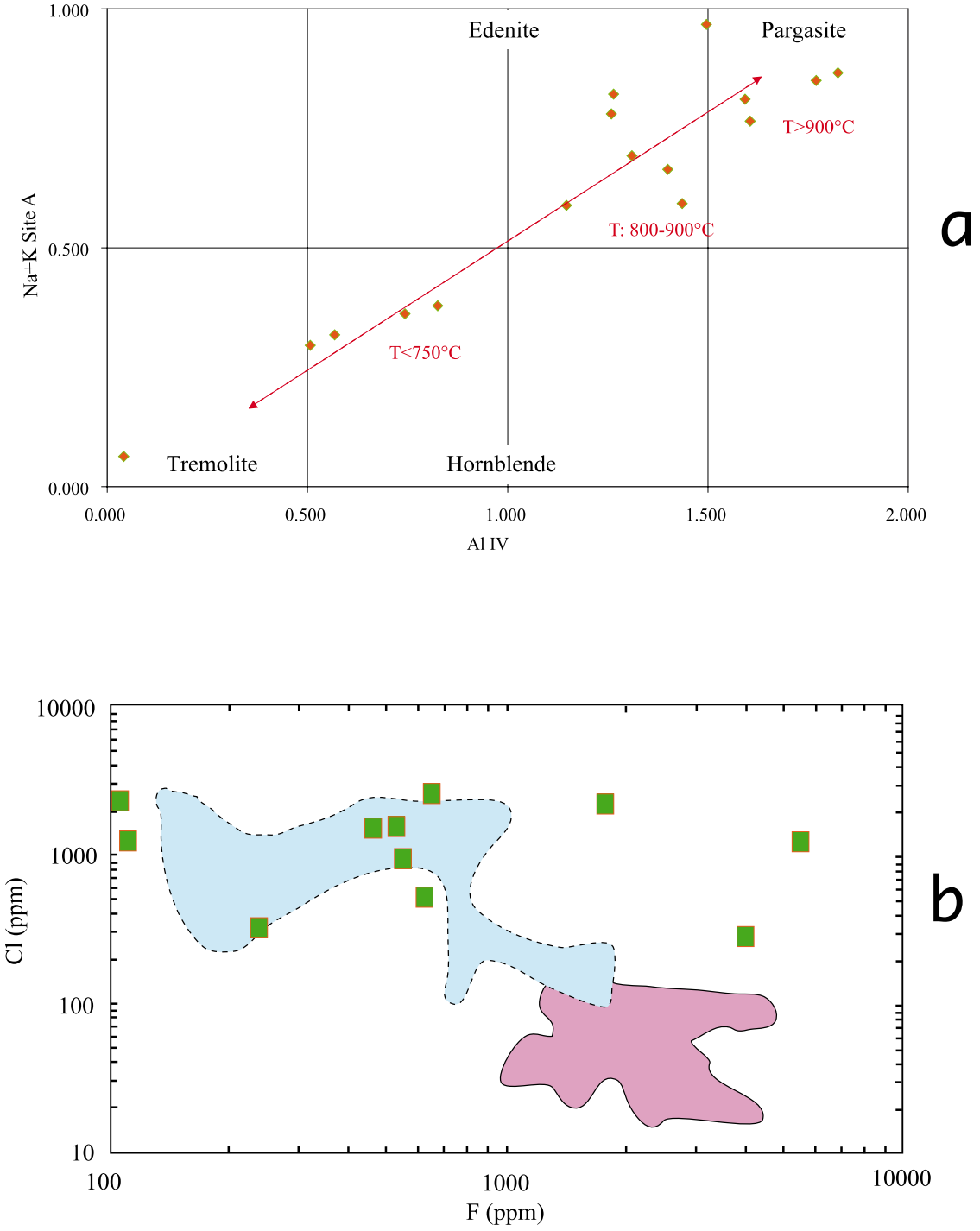

Figure 12. (a) Compositions of amphiboles from the Wadi Gaz dike rocks (see analyses in Table 1). For the estimation of equilibrium temperatures based on coexisting amphibole-plagioclase, we used the thermometer of *Holland and Blundy* [1994]. Moreover, temperatures for amphibole formation were derived by applying the semiquantitative geothermometer of *Ernst and Liou* [1998] based on the Ti content in amphiboles. For this, only those amphiboles were used which coexist with a titanian oxide phase (titanomagnetite or ilmenite). Previous studies in basaltic systems showed the general good agreement between the Ti-in-amphibole and amphibole-plagioclase temperatures [*Koepke et al.*, 2005a]. Moreover, the reliability of the TiO_2-in-amphibole thermometer was confirmed by an experimental study of *Koepke et al.* [2004] where temperatures derived from the TiO_2 content in amphiboles of experimental products correspond well to the temperatures of the experimental runs. (b) F versus Cl in amphiboles from the Wadi Gaz rocks (see analyses in Table 1). Fields shown are from *Coogan et al.* [2001], vein and replacive (dotted line), bleb and interstitial (full line).

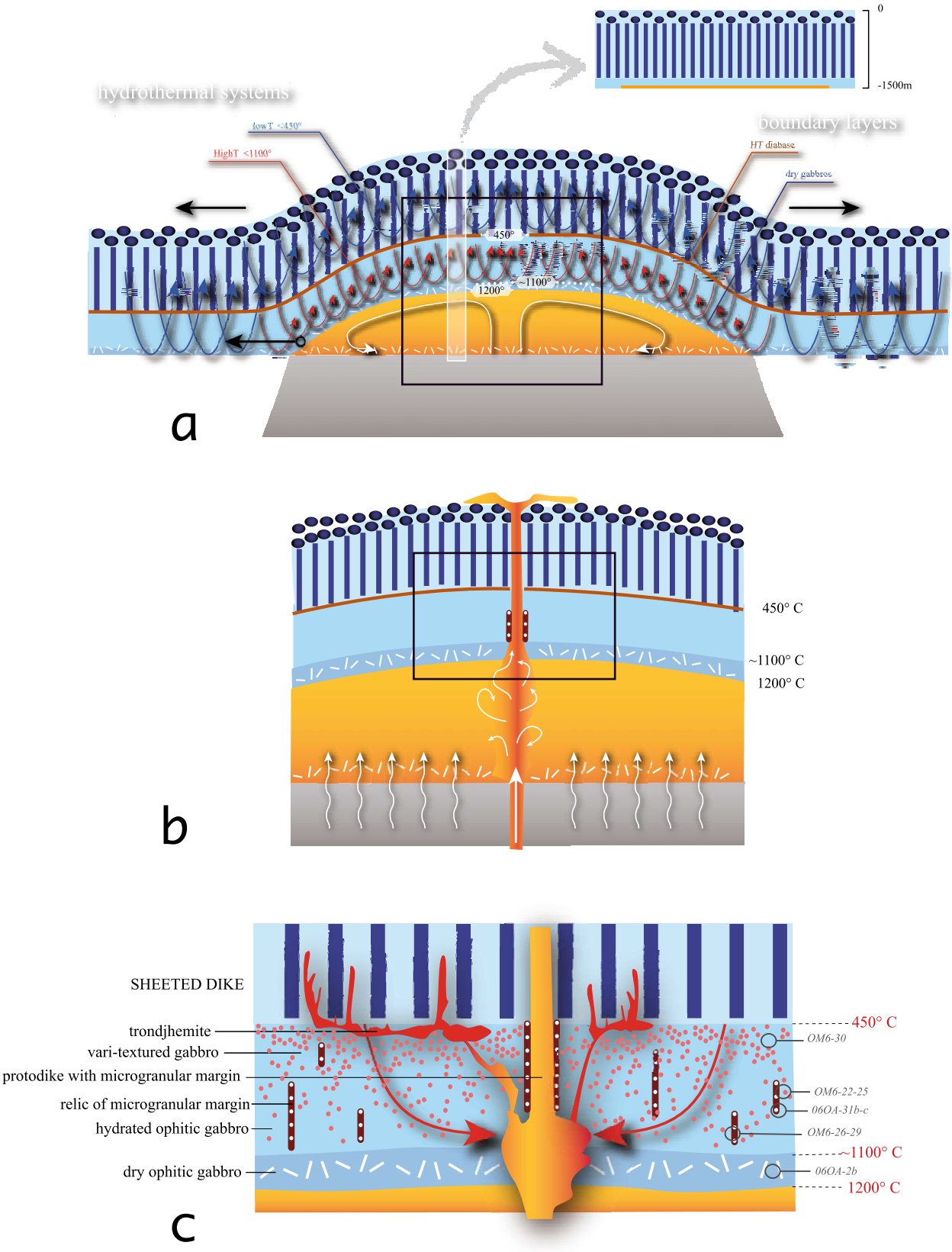
0
-1500m
hydrothermal systems
boundary layers
lowT <450°
HighT <1100°
HT diabase
dry gabbros
450°
1200°
~1100°
a
450° C
~1100° C
1200° C
b
SHEETED DIKE
trondjhemite
vari-textured gabbro
protodike with microgranular margin
relic of microgranular margin
hydrated ophitic gabbro
dry ophitic gabbro
450° C
OM6-30
OM6-22-25
06OA-31b-c
OM6-26-29
~1100° C
06OA-2b
1200° C
c

Figure 13

6.3. Hydrous Anatexis

[33] As already concluded by *Nicolas and Boudier* [1991], field observations convincingly suggest that the varitextured gabbros and their pegmatitic patches grading in pegmatite veins as well as the diorite and trondjhemite bodies are in situ products of hydrous anatexis. This interpretation has been confirmed by the discovery in Oman gabbros of a massive alteration by large fluxes of seawater heated to temperatures up to 1000°C which locally trigger hydrous anatexis [*Nicolas et al.*, 2003; *Bosch et al.*, 2004]. As the same evidence is present in RZSDC, this general interpretation is extended here, noting that seawater ingression should be easier at this shallow level than deeper in the gabbro unit. The interpretation of the observed phase relations as hydrous melting is in agreement with experiments, which have been conducted at the appropriate pressure, temperature, oxygen fugacity (see Figure 14 and Appendix A). On the basis of the mineral analyses reported in Table 2, we can extend the role of water to lower temperatures. Thus, in varitextured gabbros, hydrous reactions responsible for zonation in amphiboles record temperatures dropping from T > 900°C to T < 750°C (Figures 3b and 12a). We have also described within pegmatitic patches, the latest stage of magmatic evolution which were converted into greenschist facies probably by autometamorphism (Figure 4b). Also as a product of a very late stage magmatism, veins, dikelets or small stocks of diorite to trondjhemite can be observed. These felsic compositions can be generated either by advanced differentiation of the hydrous gabbroic mush freezing later to varitextured gabbros or by partial melting of the just frozen gabbro by the introduction of a small amount of seawater at temperatures between 900 and 980°C [*Koepke et al.*, 2004] (Figure 4c). A model-dependent confirmation is provided by *Coogan et al.* [2003]. By balancing the Cl content observed in fresh EPR MORBs with a potential contaminator, the authors conclude that ~20% of hydrothermally altered crust was assimilated and mixed in the melt lens basalt by stopping of altered dikes that can contain high amounts of water due to the presence of hydrated minerals. This also implies that the generation of hydrous magmas within the RZSDC is easily possible, since the addition of small amounts of water at the given shallow pressure may lead to high water activities (see section 6.4 and Appendix A).

6.4. Origin of Water

[34] The question raised here is whether water of mantle origin, carried by the basaltic melt to the melt lens would be sufficient to generate the hydrous reactions recorded in the RZSDC or whether seawater infiltration is necessary. In the experiments reported in Appendix A, under the chosen pressure of 50 MPa, the solubility of water in a primitive MORB melt is 2.2 wt% [*Berndt et al.*, 2002]. Thus, high water activities can be reached easily, with the addition of relative small amounts of water. Even less than 2.2 wt% water is sufficient for reaching water-saturated melts, when the melt fraction is reduced. For instance, only ~1 wt% total water is necessary, for shifting the system of Figure 14 at 1060°C from the dry solidus into a hydrous partly molten regime with ~50% water-saturated melt and 50% anhydrous crystals. Lower water contents are enough to stabilize water-saturated trondjhemitic melts at lower temperatures, where the melt fractions are low (e.g., ~0.1 to 0.4 wt% total water as a function of temperatures and melt fraction). Such low fractions of water can be attained by fractional crystallization of a basaltic melt issued from the

Figure 13. Sketches illustrating, with increasing detail, the internal structure and dynamics of the RZSDC. (a) Convective structure and RZSDC zonation above and away from the melt lens (vertical scale is exaggerated; realistic thickness shown in the close-up). The magmatic convection in the lens (white lines) is separated from the HT hydrothermal convection (red lines) by a dry isotropic ophitic gabbro horizon forming a thermal boundary layer. LT (greenschist facies) hydrothermal convection coincides with the top of the RZSDC, being separated from the underlying HT hydrothermal system by a second thermal boundary layer (amphibolite facies diabase). In the HT hydrothermal regime, hydrous melting of the isotropic gabbros and crystallization generates the varitextured gabbros and trondjhemites. (b) See box in Figure 13a. Intermittent generation of new RZSDC to replace the one drifted off-axis, by cracking of the dry gabbro layer, with injection of new melt through the crack. Dry gabbros crystallize from this new melt which can also be injected as a protodike that extends upsection into a new dike in the sheeted dike complex. (c) See box in Figure 13b. Melt surge through a protodike and minor intrusion at the base of the RZSDC, yielding the crystallization of the isotropic ophitic gabbros presumably in wet conditions, followed by abundant HT hydrous melting in the main body of the RZSDC, generating varitextured and pegmatitic gabbros, diorite, and trondjhemite.

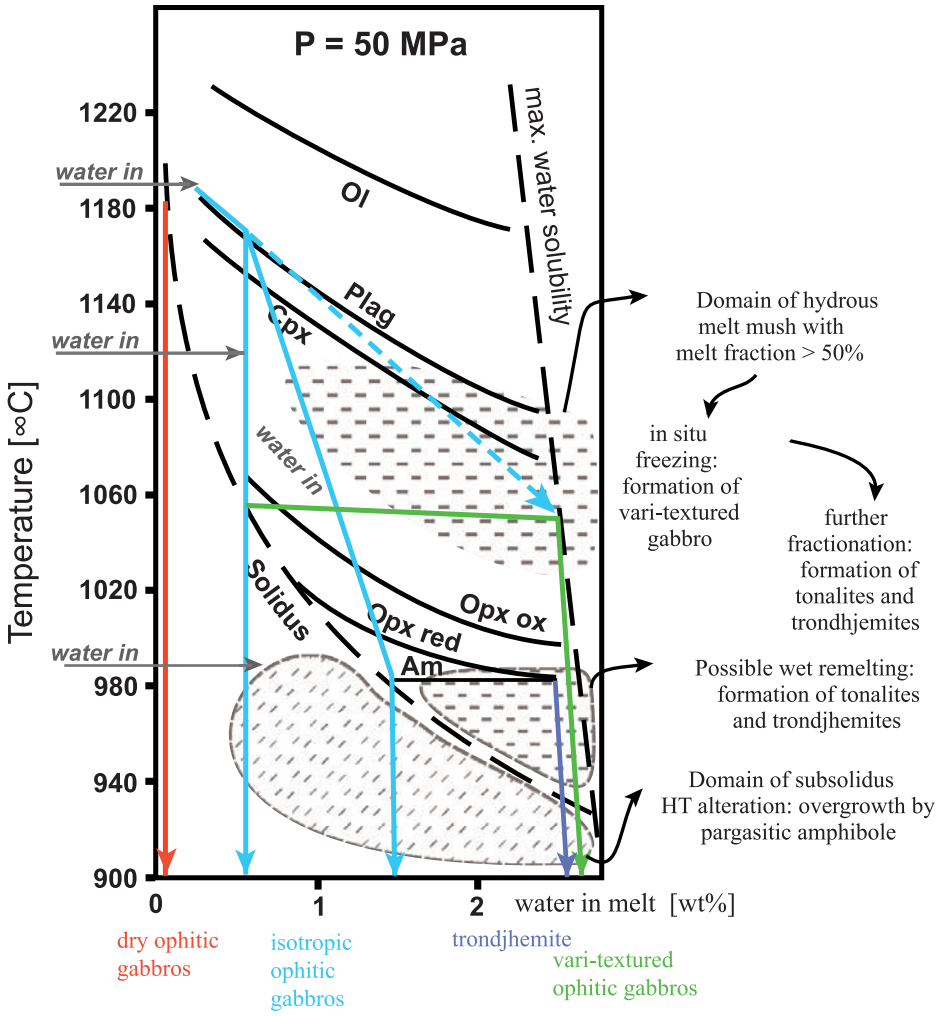

Figure 14. Phase relations in a hydrous primitive tholeiitic system at 50 MPa in the RZSDC. The solid black lines correspond to the phase boundaries of olivine (Ol), plagioclase (Plag), clinopyroxene (Cpx), orthopyroxene (Opx) under oxidizing (ox) and reducing (red) redox conditions, and amphibole (Am). See text for further details on the cooling paths and outlined fields; see Appendix A for background data of the phase diagram.

mantle where the initial water fraction is ~0.05%. The validity of the concept of fractional crystallization when dealing with a melt lens functioning in steady state conditions could be questioned. Thus, it seems quite possible that a minor fraction of deep water can be introduced within the RZSDC. However, on the basis of oxygen isotopes [*Gregory and Taylor*, 1981; *Bosch et al.*, 2004] volumes of water much larger than a few percent are probably available. They indicate that the amount water which permeated Oman gabbros at HT was of the order of magnitude of the mass of these gabbros.

[35] Most gabbros in RZSDC contain pargasitic amphiboles as interstitial or overgrowth phases. According to *Coogan et al.* [2001], the generally high chlorine content of pargasitic amphiboles, like the ones here, indicate that they crystallized in presence of seawater derived fluids. However, the Wadi Gaz pargasitic amphiboles have also a high TiO_2 content, correlated with a high fluor content (Figures 12a and 12b). High values of these two elements are considered as the signature of magmatic amphiboles [*MacLeod and Yaouancq*, 2000; *Coogan et al.*, 2001]. At this stage, we discern that the question of magmatic versus hydrothermal origin of pargasitic amphiboles cannot be settled by our data. *Koepke et al.* [2005a] point out in oceanic gabbros, a correlation of TiO_2 enrichment in pargasitic amphiboles and their association with ilmenite. This correlation is also observed here and

we refer to the discussion of this topic in their paper.

6.5. A General Model for the RZSDC Formation

[36] The model developed now integrates the observations reported above in Wadi Gaz. It applies to RZSDC generation in the situation where, as deduced from the continuity of structures over a transversal distance in map of 15 km (Figure 2), the spreading has been steady state and, expectedly, the melt lens, fairly stable over a period of ~300,000 years (assuming a half spreading rate of 5 cm/a). Subsequently, we will examine the situation of RZSDC in the environment of ridge segmentation.

[37] A dry basaltic melt crystallizes at the roof of the melt lens as a thin layer of coarse-grained and little altered ophitic gabbro. This layer is a thin thermal boundary layer between the magma convection in the melt lens, at ~1200°C, and the HT (>450°C) hydrothermal convection above. Hydrothermal convection rapidly decreases the temperature upsection but the temperature is as high as ~1100°C at the contact with the dry ophitic gabbros (Figures 13a and 14). The complex RZSDC lithology demonstrates the presence of HT fluids inducing both wet anatexis and metamorphic hydrous reactions. The mechanism by which seawater penetrates the RZSDC at high temperatures seems to be simpler here than in the case of the ubiquitous HT hydrothermal alteration of the gabbro unit located below the RZSDC [*Nicolas et al.*, 2003; *Nicolas and Mainprice*, 2005]. In contrast with the latter situation, where HT fluids have to progress several kilometers below the limit of the elastic lithosphere (~600°C), this limit is located here at the base of the sheeted dike complex, ~100 m above the RZSDC. Consequently, seawater can be introduced through tensile stress driven cracks in the elastic lithosphere.

[38] Constrained by experimental studies on the dependence of gabbro stability on water content, at 50 MPa (the approximate pressure conditions of the RZSDC at the ridge axis) (see Appendix A), the phase diagram of Figure 14 describes the formation sequence of igneous rocks in the RZSDC. The dry gabbros plated at the roof of the melt lens crystallized around 1180°C at the dry solidus. From there, they follow the red path in Figure 14. This path is also possible for the overlying isotropic ophitic gabbros which would then also be within the thermal boundary layer. However, because they display distinct textures (Figure 3), these isotropic ophitic gabbros are thought to be related to the HT hydrothermal system above the thermal boundary layer. These isotropic ophitic gabbros would crystallize from a hydrous melt which, at >1100°C following the blue path in Figure 14. This melt would result from the reaction of <1% of hydrothermal fluids with either the dry and solid gabbros from the roof of the melt lens or a dry melt injected through the protodikes.

[39] Protodikes are expected to play a major role in generating the isotropic gabbros (Figures 13b and 13c). Let us assume that a basaltic melt surge cracks the dry gabbro layer from the melt lens roof and progresses to the surface through the sheeted dike complex. It will cross the RZSDC as a melt conduit with possibly lateral injections into the surrounding medium. Just above the roof thermal boundary layer, this will be an active protodike with a microgranular margin. This margin will subsequently remain little changed, possibly because it is fine-grained and not porous. After the melt surge, the interior of the conduit crystallizes in the presence of a hydrous fluid at >1100°C, forming isotropic doleritic gabbro. Related to drifting off-axis, the RZSDC is continuously created by similar melt conduit injections and crystallizations.

[40] Above this lower horizon, more seawater-derived fluids injected at temperatures between 1100°C–1050°C locally induce, in the isotropic ophitic gabbros, hydrous anatexis resulting in crystallization of HT vary-textured and pegmatitic gabbros (Figure 14). The 1100–1050°C temperature interval for intrusion of hydrous fluids is controlled by the fact that below a melt fraction of 50%, it seems difficult, in melting varitextured gabbros, to separate and inject pegmatitic dikes without preserving restitic assemblage. Moreover no restitic assemblages are identified in the field. Due to continuous hydrous intrusion and melting, diorites and trondjhemites can be generated either by advanced closed-system differentiation of the hydrous magma or by subsequent hydrous partial melting events at lower temperatures 900 to 950°C (Figure 14) [*Koepke et al.*, 2005b]. Below this temperature, further hydrothermal alteration takes place only by solid-state metamorphic reactions.

[41] A second thermal boundary layer, located at the base of the sheeted dike complex, exists between the HT and LT hydrothermal convection systems. In Oman, it can be traced by the presence in diabase dikes of HT (amphibolite facies) alter-

ation (Figure 3a), without significant evidence of the LT (greenschist facies) ubiquitous alteration which is present in the overlying dikes.

[42] With seafloor spreading, RZSDC lithologies drift off-axis, probably without any significant change until they pass over the lateral limit of the lens. Beyond this limit, because of the related sharp drop in temperature, the dry doleritic gabbros are submitted, for a short time, to HT hydrothermal alteration. A few outcrops have nearly escaped this alteration and could still represent the roof horizon of the melt lens (Figure 3d).

[43] If melt pulses renew the gabbro boundary layer through melt fractures (Figure 13b) then each diabase dike in the sheeted dike complex is connected to one protodike in the RZSDC. However, protodikes are not that common in the RZSDC. We, therefore infer that the protodikes are massively destroyed, mainly by dike-in-dike intrusions at melting temperatures, and/or by hydrous remelting. As illustrated by Figure 13c, this hypothesis is supported by the observation of protodikes being commonly dismembered, with dispersal of microgranular margins, mainly as breccias and aligned lenses in an ophitic gabbro matrix (Figure 5). The margins of the protodikes have a tighter texture and are more resistant to assimilation than the ophitic center of protodikes. The margins are the only relicts of a former sheeted protodike complex.

6.6. RZSDC in Domains Affected by Ridge Segmentation

[44] We have selected a domain located away from ridge segment limits and related propagating rifts, where ridge segmentation has induced major ridge-related tectonic deformations and magmatic intrusions within the RZSDC. Using the presence of symptomatic gabbronorite and diorite-trondjhemite bodies, restricted to these domains, it is inferred that nearly half the lithosphere has been generated in the Oman ophiolite under the influence of ridge segmentation.

[45] In RZSDC from ridge segmentation domains, the large magmatic intrusions can induce by reheating a local contact metamorphism, as described around a gabbronorite intrusion in Troodos [*Gillis and Roberts*, 1999; *Gillis and Coogan*, 2002]. Conversely, in our RZSDC where no such intrusions are observed, reheating to HT conditions can be induced only along the protodikes emplaced in the hotter, basal part of the RZSDC (Figure 10a). Such contact metamorphism has been observed, but restricted to a centimeter scale. This is not surprising considering that, with a ~7°C/m thermal gradient, the RZSDC experiences an incredibly sharp cooling.

6.7. Comparison of RZSDC in Oman and in the IODP Hole 1256D

[46] The first results of the successful drilling through the floor of a RZSDC in the East Pacific Rise [*Wilson et al.*, 2006] show many similarities with what is observed in Oman (Figure 15) and in other ophiolites, such as Troodos [*Gillis and Roberts*, 1999]. Two features seem particularly characteristic. The IODP and Oman RZSDC have a comparable ~100 m thickness if, according to *Wilson et al.* [2006], the top gabbros from the gabbro unit are represented by the last meters of the core. Most textures observed in the Hole 1256D also match those in Oman, as illustrated by the comparison of ophitic gabbros (Figures 15a and 15b; see also for Troodos ophiolite [*Gillis and Coogan*, 2002]). Interestingly, the "completely recrystallized granoblastic" texture of Figure 4B of *Wilson et al.* [2006] observed in the lower sheeted dikes and equilibrated at ~650°C, matches, in terms of texture and position, our lowermost HT diabase dikes, which corresponds to the thermal boundary layer between the HT and LT hydrothermal systems (Figures 15c and 15d). However, in the IODP leg, the granoblastic dikes section, stratigraphically above the gabbros, is 60 m thick [*Wilson et al.*, 2006], which is somewhat thicker than the HT alteration front at the base of Oman sheeted dike complex.

[47] On the basis of the observation of prograde mineral reactions in the granoblastic dikes, the "granoblastic" textures are ascribed by *Teagle et al.* [2006] and *Wilson et al.* [2006] to "contact metamorphism by underlying gabbro intrusions." This agrees with the Troodos ophiolite study [*Gillis and Roberts*, 1999], where a large metamorphic aureole has been observed in sheeted dikes at the margins of a gabbronorite intrusion. In the part of the Oman RZSDC devoid of late magmatic intrusions, there is no evidence of any reheating, except on a centimeter scale at the margin of a dike. We suggest that Troodos ophiolite, as well as the IODP hole in the Cocos oceanic lithosphere were both accreted in a domain of ridge segmentation and not

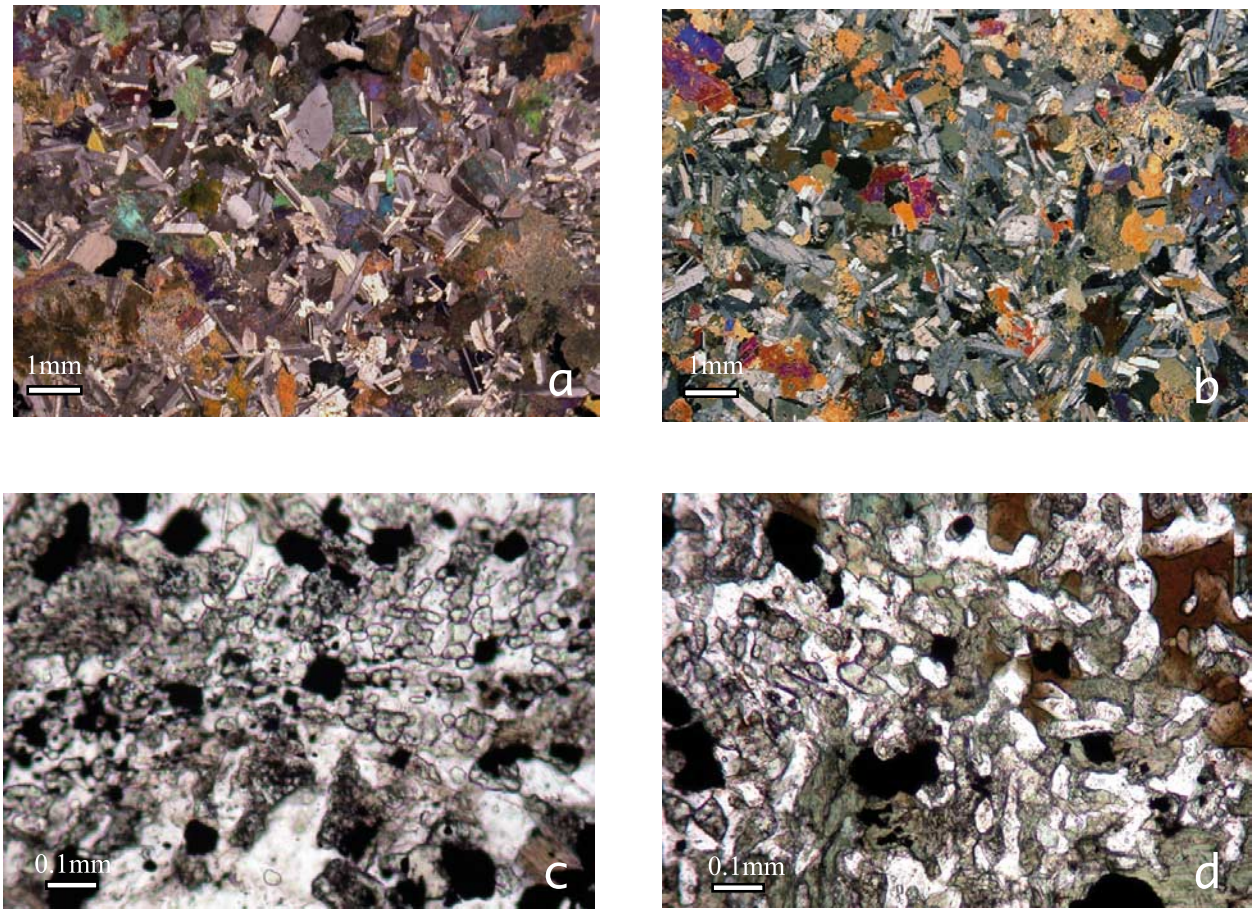

Figure 15. Comparison of textures in the Oman and IODP Hole 1256D RZSDC. The top micrographs show isotropic hydrated ophitic gabbro from (a) IODP sample 1256D216R1 and (b) site 90OF15 in Oman. The bottom micrographs show HT diabase with polygonized Cpx crystals and development of brown hornblende from (c) IODP sample 1256D194R1 and (d) site 03OA62 in Oman.

in a domain of steady state seafloor spreading as in the area selected in Oman for this study.

7. Conclusion

[48] The object of this paper was to revisit RZSDC zones in the Oman ophiolites, at a time when this critical zone has been drilled in the ocean for the first time with IODP Hole 1256D. We wish to insist on the exceptional interest of the RZSDC, as a key to understand crustal accretion at fast spreading centers. A large part of the lower crust is issued from a tiny melt lens, only ~2 km in cross section and ~30 m thick. On top of it, the slightly thicker RZSDC (~100 m) is a horizon in which the temperature drops ~800°C, from 1200°C in the melt lens to 450–400°C at the base of the sheeted dike complex. This represents the most energetic system in dynamic equilibrium at the surface of the Planet that results in the complex and varied lithology described herein. A brief comparison between the RZSDC in Oman and the first descriptions from IODP Hole 1256D suggests that the present study could help to constrain the three-dimensional context of this most important section drilled in the ocean.

Appendix A: Experimental Constraints on the Phase Relations in a Hydrous Primitive Tholeiitic System for a Pressure of 50 MPa (Figure 14)

[49] The rationale behind the understanding of the different magmatic lithologies in the RZSDC is based on the knowledge of the phase relations in a hydrous primitive to moderately evolved tholeiitic system for the pressure conditions of the RZSDC, which is assumed to be 50 MPa (corresponding to

a thickness of ~1 km for the crustal lid, plus 2–3 km water column). The role of water and oxygen fugacity on the phase equilibria and differentiation in tholeiitic, MORB-type systems at shallow pressures has been studied in recent experiments by *Feig et al.* [2006] and S. T. Feig et al. (Effect of oxygen fugacity on phase equilibria in a hydrous tholeiitic basalt, submitted to *Contributions to Mineralogy and Petrology*, 2008). They studied the pressure dependence (100, 200, and 500 MPa) and the role of oxygen fugacity (corresponding to QFM-3 to QFM+4, with QFM = quartz-fayalite-magnetite oxygen buffer) of a primitive tholeiitic system (Mg# = 73.5, with Mg# = molar 100 · MgO/(MgO + FeO)). The phase diagram of Figure 10 is based on an extrapolation of the phase relations to 50 MPa for an oxygen fugacity corresponding to ~QFM-1 at dry conditions and QFM+2 at water-saturated conditions. *Feig et al.* [2006] showed that typical thermodynamic models for predicting magmatic evolution trends like ''MELTS'' [*Ghiorso and Sack*, 1995] and "Comagmat" [*Ariskin*, 1999] fail to predict the experimental phase relations under hydrous conditions at shallow pressure. Therefore, the extrapolation of their results to 50 MPa seems the only possible way to estimate reliable evolution trends of a primitive hydrous tholeiitic system at the magmatic conditions prevailing in the RZSDC.

A1. Relation Between Water and Oxygen Fugacity

[50] In a hydrogen-buffered system, as it is the case for such experiments, the prevailing oxygen fugacity strongly depends on the water activity of the system. For the dry and water-poor conditions of Figure 10, we choose an oxygen fugacity corresponding to QFM-1 to QFM which is in accord with recent studies estimating the redox conditions of natural MORB [e.g., *Bezos and Humler*, 2005]. A further hydration of the system consequently leads to more oxidizing conditions resulting in an oxygen fugacity ~QFM+2 for a water activity of 1 (water-saturation). The quantitative treatment of the relation between water activity and redox conditions (and oxidation state of iron) is given by *Botcharnikov et al.* [2005]. The water-saturation curve included in the phase diagrams is obtained from the water solubility in a primitive MORB of *Berndt et al.* [2002] and from the temperature and pressure dependence on water solubility of *Holtz et al.* [1995].

A2. Stability of Oxides

[51] Chrome spinel, which is always stable in the experiments at near liquidus conditions, is not included into the phase diagram of Figure 10. Fe-Ti oxides were not stable under the given redox conditions in the experiments of *Feig et al.* [2006; submitted manuscript, 2008]; they are stable only at more oxidizing conditions. However, since the experimental system is primitive (FeO^{tot} content of 6.5 wt%), it is expected that in a more evolved system, Fe-Ti oxides would be stable at lower temperatures, at least at the more oxidizing conditions in the hydrated regime. The amphibole, which is stable at low temperatures typically shows a pargasite composition.

A3. Effect of Water

[52] The main effect of water on the phase relations in the given system is to displace the stability curves of the minerals at lower temperatures. Under the low pressure of 50 MPa, water is not changing the order of crystallization, in contrast to what is observed at higher pressure. The well-known depression of plagioclase stability (plagioclase crystallizing after clinopyroxene) with increasing water content was observed in the experiments of *Feig et al.* [2006] only at pressures $\geq$200 MPa. Moreover, water content also affects the mineral compositions. According to *Feig et al.* [2006], the An content of plagioclase may increase about 10 to 15 mol% when increasing the water activity from 0 to 1 at a given temperature, while the Mg# of olivine and clinopyroxene is shifted to higher values (maximum of 5 to 10) due to the increased oxygen fugacity with water. Thus, the overall effect of water is to stabilize crystal mushes with moderate or high melt fractions to lower temperatures, and thereby shifting the An content of plagioclase and the Mg# of clinopyroxene and olivine to higher values. Amphibole, the only hydrated phase in the system, is only stable at very low temperatures. Thus, it should be emphasized that the absence of amphibole in crystallized gabbro does not necessarily mean that the conditions in the magma chamber were "dry."

A4. Effect of Composition

[53] The system used for our phase diagram is fairly mafic in composition, thus corresponding to one end-member of the range of melts leaving the magma chamber. This has several consequences: (1) liquidus temperatures (and the saturation temperatures of the individual minerals) are high;

(2) olivine is stable down to the lowest temperatures; (3) the stability of orthopyroxene is restricted to the lowest temperatures while olivine is still present; (4) the iron content in the low-temperatures melts are too low for saturating Fe-Ti oxides at the applied redox condition. By using a slightly more evolved system, e.g., a normal MORB with a Mg# of 67 [*Berndt et al.*, 2005], the liquidus temperature of the system (and the saturation temperatures of the individual minerals) are slightly lower (e.g., 1220°C for the dry solidus), but the phase topology is the same and the other points mentioned above are still valid. Only when the system evolves further (e.g., Mg# < 60), notable changes in the phase relations are expected. These can be extrapolated from the experiments in hydrous MORB by *Berndt et al.* [2005], who studied both primitive and evolved MORB: (1) liquidus temperature (and the saturation temperatures of the individual minerals) are lower (e.g., ≤1200°C for the dry solidus); (2) olivine may become unstable; (3) the stability of orthopyroxene is enhanced to higher temperatures; (4) Fe-Ti oxides become stable in the lower temperature part of the diagram (but still strongly depending on the prevailing redox condition).

A5. Stability of Orthopyroxene in a Primitive System

[54] According to *Feig et al.* [2006], at a given pressure, the orthopyroxene stability is increased by oxidizing redox conditions, and decreased with increasing water activities. Therefore, two orthopyroxene saturation curves are displayed in the phase diagram of Figure 14, one for reducing and one for oxidizing conditions, related to oxygen fugacities corresponding to QFM and QFM+2 at dry conditions, respectively. In the chosen primitive system, orthopyroxene always crystallizes late, with the potential to produce typically interstitial growth. Earlier orthopyroxene crystallization can be expected at the chosen low pressure only by a significant increase of silica activity of the system.

Acknowledgments

[55] We acknowledge the support of the Universities of Montpellier and Hannover, of the CNRS, and of the European PROCOP program as well as the friendly cooperation established in Oman with the Directorate of Minerals of the MCI. The manuscript has been largely improved thanks to the constructive and patient reviews by Laurence Coogan and Nick Hayman as well as by the Editor, Vincent Salters. We are also grateful to Vincent Salters for his support.

References

Adachi, Y., and S. Miyashita (2003), Geology and petrology of the plutonic complexes in the Wadi Fizh area: Multiple magmatic events and segment structure in the northern Oman ophiolite, *Geochem. Geophys. Geosyst.*, *4*(9), 8619, doi:10.1029/2001GC000272.

Alt, J. C., et al. (1993), *Proceedings of the Ocean Drilling Program, Initial Reports*, vol. 148, Ocean Drill. Program, College Station, Tex.

Alt, J. C., et al. (1996), Hydrothermal alteration of a section of upper oceanic crust in the eastern equatorial Pacific: A synthesis of results from Site 504 (DSDP Legs 69, 70, and 83, and ODP Legs 111, 137, 140, and 148.), *Proc. Ocean Drill. Program Sci. Results*, *148*, 417–434.

Ariskin, A. A. (1999), Phase equilibria modeling in igneous petrology: Use of COMAGMAT model for simulating fractionation of ferro-basaltic magmas and the genesis of high-alumina basalt, *J. Volcanol. Geotherm. Res.*, *90*, 115–162, doi:10.1016/S0377-0273(99)00022-0.

Bach, W., B. Peucker-Ehrenbrink, S. R. Hart, and J. S. Blusztajn (2003), Geochemistry of hydrothermally altered oceanic crust: DSDP/ODP Hole 504B — Implications for seawater-crust exchange budgets and Sr- and Pb-isotopic evolution of the mantle, *Geochem. Geophys. Geosyst.*, *4*(3), 8904, doi:10.1029/2002GC000419.

Berndt, J., C. Liebske, F. Holtz, M. Freise, M. Nowak, D. Ziegenbein, D. Hurkuck, and J. Koepke (2002), A combined rapid-quench and H_2-membrane setup for internally heated pressure vessels: Description and application for water solubility in basaltic melts, *Am. Mineral.*, *87*, 1717–1726.

Berndt, J., J. Koepke, and F. Holtz (2005), An experimental investigation of the influence of water and oxygen fugacity on differentiation of MORB at 200 MPa, *J. Petrol.*, *46*, 135–167, doi:10.1093/petrology/egh066.

Bezos, A., and E. Humler (2005), The $Fe^{3+}/\Sigma Fe$ ratios of MORB glasses and their implications for mantle melting, *Geochim. Cosmochim. Acta*, *69*, 711–725, doi:10.1016/j.gca.2004.07.026.

Bosch, D., M. Jamais, F. Boudier, A. Nicolas, J. M. Dautria, and P. Agrinier (2004), Deep and high temperature hydrothermal circulation in the Oman ophiolite- Petrological and isotopic evidence, *J. Petrol.*, *45*(6), 1181–1208, doi:10.1093/petrology/egh010.

Botcharnikov, R. E., J. Koepke, F. Holtz, C. McCammon, and M. Wilke (2005), The effect of water activity on the oxidation and structural state of Fe in a ferro-basaltic melt, *Geochim. Cosmochim. Acta*, *69*, 5071–5085, doi:10.1016/j.gca.2005.04.023.

Boudier, F., M. Godard, and C. Armbruster (2000), Significance of gabbronorite occurrence in the crustal section of the Semail ophiolite, *Mar. Geophys. Res.*, *21*, 307–326, doi:10.1023/A:1026726232402.

Chenevez, J., and A. Nicolas (1997), Crustal feeding in the Oman ophiolite from the top or from the bottom? A thermal and mass balance model, *Geophys. Res. Lett.*, *24*, 1811–1814, doi:10.1029/97GL01681.

Chenevez, J., P. Machetel, and A. Nicolas (1998), Numerical models of magma chambers in the Oman ophiolite, *J. Geophys. Res.*, *103*(B7), 15,443–15,455, doi:10.1029/98JB00597.

Collier, J. S., and S. C. Singh (1997), Detailed structure of the top of the melt body beneath the East Pacific Rise at 9°40′N

from waveform inversion of seismic reflection data, *J. Geophys. Res.*, *102*(B9), 20,287–20,304, doi:10.1029/97JB01514.

Coogan, L. A. (2003), Contaminating the lower crust in the Oman ophiolite, *Geology*, *31*(12), 1065–1068, doi:10.1130/G20129.1.

Coogan, L. A., R. N. Wilson, K. M. Gillis, and C. J. MacLeod (2001), Near-solidus evolution of oceanic gabbros: Insights from amphibole geochemistry, *Geochim. Cosmochim. Acta*, *65*(23), 4339–4357, doi:10.1016/S0016-7037(01)00714-1.

Coogan, L. A., N. C. Mitchell, and M. J. O'Hara (2003), Roof assimilation at fast spreading ridges: An investigation combining geophysical, geochemical, and field evidence, *J. Geophys. Res.*, *108*(B1), 2002, doi:10.1029/2001JB001171.

Detrick, R. S., P. Buhl, E. Vera, J. Mutter, J. Orcutt, J. Madsen, and T. Brocher (1987), Multi-channel seismic imaging of a crustal magma chamber along the East Pacific Rise, *Nature*, *326*, 35–41, doi:10.1038/326035a0.

Ernst, W. G., and J. Liou (1998), Experimental phase-equilibrium study of Al- and Ti-contents of calcic amphibole in MORB—A semiquantitative thermobarometer, *Am. Mineral.*, *83*, 952–969.

Feig, S. T., J. Koepke, and J. E. Snow (2006), Effect of water on tholeiitic basalt phase equilibria: An experimental study under oxidizing conditions, *Contrib. Mineral. Petrol.*, *152*(5), 611–638, doi:10.1007/s00410-006-0123-2.

Garel, E., O. Dauteuil, and Y. Lagabrielle (2002), Deformation processes at fast to ultra-fast oceanic spreading axes: Mechanical approach, *Tectonophysics*, *346*(3–4), 223–246, doi:10.1016/S0040-1951(01)00280-3.

Ghiorso, M. S., and R. O. Sack (1995), Chemical mass transfer in magmatic processes. IV. A revised and internally consistent thermodynamic model for the interpolation and extrapolation of liquid-solid equilibria in magmatic systems at elevated temperatures and pressures, *Contrib. Mineral. Petrol.*, *119*, 197–212, doi:10.1007/BF00307281.

Gillis, K. M. (2002), The root zone of an ancient hydrothermal system exposed in the Troodos ophiolite, Cyprus, *J. Geol.*, *110*, 57–74, doi:10.1086/324205.

Gillis, K. M., and L. A. Coogan (2002), Anatectic migmatites from the roof of an ocean ridge magma chamber, *J. Petrol.*, *43*(11), 2075–2095, doi:10.1093/petrology/43.11.2075.

Gillis, K. M., and M. D. Roberts (1999), Cracking at the magma-hydrothermal transition: Evidence from the Troodos ophiolite, Cyprus, *Earth Planet. Sci. Lett.*, *169*, 227–244, doi:10.1016/S0012-821X(99)00087-4.

Gregory, R. T., and H. P. J. Taylor (1981), An oxygen isotope profile in a section of Cretaceous oceanic crust, Samail ophiolite, Oman: Evidence for $\delta^{18}O$ buffering of the oceans by deep (>5 km) seawater-hydrothermal circulation at mid-ocean ridges, *J. Geophys. Res.*, *86*, 2737–2755, doi:10.1029/JB086iB04p02737.

Harding, A. J., J. A. Orcutt, M. E. Kappus, E. E. Vera, J. C. Mutter, P. Buhl, R. S. Detrick, and T. M. Brocher (1989), Structure of young oceanic crust at 13°N on the East Pacific Rise from expanding spread profiles, *J. Geophys. Res.*, *94*(B9), 12,163–12,196, doi:10.1029/JB094iB09p12163.

Holland, T. J. B., and J. Blundy (1994), Non-ideal interactions in calcic amphiboles and their bearing on amphibole-plagioclase thermometry, *Contrib. Mineral. Petrol.*, *116*, 433–447, doi:10.1007/BF00310910.

Holtz, F., H. Behrens, D. B. Dingwell, and W. Johannes (1995), Water solubility in haplogranitic melts: Compositional, pressure and temperature dependence, *Am. Mineral.*, *80*, 94–108.

Hooft, E. E. E., R. S. Detrick, and G. M. Kent (1997), Seismic structure and indicators of magma budget along the southern East Pacific Rise, *J. Geophys. Res.*, *102*(B12), 27,319–27,340, doi:10.1029/97JB02349.

Jousselin, D., A. Nicolas, and F. Boudier (1998), Detailed mapping of a mantle diapir below a paleo-spreading center in the Oman ophiolite, *J. Geophys. Res.*, *103*(B8), 18,153–18,170, doi:10.1029/98JB01493.

Juteau, T., M. Beurrier, R. Dahl, and P. Nehlig (1988), Segmentation at a fossil spreading center: The plutonic sequence of the Wadi Haymiliyah area (Haylayn block, Sumail nappe, Oman), *Tectonophysics*, *151*, 167–197, doi:10.1016/0040-1951(88)90245-4.

Juteau, T., D. Bideau, O. Dauteuil, G. Manach, D. D. Naidoo, P. Nehlig, H. Ondreas, M. A. Tivey, K. X. Whipple, and J. R. Delaney (1995), A submersible study in the western Blanco Fracture Zone, NE Pacific: Structure and evolution during the last 1.6 Ma, *Mar. Geophys. Res.*, *17*(5), 399–430, doi:10.1007/BF01371786.

Karson, J. A., S. D. Hurst, and P. Lonsdale (1992), Tectonic rotations of dikes in fast-spread oceanic crust exposed near Hess Deep, *Geology*, *20*, 685–688, doi:10.1130/0091-7613(1992)020<0685:TRODIF>2.3.CO;2.

Karson, J. A., M. A. Tivey, and J. R. Delaney (2002a), Internal structure of uppermost oceanic crust along the Western Blanco Transform Scarp: Implications for subaxial accretion and deformation at the Juan de Fuca Ridge, *J. Geophys. Res.*, *107*(B9), 2181, doi:10.1029/2000JB000051.

Karson, J. A., et al. (2002b), Structure of uppermost fast-spread oceanic crust exposed at the Hess Deep Rift: Implications for subaxial processes at the East Pacific Rise, *Geochem. Geophys. Geosyst.*, *3*(1), 1002, doi:10.1029/2001GC000155.

Kent, G. M., et al. (2000), Evidence from three-dimensional seismic reflectivity images for enhanced melt supply beneath mid-ocean-ridge discontinuities, *Nature*, *406*(6796), 614–618, doi:10.1038/35020543.

Koepke, J., S. T. Feig, J. Snow, and M. Freise (2004), Petrogenesis of oceanic plagiogranites by partial melting of gabbros: An experimental study, *Contrib. Mineral. Petrol.*, *146*, 414–432, doi:10.1007/s00410-003-0511-9.

Koepke, J., S. Feig, and J. Snow (2005a), Late stage magmatic evolution of oceanic gabbros as a result of hydrous partial melting: Evidence from the Ocean Drilling Program (ODP) Leg 153 drilling at the Mid-Atlantic Ridge, *Geochem. Geophys. Geosyst.*, *6*, Q02001, doi:10.1029/2004GC000805.

Koepke, J., S. T. Feig, and J. Snow (2005b), Hydrous partial melting within the lower oceanic crust, *Terra Nova*, *17*, 286–291, doi:10.1111/j.1365-3121.2005.00613.x.

Lagabrielle, Y., and M. H. Cormier (1999), Formation of large summit troughs along the East Pacific Rise as collapse calderas: An evolutionary model, *J. Geophys. Res.*, *104*(B6), 12,971–12,988, doi:10.1029/1999JB900015.

Lippard, S. J., A. W. Shelton, and I. G. Gass (1986), *The Ophiolite of Northern Oman*, *Geol. Soc. Mem. 11*, 178 pp., Blackwell Sci., Malden, Mass.

MacLeod, C. J., and D. A. Rothery (1992), Ridge axial segmentation in the Oman ophiolite: Evidence from along-strike variations in the sheeted dyke complex, in *Ophiolites and Their Modern Analogues*, edited by L. M. Parson, B. J. Murton, and P. Browning, *Geol. Soc. Spec. Publ.*, *60*, 39–63.

MacLeod, C. J., and G. Yaouancq (2000), A fossil melt lens in the Oman ophiolite: Implications for magma chamber processes at fast spreading ridges, *Earth Planet. Sci. Lett.*, *176*, 357–373, doi:10.1016/S0012-821X(00)00020-0.

Manning, C. E., P. E. Weston, and K. I. Mahon (1996), Rapid high-temperature metamorphism of East Pacific Rise gab-

bros from Hess deep, *Earth Planet. Sci. Lett.*, *144*(1–2), 123–132, doi:10.1016/0012-821X(96)00153-7.

Manning, C. E., C. J. MacLeod, and P. E. Weston (2000), Lower-cracking front at fast-spreading ridges: Evidence from the East Pacific Rise and the Oman ophiolite, in *Ophiolites and Oceanic Crust: New Insights From Field Studies and the Ocean Drilling Program*, *Spec. Pap. Geol. Soc. Am.*, *349*, 261–272.

Ministry of Petroleum and Minerals (1986), Geological map of the Sultanate of Oman, scale 1:100,000, Dir. Gen. of Miner., Muscat.

Ministry of Petroleum and Minerals (1992), Geological map of the Sultanate of Oman, scale 1:250,000, Dir. Gen. of Miner., Muscat.

Miyashita, S., Y. Adachi, and S. Umino (2003), Along-axis magmatic system in the northern Oman ophiolite: Implications of compositional variation of the sheeted dike complex, *Geochem. Geophys. Geosyst.*, *4*(9), 8617, doi:10.1029/2001GC000235.

Nehlig, P., T. Juteau, V. Bendel, and J. Cotten (1994), The root zone of oceanic hydrothermal systems: Constraints from the Samail ophiolite (Oman), *J. Geophys. Res.*, *99*(B3), 4703–4713, doi:10.1029/93JB02663.

Nicolas, A., and F. Boudier (1991), Rooting of the sheeted dike complex in the Oman ophiolite, in *Ophiolite Genesis and Evolution of the Oceanic Lithosphere*, edited by T. Peters, A. Nicolas, and R. G. Coleman, pp. 39–54, Kluwer Acad., Dordrecht, Netherlands.

Nicolas, A., and F. Boudier (1995), Mapping oceanic ridge segments in Oman ophiolites, *J. Geophys. Res.*, *100*(B4), 6179–6197, doi:10.1029/94JB01188.

Nicolas, A., and D. Mainprice (2005), Burst of high-temperature seawater injection throughout accreting oceanic crust: A case study in Oman ophiolite, *Terra Nova*, *17*, 326–330, doi:10.1111/j.1365-3121.2005.00617.x.

Nicolas, A., I. Reuber, and K. Benn (1988), A new magma chamber model based on structural studies in the Oman ophiolite, *Tectonophysics*, *151*, 87–105.

Nicolas, A., F. Boudier, B. Ildefonse, and E. Ball (2000), Accretion of Oman and United Arab Emirates ophiolite: Discussion of a new structural map, *Mar. Geophys. Res.*, *21*, 147–179, doi:10.1023/A:1026769727917.

Nicolas, A., D. Mainprice, and F. Boudier (2003), High-temperature seawater circulation throughout crust of oceanic ridges: A model derived from the Oman ophiolites, *J. Geophys. Res.*, *108*(B8), 2371, doi:10.1029/2002JB002094.

Pallister, J. S., and C. A. Hopson (1981), Samail Ophiolite Plutonic Suite: Field relations, phase variation, cryptic variation and layering, and a model of a spreading ridge magma chamber, *J. Geophys. Res.*, *86*(B4), 2593–2644, doi:10.1029/JB086iB04p02593.

Quick, J. E., and R. P. Denlinger (1993), Ductile deformation and the origin of layered gabbro in ophiolites, *J. Geophys. Res.*, *98*, 14,015–14,027.

Rothery, D. A. (1983), The base of a sheeted dyke complex, Oman ophiolite: Implications for magma chambers at oceanic spreading axes, *J. Geol. Soc. London*, *140*, 287–296, doi:10.1144/gsjgs.140.2.0287.

Singh, S. C., G. M. Kent, J. S. Collier, A. J. Harding, and J. A. Orcutt (1998), Melt to mush variations in crustal magma properties along the ridge crest at the southern East Pacific Rise, *Nature*, *394*(6696), 874–878, doi:10.1038/29740.

Singh, S. C., et al. (2006), Seismic reflection images of the Moho underlying melt sills at the East Pacific Rise, *Nature*, *442*, 287–290, doi:10.1038/nature04939.

Stakes, D. S., and H. P. Taylor (1992), The Northern Samail Ophiolite: An oxygen isotope, microprobe and field study, *J. Geophys. Res.*, *97*, 7043–7080, doi:10.1029/91JB02743.

Teagle, D. A. H., J. C. Alt, S. Umino, S. Miyashita, N. R. Banerjee, D. S. Wilson, and the Expedition 309/312 Scientists (2006), Superfast Spreading Rate Crust 2 and 3, *Proc. Integr. Ocean Drill. Program*, *309/312*, doi:10.2204/iodp.proc.309312.2006.

Umino, S., S. Miyashita, F. Hotta, and Y. Adachi (2003), Along-strike variation of the sheeted dike complex in the Oman Ophiolite: Insights into subaxial ridge segment structures and the magma plumbing system, *Geochem. Geophys. Geosyst.*, *4*(9), 8618, doi:10.1029/2001GC000233.

Wilson, D. S., et al. (2006), Drilling to gabbro in intact ocean crust, *Science*, *312*(5776), 1016–1020, doi:10.1126/science.1126090.

Annex A3.

“A New Method to Estimate the Oxidation State of Basaltic Series from Microprobe Analyses”

Elsevier Editorial System(tm) for Journal of Volcanology and Geothermal Research
Manuscript Draft

Manuscript Number: VOLGEO3036

Title: A New Method to Estimate the Oxidation State of Basaltic Series from Microprobe Analyses

Article Type: Research Paper

Keywords: oxygen fugacity; partition coefficient; clinopyroxene; plagioclase; EPMA

Corresponding Author: Dr. Lydéric France, Ph.D.

Corresponding Author's Institution: Université Montpellier 2

First Author: Lydéric France, Ph.D.

Order of Authors: Lydéric France, Ph.D.; Juergen Koepke; Benoit Ildefonse; Florent Bech

Abstract: The oxygen fugacity and therefore the iron redox state of a melt is known to have a strong influence on the liquid line of descent of magmas and thus on the composition of the coexisting melts and crystals. We present a new method to estimate this critical parameter from electron probe microanalyses of two of the most common minerals of basaltic series, plagioclase and clinopyroxene. This method is not based on stoichiometric calculations, but on the different partioning behaviour of Fe3+ and Fe2+ between both minerals and a melt phase: plagioclase can incorporate more Fe3+ than Fe2+, while clinopyroxene can incorporate more Fe2+ than Fe3+. For example, the effect of oxidizing a basaltic partly molten system (Fe3+ is stabilized with respect to Fe2+) results in an increase of FeOtotal in plagioclase, but a decrease in the associated clinopyroxene. We propose an equation, based on published partition coefficients, that allows estimating the redox melt state from these considerations. An application to a set of experimental and natural data attests the validity of the proposed model. The associated error can be calculated and is in average ±1 log unit of the prevailing oxygen fugacity.
In order to reduce the different variables influencing the Fe2+/Fe3+ mineral/melt equilibrium, our model is restricted to basaltic series with $SiO_2 < 60\%$ that have crystallised at intermediate to low pressure (< 0.5 GPa) and under relatively oxidizing conditions ($\Delta FMQ > 0$; where FMQ is the fayalite-magnetite-quartz oxygen buffer equilibrium), but may be parameterized for other conditions. A spreadsheet is provided to assist the use of equations, and to performe the error propagation analysis.

Suggested Reviewers: Gilles Chazot
Gilles.Chazot@univ-brest.fr

Pierre Boivin
P.Boivin@opgc.univ-bpclermont.fr

Dominique Lattard
dlattard@min.uni-heidelberg.de

Carole Cordier
cordier@unisi.it

Cover Letter

Click here to view linked References

Lydéric France
Géosciences Montpellier
CC 060 Bâtiment 22
Université de Montpellier 2,
Place Eugène Bataillon
34095 Montpellier cedex 05
france@gm.univ-montp2.fr

Montpellier, August 4th, 2009

Dear Editor,

Please find attached the manuscript "A New Method to Estimate the Oxidation State of Basaltic Series from Microprobe Analyses" by France L., Koepke J., Ildefonse B., and Bech F., which we are submitting for publication in Journal of Volcanology and Geothermal Research.

The redox state of a melt is a key controlling parameter in magmatology. It can influence its liquid line of descent, modify its crystallization sequence, and influence the liquidus and solidus temperatures as well as the temperature of stability of the different minerals. It is also closely linked to the fluids activity and its determination is of major importance to discuss geochemical and petrological processes. We present here a new tool to estimate the redox state of a melt from electronic microprobe measurements of clinopyroxene and plagioclase, two of the most common magmatic minerals. We believe that this new tool will be useful for many studies in magmatology.

This manuscript is original; no material has been submitted elsewhere.

Best regards,
Lydéric France

Date: 30 Sep 2009 From: "J. Volcanology Geothermal Research" Subject: VOLGEO3036

- Editor decision - moderate revision

Dear Dr. France,

I can now inform you that the reviewers and editor have evaluated the manuscript "A New Method to Estimate the Oxidation State of Basaltic Series from Microprobe Analyses" (Dr. Lydéric France). As you will see from the comments below and on http://ees.elsevier.com/volgeo/, moderate revision has been requested.

Please consider the reviews to see if revision would be feasible. Should you wish to resubmit you should explain how and where each point of the reviewers' comments has been incorporated. For this, use submission item "Revision Notes" when uploading your revision. Also, indicate the changes in an annotated version of the revised manuscript (submission item "Revision, changes marked"). Should you disagree with any part of the reviews, please explain why. To facilitate further review, add line numbers in the text of your manuscript.

Please strictly follow the formatting requirements as presented in the Guide for Authors.

Given that the requested revisions are moderate the new version is required within six weeks.

To submit a revision, go to http://ees.elsevier.com/volgeo/ and log in as an Author. You will find your submission record under Submission(s) Needing Revision.

When resubmitting, please present any figures, tables etc. as separate files. See the Artwork Guidelines on the home page right menu for further file naming conventions, referencing and format issues.

I hope that you will find the comments to be of use to you and am looking forward with interest to receiving your revision.

Thank you for submitting your work to this journal.

Kind regards,

Dr. Malcolm J. Rutherford
Editor
Journal of Volcanology and Geothermal Research

.....
Important note: If a reviewer has provided a review or other materials as attachments, those items will not be in this letter. Please ensure therefore that you log on to the journal site and check if any attachments have been provided.

COMMENTS FROM EDITORS AND REVIEWERS

Editors Decision

This paper is generally well written and deals with a new way to estimate the oxidation state of basaltic magmas, an interesting problem that is well within the range of interests for

this journal. I agree with almost all of the comments from the three reviewers. A modest revision is required to modify some of the details of the introduction and discussion of the results presented. The core data and ideas in the paper appear sound and publication should be timely after the authors address the reviewers comments. I particularly support the suggestions of reviewer Robert Luth who suggests a little more discussion of some of the statements made in the introduction section regarding the nature and importance of oxygen fugacity, and on the previous work on this topic. I Do not anticpate that I will have to send the revised submission out to external reviewers when we receive it.

Malcolm J Rutherford
Editor

Reviewer #1: #60 An other method is the intrinsic fugacity measurement on the bulk rock
#99-105 Lundgaard and Tegner (2004) pointed to the extreme difficulty to properly analyse the iron concentration in small(5-10µ) plagioclase crystals (specially in experimental works) with the electron microprobe. In case of basaltic lavas, plagioclase microlites are larger than in experimental products but only the rim of these crystals is expected to be in chemical equilibrium with the glass matrix. Unfortunatly the rim is generally 5-10µ thick and the same analytical problems as in experimental run products arise. For this reason Lundgaard did not use the measured Fe content BUT the content computed using Sugawara's method. You should adress this problem as the application of your method requires accurate estimates of iron in plagioclase.
#155-159 Kress and Carmichael (1991) empirical equations write : ln(XFe2O3/XFeO) = f(ln(fO2)). Because they are computed from regression calculation with correlation coefficient ? 1, the inverse equation ln(fO2)= g(ln(XFe2O3/XFeO)) should be computed from a specific regression calculation and not deduced by the simple algebraic transformation ln(fO2)= f^-1(ln(XFe2O3/XFeO))

Apparent contradiction : you use first reduced experiments to estimated the FERROUS iron partition coefficient (#206-208) and then lines #215-217 you use McCanta's reduced experiments to estimate the FERRIC iron partition coefficient
#218-235 Confused discussion. McCanta relationship (fig 3a) is poorly constrainted at ?FMQ>-1 because of the very large uncertainties and your best fit don't take in account this uncertainty. Probably this is the reason why the dashed curve does not fit the experimental data at high fO2. You reintroduce the uncertainty effect when you use the 0.4±0.4 constant value (dotted curve)
#391 reference omitted : Contrib Mineral Petrol
fig 1 : not useful
Excel spreadsheet : the Xoxydename nomenclature is confusing to indicate the oxyde wt%. Usually X prefix is used to indicate a fraction (i.e. XFe = Fe molar fraction)

Reviewer #2: This is an excellent paper, and I strongly recommend it for publication. It embodies an idea that I would never have thought of (perhaps many others, too?). There are indeed many problems with current methods available for estimating the redox conditions of basaltic magma. Although this new method has a +-1 log unit uncertainty, its ease of use for the average petrologist makes it an oxybarometer that I suspect will be widely employed.
I could not find any problems with the way it has been formulated, although I confess to being

not too familiar with most of the literature cited.
I will forward an annotated copy of the ms to the journal office. I made some changes in word order, deleted a lot of "have"s, changed "could" to "can", etc. I would suggest the authors not use "evolution" on page 10, because it is not quite the same as "magma evolution", in which deltaFMQ can go either way. They might add: Ghiorso & Evans, Am J Sci 2008, 308, 957-1039 to the references on the FeTi oxybarometer.

Bernard W. Evans, Sept. 2, 2009

Reviewer #3: None - the attached review can go in full to the authors; I have identified myself explicitly at the end of the review. Robert W. Luth

Comments on "A new method to estimate the oxidation state of basaltic series from microprobe analyses" by L. France, J. Koepke, B. Ildefonse, and F. Bech. Submitted to JVGR.

General comments:

The goal of producing a technique by which one could infer the relative fO_2 of a basaltic melt using only the electron microprobe is truly a 'holy grail' of igneous petrology and petrologists. The authors propose such a technique, based on the different partitioning of iron between basaltic melt and clinopyroxene, and basaltic melt and plagioclase. I think the authors are on the right track, but suggest that their model could be significantly improved by a more comprehensive analysis of the partitioning behaviour of Fe^{2+} between melt and clinopyroxene. Figure 2 illustrates the inadequacy of the approach in the current paper, so I would suggest that they do such an analysis prior to publication.

Specific comments:

lines 33-36: This introduction presumes that fO_2 is an independent variable in magmatic systems, rather than merely a convenient monitor of oxidation state. The authors might want to clarify their thinking here.

lines 51-54: C. Herd had a useful article on estimation of fO_2 in basalts in the recent 'Oxygen in the Solar System" RIMG volume. Would be useful to reference it for other techniques for estimation of fO_2 beyond those discussed here.

lines 67-68: Luth and Canil (1993) never claimed their oxybarometer was useful for basaltic systems; their interest was in more ultramafic systems.

lines 76-78: I'm puzzled by the apparent contradiction in the statement that $D_{Pl-melt}^{Fe-total}$ is dependent on fO_2 but the two components of that D ($D_{Pl-melt}^{Fe2+}$and $D_{Pl-melt}^{Fe3+}$d) do not. A bit more explanation would be most helpful here.

lines 83-84: In what sense is a 'tholeiitic basalt system' be a 'precisely constrained compositional system'? Wouldn't you have a large range in Mg/(Mg+Fe) in such a system? How might that affect the partitioning behaviour of Fe? And would a 'tholeiitic' system really be appropriate at oxidizing conditions, such as those for which this calibration is intended?

line 85: It would be useful to define the difference between the notation used for plag (e.g., $D_{Pl-melt}^{Fe-total}$) and that used for cpx (e.g., $D_{cpx-melt}^{*Fe2+}$).

lines 87-95: The authors might want to rephrase this – measurements of Fe^{2+}/Fe^{3+} cannot be correlated to the fO_2 of a magmatic system without knowledge of the functional relationship between Fe^{2+}/Fe^{3+} and fO_2.

Throughout the manuscript, the authors need to specify the units for Fe2O3, FeO, Fe_{cpx}^{3+}, Fe_{cpx}^{2+}, etc – are these wt.% oxides, molar quantities, cations per six oxygens or ?

A more logical arrangement of the manuscript would place the section on 'Controlling parameters' BEFORE the section on the "Model".

line 131: again, specify units of concentration. wt. %? molar?

There is an irritating change in notation between equations (3) and (5).

In equation (6), the authors need to specify how the mole fractions are calculated – are these mole fractions of the oxides assuming an anhydrous composition?

line 171: The authors should discuss why they consider the model of Kress and Carmichael (1991) appropriate for hydrous melts.

lines 205-206: Given the poor quality of fit (R^2= 0.60), the authors need to justify why they did not regress against other compositional parameters in the same fashion as Lundgaard and Tegner (2004) did. I suspect had they done so, they could have improved the fit of this parameter (D) considerably.

Also, crucial in their analysis is the assumption that there was no Fe^{3+} in either the liquid or the cpx in the experiments they selected. Based on McCanta et al's work, I could agree with the latter assumption, but they should outline their justification for the former.

line 210: Again, if this parameter is so strongly influenced by melt composition, why was only SiO_2 regressed against?

lines 217-218: Maybe I missed it, but I did not see where McCanta et al (2004) "proposed an estimation of $D_{cpx-melt}^{Fe3+}$ as a function of the redox conditions."

line 220: The authors need to justify why they chose to fit five data points with a quadratic equation, especially given the uncertainties attributed to the two values at more oxidized conditions. Further, given that they show in the next paragraph that this equation does not extrapolate well to higher fO_2, and abandon it in favour of an fO_2-independent $D_{cpx-melt}^{Fe3+}$, should this section be re-written or omitted entirely?

lines 231-232: How does a constant $D_{cpx-melt}^{Fe3+}$ of 0.4 agree with the data of McCanta et al? If anything, a lower value would agree better with the low fO_2 data…

lines 257-258: In the error propagation analysis, the authors need to justify the neglect of covariance. Having said that, I congratulate the authors for even this level of analysis of propagation of errors; more papers should do this.

lines 261-273 (Model Testing section): I think this section needs to be expanded. First, did all these data fulfill the criteria (e.g., $SiO_2 < 60$ wt.% and $fO_2 > \Delta FMQ$)? Second, there are "error" bars plotted in Figure 4 – are these from propagating the errors as per above, and are they 1σ or 2σ? The agreement of the data points to the predicted values needs to be addressed. For example, the model appears to predict a systematic trend in the fO_2 of the data of Berndt et al. (2005) that appears to be an artefact, but what caused this trend?

line 473: This is not a linear regression in Figure 3.

Robert W. Luth
Edmonton, Alberta
22 September 2009

A New Method to Estimate the Oxidation State of Basaltic Series from Microprobe Analyses

Lydéric France[1,2*], Juergen Koepke[2], Benoit Ildefonse[1], Florent Bech

1: Géosciences Montpellier, CNRS, Université Montpellier 2, CC 60, 34095 Montpellier cedex 05, France
2: Institut fuer Mineralogie, Universitaet Hannover, Callinstrasse 3, 30167 Hannover, Germany
*: Corresponding author: lfrance@um2.fr

Abstract

The oxygen fugacity and therefore the iron redox state of a melt is known to have a strong influence on the liquid line of descent of magmas and thus on the composition of the coexisting melts and crystals. We present a new method to estimate this critical parameter from electron probe microanalyses of two of the most common minerals of basaltic series, plagioclase and clinopyroxene. This method is not based on stoichiometric calculations, but on the different partioning behaviour of Fe^{3+} and Fe^{2+} between both minerals and a melt phase: plagioclase can incorporate more Fe^{3+} than Fe^{2+}, while clinopyroxene can incorporate more Fe^{2+} than Fe^{3+}. For example, the effect of oxidizing a basaltic partly molten system (Fe^{3+} is stabilized with respect to Fe^{2+}) results in an increase of FeO_{total} in plagioclase, but a decrease in the associated clinopyroxene. We propose an equation, based on published partition coefficients, that allows estimating the redox melt state from these considerations. An application to a set of experimental and natural data attests the validity of the proposed model. The associated error can be calculated and is in average ±1 log unit of the prevailing oxygen fugacity.

In order to reduce the different variables influencing the Fe^{2+}/Fe^{3+} mineral/melt equilibrium, our model is restricted to basaltic series with $SiO_2 < 60\%$ that have crystallised at intermediate to low pressure (< 0.5 GPa) and under relatively oxidizing conditions ($\Delta FMQ > 0$; where FMQ is the fayalite-magnetite-quartz oxygen buffer equilibrium), but may be parameterized for other conditions. A spreadsheet is provided to assist the use of equations, and to performe the error propagation analysis.

Key words: *oxygen fugacity, partition coefficient, clinopyroxene, plagioclase, EPMA*

1. Introduction

The oxygen fugacity (fO_2) of basaltic melts is a critical controlling parameter of magmatic processes. It controls the iron redox state of the melt (Kilinc et al., 1983; Kress and Carmichael, 1991; Ottonello et al., 2001; Moretti, 2005; Botcharnikov et al., 2005), and it strongly influences the crystallisation sequences and the composition of crystallising minerals. Grove and Baker (1984), and references therein have shown that the tholeiitic differentiation trend leads to an iron-enrichment of the magma (the "Fenner trend"), while calc-alkaline differentiation trend, which usually corresponds to more oxidizing conditions, allows the early appearance of orthopyroxene and oxides thus forcing a silica enrichment (the "Bowen trend"). More recently Berndt et al. (2005) and Feig et al. (2006) have shown that in a given tholeiitic series, the oxidation state modifies *(i)* the liquidus temperature of the different mineral phases, and *(ii)* the order of crystallization of mineral phases. In a H_2-buffered system the iron redox state of the melt is closely linked to the H_2O content (e.g., Botcharnikov et al., 2005), the knowledge of the redox state therefore brings information on the evolution of magmatic series (e.g., wet versus dry trends) and finally on processes/reactions occurring in magma chambers (e.g., Kuritani, 1998; Ginibre et al., 2002; Cordier et al., 2007). The iron redox state of basaltic magmas is also considered to place an upper limit to the fO_2 of their mantle source (e.g., Basaltic Volcanism Study Project, 1981; Carmichael and Ghiorso, 1986; Wood et al., 1990; Carmichael, 1991; Ballhaus, 1993; Ballhaust and Frost, 1994).

In basaltic series, the fO_2 is usually estimated by using the geooxybarometer based on the equilibrium between ilmenite and magnetite (Buddington and Lindsley, 1964; Anderson and Lindsley, 1985; Bacon and Hirschmann, 1988; Ghiorso and Sack, 1991; Sauerzapf et al., 2008). However, this method has limitations as coexisting ilmenite and magnetite are not always present in basaltic series. Moreover, oxide minerals are easily reequilibrated at lower temperature (e.g., Venezky and Rutherford, 1999; Koepke et al., 2008), either during slow

cooling or during hydrothermal alteration processes. Another common method is to measure the Fe^{3+}/Fe^{2+} ratio (or Fe_2O_3/FeO) of either fresh glasses representing frozen melts, or minerals. For fresh lavas, this ratio can be directly determined from the whole rock composition (e.g., Rhodes and Vollinger, 2005), by measuring both ferrous iron and total iron contents. The alternate solution is to determine the Fe^{3+}/Fe^{2+} ratio in minerals and to calculate the value of the corresponding melt using partition coefficients (Tegner et al., 2003). The Fe^{3+} content in minerals is commonly estimated using formula calculations based on appropriate mineral stoichiometry. However, Canil and O'Neill (1996) and Sobolev et al. (1999) have shown that these calculations for silicates such as clinopyroxene (Cpx) or plagioclase (Pl) are not valid. Therefore, the best way to constrain the prevailing fO_2 in a magmatic system is to measure the Fe^{3+}/Fe^{2+} ratio in minerals directly. For example, Luth and Canil (1993) proposed an oxybarometer based on Mössbauer spectroscopy analysis of Fe^{3+} and Fe^{2+} in Cpx. Delaney et al. (1998) have shown that synchrotron micro-XANES probe can be used to measure Fe^{3+}/Fe^{2+} even in minerals like Pl that have only very small bulk iron contents. Thanks to this method, Tegner et al. (2003) constrained the fO_2 in the Skaergaard layered intrusion by measuring the Fe^{3+} contents in Pl. However, one problem by constraining the redox conditions of melt from Fe^{3+}/Fe^{2+} ratio in minerals is that the partition coefficient of Fe^{3+} and of Fe^{2+} between mineral and melt must be known (Tegner et al., 2003). For Pl, Sato (1989) and Phinney (1992) have proposed that the partition coefficient of FeO_{total} ($D_{Pl-melt}^{Fe\_total}$) increases with the fO_2 due to substitution of Al_2O_3 by Fe_2O_3. Lundgaard and Tegner (2004), using the same thermodynamic model as Sugawara (2000, 2001), have shown that $D_{Pl-melt}^{Fe2+}$ and $D_{Pl-melt}^{Fe3+}$ do not depend on fO_2, while $D_{Pl-melt}^{Fe\_total}$ does. In addition, their data show that $D_{Pl-melt}^{Fe3+}$ is much larger than $D_{Pl-melt}^{Fe2+}$ (0.19-0.92 and 0.008-0.05, respectively) and that both depend on the melt composition. Consequently, Pl incorporates Fe^{3+} better than Fe^{2+}. In Cpx,

McCanta et al. (2004) give $D^{Fe3+}_{Cpx-melt}$ values ranging from 0 to 0.77. As Fe^{2+} in typical magmatic Cpx is a major element, it does not follow the Henry's law, and partition coefficients should be used with caution. Nevertheless, for a precisely constrained compositional system, as it is the case for the tholeiitic basaltic system, a rough estimate of an "apparent partition coefficient" (noted $D*^{Fe2+}_{Cpx-melt}$) could be made by the evaluation of available experimental data (see section "Controlling parameters").

Other methods are available to determine the fO_2 of magmatic systems, such as measurements with the EELS technique (e.g., Van Aken et al., 1998; Van Aken and Liebscher, 2002). King et al. (2000) have shown that the partitioning of Fe^{3+}/Fe_{total} between amphibole and melt is close to unity and thus Fe^{3+} contents in Amphibole reflect the fO_2 of the melt.

Fialin et al. (2001 and 2004) have shown that the Fe^{3+}/Fe_{total} of some minerals and glasses could be estimated with the electron microprobe using the self-absorption-induced shift of the Fe$L\alpha$ peak. Estimating the fO_2 from the partitioning of Eu between Pl and melt (Wilke and Behrens, 1999) or from the partitioning of V between olivine and melt (Canil, 1997) is also largely used.

A problem resulting from constraining the melt fO_2 from micro-XANES via synchrotron radiation, EELS, Mössbauer or trace element in plagioclase or olivine is that such facilities are not easily accessible to the whole community and couldn't be use as routine analyses.

In the present paper we propose a new simple method to estimate the fO_2 of basaltic series based on microprobe analyses of two of the most common minerals of basaltic series (Pl and Cpx). This method does not include stoichiometric estimations based on formula calculations; it is restricted to basaltic systems under relatively oxidizing conditions ($\Delta FMQ>0$). Hence, it is well-suited for an application to subduction zone-related basaltic series which are characterized by relatively oxidizing redox conditions (e.g., Johnson et al., 1994; Kelley and Cottrell, 2009). Moreover, since the presence of water has generally an oxidizing effect on the

redox conditions (e.g., Botcharnikov et al., 2005), this method is also well-suited for an application to hydrous MORB-type systems, e.g., the melts produced at the gabbro/dike transition from fast-spreading mid-ocean ridges, where magmatic and hydrothermal reactions interfere (e.g., Nicolas et al., 2008; Koepke et al., 2008; France et al., 2009a, 2009b).

2. Model

The model presented here allows the estimation of the redox conditions, expressed as ΔFMQ, at which a basaltic rock has crystallised, based on microprobe analyses of FeO_{total} in Cpx and Pl.

Our model is based on the different behaviour of the partioning coefficients $K_{DFe_2O_3/FeO}^{Cpx-melt}$ and $K_{DFe_2O_3/FeO}^{Pl-melt}$. These K_D are equivalent to the ratio of the partition coefficient of Fe_2O_3 and FeO between Cpx and melt, and between Pl and melt, respectively: $K_{DFe_2O_3/FeO}^{Cpx-melt} = D_{Cpx-melt}^{Fe3+} / D*_{Cpx-melt}^{Fe2+}$ and $K_{DFe_2O_3/FeO}^{Pl-melt} = D_{Pl-melt}^{Fe3+} / D_{Pl-melt}^{Fe2+}$. In basaltic series the K_D are around 0.4 and 18 for Cpx and Pl, respectively (see the next section "controlling parameters" for estimation of $D_{Cpx-melt}^{Fe3+}$, $D*_{Cpx-melt}^{Fe2+}$, $D_{Pl-melt}^{Fe3+}$ and $D_{Pl-melt}^{Fe2+}$). Thus, $D_{Cpx-melt}^{Fe3+}$ is lower than $D*_{Cpx-melt}^{Fe2+}$ and $D_{Pl-melt}^{Fe3+}$ is significantly higher than $D_{Pl-melt}^{Fe2+}$. Consequently, when a melt is oxidized (Fe^{2+} content decreases and Fe^{3+} content increases) FeO_{total} decreases in Cpx and increases in Pl (Figure 1).

The ratio between the total iron contents in Cpx and Pl could be written as the ratio of the sums of ferric and ferrous iron in Cpx and Pl, respectively :

$$\frac{FeO_{Cpx}^{total}}{FeO_{Pl}^{total}} = \frac{Fe_{Cpx}^{total}}{Fe_{Pl}^{total}} = \frac{Fe_{Cpx}^{3+} + Fe_{Cpx}^{2+}}{Fe_{Pl}^{3+} + Fe_{Pl}^{2+}} \qquad (1)$$

The partition coefficients ("D" for trace elements) and apparent partition coefficients ("D*" for major element for a small range of melt composition) are defined by the relation: $D^{element}_{\min eral-melt} = [conc.]_{\min eral} / [conc.]_{melt}$.

Where "conc." is the concentration of the considered element. By using partition coefficients, the ratio between the total iron contents in Cpx and Pl can be expressed from the composition of the melt :

$$\frac{\mathrm{FeO}^{\mathrm{total}}_{Cpx}}{FeO^{total}_{Pl}} = \frac{\left[\left(Fe^{3+}_{melt} \times D^{Fe3+}_{Cpx-melt}\right) + \left(Fe^{2+}_{melt} \times D*^{Fe2+}_{Cpx-melt}\right)\right]}{\left[\left(Fe^{3+}_{melt} \times D^{Fe3+}_{Pl-melt}\right) + \left(Fe^{2+}_{melt} \times D^{Fe2+}_{Pl-melt}\right)\right]} \qquad (2)$$

A factorisation of (2) leads to :

$$\frac{\mathrm{FeO}^{\mathrm{total}}_{Cpx}}{FeO^{total}_{Pl}} = \frac{\left[\left(D^{Fe3+}_{Cpx-melt} \times \frac{Fe^{3+}_{melt}}{Fe^{2+}_{melt}}\right) + D*^{Fe2+}_{Cpx-melt}\right]}{\left[\left(D^{Fe3+}_{Pl-melt} \times \frac{Fe^{3+}_{melt}}{Fe^{2+}_{melt}}\right) + D^{Fe2+}_{Pl-melt}\right]} \qquad (3)$$

A reorganisation of equation (3) by using the relation (4) (where M_{FeO} and M_{Fe2O3} are the molar masses of the oxides: 71.85 and 159.69g/mol, respectively) leads to equation 5 :

$$\frac{Fe^{3+}_{melt}}{Fe^{2+}_{melt}} = \left(\frac{Fe_2O_3}{FeO}\right)_{melt} \times \frac{M_{FeO} \times 2}{M_{Fe_2O_3}} \qquad (4)$$

$$\left(\frac{Fe_2O_3}{FeO}\right)_{melt} = \frac{D*^{2+}_{Cpx-melt} - \left(FeO^{total}_{Cpx} \Big/ FeO^{total}_{Pl} \times D^{2+}_{Pl-melt}\right)}{-D^{3+}_{Cpx\_melt} + \left(FeO^{total}_{Cpx} \Big/ FeO^{total}_{Pl} \times D^{3+}_{Pl-melt}\right)} \times \frac{M_{Fe2O3}}{M_{FeO} \times 2} \qquad (5)$$

Equation (5) links the Fe_2O_3/FeO ratio of the melt to the total iron content of the Cpx and Pl for a set of parameters (partitions coefficients and molar masses). The Fe_2O_3/FeO ratio is directly linked to the oxidation state of the melt. According to Kress and Carmichael (1991) the Fe_2O_3/FeO ratio of the melt is linked to its fO_2 by the empirical relation :

$$\log(fO_2) = \log\left\{\exp\left(\frac{\ln\left(\frac{Fe_2O_3}{FeO}\right)_{melt} - \frac{b}{T} - c - \sum_i diXi}{a}\right)\right\} \quad (6)$$

with a=0.207; b=12 980; c=-6.115; d_{SiO2}=-2.368; d_{Al2O3}=-1.622 and d_{CaO}=2.073. With T the temperature in K and Xi between 0 and 1. The equation (7) should be used if high pressure and high temperature (>1630°) are considered :

$$\log(fO_2) = \log\left\{\exp\left(\frac{\ln\left(\frac{Fe_2O_3}{FeO}\right)_{melt} - \frac{b}{T} - c - \sum_i diXi - e\left[1 - \frac{T_0}{T} - \ln\left(\frac{T}{T_0}\right)\right] - f\frac{P\times10^9}{T} - g\frac{(T-T_0)P\times10^9}{T} - h\frac{(P\times10^9)^2}{T}}{a}\right)\right\} \quad (7)$$

with a=0.196; b=11 492; c=-6.675; e=-3.36; f=-7.01 10-7; g=-1.54 10-10; h=3.85 10-17; d_{Al2O3}=-2.243; d_{FeO*}=-1.828; d_{CaO}=3.201; d_{Na2O}=5.854; d_{K2O}=6.215 and T_0=1673. With P the pressure in GPa and T in K and Xi between 0 and 1.

Ottonello et al. (2001) have proposed a new thermodynamic model for calculating the oxidation state of Fe in dry silicate melts and glasses at atmospheric pressure. Moretti (2005) have extended this model considering the pressure and water content effect. In their Figure 12, Botcharnikov et al. (2005) have shown that the differences between these different models are small. The use of the model proposed by Moretti (2005) is restricted to melt of known water content. However, since the water content of those natural melts crystallizing plagioclase and pyroxene is generally unknown, the general application of the model of Moretti (2005) is hampered. Therefore, we use the model of Kress and Carmichael (1991).

The redox state of a melt can be better understood by comparing the fO_2 to oxygen buffers. We recall here the relations corresponding to the FMQ (equation 8) and to the NNO (where NNO is the Ni-NiO solid oxygen buffer equilibrium; equation 9) oxygen buffers from Ballhaus et al. (1991):

$$\Delta FMQ = \log fO_2 - \left(82.75 + 0.00484T - 30681/T - 24.45\log T + 940\,P/T - 0.02P\right) \quad (8)$$

$$\Delta NNO = \log fO_2 - \left(12.78 - 25073/T - 1.1\log T + 450\,P/T + 0.025P\right) \quad (9)$$

From (8) and (9) the redox state of a melt could be obtained by knowing P, T, the composition of the melt, and the composition in total iron of Cpx and Pl (FeO_{Cpx}^{total} and FeO_{Pl}^{total}). We provide an EXCEL spreadsheet (supplementary material) in order to facilitate the use of equations (5), (6) and (8). The estimation of partition coefficients $D_{Cpx-melt}^{Fe3+}$, $D_{Pl-melt}^{Fe3+}$, $D_{Pl-melt}^{Fe2+}$ and apparent partition coefficient $D*_{Cpx-melt}^{Fe2+}$ is discussed in the following part.

2.1. Controlling parameters

To estimate the redox state of a melt with the model presented here, it is necessary to know the partition coefficients $D_{Pl-melt}^{Fe3+}$, $D_{Pl-melt}^{Fe2+}$, $D_{Cpx-melt}^{Fe3+}$ and apparent partition coefficient $D*_{Cpx-melt}^{Fe2+}$ (equation 5).

We estimate these parameters by evaluating the existing literature data. It should be noted that the accuracy of our model can by improved in the future, with new data on partition coefficients.

$D_{Pl-melt}^{Fe3+}$ and $D_{Pl-melt}^{Fe2+}$ can be calculated from the melt composition by using equation (10) determined by Lundgaard and Tegner (2004) who presented an important and detailed study on this subject:

$$\ln(D) = a\sum_i biXi \quad (10)$$

Parameters determined by Lundgaard and Tegner (2004) for equation (10) are summarized in Table 1.

198 $D^{*Fe2+}_{Cpx-melt}$ and $D^{Fe3+}_{Cpx-melt}$ remain poorly constrained in literature. As recalled in the
199 introduction, a prerequisite for the estimation of $D^{*Fe2+}_{Cpx-melt}$ is to identify the compositional
200 field of interest, since $D^{*Fe2+}_{Cpx-melt}$ is strongly dependent on the composition of the system.
201 Since our study focuses on basaltic systems, we derive $D^{*Fe2+}_{Cpx-melt}$ empirically by evaluating
202 experimental data in basaltic and andesitic systems with SiO_2<60 wt%. For this, we use the
203 studies of Snyder et al. (1993), Toplis et al. (1994), Toplis et Carroll (1995), Berndt et al.
204 (2005), Freise et al. (2009), Botcharnikov et al. (2008), and unpublished data from S. Feig.
205 Based on more than 100 experiments, we find a correlation between the SiO_2 content of the
206 melt and the $D^{*Fe2+}_{Cpx-melt}$ (R^2=0.6; Figure 2): SiO_2= 10.431 $D^{*Fe2+}_{Cpx-melt}$ + 41.784. Because we
207 use only experimental data from reducing experiments (ΔFMQ<0), we assume that the
208 estimated apparent partition coefficient is a good approximation for the case of ferrous iron.
209 Taking into account that the parameter $D^{*Fe2+}_{Cpx-melt}$ is only an apparent partition coefficient,
210 strongly influenced by the melt composition, we chose to consider a relatively large error for
211 this parameter, corresponding to twice the standard deviation (Figure 2). Several studies on
212 basaltic series (e.g., Dale and Henderson, 1972; Bougault and Hekinian, 1974; Jones and
213 Layne, 1997) have bracketed $D^{*Fe2+}_{Cpx-melt}$ between 0.714 and 1, which is in agreement with
214 Figure 2.
215 To estimate $D^{Fe3+}_{Cpx-melt}$, we use the work of McCanta et al. (2004), who have performed
216 experiments at reducing conditions (ΔFMQ varies between -5.0 and 0.5), and calculated the
217 associated $D^{Fe3+}_{Cpx-melt}$. Despite the large standard deviations in their results (Figure 3a),
218 McCanta et al. (2004) have proposed an estimation of $D^{Fe3+}_{Cpx-melt}$ as a function of the redox
219 conditions. This evolution is best fitted (R^2=0.998) by equation 11 (Figure 3a):

$$D_{Cpx-melt}^{Fe3+} = 0.0348 \times (\Delta FMQ)^2 + 0.3038 \times \Delta FMQ + 0.6522 \quad (11)$$

With this equation, the evolution of $D_{Cpx-melt}^{Fe\_total}$ with increasing ΔFMQ values can be calculated. Figure 3b displays the evolution of the $D_{Cpx-melt}^{Fe\_total} / D*_{Cpx-melt}^{Fe2+}$ ratio, for increasing ΔFMQ values if equation (11) is applied (dashed curve). In the Figure 3b model (dashed curve) we use an average temperature of 1150°C and a $D*_{Cpx-melt}^{Fe2+}$ = 1 that correspond to the average values of the experimental data (diamonds); for this reason, the scattering of experimental data cannot be reproduced by the model. It is obvious that the curve calculated using equation (11) does not reproduce oxidizing experimental data (ΔFMQ>0) from literature (Figure 3b). For oxidizing conditions, data from literature display a $D_{Cpx-melt}^{Fe\_total} / D*_{Cpx-melt}^{Fe2+}$ ratio which is on average lower than 1 (Figure 3b). As a melt oxidation results in an increase of its ferric content, the variation of $D_{Cpx-melt}^{Fe\_total} / D*_{Cpx-melt}^{Fe2+}$ with the ΔFMQ value, attests to the influence of $D_{Cpx-melt}^{Fe3+}$ on $D_{Cpx-melt}^{Fe\_total}$. It shows that $D*_{Cpx-melt}^{Fe2+} > D_{Cpx-melt}^{Fe3+}$. If we use $D_{Cpx-melt}^{Fe3+}$ =0.4±0.4, which is in agreement (Figure 3a) with the data of McCanta et al. (2004), without considering the evolution of this partition coefficient with the redox conditions (equation 11), the oxidizing experimental data (ΔFMQ>0) from literature are better reproduced (Figure 3b; dotted curve).

2.2. Limitations

The model is valid for Cpx-Pl pairs crystallized under equilibrium conditions. As the partition coefficients are derived from basaltic series with SiO_2<60%, the model should be restricted to such compositions. Moreover, it has been elaborated for lavas and since the partition coefficients have been derived from experiments performed under shallow pressures ranging between 10^{-4} GPa (1 atm) and 0.5 GPa, we recommend using the model within this pressure

interval. To apply this model to other systems or pressures, a re-evaluation of the corresponding partition coefficients is necessary.

Another important limitation comes from the concept of the model itself. Discriminating between reducing and oxidizing conditions is possible because of the different partioning behaviour of Fe^{3+} with respect to Pl/melt and Cpx/melt. Since under reducing conditions, the Fe^{3+} content of the melt is very small, the error in the estimation increases drastically. Therefore, we recommend to apply the model only for relatively oxidizing conditions with an oxygen fugacity equal to, or higher than the FMQ oxygen buffer.

2.3. Error propagation analysis

For each parameter (partition coefficients), an associated error is given. For $D^{Fe3+}_{Cpx-melt}$ and $D*^{Fe2+}_{Cpx-melt}$ the used associated errors are large (± 0.4 for $D^{Fe3+}_{Cpx-melt}$ and ± 0.2 for $D*^{Fe2+}_{Cpx-melt}$) to account for the poor constrains on these parameters. Errors on FeO^{total}_{Cpx}, FeO^{total}_{Pl}, melt composition, T and P are also considered in the error propagation analysis. The error propagation analysis has been performed following Ku (1966) by considering all variables as independent. Details of the calculation are summarized in the Appendix. The error propagation analysis is also included in the spreadsheet provided as supplementary material.

3. Model Testing

In order to test our model, we have selected a set of natural and experimental data (Figure 4), where Cpx, Pl and melt compositions are given together with an estimation of the redox state for basaltic compositions with SiO_2 contents below 60 wt%. For natural data, we use the study of Cordier et al. (2007) from the Blanco Deep at the East Pacific Rise. Experimental data are taken from Berndt et al. (2005), Feig et al. (2006), Freise et al. (2009), Parat et al.

(2008), and Feig (personal communication). It should be noted that the experimental data from Berndt et al. (2005), Freise et al. (2009), and Feig (personal communication) used in Figure 2 for calibration under reducing condition are not the same as those under oxidizing conditions used here to test the model.

Taking into account the errors calculated for our model, most of the calculated oxygen fugacity expressed in log units relative to the FMQ oxygen buffer are in good agreement with the published ones (Figure 4).

4. Conclusion

The model presented here allows us to estimate the redox state in basaltic rocks that contain plagioclase and clinopyroxene. It is based on the different partitioning behaviour of ferric and ferrous iron between clinopyroxene and melt and plagioclase and melt. Input data are FeO_{total} contents of these minerals which can be easily measured using an electron microprobe, melt composition and approximate equilibrium temperature. The application of our model is restricted to basaltic series containing less than 60% of SiO_2 equilibrated under shallow pressures and under oxidizing conditions ($\Delta FMQ>0$). The accuracy of this method is about ±1 log unit, and the exact associated error can easily be calculated along with the ΔFMQ using a spreadsheet provided within the supplementary material.

Acknowledgments

Ariel Provost (LMV, Clermont-Ferrand, France) is thanked for checking the error propagation analysis. Carole Cordier (MNA, Siena, Italy) is thanked for providing unpublished data and discussions. Roberto Moretti (INVG, Naples, Italy) is thanked for providing the software associated with his redox determination model that has been used in the first steps of elaboration of our model.

Appendix: Error-propagation analysis

Error associated to the ΔFMQ value obtained with equations (8-6-5) can be calculated using the equation:

$$\sigma_{\Delta FMQ}{}^{2} = \left[\frac{\partial \Delta_{FMQ}}{\partial Sc} \times \sigma_{Sc}\right]^2 + \left[\frac{\partial \Delta_{FMQ}}{\partial Sp} \times \sigma_{Sp}\right]^2 + \left[\frac{\partial \Delta_{FMQ}}{\partial D^{++}_{Cpx-melt}} \times \sigma_{D^{++}_{Cpx-melt}}\right]^2 + \left[\frac{\partial \Delta_{FMQ}}{\partial D^{+++}_{Cpx-melt}} \times \sigma_{D^{+++}_{Cpx-melt}}\right]^2 + \left[\frac{\partial \Delta_{FMQ}}{\partial D^{++}_{Pl-melt}} \times \sigma_{D^{++}_{Pl-melt}}\right]^2 + \left[\frac{\partial \Delta_{FMQ}}{\partial D^{+++}_{Pl-melt}} \times \sigma_{D^{+++}_{Pl-melt}}\right]^2 + \ldots$$

$$\ldots + \left[\frac{\partial \Delta_{FMQ}}{\partial P} \times \sigma_{P}\right]^2 + \left[\frac{\partial \Delta_{FMQ}}{\partial T} \times \sigma_{T}\right]^2 + \left[\frac{\partial \Delta_{FMQ}}{\partial Xi} \times \sigma_{Xi}\right]^2$$

Where *Sc* and *Sp* represent the FeO_{total} content of clinopyroxene and plagioclase, respectively.

With:

$$\frac{\partial \Delta_{FMQ}}{\partial Sc} \times \sigma_{Sc} = \frac{1}{a \ln 10}\left\{\frac{\left(1/Sp\right)\left(D^{+++}_{Cpx-melt}D^{++}_{Pl-melt} - D^{+++}_{Pl-melt}D^{++}_{Cpx-melt}\right)}{\left[-D^{+++}_{Cpx-melt} + \left(\frac{Sc}{Sp} \times D^{+++}_{Pl-melt}\right)\right]\left[D^{++}_{Cpx-melt} - \left(\frac{Sc}{Sp} \times D^{++}_{Pl-melt}\right)\right]}\right\}$$

$$\frac{\partial \Delta_{FMQ}}{\partial Sp} \times \sigma_{Sp} = \frac{1}{a \ln 10}\left\{\frac{\left(Sc/Sp^{2}\right)\left(D^{+++}_{Pl-melt}D^{++}_{Cpx-melt} - D^{+++}_{Cpx-melt}D^{++}_{Pl-melt}\right)}{\left[-D^{+++}_{Cpx-melt} + \left(\frac{Sc}{Sp} \times D^{+++}_{Pl-melt}\right)\right]\left[D^{++}_{Cpx-melt} - \left(\frac{Sc}{Sp} \times D^{++}_{Pl-melt}\right)\right]}\right\}$$

$$\frac{\partial \Delta_{FMQ}}{\partial D^{++}_{Cpx-melt}} \times \sigma_{D^{++}_{Cpx-melt}} = \frac{1}{a \ln 10} \times \frac{1}{\left[D^{++}_{Cpx-melt} - \left(Sc/Sp \times D^{++}_{Pl-melt}\right)\right]}$$

301 $$\frac{\partial \Delta_{FMQ}}{\partial D^{+++}_{Cpx-melt}} \times \sigma_{D^{+++}_{Cpx-melt}} = \frac{1}{a \ln 10} \times \frac{1}{\left[- D^{+++}_{Cpx-melt} + \left(Sc \diagup Sp \times D^{+++}_{Pl-melt} \right) \right]}$$

302 $$\frac{\partial \Delta_{FMQ}}{\partial D^{++}_{Pl-melt}} \times \sigma_{D^{++}_{Pl-melt}} = \frac{1}{a \ln 10} \times \frac{\left(- Sc \diagup Sp \right)}{\left[D^{++}_{Cpx-melt} - \left(Sc \diagup Sp \times D^{++}_{Pl-melt} \right) \right]}$$

303 $$\frac{\partial \Delta_{FMQ}}{\partial D^{+++}_{Pl-melt}} \times \sigma_{D^{+++}_{Pl-melt}} = \frac{1}{a \ln 10} \times \frac{\left(Sc \diagup Sp \right)}{\left[- D^{+++}_{Cpx-melt} + \left(Sc \diagup Sp \times D^{+++}_{Pl-melt} \right) \right]}$$

304 $$\frac{\partial \Delta_{FMQ}}{\partial P} \times \sigma_P = - \frac{940}{T} + 0.02$$

305 $$\frac{\partial \Delta_{FMQ}}{\partial T} \times \sigma_T = \left(\frac{1}{T^2} \right) \left[\frac{b}{a \ln 10} + 940P - 30681 \right] + \frac{24.45}{T \ln 10} - 0.00484$$

306 $$\frac{\partial \Delta_{FMQ}}{\partial Xi} \times \sigma_{Xi} = - \frac{di}{a \ln 10}$$

References

Andersen, D.J., Lindsley, D.H., 1985. New (and final!) models for the Ti-magnetite/ilmenite geothermometer and oxygen barometer. Abstract AGU 1985 Spring Meeting Eos Transactions. American Geophysical Union 66-416.

Bacon, C.R., Hirschmann, M.M., 1988. Mg/Mn partitioning as a test for equilibrium between coexisting Fe-Ti oxides. Am. Mineral. 73, 57-61.

Ballhaus, C., Berry, R.F., Green, D.H., 1991. High pressure experimental calibration of the olivine-orthopyroxene-spinel oxygen geobarometer: implications for the oxidation state of the upper mantle. Contrib. Mineral. Petrol. 107, 27-40.

Ballhaus, C., 1993. Redox states of lithospheric and asthenospheric upper mantle. Cont. Min. Pet. 114, 331-348.

Ballhaus, C., Frost, B.R., 1994. The generation of oxidized CO_2-bearing basaltic melts from reduced CH_4-bearing upper mantle sources. Geochim. Cosmochim. Acta 58, 4931-4940.

Basaltic Volcanism Study Project, 1981. Temperature and gas fugacities of planetary basalts. Pergamon Press Inc., New York, 371-384.

Berndt, J., Koepke, J., Holtz, F., 2005. An experimental investigation of the influence of water and oxygen fugacity on differentiation of MORB at 200MPa. J. Petrol. 46, 135-167.

Botcharnikov, R.E., Koepke, J., Holtz, F., McCammon, C., Wilke, M., 2005. The effect of water activity on the oxidation and structural state of Fe in a ferro-basaltic melt. Geochim. Cosmochim. Acta 69, 5071-5085.

Botcharnikov, R.E., Almeev, R.R., Koepke, J., Holtz, F., 2008. Phase Relations and Liquid Lines of Descent in Hydrous Ferrobasalt-Implications for the Skaergaard Intrusion and Columbia River Flood Basalts. J. Petrol. 49-9, 1687-1727.

Bougault, H., Hekinian, R., 1974. Rift valley in the Atlantic Ocean near 36 degrees 50'N; petrology and geochemistry of basalt rocks. Earth Planet. Sci. Lett. 24, 249-261.

Buddington, A.F., Lindsley D.H., 1964. Iron-titanium oxide minerals and synthetic equivalents. J. Petrol. 5, 310-357.

Canil, D., 1997. Vanadium partitioning and the oxidation state of Archaean komatiite magmas. Nature 389, 842-845.

Canil, D., O'Neill, H.St.C., 1996. Distribution of Ferric Iron in some Upper-Mantle Assemblages. J. Petrol. 37, 609-635.

Carmichael, I.S.E., 1991. The redox state of basic and silicic magmas: a reflection of their source regions? Cont. Min. Pet. 106, 129-141.

Carmichael, I.S.E., Ghiorso, M.S., 1986. Oxidation-reduction in basic magmas: a case for homogeneous equilibria. Earth Planet. Sci. Letters 78, 200-210.

Cordier, C., Caroff, M., Juteau, T., Fleutelot, C., Hémond, C., Drouin, M., Cotton, J., Bollinger, C., 2007. Bulk-rock geochemistry and plagioclase zoning in lavas exposed along the northern flank of the Western Blanco Depression (Northeast Pacific): Insight into open-system magma chamber processes. Lithos 99, 289-311.

Dale, I. M., Henderson, P., 1972. The Partition of Transition Elements in Phenocryst-bearing Basalts and the Implications about Melt Structure. 24th Int Geol Congr Sect 10, 105-111.

Delaney, J.S., Dyar, M.D., Sutton, S.R., Bajt, S., 1998. Redox ratio with relevant resolution; solving an old problem by using the synchrotron micro-XANES probe. Geology 26, 139-142.

Feig, S.T., Koepke, J., Snow, J.E., 2006. Effect of water on tholeiitic basalt phase equilibria: an experimental study under oxidizing conditions. Cont. Min. Pet. 152, 611-638.

Fialin, M., Wagner, C., Métrich, N., Humler, E., Galoisy, L., Bézos, A., 2001. Fe^{3+}-ΣFe vs. Fe Lα peak energy for minerals and glasses: Recent advances with electron microprobe. American Mineralogist 86, 456-465.

Fialin, M., Bézos, A., Wagner, C., Magnien, V., Humler, E., 2004. Quantitative electron microprobe analysis of Fe^{3+}-ΣFe: Basic concepts and experimental protocol for glasses. American Mineralogist 89, 654-662.

France, L., Ildefonse, B., Koepke, J., 2009a. Interactions between magma and the hydrothermal system in the Oman ophiolite and in IODP hole 1256D: fossilization of a dynamic melt lens at fast spreading ridges. Accepted for publication to Geochem Geophys Geosyst.

France, L., Koepke, J., Ildefonse, B., Cichy, S.B., Deschamps, F., 2009b. Hydrous partial melting in the sheeted dike complex at fast spreading ridges: Experiments and nature. Submitted to Contrib. Mineral. Petrol.

Freise, M., Holtz, F., Nowak, M., Scoates, J.S., Strauss, H., 2009. Differentiation and crystallization conditions of basalts from the Kerguelen large igneous province: An experimental study. Contrib. Mineral. Petrol. on line first Doi: 10.1007/s00410-009-0394-5

Ghiorso, M.S., Sack, R.O., 1991. Fe-Ti oxide geothermometry: thermodynamic formulation and the estimation of intensive variables in silicic magmas. Cont. Min. Pet. 108, 485-510.

Ginibre, C., Wörner, G., Kronz, A., 2002. Minor- and trace-element zoning in plagioclase: implications for magma chamber processes at Parinacota volcano, northern Chile. Cont. Min. Pet. 143, 300-315.

Grove, T.L., Baker, M.B., 1984. Phase equilibrium controls on the tholeiitic versus calc-alkaline differentiation trends. J. Geophys. Res. 85, 3253-3274.

Johnson, M.C., Anderson, A.T., Rutherford, M.J., 1994. Pre-eruptive volatile contents of magmas. In: Carroll, M.R., Holloway, J.R., (eds) Volatiles in magmas. Rev. Mineral. vol. 30. Mineralogical Society of America, Washington, DC, United States, pp 281-330.

Jones, R.H., Layne, G.D., 1997. Minor and trace element partitioning between pyroxene and melt in rapidly cooled chondrules. Am. Mineral. 82, 534-545.

Kelley, K.A., Cottrell, E., 2009. Water and the oxidation state of subduction zone magmas. Science 325:605-607, doi: 10.1126/science.1174156.

Kilinc, A., Carmichael, I.S.E., Rivers, M.L., Sack, R.O., 1983. The ferric-ferrous ratio of natural silicate liquids equilibrated in air. Cont. Min. Pet. 83, 136-140.

King, P.L., Hervig, R.L., Holloway, J.R., Delaney, J.S., Dyar, M.D., 2000. Partitioning of Fe^{3+}-Fe_{total} between amphibole and basanitic melt as a function of oxygen fugacity. Earth Planet. Sci. Letters 178, 97-112.

Koepke, J., Christie, D.M., Dziony, W., Holtz, F., Lattard, D., Maclennan, J., Park, S., Scheibner, B., Yamasaki T., and Yamazaki S., 2008. Petrography of the Dike/Gabbro Transition at IODP Site 1256 (Equatorial Pacific): The evolution of the Granoblastic Dikes. Geochem. Geophys. Geosyst. 9-7, Q07O09, doi:10.1029/2008GC001939.

Kress, V.C., Carmichael, I.S.E., 1991. The compressibility of silicate liquids containing Fe_2O_3 and the effect of composition, temperature, oxygen fugacity and pressure on their redox states. 108, 82-92.

Ku, H., 1966. Notes on the Use of Propagation of Error Formulas. J Research of National Bureau of Standards-C. Engineering and Instrumentation, Vol. 70C, No.4, 263-273.

Kuritani, T., 1998. Boundary layer crystallisation in a basaltic magma chamber: Evidence from Rishiri volcano, Northern Japan. J. Petrol. 39, 1619-1640.

Lundgaard, K.L., Tegner, C., 2004. Partitioning of ferric and ferrous iron between plagioclase and silicate melt. Cont. Min. Pet. 147, 470-483.

Luth, R.W., Canil, D., 1993. Ferric iron in mantle-derived pyroxenes and a new oxybarometer for the mantle. Cont. Min. Pet. 113, 236-248.

McCanta, M.C., Dyar, M.D., Rutherford, M.J., Delaney, J.S., 2004. Iron partitioning between basaltic melts and clinopyroxene as a function of oxygen fugacity. Am. Mineral. 89, 1685-1693.

Moretti, R., 2005. Polymerization, basicity, oxidation state and their role in ionic modelling of silicate melts. Ann. Geoph. 48, 583-608.

Nicolas, A., Boudier, F., Koepke, J., France, L., Ildefonse, B., Mevel, C., 2008. Root zone of the sheeted dike complex in the Oman ophiolite. Geochem. Geophys. Geosyst. 9:Q05001, doi:10.1029/2007GC001918.

Ottonello, G., Moretti, R., Marini, L., Zuccolini, M.V., 2001. Oxidation state of iron in silicate glasses and melts: a thermochemical model. Chem. Geol. 174, 157-179.

Parat, F., Holtz, F., Feig, S., 2008. Pre-eruptive conditions of the Huerto andesite (Fish canyon system, San Juan volcanic field, Colorado): Influence of volatiles (C-O-H-S) on phase equilibria and mineral composition. J. Petrol. 49-5, 911-935.

Phinney, W.C., 1992. Partition coefficients for iron between plagioclase and basalts as a function of oxygen fugacity: Implications for Archean and lunar anorthosites. Geochim. Cosmochim. Acta 56, 1885-1895.

Rhodes, J.M., Vollinger, M.J., 2005. Ferric/Ferrous ratio in 1984 Mauna Loa lavas: a contribution to understanding the oxidation state of Hawaiian magmas. Cont. Min. Pet. 149, 666-674.

Sato, H., 1989. Mg-Fe partitioning between plagioclase and liquid in basalts of Hole 504B, ODP Leg 111: A study of melting at 1atm. Proc Ocean Drilling Program Sci Results 111, 17-26.

Sauerzapf, U., Lattard, D., Burchard, M., Engelmann, R., 2008. The titanomagnetite-ilmenite equilibrium: new experimental data and thermo-oxybarometric application to the crystallisation of basic to intermediate rocks. J. Petrol. 49-6, 1161-1185.

Snyder, D., Carmichael, I.S.E., Wiebe, R.A., 1993. Experimental study of liquid evolution in an Fe-rich, layered mafic intrusion: constraints of Fe-Ti oxide precipitation on the T-f_{O2} and T-ρ paths of tholeiitic magmas. Cont. Min. Pet. 113, 73-86.

Sobolev, V.N., McCammon, C.A., Taylor, L.A., Snyder, G.A., Sobolev, N.V., 1999. Precise Moessbauer milliprobe determination of ferric iron in rock-forming minerals and limitations of electron microprobe analysis. Am. Mineral. 88, 1145-1152.

Sugawara, T., 2000. Thermodynamic analysis of Fe and Mg partitioning between plagioclase and silicate liquid. Cont. Min. Pet. 138, 101-113.

Sugawara, T., 2001. Ferric iron partitioning between plagioclase and silicate liquid: thermodynamics and petrologicaly applications. Cont. Min. Pet. 141, 659-686.

Tegner, C., Delaney, J.S., Dyar, M.D., Lundgaard, K.L., 2003. Iron in Plagioclase as a monitor of oxygen fugacity in Skaergaard, Bushveld and Bjerkreim-Sokndal layered intrusions, and anorthosite of the Rogaland igneous province. Geophysical Research Abstracts 5, 08789.

Toplis, M.J., Libourel, G., Carroll, M.R., 1994. The role of phosphorus in crystallisation processes of basalt: An experimental study. Geochim. Cosmochim. Acta 58-2, 797-810.

Toplis, M.J., Carroll, M.R., 1995. An Experimental Study of the Influence of Oxygen Fugacity on Fe-Ti Oxide Stability, Phase Relations, and Mineral-Melt Equilibria in Ferro-Basaltic Systems. J. Petrol. 36-5, 1137-1170.

Van Aken, P.A., Liebscher, B., Styrsa, V.J., 1998. Quantitative determination of iron oxidation states in minerals using Fe $L_{2,3}$-edge electron energy-loss near-edge structure spectroscopy. Phys. Chem. Minerals 25, 323-327.

Van Aken, P.A., Liebscher, B., 2002. Quantification of ferrous/ferric ratio in minerals: new evaluation schemes of Fe L_{23} electron energy-loss near-edge spectra. Phys. Chem. Minerals 29, 188-200.

Venezky, D.Y., Rutherford, M.J., 1999. Petrology and Fe-Ti oxide reequilibration of the 1991 Mount Unzen mixed magma. J. Volcanol. Geotherm. Res. 89, 213-230.

Wilke, M., Behrens, H., 1999. The dependence of the partitioning of iron and europium between plagioclase and hydrous tonalitic melt on oxygen fugacity. Cont. Min. Pet. 137, 102-114.

Wood, B.J., Bryndzia, L.T., Johnson, K.E., 1990. Mantle oxidation state and its relationship to tectonic environment and fluid speciation. Science 248, 337-345.

Table 1: Parameters determined by Lundgaard and Tegner (2004) to use in equation (10).

	Sub-alkaline		Alkaline	
	$\ln(D_{Pl-melt}^{Fe_2O_3})$	$\ln(D_{Pl-melt}^{FeO})$	$\ln(D_{Pl-melt}^{Fe_2O_3})$	$\ln(D_{Pl-melt}^{FeO})$
Regression coefficients b_i				
SiO_2	0.0167	0.00298	0.0176	0.0655
TiO_2	-0.0578	-0.0201	-0.0509	0.0205
Al_2O_3	-0.0394	-0.0589	-0.0395	-0.0155
FeO_{total}	-0.0779	-0.0559	-0.107	0.0115
MgO	-0.0295	-0.107	-0.0872	-0.0363
CaO	-0.000558	-0.00484	-0.0252	0.100
Na_2O	-0.0292	-0.140	-0.114	0.0122
K_2O	0.130	-0.0430	0.0530	0.0642
a	-0.211	-1.555	0.980	-8.263

462 ***Figures captions:***

463 Figure 1: Rationale for the proposed model. FeO_{total} decreases in Cpx and increases in Pl
464 when the parental melt is oxidized.

465

466 Figure 2: SiO_2 vs. $D*^{Fe2+}_{Cpx-melt}$ plot for experimental data of experiments performed under
467 reducing conditions. Data are from Snyder et al. (1993), Toplis et al. (1994), Toplis & Carroll
468 (1995), Berndt et al. (2005), Freise et al. (2009), Botcharnikov et al. (2008), and Feig
469 (personal communication). The thick lines correspond to the range of accepted error (~2σ).
470 The thin line is the regression line with SiO_2=10.431 $D*^{Fe2+}_{Cpx-melt}$ +41.784 (R^2~0.6).

471

472 Figure 3: a) Values for $D^{Fe3+}_{Cpx-melt}$ as a function of the oxygen fugacity expressed in log units
473 relative to the FMQ oxygen buffer; after McCanta et al. (2004). The equation is for the linear
474 regression (black line); standard deviations (black bars) are given in McCanta et al. (2004). b)
475 Oxygen fugacity expressed in log units relative to the FMQ oxygen buffer as function of
476 $D^{Fe\_total}_{Cpx-melt} / D*^{Fe2+}_{Cpx-melt}$, showing the influence of $D^{Fe3+}_{Cpx-melt}$ on the evolution of $D^{Fe\_total}_{Cpx-melt}$ when
477 oxidizing conditions are varying. The dashed curve is calculated using equation (11), after
478 McCanta et al. (2004), and the doted curve is calculated using a value of $D^{Fe3+}_{Cpx-melt}$ =0.4 (±0.4),
479 which is in agreement with the data of McCanta et al. (2004). In b), both models (dotted and
480 dashed lines) use fixed values: T=1150°C and $D*^{Fe2+}_{Cpx-melt}$ = 1. Data in b) are from Snyder et
481 al. (1993), Toplis et al. (1994), Toplis & Carroll (1995), Berndt et al. (2005), and Feig et al.
482 (2006).

483

484 Figure 4: Comparison of oxygen fugacity expressed in log units relative to the FMQ oxygen
485 buffer calculated with our model and given in literature for the same data. Data are from
486 Berndt et al. (2005), Feig et al. (2006), Cordier et al. (2007), Parat et al. (2008), Freise et al.
487 (2009), and Feig et al. (personal communication). Error bars are those for values calculated
488 with our model. Most of the calculated values are consistent with literature in the range of ±1
489 log unit (shaded area), which corresponds to the average standard deviation calculated with
490 the model.

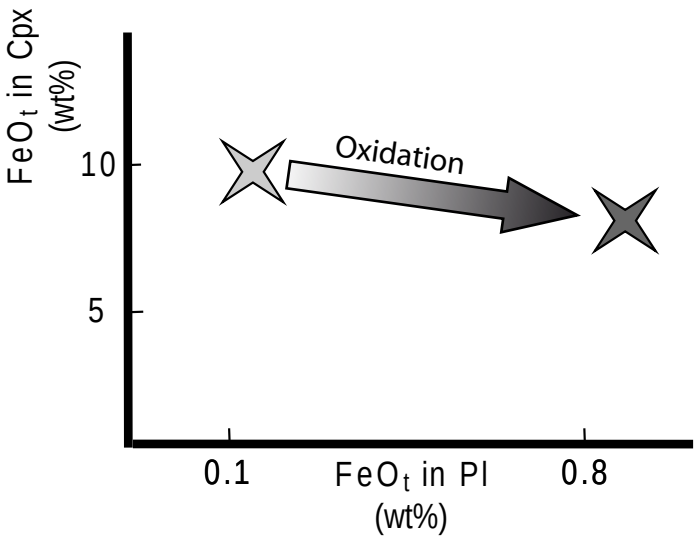

France et al., Fig. 1

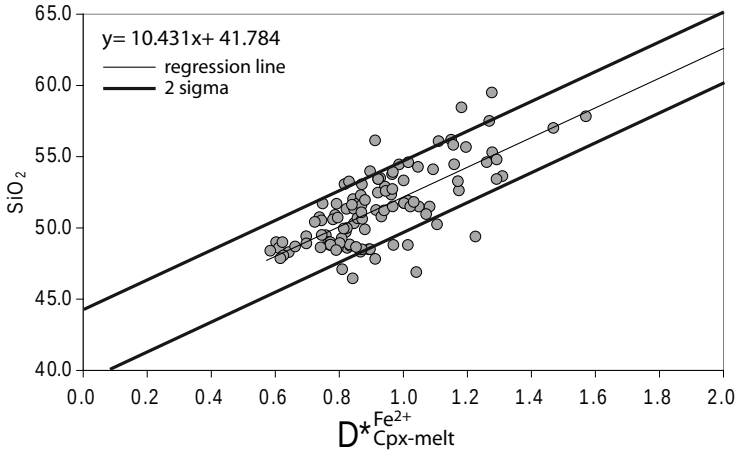

France et al., Fig. 2

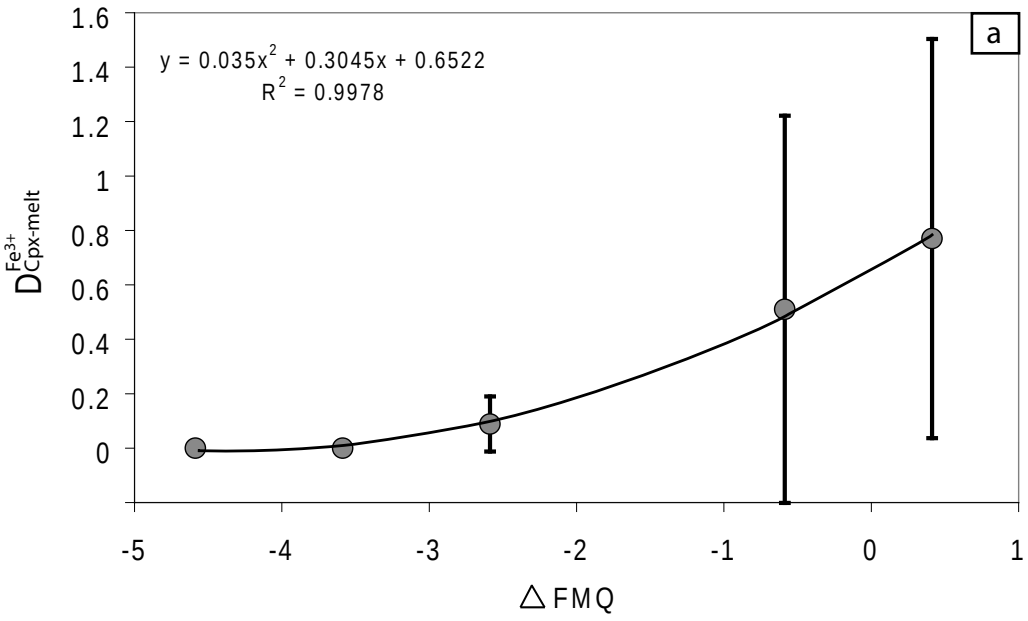

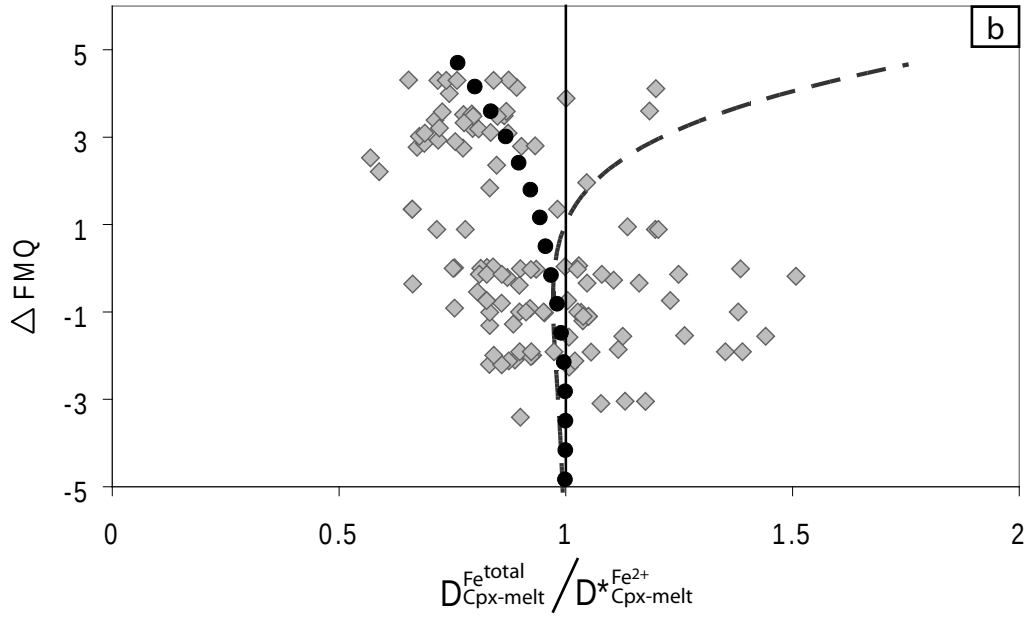

France et al., Fig. 3

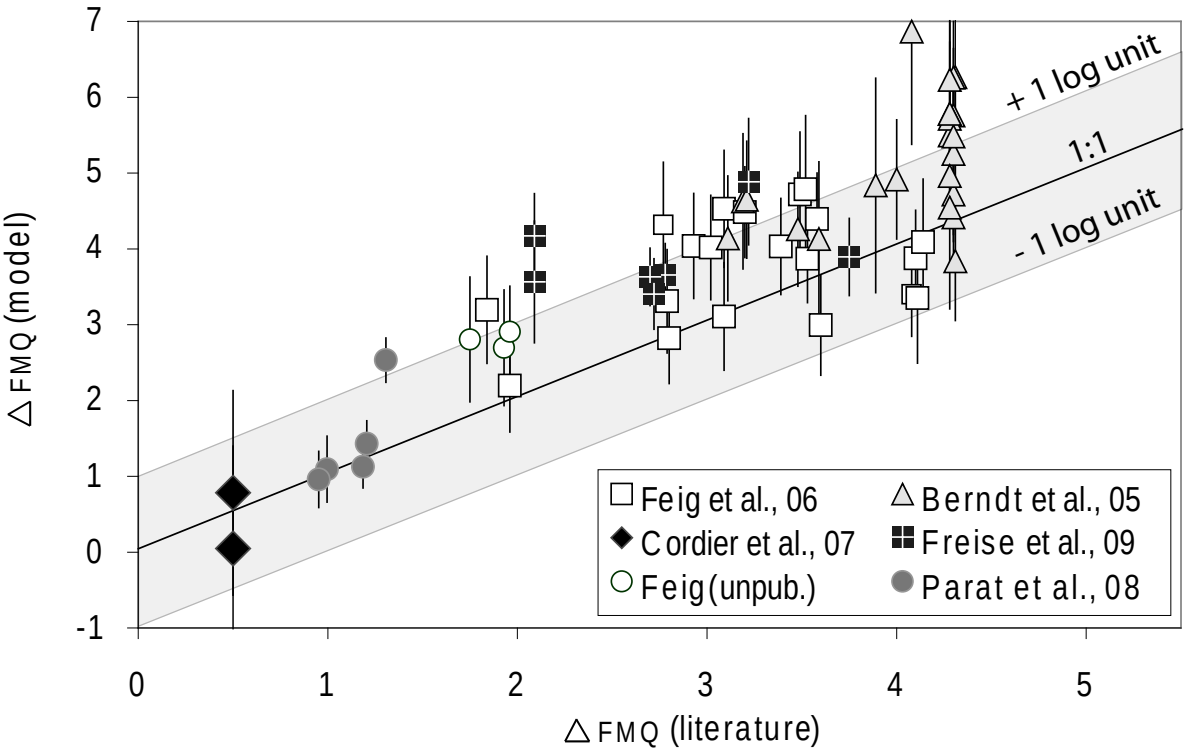

France et al., Fig. 4

Annex A4.

“Gabbros from IODP Site 1256 (Equatorial Pacific): Insight into axial magma chamber processes at fast-spreading ocean ridges”

Gabbros from IODP Site 1256 (Equatorial Pacific): Insight into axial magma chamber processes at fast-spreading ocean ridges

J. Koepke [a,*], W. Dziony [a], L. France [b,a]

[a] Institut fuer Mineralogie, Leibniz University Hannover, Callinstr. 3, 30167 Hannover, Germany
[b] Géosciences Montpellier, CNRS, Université Montpellier 2, CC60, F-34095 Montpellier Cedex 05, France

Submitted to Geochemistry, Geophysics, Geosystems

within the theme

"Formation and Evolution of Oceanic Crust Formed at Fast Spreading Rates"

* corresponding author:
Dr. Jürgen Koepke
Institut für Mineralogie der Leibniz Universität Hannover
Callinstrasse 3
D-30167 Hannover
Germany
e-mail: koepke@mineralogie.uni-hannover.de
Tel.: 0049 511 7624084
Fax: 0049 511 7623045

Abstract

The ODP/IODP three-leg campaign at Site 1256 (Leg 206, Expeditions 309 and 312) provides the first continuous in situ sampling of fast-spread ocean crust from the extrusive lavas, through the sheeted dikes and down into the uppermost gabbros (Cocos plate; East Pacific Rise; eastern equatorial Pacific). This paper focuses on a detailed petrographic and microanalytical investigation of the gabbro section drilled during Expedition 312.

We identified three principal components making up the gabbros of Hole 1256D which are closely associated in domains of different lithologies/textures and of varying amounts and which are responsible for the marked patchiness and spotty appearances observed in many gabbros: (1) subophitic, (2) granular, and (3) microgranular domains. Each of these units derived from different parental sources and was formed under quite different conditions of crystallization. In a first high-temperature stadium, a relative primitive high-temperature component of an ascending axial melt lens progressed into the overlying conducting boundary layer. Stoping and assimilation of previously metamorphosed dikes (the "granoblastic" dikes) were very effective, expressed by high amounts of microgranular patches in the gabbros. At a later stage, at distinctly lower temperatures, the high temperature mush was intermingled by a low-temperature magma of highly evolved composition.

None of the analyzed minerals in the investigated domains match those compositions to be expected for the crystallization of normal MORB. Instead, it is implied that the magma chamber was filled with melts/magmas of strange compositions, e.g., of highly fractionated, uneruptable liquids.

Index Terms

3625 Petrography, microstructures, and textures; 3660 Metamorphic petrology; 1012 Reactions and phase equilibria; 1021 Composition of the oceanic crust; 8416 Mid-oceanic ridge processes.

1. Introduction

1.1. IODP Hole 1256D

IODP (Integrated Ocean Drilling Program) Site 1256 is located in the eastern equatorial Pacific on 15 Ma oceanic crust of the Cocos plate formed at the East Pacific Rise under superfast spreading conditions (220 mm/yr full spreading rate). Hole 1256D, initiated by ODP Leg 206 and continued by IODP Expeditions 309 and 312 penetrated the entire upper oceanic crust, passing through a ~ 250-m thick sediment sequence, a ~ 800-m thick lava series and a relatively thin, ~350-m thick sheeted dike complex before finally extending ~100 m into the uppermost gabbros [*Teagle et al.*, 2006; *Wilson et al.*, 2006]. Hole 1256D represents the first complete penetration of the upper oceanic crust reaching the gabbroic section and is necessarily an important reference section for the dike/gabbro transition of fast-spreading ocean crust. Initial drilling results from Site 1256, together with site maps and details on the geological setting and the observed lithostratigraphic units can be found in *Teagle et al.*, [2006] and *Teagle et al.* [2007].

Previous paper related to the petrology and geochemistry of the drilled rocks at Site 1256 dealt with basalt alteration processes [*Busigny et al.*, 2005; *Laverne et al.*, 2006; *Sano et al.*, 2008] and with basalt formation [*Umino et al.*, 2008; *Tartarotti et al.*, 2009]. *Koepke et al.* [2008] identified the so-called “granoblastic dikes”, a ~ 60 m thick horizon of contact-metamorphic, previously altered sheeted dikes as a boundary layer between the active magma

system of the melt lens and the low-temperature, convecting hydrothermal system within the sheeted dike section. Hole 1256D provides the first in situ access for petrological and geochemical investigation of this geochemically important zone. Two pyroxene equilibrium temperatures for this zone range between 930°C and 1050°C, implying that conditions within the granoblastic zone were appropriate for hydrous anatexis, with the potential to generate partial melts of trondhjemitic composition. The downhole evolution of the granoblastic overprint is expressed by systematic changes in texture, phase composition and calculated equilibrium temperature, consistent with thermal metamorphism by a deeper heat source. Thermal modeling implies a long-lasting heat source located beneath the granoblastic dikes, corresponding to a steady-state, high-level axial magma chamber (AMC) located at the base of the sheeted dike section.

The drilled record of the gabbro section below the granoblastic dikes was initially interpreted to be composed of two individual bodies (named "Gabbro 1" and "Gabbro 2" in this paper) separated by a screen of granoblastic dikes ("Upper Dike Screen") and underlain by another horizon of granoblastic dikes ("Lower Dike Screen") as depicted in Fig. 1a [*Teagle et al.*, 2006; *Wilson et al.*, 2006; *Koepke et al.*, 2008]. Investigations in sections displaying the dike/gabbro transition in the Oman ophiolite revealed very similar petrographic and structural features compared to Site 1256 [*France et al.*, 2009]. In a comparative petrographical and geochemical study, *France et al.* [2009] re-interpreted the drilled gabbro section at Site 1256 as one continuous gabbro body representing the fossilized axial melt lens (AML), where the upper and the lower dike screens correspond to stoped clasts of partially resorbed granoblastic dikes which were accumulated in the lower part of the axial melt lens (Fig. 1b).

This paper focuses on a detailed petrographic and microanalytical investigation of the gabbro section drilled during Expedition 312, and is based on the shipboard petrographical work. The basic materials for this paper are the original shipboard thin sections, which were

petrographically initially investigated during the ship cruise. In the course of this study, the same sections were carefully reinvestigated including a very detailed microanalytical survey. Individual descriptions of the analyzed sections can be found in *Teagle et al.* [2006] including detailed information about structural and metamorphic features, estimates of the modal amounts of primary and secondary minerals, and presentation of various microscopic images. Corresponding numbers of those figures of *Teagle et al.* [2006] presenting petrographic details of samples used in this study are included in Table 1.

1.2. Methods

Sample names are shortened from the original IODP descriptions [see *Teagle et al.*, 2006]. Details are given in Table 1. Petrographic features of the investigated samples are given in Table 2. Electron probe microanalyses (EPMA) were performed using a Cameca SX100 electron microprobe equipped with 5 spectrometers and an operating system "Peak sight". All data were obtained using 15 kV acceleration potential, a static (fixed) beam, Kα emission from all elements, and the "PAP" matrix correction [*Pouchou and Pichoir*, 1991]. Most element concentrations were obtained with a beam current of 15 nA and a counting time of 20 to 120 seconds on peak and background. Averages are presented in Table 3. For completeness and comparison, some diagrams also include mineral compositions from lavas and dikes of the upper section [*Dziony et al.*, 2008; *Yamazaki et al.*, 2009], as well as from selected lithologies of the gabbroic section [e.g., upper and lower dike screen, xenoliths, from *France et al.*, 2009; *Yamazaki et al.*, 2009]. The whole data set of mineral compositions from lavas, dikes, granoblastic dikes, and gabbros based on more than 5000 single analyses can be provided as spreadsheet on request.

We used three independent geothermometers to estimate equilibrium temperatures: the 2-pyroxene thermometer ["QUILF", *Andersen et al.*, 1993]; the amphibole-plagioclase thermometer [*Holland and Blundy*, 1994], and the Ti-in-amphibole thermometer [*Ernst and*

98 *Liu*, 1998] which is applicable, since all amphiboles considered coexist with Fe-Ti oxides.
99 The results are presented in Table 2.

100 2. Petrography of the gabbro section

101 *2.1. Primary magmatic features*

102 2.1.1. General characteristics

103 Gabbroic rocks from Hole 1256D span a wide range of compositions covering gabbro
104 (clinopyroxene gabbro), oxide gabbro, gabbronorite, norite, and highly differentiated rocks
105 like quartz-rich diorites. Detailed petrographic descriptions of the different gabbroic units as
106 well as of the upper and lower dike screens can be found in *Teagle et al.* [2006]. Primitive
107 members characteristic for the lower oceanic crust from fast-spreading ridges like olivine
108 gabbros [see review in *Coogan*, 2007] are missing. The olivines observed in the 1256D
109 gabbros are relatively iron-rich and coexist with orthopyroxene and oxide mostly in the
110 absence of clinopyroxene, thus not typical for primitive olivine gabbros. Typical "foliated
111 gabbros" where constituent minerals show in general a steep magmatic foliation observed in a
112 high crustal level from Hess Deep [*MacLeod et al.*, 1996] or from the Oman ophiolite
113 [parallel to the strike of the sheeted dyke complex, *MacLeod et al.*, 2002; *Nicolas et al.*, 2008;
114 *France et al.*, 2009; *Nicolas et al.*, 2009], are not recovered.

115 Compared to the Oman ophiolite, the recovered gabbros at Site 1256 show some
116 similarities with the uppermost gabbro horizon, directly below the sheeted dikes often named
117 "varitextured gabbro" [*Lippard et al.*, 1986; *MacLeod et al.*, 2002; *Nicolas et al.*, 2008], a 50
118 to 100 m thick horizon characterized by extreme variability in texture, grain size and chemical
119 composition, generally lacking any foliation. However there are some differences between
120 both locations. First, pegmatitic varieties with grain sizes of several cm common in Oman
121 were not observed in the 1256D gabbros. Second, different gabbro types like subophitic and

granular facies mixed together in the Oman ophiolite are more coherent units with uniform lithologies within a meter to decameter level, while the varitextured characteristics in the 1256D gabbros are varying in a very small scale, often within a thin section level, as demonstrated below.

A key feature of the 1256D gabbros is the strong variation in mineralogy and texture within a mm to cm scale. This is expressed by a marked patchiness and spotty appearances in many gabbros [*Teagle et al.*, 2006]. Detailed petrographic investigations revealed that this is mostly due to different domains closely associated representing different types of gabbro, mostly also contrasting in texture. Best examples for very patchy rocks are represented by Gabbro 1, where locally two domains of different lithologies are intimately mixed together: cm-sized spots of gabbro composed only of plagioclase enclosed in clinopyroxene oikocrysts in a subophitic style swimming in a network of granular oxide norite [e.g., Fig. F210 in *Teagle et al.,* 2006]. An overview of the petrographic characteristic of the investigated 1256D gabbros is presented in Table 2.

2.1.2. Principal lithological/textural components

We identified three principal components making up the gabbros of Hole 1256D which are closely associated in domains of different lithologies/textures and of varying amounts (Fig. 2):

(1) Subophitic domains - composed of mm-sized poikilitic clinopyroxene enclosing plagioclase chadacrysts which sometimes show hollows and skeletal growth (for details see section 2.1.3). No other minerals are present. Characteristic are very primitive compositions of both phases (see section 3.1.).

(2) Granular domains - mostly composed of prismatic plagioclase, amphibole, orthopyroxene, and granular oxide. True primary amphiboles characterized by pargasitic composition and idiomorphic crystal shape [e.g., Fig. AF3D in *Teagle et al.,* 2006] only rarely survived a

147 secondary overprint where they were altered to hornblende or actinolitic aggregates. While
148 clinopyroxene is widely absent, relatively iron-rich olivine may join this assemblage. Rarely,
149 quartz is present forming interstitial graphophyric intergrowths with plagioclase. The phase
150 assemblage and the generally evolved mineral compositions (see section 3.1.) imply that this
151 lithology represents a more differentiated stage of magmatic evolution.
152 (3) Microgranular domains - composed of wormy intergrowth of plagioclase, clinopyroxene,
153 orthopyroxene and oxide mostly as roundish inclusions within the granular gabbro. Often,
154 clinopyroxene grains bear numerous inclusions of tiniest oxide spots. This feature, the overall
155 textural appearance, and the mineral compositions (see section 3.1.) imply that these domains
156 represent relics of previously stoped granoblastic dikes. A variety within this domain are
157 patches composed of poikilitic orthopyroxenes filled with numerous very small inclusions of
158 clinopyroxene, which are also interpreted to represent relics of former granoblastic dikes stage
159 (see section 3.4.2. for details).

160 In all rocks investigated in this study at least two domains were indentified (Table 2).
161 Rocks with subophitic domains are more common in Gabbro 1, whereas rocks with
162 microgranular patches are more common in Gabbro 2. The arrangement of different domains
163 can be rather complex as demonstrated in Fig. 3 showing sample 232_2_98_100 from Gabbro
164 2 composed of 4 different domains.

165 It is important to note that the contacts between the different domains are always
166 smooth and continuous, sometimes of lobate style [Fig. 3 and Fig. F210 in *Teagle et al.,*
167 2006], reflecting the result of mingling of different crystal mushes or magmas in the pure
168 magmatic regime. Only in Gabbro 2 typical comb layering developed in medium grained
169 oxide gabbro at the contact to fine-grained gabbros characterized by high amounts of
170 microgranular domains [Table 2; Fig. F236E in *Teagle et al.,* 2006], implying the presence of
171 a larger thermal contrast between these units. This is discussed in section 4. 1.

2.1.3. Record of fast quenching processes within the subophitic domains

Some plagioclase chadacrysts within clinopyroxene oikocrysts in the subophitic domains of Gabbro 1 show characteristic fillings and skeletal growth, as demonstrated in Fig. 2a and 4a, b. Such features are indicative for fast crystal growth [e.g., *Bryan*, 1972], not typical for slow crystal growth conditions in oceanic magma chambers. Similar features, but generally in a finer scale, are well known from the dikes and basalts of the upper section [e.g., Figs. F222 and AF1 in *Teagle et al.,* 2006], where a high degree of undercooling is indicated, due to the efficiently hydrothermally cooled environment.

The filling of the 1 mm long plagioclase needles in Fig. 4 is composed of clinopyroxene with identical composition as the hosting oikocryst, suggesting a formation simultaneously to the crystallization of the oikocryst framework. This implies the following scenario. First, plagioclases crystallized initially very fast under high undercooling conditions, producing well-known effects, such as skeletal growth and the presence of cavities and hollows. Continuous undercooling supported further growth of plagioclase (including the hollows) up to mm-sized aggregates, until clinopyroxene started to grow from the intercumulus liquid enclosing plagioclases and filling the hollows and cavities within the latter.

The source of cooling is probably the relative cold conducting boundary layer (CBL) at the roof of a dynamic AML, which is a decameter-thick zone with a very strong temperature gradient [e.g., *Coogan et al.*, 2003]. This is conform with the lithostratigraphy of Hole 1256D, where the interval of granoblastic dikes directly above the gabbros was recently identified as part of a dynamic CBL overlying the AML [*Koepke et al.,* 2008]. Provided that an upward moving melt lens progresses fast into the granoblastic dikes, thereby consuming the lowermost thin zone of the CBL which is in thermal equilibrium with the magma, colder zones of the CBL may be reached by the ascending magma, maintaining the very special conditions of undercooling in such a dynamic system. It should be noted that such features up

198 to now are not described from any oceanic gabbro. Such features are also unknown from
199 typical static magma chamber systems like Layered Intrusions, where characteristic roof
200 crystallization at the top of the magma chamber occurs, displaying textures identical with
201 those resulting from the main crystallization in the interior of the magma body [e.g., *Wager*
202 *and Brown*, 1968]. Possible petrological consequences of such reactions (e.g., the addition of
203 water to the system) are discussed below.

204 *2.2. Hydrothermal alteration*

205 All gabbroic rocks suffered a pervasive hydrothermal alteration mostly under greenschist
206 facies condition, expressed by the presence of patches and veins mainly filled with chlorite,
207 epidote, actinolite, secondary plagioclase, and secondary magnetite. Moreover, many gabbros
208 show the record of an isostatic hydrothermal overprint at significantly higher temperatures,
209 expressed by the presence of diopsidic pyroxene and true hornblende which often forms
210 pseudomorphs after idiomorphic magmatic amphibole, which is pargasitic in composition.
211 Single-clinopyroxene thermometry using QUILF for secondary diopsides of two samples
212 (compositions in Table 3) revealed equilibration temperatures between 740 and 760°C, so
213 well within the amphibolite facies, matching also the observation of secondary ortho-
214 amphibole overgrowth in Gabbro 1 [*Teagle et al.,* 2006]. The Ti-in-amphibole temperatures
215 estimated for hornblendes vary between 601 and 714 °C (Table 2).

216 3. Microanalytical investigations

217 *3.1. Mineral compositions in the principal domains*

218 The strong difference in texture and mineralogy between the different domains composing the
219 1256D gabbros is also reflected by a significant contrast in phase chemistry.

3.1.1. Subophitic domain

Clinopyroxene and plagioclase of the subophitic domain from Gabbro 1 are significantly more primitive in composition compared to all the other lithologies of the gabbroic section (Fig. 5). While the TiO_2 and Al_2O_3 contents of the clinopyroxenes show similar values like those from fresh lavas and dikes (Fig. 5a), the Mg# (MgO/(MgO+FeO)*100; molar) with values between 82 – 85 are generally very high, even higher than most of the corresponding values from fresh lavas and dikes (Fig. 5b). Plagioclase chadacrysts vary only slightly in An content, showing generally extreme high values between 76 and 80 mol%. Three of four averages are higher in An content than the highest values from plagioclases from fresh lava and dikes (Fig. 5b). In the plagioclase An content versus clinopyroxene Mg# diagram of Fig. 5b, a crystallization path is included which was modeled with COMAGMAT [*Ariskin*, 1999] for the case of equilibrium crystallization using the most primitive basalt composition of recovered lava and dikes as starting composition [sample 1256D, 309, 161R, 2-1cm, piece 9; composition in *Teagle et al.*, 2006]. While the analyzed minerals of fresh lavas and dikes fit well with the modeled trend, the plagioclase chadacrysts of the subophitic domain clearly plot away from the trend, mainly due to too An-rich plagioclases. The most plausible explanation for this is a crystallization in a hydrous system instead of in a dry system, shifting the An content of the plagioclase to significant higher values [*Gaetani et al.*, 1993; *Feig et al.*, 2006; *Koepke et al.*, 2009]. Due to the oxidizing effect of water, the Mg# of the clinopyroxenes is also shifted to higher values in such a case [*Feig et al.*, 2006; *Koepke et al.*, 2009]. We assume that the source of water is due to the incorporation of granoblastic dikes typically containing hydrous phases [*Koepke et al.,* 2008; *France et al.,* 2009] at the top of an ascending AML. This interpretation is also in agreement with the observed strong undercooling effects during the crystallization of the subophitic domains of Gabbro 1 (see section 2.1.3.)

245 Both clinopyroxenes and plagioclases show typical normal zoning effects towards the
246 rims of the crystals, which is expressed by lower Mg# and Cr_2O_3 contents (Fig. 4c), and lower
247 An contents (Fig. 6b), respectively (Table 3).

248 Some clinopyroxene oikocrysts in the subophitic domains show a characteristic
249 structure of wormy lamellae in the outer rims, in part with symplectitic quartz-plagioclase
250 intergrowths at the contact to primary amphibole of the granular network domain. For details
251 see Fig. AF3 in *Teagle et al.* [2006]. The composition of these zones is distinct from the
252 clinopyroxene core compositions, with lower Mg# and contents of Ti, Al, Na (Fig. 4d, Table
253 3). Striking is the low Cr_2O_3 content approaching zero, while the corresponding values of the
254 core vary between 0.3 and 0.7 wt%. These zones are also compositionally different from the
255 "normal" zoned rims of the clinopyroxene oikocrysts which have Cr_2O_3 contents between 0.2
256 and 0.6 wt% and which develop more or less continuously from the cores towards the borders
257 of the crystals (Fig. 4c, Table 3).

258 We interpret the complex zoning effects observed in the clinopyroxene oikocrysts as a
259 result of magma reactions at two different stages during the magmatic evolution. The
260 continuous zoning (Fig. 4c) reflects variations in melt composition from a very primitive
261 MORB (Mg# of the cores from 82-85) to a less primitive compositions (Mg# of the rims 74-
262 78) during a primary high-temperature stage. On the other hand, the wormy intergrowth was
263 formed by reaction with a much more differentiated melt (Cr_2O_3 content near zero) during a
264 secondary stage at much lower temperatures probably under hydrous conditions (involvement
265 of primary amphibole).

266 3.1.2. Granular domain

267 The principal phases of the granular domain are significantly more evolved compared to the
268 corresponding phases in the subophitic domain, as shown for clinopyroxene and plagioclase
269 in Fig. 5 with Mg# varying from 68 to 74, and An contents varying from 50 to 65 mol%,

respectively (Table 3). Relatively low Mg# were also obtained for coexisting orthopyroxene (63 -75; Table 3). Low values in Mg# are also typical for the coexisting olivines in this domain with values between 65 and 74 [Table 3 and data of *Yamazaki et al.,* 2009], thus not corresponding to the olivines with higher forsterite contents of typical primitive olivine gabbros. Most data fit with the modeled evolution trend of Figure 5b, but plot at the end of these paths, compatible with 50 to 80 % of crystallization starting from the most primitive basaltic composition recovered.

The plagioclases of the granular domain show a marked and often very complex zoning. Within a single microprobe profile, An contents may vary from ~ 30 up to ~80 mol% as demonstrated in Fig. 6a for sample 214_2_0_6 (Gabbro 1). The high An contents in this profile are related to more or less euhedral "ghost" crystals enclosed by plagioclase with equilibrium composition significantly lower in An (Fig. 6a). Since the An contents of the "ghost" crystals approach those values typical for plagioclase chadacrysts from the adjacent subophitic domains, we interpret these as relics from the high-temperature subophitic stage survived during the magmatic reaction with a low-temperature evolved magma.

Interestingly, the data for the subophitic and the granular domain, even from the same sample, form distinct fields at the beginning and the end of the modeled evolution path, without any overlap (Fig. 5b), in accord with a scenario that two different magmas were mechanically mingled together without significant chemical mixing producing intermediate compositions. However this is only valid when considering the averages of the corresponding minerals interpreted as equilibrium compositions. Reaction rims at the border between clinopyroxene of the subophitic domains and hornblende of the granular domains (see above), as well as the "ghost" plagioclases strongly enriched in An inherited in the plagioclases of the granular domain content, are identified products of magmatic reactions related to the mixing event.

3.1.3. Microgranular domain

As shown in Fig. 5a, most of the clinopyroxenes in the microgranular domain plot in the TiO_2 versus Al_2O_3 diagram in the field for the "granoblastic trend" of *France et al.* [2009], supporting the hypothesis based on textural arguments (e.g., Fig. 2c) that these domains represent former granoblastic dikes incorporated and assimilated during the ascent of the AML. With one exception, there is no overlap with the clinopyroxenes from fresh lavas and dikes, which should be the case when these domains would be related to cumulates derived from the main crystallization process in the AML. The high amount of survived microgranular patches, and their individual clinopyroxene compositions preserved from the granoblastic stage, which were mostly not reset to equilibrium values, implies that assimilation was highly incomplete and that the AML persisted in a general state of disequilibrium until it finally was frozen. Similar microgranular patches have been described in gabbros from the Oman ophiolite, and ascribed to assimilation of the granoblastic dikes [*France et al.,* 2009]

3.2. Record of striking intra-sample heterogeneity in mineral compositions

It is a striking feature of the 1256D gabbros that they generally consist of domains with strongly contrasting mineralogy which is reflected in a marked heterogeneity of mineral compositions even within one section. This is demonstrated in Fig. 3, showing gabbro 232_2_98_100 (Gabbro 2) with 4 different lithological/textural domains within one thin section and the corresponding mineral compositions for plagioclase and clinopyroxene. As expected, the intra-sample variation for the minerals is extremely large, e.g. for plagioclase spanning a range in An content from 20 to 65 mol%. The clinopyroxene compositions enable the assignment to the main crystallization stage ("fresh lava/dikes" field for the compositions of the subophitic domain) or to the granoblastic stage ("granoblastic" field for the

compositions of the granular fine and the microgranular domains). No clinopyroxene was observed in the granular coarse domain.

Another example for a large intra-sample contrast is shown for plagioclase from gabbro 214_2_0_6 (Gabbro 1) where subophitic domains and granular domains are in intimate contact. All these examples reveal that the chemical composition of a given sample is governed by the presence and amount of different domains implying that bulk chemical approaches for these rocks are of less value.

3.3. Comparison with oceanic gabbros from recent oceans

For comparison with oceanic gabbros from other locations, only data points of the subophitic and the granular domains are considered, since the microgranular domain is a very special feature of the 1256D gabbros, not observed in other oceanic gabbros from recent oceans. In the TiO_2 versus Al_2O_3 diagram (Fig. 7a), the clinopyroxenes of the subophitic domains plot into the middle of the field spanned by most ocean gabbros, while clinopyroxenes from the granular domain plot at the left margin of the field, towards more evolved compositions. This is in accord with our findings from above that the formation of the subophitic domains corresponds to a (early) high-temperatures crystallization stage and the formation of the granular domains to a (late) evolved magmatic stage at lower temperatures.

In Fig. 7b, the plagioclase An content versus clinopyroxene Mg# is plotted, including the differentiation trend modeled with COMAGMAT using the most primitive bulk composition from lava/dike recovered at Site 1256 as starting composition. Data from the fast-spreading East Pacific Rise (Hess Deep and Pito Deep) match the trend, as well as most of the data from the granular domains of the 1256D gabbros which plot towards the more evolved compositions of the trend. However, the modeled path does not fit with the compositions from the slow-spreading ridges which follow a trend with a generally lower Ca/Na ratio, which was also demonstrated by *Coogan* [2007] who successfully modeled the

magma evolution from slow-spreading systems by using a more evolved starting composition compared to that used in this study.

Fig. 7b points out that the data for the subophitic domains in Gabbro 1 show the highest An content for a given clinopyroxene Mg# compared to all oceanic gabbros from the different locations, emphasizing the very special compositional feature of these domains, which we interpret as consequence of the presence of water in the system.

3.4. Record of incorporation/assimilation of granoblastic dikes

The results of the petrographic investigation of the gabbros performed during the Expedition 312 emphasized the significance of metamorphic effects in the 1256D gabbros, not observed in other oceanic gabbros so far [*Teagle et al.,* 2006]. Particularly, these are : (1) large orthopyroxene grains that contain tiny inclusions of granular clinopyroxene, and appear to have formed in the solid state; (2) typical crystalloblastic intergrowths that include orthopyroxene and clinopyroxene, and are similar to those described for the granoblastic dikes (e.g., *Koepke et al.*, 2008]; (3) concentration of orthopyroxene along veins; (4) the presence of microgranular patches interpreted as former domains of granoblastic dikes. The results of the microanalytical characterization of such features presented in the following imply that most of these effects can be attributed to the incorporation of granoblastic dikes into an ascending magma and to assimilation processes involved in a regime were magmatic and metamorphic processes interfere.

3.4.1. Inclusions in pyroxenes

Many pyroxenes in granular and microgranular domains especially from Gabbro 2 contain numerous inclusions of tiniest roundish minerals with typical structures well-known from metamorphic rocks but not from oceanic gabbros. Mostly, these are clinopyroxenes included in orthopyroxene [Fig. 8; see also Figure F241 in *Teagle et al.*, 2006], sometimes plagioclases included in orthopyroxene and clinopyroxene [Figure F240 in *Teagle et al.*, 2006]. Textural

arguments, as "classical" poikiloblastic structures and the dihedral nature of the inclusions, exclude that these are simple poikilitic assemblages formed in a magmatic regime. Analyzed inclusions of clinopyroxene in orthopyroxene follow the granoblastic trend in the TiO_2 versus Al_2O_3 diagram of Fig. 5, implying that these could be regarded as constituents of former granoblastic dikes, especially the analyzed inclusion with only 0.7 wt% of Al_2O_3 and 0.2 wt% of TiO_2 which can hardly be attributed to "normal" crystallization within an axial magma chamber.

Details of the microanalytical investigation are presented in Fig. 8 where an orthopyroxene is shown which is filled with numerous of roundish 10 to 20 µm sized clinopyroxene inclusions. Some of the clinopyroxene inclusions show, in turn, µm-sized inclusions of ilmenite. This is a key feature for the granoblastic stage, implying that the roundish clinopyroxene grains within the orthopyroxene correspond to inherited, relictic dike material once incorporated into the gabbroic mush.

Another interesting feature is that prismatic orthopyroxene in the granular domain of Gabbro 2 may contain Fe-Ti oxide [Figure F240 and F243 in *Teagle et al.*, 2006] and even sulfide as inclusion (Fig. 9b), a feature fully unknown for oceanic gabbros. Orthopyroxene - sulfide assemblages and sulfide inclusion within orthopyroxene are well-known from the granoblastic dikes, which were grown there during the granoblastic re-crystallization event [*Koepke et al.,* 2008]. Most probably, the granoblastic orthopyroxene grew from alteration haloes which included sulfide minerals produced by the first hydrothermal alteration prior to the prograde metamorphic event. We interpret the presence of primary sulfide inclusion in orthopyroxene of the 1256D gabbros as robust evidence that orthopyroxene-sulfide cluster from the granoblastic stage were involved during the formation of these gabbros

3.4.2. Effect of hydrous partial melting of granoblastic dikes

A marked feature of both Gabbro 1 and 2 are plagioclases in granular and microgranular domains showing structures implying that partial melting reactions proceeded. Typical are zones of An-enriched plagioclase, representing the residual plagioclase after such an event, and more or less rectangular zones corresponding to the former melt pools, now frozen to Ab-richer plagioclase. BSE image and related concentration profiles are shown in Fig. 10 for plagioclases from Gabbro 1 and 2. Striking is the similarity of the observed structures with those produced by experiments in the partly molten regime [e.g., Figures in *Johannes and Holtz*, 1992].

3.5. Basaltic xenoliths in the gabbros

A characteristic feature especially within Gabbro 2 is the presence of basaltic enclaves. Among the investigated samples was also one (sample 230_1_54_56) where the contact to a basaltic enclave is displayed. The main lithology of the xenolith is gabbronoritic with fine-grained granular to microgranular texture, similar in appearance as other domains observed in the gabbro section. Directly at the contact, a mm-sized zone enriched in oxides is developed where no clinopyroxene was observed. The matrix is a granular hornblende-bearing oxide gabbro, with a zone at the contact where the amount of oxide decreases.

The clinopyroxene of the xenoliths [included those from *France et al.,* 2009] clearly follow the granoblastic trend in the TiO_2 versus Al_2O_3 diagram in Fig. 5, confirming the hypothesis that these xenoliths went through a stage of granoblastic overprint before incorporation into the gabbroic mush. Temperature of equilibration for the xenolith center (ortho- and clinopyroxene stable) was estimated using QUILF to 1014 ± 73°C.

3.6. The Upper and Lower Dike screen

Gabbro 1 and Gabbro 2 are separated by the Upper Dike Screen, while Gabbro 2 is underlain by another dike screen named the Lower Dike screen [*Teagle et al.*, 2006]. Although assigned to the granoblastic dikes, some of the samples of the dike screens show typical magmatic, granular textures very similar to those observed in other domains of the gabbroic section. Characteristic is the stability of euhedral orthopyroxene, and the presence of numerous of tiniest inclusions in both pyroxenes and even in plagioclases, implying a derivation from the granoblastic dikes (see above). Concerning the decision whether these rocks are metamorphic or magmatic, the shipboard scientists from Expedition 312 stated "The multiplicity of orthopyroxene occurrences, including magmatic orthopyroxene in gabbronorite, apparently metamorphic orthopyroxene in granoblastic domains within gabbronorite, and similar orthopyroxene along contact zones, both in the intruding gabbronorite and in the host metabasalt, emphasizes that within and beneath the dike screen there is an important interface where the distinction between magmatic and metamorphic processes is blurred " [*Teagle et al.*, 2006].

In the TiO_2 versus Al_2O_3 diagram the clinopyroxenes of both dike screens clearly follow the granoblastic trend of *France et al.* [2009]. Some clinopyroxenes high in Al_2O_3 and TiO_2 overlap with the true magmatic granular or microgranular domains, conform with the evaluation of *Teagle et al.* [2006] that these rocks represent an interface between magmatic and metamorphic processes. One important feature of theses rocks is that the change in metamorphic/magmatic facies from sample to sample is highly abrupt. Since many samples of the dike screens show rather a "magmatic" than a "metamorphic" texture, implying a direct involvement into magma chamber processes, we follow the hypothesis of *France et al.* [2009], that the upper and the lower dike screens correspond rather to stoped clasts of partially resorbed granoblastic dikes which were accumulated in the lower part of the axial melt lens (Fig. 1b), than to contact-metamorphosed dikes.

4. Discussion

4.1. Hydrous magma mixing/mingling processes in the AML

The microanalytical results for the three principal lithological/textural units (subophitic, granular, and microgranular domains) composing the gabbroic section at Site 1256 reveal quite different ways of formation for the each different unit.

The subophitic domains were most likely formed under high water activities and under high undercooling conditions, probably at the top of the AML progressing into the relatively cold environment of a CBL. This fits with the observation, that these domains, characterized by plagioclases very high in An (for a given Mg# in clinopyroxene), only occur in the uppermost section of the gabbro core but not in the deeper part, e.g., in Gabbro 2. The only analyzed domain with subophitic texture in a sample from Gabbro 2 (232_2_98_100; see Fig. 3) is quite evolved (Table 3). The evaluation of the parental magma for the subophitic domains of Gabbro 1 seems difficult. Primitive MORB would crystallize olivine before clinopyroxene, which is not the case for the observed domains. Probably, the silica activity was increased preventing the crystallization of early olivine. Temperatures of crystallization could be estimated from phase relations in hydrous MORB at shallow pressures [e.g., *Berndt et al.*, 2005; *Feig et al.*, 2006; *Botcharnikov et al.*, 2008] to values of 1100 and 1150°C (assumed stability of clinopyroxene and a water content of 2 wt%).

Quite different are the assumed parental composition and temperature conditions for the formation of the typical granular domain. According to experiments on hydrous partial melting of different oceanic gabbros at a pressure of 200 MPa from *Koepke et al.* [2004], the stability of orthopyroxene ± olivine ± amphibole and absence of clinopyroxene limits the temperature of formation to below 980°C. The observation of euhedral amphibole with primary compositions (pargasite, sample 215_1_84_88, Table 3) is of importance, since it is a first-order observation that the corresponding magmas prevailed under high $a\mathrm{H_2O}$ [*Johnson*

465 *et al.*, 1994]. Moreover, it limits the temperature of the magma at this crystallization stage to
466 the relatively low value of ~1050°C, since this is the maximum temperature for amphibole
467 stability observed in basaltic systems at shallow pressure [e.g., *Ernst and Liu*, 1998]. 2 –
468 pyroxene geothermometry using QUILF reveal equilibrium temperatures varying between
469 981 and 1059°C, and Ti-in-amphibole thermometry for the most freshest amphiboles revealed
470 temperatures between 906 and 1003°C (Table 2). To summarize, temperatures for
471 crystallization of the granular domains can be averaged to values from ~950 to 1050°C. Phase
472 chemistry of the phases of the granular domains reveal quite evolved compositions, which is
473 in accord with the presence of quartz in some of these domains. Thus it seems very probable
474 that the parental composition correspond to a highly evolved, FeO- and TiO_2-rich late stage
475 composition corresponding to typical Fe-Ti basalts, which are interpreted as the final product
476 of MORB differentiation, and which can be rarely found as erupted liquids at the seafloor
477 [e.g., *Ludden et al.*, 1980; *Fornari et al.*, 1983].

478 Temperatures for the equilibration of the microgranular domains estimated with
479 QUILF for two patches vary within a small interval between 1021 and 1041°C (Table 2). This
480 fits well with the observed partial melting of granoblastic protoliths, provided high water
481 activities prevailed. This is in concordance with the phase relations obtained for MORB-type
482 systems at shallow pressures under hydrous conditions [e.g., *Berndt et al.*, 2005; *Feig et al.*,
483 2006; *Botcharnikov et al.*, 2008]. The addition of water into the otherwise rather dry MORB-
484 system can be explained by the incorporation of granoblastic dikes, which typically bear
485 considerable amounts of hornblende, which may deliberate water during its breakdown at
486 temperatures above ~ 1000°C. The required high aH_2O for stabilizing hydrous partial melting
487 of plagioclase of ~ An 70 in a MORB mush can be easily achieved, since the water solubility
488 in MORB melts at those shallow pressures prevailing in the AML is low [e.g., only ~2.5 wt%
489 at 100 MPa according to *Berndt et al.*, 2002].

To summarize, the petrography and phase chemistry of the gabbroic section drilled at Site 1256 revealed highly complex magmatic mingling and mixing processes which probably proceeded under hydrous conditions. In a first high-temperature stadium, a relative primitive high-temperature component of an ascending AML, eventually related to a replenishment event of the AML, progressed into the overlying CBL. Stoping, incorporation, and assimilation of previously metamorphosed granoblastic dikes were very effective, expressed by the numerous amounts of microgranular patches. Hydrous partial melting of the stoped granoblastic roof material produced silicic melts, which were obviously mixed with the high-temperatures melts, thereby increasing the silica activity of the melt. The residuals after the partial melting of the granoblastic protolith, now denser than the basaltic melts [see density calculation in *France et al.,* 2009], were accumulated in the lower part of the AML (level of Gabbro 2) as enclaves difficult to 'digest'. At a later stage, at distinctly lower temperatures, the high temperature mush was intermingled by a low-temperature magma of highly evolved composition. The temperature contrast is also expressed by typical comb layering developed in some oxide gabbros.

Interestingly, none of the investigated domains match those clinopyroxene and plagioclase compositions typical for the fresh lavas and dikes (Fig. 5 b). Thus, it seems that the corresponding AML was filled with melts/magmas of strange compositions, e.g., highly fractionated, uneruptable liquids [e.g., *Natland and Dick*, 1996], and not by pooled basaltic liquids derived from the underlying mush pile and equivalent in composition to the upper crust [e.g., *Sinton and Detrick*, 1992].

4.2. Mechanism of MORB contamination at the top of the melt lens

Geochemical studies on chlorine contents in MORB imply that assimilation is much more pronounced at fast-spreading ridges than at slow-spreading systems (using Cl as proxy for contamination [e.g., *Michael and Schilling*, 1989; *Jambon et al.*, 1994; *Michael and Cornell*,

515 1998]. Our petrographic and microanalytical results reveal that a considerable part of AML is
516 composed of enclaves of stoped granoblastic dike material from the roof region of the AML.
517 Thus, it is indicated that this process can be responsible for the observed
518 contamination/assimilation processes ongoing at fast-spreading ridges. The most relevant
519 parameters necessary to understand this important process, are only poorly constrained: e.g.,
520 source of the contaminant, the detailed mechanisms, the involved volumes, the contamination
521 rate. One of the most sophisticated studies aimed to understand details of the contamination
522 process is provided by *Coogan et al.* [2003] who presented a hypothesis based on
523 geochemical modeling that contamination occurs at the roof of a vertical oscillating AMC by
524 assimilation/stoping of previously hydrothermalized dikes. For the vertical fluctuations, a
525 timescale of decades was assumed. Compared with the compilation of possible time scales in
526 section 2.1.3., this value is extremely short. The model allows to extract a "contamination
527 rate", which is ~ 20 cm/year in average, corresponding to an assimilation of 20 cm of dikes
528 per year. However, some of the input parameters of this model are uncertain. Most important,
529 the accumulation of extreme chlorine-enriched material derived by brines was neglected,
530 although it is known that brines generated after fluid phase separation may form a dense layer
531 at the base of the sheeted dikes [e.g., *Bischoff and Rosenbauer*, 1989]. Interestingly, the only
532 analyzed amphibole with primary magmatic amphibole from a granular domain composition
533 (pargasite from sample 215_1_84_88 with 10.9 wt% Al_2O_3 and 0.7 wt% K_2O, Table 3) shows
534 with 0.61 wt% Cl the highest Cl values of all analyzed amphiboles (including those of the
535 granoblastic dikes), implying that the incorporation of brines eventually cannot be neglected.
536 Further studies will shed light on this important topic.

537 5. Conclusion

538 The IODP drilling at Site 1256 provides the first continuous in situ sampling of fast-spread
539 ocean crust from the extrusive lavas, through the sheeted dikes and down into the uppermost

gabbros. The detailed investigation of the petrography and the phase chemistry of the drilled gabbros from Site 1256 revealed an amazing insight into highly complex magmatic reaction including mingling, mixing, and partial melting of previously altered dike proceeding in the axial melt lens. Surprisingly, a high water activity was involved, although it is well-known that typical MORB differentiation at fast-spreading ridges occurs under dry conditions.

One of the most unexpected results of our study is that none of the analyzed minerals in the investigated gabbros match those compositions to be expected for the crystallization of normal MORB. Instead, it is implied that the magma chamber was filled with melts/magmas of strange compositions, e.g., of highly fractionated, uneruptable liquids.

The first in-situ drilling of the gabbro/dike transition at Site 1256 presents now direct evidence for stoping and assimilation of previously hydrothermalized dikes, thus providing an opportunity to shed light on the important contamination process by future detailed geochemical and microanalytical investigation.

Acknowledgments

We gratefully acknowledge the Captain and shipboard crew of IODP Expedition 312 for their assistance in data collection at sea. We wish to thank the Scientific Party of IODP Expedition 312 for fruitful discussion during the cruise. This work benefited from fruitful discussions during field work in Oman with F. Boudier, A. Nicolas, B. Ildefonse. This study used samples provided by the Integrated Ocean Drilling Program. Funding for this research was provided by grants from the Deutsche Forschungsgemeinschaft.

Reference

Andersen, D.J., D.H. Lindsley, and P.M. Davidson (1993), Quilf - a Pascal Program to Assess Equilibria among Fe-Mg-Mn-Ti Oxides, Pyroxenes, Olivine, and Quartz, *Comput. Geosci.*, *19*, 1333-1350.

564 Ariskin, A.A. (1999), Phase equilibria modeling in igneous petrology: use of COMAGMAT
565 model for simulating fractionation of ferro-basaltic magmas and the genesis of high-
566 alumina basalt, *J. Volcanol. Geotherm. Res.*, *90*, 115-162.
567 Berndt, J., C. Liebske, F. Holtz, M. Freise, M. Nowak, D. Ziegenbein, D. Hurkuck, and J.
568 Koepke (2002), A combined rapid-quench and H_2-membrane setup for internally
569 heated pressure vessels: Description and application for water solubility in basaltic
570 melts, *Am. Mineral.*, *87*, 1717-1726.
571 Berndt, J., J. Koepke, and F. Holtz (2005), An experimental investigation of the influence of
572 water and oxygen fugacity on differentiation of MORB at 200 MPa, *J. Petrol.*, *46*,
573 135-167.
574 Bischoff, J.L., and R.J. Rosenbauer (1989), Salinity variations in submarine hydrothermal
575 systems by layered double-diffusive convection, *J. Geol.*, *97*, 613-623.
576 Botcharnikov, R.E., R. Almeev, J. Koepke, and F. Holtz (2008), Phase relations and liquid
577 lines of descent in hydrous ferrobasalt - Implications for the Skaergaard Intrusion and
578 Columbia River Flood Basalts, *J. Petrol.*, *49*, 1687-1727.
579 Bryan, W.B. (1972), Morphology of quench crystals in submarine basalts, *J. Geophys. Res.*,
580 *77*, 5812-5819.
581 Busigny, V., C. Laverne, and M. Bonifacie (2005), Nitrogen content and isotopic composition
582 of oceanic crust at a superfast spreading ridge: A profile in altered basalts from ODP
583 Site 1256, Leg 206, *Geochem. Geophys. Geosyst.*, *6*, doi:10.1029/2005GC001020.
584 Coogan, L.A., P.D. Kempton, A.D. Saunders, and M.J. Norry (2000a), Melt aggregation
585 within the crust beneath the Mid-Atlantic Ridge: evidence from plagioclase and
586 clinopyroxene major and trace element compositions, *Earth Planet. Sci. Lett.*, *176*,
587 245-257.

588 Coogan, L.A., A.D. Saunders, P.D. Kempton, and M.J. Norry (2000b), Evidence from
589 oceanic gabbros for porous melt migration within a crystal mush beneath the Mid-
590 Atlantic Ridge, *Geochem. Geophys. Geosyst.*, *1*, 2000GC000072.
591 Coogan, L.A., K.M. Gillis, C.J. MacLeod, G.M. Thompson, and R. Hekinian (2002),
592 Petrology and geochemistry of the lower ocean crust formed at the East Pacific Rise
593 and exposed at Hess Deep: A synthesis and new results, *Geochem. Geophys. Geosyst.*,
594 *3*.
595 Coogan, L.A., N.C. Mitchell, and M.J. O'Hara (2003), Roof assimilation at fast spreading
596 ridges: An investigation combining geophysical, geochemical, and field evidence, *J.*
597 *Geophys. Res.-Solid Earth*, *108*, doi:10.1029/2001JB001171.
598 Coogan, L.A. (2007), The lower oceanic crust, in *Treatise on Geochemistry*, vol. edited by K.
599 Turekian, and H.D. Holland, pp. 1-45, Elsevier, Amsterdam.
600 Dick, H.J.B., and J.H. Natland (1996), Late-stage melt evolution and transport in the shallow
601 mantle beneath the East Pacific Rise, *Proc. ODP, Sci. Results*, *147*, 103 -134.
602 Dick, H.J.B., K. Ozawa, P.S. Meyer, Y. Niu, P.T. Robinson, M. Constantin, R. Hebert, J.
603 Maeda, J.H. Natland, J.G. Hirth, and S.M. Mackie (2002), Primary silicate mineral
604 chemistry of a 1.5-km section of very slow spreading lower ocean crust: ODP Hole
605 735B, Southwest Indian Ridge, *Proc. ODP, Sci. Results*, *176, chap. 10*, 1-61.
606 Dziony, W., J. Koepke, and F. Holtz (2008), Data report: Petrography and phase analyses in
607 lavas and dikes from the hole 1256D (ODP Leg 206 and IODP Expedition 309, East
608 Pacific Rise), in *Proc. IODP, Sci. Results, 309/312,*
609 *doi:10.2204/iodp.proc.309312.201.2008*, vol. edited by D.A.H. Teagle et al., College
610 Station, TX, Ocean Drilling Program.
611 Ernst, W.G., and J. Liu (1998), Experimental phase-equilibrium study of Al- and Ti-contents
612 of calcic amphibole in MORB - a semiquantitative thermobarometer, *Am. Mineral.*,
613 *83*, 952-969.

614 Feig, S., J. Koepke, and J. Snow (2006), Effect of water on tholeiitic basalt phase equilibria:
615 An experimental study under oxidizing conditions, *Contrib. Mineral. Petrol.*, *152*,
616 611-638.
617 Fornari, D.J., M.R. Perfit, A. Malahoff, and R.U. Embley (1983), Geochemical studies of
618 abyssal lavas recovered by DSRV Alvin from Eastern Galapagos Rift, Inca
619 Transform, and Ecuador Rift. 1. Major element variations in natural glasses and
620 spatial distribution of lavas, *J. Geophys. Res.*, *88*, 10519-10529.
621 France, L., B. Ildefonse, and J. Koepke (2009), Interactions between magma and the
622 hydrothermal system in the Oman ophiolite and in IODP hole 1256D: fossilisation of
623 a dynamic melt lens at fast spreading ridges, *Geochem. Geophys. Geosyst.*, *10*,
624 doi:10.1029/2009GC002652.
625 Gaetani, G.A., T.L. Grove, and W.B. Bryan (1993), The influence of water on the
626 petrogenesis of subduction-related igeneous rocks, *Nature*, *365*, 332-334.
627 Holland, T.J.B., and J. Blundy (1994), Non-ideal Interactions in calcic amphiboles and their
628 bearing on amphibole-plagioclase thermometry, *Contrib. Mineral. Petrol.*, *116*, 433-
629 447.
630 Jambon, A., B. Deruelle, G. Dreibus, and F. Pineau, 1994. Chlorine and bromine abundance
631 in MORB: The contrasting behaviour of the Mid-Atlantic Ridge and East Pacific Rise
632 and implications for chlorine geodynamic cycle, Workshop on the Mantle-Ocean
633 Connection, Amsterdam, Netherlands, pp. 101-117.
634 Johannes, W., and F. Holtz (1992), Melting of plagioclase in granite and related systems -
635 Composition of coexisting phases and kinetic observations, *Trans. R. Soc. Edinburgh*
636 *Earth Sci.*, *83*, 417-422.
637 Johnson, M.C., A.T. Anderson, and M.J. Rutherford (1994), Pre-eruptive volatile contents of
638 magmas, in *Volatiles in magmas. Rev. Mineral.*, vol. 30, edited by M.R. Carroll, and

639 J.R. Holloway, pp. 281-330, Mineralogical Society of America, Washington, DC,
640 United States.
641 Koepke, J., S.T. Feig, J. Snow, and M. Freise (2004), Petrogenesis of oceanic plagiogranites
642 by partial melting of gabbros: An experimental study, *Contrib. Mineral. Petrol.*, *146*,
643 414-432.
644 Koepke, J., S.T. Feig, and J. Snow (2005), Late-stage magmatic evolution of oceanic gabbros
645 as a result of hydrous partial melting: Evidence from the ODP Leg 153 drilling at the
646 Mid-Atlantic Ridge, *Geochem. Geophys. Geosyst.*, *6*, 2004GC000805, pp. 1-27.
647 Koepke, J., D.M. Christie, W. Dziony, F. Holtz, D. Lattard, J. Maclennan, S. Park, B.
648 Scheibner, T. Yamasaki, and S. Yamasaki (2008), Petrography of the Dike/Gabbro
649 Transition at IODP Site 1256D (Equatorial Pacific): The evolution of the Granoblastic
650 Dikes, *Geochem. Geophys. Geosyst.*, *9*, doi:10.1029/2008GC001939.
651 Koepke, J., S. Schoenborn, M. Oelze, H. Wittmann, S. Feig, E. Hellebrand, F. Boudier, and
652 R. Schoenberg (2009), Petrogenesis of crustal wehrlites in the Oman ophiolite:
653 Experiments and natural rocks, *Geochem. Geophys. Geosyst.*, *10*,
654 doi:10.1029/2009GC002488.
655 Laverne, C., O. Grauby, J.C. Alt, and M. Bohn (2006), Hydroschorlomite in altered basalts
656 from Hole 1256D, ODP Leg 206: The transition from low-temperature to
657 hydrothermal alteration, *Geochem. Geophys. Geosyst.*, *7*, Q10O03.
658 doi:10.1029/2005GC001180.
659 Lippard, S.J., A.W. Shelton, and I.G. Gass, (1986), *The ophiolite of Northern Oman*. *Geol.*
660 *Soc. Mem.*, 11, 178 pp., Blackwell Scientific Publ., Oxford.
661 Lissenberg, C.J., and H.J.B. Dick (2008), Melt-rock reaction in the lower oceanic crust and its
662 implications for the genesis of mid-ocean ridge basalt, *Earth Planet. Sci. Lett.*, *271*,
663 311-325.

664 Ludden, J.N., G. Thompson, W.B. Bryan, and F.A. Frey (1980), The origin of lavas from the
665 Ninetyeast Ridge, Eastern Indian Ocean: An evaluation of fractional crystallization
666 models, *J. Geophys. Res.*, *85*, 4405-4420.
667 MacLeod, C.F., F. Boudier, G. Yaouancq, and C. Richter (1996), Gabbro fabrics from ODP
668 Site 894, Hess Deep: implications for magma chamber processes at the East Pacific
669 Rise, *Proc. ODP, Sci. Res.*, *147*, 317-328.
670 MacLeod, C.J., J. Escartin, D. Banerji, G.J. Banks, M. Gleeson, D.H.B. Irving, R.M. Lilly,
671 A.M. McCaig, Y.L. Niu, S. Allerton, and D.K. Smith (2002), Direct geological
672 evidence for oceanic detachment faulting: The Mid-Atlantic Ridge, 15 degrees 45 ' N,
673 *Geology*, *30*, 879-882.
674 Michael, P.J., and J.-G. Schilling (1989), Chlorine in mid-ocean ridge magmas: evidence for
675 assimilation of seawater-influenced components., *Geochim. Cosmochim. Acta*, *53*,
676 3131-3143.
677 Michael, P.J., and W.C. Cornell (1998), Influence of spreading rate and magma supply on
678 crystallization and assimilation beneath mid-ocean ridges: Evidence from chlorine and
679 major element chemistry of mid-ocean ridge basalts, *J. Geophys. Res.-Solid Earth*,
680 *103*, 18325-18356.
681 Miller, D.J., G.J. Iturrino, and N.I. Christensen (1996), Geochemical and petrological
682 constraints on velocity behavior of lower crustal and upper mantle rocks from the fast-
683 spreading ridge at Hess Deep, *Proc. ODP, Sci. Results*, *147*, 477-490.
684 Natland, J.H., and H.J.B. Dick (1996), Melt migration through high-level gabbroic cumulates
685 of the East Pacific Rise at Hess Deep: the origin of magma lenses and the deep crustal
686 structure of fast-spreading ridges, *Proc. ODP, Sci. Results*, *147*, 21-58.
687 Nicolas, A., F. Boudier, J. Koepke, L. France, B. Ildefonse, and C. Mevel (2008), Root zone
688 of the sheeted dike complex in the Oman ophiolite, *Geochem. Geophys. Geosyst.*, *9*,
689 doi:10.1029/2007GC001918, 29 pages.

690 Nicolas, A., F. Boudier, and L. France (2009), Subsidence in magma chamber and the
691 development of magmatic foliation in Oman ophiolite gabbros, *Earth Planet. Sci.*
692 *Lett.*, *284*, 76-87.
693 Perk, N.W., L.A. Coogan, J.A. Karson, E.M. Klein, and H.D. Hanna (2007), Petrology and
694 geochemistry of primitive lower oceanic crust from Pito Deep: implications for the
695 accretion of the lower crust at the Southern East Pacific Rise, *Contrib. Mineral.*
696 *Petrol.*, *154*, 575-590.
697 Pouchou, J.L., and F. Pichoir (1991), Quantitative analysis of homogeneous or stratified
698 microvolumes applying the model "PAP", in *Electron probe quantification*, vol. edited
699 by K.F.J. Heinrich, and D.E. Newbury, pp. 31-75, Plenum Press, New York.
700 Sano, T., M. Miyoshi, S. Ingle, N.R. Banerjee, M. Ishimoto, and T. Fukuoka (2008), Boron
701 and chlorine contents of upper oceanic crust: Basement samples from IODP Hole
702 1256D, *Geochem. Geophys. Geosyst.*, *9*.
703 Sinton, J.M., and R.S. Detrick (1992), Midocean ridge magma chambers, *J. Geophys. Res.-*
704 *Solid Earth*, *97*, 197-216.
705 Suhr, G., E. Hellebrand, K. Johnson, and D. Brunelli (2008), Stacked gabbro units and
706 intervening mantle: A detailed look at a section of IODP Leg 305, Hole U1309D,
707 *Geochem. Geophys. Geosyst.*, *10*, doi:10.1029/2008GC002012.
708 Tartarotti, P., E. Fontana, and L. Crispini (2009), Deformation pattern in a massive ponded
709 lava flow at ODP-IODP Site 1256: A core and log approach, *Geochem. Geophys.*
710 *Geosyst.*, *10*, doi: 10.1029/2008gc002346.
711 Teagle, D.A.H., J.C. Alt, S. Umino, S. Miyashita, N.R. Banerjee, D.S. Wilson, and and the
712 Expedition 309/312_Scientists (2006), *Proc. IODP*, *309/312*,
713 doi:10.2204/iodp.proc.309312.2006.
714 Teagle, D.A.H., D.S. Wilson, G.D. Acton, and D.A.E. Vanko (2007), *Proc. ODP*, *206*,
715 doi:10.2973/odp.proc.sr.206.2007.

716 Umino, S., L. Crispini, P. Tartarotti, D.A.H. Teagle, J.C. Alt, S. Miyashita, and N.R. Banerjee
717 (2008), Origin of the sheeted dike complex at superfast spread East Pacific Rise
718 revealed by deep ocean crust drilling at Ocean Drilling Program Hole 1256D,
719 *Geochem. Geophys. Geosyst.*, *9*, doi:10.1029/2007gc001760.
720 Wager, L.R., and G.M. Brown, (1968), *Layered igneous rocks*, 588 pp., Oliver and Boyd,
721 Edinburgh and London.
722 Wilson, D.S., D.A.H. Teagle, J.C. Alt, N.R. Banerjee, S. Umino, S. Miyashita, G.D. Acton, R.
723 Anma, S.R. Barr, A. Belghoul, J. Carlut, D.M. Christie, R.M. Coggon, K.M. Cooper,
724 C. Cordier, L. Crispini, S.R. Durand, F. Einaudi, L. Galli, Y. Gao, J. Geldmacher,
725 L.A. Gilbert, N.W. Hayman, E. Herrero-Bervera, N. Hirano, S. Holter, S. Ingle, S.
726 Jiang, U. Kalberkamp, M. Kerneklian, J. Koepke, C. Laverne, H.L.L. Vasquez, J.
727 Maclennan, S. Morgan, N. Neo, H.J. Nichols, S.-H. Park, M.K. Reichow, T.
728 Sakuyama, T. Sano, R. Sandwell, B. Scheibner, C.E. Smith-Duque, S.A. Swift, P.
729 Tartarotti, A.A. Tikku, M. Tominaga, E.A. Veloso, T. Yamasaki, S. Yamazaki, and C.
730 Ziegler (2006), Drilling to gabbro in intact ocean crust, *Science*, *312*, 1016-1020.
731 Yamazaki, S., N. Neo, and S. Miyashita (2009), Data report: whole-rock major and trace
732 elements and mineral compositions of the sheeted dike–gabbro transition in ODP Hole
733 1256D1, in *Proc. IODP, Sci. Results, 309/312,*
734 *doi:10.2204/iodp.proc.309312.203.2009*, vol. edited by D.A.H. Teagle et al., College
735 Station, TX, Ocean Drilling Program.

736 Figure captions

737 **Figure 1.** Cartoons illustrating the drilled dike/gabbro transition at Site 1256D, as interpreted
738 by the results of different authors. Included is the location of the drill core. Both cartoons
739 reproduce the lithostratigraphy recorded in the drill core of Hole 1256D as presented in
740 *Teagle et al.* [2006]. The size of the fragments of granoblastic dikes observed in the gabbros

741 is out of scale. See text for detail. For clarity, the lowermost rock recovered from Hole
742 1256D, a basaltic dike that lacks granoblastic textures, which is interpreted to be a late dike
743 crosscutting the gabbros [*Teagle et al.,* 2006] is not included into the cartoon.
744
745 **Figure 2.** Microphotographs showing the principle textural/lithological domains occurring in
746 the 1256D gabbros. For details see text and Table 2. All images with plane-polarized light.
747 Images are from the data base of Expedition 312 in *Teagle et al.* [2006].
748 (a) Subophitic domain: Medium grained gabbro showing mm-sized poikilitic clinopyroxene.
749 Note that the enclosed plagioclase shows hollows and skeletal growth. These features are
750 discussed in section 2.1.1. Sample 215_1_84_88; field of view 2.4 mm.
751 (b) Granular domain: Medium grained oxide noritic domain showing a framework composed
752 of prismatic plagioclase, orthopyroxene, and granular oxide. This sample shows some
753 peculiar features which are not so often visible in similar domains: the presence of interstitial
754 quartz (lower left) and slightly curved grain boundaries between the interlocking plagioclase
755 crystals which is interpreted as typical cumulate features. Sample 232_2_98_100; field of
756 view 2.4 mm.
757 (c) Microgranular domain: wormy intergrowth of plagioclase, clinopyroxene and oxide as
758 inclusion within a granular oxide gabbro. Note that the clinopyroxene grains bear numerous
759 inclusions of tiniest oxide spots. This feature and the overall textural appearance are well-
760 known from the granoblastic dikes, implying that these domains present relics of previously
761 stoped granoblastic dikes. Sample 223_2_57_60; field of view 1.2 mm.
762
763 **Figure 3.** Sample 232_2_98_100 from Gabbro 2 as example for extreme patchiness in the
764 1256D gabbros showing 4 different lithological/textural domains within one thin section. For
765 details see text. Images a-c with plane-polarized light. Image d with cross-polarized light is
766 from the data base of Expedition 312 in *Teagle et al.* [2006].

(a) Thin section scan with marked boundaries between the different domains. This is not the original ship section but a reproduced one from the shipboard rock billet. Length of the section is 4.8 cm.

(b) Subophitic gabbronoritic domain ("subophitic" in Table 1, 2). Clinopyroxene (cpx) and one orthopyroxene (opx) oikocrysts with plagioclase (pl) laths as chadacrysts form subophitic domains. Note the dusty appearance of the plagioclase which is a common feature for gabbro 2.

(c) Microgranular gabbronoritic domain ("microgranular" in Table 1, 2). Wormy intergrowths between granular ortho- and clinopyroxene and plagioclase forming a typical microgranular network which is well-known from the granoblastic dikes. Note the numerous inclusions of tiny oxides and silicates crystals in the pyroxenes which are interpreted as inherited from the former granoblastic stage. Some inclusions in orthopyroxene could be identified as clinopyroxene (white arrows) with the same composition as those from the microgranular network..

(d) Granular noritic domain ("granular coarse" in Table 1, 2). Characteristic are strongly zoned, tabular plagioclases forming an interlocking network with granophyric intergrowth between quartz and plagioclase (qz/pl) in the interstices. Note that tabular plagioclases show corroded boundaries at the contact (blue arrows) implying reactions between the tabular plagioclase and the late quartz-saturated melt. Primary mafic minerals within the interstices are orthopyroxene and probably amphibole, now completely altered to a mix of actinolite/chlorite (act).

(e) Compositional relations between the plagioclases in the different lithological domains including zoning effects within individual grains. "Coarse" and "fine" means "granular coarse" and "granular fine", respectively. Filled symbols: core compositions; open symbols: rim compositions (for granular coarse domain: normal rim [open circle with thick line] and outermost rim [open circle with thin line]).

(f) Compositional relations between clinopyroxene cores in the different lithological domains. Included are the fields for fresh lava/dikes and for the granoblastic dikes of the extrusive section of Hole 1256D from *Koepke et al.* [2008]. Symbols as in (e).

Figure 4. Microphotographs of clinopyroxene oikocrysts in subophitic domains of Gabbro 1 showing assumed quench effects (a, b), zoning effects (c), and high-temperature reaction effects (d). Numbers in c and d correspond to the average Cr_2O_3 contents (wt%) as listed in Table 3.

(a, b) 1 mm long plagioclase needle as chadacrysts within a clinopyroxene oikocryst showing characteristic fillings composed of clinopyroxene (arrows) with identical composition as the oikocryst in sample 214_2_15_17. Such features are indicative for very fast growth, not compatible with a crystal growth in typical magma chamber. These textural features are well known from the dike rocks (see Fig. 1-8). See text for details. (a) with plane-polarized light; (b) BSE image.

(c) "Normal", continuous zoning at the borders to the plagioclase chadacrysts with lower Mg#, Ti, Al, and Cr. Note that the adjacent plagioclases also show normal zoning towards the rim, indicated by slightly darker grey levels. Sample 215_1_84_88 (BSE image).

(b) Symplectitic intergrowth in the upper part of the image at the rim of a clinopyroxene oikocryst in the lower part (with exsolution lamellae) in sample 214_2_15_17 (BSE image). The wormy inclusions in the intergrowth are composed of orthoamphibole (EDX-checked), which are mostly heavily altered to chlorite.

Figure 5. Selected compositional parameters for clinopyroxenes and plagioclases from the gabbroic section of Hole 1256D. Data points correspond to averages presented in Table 3 (only compositions of the central parts of the grains). Included are data points from fresh lavas and dikes from Leg 206 and Expedition 309 published in *Dziony et al.* [2008] and

819 *Yamazaki et al.* [2009], and from granoblastic dikes published in *Koepke et al.* [2008].
820 Analyses from basaltic enclaves ("xenolith") are from this study and from *France et al.*
821 [2009]. Data points from the upper dike screen and from the subophitic domain (only Gabbro
822 1) include data from *Yamazaki et al.* [2009]. Data from the lower dike screen are from
823 *Yamazaki et al.* [2009].
824 (a) TiO_2 versus Al_2O_3 in the clinopyroxenes. The red field for the granoblastic trend is from
825 *France et al.* [2009]; the blue field for oceanic gabbro corresponds to data from key locations
826 for oceanic gabbro presented in Fig. 7.
827 (b) Plagioclase An content versus clinopyroxene Mg#. The modeling trend included was
828 calculated with COMAGMAT [*Ariskin*, 1999] using the most primitive bulk composition of
829 recovered lava as starting composition. Note that the analyzed minerals of the fresh lavas and
830 dikes fit well with the modeled trend. The data points from the subophitic domain, however,
831 plot away from the trend, mainly due to too An-rich plagioclases implying a crystallization in
832 a wet system.
833
834 **Figure 6.** BSE images of clusters of plagioclases showing striking zoning patterns of two
835 different lithological domains from the sample 214_2_0_6 (Gabbro 1) and related
836 concentration profiles for An content. The arrows in the BSE images indicate the position of
837 the profile acquisition. Averages of the compositions of the different zones are presented in
838 Table 3.
839 (a) Granular domain.
840 (b) Subophitic domain.
841
842 **Figure 7.** Variation in the major-element composition of minerals in the 1256D rocks and in
843 gabbros from key locations for deep crustal rocks in recent oceans. Data points correspond to
844 averages presented in Table 3. The subophitic domain data (only Gabbro 1) includes analyses

845 from *Yamazaki et al.* [2009]; analyses from fresh lavas and dikes are from *Dziony et al.*
846 [2008] and *Yamazaki et al.* [2009].
847 (a) TiO_2 versus Al_2O_3 in the clinopyroxenes.
848 (b) Plagioclase An content versus clinopyroxene Mg#. The modeling trend included was
849 calculated with COMAGMAT [*Ariskin*, 1999] using the most primitive bulk composition of
850 recovered lava as starting composition.
851 Data are from Southwest Indian Ridge [SWIR, *Dick et al.*, 2002], Mid-Atlantic Ridge near
852 Kane fracture zone [MARK, *Coogan et al.*, 2000a; *Coogan et al.*, 2000b; *Koepke et al.*, 2005;
853 *Lissenberg and Dick*, 2008], Mid-Atlantic Ridge near Atlantis Massif [Atlantis M., *Suhr et*
854 *al.*, 2008], East Pacific Rise from Pito Deep [*Perk et al.*, 2007], and East Pacific Rise from
855 Hess Deep [*Dick and Natland*, 1996; *Miller et al.*, 1996; *Natland and Dick*, 1996; *Coogan et*
856 *al.*, 2002].
857
858 **Figure 8.** Microphotographs of orthopyroxene containing millions of inclusions of tiniest
859 roundish clinopyroxenes within a granular noritic gabbro (sample 230_2_36_40). See text for
860 details.
861 (a) cross-polarized light. Image is from the data base of Expedition 312 in *Teagle et al.*
862 [2006].
863 (b) BSE image. The identified cpx inclusions are indicated by white arrows. Note that some
864 of the cpx inclusions show very small inclusions of ilmenite (black arrows). This is a key
865 feature for the granoblastic stadium, implying that the roundish clinopyroxene grains within
866 the orthopyroxene are relics of former granoblastic dikes incorporated into the gabbroic mush.
867 Alteration patches are also visible. In principle, the tiny oxide spots could also be explained
868 by a later alteration processes. However, the composition of typical secondary oxides in the
869 1256D gabbros is always magnetite with very low concentrations of TiO_2, but never ilmenite
870 as in the situation presented.

871

872 **Figure 9.** BSE images showing sulfide inclusions in orthopyroxene formed metamorphically
873 in a granoblastic dike and magmatically in a gabbro.
874 (a) In the granoblastic dike orthopyroxene forms clusters of single grains that are surrounded
875 by fine coronas of sulfide granules (arrows). The pyroxene-sulfide assemblage is clearly
876 grown during the granoblastic recrystallization event, and is not product of the later
877 hydrothermal alteration process. Two-pyroxene thermometry implies equilibration
878 temperatures >1000°C for the formation. Sample 209_1_8_10.
879 (b) Inclusion of sulfide (arrows) and plagioclase (~An 55 mol%) in a mm-sized prismatic
880 orthopyroxene in a complex 4-domain gabbro from Gabbro 2. Carefully evaluation of the
881 textural relations reveals a primary formation of the sulfides (also evidenced from other
882 samples), despite signs of a secondary alteration (plagioclase inclusion with albitic rims,
883 patches of actinolite/chlorite in the orthopyroxene). Sample 232_2_98_100.
884

885 **Figure 10.** BSE images of plagioclases from both Gabbro 1 and 2 showing the record of
886 proceeded partial melting reactions and related concentration profiles for An content. The
887 arrows in the BSE images indicate the position of the profile acquisition. Averages of the
888 compositions of the different zones (An-rich, Ab-rich) are presented in Table 3.
889 (a) Record of a more or less single partial melting event in a plagioclase grain of the
890 microgranular domain of sample 223_3_1_6 (Gabbro 1), expressed by zones strongly
891 enriched in An rimming more or less rectangular zones of Ab-rich plagioclase. Note further
892 similar structures visible in the smaller plagioclase grains in the lower left corner. We
893 interpret these structures as evidence for proceeded partial melting within the microgranular
894 domain, where the An-rich zones correspond to residual plagioclase, and the rectangular
895 zones to former melt pools, now frozen to Ab-rich plagioclase. Striking is the similarity of the

observed structures with those produced by experiments in the partly molten regime [e.g., Fig. 2 in *Koepke et al.*, 2005].

(b) Very complex zoning pattern interpreted as partial melting structures visible in a plagioclase grain of the granular domain of sample 230_2_36_40 (Gabbro 2) and related microprobe profile. Identical structures were obtained experimentally by partial melting of a plagioclase single crystal by [*Johannes and Holtz*, 1992] , Fig. 2].

Table 1. Samples from the drillcore of Hole 1256D used in this study

Exp[a]	Core	Sc[b]	Top (cm)	Bot. (cm)	Piece	Depth (mbsf)	Unit	Lithology	Thin-section [c]	Description [d]
312	214	2	0	6	1	1412.4	84	Gabbro 1	63	214_2_0_6
312	214	2	15	17	4a	1412.5	84	Gabbro 1	69	214_2_15_17
312	215	1	84	88	17	1416.5	85	Gabbro 1	71	215_1_84_88
312	223	2	57	60	1a	1451.4	89A	Gabbro 1	93	223_2_57_60
312	223	3	1	6	1	1452.3	89A	Gabbro 1	95	223_3_1_6
312	225	1	10	14	3	1459.0	90A	Up. dike screen	-	225_2_10_14
312	227	1	23	28	5a	1468.7	90A	Up. dike screen	100	227_1_23_28
312	230	1	54	56	8	1483.5	91A	Gabbro 2	-	230_1_54_56
312	230	2	36	40	6b	1484.9	91A	Gabbro 2	110	230_2_36_40
312	232	1	97	100	5c	1493.9	91A	Gabbro 2	113	232_1_97_100
312	232	2	52	54	2	1494.5	93	Gabbro 2	115	232_2_52_54
312	232	2	98	100	9	1495.0	93/94	Gabbro 2	116	232_2_98_100

[a)] Expedition [b)] Section of the core [c)] Shipboard thin section #

[d)] Abbreviated sample designation used in this study

Table 2. Petrographic features of the investigated samples and calculated equilibrium temperatures

Sample	Textural domains	Primary phases [a]	Special petrographic features	Equilibrium temperatures [b]	Figure# in *Teagle et al.* [2006] [c]
214_2_0_6	subophitic	cpx,plag			F210; F233B; F303E
	granular	plag,am,ox		Ti-in-am: 611	
214_2_15_17	subophitic	cpx,plag	rapid quench features; high-temperature reactions in cpx		F233A; F303C
	granular	plag,am,ox		Ti-in-am: 601	
215_1_84_88	subophitic	cpx,plag	rapid quench features; high-temperature reactions in cpx		F286A,B; F289; F303D; AF3B,C,D
	granular	opx,plag,am,ox	opx with granular inclusions of cpx; hydrous partial melting structures in plag	2-pyr: 1071±54[d] Ti-in-am: 1009 am-plag: 925	
223_2_57_60	subophitic	cpx,plag	high-temperature reactions in cpx		F236C,D
	granular	opx,ol,plag,am,ox	textural relics of granoblastic dikes; poikilitic oxides	Ti-in-am: 908	
	microgranular	cpx,plag,ox			
223_3_1_6	granular	opx,ol,plag,am,ox	textural relics of granoblastic dikes; hydrous partial melting structures in plag; opx with tiny granular inclusions of cpx	Ti-in-am: 906	F295
	microgranular	cpx,plag,ox			
225_2_10_14	granoblastic	cpx,plag,am,ox		1-py: 971	no shipboard section
227_1_23_28	granular	cpx,opx,pl,am,ox	tiny cpx and opx inclusions in plag	2-py: 981±91	F290A; F291; F308I
230_1_54_56	granular	cpx,plag,am,ox	close to xenolith contact: no more oxides		no shipboard section
	xenolith	cpx,opx,pl,ox	xenolith core; at the contact more oxides and absence of cpx	2-py: 1014±73	
230_2_36_40	granular	opx,plag,am,ox	millions of cpx inclusions in opx; cpx inclusions bear tiniest inclusions of il; hydrous partial melting structures in plag	Ti-in-am: 682	F241
	microgranular	cpx,opx,plag,ox		2-py: 1043±35	
232_1_97_100	granular	cpx,opx,plag,am,ox	both pyroxenes are poikilitic containing numerous plag grains; plag contains tiny inclusions of opx and cpx; contains secondary diopside	2-py: 1045+57 Ti-in-am: 714	F240
	microgranular	cpx,plag,ox			
232_2_52_54	granular	cpx,opx,plag,ox	comb structure at the contact between both lithologies; opx with inclusions of oxides and plag	2-py: 1084±70	F243; F245
	microgranular	cpx,opx,plag,ox	poikilitic sulfides	2-py: 1021±40	
232_2_98_100	subophitic	cpx,opx,plag	texturally and compositionally different compared to the subophitic domains from Gabbro 1		F242; F244; F246; F247; F286E,F
	granular coarse	opx,plag,am,qz,ox	quarz-bearing; typical cumulate features; opx with sulfide inclusions; contains secondary diopside		
	granular fine	cpx,opx,plag,ox		2-py:1059±36	
	microgranular	cpx,plag,ox			

[a] cpx - clinopyroxene, opx - orthopyroxene, ol - olivine, plag - plagioclase, am - amphibole, qz - quartz, ox - oxides, il - ilmenite.

[b] Used thermometers: 1-pyr, 2-pyr: single- and two-pyroxenes (QUILF); Ti-in-am: TiO_2-in-amphibole; am-plag: amphibole-plagioclase; see text for details.

[c] Number of Fig. in *Teagle et al.* [2006] in which petrographic details of the corresponding samples are presented.

[d] Calculated for opx host and cpx inclusions.

Table 3. Mineral compositions

lith[a]	dom[b]	tex dom[c]	pha[d]	an[e]	qual[f]	no[g]	SiO_2	TiO_2	Al_2O_3	Cr_2O_3	FeO	MnO	NiO	MgO	CaO	Na_2O	K_2O	F	Cl	Total	Mg#[h]	An[i]
214_2_0_6																						
gb1	2-dom	suboph	cpx			21	51.90	0.59	2.82	0.40	6.37	0.16		16.27	20.75	0.24	-			99.49	81.99	
							0.48	*0.09*	*0.54*	*0.15*	*0.26*	*0.03*		*0.50*	*0.64*	*0.03*					*0.96*	
		suboph	pl	co		14	47.92		32.88		0.44			0.05	16.66	2.33	0.02			100.31		79.72
							0.35		*0.27*		*0.04*			*0.03*	*0.29*	*0.17*	*0.01*					*1.41*
		suboph	pl	ri		44	50.74		30.83		0.52			0.10	14.29	3.61	0.06			100.15		68.41
							0.96		*0.64*		*0.17*			*0.12*	*0.53*	*0.33*	*0.12*					*2.61*
		granul	pl	co	rel	30	47.30		32.20		0.67			0.06	16.24	2.22	0.24			98.93		79.05
							1.76		*1.41*		*0.15*			*0.11*	*0.99*	*0.23*	*0.65*					*1.42*
		granul	pl	co	matrix	57	53.37		28.35		0.63			0.05	11.77	4.94	0.16			99.28		56.33
							1.60		*1.07*		*0.17*			*0.07*	*0.80*	*0.44*	*0.04*					*3.39*
		granul	am			12	51.34	0.63	3.51		13.84	0.20		15.21	11.42	0.90	0.05	0.07	0.16	97.33	66.19	
							1.38	*0.11*	*0.90*		*2.65*	*0.06*		*1.61*	*0.81*	*0.11*	*0.02*	*0.05*	*0.02*		*6.42*	
		granul	il	int		7	-	47.07	0.03	-	50.73	1.07		0.33	-	-	-			99.24		
								0.67	*0.01*		*1.17*	*0.18*		*0.04*								
		granul	mt	int		9	0.18	20.06	0.62	-	73.95	0.52		0.30	-	-	-			95.62		
							0.20	*4.49*	*0.11*		*4.23*	*0.21*		*0.13*								
214_2_15_17																						
gb1	2-dom	suboph	cpx			9	51.76	0.60	2.82	0.34	6.52	0.18		17.13	20.76	0.24	-			100.36	82.42	
							0.24	*0.07*	*0.26*	*0.06*	*0.40*	*0.04*		*0.27*	*0.69*	*0.04*					*0.77*	
		suboph	cpx		intergr	9	51.99	0.57	2.22	0.08	8.18	0.23		16.61	20.30	0.21	-			100.38	78.35	
							0.16	*0.02*	*0.10*	*0.04*	*0.24*	*0.03*		*0.15*	*0.22*	*0.02*					*0.58*	
		suboph	pl		rel	5	47.16		31.78		0.58			0.05	16.24	2.42	0.06			98.27		78.53
							2.49		*1.61*		*0.04*			*0.09*	*0.46*	*0.16*	*0.04*					*1.44*
		granul	pl		matrix	41	54.65		27.75		0.60			0.03	10.96	5.37	0.14			99.49		52.59
							1.74		*0.92*		*0.09*			*0.03*	*0.58*	*0.39*	*0.06*					*2.91*
		granul	am		cluster	19	49.42	0.58	4.34	-	17.46	0.27	-	12.71	11.22	0.93	0.14	-	0.26	97.33	56.36	
							0.84	*0.19*	*0.57*		*2.25*	*0.04*		*1.69*	*0.34*	*0.15*	*0.08*		*0.09*		*6.58*	
		granul	il	foc		5	-	45.57	0.04	-	49.97	0.90		0.24	0.06	-	-			96.78		
								0.51	*0.01*		*0.36*	*0.04*		*0.01*	*0.06*							
		granul	mt	int		6	0.16	25.48	0.69	0.07	66.95	0.28		0.12	-	-	-			93.75		
							0.07	*12.03*	*0.18*	*0.03*	*11.20*	*0.22*		*0.06*								
215_1_84_88																						
gb1	2-dom	suboph	cpx	co		27	52.21	0.52	2.56	0.42	6.25	0.17		17.18	20.71	0.24	-			100.25	83.07	
							0.48	*0.10*	*0.51*	*0.13*	*0.53*	*0.03*		*0.41*	*0.55*	*0.04*					*1.21*	
		suboph	cpx	ri		4	51.56	1.06	1.98	0.19	9.66	0.26		15.59	19.76	0.23	-			100.29	74.22	
							0.23	*0.17*	*0.06*	*0.00*	*0.66*	*0.01*		*0.69*	*1.34*	*0.01*					*0.91*	
		suboph	cpx		intergr	5	52.56	0.50	1.59	-	8.32	0.23		17.36	19.43	0.22	-			100.22	78.81	
							0.13	*0.02*	*0.04*		*0.26*	*0.03*		*0.12*	*0.17*	*0.01*					*0.63*	
		granul	cpx		inc/opx	3	51.44	0.76	1.70	-	12.12	0.34		14.68	18.88	0.24	-			100.16	68.36	
							0.25	*0.07*	*0.18*		*0.63*	*0.04*		*0.28*	*0.21*	*0.01*					*1.49*	
		granul	opx		prism	3	52.56	0.44	0.86	-	22.42	0.50		21.86	2.06	0.03	-			100.72	63.47	
							0.23	*0.06*	*0.19*		*1.10*	*0.08*		*0.75*	*0.03*	*0.03*					*1.93*	
		suboph	pl	co		54	48.22		32.44		0.43			0.06	16.22	2.53	0.03			99.92		77.87
							0.41		*0.31*		*0.05*			*0.07*	*0.31*	*0.18*	*0.01*					*1.55*
		suboph	pl	ri		30	50.61		30.88		0.46			0.08	14.30	3.67	0.05			100.06		68.11
							0.39		*0.30*		*0.07*			*0.08*	*0.30*	*0.18*	*0.01*					*1.49*
		granul	pl		rel	8	51.70		30.03		0.63			0.06	13.59	4.08	0.07			100.16		64.57
							0.58		*0.47*		*0.07*			*0.03*	*0.55*	*0.30*	*0.04*					*2.60*
		granul	pl	co	matrix	59	54.70		27.90		0.61			0.05	10.98	5.56	0.14			99.94		51.75
							0.77		*0.50*		*0.05*			*0.03*	*0.56*	*0.33*	*0.05*					*2.71*
		granul	pl	ri	matrix	22	61.52		24.05		0.45			-	5.64	8.53	0.22			100.41		26.41
							2.66		*1.47*		*0.08*				*1.97*	*1.06*	*0.07*					*9.28*
		granul	am		cluster	3	40.85	3.98	10.93		16.92	0.19		9.96	11.39	2.42	0.70	-	0.61	97.95	51.22	
							0.39	*0.77*	*0.36*		*0.35*	*0.04*		*0.17*	*0.21*	*0.39*	*0.49*		*0.11*		*0.89*	
		granul	il	int		13	-	47.23	0.11	-	51.08	0.98		0.22	-	-	-			99.63		
								1.02	*0.04*		*0.82*	*0.12*		*0.09*								
		granul	il	foc	exsol	10	-	48.21	0.05	-	49.87	1.03		0.05	-	-	-			99.21		
								0.62	*0.02*		*0.47*	*0.09*		*0.05*								
		granul	il	foc	host	5	-	48.79	0.05	-	49.38	0.97		0.23	-	-	-			99.42		
								0.32	*0.02*		*0.53*	*0.04*		*0.10*								
		granul	mt	int	image		0.03	19.84	1.04	0.06	74.37	0.47		0.08		-	-			95.89		
		granul	mt	foc	exsol	5	-	2.71	0.66	0.07	91.01	0.04		-	-	-	-			94.48		
								0.26	*0.35*	*0.04*	*1.03*	*0.02*										
		granul	mt	foc	host	16	0.05	4.40	1.58	0.08	87.71	0.16		0.10	-	-	-			94.07		
							0.02	*0.46*	*0.17*	*0.02*	*0.74*	*0.03*		*0.04*								
223_2_57_60																						
gb1	3-dom	suboph	cpx	co		17	51.78	0.43	2.57	0.69	5.39	0.16		17.40	20.73	0.24	-			99.39	85.21	
							0.59	*0.05*	*0.47*	*0.27*	*0.24*	*0.03*		*0.32*	*0.37*	*0.02*					*0.47*	
		suboph	cpx	ri		6	51.30	0.48	2.39	0.63	7.69	0.21		15.59	20.53	0.34	-			99.16	78.33	
							0.30	*0.13*	*0.16*	*0.11*	*0.30*	*0.06*		*0.33*	*0.44*	*0.05*					*0.88*	
		microgran	cpx	co		6	52.15	0.40	2.31	0.50	6.41	0.16		16.79	20.90	0.26	-			99.87	82.36	
							0.21	*0.03*	*0.06*	*0.08*	*0.78*	*0.04*		*0.33*	*0.53*	*0.02*					*2.00*	
		microgran	cpx	ri	pop1	5	51.30	0.73	2.13	0.25	8.41	0.27		15.74	20.11	0.34	-			99.29	76.93	
							0.51	*0.23*	*0.13*	*0.07*	*0.37*	*0.04*		*0.46*	*0.41*	*0.07*					*1.08*	
		microgran	cpx	ri	pop2Cr	3	50.27	0.57	2.93	1.07	9.34	0.26		14.64	20.02	0.38	-			99.48	73.65	
							0.08	*0.09*	*0.05*	*0.05*	*0.17*	*0.06*		*0.08*	*0.54*	*0.02*					*0.28*	
		granul	opx			11	52.97	0.52	1.02	-	18.18	0.42		24.15	1.99	0.04	-			99.29	70.31	
							0.38	*0.07*	*0.15*		*0.48*	*0.05*		*0.27*	*0.15*	*0.02*					*0.75*	
		granul	ol			5	37.11	-	-	-	29.66	0.46	0.11	32.42	0.08	-	-			99.84	66.09	
							0.11				*0.17*	*0.03*	*0.02*	*0.19*	*0.03*						*0.23*	
		suboph	pl			12	47.99		31.43		0.59			0.04	15.73	2.72	0.02			98.52		76.08

Table 3. (continued)

lith[a]	dom[b]	tex dom[c]	pha[d]	an[e]	qual[f]	no[g]	SiO_2	TiO_2	Al_2O_3	Cr_2O_3	FeO	MnO	NiO	MgO	CaO	Na_2O	K_2O	F	Cl	Total	Mg#[h]	An[i]
							0.45		*0.40*		*0.08*			*0.02*	*0.36*	*0.19*	*0.01*					*1.63*
		granul	pl		rel	30	48.14		31.24		0.63			-	15.78	2.79	0.02			98.60		75.67
							0.65		*0.37*		*0.09*				*0.41*	*0.25*	*0.01*					*2.15*
		granul	pl		matrix	27	51.20		29.22		0.53			-	13.19	4.22	0.04			98.41		63.19
							1.57		*1.15*		*0.12*				*0.65*	*0.34*	*0.02*					*2.82*
		microgran	pl	co		10	49.12		31.59		0.61			-	15.16	3.02	0.02			99.53		73.42
							0.62		*0.42*		*0.12*				*0.55*	*0.30*	*0.01*					*2.63*
		microgran	pl	ri		8	52.05		29.57		0.50			-	12.76	4.45	0.04			99.36		61.18
							0.12		*0.07*		*0.09*				*0.11*	*0.08*	*0.00*					*0.57*
		granul	am		cluster	17	43.03	2.63	9.52	0.04	13.11	0.14	-	13.10	11.38	2.62	0.18	-	0.43	96.18	64.05	
							0.46	*0.21*	*0.26*	*0.01*	*0.39*	*0.02*		*0.28*	*0.12*	*0.07*	*0.02*		*0.03*		*1.04*	
		granul	il	int		9	0.03	49.38	0.08	0.08	48.11	2.12		0.07	-	-	-			99.87		
							0.01	*0.94*	*0.04*	*0.03*	*0.76*	*0.14*		*0.02*								
		granul	mt	int		7	0.07	4.74	1.75	0.81	84.82	0.20		0.22	-	-	-			92.62		
							0.02	*0.96*	*0.07*	*0.06*	*1.08*	*0.06*		*0.04*								
223_3_1_6																						
gb1	2-dom	microgran	cpx			11	51.93	0.71	1.95	0.18	9.47	0.26		15.21	20.49	0.34	-			100.54	74.15	
							0.57	*0.09*	*0.10*	*0.12*	*0.61*	*0.06*		*0.41*	*0.97*	*0.04*					*1.00*	
		granul	opx		poik	8	53.19	0.55	1.09	-	18.08	0.38		24.98	1.99	0.04	-			100.29	71.13	
							0.28	*0.04*	*0.07*		*0.35*	*0.05*		*0.15*	*0.10*	*0.01*					*0.47*	
		granul	opx		prism	4	55.00	0.37	1.16	-	15.58	0.38		26.91	2.24	0.05	-			101.70	75.49	
							0.19	*0.02*	*0.06*		*0.19*	*0.04*		*0.20*	*0.11*	*0.01*					*0.14*	
		granul	ol			18	36.93	-	-	-	30.86	0.43	0.08	32.59	0.17	-	-			101.06	65.31	
							0.51				*1.28*	*0.05*	*0.03*	*0.76*	*0.35*						*1.45*	
		microgran	pl		An-rich	17	49.21		31.77		0.63			-	15.64	2.83	0.03			100.12		75.18
							0.49		*0.30*		*0.05*				*0.28*	*0.15*	*0.01*					*1.32*
		microgran	pl		matrix	28	51.61		30.08		0.62			0.05	13.62	3.95	0.04			99.96		65.42
							0.63		*0.54*		*0.25*			*0.09*	*0.47*	*0.22*	*0.01*					*1.88*
		microgran	pl		Ab-rich	24	54.05		28.65		0.61			0.05	11.85	4.98	0.06			100.25		56.63
							0.80		*0.49*		*0.14*			*0.08*	*0.59*	*0.33*	*0.01*					*2.83*
		granul	pl			7	53.94		28.78		0.64			0.09	12.20	4.87	0.05			100.57		57.90
							0.19		*0.23*		*0.19*			*0.15*	*0.13*	*0.12*	*0.01*					*0.79*
		microgran	am		cluster	9	44.85	2.61	9.36	0.10	12.60	0.17	-	14.22	11.50	2.48	0.25	0.06	0.41	98.59	66.79	
							0.49	*0.16*	*0.31*	*0.03*	*0.25*	*0.02*		*0.23*	*0.17*	*0.07*	*0.02*	*0.05*	*0.01*		*0.64*	
		granul	il	int		14	0.08	50.09	0.08	0.05	48.77	1.50		0.23	-	-	-			100.80		
							0.06	*0.33*	*0.04*	*0.03*	*0.56*	*0.22*		*0.07*								
		granul	mt	int		21	0.16	4.45	2.34	0.62	85.65	0.21		0.32	-	-	-			93.75		
							0.09	*0.93*	*0.24*	*0.12*	*1.18*	*0.08*		*0.08*								
225_1_10_14																						
Udi-s	1-dom	granbl	cpx			10	51.99	0.68	1.49	-	9.66	0.24		15.19	20.79	0.33	-			100.36	73.70	
							0.22	*0.08*	*0.15*		*0.31*	*0.04*		*0.19*	*0.31*	*0.02*					*0.62*	
		granbl	pl			22	54.21		28.47		0.65			0.03	11.31	5.35	0.06			100.07		53.73
							0.41		*0.28*		*0.12*			*0.03*	*0.30*	*0.18*	*0.01*					*1.43*
		granbl	am		flaky	6	51.12	0.94	4.48	-	10.78	0.15	-	16.64	11.58	1.18	0.08	-	0.14	97.08	73.33	
							1.08	*0.22*	*0.61*		*0.35*	*0.04*		*0.47*	*0.20*	*0.17*	*0.01*		*0.04*		*1.09*	
227_1_23_28																						
Udi-s	1-dom	granul	cpx			19	52.52	0.13	0.48	-	9.42	0.32		14.13	22.15	0.31	-			99.46	72.82	
							0.57	*0.08*	*0.23*		*0.99*	*0.04*		*0.36*	*1.04*	*0.13*					*2.35*	
		granul	cpx		inc/plag	6	52.10	0.24	0.70	0.05	10.54	0.31		13.94	21.09	0.38	-			99.35	70.20	
							0.33	*0.09*	*0.24*	*0.06*	*0.39*	*0.04*		*0.41*	*0.27*	*0.18*					*1.04*	
		granul	opx			15	52.19	0.40	0.80	-	22.34	0.52		21.78	2.04	0.04	-			100.10	63.48	
							0.15	*0.01*	*0.02*		*0.30*	*0.04*		*0.22*	*0.12*	*0.01*					*0.40*	
		granul	opx		inc/plag	9	51.90	0.41	0.81	-	22.63	0.54		21.50	2.02	0.03	-			99.84	62.88	
							0.20	*0.01*	*0.04*		*0.29*	*0.05*		*0.12*	*0.04*	*0.02*					*0.42*	
		granul	pl	co		22	53.27		28.19		0.68			0.05	11.69	5.08	0.06			99.01		55.80
							1.00		*0.52*		*0.36*			*0.04*	*0.73*	*0.44*	*0.01*					*3.63*
		granul	pl	ri		3	58.73		25.09		0.47			-	7.66	7.24	0.09			99.29		36.71
							0.71		*0.31*		*0.04*				*0.37*	*0.18*	*0.01*					*1.64*
		granul	am		inc/plag	2	46.14	0.78	8.27	-	13.56	0.18		14.36	11.55	1.90	0.15			96.90	65.38	
							0.18	*0.05*	*0.41*		*0.10*	*0.02*		*0.21*	*0.04*	*0.06*	*0.02*				*0.17*	
		granul	il	int		7	-	47.40	0.06	0.04	49.71	1.44		0.23	-	-	-			98.89		
								1.11	*0.05*	*0.01*	*1.00*	*0.06*		*0.11*								
		granul	mt	int		8	0.07	3.40	1.02	0.34	86.97	0.22		0.19	-	-	-			92.20		
							0.05	*0.19*	*0.07*	*0.03*	*0.49*	*0.03*		*0.12*								
230_1_54_56																						
gb2	gb/xeno	m granul	cpx			8	51.92	0.50	1.10	-	12.00	0.34		13.99	20.03	0.26				100.18	67.53	
							0.24	*0.07*	*0.05*		*0.15*	*0.03*		*0.14*	*0.32*	*0.02*				*0.36*	*0.26*	
		m granul(-)	cpx			7	51.91	0.43	1.09	-	12.19	0.34		13.82	20.16	0.27				100.24	66.91	
							0.20	*0.11*	*0.20*		*0.08*	*0.03*		*0.31*	*0.43*	*0.02*				*0.12*	*0.96*	
		xeno core	cpx			8	52.03	0.47	1.19	-	11.35	0.29		14.13	20.62	0.28				100.39	68.94	
							0.19	*0.09*	*0.12*		*0.25*	*0.04*		*0.07*	*0.32*	*0.02*				*0.26*	*0.53*	
		xeno core	opx			6	52.05	0.40	0.83	-	23.44	0.52		20.77	1.95	0.03				100.02	61.23	
							0.14	*0.02*	*0.03*		*0.20*	*0.03*		*0.26*	*0.19*	*0.01*				*0.21*	*0.41*	
		xeno rim	opx			10	52.37	0.43	0.78	-	22.98	0.51		21.21	1.99	0.03				100.31	62.20	
							0.22	*0.01*	*0.06*		*0.24*	*0.02*		*0.20*	*0.20*	*0.01*				*0.43*	*0.27*	
		m granul	pl			8	55.28		27.79		0.60			-	10.31	5.62	0.07			99.75		50.14
							0.24		*0.19*		*0.15*				*0.12*	*0.13*	*0.01*			*0.27*		*0.81*
		m granul(-)	pl			10	54.62		28.01		0.80			-	10.47	5.52	0.12			99.65		50.83
							1.16		*0.33*		*0.85*				*0.49*	*0.33*	*0.16*			*0.53*		*2.33*
		xeno core	pl	co		8	53.50		29.04		0.47			-	11.80	4.85	0.05			99.82		57.20
							0.54		*0.45*		*0.06*				*0.68*	*0.36*	*0.00*			*0.50*		*3.18*
		xeno core	pl	ri		5	56.63		27.05		0.49			-	9.53	6.18	0.07			100.01		45.83
							1.18		*0.69*		*0.06*				*0.78*	*0.44*	*0.00*			*0.42*		*3.74*

Table 3. (continued)

lith[a]	dom[b]	tex dom[c]	pha[d]	an[e]	qual[f]	no[g]	SiO_2	TiO_2	Al_2O_3	Cr_2O_3	FeO	MnO	NiO	MgO	CaO	Na_2O	K_2O	F	Cl	Total	Mg#[h]	An[i]
		xeno rim	pl	co		5	50.92		30.58		0.45			-	14.16	3.60	0.04			99.82		68.31
							1.48		*0.97*		*0.09*				*1.25*	*0.71*	*0.02*			*0.23*		*6.20*
		xeno rim	pl	ri		5	47.70		26.53		0.52			-	11.41	4.11	0.06			90.40		60.31
							0.56		*0.44*		*0.20*				*0.31*	*0.21*	*0.04*			*0.36*		*1.66*
		m granul	il	int		6	-	46.71	0.09	0.04	51.05	1.46		0.07	-	-	-			99.48		
								0.51	*0.01*	*0.06*	*0.51*	*0.38*		*0.02*								
		xeno core	il	int		8	-	45.60	0.06	0.05	51.96	1.07		0.07	-	-	-			98.83		
								0.51	*0.02*	*0.04*	*0.36*	*0.08*		*0.02*						*0.70*		
		xeno rim	il	int		8	-	46.66	0.07	0.06	51.01	1.18		0.08	-	-	-			99.10		
								0.49	*0.01*	*0.06*	*0.60*	*0.08*		*0.02*						*0.38*		
		m granul	mt	int		6	-	3.56	1.61	0.19	87.70	0.21		0.53	-	-	-			93.83		
								0.05	*0.04*	*0.07*	*0.40*	*0.05*		*0.09*								
		xeno core	mt	int		8	-	3.27	0.90	0.35	88.13	0.17		0.15	-	-	-			93.05		
								0.48	*0.11*	*0.03*	*0.54*	*0.04*		*0.09*						*0.23*		
		xeno rim	mt	int		8	-	3.51	1.71	0.30	87.20	0.16		0.37	-	-	-			93.34		
								0.13	*0.08*	*0.04*	*0.38*	*0.04*		*0.11*						*0.44*		
230_2_36_40																						
gb2	2-dom	granul	cpx		inc/opx	3	51.73	0.68	1.71	-	10.90	0.29		15.50	19.02	0.30	-			100.14	71.78	
							0.20	*0.08*	*0.15*		*1.33*	*0.02*		*0.65*	*1.64*	*0.02*					*1.67*	
		microgran	cpx			13	51.33	0.62	1.61	-	10.25	0.30		14.49	20.33	0.28	-			99.21	71.59	
							0.23	*0.03*	*0.07*		*0.28*	*0.03*		*0.21*	*0.37*	*0.03*					*0.54*	
		granul	opx			14	52.42	0.49	0.94	-	20.71	0.48		22.55	1.90	0.03	-			99.52	66.00	
							0.39	*0.03*	*0.05*		*0.60*	*0.04*		*0.36*	*0.19*	*0.01*					*0.92*	
		microgran	opx			9	52.42	0.47	1.01	-	19.74	0.47		23.45	1.80	-	-			99.36	67.93	
							0.14	*0.04*	*0.10*		*0.35*	*0.04*		*0.13*	*0.14*						*0.47*	
		granul	pl	co		12	51.36		29.86		0.62			0.06	12.98	4.19	0.07			99.16		62.85
							0.97		*0.45*		*0.12*			*0.11*	*0.64*	*0.36*	*0.04*					*3.03*
		granul	pl	ri		6	53.43		28.63		0.55			0.04	11.62	5.04	0.08			99.38		55.79
							0.55		*0.29*		*0.05*			*0.03*	*0.33*	*0.19*	*0.01*					*1.54*
		granul	pl		An-rich	53	47.08		33.26		0.26			-	16.76	2.08	0.02			99.47		81.51
							0.40		*0.27*		*0.07*				*0.32*	*0.17*	*0.01*					*1.52*
		granul	pl		Ab-rich	13	51.32		30.31		0.42			0.04	13.38	4.07	0.06			99.61		64.23
							0.39		*0.28*		*0.11*			*0.07*	*0.34*	*0.21*	*0.02*					*1.75*
		microgran	pl			15	51.98		29.53		0.65			0.04	12.52	4.57	0.08			99.37		59.95
							0.98		*0.67*		*0.14*			*0.03*	*0.73*	*0.42*	*0.03*					*3.55*
		granul	am			6	49.91	1.01	4.52	0.03	12.85	0.20	-	15.32	11.43	1.08	0.10	-	0.25	96.70	68.02	
							0.48	*0.08*	*0.37*	*0.01*	*0.45*	*0.02*		*0.27*	*0.12*	*0.06*	*0.02*		*0.03*		*1.09*	
		granul	il	foc		13	-	47.84	0.07	0.08	50.65	1.17		0.14	-	-	-			99.95		
								0.57	*0.01*	*0.05*	*0.50*	*0.14*		*0.06*								
		granul	mt	foc		15	0.07	4.22	1.66	0.59	85.85	0.22		0.26	-	-	-			92.88		
							0.03	*0.45*	*0.47*	*0.48*	*0.45*	*0.06*		*0.10*								
232_1_97_100																						
gb2	2-dom	granul	cpx		poik	10	51.30	0.72	1.89	0.20	9.16	0.24		14.91	20.48	0.29	-			99.20	74.37	
							0.33	*0.06*	*0.19*	*0.21*	*0.32*	*0.03*		*0.21*	*0.40*	*0.03*					*0.59*	
		granul	cpx		diop	13	52.75	0.11	0.53	-	9.08	0.26		14.21	22.35	0.28	-			99.55	73.62	
							0.27	*0.04*	*0.15*		*0.72*	*0.05*		*0.38*	*0.42*	*0.05*					*2.01*	
		microgran	cpx			10	51.35	0.87	1.85	-	10.62	0.24		14.77	19.89	0.35	-			99.94	71.29	
							0.70	*0.15*	*0.09*		*1.00*	*0.05*		*0.40*	*0.86*	*0.03*					*2.04*	
		granul	opx		poik	14	52.90	0.50	0.99	-	18.68	0.43		24.09	1.85	-	-			99.44	69.69	
							0.20	*0.03*	*0.05*		*0.14*	*0.04*		*0.13*	*0.13*						*0.16*	
		granul	pl	co		48	52.28		29.36		0.62			0.07	12.56	4.50	0.06			99.45		60.44
							1.03	*0.02*	*0.63*	*0.02*	*0.16*	*0.02*		*0.11*	*0.72*	*0.44*	*0.01*					*3.62*
		granul	pl	ri		7	55.22		27.60		0.55			-	10.33	5.82	0.08			99.59		49.27
							1.59	*0.04*	*0.77*	*0.00*	*0.13*	*0.02*			*1.19*	*0.74*	*0.02*					*6.02*
		microgran	pl			12	54.43		28.33		0.59			0.04	11.06	5.47	0.07			99.99		52.55
							0.54		*0.41*		*0.13*			*0.03*	*0.35*	*0.22*	*0.01*					*1.75*
		granul	am		cluster	19	49.69	1.20	5.05	0.07	12.49	0.18	-	15.48	11.37	1.34	0.11	0.05	0.23	97.26	68.79	
							1.34	*0.26*	*0.97*	*0.02*	*0.75*	*0.03*		*0.85*	*0.13*	*0.20*	*0.03*	*0.03*	*0.07*		*2.45*	
		granul	il	foc		11	-	47.46	0.07	0.15	50.86	1.09		0.36	-	-	-			99.99		
								0.27	*0.02*	*0.03*	*0.37*	*0.10*		*0.37*								
		microgran	il	foc		10	-	49.01	0.05	0.04	45.60	5.66		0.07	0.08	-	-			100.51		
								0.31	*0.02*	*0.02*	*0.50*	*0.24*		*0.01*	*0.04*							
		granul	mt	int		11	0.07	4.11	1.64	1.23	85.46	0.22		0.62	-	-	-			93.34		
							0.04	*0.52*	*0.26*	*0.05*	*0.57*	*0.04*		*0.22*								
		microgran	mt	int		7	2.04	2.42	1.73	0.40	84.44	0.35		0.76	0.53	-	-			92.67		
							1.27	*1.33*	*0.69*	*0.03*	*2.41*	*0.17*		*0.53*	*1.02*							
232_2_52_54																						
gb2	2-dom	granul	cpx			27	51.67	0.68	1.85	0.08	10.09	0.26		15.48	20.05	0.28	-			100.44	73.23	
							0.60	*0.32*	*0.37*	*0.06*	*1.22*	*0.05*		*0.87*	*1.18*	*0.03*					*2.90*	
		microgran	cpx			10	51.91	0.75	1.65	-	9.82	0.28		14.89	20.79	0.28	-			100.36	73.02	
							0.24	*0.10*	*0.18*		*0.43*	*0.03*		*0.22*	*0.72*	*0.02*					*0.64*	
		granul	opx			18	53.32	0.50	1.02	-	18.73	0.41		24.62	1.99	0.05	-			100.64	70.08	
							0.29	*0.06*	*0.11*		*0.91*	*0.04*		*0.85*	*0.21*	*0.02*					*1.71*	
		microgran	opx			8	52.78	0.49	0.95	-	20.15	0.45		23.93	1.66	0.03	-			100.45	67.92	
							0.25	*0.05*	*0.09*		*0.27*	*0.04*		*0.21*	*0.14*	*0.02*					*0.39*	
		granul	pl			47	52.85		29.47		0.58			0.04	12.65	4.64	0.06			100.29		59.91
							1.53		*1.01*		*0.15*			*0.04*	*1.16*	*0.66*	*0.01*					*5.60*
		microgran	pl			10	53.75		28.91		0.55			0.04	11.91	5.05	0.06			100.27		56.39
							0.73		*0.44*		*0.09*			*0.04*	*0.49*	*0.31*	*0.01*					*2.49*
		granul	il	int		8	-	46.04	0.03	0.15	51.56	0.93		0.56	-	-	-			99.27		
								0.30	*0.01*	*0.02*	*0.28*	*0.20*		*0.21*								
		granul	mt	int		4	0.34	2.69	0.66	1.54	87.30	0.16		0.17	0.06	-	-			92.94		
							0.21	*0.45*	*0.04*	*0.08*	*0.54*	*0.06*		*0.12*	*0.04*							

Table 3. (continued)

lith[a]	dom[b]	tex dom[c]	pha[d]	an[e]	qual[f]	no[g]	SiO_2	TiO_2	Al_2O_3	Cr_2O_3	FeO	MnO	NiO	MgO	CaO	Na_2O	K_2O	F	Cl	Total	Mg#[h]	An[i]
232_2_98_100																						
gb2	4-dom	coarse	cpx		diop	24	53.12	0.07	0.38	-	9.21	0.25		14.20	22.57	0.32	-			100.12	73.33	
							0.34	*0.03*	*0.12*		*0.71*	*0.06*		*0.48*	*0.50*	*0.11*					*2.01*	
		fine	cpx			16	51.84	0.58	1.23	-	11.51	0.30		14.43	19.99	0.29	-			100.16	69.09	
							0.17	*0.04*	*0.10*		*0.34*	*0.04*		*0.23*	*0.46*	*0.03*					*0.40*	
		microgran	cpx			18	51.45	0.68	1.70	0.09	10.50	0.30		14.40	19.93	0.34	-			99.38	71.00	
							0.29	*0.07*	*0.13*	*0.04*	*0.63*	*0.04*		*0.26*	*0.64*	*0.03*					*1.04*	
		suboph	cpx			37	50.77	0.92	2.52	0.06	8.46	0.23		14.83	21.17	0.28	-			99.24	75.76	
							0.41	*0.09*	*0.25*	*0.03*	*0.53*	*0.05*		*0.41*	*0.82*	*0.04*					*1.07*	
		coarse	opx			21	52.88	0.43	0.89	-	20.22	0.45		23.49	1.98	0.03	-			100.39	67.43	
							0.25	*0.05*	*0.11*		*0.67*	*0.05*		*0.43*	*0.07*	*0.01*					*1.10*	
		fine	opx			14	52.50	0.48	0.88	-	21.60	0.50		22.61	1.94	0.04	-			100.55	65.11	
							0.21	*0.05*	*0.06*		*0.63*	*0.04*		*0.46*	*0.19*	*0.01*					*1.09*	
		coarse	pl	co		16	54.44		27.93		0.67			0.03	10.91	5.48	0.05			99.52		52.26
							0.97		*0.45*		*0.13*			*0.02*	*0.64*	*0.37*	*0.01*					*3.07*
		coarse	pl	ri		4	59.83		24.89		0.41			-	6.82	7.78	0.08			99.81		32.50
							1.03		*0.62*		*0.07*				*0.59*	*0.33*	*0.01*					*2.79*
		coarse	pl	ri	out rim	6	64.34		22.68		0.33			-	3.71	9.49	0.11			100.67		17.67
							0.43		*0.31*		*0.11*				*0.31*	*0.17*	*0.02*					*1.48*
		fine	pl	co		9	51.28		30.01		0.64			0.03	13.50	3.99	0.04			99.48		65.02
							0.54	*0.01*	*0.46*	*0.01*	*0.21*			*0.03*	*0.48*	*0.23*	*0.01*					*2.09*
		fine	pl	ri		5	55.13		27.62		0.66			0.05	10.42	5.61	0.06			99.56		50.47
							1.51	*0.03*	*0.74*	*0.02*	*0.26*			*0.07*	*1.19*	*0.63*	*0.01*					*5.70*
		microgran	pl	co		8	52.49		29.28		0.66			-	12.60	4.45	0.05			99.53		60.86
							0.80	*0.01*	*0.47*	*0.01*	*0.09*				*0.55*	*0.34*	*0.01*					*2.81*
		microgran	pl	ri		9	53.86		28.31		0.74			-	11.43	5.10	0.05			99.48		55.15
							0.42	*0.01*	*0.23*	*0.01*	*0.15*				*0.30*	*0.15*	*0.00*					*1.30*
		suboph	pl			20	52.04	0.07	29.24		0.63			0.05	12.82	4.40	0.04			99.31		61.54
							0.58	*0.03*	*0.27*		*0.16*			*0.06*	*0.29*	*0.21*	*0.01*					*1.56*
		fine	il	int		10	-	44.59	0.09	0.21	53.32	1.03		0.26	-	-	-			99.49		
								0.58	*0.01*	*0.03*	*0.41*	*0.11*		*0.10*								
		coarse	il	int		7	-	45.98	0.03	0.09	52.34	0.90		0.31	-	-	-			99.65		
								0.33	*0.01*	*0.03*	*0.25*	*0.20*		*0.07*								
		fine	mt	int		16	0.09	3.58	1.39	1.84	86.66	0.19		0.23	-	-	-			93.98		
							0.18	*0.70*	*0.09*	*0.05*	*0.79*	*0.04*		*0.09*								

[a] Lithology: *gb1* - Gabbro 1; *gb2* - Gabbro 2; *Udi-s* - upper dike screen

[b] Domains: number of identified textural/lithological domains; *gb/xeno* - gabbro hosting a xenolith

[c] Textural domain: *coarse* - granular coarse-grained; *fine* - granular fine-grained; *granbl* - granoblastic; *granul* - granular; *m granul* - granular matrix hosting xenolith; *m granul(-)* - granular matrix near the contact to a xenolith without oxides; *microgran* - microgranular; *suboph* - subophitic; *xeno core* - core region of a xenolith; *xeno rim* - rim of a xenolith

[d] Phase: *am* - amphibole; *cpx* - clinopyroxene; *il* - ilmenite; *mt* - magnetite; *ol* - olivine; *opx* - orthopyroxene; *pl* - plagioclase

[e] Details of the analysis: *co* - core; *ri* - rim; empty space: central part of the crystal. For oxides: *foc* - focused analysed; *int* - integral analysed

[f] Phase qualifier: *Ab-rich, An-rich* - Ab- and An-enriched zone in partial molten plagioclase; *diop* - diopsidic clinopyroxene; *exsol* - exsolutions; *host* - host crystal bearing exsolutions; *image* - calculated composition via image analysis; *inc/opx*, *inc/plag*: tiny inclusions in orthopyroxene and plagioclase, respectively; *intergr* - intrgrowth formed by reaction; *out rim* - outermost rim; *poik* - poikilitic; *poikbl* - poikiloblastic; *pop1* - population 1; *pop2Cr* - population 2 rich in Cr; *prism* - prismatic; *rel* - An-rich relict. For details see text

[g] Number of analyses [h] $MgO/(MgO + FeO^{tot})*100$, molar [i] An content of the plagioclase, mol %

- below limit of detection; empty space - not analyzed; FeO = FeO^{tot}; italics: one standard deviation

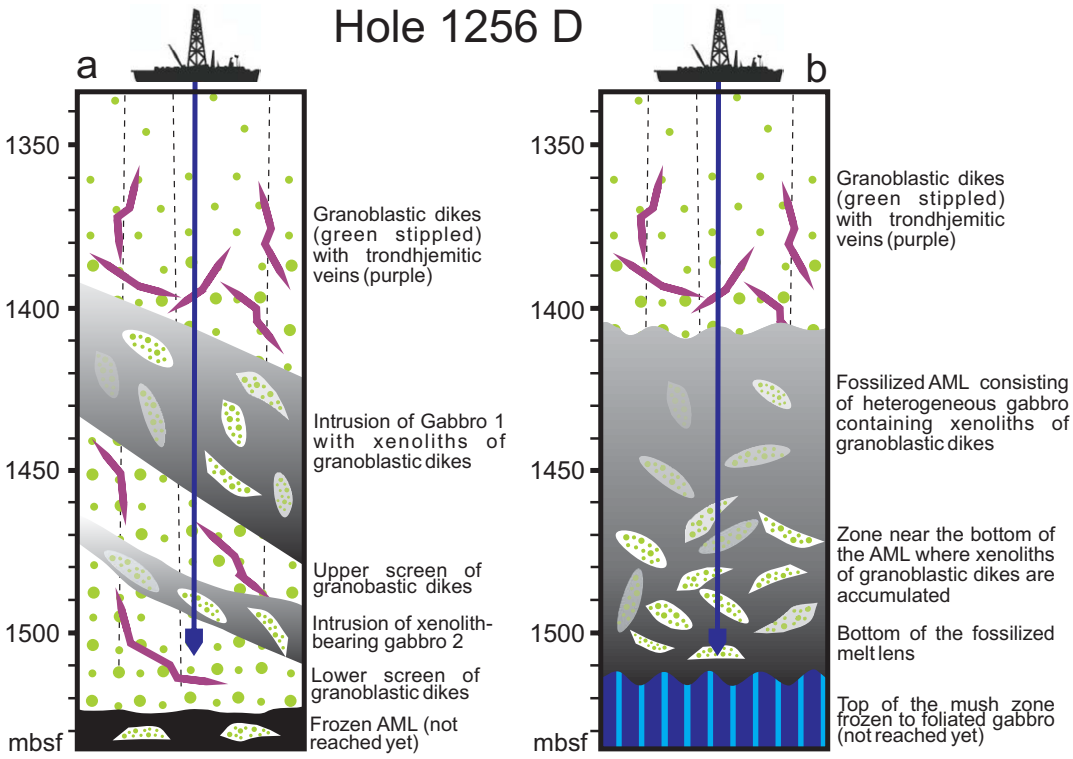

Wilson et al. [2006]; *Teagle et al.* [2006]; *Koepke et al.* [2008]

France et al. [2009]

Figure 1; Koepke et al.

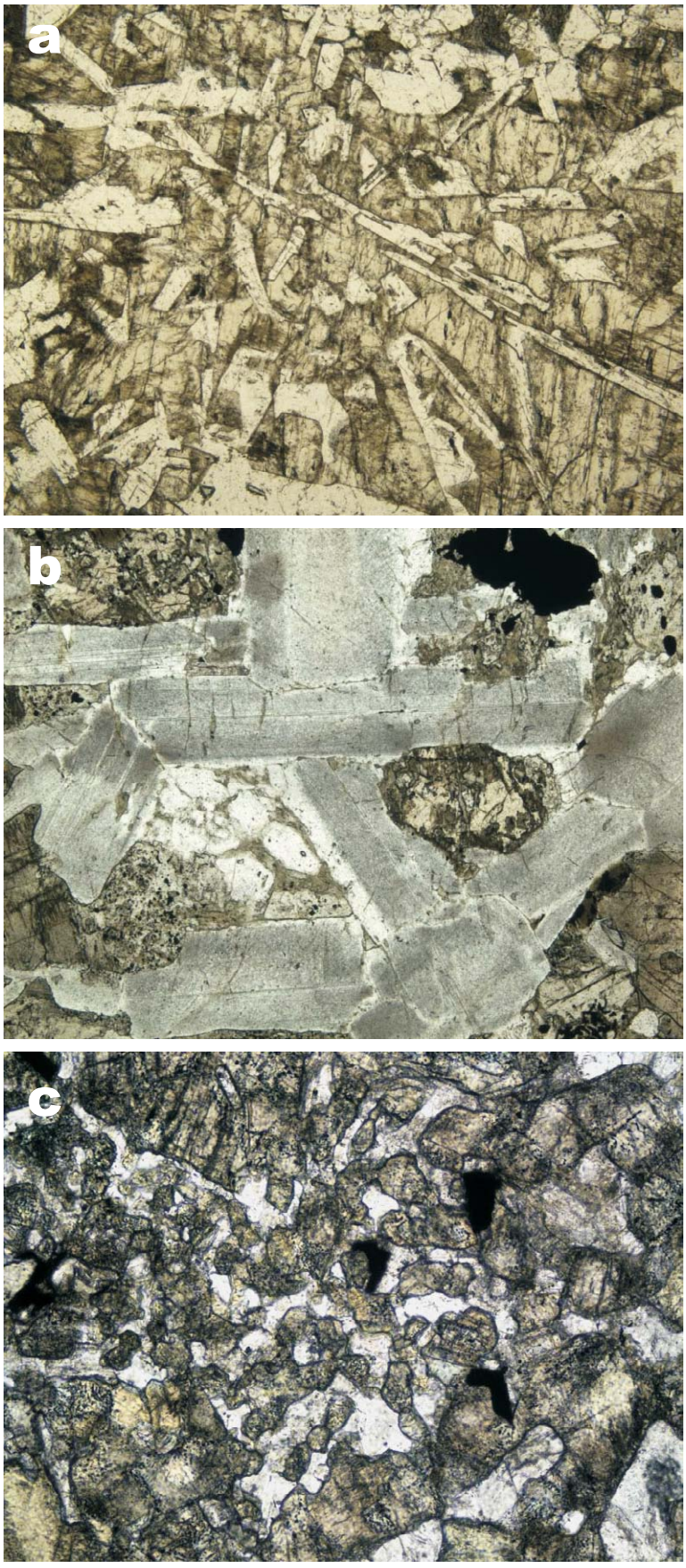

Fig. 2; Koepke et al.

Gabbro 232_2_98_100:
4 domains with different textures, phase relations and phase compositions

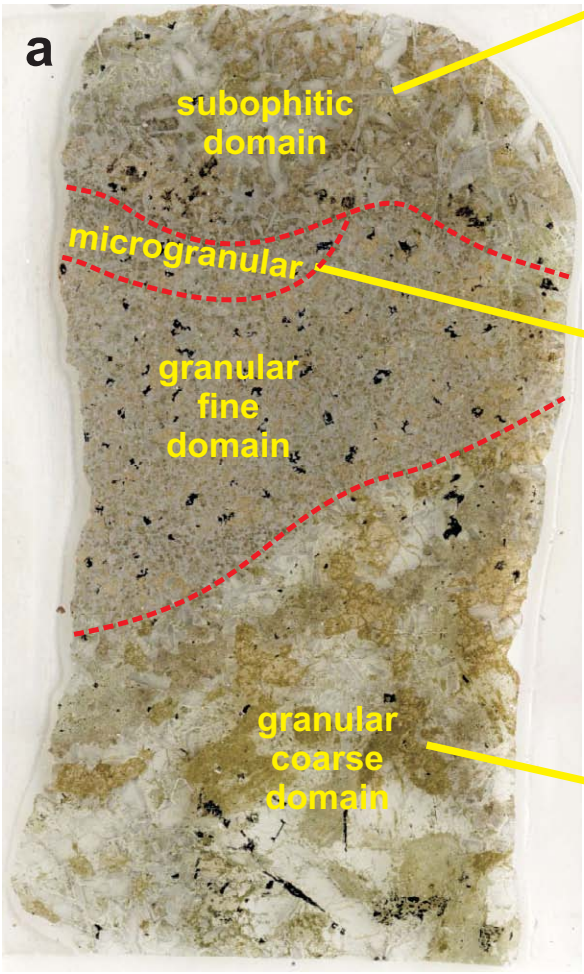

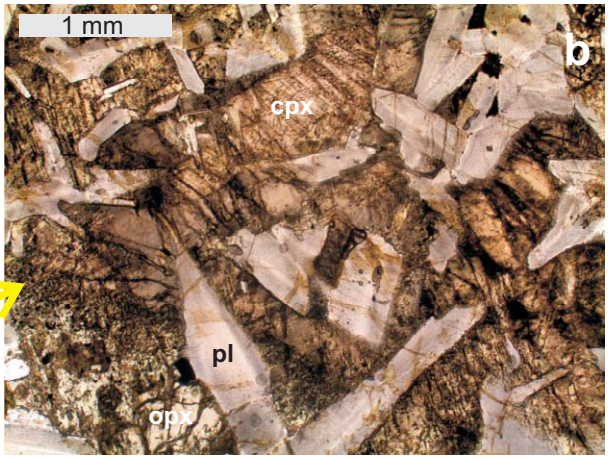

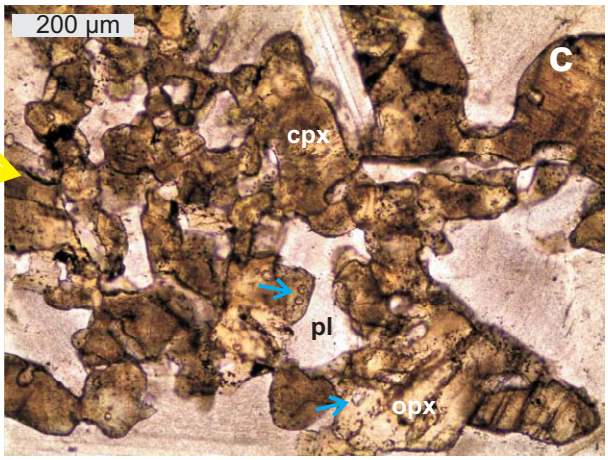

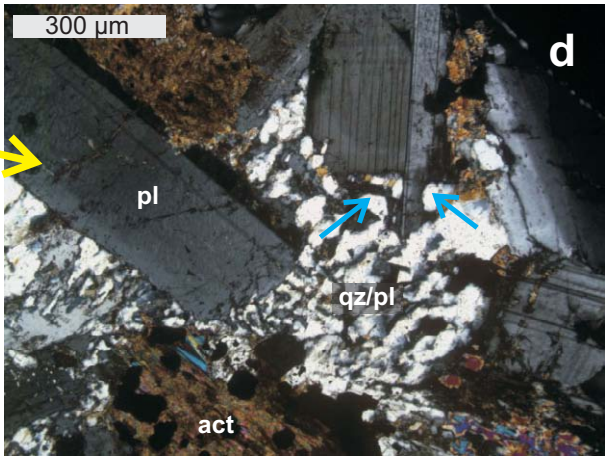

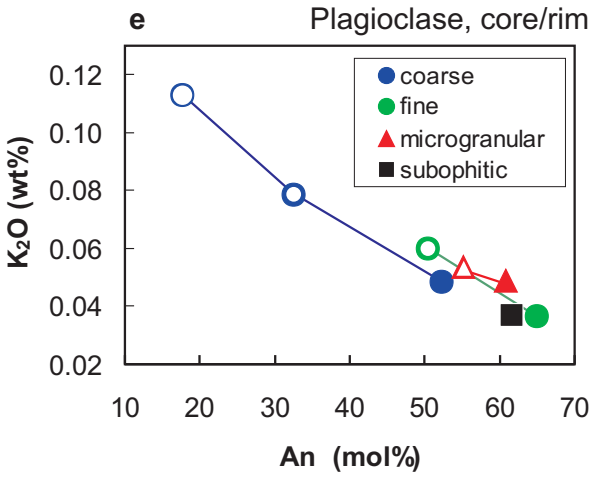

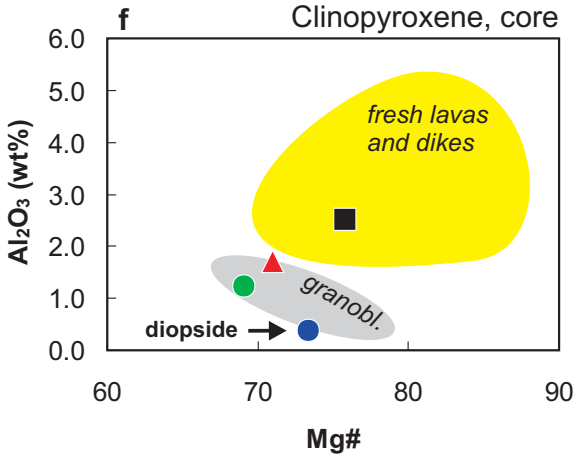

Fig. 3, Koepke et al.

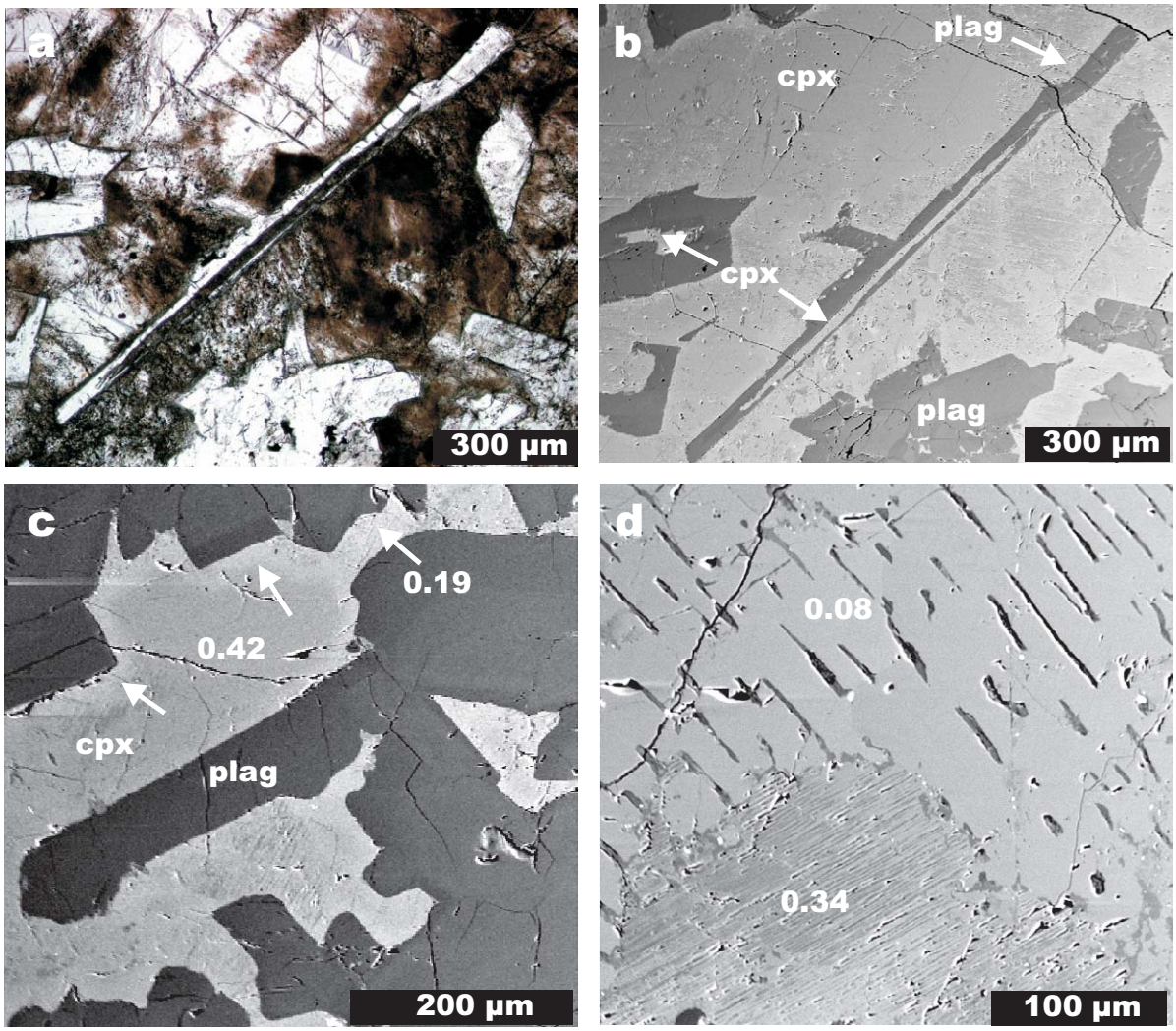

Fig. 4; Koepke et al.

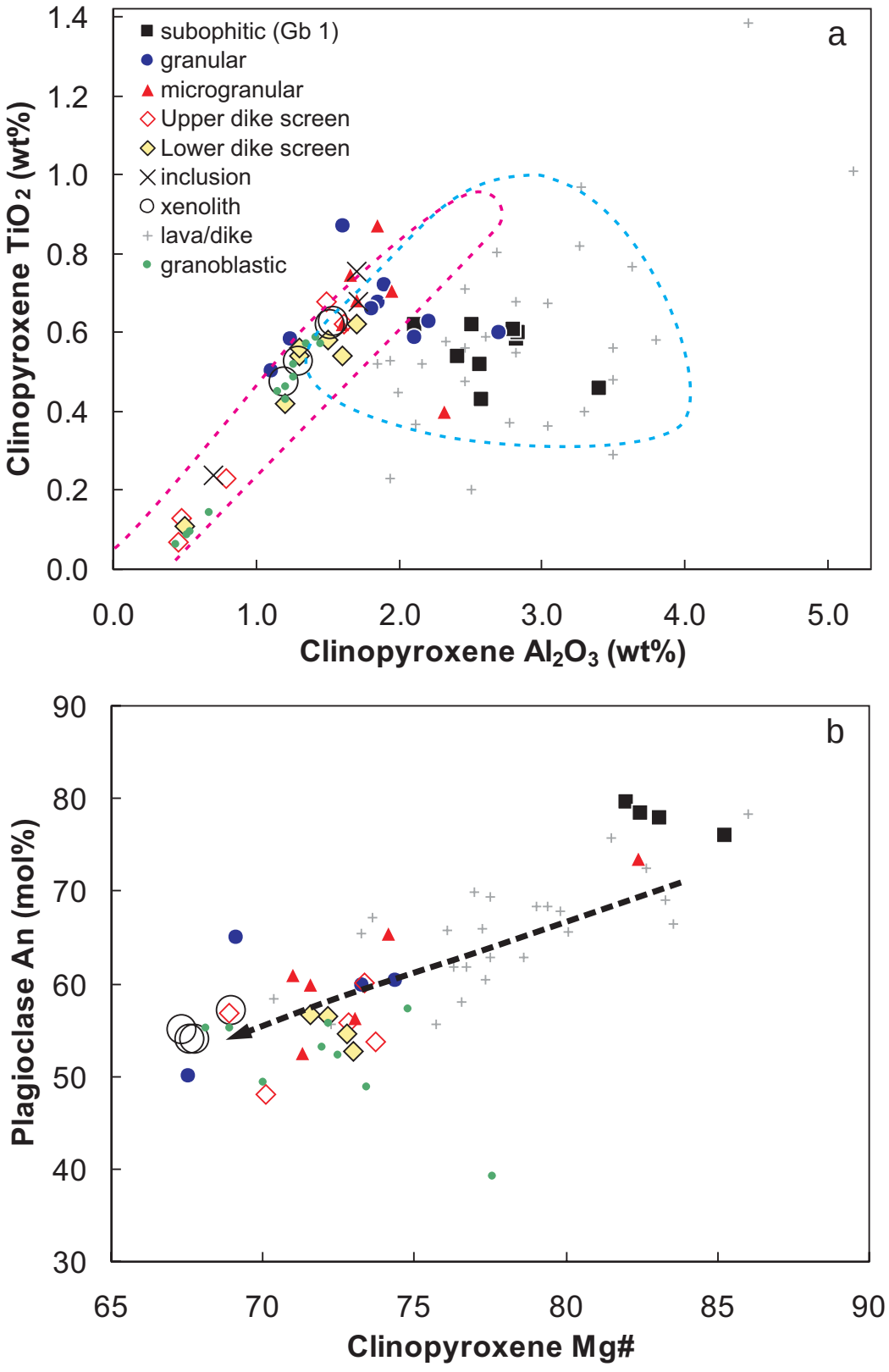

Fig. 5; Koepke et al.

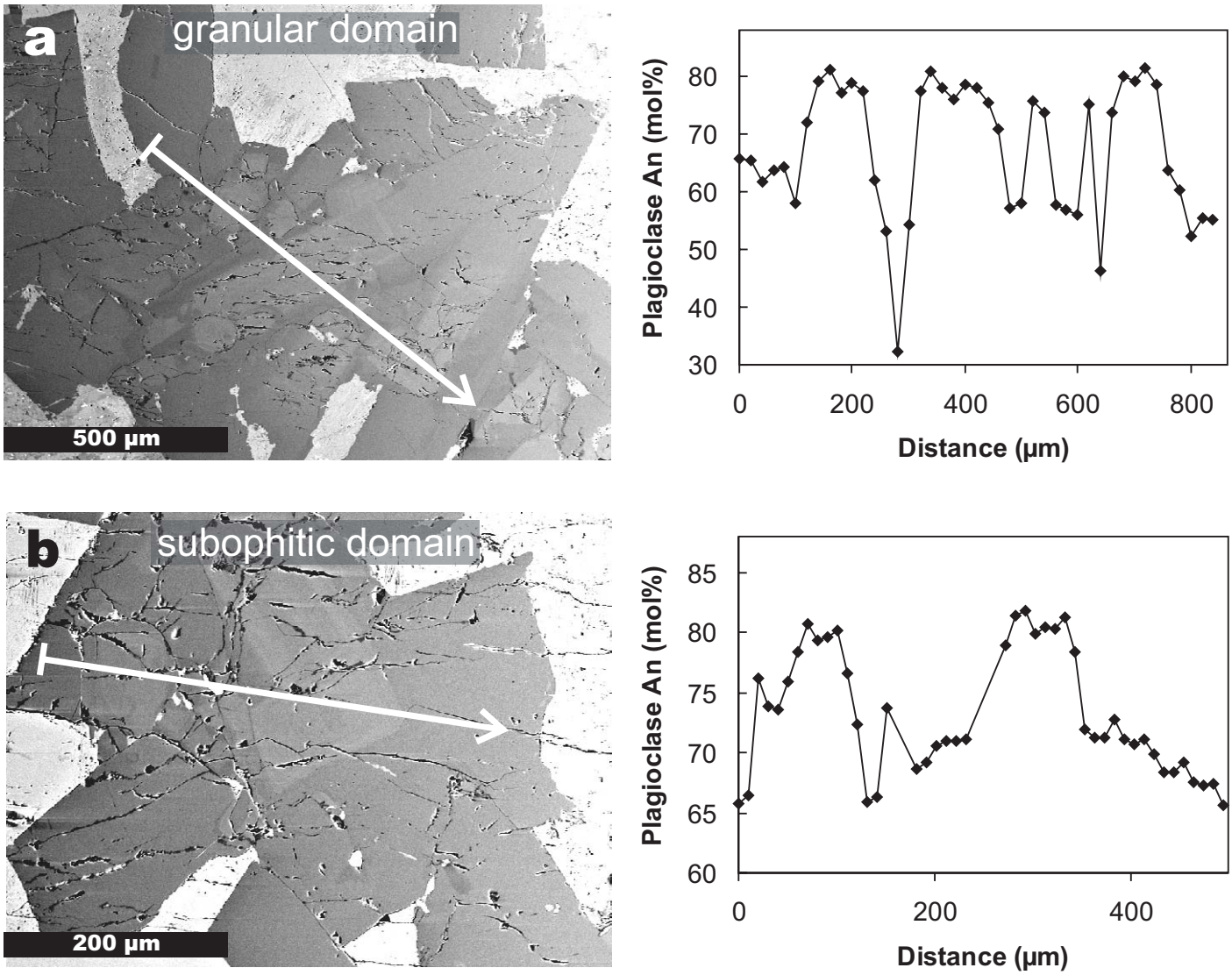

Fig. 6; Koepke et al.

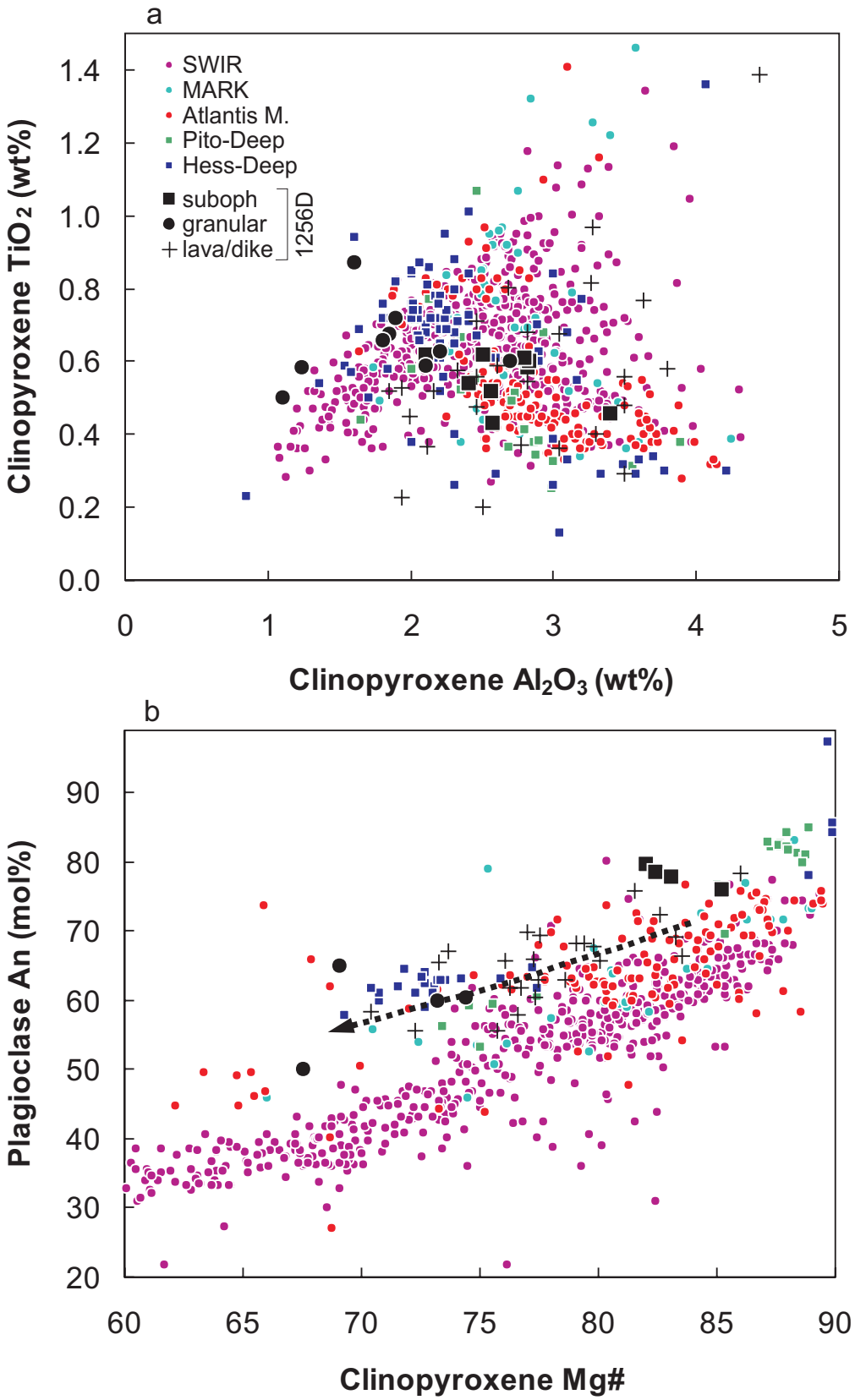

Fig. 7; Koepke et al.

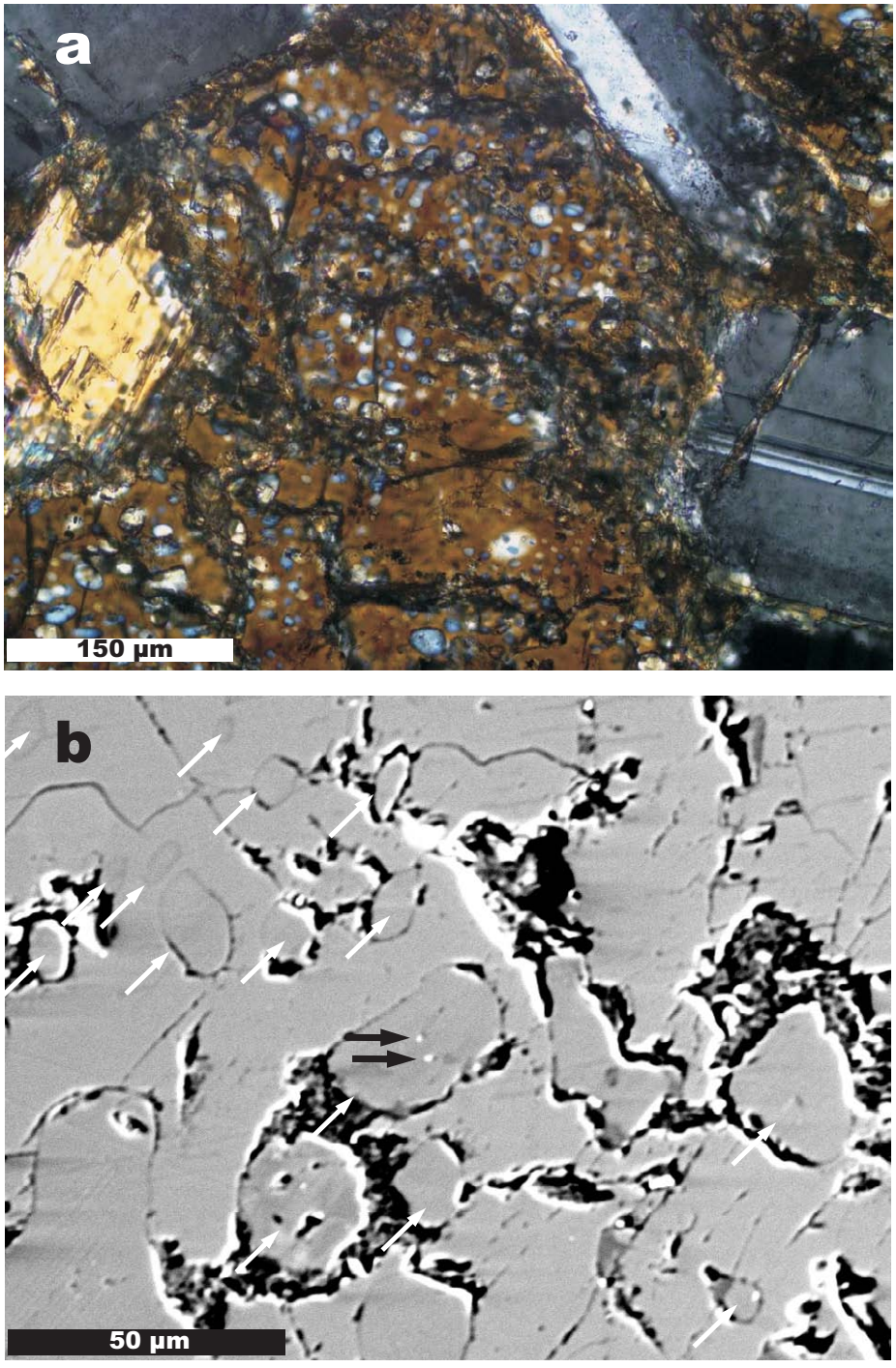

Fig. 8; Koepke et al.

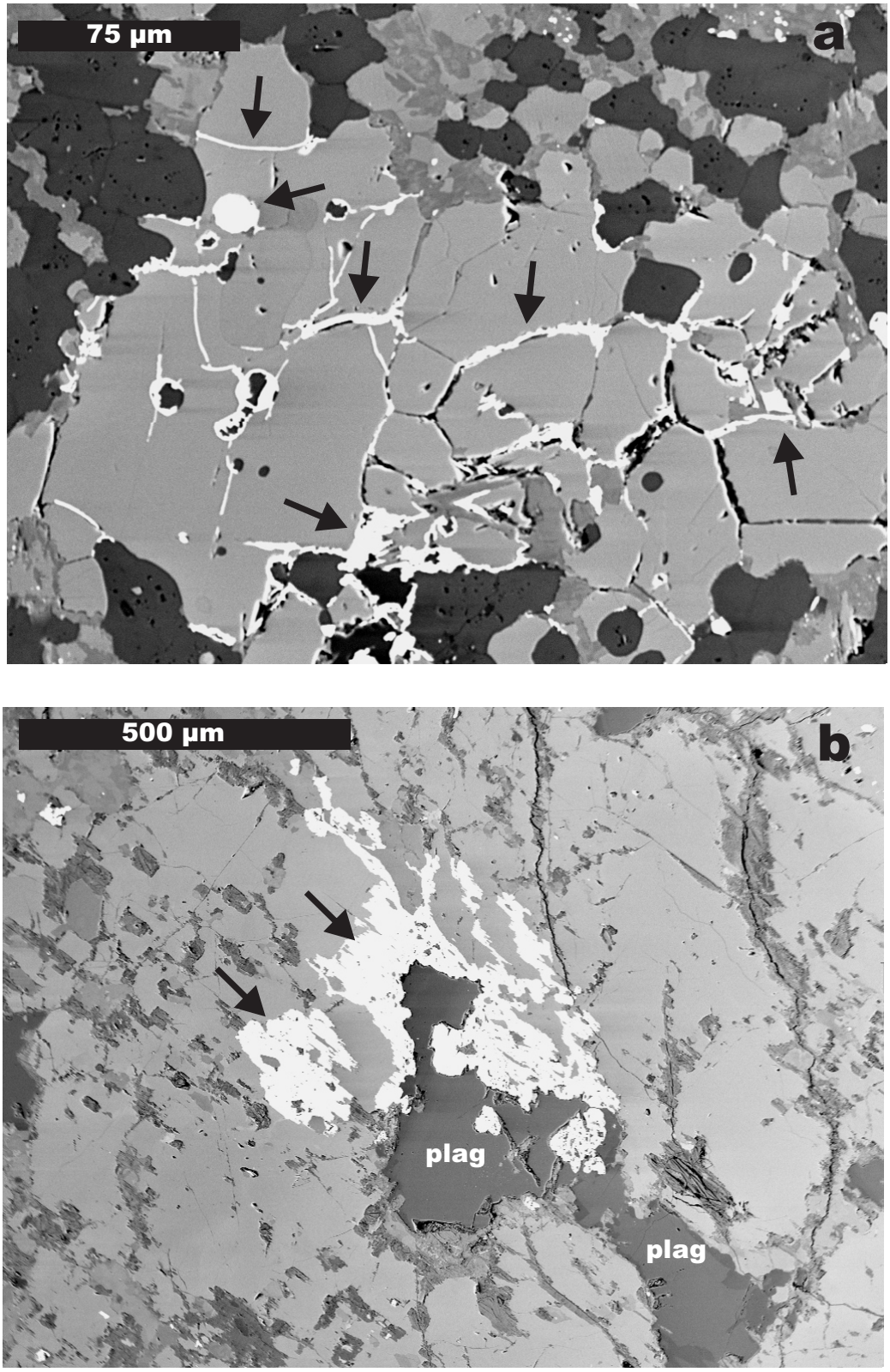

Fig. 9; Koepke et al.

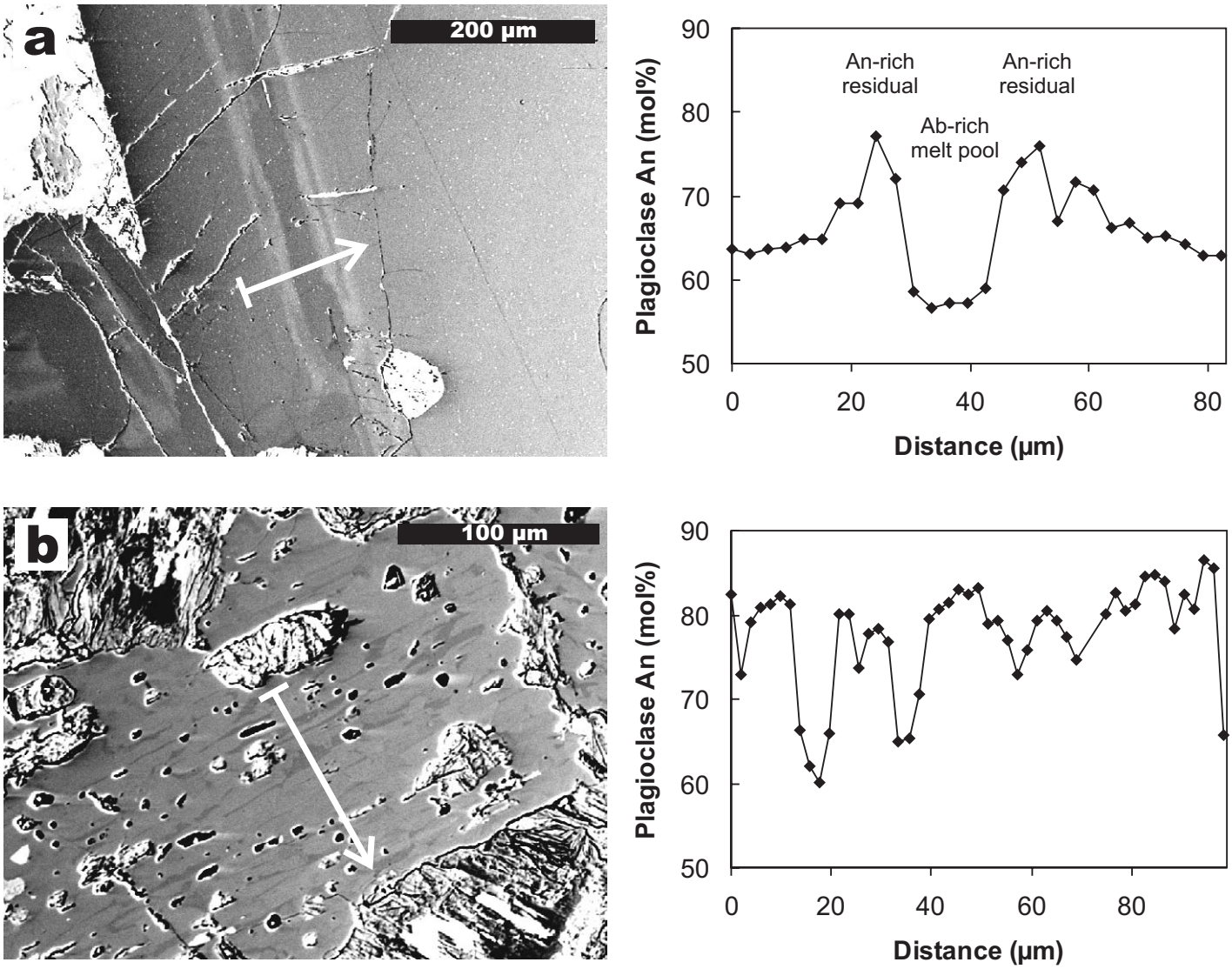

Fig. 10; Koepke et al.

Annex B.

Dataset

Annex B1: Mineral compositions (weight %) of rocks from the bottom of IODP Hole 1256D.

mbsf	*sample*	*min.*	*unit*	*thermometry*	*SiO_2*	*Al_2O_3*	*TiO_2*	*CaO*	*Na_2O*	*K2O*	*MnO*	*MgO*	*FeO*	*Cr_2O_3*	*NiO*	*P_2O_5*	*Total*	*n*	*Mg#*	*An%*
~300	**9R-2, 7-10**	Cpx	***pond***	914	52.65	1.85	0.52	18.51	0.27	-	0.25	17.18	8.96	-	-	-	100.33	*8*	77	-
~300	**9R-2, 7-10**	pig	***pond***	-	53.27	0.88	0.37	4.82	0.08	-	0.49	21.90	18.95	-	-	-	100.77	*17*	67	-
~300	**9R-2, 7-10**	Pl	***pond***	-	53.21	28.78	-	12.48	4.50	0.05	-	0.16	0.75	-	-	-	99.93	*5*	-	60
~300	**9R-2, 7-10**	Ilm	***pond***	-	-	0.04	49.36	-	-	-	0.54	0.43	47.90	-	-	-	98.35	*10*	-	-
~300	**9R-2, 7-10**	Ti-magt	***pond***	-	0.14	0.86	20.96	-	-	-	1.00	0.30	71.75	0.05	-	-	95.08	*21*	-	-
~700	**flow average**	Cpx	***flow***	1009	51.84	2.86	0.61	17.17	0.19	0.01	0.23	18.42	8.64	0.30	-	-	100.19	*12*	79	-
~700	**flow average**	pig	***flow***	-	54.69	0.87	0.19	4.82	0.06	-	0.34	26.89	12.80	-	-	-	100.72	*4*	79	-
~700	**flow average**	Pl	***flow***	-	52.08	29.16	-	13.38	3.95	0.06	-	0.24	0.85	-	-	-	99.71	*12*	-	65
~700	**flow average**	Ti-magt	***flow***	-	0.23	1.99	21.50	0.11	-	-	1.21	0.29	69.30	-	-	-	94.57	*10*	-	-
~1100	**dike average**	Cpx	***dike***	969	51.20	2.43	0.68	17.33	0.22	-	0.28	16.75	11.03	-	-	-	100.01	*3*	73	-
~1100	**dike average**	Pl	***dike***	-	53.54	28.19	-	12.09	4.70	0.05	-	0.14	0.87	-	-	-	99.58	*3*	-	59
~1100	**dike average**	Ti-magt	***dike***	-	0.63	1.39	23.04	0.51	-	-	1.44	0.11	66.27	-	-	-	93.43	*3*	-	-
1373	**202R-1_8-10**	Amp	***zone 2***	Tmax=592	52.64	2.42	0.34	9.61	0.35	0.00	0.47	15.51	16.40	0.01	0.01	0.03	97.81	*4*	65	-
1373	**202R-1_8-10**	Pl	***zone 2***	604	54.31	28.52	0.06	11.46	5.04	0.00	0.00	0.05	0.88	0.00	0.00	0.02	100.41	*5*	-	56
1373	**202R-1_8-10**	Cpx	***zone 2***	856	51.63	1.22	0.52	19.19	0.24	0.00	0.41	13.54	13.31	0.02	0.01	0.04	100.14	*3*	64	-
1373	**202R-1_8-10**	Opx	***zone 2***	1010+-24	52.53	0.59	0.32	1.88	0.02	0.00	0.69	19.73	24.86	0.00	0.00	0.01	100.63	*2*	59	-
1373	**202R-1_8-10**	Ilm	***zone 2***	-	0.48	0.10	42.48	0.56	0.00	0.00	1.48	0.06	51.87	0.09	0.01	0.02	97.16	*4*	-	-
1373	**202R-1_8-10**	Ti-magt	***zone 2***	-	0.33	0.86	10.85	0.64	0.02	0.00	0.30	0.83	77.71	0.18	0.01	0.02	91.76	*1*	-	-
1373	**202R-1_8-10**	magt	***zone 2***	-	0.98	0.65	1.52	0.61	0.07	0.00	0.10	0.11	87.80	0.32	0.01	0.00	92.20	*2*	-	-
1375	**203R-1_0-2**	Amp	***zone 2***	Tmax=589	52.09	2.70	0.38	10.95	0.39	0.04	0.30	15.20	13.41	0.02	0.02	0.06	95.56	*3*	69	-
1375	**203R-1_0-2**	Pl	***zone 2***	660	52.65	29.02	0.05	11.85	4.89	0.07	0.02	0.05	0.82	-	-	0.05	99.48	*2*	-	57
1375	**203R-1_0-2**	Cpx	***zone 2***	872	50.64	1.39	0.53	19.34	0.26	0.01	0.33	13.63	11.17	0.03	0.02	0.06	97.40	*2*	68	-
1375	**203R-1_0-2**	Ilm	***zone 2***	-	2.04	0.12	45.55	0.36	0.04	0.00	1.60	0.19	45.76	0.02	-	0.00	95.68	*1*	-	-
1375	**203R-1_0-2**	magt	***zone 2***	-	0.33	0.66	1.48	0.28	0.03	-	0.02	0.01	85.33	0.32	0.01	0.06	88.53	*1*	-	-
1396.5	**209R-1_4-7**	Amp	***zone 2***	Tmax=552	52.55	2.22	0.31	10.83	0.31	0.03	0.33	16.74	11.32	0.01	0.01	0.02	94.69	*2*	74	-
1396.5	**209R-1_4-7**	Pl	***zone 2***	538	52.57	28.69	0.06	11.45	5.07	0.05	0.00	0.06	0.76	0.00	-	0.02	98.74	*7*	-	56
1396.5	**209R-1_4-7**	Cpx	***zone 2***	852	50.91	1.18	0.42	20.33	0.28	0.00	0.37	14.13	9.45	0.01	-	0.04	97.11	*3*	73	-
1396.5	**209R-1_4-7**	Opx	***zone 2***	1011+-48	51.99	0.65	0.27	2.02	0.02	0.00	0.73	21.59	20.48	-	0.00	-0.03	97.76	*2*	65	-

mbsf	*sample*	*min.*	*unit*	*thermometry*	*SiO_2*	*Al_2O_3*	*TiO_2*	*CaO*	*Na_2O*	*K2O*	*MnO*	*MgO*	*FeO*	*Cr_2O_3*	*NiO*	*P_2O_5*	*Total*	*n*	*Mg#*	*An%*
1411	**214R-1_43-47**	Pl	***diorite***	618	55.32	27.09	0.05	10.03	5.93	0.00	0.01	0.06	0.60	0.01	0.00	0.04	99.22	*9*	-	48
1411	**214R-1_43-47**	Ilm	***diorite***	-	0.08	0.02	49.99	0.01	0.00	0.00	1.76	0.23	46.85	0.01	0.00	0.01	98.98	*3*	-	-
1411	**214R-1_43-47**	magt	***diorite***	-	0.66	0.50	1.58	0.13	0.00	0.00	0.07	0.21	90.19	0.04	0.02	0.03	93.43	*2*	-	-
1411	**214R-1_43-47**	Qz	***diorite***	-	99.01	0.06	0.07	0.01	0.01	0.00	0.00	0.00	0.01	0.00	0.00	0.00	99.17	*3*	-	-
1411	**214R-1_43-47**	Amp	***diorite***	Tmax=651	52.86	1.66	0.28	12.05	0.39	0.00	0.23	13.71	16.52	0.00	0.01	0.02	97.75	*9*	61	-
1416	**215R-1_20-23**	Amp	***zone 3 (white patches)***	Tmax=599	52.76	2.04	0.40	11.47	0.45	0.00	0.21	14.84	15.19	0.00	0.04	0.05	97.48	*3*	65	-
1416	**215R-1_20-23**	Pl	***zone 3 (white patches)***	632	57.03	26.69	0.06	8.90	6.60	0.00	0.01	0.03	0.44	0.01	0.01	0.04	99.93	*7*	-	43
1416	**215R-1_20-23**	Prehnite	***zone 3 (white patches)***	-	41.12	29.08	0.09	22.00	0.78	0.00	0.03	0.15	1.82	0.01	0.01	0.05	95.13	*1*	-	-
1416	**215R-1_20-23**	Pumpellyite	***zone 3 (white patches)***	-	37.43	24.91	0.07	22.88	0.03	0.00	0.09	1.06	7.42	0.02	0.00	0.12	94.03	*4*	-	-
1416	**215R-1_20-23**	Chlo	***zone 3 (gabbro)***	-	41.91	10.04	0.02	3.32	0.07	0.00	0.07	15.29	15.96	0.01	0.12	0.04	86.88	*7*	63	-
1416	**215R-1_20-23**	Ilm	***zone 3 (gabbro)***	-	0.16	0.04	48.59	0.01	0.00	0.00	1.20	0.08	49.60	0.01	0.02	0.01	99.72	*3*	-	-
1416	**215R-1_20-23**	magt	***zone 3 (gabbro)***	-	1.77	1.34	2.64	0.49	0.01	0.00	0.09	0.66	84.81	0.04	0.03	0.10	91.97	*3*	-	-
1416	**215R-1_20-23**	Pl	***zone 3 (gabbro)***	-	50.51	30.87	0.06	14.28	3.58	0.00	0.01	0.07	0.52	0.00	0.01	0.02	99.98	*20*	-	69
1416	**215R-1_20-23**	Cpx	***zone 3 (gabbro)***	970	51.73	2.44	0.59	19.95	0.24	0.00	0.22	16.30	8.03	0.30	0.02	0.05	99.89	*22*	78	-
1430.4	**219R-1_38-41**	Pl	***zone 4 (coarse-grained)***	-	51.78	30.18	0.05	13.37	3.93	0.05	0.00	0.07	0.62	0.00	0.01	-	100.06	*6*	-	65
1430.4	**219R-1_38-41**	Cpx	***zone 4 (coarse-grained)***	921	53.45	1.92	0.40	19.61	0.21	0.00	0.19	17.34	6.48	0.18	0.02	-	99.80	*5*	83	-
1430.4	**219R-1_38-41**	Ol	***zone 4 (fine-grained)***	-	37.32	0.00	0.02	0.11	0.01	0.00	0.47	31.00	31.66	0.00	0.07	-	100.67	*3*	64	-
1430.4	**219R-1_38-41**	Pl	***zone 4 (fine-grained)***	-	50.93	30.86	0.03	14.26	3.35	0.06	0.00	0.05	0.57	0.00	0.00	-	100.12	*1*	-	70
1430.4	**219R-1_38-41**	Cpx	***zone 4 (fine-grained)***	871	51.91	1.39	0.65	19.19	0.23	0.00	0.30	14.67	10.69	0.01	0.01	-	99.05	*1*	71	-
1430.4	**219R-1_38-41**	Opx	***zone 4 (fine-grained)***	1051+-24	53.78	0.83	0.42	1.96	0.02	0.00	0.47	22.53	20.39	0.00	0.04	-	100.44	*2*	66	-
1430.4	**219R-1_38-41**	Serp	***zone 4 (fine-grained)***	-	52.51	0.01	0.02	0.54	0.08	0.05	0.05	24.88	12.97	0.01	0.10	-	91.20	*2*	77	-

mbsf	*sample*	*min.*	*unit*	*thermometry*	*SiO_2*	*Al_2O_3*	*TiO_2*	*CaO*	*Na_2O*	*K2O*	*MnO*	*MgO*	*FeO*	*Cr_2O_3*	*NiO*	*P_2O_5*	*Total*	*n*	*Mg#*	*An%*
1451.4	**223R-2_50-53**	Pl	***zone 4 (coarse-grained)***	-	51.04	30.71	0.05	13.89	3.59	0.04	0.00	0.05	0.65	0.01	0.00	-	100.03	*9*	-	68
1451.4	**223R-2_50-53**	Cpx	***zone 4 (coarse-grained)***	935	52.96	2.08	0.43	20.87	0.23	0.00	0.21	16.39	6.13	0.26	0.02	-	99.58	*10*	83	-
1453	**223R-3_5-7**	Amp	***zone 4 (coarse-grained)***	**Tmax=553**	53.07	2.81	0.33	11.31	0.60	0.00	0.15	15.55	14.36	0.00	0.05	0.04	98.31	*2*	69	-
1453	**223R-3_5-7**	Ilm	***zone 4 (coarse-grained)***	**-**	0.13	0.01	48.12	0.00	0.00	0.00	0.89	0.37	49.94	0.06	0.00	0.01	99.53	*1*	-	-
1453	**223R-3_5-7**	Pl	***zone 4 (coarse-grained)***	688	52.81	29.27	0.08	12.41	4.62	0.00	0.01	0.14	0.79	0.01	0.01	0.03	100.20	*7*	-	60
1453	**223R-3_5-7**	Cpx	***zone 4 (coarse-grained)***	926	52.03	1.97	0.63	19.54	0.26	0.00	0.23	16.65	8.47	0.13	0.02	0.04	99.97	*4*	78	-
1453	**223R-3_5-7**	Opx	***zone 4 (coarse-grained)***	1055+-68	53.61	1.03	0.49	2.10	0.04	0.00	0.41	24.72	18.32	0.02	0.02	0.00	100.77	*3*	71	-
1453	**223R-3_5-7**	Ol	***zone 4 (fine-grained)***	-	37.14	0.01	0.03	0.07	0.00	0.00	0.42	32.35	31.60	0.01	0.12	0.06	101.82	*2*	65	-
1453	**223R-3_5-7**	Pl	***zone 4 (fine-grained)***	-	50.90	30.43	0.07	13.65	3.88	0.00	0.01	0.08	0.63	0.01	0.01	0.05	99.76	*6*	-	66
1453	**223R-3_5-7**	Cpx	***zone 4 (fine-grained)***	929	51.37	2.00	0.78	19.75	0.31	0.00	0.26	15.09	10.17	0.16	0.02	0.06	99.98	*9*	73	-
1454.4	**224R-1_7-9**	Amp	***diorite (contact zone 4/5)***	Tmax=726	50.80	2.76	0.53	11.54	0.61	0.00	0.28	12.88	18.67	0.01	0.07	0.03	98.26	*6*	56	-
1454.4	**224R-1_7-9**	Pl	***diorite (contact zone 4/5)***	756	57.23	26.31	0.07	8.62	6.78	0.00	0.00	0.09	0.68	0.01	0.01	0.03	99.89	*8*	-	41
1454.4	**224R-1_7-9**	Cpx	***diorite (contact zone 4/5)***	845	52.24	1.10	0.39	20.98	0.27	0.00	0.35	14.09	10.85	0.00	0.01	0.05	100.33	*7*	70	-
1454.4	**224R-1_7-9**	Pl?	***diorite (contact zone 4/5)***	-	41.48	24.18	0.07	9.72	4.81	0.00	0.00	0.07	0.66	0.01	0.01	0.09	81.15	*10*	-	-
1454.4	**224R-1_7-9**	Apat.	***diorite (contact zone 4/5)***	-	0.51	0.01	0.02	51.10	0.01	0.00	0.04	0.00	0.14	0.00	0.01	38.5	90.34	*2*	-	-
1454.4	**224R-1_7-9**	Ilm	***diorite (contact zone 4/5)***	-	0.25	0.07	47.34	0.10	0.00	0.00	1.71	0.12	49.25	0.02	0.01	0.00	98.89	*2*	-	-

mbsf	*sample*	*min.*	*unit*	*thermometry*	*SiO_2*	*Al_2O_3*	*TiO_2*	*CaO*	*Na_2O*	*K2O*	*MnO*	*MgO*	*FeO*	*Cr_2O_3*	*NiO*	*P_2O_5*	*Total*	*n*	*Mg#*	*An%*
1454.4	**224R-1_7-9**	magt	***diorite (contact zone 4/5)***	-	0.66	4.12	5.99	0.01	0.00	0.00	0.20	0.63	79.93	0.08	0.03	0.00	91.66	*1*	-	-
1454.4	**224R-1_7-9**	Qz	***diorite (contact zone 4/5)***	-	99.57	0.03	0.05	0.01	0.00	0.00	0.01	0.01	0.02	0.00	0.01	0.01	99.72	*3*	-	-
1459	**225R-1_4-8**	Amp	***zone 5 (top)***	Tmax=887	51.05	4.17	1.10	11.27	0.90	0.00	0.22	16.22	12.88	0.07	0.02	0.03	98.07	*16*	72	-
1459	**225R-1_4-8**	Ilm	***zone 5 (top)***	-	0.18	0.02	46.57	0.26	0.01	0.00	1.47	0.13	49.93	0.16	0.01	0.01	98.75	*4*	-	-
1459	**225R-1_4-8**	magt	***zone 5 (top)***	-	0.24	1.18	2.63	0.19	0.01	0.00	0.16	0.15	86.62	1.38	0.04	0.02	92.62	*4*	-	-
1459	**225R-1_4-8**	Pl	***zone 5 (top)***	742	52.51	29.69	0.07	12.71	4.38	0.00	0.01	0.05	0.74	0.01	0.01	0.04	100.26	*11*	-	62
1459	**225R-1_4-8**	Cpx	***zone 5 (top)***	816	53.13	0.79	0.23	22.26	0.24	0.00	0.29	14.26	9.26	0.07	0.00	0.04	100.58	*3*	73	-
1459	**225R-1_4-8**	Opx	***zone 5 (top)***	973+-77	52.88	0.87	0.39	2.00	0.03	0.00	0.46	22.55	21.36	0.03	0.01	0.01	100.60	*5*	65	-
1463.9	**226R-1_4-6**	Amp	***zone 5***	Tmax=823	53.73	4.12	1.11	10.69	1.06	0.05	0.17	16.95	11.22	0.01	0.01	-	99.12	*2*	76	-
1463.9	**226R-1_4-6**	Pl	***zone 5***	724	54.11	28.65	0.07	11.60	4.93	0.03	0.02	0.23	1.03	0.00	0.00	-	100.69	*16*	-	57
1463.9	**226R-1_4-6**	Cpx	***zone 5***	892	52.56	1.62	0.62	19.67	0.37	0.00	0.28	13.96	11.22	0.02	0.02	-	100.34	*4*	69	-
1463.9	**226R-1_4-6**	Opx	***zone 5***	1019+-34	53.50	0.79	0.37	1.87	0.03	0.00	0.53	20.90	22.38	0.01	0.02	-	100.41	*4*	62	-
1463.9	**226R-1_4-6**	Apat.	***zone 5***	-	11.47	0.49	0.06	44.94	0.07	0.01	0.13	2.96	2.84	0.01	0.01	-	62.99	*2*	-	-
1463.9	**226R-1_4-6**	magt	***zone 5***	-	0.74	0.57	0.86	0.22	0.00	0.00	0.10	0.33	87.60	0.44	0.05	-	90.91	*1*	-	-
1469	**227R-1_30-34**	Amp	***zone 5***	Tmax=632	52.70	2.59	0.50	11.32	0.51	0.00	0.24	16.21	13.36	0.02	0.02	0.01	97.52	*2*	71	-
1469	**227R-1_30-34**	Ilm	***zone 5***	-	0.15	0.00	47.84	0.22	0.00	0.00	1.45	0.12	48.86	0.03	0.02	0.01	98.71	*1*	-	-
1469	**227R-1_30-34**	Pl	***zone 5***	665	55.55	27.55	0.05	9.98	5.96	0.00	0.01	0.04	0.70	0.00	0.01	0.03	99.94	*3*	-	48
1469	**227R-1_30-34**	Cpx	***zone 5***	784	52.43	0.46	0.07	22.14	0.17	0.00	0.31	13.61	10.35	0.01	0.00	0.03	99.57	*2*	70	-
1469	**227R-1_30-34**	Opx	***zone 5***	956+-77	52.11	0.86	0.40	2.11	0.01	0.00	0.52	21.40	22.59	0.01	0.01	0.02	100.06	*3*	63	-
1469	**227R-1_30-34**	Qz	***zone 5***	-	99.11	0.03	0.11	0.04	0.00	0.00	0.00	0.00	0.36	0.00	0.00	0.00	99.65	*1*	-	-
1483.2	**230R-1_15-20**	Ilm	***zone 6 (xenolith)***	-	0.11	0.01	46.13	0.06	0.01	0.00	2.59	0.07	50.28	0.08	0.01	0.01	99.37	*2*	-	-
1483.2	**230R-1_15-20**	magt	***zone 6 (xenolith)***	-	0.16	1.01	3.03	0.10	0.00	0.00	0.12	0.18	87.39	0.64	0.03	0.03	92.69	*3*	-	-
1483.2	**230R-1_15-20**	Pl	***zone 6 (xenolith)***	-	53.87	28.67	0.07	11.25	5.27	0.00	0.01	0.02	0.71	0.01	0.00	0.05	99.98	*5*	-	54
1483.2	**230R-1_15-20**	Cpx	***zone 6 (xenolith)***	883	51.58	1.51	0.62	20.27	0.33	0.00	0.26	13.93	11.83	0.04	0.00	0.10	100.48	*1*	68	-
1483.2	**230R-1_15-20**	Opx	***zone 6 (xenolith)***	1017+-30	52.27	0.86	0.41	1.90	0.02	0.00	0.53	20.69	23.68	0.02	0.01	0.01	100.41	*5*	61	-
1483.7	**230R-1_73-80**	Amp	***zone 6 (xenolith)***	Tmax=713	49.66	5.28	1.16	11.37	1.37	0.00	0.20	15.55	12.92	0.04	0.02	0.04	97.71	*2*	74	-
1483.7	**230R-1_73-80**	Ilm	***zone 6 (xenolith)***	-	0.16	0.05	46.15	0.05	0.00	0.00	1.30	0.03	50.83	0.05	0.02	0.03	98.69	*2*	-	-

mbsf	*sample*	*min.*	*unit*	*thermometry*	*SiO_2*	*Al_2O_3*	*TiO_2*	*CaO*	*Na_2O*	*K2O*	*MnO*	*MgO*	*FeO*	*Cr_2O_3*	*NiO*	*P_2O_5*	*Total*	*n*	*Mg#*	*An%*
1483.7	**230R-1_73-80**	magt	***zone 6 (xenolith)***	-	4.44	0.81	2.52	1.96	0.03	0.00	0.20	1.29	82.68	0.26	0.04	0.01	94.24	*5*	-	-
1483.7	**230R-1_73-80**	Pl	***zone 6 (xenolith)***	769	53.80	28.84	0.07	11.38	5.13	0.00	0.01	0.02	0.63	0.00	0.01	0.03	99.96	*10*	-	55
1483.7	**230R-1_73-80**	Cpx	***zone 6 (xenolith)***	862	51.67	1.29	0.53	20.10	0.31	0.00	0.33	13.71	11.88	0.02	0.01	0.04	99.90	*5*	67	-
1483.7	**230R-1_73-80**	Opx	***zone 6 (xenolith)***	1030+-35	52.34	0.75	0.36	1.89	0.02	0.00	0.50	21.08	22.90	0.02	0.02	0.01	99.89	*5*	62	-
1483.9	**230R-1_87-90**	Amp	***zone 6 (xenolith)***	Tmax=704	49.77	7.96	1.14	11.16	1.67	0.00	0.16	14.78	13.26	0.01	0.05	0.05	100.23	*1*	76	-
1483.9	**230R-1_87-90**	Ilm	***zone 6 (xenolith)***	-	0.10	0.06	46.43	0.06	0.00	0.00	1.11	0.14	50.84	0.04	0.01	0.00	98.80	*3*	-	-
1483.9	**230R-1_87-90**	magt	***zone 6 (xenolith)***	-	0.15	1.43	3.35	0.02	0.00	0.00	0.15	0.29	87.64	0.28	0.02	0.01	93.33	*2*	-	-
1483.9	**230R-1_87-90**	Pl	***zone 6 (xenolith)***	753	54.00	28.60	0.08	11.23	5.28	0.02	0.01	0.02	0.59	0.01	0.00	0.04	99.92	*6*	-	54
1483.9	**230R-1_87-90**	Cpx	***zone 6 (xenolith)***	886	51.38	1.54	0.63	19.63	0.33	0.00	0.32	14.12	12.08	0.01	0.01	0.03	100.10	*6*	68	-
1483.9	**230R-1_87-90**	Opx	***zone 6 (xenolith)***	1028+-21	52.55	0.77	0.39	1.78	0.02	0.00	0.53	21.12	23.49	0.00	0.01	0.01	100.67	*4*	62	-
1484.2	**230R-1_118-121**	Pl	***zone 6 (gabbro)***	-	53.65	28.04	0.08	11.34	5.07	0.05	0.01	0.18	0.82	0.00	0.00	-	99.23	*4*	-	55
1484.2	**230R-1_118-121**	Cpx	***zone 6 (gabbro)***	819	52.09	0.82	0.42	21.08	0.45	0.00	0.29	14.28	10.41	0.03	0.01	-	99.87	*5*	71	-
1485.2	**230R-2_71-73**	Pl	***zone 6 (gabbro)***	714	51.91	29.28	0.07	12.57	4.36	0.07	0.00	0.10	0.67	0.01	0.01	-	99.05	*12*	-	61
1485.2	**230R-2_71-73**	Cpx	***zone 6 (gabbro)***	925	51.18	1.96	0.73	19.08	0.30	0.00	0.27	15.38	10.46	0.06	0.01	-	99.43	*9*	72	-
1485.2	**230R-2_71-73**	Opx	***zone 6 (gabbro)***	1065+-20	52.85	0.91	0.51	1.88	0.02	0.00	0.43	23.72	20.14	0.02	0.02	-	100.50	*2*	68	-
1485.2	**230R-2_71-73**	Amp	***zone 6 (gabbro)***	Tmax=652	50.93	4.03	0.79	11.04	0.86	0.08	0.23	15.46	13.94	0.03	0.02	-	97.41	*2*	70	-
1485.2	**230R-2_71-73**	Ilm	***zone 6 (gabbro)***	-	0.18	0.04	46.14	0.03	0.00	0.00	1.53	0.09	50.66	0.11	0.00	-	98.80	*5*	-	-
1485.2	**230R-2_71-73**	Magt	***zone 6 (gabbro)***	-	0.20	1.14	3.51	0.01	0.01	0.00	0.19	0.16	87.36	1.16	0.02	-	93.76	*5*	-	-
1492	**231R-4_7-10**	Pl	***zone 6 (gabbro)***	707	51.12	29.88	0.05	13.23	4.07	0.03	0.01	0.14	0.72	0.00	0.00	-	99.25	*5*	-	64
1492	**231R-4_7-10**	Cpx	***zone 6 (gabbro)***	1011	51.54	2.89	0.45	20.14	0.26	0.00	0.18	16.47	7.12	0.69	0.03	-	99.77	*5*	80	-
1492	**231R-4_7-10**	Opx	***zone 6 (gabbro)***	1000+-121	52.59	0.92	0.49	2.03	0.03	0.01	0.46	22.93	20.77	0.02	0.01	-	100.25	*4*	66	-
1492	**231R-4_7-10**	Amp	***zone 6 (gabbro)***	Tmax=709	50.52	4.31	0.61	11.30	0.89	0.06	0.20	14.38	15.24	0.05	0.02	-	97.58	*6*	67	-
1493.7	**232R-1_82-85**	Ol	***zone 6 (xenolith)***	-	37.86	0.01	0.03	0.04	0.00	0.00	0.46	36.02	26.86	0.00	0.07	-	101.36	*2*	70	-

mbsf	*sample*	*min.*	*unit*	*thermometry*	*SiO_2*	*Al_2O_3*	*TiO_2*	*CaO*	*Na_2O*	*K2O*	*MnO*	*MgO*	*FeO*	*Cr_2O_3*	*NiO*	*P_2O_5*	*Total*	*n*	*Mg#*	*An%*
1493.7	**232R-1_82-85**	Pl_c	***zone 6 (xenolith)***	-	53.25	29.27	0.08	12.07	4.79	0.10	0.00	0.04	0.60	0.01	0.00	-	100.22	*3*	-	58
1493.7	**232R-1_82-85**	Pl_m	***zone 6 (xenolith)***	-	48.69	31.76	0.02	15.31	2.86	0.05	0.01	0.11	0.82	0.00	0.01	-	99.65	*5*	-	75
1493.7	**232R-1_82-85**	Opx	***zone 6 (xenolith)***	-	54.21	0.93	0.25	1.08	0.01	0.00	0.43	26.72	17.07	0.01	0.01	-	100.73	*10*	74	-
1493.7	**232R-1_82-85**	magt	***zone 6 (xenolith)***	-	0.25	2.30	0.89	0.03	0.02	0.00	0.19	0.54	89.22	0.02	0.06	-	93.53	*2*	-	-
1497.6	**233R-1_8-12**	Ilm	***zone 7***	-	0.16	0.05	47.64	0.03	-	-	0.95	0.16	47.85	0.00	0.01	-	96.84	*1*	-	-
1497.6	**233R-1_8-12**	magt	***zone 7***	-	0.49	1.61	4.00	0.22	0.05	-	0.15	0.33	83.60	0.15	0.01	0.01	90.63	*4*	-	-
1497.6	**233R-1_8-12**	Pl	***zone 7***	-	52.27	29.18	0.06	11.89	4.94	0.04	0.01	0.03	0.58	0.00	0.00	0.03	99.06	*21*	-	57
1497.6	**233R-1_8-12**	Cpx	***zone 7***	883	50.81	1.51	0.53	20.28	0.37	0.00	0.26	14.16	9.80	0.02	0.01	0.05	97.80	*8*	72	-
1497.6	**233R-1_8-12**	Opx	***zone 7***	956+-31	51.93	0.81	0.38	1.58	0.03	-	0.48	22.49	20.26	0.00	0.01	0.01	98.00	*3*	66	-
1497.64	**233R-1_14-18**	Ilm	***zone 7***	-	0.22	0.04	46.79	0.08	0.02	0.00	1.84	0.11	49.78	0.07	0.01	0.01	98.98	*3*	-	-
1497.64	**233R-1_14-18**	magt	***zone 7***	-	0.17	0.79	3.03	0.16	0.00	0.00	0.14	0.14	87.68	0.83	0.05	0.02	93.01	*5*	-	-
1497.64	**233R-1_14-18**	Pl	***zone 7***	-	53.44	29.16	0.05	11.84	5.00	0.00	0.00	0.02	0.57	0.01	0.01	0.03	100.15	*6*	-	57
1497.64	**233R-1_14-18**	Cpx	***zone 7***	854	52.10	1.20	0.42	21.24	0.30	0.00	0.28	14.38	10.21	0.02	0.00	0.04	100.18	*6*	72	-
1497.64	**233R-1_14-18**	Opx	***zone 7***	1003+-50	52.49	0.88	0.41	1.90	0.03	0.00	0.49	22.27	21.78	0.01	0.00	0.01	100.28	*3*	65	-
1502.6	**234R-1_10-13**	Pl	***zone 8 (off axis dolerite)***	-	55.90	27.15	0.09	10.25	5.65	0.00	0.01	0.11	0.91	0.01	0.01	0.07	100.23	*2*	-	50
1502.6	**234R-1_10-13**	Cpx	***zone 8 (off axis dolerite)***	986	49.93	2.61	1.03	17.83	0.29	0.00	0.32	13.10	14.99	0.02	0.01	0.04	100.19	*5*	61	-
1502.6	**234R-1_10-13**	Qz	***zone 8 (off axis dolerite)***	-	99.57	0.12	0.04	0.02	0.00	0.00	0.00	0.00	0.12	0.02	0.00	0.01	99.90	*1*	-	-

Mineral compositions for lava-pond, lava flow, and sheeted dike are averages calculated from Dziony et al. (2008). Abbreviations are: mbsf=meter below sea-floor; min=mineral; n=number of analyses; Mg#=Mg/(Mg+Fe) in moles; An%=Ca/(Ca+Na+K) in moles; -=not analyzed or below detection limit; Cpx=clinopyroxene; pig=pigeonite; Pl=plagioclase; Pl_m=plagioclase margin; Pl_c=plagioclase core; Ilm=ilmenite; Ti-magt=titanomagnetite; Amp=amphibole; Opx=orthopyroxene; magt=magnetite; Qz=quartz; Chlo=chlorite; Ol=olivine; Serp=serpentine; Apat.=apatite. Temperature estimations indicated for amphibole are from Ernst and Liu (1998); for plagioclase from Holland and Blundy (1994); for Opx from Andersen et al. (1993), and for Cpx from France et al. (2009b; see section IV).

Annex B2: Major element composition (weight %) of starting material (08OL30), and of the experimental products.

Sample	Phase	AVG / +/-	SiO_2	Al_2O_3	TiO_2	CaO	Na_2O	K_2O	MnO	MgO	FeO	Cr_2O_3	P_2O_5	Total	*n*	**Mg#**	**An%**	*T max*	*T AVG*
Start. mat.	Amp	AVG	52.46	2.47	0.31	11.70	0.42	0.05	0.22	13.82	16.01	0.00	-	97.47	*29*	62.28	-	-	550
-	-	+/-	*1.16*	*0.99*	*0.08*	*0.69*	*0.42*	*0.03*	*0.06*	*0.57*	*1.20*	*0.04*	-	*1.17*	-	-	-	-	*17*
Start. mat.	magt	AVG	0.67	0.28	0.96	0.20	0.03	0.00	0.02	0.08	88.45	0.06	-	90.77	*12*	-	-	-	-
-	-	+/-	*0.40*	*0.19*	*0.39*	*0.09*	*0.03*	*0.01*	*0.05*	*0.08*	*1.24*	*0.02*	-	*0.89*	-	-	-	-	-
Start. mat.	Pl	AVG	67.92	20.27	0.01	0.54	11.46	0.07	0.01	0.01	0.15	0.00	-	100.45	*16*	-	2.53	-	-
-	-	+/-	*0.76*	*0.44*	*0.02*	*0.28*	*0.31*	*0.07*	*0.03*	*0.02*	*0.10*	*0.03*	-	*0.66*	-	-	-	-	-
Start. mat.	Prehnite	AVG	43.48	23.64	0.00	27.09	0.12	0.01	0.05	0.00	0.11	0.01	-	94.52	*3*	-	-	-	-
-	-	+/-	*0.15*	*0.15*	*0.01*	*0.13*	*0.05*	*0.00*	*0.02*	*0.01*	*0.02*	*0.00*	-	*0.07*	-	-	-	-	-
Start. mat.	Pumpellyite	AVG	38.97	21.62	0.10	22.44	0.05	0.01	0.06	1.61	11.68	0.02	-	96.56	*6*	-	-	-	-
-	-	+/-	*2.12*	*2.95*	*0.07*	*1.55*	*0.05*	*0.01*	*0.08*	*2.06*	*0.49*	*0.02*	-	*0.50*	-	-	-	-	-
Start. mat.	sphene	AVG	30.61	1.12	36.66	28.34	0.02	0.01	0.01	0.22	1.79	0.02	-	98.83	*7*	-	-	-	-
-	-	+/-	*0.77*	*0.68*	*1.92*	*0.44*	*0.02*	*0.01*	*0.03*	*0.43*	*0.34*	*0.04*	-	*0.28*	-	-	-	-	-
-	-	-	-	-	-	-	-	-	-	-	-	-	-	-	-	-	-	-	-
1030	melt	AVG	53.48	16.62	1.48	7.49	4.90	0.20	0.05	3.52	8.62	0.00	-	96.39	*58*	42.2	-	-	-
-	-	+/-	*0.28*	*0.15*	*0.07*	*0.07*	*0.10*	*0.07*	*0.02*	*0.07*	*0.17*	*0.02*	-	*0.40*	-	-	-	-	-
1000	melt	AVG	55.15	16.60	1.20	5.50	5.58	0.25	0.06	2.58	6.30	-	-	93.22	*33*	42.2	-	-	-
-	-	+/-	*0.86*	*0.31*	*0.09*	*0.18*	*0.68*	*0.04*	*0.07*	*0.11*	*0.31*	-	-	*1.28*	-	-	-	-	-
970	melt	AVG	60.50	17.11	1.13	4.23	5.62	0.35	0.05	1.91	5.08	0.00	0.09	96.05	*38*	40.2	-	-	-
-	-	+/-	*0.61*	*0.27*	*0.07*	*0.17*	*0.74*	*0.07*	*0.03*	*0.09*	*0.25*	*0.10*	*0.03*	*0.76*	-	-	-	-	-
955	melt	AVG	60.18	16.51	0.97	3.58	5.39	0.41	0.04	1.56	4.66	0.01	0.10	93.51	*22*	37.3	-	-	-
-	-	+/-	*0.54*	*0.16*	*0.05*	*0.15*	*1.00*	*0.03*	*0.03*	*0.06*	*0.23*	*0.15*	*0.05*	*0.90*	-	-	-	-	-
940	melt	AVG	63.85	16.63	0.82	2.35	4.62	0.77	0.02	0.87	2.94	0.01	0.11	93.11	*94*	29.6	-	-	-
-	-	+/-	*2.11*	*1.03*	*0.40*	*1.23*	*1.62*	*0.26*	*0.07*	*0.92*	*1.35*	*0.20*	*0.04*	*1.74*	-	-	-	-	-
910	melt	AVG	66.05	16.54	0.47	2.15	5.21	1.11	0.02	0.62	2.79	0.12	0.06	95.32	*27*	28.5	-	-	-
-	-	+/-	*0.98*	*1.18*	*0.11*	*0.70*	*0.84*	*0.20*	*0.10*	*0.10*	*0.37*	*0.31*	*0.04*	*1.60*	-	-	-	-	-
880	melt	AVG	68.04	16.15	0.38	1.79	5.31	1.26	0.02	0.40	1.92	0.06	0.04	95.58	*27*	27.0	-	-	-
-	-	+/-	*1.68*	*1.16*	*0.08*	*0.62*	*0.71*	*0.23*	*0.07*	*0.12*	*0.48*	*0.37*	*0.04*	*1.70*	-		-	-	-
850	melt	AVG	68.76	15.66	0.28	1.23	4.66	2.09	0.00	0.24	1.54	0.08	0.02	94.67	*12*	22.0	-	-	-
-	-	+/-	*1.25*	*1.22*	*0.07*	*0.38*	*0.73*	*0.33*	*0.09*	*0.08*	*0.38*	*0.14*	*0.02*	*2.31*	-	-	-	-	-
1030	melt_recalc.	AVG	55.48	17.25	1.54	7.77	5.09	0.20	0.05	3.66	8.94	0.00	0.00	100.00	-	-	-	-	-
1000	melt_recalc.	AVG	59.16	17.80	1.29	5.90	5.98	0.27	0.07	2.77	6.76	0.00	0.00	100.00	-	-	-	-	-
970	melt_recalc.	AVG	62.99	17.81	1.18	4.40	5.85	0.37	0.05	1.99	5.29	0.00	0.09	100.00	-	-	-	-	-

Sample	Phase	AVG / +/-	SiO_2	Al_2O_3	TiO_2	CaO	Na_2O	K_2O	MnO	MgO	FeO	Cr_2O_3	P_2O_5	Total	*n*	**Mg#**	**An%**	*T max*	*T AVG*
955	melt_recalc.	AVG	64.36	17.66	1.03	3.83	5.76	0.44	0.04	1.67	4.99	0.02	0.11	100.00	-	-	-	-	-
940	melt_recalc.	AVG	68.58	17.86	0.88	2.53	4.96	0.83	0.02	0.93	3.16	0.01	0.12	100.00	-	-	-	-	-
910	melt_recalc.	AVG	69.29	17.35	0.49	2.25	5.46	1.16	0.02	0.65	2.93	0.13	0.06	100.00	-	-	-	-	-
880	melt_recalc.	AVG	71.19	16.90	0.40	1.88	5.56	1.32	0.02	0.42	2.01	0.06	0.04	100.00	-	-	-	-	-
850	melt_recalc.	AVG	72.63	16.54	0.29	1.30	4.92	2.21	0.00	0.25	1.62	0.08	0.02	100.00	-	-	-	-	-
-	-	-	-	-	-	-	-	-	-	-	-	-	-	-	-	-	-	-	-
1030	Ol	AVG	39.21	0.11	0.06	0.32	0.01	0.00	0.14	37.87	22.79	0.00	-	100.54	*40*	74.76	-	-	-
-	-	+/-	*0.40*	*0.36*	*0.06*	*0.28*	*0.03*	*0.02*	*0.01*	*0.78*	*0.63*	*0.01*	-	*0.37*	-	-	-	-	-
1000	Ol	AVG	38.40	0.17	0.04	0.29	0.04	0.01	0.17	38.68	23.21	-	-	101.01	*37*	74.80	-	-	-
-	-	+/-	*0.38*	*0.44*	*0.02*	*0.13*	*0.09*	*0.01*	*0.05*	*0.97*	*0.49*	-	-	*0.56*	-	-	-	-	-
970	Ol	AVG	38.44	0.09	0.04	0.30	0.02	0.00	0.21	36.63	24.25	0.00	-	99.98	*26*	72.91	-	-	-
-	-	+/-	*0.26*	*0.18*	*0.02*	*0.26*	*0.03*	*0.01*	*0.01*	*0.48*	*0.41*	*0.01*	-	*0.45*	-	-	-	-	-
955	Ol	AVG	37.39	0.05	0.04	0.25	0.03	0.01	0.22	33.34	27.95	0.02	-	99.34	*21*	68.01	-	-	-
-	-	+/-	*0.41*	*0.08*	*0.03*	*0.05*	*0.02*	*0.01*	*0.06*	*0.39*	*0.64*	*0.09*	-	*0.58*	-	-	-	-	-
940	Ol	AVG	38.64	0.44	0.05	0.46	0.09	0.01	0.23	32.99	27.41	0.00	-	100.34	*19*	68.21	-	-	-
-	-	+/-	*0.68*	*0.54*	*0.03*	*0.25*	*0.10*	*0.01*	*0.01*	*0.81*	*0.88*	*0.02*	-	*0.74*			-	-	-
1030	Cpx	AVG	51.92	2.98	0.70	21.37	0.39	0.00	0.08	15.26	7.77	0.01	-	100.50	*42*	77.77	-	-	-
-	-	+/-	*0.43*	*0.40*	*0.15*	*0.79*	*0.03*	*0.04*	*0.02*	*0.48*	*0.39*	*0.02*	-	*0.49*	-	-	-	-	-
1000	Cpx	AVG	51.18	2.93	0.65	20.90	0.44	0.01	0.11	15.78	8.16	0.03	-	100.17	*34*	77.52	-	-	-
-	-	+/-	*0.61*	*0.37*	*0.19*	*0.72*	*0.05*	*0.01*	*0.04*	*0.44*	*0.58*	*0.04*	-	*0.65*	-	-	-	-	-
970	Cpx	AVG	51.79	2.50	0.60	20.34	0.48	0.01	0.13	15.36	8.53	0.01	-	99.74	*30*	76.25	-	-	-
-	-	+/-	*0.36*	*0.23*	*0.11*	*0.75*	*0.07*	*0.01*	*0.02*	*0.36*	*0.41*	*0.01*	-	*0.47*	-	-	-	-	-
955	Cpx	AVG	51.92	2.17	0.58	19.90	0.48	0.01	0.14	15.07	9.16	0.00	-	99.46	*39*	74.56	-	-	-
-	-	+/-	*0.38*	*0.26*	*0.15*	*0.62*	*0.05*	*0.01*	*0.05*	*0.47*	*0.54*	*0.12*	-	*0.44*	-	-	-	-	-
940	Cpx	AVG	52.76	2.13	0.47	18.83	0.57	0.00	0.16	15.17	10.08	0.01	-	100.20	*25*	72.87	-	-	-
-	-	+/-	*0.55*	*0.49*	*0.13*	*0.85*	*0.09*	*0.06*	*0.02*	*0.52*	*0.89*	*0.01*	-	*0.51*	-	-	-	-	-
910	Cpx	AVG	52.54	1.73	0.41	18.86	0.53	0.02	0.16	14.61	11.11	0.00	-	99.99	*47*	70.14	-	-	-
-	-	+/-	*0.78*	*0.40*	*0.17*	*1.38*	*0.06*	*0.02*	*0.03*	*0.57*	*0.95*	*0.05*	-	*0.75*	-	-	-	-	-
880	Cpx	AVG	52.56	1.47	0.42	18.60	0.56	0.01	0.17	15.52	10.49	0.00	-	99.83	*1*	72.56	-	-	-
-	-	+/-	*0.74*	*0.31*	*0.12*	*1.55*	*0.09*	*0.03*	*0.04*	*0.70*	*1.17*	*0.05*	-	*0.94*	-	-	-	-	-
850	Cpx	AVG	51.42	1.26	0.37	18.22	0.47	0.02	0.16	14.17	13.01	0.00	-	99.13	*33*	66.08	-	-	-
-	-	+/-	*0.49*	*0.39*	*0.11*	*1.67*	*0.12*	*0.02*	*0.04*	*0.64*	*1.39*	*0.09*	-	*0.99*	-	-	-	-	-
850	Cpx_reaction	AVG	49.69	2.59	0.49	22.02	0.45	0.02	0.11	11.51	13.13	0.06	-	100.07	*5*	60.80	-	-	-
-	-	+/-	*1.47*	*0.47*	*0.13*	*1.32*	*0.19*	*0.01*	*0.03*	*1.49*	*1.62*	*0.10*	-	*0.23*	-	-	-	-	-
800	Cpx_reaction	AVG	50.81	1.94	0.47	21.14	0.27	0.00	0.12	12.12	13.19	0.05	-	100.10	*2*	62.09	-	-	-
-	-	+/-	*0.02*	*0.03*	*0.00*	*0.22*	*0.01*	*0.00*	*0.01*	*0.05*	*0.09*	*0.01*	-	*0.24*	-	-	-	-	-
750	Cpx_reaction	AVG	50.30	2.19	0.56	20.05	0.50	0.02	0.20	12.21	12.55	0.00	-	98.61	*17*	63.40	-	-	-
-	-	+/-	*0.94*	*0.76*	*0.44*	*1.81*	*0.17*	*0.03*	*0.12*	*0.88*	*0.86*	*0.09*	-	*0.74*	-	-	-	-	-

Sample	Phase	AVG / +/-	SiO_2	Al_2O_3	TiO_2	CaO	Na_2O	K_2O	MnO	MgO	FeO	Cr_2O_3	P_2O_5	Total	*n*	**Mg#**	**An%**	*T max*	*T AVG*
1000	Pl	AVG	52.87	28.92	0.06	12.15	4.59	0.03	0.00	0.12	0.94	-	-	99.69	*19*	-	59.38	-	-
-	-	+/-	*0.46*	*0.36*	*0.03*	*0.31*	*0.18*	*0.01*	*0.04*	*0.06*	*0.13*	-	-	*0.44*	-	-	-	-	-
970	Pl	AVG	55.34	27.78	0.08	10.54	5.62	0.04	0.00	0.10	0.79	-	-	100.31	*27*	-	50.92	-	-
-	-	+/-	*0.60*	*0.47*	*0.05*	*0.40*	*0.29*	*0.01*	*0.01*	*0.12*	*0.24*	-	-	*0.41*	-	-	-	-	-
955	Pl	AVG	56.51	27.03	0.05	9.69	5.94	0.04	0.00	0.05	0.59	-	-	99.96	*28*	-	47.43	-	-
-	-	+/-	*0.37*	*0.24*	*0.01*	*0.28*	*0.19*	*0.01*	*0.03*	*0.01*	*0.07*	-	-	*0.34*	-	-	-	-	-
940	Pl	AVG	58.76	25.88	0.06	8.20	6.97	0.05	0.00	0.06	0.66	-	-	100.66	*24*	-	39.37	-	-
-	-	+/-	*0.59*	*0.35*	*0.03*	*0.45*	*0.22*	*0.04*	*0.01*	*0.06*	*0.12*	-	-	*0.36*	-	-	-	-	-
910	Pl	AVG	60.98	24.28	0.05	6.46	7.81	0.16	0.00	0.05	0.67	-	-	100.48	*26*	-	31.41	-	-
-	-	+/-	*0.88*	*0.40*	*0.03*	*0.49*	*0.56*	*0.03*	*0.01*	*0.05*	*0.26*	-	-	*0.75*	-	-	-	-	-
880	Pl	AVG	61.37	23.92	0.06	5.86	7.92	0.17	0.01	0.03	0.55	-	-	99.91	*17*	-	29.10	-	-
-	-	+/-	*0.80*	*0.43*	*0.03*	*0.49*	*0.56*	*0.02*	*0.02*	*0.01*	*0.09*	-	-	*1.07*	-	-	-	-	-
850	Pl	AVG	61.48	23.76	0.04	5.21	8.35	0.30	0.00	0.02	0.41	-	-	99.62	*24*	-	25.66	-	-
-	-	+/-	*0.78*	*0.44*	*0.02*	*0.53*	*0.31*	*0.03*	*0.03*	*0.02*	*0.09*	-	-	*0.56*	-	-	-	-	-
800	Pl	AVG	60.02	24.49	0.02	6.35	7.62	0.22	0.01	-	0.35	-	-	99.12	*21*	-	31.54	-	-
-	-	+/-	*0.92*	*0.53*	*0.01*	*0.34*	*0.22*	*0.02*	*0.03*	-	*0.07*	-	-	*1.34*	-	-	-	-	-
750	Pl	AVG	60.87	24.00	0.02	5.57	8.22	0.27	0.00	0.02	0.35	-	-	99.35	*36*	-	27.22	-	-
-	-	+/-	*1.36*	*0.77*	*0.01*	*0.96*	*0.48*	*0.05*	*0.04*	*0.05*	*0.12*	-	-	*0.42*	-	-	-	-	-
1000	Pl_m	AVG	47.99	30.55	0.27	15.74	2.09	0.05	0.01	0.53	2.61	-	-	99.86	*3*	-	80.62	-	-
-	-	+/-	*0.22*	*0.66*	*0.05*	*0.44*	*0.17*	*0.01*	*0.05*	*0.08*	*0.43*	-	-	*0.86*	-	-	-	-	-
970	Pl_m	AVG	51.16	29.45	0.20	13.73	3.32	0.06	0.01	0.32	1.76	-	-	100.04	*18*	-	69.60	-	-
-	-	+/-	*2.06*	*1.73*	*0.15*	*1.59*	*0.91*	*0.03*	*0.01*	*0.25*	*0.83*	-	-	*0.79*	-	-	-	-	-
955	Pl_m	AVG	50.27	29.98	0.12	14.14	3.11	0.04	0.00	0.18	1.38	-	-	99.29	*10*	-	71.44	-	-
-	-	+/-	*2.55*	*1.46*	*0.06*	*1.81*	*0.89*	*0.02*	*0.03*	*0.07*	*0.42*	-	-	*0.59*	-	-	-	-	-
940	Pl_m	AVG	55.64	27.50	0.10	11.01	5.22	0.07	0.00	0.14	0.99	-	-	100.67	*8*	-	53.79	-	-
-	-	+/-	*1.16*	*1.08*	*0.09*	*0.89*	*0.32*	*0.03*	*0.01*	*0.08*	*0.28*	-	-	*0.79*	-	-	-	-	-
910	Pl_m	AVG	58.54	24.93	0.07	7.58	6.56	0.17	0.02	0.08	0.98	0.04	-	98.96	*3*	-	39.02	-	-
-	-	+/-	*0.50*	*0.41*	*0.03*	*0.26*	*0.40*	*0.06*	*0.00*	*0.03*	*0.52*	*0.05*	-	*0.72*	-	-	-	-	-
880	Pl_m	AVG	60.74	24.50	0.07	6.79	6.60	0.21	0.03	0.06	0.71	0.01	-	99.13	*2*	-	36.23	-	-
-	-	+/-	*0.89*	*0.27*	*0.02*	*0.32*	*1.28*	*0.04*	*0.01*	*0.02*	*0.09*	*0.01*	-	*0.76*	-	-	-	-	-
850	Pl_m	AVG	52.79	28.06	0.03	12.57	4.56	0.11	-	0.31	1.41	0.08	-	99.94	*2*	-	60.53	-	-
-	-	+/-	*2.34*	*1.55*	*0.01*	*1.47*	*1.05*	*0.03*	*0.01*	*0.17*	*0.42*	*0.01*	-	*0.16*	-	-	-	-	-
800	Pl_m	AVG	58.48	25.82	0.02	7.97	7.00	0.17	0.02	0.04	0.48	0.01	-	100.03	*11*	-	38.62	-	-
-	-	+/-	*0.93*	*0.52*	*0.01*	*0.68*	*0.31*	*0.01*	*0.01*	*0.09*	*0.19*	*0.06*	-	*0.68*	-	-	-	-	-
750	Pl_m	AVG	49.43	28.54	0.04	14.32	3.34	0.09	0.01	0.8	1.24	0.02	-	97.88	*11*	-	70.35	-	-
-	-	+/-	*2.65*	*4.00*	*0.05*	*1.96*	*1.13*	*0.03*	*0.02*	*1.36*	*1.24*	*0.10*	-	*0.87*	-	-	-	-	-

Sample	Phase	AVG / +/-	SiO_2	Al_2O_3	TiO_2	CaO	Na_2O	K_2O	MnO	MgO	FeO	Cr_2O_3	P_2O_5	Total	*n*	**Mg#**	**An%**	*T max*	*T AVG*
1000	TiMagt	AVG	0.32	4.21	10.42	0.18	0.02	0.00	0.15	4.39	75.38	-	-	95.08	*25*	-	-	-	-
-	-	+/-	*0.57*	*0.13*	*0.95*	*0.27*	*0.05*	*0.01*	*0.05*	*0.22*	*0.84*	-	-	*0.71*	-	-	-	-	-
970	TiMagt	AVG	0.33	3.61	11.98	0.15	0.01	0.00	0.17	3.89	74.47	0.06	-	94.69	*20*	-	-	-	-
-	-	+/-	*0.26*	*0.10*	*0.47*	*0.07*	*0.02*	*0.01*	*0.01*	*0.07*	*0.69*	*0.02*	-	*0.65*	-	-	-	-	-
955	TiMagt	AVG	0.11	3.07	13.75	0.11	0.04	0.00	0.18	3.40	73.52	0.04	-	94.25	*14*	-	-	-	-
-	-	+/-	*0.03*	*0.06*	*0.40*	*0.05*	*0.03*	*0.01*	*0.07*	*0.09*	*0.82*	*0.10*	-	*0.78*	-	-	-	-	-
940	TiMagt	AVG	0.53	2.80	11.01	0.24	0.04	0.00	0.17	3.02	76.58	0.04	-	94.45	*16*	-	-	-	-
-	-	+/-	*0.54*	*0.09*	*0.44*	*0.16*	*0.17*	*0.01*	*0.02*	*0.14*	*0.58*	*0.02*	-	*0.85*	-	-	-	-	-
910	TiMagt	AVG	1.57	2.13	11.21	0.63	0.03	0.01	0.16	2.53	76.81	0.04	-	95.11	*3*	-	-	-	-
-	-	+/-	*1.73*	*0.06*	*0.54*	*0.58*	*0.00*	*0.00*	*0.00*	*0.45*	*0.85*	*0.01*	-	*1.34*	-	-	-	-	-
880	TiMagt	AVG	0.24	1.74	8.27	0.15	0.01	0.00	0.13	2.01	81.32	0.04	-	93.91	*5*	-	-	-	-
-	-	+/-	*0.11*	*0.09*	*0.87*	*0.02*	*0.02*	*0.00*	*0.01*	*0.09*	*0.67*	*0.02*	-	*0.24*	-	-	-	-	-
850	TiMagt	AVG	0.27	1.55	9.61	0.20	0.04	0.00	0.14	1.26	82.28	0.05	-	95.42	*12*	-	-	-	-
-	-	+/-	*0.13*	*0.05*	*2.15*	*0.07*	*0.03*	*0.01*	*0.03*	*0.27*	*2.65*	*0.10*	-	*1.70*	-	-	-	-	-
800	TiMagt	AVG	0.51	1.69	10.38	0.18	0.03	0.01	0.13	1.09	80.65	0.07	-	94.79	*4*	-	-	-	-
-	-	+/-	*0.16*	*0.03*	*0.79*	*0.08*	*0.04*	*0.00*	*0.01*	*0.13*	*1.54*	*0.02*	-	*0.48*	-	-	-	-	-
750	TiMagt	AVG	0.35	1.85	8.21	0.23	0.05	0.01	0.14	1.04	81.41	0.06	-	93.36	*15*	-	-	-	-
-	-	+/-	*0.30*	*0.15*	*2.53*	*0.37*	*0.06*	*0.01*	*0.05*	*0.36*	*4.16*	*0.07*	-	*1.02*	-	-	-	-	-
955	Ilm	AVG	0.62	0.37	45.13	0.45	0.05	0.01	0.21	4.85	45.93	0.00	-	97.65	*7*	-	-	-	-
-	-	+/-	*0.68*	*0.04*	*0.80*	*0.35*	*0.02*	*0.01*	*0.02*	*0.19*	*0.67*	*0.08*	-	*0.55*	-	-	-	-	-
940	Ilm	AVG	2.53	0.78	41.41	1.03	0.12	0.00	0.19	4.49	46.76	0.02	-	97.35	*6*	-	-	-	-
-	-	+/-	*1.74*	*0.52*	*1.30*	*1.02*	*0.09*	*0.04*	*0.01*	*0.33*	*1.51*	*0.01*	-	*0.87*	-	-	-	-	-
910	Ilm	AVG	1.78	0.69	43.22	0.46	0.42	0.02	0.18	3.61	47.60	0.00	-	98.00	*3*	-	-	-	-
-	-	+/-	*2.17*	*0.61*	*1.68*	*0.27*	*0.57*	*0.02*	*0.02*	*0.04*	*1.55*	*0.01*	-	*0.44*	-	-	-	-	-
880	Ilm	AVG	0.32	0.29	42.65	0.46	0.04	0.00	0.18	3.34	50.18	0.00	-	97.49	*3*	-	-	-	-
-	-	+/-	*0.31*	*0.12*	*1.49*	*0.16*	*0.04*	*0.00*	*0.01*	*0.13*	*0.66*	*0.04*	-	*1.04*	-	-	-	-	-
850	Ilm		0.03	0.12	46.84	0.34	0.00	0.00	0.14	2.03	50.51	0.00	-	100.00	*1*	-	-	-	-
750	Ilm	AVG	4.31	0.50	45.21	2.00	0.16	0.04	0.29	2.26	44.53	0.00	-	99.30	*5*	-	-	-	-
-	-	+/-	*4.47*	*0.44*	*4.28*	*1.33*	*0.18*	*0.07*	*0.06*	*0.78*	*3.53*	*0.05*	-	*1.14*	-	-	-	-	-
940	Opx	AVG	54.72	1.42	0.19	1.96	0.09	0.00	0.23	24.60	17.02	0.01	-	100.26	*9*	72.03	-	-	-
-	-	+/-	*0.42*	*0.25*	*0.06*	*0.28*	*0.04*	*0.02*	*0.01*	*0.30*	*0.24*	*0.02*	-	*0.52*	-	-	-	-	-
910	Opx	AVG	53.74	0.99	0.19	1.71	0.07	0.01	0.25	23.38	19.24	0.00	-	99.60	*18*	68.41	-	-	-
-	-	+/-	*0.78*	*0.21*	*0.03*	*0.19*	*0.04*	*0.01*	*0.03*	*0.39*	*0.44*	*0.05*	-	*1.21*	-	-	-	-	-
880	Opx	AVG	54.15	1.24	0.23	1.59	0.15	0.02	0.24	24.93	17.35	0.01	-	99.94	*7*	71.91	-	-	-
-	-	+/-	*0.78*	*0.43*	*0.06*	*0.28*	*0.11*	*0.06*	*0.04*	*0.76*	*0.64*	*0.05*	-	*1.22*	-	-	-	-	-
850	Opx	AVG	51.82	0.76	0.23	1.96	0.10	0.01	0.27	21.27	22.16	0.01	-	98.62	*9*	63.11	-	-	-
-	-	+/-	*0.33*	*0.24*	*0.06*	*0.19*	*0.07*	*0.01*	*0.05*	*0.52*	*0.81*	*0.06*	-	*1.41*	-	-	-	-	-

Sample	Phase	AVG / +/-	SiO_2	Al_2O_3	TiO_2	CaO	Na_2O	K_2O	MnO	MgO	FeO	Cr_2O_3	P_2O_5	Total	*n*	**Mg#**	**An%**	*T max*	*T AVG*
800	Opx	AVG	52.41	1.15	0.18	1.82	0.05	0.00	0.22	18.85	26.28	0.01	-	100.98	*3*	56.11	-	-	-
-	-	+/-	*0.41*	*0.45*	*0.04*	*0.28*	*0.04*	*0.00*	*0.02*	*0.30*	*0.86*	*0.01*	-	*0.26*	-	-	-	-	-
750	Opx	AVG	51.37	1.14	0.17	1.52	0.10	0.01	0.25	19.30	24.26	0.03	-	98.16	*16*	58.60	-	-	-
-	-	+/-	*0.65*	*0.60*	*0.03*	*0.35*	*0.08*	*0.01*	*0.05*	*1.11*	*1.25*	*0.06*	-	*0.97*	-	-	-	-	-
940	Amp	AVG	45.37	9.32	3.21	11.03	2.89	0.09	0.09	14.45	11.86	-	-	98.31	*27*	74.52	-	1020	950
-	-	+/-	*1.56*	*1.11*	*0.62*	*0.54*	*0.42*	*0.04*	*0.02*	*0.44*	*0.38*	-	-	*0.51*	-	-	-	-	*60*
910	Amp	AVG	50.18	5.18	1.03	11.40	1.54	0.09	0.14	14.46	12.76	-	-	96.81	*13*	71.06	-	888	680
-	-	+/-	*2.16*	*2.44*	*0.64*	*0.92*	*0.61*	*0.04*	*0.04*	*0.65*	*0.90*	-	-	*1.21*	-	-	-	-	*106*
880	Amp	AVG	52.23	3.78	0.57	11.37	1.12	0.07	0.17	15.08	13.17	-	-	97.59	*9*	71.20	-	820	600
-	-	+/-	*1.35*	*0.94*	*0.47*	*0.64*	*0.30*	*0.04*	*0.03*	*0.79*	*1.36*	-	-	*1.20*	-	-	-	-	*80*
850	Amp	AVG	51.90	3.31	0.37	10.98	1.04	0.06	0.17	14.49	14.43	-	-	96.78	*25*	66.95	-	620	558
-	-	+/-	*0.55*	*2.22*	*0.10*	*1.56*	*0.43*	*0.02*	*0.03*	*0.73*	*0.98*	-	-	*0.91*	-	-	-	-	*20*
800	Amp	AVG	52.13	3.61	0.55	11.52	1.18	0.06	0.17	14.11	15.55	-	-	98.89	*23*	66.33	-	810	590
-	-	+/-	*1.87*	*1.82*	*0.42*	*0.53*	*0.51*	*0.03*	*0.05*	*0.49*	*0.67*	-	-	*0.83*	-	-	-	-	*75*
750	Amp	AVG	50.71	3.87	0.47	10.98	1.26	0.14	0.16	13.76	15.06	-	-	96.45	*53*	64.97	-	910	580
-	-	+/-	*1.46*	*2.70*	*0.37*	*1.98*	*0.43*	*0.28*	*0.06*	*1.07*	*1.57*	-	-	*0.71*	-	-	-	-	*60*
800	“Dry prehnite”	AVG	45.50	25.39	-	26.76	0.36	0.01	0.08	-	0.91	-	-	99.01	*1*	-	-	-	-
750	“Dry prehnite”	AVG	45.65	25.77	0.01	26.68	0.48	0.02	0.02	0.00	0.86	-	-	99.49	*5*	-	-	-	-
		+/-	*0.11*	*0.20*	*0.01*	*0.46*	*0.08*	*0.00*	*0.04*	*0.01*	*0.08*	-	-	*0.49*	-	-	-	-	-

Composition of the experimental phases and of the starting material minerals. In the sample name column, numbers correspond to the experimental temperature. Compositional values are averages, the detailed compositions of all experiments with and without water addition are provided as supplementary material. Abbreviations are the same as Table 2 and: Start. Mat.=starting material, T_{max}=maximum temperature calculated with Ernst and Liu (1998), T_{AVG}=average temperature calculated with Ernst and Liu (1998), Mg#=Mg/(Mg+Fe_{total}) (molar basis), An%=Ca/(Ca+Na+K) (molar basis), AVG=average, *n*=number of analyses, ±=standard deviations, melt_recalc.=melt composition recalculated for a sum=100%, Cpx_reaction=Ca-Al-rich clinopyroxene observed in the coronitic assemblages (see “prehnite break-down reaction” part for more details).

Annex B3: Trace element composition of experimental melts, and of natural samples from the Oman ophiolite. Sample name format for experimental products is: [run]-[analyzed point]_[temperature]; AVG: average; +/- is the standard deviation for a given experiment; 08OL30: starting material; SDC: sheeted dike complex; coarse: coarser grained SDC; fine: finer grained SDC; PG: plagiogranite.

sample	Ti	Zr	Nb	Ba	La	Ce	Nd	Sm	Eu	Tb	Gd	Dy	Er	Yb	Lu	Hf	Th	U	Sc	V	Sr	Y
10-01_1030	8392.38	70.13	2.01	9.05	3.01	8.84	7.65	2.72	0.85	0.71	4.07	4.26	2.89	2.89	0.46	2.31	0.19	0.11	41.56	374.99	100.89	26.72
10-02_1030	8344.32	69.64	1.89	9.08	2.96	8.58	7.72	2.45	0.93	0.66	3.74	4.62	2.96	2.93	0.42	2.54	0.19	0.09	39.93	373.68	99.32	27.37
10-03_1030	8366.52	72.24	2.03	9.06	2.87	8.68	8.23	2.38	0.94	0.67	3.56	4.41	2.70	2.64	0.47	2.39	0.22	0.09	41.53	369.28	97.79	26.79
10_1030-AVG	**8367.74**	**70.67**	**1.97**	**9.06**	**2.95**	**8.70**	**7.87**	**2.52**	**0.91**	**0.68**	**3.79**	**4.43**	**2.85**	**2.82**	**0.45**	**2.41**	**0.20**	**0.10**	**41.01**	**372.65**	**99.33**	**26.96**
10_1030_+/-	*19.64*	*1.13*	*0.06*	*0.01*	*0.06*	*0.10*	*0.26*	*0.15*	*0.04*	*0.02*	*0.21*	*0.15*	*0.11*	*0.13*	*0.02*	*0.10*	*0.01*	*0.01*	*0.76*	*2.44*	*1.27*	*0.29*
12-01_1030	8032.67	70.45	2.06	8.34	2.93	8.50	7.41	2.58	0.86	0.62	3.59	4.27	2.84	2.92	0.44	2.44	0.19	0.13	37.95	389.05	99.01	26.38
12-02_1030	7922.54	69.96	2.11	9.68	2.91	8.31	7.81	2.58	0.87	0.65	3.67	4.24	2.76	2.91	0.42	2.32	0.17	0.12	41.05	350.97	97.81	24.62
12-03_1030	7886.61	72.42	2.03	9.51	2.91	8.30	7.39	2.32	0.88	0.63	3.67	4.35	2.83	2.54	0.45	2.63	0.20	0.12	38.47	376.99	102.60	26.75
12_1030-AVG	**7947.28**	**70.94**	**2.07**	**9.18**	**2.92**	**8.37**	**7.54**	**2.49**	**0.87**	**0.63**	**3.64**	**4.29**	**2.81**	**2.79**	**0.44**	**2.47**	**0.19**	**0.12**	**39.16**	**372.34**	**99.80**	**25.92**
12_1030_+/-	*62.14*	*1.07*	*0.03*	*0.60*	*0.01*	*0.09*	*0.20*	*0.13*	*0.01*	*0.01*	*0.04*	*0.05*	*0.03*	*0.18*	*0.01*	*0.13*	*0.02*	*0.01*	*1.36*	*15.89*	*2.04*	*0.93*
C-01_1000	7538.50	94.03	3.92	13.65	4.48	12.70	10.71	3.36	1.17	0.82	5.03	5.53	3.53	3.34	0.51	3.26	0.29	0.13	34.21	226.45	98.62	34.13
C-02_1000	7642.16	95.17	3.25	12.69	3.96	11.79	9.45	3.39	1.15	0.84	4.81	5.23	3.26	3.40	0.52	3.29	0.28	0.18	29.25	235.25	97.62	33.64
C-03_1000	7584.36	98.31	2.62	12.29	3.89	11.22	9.61	3.29	1.08	0.79	4.54	5.19	3.46	3.46	0.54	3.48	0.27	0.18	32.30	220.85	95.70	31.46
C_1000-AVG	**7588.34**	**95.83**	**3.26**	**12.88**	**4.11**	**11.91**	**9.92**	**3.34**	**1.13**	**0.81**	**4.79**	**5.32**	**3.42**	**3.40**	**0.53**	**3.34**	**0.28**	**0.16**	**31.92**	**227.52**	**97.31**	**33.08**
C_1000_+/-	*42.41*	*1.81*	*0.53*	*0.57*	*0.26*	*0.61*	*0.56*	*0.04*	*0.04*	*0.02*	*0.20*	*0.15*	*0.11*	*0.05*	*0.01*	*0.10*	*0.01*	*0.02*	*2.04*	*5.93*	*1.21*	*1.16*
B-01_1000	6850.56	89.93	2.88	12.62	3.51	10.51	9.25	3.22	1.05	0.71	4.19	4.56	3.06	3.19	0.49	3.35	0.26	0.14	29.60	228.97	97.60	30.23
B-02_1000	7025.84	84.02	3.99	13.26	3.49	9.99	8.36	2.84	0.93	0.68	4.17	4.30	3.07	3.26	0.53	3.13	0.23	0.14	33.76	217.23	93.53	26.29
B-03_1000	7006.44	88.98	3.22	12.23	3.45	10.04	7.91	2.79	0.87	0.74	4.01	5.02	3.23	3.18	0.49	3.04	0.25	0.13	29.60	223.23	96.86	29.40
B_1000-AVG	**6960.95**	**87.64**	**3.36**	**12.70**	**3.48**	**10.18**	**8.51**	**2.95**	**0.95**	**0.71**	**4.13**	**4.63**	**3.12**	**3.21**	**0.50**	**3.17**	**0.25**	**0.14**	**30.99**	**223.14**	**96.00**	**28.64**
B_1000_+/-	*78.45*	*2.59*	*0.46*	*0.43*	*0.03*	*0.23*	*0.56*	*0.19*	*0.07*	*0.02*	*0.08*	*0.30*	*0.08*	*0.04*	*0.02*	*0.13*	*0.01*	*0.00*	*1.96*	*4.79*	*1.77*	*1.69*
13-01_970	6100.81	121.44	3.45	18.42	5.01	14.30	12.19	3.61	1.08	0.91	5.31	5.61	3.97	4.04	0.65	3.96	0.43	0.26	30.37	121.49	74.12	34.37
13-02_970	6095.83	122.94	3.50	17.88	5.12	14.02	11.98	3.61	1.02	0.95	5.35	5.72	3.92	4.10	0.60	3.94	0.38	0.24	27.37	137.55	78.67	38.33
13_970-AVG	**6098.32**	**122.19**	**3.48**	**18.15**	**5.06**	**14.16**	**12.09**	**3.61**	**1.05**	**0.93**	**5.33**	**5.66**	**3.94**	**4.07**	**0.62**	**3.95**	**0.41**	**0.25**	**28.87**	**129.52**	**76.39**	**36.35**
13_970_+/-	*2.49*	*0.75*	*0.03*	*0.27*	*0.06*	*0.14*	*0.11*	*0.00*	*0.03*	*0.02*	*0.02*	*0.06*	*0.02*	*0.03*	*0.02*	*0.01*	*0.03*	*0.01*	*1.50*	*8.03*	*2.27*	*1.98*
14-01_970	6343.26	115.54	3.79	15.06	5.03	14.67	12.63	3.65	1.11	0.88	5.69	5.82	4.08	3.80	0.60	3.81	0.32	0.21	32.04	136.64	78.10	33.84
14-02_970	6228.12	123.50	3.62	15.71	4.94	14.44	11.95	3.99	1.11	0.97	5.19	5.90	3.68	3.88	0.61	4.39	0.36	0.21	26.45	147.61	78.54	38.67
14_970-AVG	**6285.69**	**119.52**	**3.71**	**15.39**	**4.99**	**14.55**	**12.29**	**3.82**	**1.11**	**0.93**	**5.44**	**5.86**	**3.88**	**3.84**	**0.60**	**4.10**	**0.34**	**0.21**	**29.24**	**142.12**	**78.32**	**36.26**
14_970_+/-	*57.57*	*3.98*	*0.08*	*0.33*	*0.05*	*0.11*	*0.34*	*0.17*	*0.00*	*0.05*	*0.25*	*0.04*	*0.20*	*0.04*	*0.01*	*0.29*	*0.02*	*0.00*	*2.79*	*5.49*	*0.22*	*2.41*
23-01_955	4713.45	131.64	3.77	18.25	5.77	16.45	13.14	3.82	1.10	0.93	4.47	5.63	4.35	4.35	0.59	4.38	0.37	0.23	30.49	102.78	72.01	47.48
23-03_955	5402.62	148.45	4.20	19.56	6.61	19.10	15.46	4.63	1.21	1.13	5.49	6.53	4.46	4.72	0.71	5.56	0.51	0.27	27.36	79.50	68.13	43.22
23_955-AVG	**5058.04**	**140.04**	**3.98**	**18.91**	**6.19**	**17.78**	**14.30**	**4.22**	**1.16**	**1.03**	**4.98**	**6.08**	**4.40**	**4.54**	**0.65**	**4.97**	**0.44**	**0.25**	**28.93**	**91.14**	**70.07**	**45.35**
23_955_+/-	*344.59*	*8.40*	*0.21*	*0.66*	*0.42*	*1.33*	*1.16*	*0.40*	*0.05*	*0.10*	*0.51*	*0.45*	*0.06*	*0.19*	*0.06*	*0.59*	*0.07*	*0.02*	*1.57*	*11.64*	*1.94*	*2.13*
25-01_955	5258.30	155.88	4.17	18.82	6.49	18.50	13.66	4.30	1.11	1.04	6.37	6.56	4.55	4.79	0.71	5.49	0.49	0.32	3.69	97.55	80.90	43.55
25-02_955	5479.43	141.83	5.33	19.90	6.50	18.81	15.45	4.48	1.23	0.94	6.16	6.69	4.48	4.30	0.71	5.15	0.52	0.31	27.36	96.55	70.04	39.52

sample	Ti	Zr	Nb	Ba	La	Ce	Nd	Sm	Eu	Tb	Gd	Dy	Er	Yb	Lu	Hf	Th	U	Sc	V	Sr	Y
25-03_955	5540.13	136.10	5.09	17.89	6.19	18.53	14.13	3.97	1.15	1.05	5.71	6.42	4.26	4.57	0.74	5.06	0.40	0.25	23.41	104.78	68.46	43.38
25-04_955	5183.15	130.26	4.62	18.58	6.21	17.58	14.34	4.65	1.10	1.12	6.15	6.81	4.92	4.34	0.62	4.52	0.39	0.27	70.61	182.56	54.41	66.84
25_955-AVG	**5365.25**	**141.02**	**4.80**	**18.80**	**6.35**	**18.35**	**14.40**	**4.35**	**1.15**	**1.03**	**6.10**	**6.62**	**4.55**	**4.50**	**0.69**	**5.05**	**0.45**	**0.29**	**31.27**	**120.36**	**68.45**	**48.32**
25_955_+/-	*148.51*	*9.50*	*0.45*	*0.72*	*0.15*	*0.46*	*0.66*	*0.25*	*0.05*	*0.06*	*0.24*	*0.15*	*0.24*	*0.20*	*0.05*	*0.35*	*0.05*	*0.03*	*24.42*	*36.05*	*9.42*	*10.81*
08OL30	**8872.59**	**69.00**	**2.00**	**18.00**	**2.90**	**8.10**	**7.60**	**2.40**	**1.08**	**0.70**	**3.40**	**4.60**	**2.80**	**2.50**	**0.39**	**2.10**	**0.30**	**0.10**	**29.00**	**396.00**	**120.00**	**23.00**
residue-955_60	*11313.22*	*21.31*	*0.41*	*17.43*	*0.65*	*1.46*	*3.10*	*1.14*	*1.03*	*0.48*	*1.97*	*3.43*	*1.68*	*1.15*	*0.20*	*0.16*	*0.20*	*0*	*28.27*	*589.50*	*153.83*	*7.11*
granoblastic dike_95OC42	7479.37	7.55	0.42	53.43	0.42	1.30	1.96	0.97	0.76	0.38	1.69	2.61	1.51	1.50	0.23	-	0.04	0.02	-	306.24	148.56	12.01
granoblastic dike_95OC43	5275.59	6.21	0.19	100.59	0.33	1.10	1.77	0.91	0.78	0.33	1.58	2.35	1.45	1.27	0.19	-	0.00	-	-	262.48	150.69	10.92
granoblastic xenolith_95OG27	1829.38	20.44	1.10	17.81	0.43	1.36	1.56	0.61	0.34	0.18	1.00	1.23	0.79	0.73	0.12	-	0.02	-	-	140.63	103.52	7.51
granoblastic dike_97OC25	4583.89	15.47	0.44	26.14	0.69	2.35	3.47	1.55	0.93	0.55	2.40	3.81	2.17	2.08	0.31	-	0.04	0.02	-	254.83	154.43	17.33
granoblastic dike_97OC29	6779.07	18.48	0.67	315.34	0.95	3.07	4.22	1.95	1.39	0.64	2.93	4.47	2.70	2.57	0.38	-	0.02	0.02	-	248.85	185.15	21.09
AVG_ granoblastic rocks	**5167.92**	**13.63**	**0.56**	**102.66**	**0.57**	**1.83**	**2.60**	**1.20**	**0.84**	**0.42**	**1.92**	**2.89**	**1.72**	**1.63**	**0.25**	**-**	**0.02**	**0.02**	**-**	**242.61**	**148.47**	**13.77**
SDC_99OC215	12126.14	52.63	3.00	73.63	3.18	9.55	9.66	3.49	1.30	0.89	4.68	5.86	3.91	3.69	0.55	1.52	0.15	0.04	-	554.33	152.96	37.42
SDC_01OC14	6938.39	50.62	1.70	152.8	3.79	9.06	7.26	2.51	1.05	0.62	3.23	4.10	2.70	2.52	0.38	1.31	0.24	0.08	-	333.36	132.55	26.54
SDC_01OC18	5290.36	53.99	1.84	65.80	2.34	6.39	5.97	2.12	0.83	0.54	2.82	3.62	2.40	2.26	0.34	1.43	0.21	0.05	-	243.10	110.17	23.22
SDC (N-S)_01OC19	11061.66	128.71	4.25	57.81	5.70	15.31	12.97	4.14	1.40	1.01	5.37	6.63	4.46	4.34	0.66	3.16	0.50	0.20	-	412.16	137.97	43.28
SDC_01OC20	10850.04	96.75	3.54	26.22	5.29	14.33	12.24	3.96	1.43	0.91	4.93	6.04	3.99	3.82	0.57	2.41	0.44	0.15	-	426.65	116.48	39.31
SDC (coarse)_01OC21	8414.91	50.89	2.57	44.03	3.23	8.93	8.14	2.79	1.05	0.71	3.71	4.69	3.15	2.96	0.45	1.48	0.34	0.09	-	456.03	120.79	30.57
SDC (fine)_01OC22	12902.42	94.78	3.96	59.46	3.92	12.14	11.51	3.93	1.40	0.95	5.03	6.25	4.22	4.00	0.61	2.44	0.36	0.13	-	600.03	109.41	40.58
SDC_01OC24	12421.38	116.33	3.72	34.47	5.77	15.91	13.77	4.63	1.58	1.11	5.77	7.23	4.84	4.62	0.70	2.91	0.48	0.21	-	541.17	113.56	47.75
AVG Abyad SDC	**10000.66**	**80.59**	**3.07**	**64.28**	**4.15**	**11.45**	**10.19**	**3.45**	**1.26**	**0.84**	**4.44**	**5.55**	**3.71**	**3.53**	**0.53**	**2.08**	**0.34**	**0.12**	**-**	**445.85**	**124.24**	**36.08**
PG intruding SDC_97OC68	3991.80	762.56	4.18	5.65	11.12	31.54	25.86	7.45	1.66	1.93	10.78	12.47	7.57	7.47	0.99	-	0.54	0.07	-	21.71	56.91	74.76

Annex B4: Mineral compositions (weight %) of samples 07OL34 and 07OL36 from the Rajmi area of the Oman ophiolite.

	mineral	*Comment*	*SiO_2*	*Al_2O_3*	*TiO_2*	*CaO*	*Na_2O*	*K_2O*	*MnO*	*MgO*	*FeO*	*Cr_2O_3*	*NiO*	*Total*	*n*	*Mg#*	*An%*
07OL34																	
AVG	Cpx	bright on BSE images	53.66	0.74	0.14	24.51	0.20	0.00	0.18	15.67	5.54	0.04	0.00	100.69	*42*	83	-
+/-	***Cpx***		***0.78***	***0.35***	***0.09***	***0.80***	***0.08***	***0.00***	***0.07***	***0.83***	***1.38***	***0.05***	***0.00***	***0.68***	-	***4***	-
AVG	Cpx	dark on BSE images	54.34	0.85	0.10	25.14	0.16	0.00	0.07	16.82	2.71	0.03	0.02	100.24	*50*	92	-
+/-	***Cpx***		***0.68***	***0.66***	***0.13***	***0.39***	***0.08***	***0.00***	***0.04***	***0.52***	***0.61***	***0.04***	***0.01***	***0.70***	-	***2***	-
AVG	Pl	An_max=99	44.08	35.79	0.00	19.51	0.50	0.00	0.01	0.01	0.06	0.01	0.01	99.98	*32*	-	96
+/-	***Pl***		***1.47***	***0.93***	***0.01***	***1.15***	***0.71***	***0.00***	***0.01***	***0.02***	***0.03***	***0.02***	***0.01***	***0.43***	-	-	***6***
AVG	Amp	T max=841°C	50.89	5.42	0.78	12.67	0.87	0.03	0.12	17.77	8.91	0.19	0.00	97.66	*37*	84	-
+/-	***Amp***		***2.88***	***2.33***	***0.55***	***0.33***	***0.48***	***0.04***	***0.03***	***1.39***	***1.03***	***0.17***	***0.00***	***0.58***	-	***2***	-
07OL36																	
AVG	Cpx	"magmatic"	52.28	1.93	0.39	22.02	0.29	0.00	0.19	14.79	7.86	0.24	0.02	100.00	*26*	77	-
+/-	***Cpx***	***"magmatic"***	***0.41***	***0.19***	***0.10***	***0.38***	***0.02***	***0.00***	***0.03***	***0.33***	***0.35***	***0.05***	***0.01***	***0.34***	-	***1***	-
AVG	Cpx	"recrystallized"	53.24	0.86	0.19	23.13	0.20	0.00	0.20	15.01	7.36	0.10	0.01	100.28	*34*	78	-
+/-	***Cpx***	***"recrystallized"***	***0.45***	***0.31***	***0.09***	***0.82***	***0.06***	***0.00***	***0.03***	***0.36***	***0.42***	***0.05***	***0.01***	***0.31***	-	***1***	-
AVG	Cpx	margins of "recrystallized"	51.90	1.84	0.45	22.15	0.27	0.00	0.17	15.09	7.99	0.16	-	100.01	*4*	77	-
+/-	***Cpx***	***margins of "recrystallized"***	***0.17***	***0.26***	***0.06***	***0.24***	***0.02***	***0.00***	***0.03***	***0.15***	***0.16***	***0.06***	-	***0.22***	-	***0***	-
AVG	Opx		54.39	1.20	0.13	1.14	0.01	0.00	0.35	24.63	18.50	0.11	0.02	100.49	*19*	70	-
+/-	***Opx***		***0.43***	***0.22***	***0.06***	***0.37***	***0.01***	***0.00***	***0.04***	***0.82***	***1.19***	***0.02***	***0.01***	***0.31***	-	***2***	-
AVG	Pl	An_max=93	45.93	34.09	0.01	17.95	1.36	0.03	0.01	0.01	0.39	0.01	0.00	99.79	*39*	-	88
+/-	***Pl***		***0.80***	***0.70***	***0.01***	***0.61***	***0.35***	***0.02***	***0.01***	***0.01***	***0.07***	***0.02***	***0.01***	***0.50***	-	-	***3***
AVG	Amp	T max=780°C	52.10	4.39	0.76	11.66	0.70	0.09	0.18	17.56	10.12	0.20	0.02	97.79	*42*	79	-
+/-	***Amp***		***2.96***	***2.37***	***0.55***	***1.01***	***0.45***	***0.07***	***0.11***	***1.70***	***1.87***	***0.12***	***0.02***	***0.40***	-	***4***	-
AVG	Magt		1.31	0.20	0.35	0.78	0.02	0.00	0.19	0.39	83.26	3.80	-	90.30	*15*	-	-
+/-	***Magt***		***2.71***	***0.18***	***0.25***	***0.75***	***0.02***	***0.01***	***0.11***	***0.79***	***3.36***	***1.72***	-	***2.14***	-	-	-
AVG	Ilm		0.19	0.02	51.13	0.71	0.01	0.00	2.50	0.20	43.85	0.13	-	98.74	*6*	-	-
+/-	***Ilm***		***0.10***	***0.01***	***0.89***	***0.19***	***0.01***	***0.01***	***0.97***	***0.11***	***1.13***	***0.07***	-	***0.87***	-	-	-
AVG	Qz		99.70	0.03	0.04	0.02	0.01	0.00	0.01	0.00	0.03	0.03	-	99.88	*23*	-	-
+/-	***Qz***		***0.21***	***0.01***	***0.01***	***0.02***	***0.01***	***0.00***	***0.01***	***0.01***	***0.06***	***0.04***	-	***0.21***	-	-	-

Abbreviations are: n=number of analyses; Mg#=Mg/(Mg+Fe) in moles; An%=Ca/(Ca+Na+K) in moles; -=not analyzed or below detection limit; Cpx=clinopyroxene; Pl=plagioclase; Ilm=ilmenite; Amp=amphibole; Opx=orthopyroxene; magt=magnetite; Qz=quartz.

Annex C.

Other papers written during the PhD work

Computers & Geosciences 35 (2009) 1304–1310

Contents lists available at ScienceDirect

Computers & Geosciences

journal homepage: www.elsevier.com/locate/cageo

CMAS 3D, a new program to visualize and project major elements compositions in the CMAS system ☆

L. France *,[1], N. Ouillon, G. Chazot [2], J. Kornprobst, P. Boivin

Laboratoire Magmas et Volcans, OPGC–UBP–CNRS, 5, Rue Kessler, 63038 Clermont-Ferrand Cedex, France

ARTICLE INFO

Article history:
Received 14 January 2008
Received in revised form
1 July 2008
Accepted 9 July 2008

Keywords:
CMAS system
3D
Projection

ABSTRACT

CMAS 3D, developed in MATLAB®, is a program to support visualization of major element chemical data in three dimensions. Such projections are used to discuss correlations, metamorphic reactions and the chemical evolution of rocks, melts or minerals. It can also project data into 2D plots. The CMAS 3D interface makes it easy to use, and does not require any knowledge of Matlab® programming. CMAS 3D uses data compiled in a Microsoft Excel™ spreadsheet. Although useful for scientific research, the program is also a powerful tool for teaching.

1. Introduction

Major element chemical data of rocks and minerals are of great use in the study of the origins and evolution of magmatic and metamorphic rocks. Petrologists mostly use binary plots to evaluate correlation between chemical elements or oxides, but some reduced systems have been developed to take into account more than 2 elements in the same diagram. For example some software packages such as MinPet (Richard, 1997), IgPet (Carr, 1995), NewPet (Clarke, 1993), Petrograph (Petrelli, 2003) or GeoPlot (Zhou and Li, 2006) have been developed for better data visualization and interpretation. Smith and Beermann (2006) proposed to use multivector diagrams to represent up to nine components. O'Hara (1968) introduced the use of the $CaO–MgO–Al_2O_3–SiO_2$ (CMAS) system allowing representation of 13 oxides in a 4D representation. This pseudo-quaternary projection has been largely used as it is the simplest way to represent the major element composition of mafic and ultramafic rocks (Garrido and Bodinier, 1999), as well as the main crustal and mantle minerals (Kornprobst, 1970; Kornprobst and Conquéré, 1972) or extraterrestrial objects (Grossman and Fedkin, 2003; Grossman et al., 2002; Yoneda and Grossman, 1995) and serves as a good model for dry basaltic melts (Schiano et al., 2000, 2004). It is also largely used in experimental petrology (Hirschmann et al., 2003; Kogiso et al., 2003, 2004).

Here we present CMAS 3D, a program written in MATLAB 6.5®. It converts oxide data to CMAS coordinates and allows visualization of these data in three dimensions, and projects the data onto 2D plots. Using CMAS 3D does not require MATLAB programming expertise. It reads data from a Microsoft Excel™ spreadsheet. The visualization uses the virtual reality modeling language (VRML) allowing the rotation of the CMAS tetrahedron in all directions in order to evaluate different correlations and reactions. CMAS 3D also permits the addition of lines or planes

☆ Code available from server at http://www.iamg.org/CGEditor/index.htm.

* Corresponding author at: Equipe Manteau-Noyau, University Montpellier II–CNRS, Laboratoire Geosciences Montpellier, Geosciences Montpellier, CC 060, Place Eugene Bataillon 34095, Montpellier cedex 05, France. Tel.: +334 67 14 39 44; fax: +334 67 14 36 03.
E-mail address: France@gm.univ-montp2.fr (L. France).
[1] Present address: Géosciences Montpellier, Université Montpellier 2-CNRS, 34095 Montpellier cedex 05, France.
[2] Present address: UMR 6538 "Domaines Océaniques", IUEM, Université de Bretagne Occidentale, Place Copernic, 29280 Plouzané, France.

0098-3004/$ - see front matter © 2008 Elsevier Ltd. All rights reserved.
doi:10.1016/j.cageo.2008.07.002

Elsevier Editorial System(tm) for Computers & Geosciences
Manuscript Draft

Manuscript Number:

Title: MetaRep, an extended CMAS 3D program to visualize mafic (CMAS, ACF-S, ACF-N) and pelitic (AFM-K, AFM-S, AKF-S) projections.

Article Type: Short Note

Keywords: projections; 3D representation; major element; pelitic rocks; mafic rocks

Corresponding Author: PhD student Lydéric france,

Corresponding Author's Institution: University Montpellier II

First Author: Lydéric France, Dr

Order of Authors: Lydéric France, Dr; Christian Nicollet, Pr

Abstract: MetaRep is a program based on our earlier program, CMAS 3D; it is developed in MATLAB® script. MetaRep objectives are to visualize and project major element compositions of mafic and pelitic rocks and their minerals in the pseudo quaternary projections of the ACF-S, ACF-N, CMAS, AFM-K, AFM-S and AKF-S systems. These six systems are commonly used to describe metamorphic mineral assemblages and magmatic evolutions. Each system, made of four apices, can be represented in a tetrahedron that is visualizable in three dimensions with MetaRep; the four tetrahedron apices represent oxides or combination of oxides that define the composition of the projected rock or mineral. From these systems, MetaRep can also project data in triangular plots (for example, the ACF, AFM and AKF triangular projections can be generated). A functional interface makes it easy to use, and does not require any knowledge of MATLAB ® programming. To facilitate the use, MetaRep loads, from the main interface, data compiled in a Microsoft ExcelTM spreadsheet. Although useful for scientific research, the program is also a powerful tool for teaching. We propose an application example which, by using two combined systems (ACF-S and ACF-N), brings a strong confirmation to the petrological interpretations.

Petrological and Geochemical Study of Late-Orogenic Mantle Garnet Pyroxenites. Implications on Magmatism in Old Orogenic Regions.

To be submitted to Journal of Petrology

FRANCE Lydéric[1,2*], CHAZOT Gilles[3,4] , KORNPROBST Jacques[5], DALLAI Luigi[6], VANNUCCI Riccardo[7], TEMDJIM Robert[8].

Abstract

Pyroxenites are mantle heterogeneities which could represent recycling of oceanic crust in mantle domains or mantle cumulates. Uncommon petrological and geochemical (major and trace elements, Sr-Nd and O isotopes) data of xenolith samples coming from various localities (French Massif-Central, Jordan, Morocco and Cameroon) show that they represent crystallized melts. They formed in the mantle domains at pressures of 1-2 GPa during post-collisional magmatism that follows orogenic events (Hercynian for the French Massif-Central and Morocco, and Panafrican for the others). Most of the samples display metasomatic overprint that is probably linked to the recent volcanism episodes of the different studied regions. The thermal reequilibration of lithospheric domains, typical of the late stage of exhumations, is also recorded by the samples.

The pyroxenites crystallization during late orogenic events has implications on the subsequent evolution of the mantle domains. The presence of large amounts of mantle pyroxenites in old orogenic regions indeed confers physical and chemical particularities to these domains. Among others, global solidus temperature of the whole lithospheric domain will be lowered; it follows that old orogenic regions are refertilized zones where the magmatic activity would be enhanced.

Annex D.

Conference abstracts

Root zone of sheeted dike complex in Oman ophiolite-petrological model

F. BOUDIER[1], J. KOEPKE[2], L. FRANCE[1] AND C. MEVEL[3]

[1]Univ. Montpellier II, France (boudier@gm.univ-montp2.fr)
[2]Institut fuer Mineralogie der Universitaet Hannover, Germany (koepke@mineralogie.uni-hannover.de)
[3]IPGP, Paris (mevel@ipgp.jussieu.fr)

Recently, IODP (Integrated Ocean Drilling Program) has penetrated in the eastern Pacific Ocean (Hole 1256D) the root zone of the sheeted dike complex (RZSDC). In Oman ophiolites, it is a well exposed horizon ~100m thick between the main gabbro unit and above, the crustal lid (sheeted dikes and lavas). To compare with the IODP hole, a new petro-structural study was conducted in Oman. We explain this complex zone by interference between the magmatic system of the melt lens present in fast spreading ridges, and a hydrothermal system operating at very high temperatures penetrating down to the roof of this lens where it induces successive stages of hydrous anatexis. This results in a crude stratigraphy throughout the RZSDC with doleritic isotropic gabbros evolving upwards in vari-textured, pegmatitic gabbros and trondjhemite intrusions. New melt intrusions from the melt lens proceed through basaltic 'protodikes' which are, in the RZSDC, a relay to the overlying sheeted dikes. Injected in gabbros still at solidus temperature, protodikes develop against these gabbros a typical microgranular margin. The following phase diagram constructed for pressure 50MPa, issued from Feig *et al*., 2006 allows to follow the sequence of formation of the successive magmatic facies described in the RZSDC.

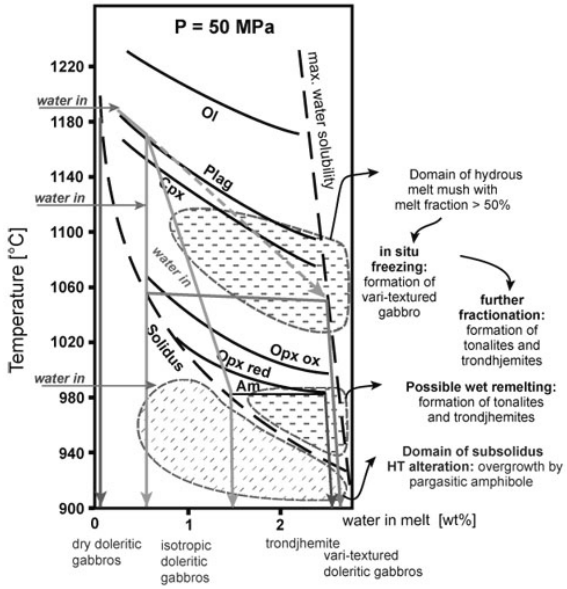

References

Feig, S., Koepke, J., Snow, J., 2006. *Contrib. Mineral. Petrol.* **152**, 611-638

Geophysical Research Abstracts,
Vol. 10, EGU2008-A-00000, 2008
EGU General Assembly 2008

Processes governing the magmatic-hydrothermal interface at the sheeted dike complex-gabbro transition: From the comparison between the IODP Hole 1256D and the Oman ophiolite to a general model?

L. France (1), B. Ildefonse(1), J. Koepke(2)

(1) Université Montpellier 2/ CNRS, France, (2) Institut fuer Mineralogie, Universitaet Hannover, Germany, (lyderic.france@gm.univ-montp2.fr / Fax: +334 67 14 36 03 / Phone: +334 67 14 39 44)

The Integrated Ocean Drilling Program (IODP) has recently cored the root zone of the sheeted dike complex in the eastern Pacific Ocean (IODP Hole 1256D). In the Oman ophiolite, this zone is a well exposed horizon, $\sim$100m thick, between the main gabbro unit and the basaltic (sheeted dikes and lavas) upper crustal lid. To compare with recent observations in IODP Hole 1256D, we have performed detailed mapping and petrological analysis in various areas in the Oman ophiolite. The complex lithologies of the transition zone between sheeted dikes and gabbros most probably results from vertical movements of the magma lens, which in turn allow the hydrothermal system to move up and down. Ascent of the melt lens seems to be accompanied by reheating and assimilation of the root zone lithologies, as observed in the studied areas. This reheating lead to dehydration metamorphic reactions (such as Hornblende=>Clinopyroxene+Orthopyroxene+Plagioclase+H_2O) and to dehydration melting processes (this latter being linked to hydrous partial melting). These reactions mark the transition from green-schist/amphibolite facies to dry and wet granulitic facies, respectively, probably depending on the kinetics of reheating. Dehydration reactions also occur in stopped dike fragments that are observed in the underlying gabbros, and allow the introduction of water in the melt lens.

Geophysical Research Abstracts,
Vol. 10, EGU2008-A-00000, 2008
EGU General Assembly 2008

A new method to constrain the oxidation state of basaltic series from microprobe analysis.

L. France (1), B. Ildefonse (1), J. Koepke (2), C. Cordier (1), F. Bech (3).

(1) Université Montpellier 2/ CNRS, France, (2) Institut fuer Mineralogie, Universitaet Hannover, Germany, (3) Université de Clermont-Ferrand/ CNRS, France, (lyderic.france@gm.univ-montp2.fr / Fax: +334 67 14 36 03 / Phone: +334 67 14 39 44)

The oxygen fugacity (fO_2) of basaltic magmas is a critical controlling parameter of magmatic processes. It controls the iron redox state of the melt, and it strongly influences the crystallisation sequences and the composition of minerals crystallising. We propose a new simple method for constraining fO_2 of parental magmas of igneous rocks. It uses FeO_{tot} electronic microprobe analysis in clinopyroxene (Cpx) and plagioclase (Pl). The results do not depend on stoechiometric calculations. The method is based on the difference between the exchange coefficients: $K_D{}^{Cpx-melt}_{Fe2O3/FeO}$ and $K_D{}^{Pl-melt}_{Fe2O3/FeO}$. These coefficients are equivalent to the ratio of the partition coefficient of Fe_2O_3 and FeO between Cpx and melt and between Pl and melt**,** respectively: $K_D^{Pl-melt}(Fe_2O_3/FeO) = D^{Fe3+}_{Pl-melt}/D^{Fe2+}_{Pl-melt}$. Using published partition coefficients, these K_D are around 0.5 and 20 for Cpx and Pl, respectively. These values show that increasing oxidation of a melt results in a decreasing of FeO_{tot} in Cpx and an increasing of FeO_{tot} in Pl. We propose an equation, based on these partition coefficients, that allows calculating the redox conditions of a partly molten system expressed in ΔFMQ values (FMQ = oxygen fugacity corresponding to the fayalite-magnetite-quartz oxygen buffer), by the input of analysed FeO_{tot} in Cpx and Pl, and an estimation of the pressure, temperature and melt composition. Error propagation reveals the limits of the model. An application to literature data attests the validity of the proposed model.

Geophysical Research Abstracts,
Vol. 10, EGU2008-A-00000, 2008
EGU General Assembly 2008

Petrological and geochemical study of late-orogenic mantle garnet pyroxenites. Implications on magmatism in old orogenic regions.

L. FRANCE (1), G. CHAZOT (2), J. KORNPROBST (3), L. DALLAI (4), R. VANNUCCI (5), C. BOSQ (3).

(1) Université de Montpellier 2/ CNRS, Montpellier, France, (2) Université de Bretagne Occidentale/ CNRS, Plouzané, France, (3) Université de Clermont-Ferrand II/ CNRS, Clermont-Ferrand, France, (4) CNR-IGG, Pisa, Italia, (5) Università degli Studi di Pavia/ CNR, Italia, (lyderic.france@gm.univ-montp2.fr / Fax: +334 67 14 36 03 / Phone: +334 67 14 39 44)

The petrological and geochemical study of garnet bearing pyroxenites from four localities (FMC, Morocco, Jordan, Cameroon) demonstrates that these rocks are cumulates crystallised in the lithospheric mantle domain. Metamorphic reactions, exsolutions and trace elements WR analysis demonstrate that their crystallisation pressure ranges between 1 and 2GPa (30 to 60km). The elaboration of the PTt paths for the studied samples attests of important movements in the respective lithospheres. Replaced in the geodynamical contexts, the samples are interpreted to represent the crystallisation of melts formed during exhumation of orogenic domains. Radiogenic isotopes (Sr-Nd) show that in a very same region, the samples are isotopicaly heterogeneous but are similar to the respective regional lithosphere. Initial isotopic ratios lead to propose that the FMC samples have crystallised at the end of the Hercynian orogen and that the samples from the other localities (Morocco, Jordan and Cameroon) have crystallised at the end of the Pan-African orogen. After recalculation at the crystallisation time, the isotopic compositions are in good agreement with the respective regional lithosphere ones and so samples of this study could represent the product of the melting of these lithospheres. The analyses of oxygen stable isotopes allow to precise the model; they show that twelve of the samples come from the melting of a lherzolitic mantle and that the four others come from the melting of a heterogeneous mantle formed of lherzolites and eclogites. The presence of some hydrous minerals such as amphiboles and micas

and the trace elements WR analyses show that some of the samples were affected by a late metasomatic event.

Results of our study show that thermal relaxation following orogenic events lead to the crystallisation of pyroxenites in the lithosphere. The presence of lage amounts of mantle pyroxenites in old orogenic regions confers physical and chemical particularities to these domains. Among others, global solidus temperature of the whole lithospheric domain will be lowered; it follows that old orogenic regions such as FMC, Morocco, Jordan and Cameroon represent more fertile lithospheric zones in which magmatic activity will be facilitated.

Cite abstracts as **Author(s) (2008), Title,** *Eos Trans. AGU, 89***(53), Fall Meet. Suppl., Abstract xxxxx-xx**

Your query was:
ildefonse

0800h
V51F-2111

The fossilisation of a dynamic melt lens at fast spreading centers: insights from the Oman ophiolite

*** France, L**
france@gm.univ-montp2.fr
Géosciences Montpellier Université Montpellier 2 CNRS, CC60 Place Eugène Bataillon, Montpellier, 34095, France
Ildefonse, B
ildefonse@gm.univ-montp2.fr
Géosciences Montpellier Université Montpellier 2 CNRS, CC60 Place Eugène Bataillon, Montpellier, 34095, France
Koepke, J
koepke@mineralogie.uni-hannover.de
Institut fuer Mineralogie Leibniz Universitaet Hannover, Callinstrasse 3, Hannover, D-30167, Germany

Thin and narrow melt lenses are observed on top of crystal-rich magma chambers at fast spreading ridges. This particular horizon, which marks the interface between the magmatic and the hydrothermal system, presents complex petrological and structural features. Its dynamics remain poorly constrained. We present here new detailed mapping of continuous, undisturbed areas of the Oman ophiolite and discuss evidences for a dynamic system with upward and downward vertical movements of the melt lens. These observations are consistent with episodic dikes injections in a steady state model, but also suggest that the root of the sheeted dike complex is generally overprinted by the upward vertical movements of the melt lens. The latter trigger prograde recrystallization in the dikes. However, because of later, low-temperature alteration, the upward extent of such a possible recrystallization front is unconstrained. Dike assimilation is evidenced in the field; it provides a mechanism for the incorporation of hydrated phases in the melt lens during its upward migrations. Recrystallized-dike-enclaves accumulations are observed at the foliated gabbro/isotropic gabbro transition, and inferred to represent fragment of the assimilated dikes, stoped at the bottom of the melt lens during its upward migration. In the isotropic gabbro horizon, some coarse grained gabbros display a crystallisation sequence with the clinopyroxenes crystallizing earlier than the plagioclases, which is uncommon in oceanic gabbros. Plagioclase composition is also abnormal with anorthite content reaching An99. These unusual observations are consistent with crystallization under hydrous conditions. In these samples relict domains (reaching 5mm) display Al-Ti poor clinopyroxenes. They contain small oxide inclusions (1mm), which we interpret as an evidence of prograde metamorphic recrystallization of amphiboles. These domains illustrate the recycling of previously hydrothermalized lithologies in the melt lens. The described melt lens upward migration, which results in reheating and

assimilation of hydrothermalized sheeted dikes, is consistent with observations made in IODP Hole 1256D. A general dynamic model for the melt lens evolution at fast spreading ridges is proposed, in which episodic dike injections during steady state regime stages alternate with vertical migrations of the melt lens. Upward and downward movements of the lens result in reheating/assimilation of dikes, and crystallization of varitextured isotropic gabbros, respectively.

3614 Mid-oceanic ridge processes (1032, 8416)

3618 Magma chamber processes (1036)

3690 Field relationships (1090, 8486)

8140 Ophiolites (3042)

8424 Hydrothermal systems (0450, 1034, 3017, 3616, 4832, 8135)

Volcanology, Geochemistry, Petrology [V]

2008 Fall Meeting

New Search

AGU 2008_The Influence of Geologic Processes in the Lower Continental Crust and Upper Mantle on Crustal Formation and Mantle Geochemistry From Field, Petrological, Geochemical, and Geophysical Perspectives
V31C-2173

Late-orogenic mantle garnet pyroxenites evidence mantle refertilization during exhumation of orogenic belt.

Chazot G. [1], France L.[2,*], Kornprobst J.[3], Dallai L.[4], Vannucci R.[5]
(1) Université de Bretagne Occidentale/ CNRS, Plouzané, France, (2) Université de Montpellier 2/ CNRS, Montpellier, France, (3) Université de Clermont-Ferrand II/ CNRS, Clermont-Ferrand, France, (4) CNR-IGG, Pisa, Italia, (5) Università degli Studi di Pavia/ CNR, Italia, *corresponding author (lyderic.france@gm.univ-montp2.fr / Fax: +334 67 14 36 03 / Phone: +334 67 14 39 44)

The petrological and geochemical study of garnet bearing pyroxenites from four localities (FMC, Morocco, Jordan, Cameroon) demonstrates that these rocks are cumulates crystallised in the lithospheric mantle domain. Metamorphic reactions, exsolutions and trace elements WR analysis demonstrate that their crystallisation pressure ranges between 1 and 2GPa (30 to 60km). The elaboration of the PTt paths for the studied samples attests of important movements in the respective lithospheres. Replaced in the geodynamical contexts, the samples are interpreted to represent the crystallisation of melts formed during exhumation of orogenic domains. Radiogenic isotopes (Sr-Nd) show that in a very same region, the samples are isotopicaly heterogeneous but are similar to the respective regional lithosphere. Initial isotopic ratios lead to propose that the FMC samples have crystallised at the end of the Hercynian orogen and that the samples from the other localities (Morocco, Jordan and Cameroon) have crystallised at the end of the Pan-African orogen. After recalculation at the crystallisation time, the isotopic compositions are in good agreement with the respective regional lithosphere ones and so samples of this study could represent the product of the melting of these lithospheres. The analyses of oxygen stable isotopes allow to precise the model; they show that twelve of the samples come from the melting of a lherzolitic mantle and that the four others come from the melting of a heterogeneous mantle formed of lherzolites and eclogites. The presence of some hydrous minerals such as amphiboles and micas and the trace elements WR analyses show that some of the samples were affected by a late metasomatic event.

Results of our study show that thermal relaxation following orogenic events lead to the crystallisation of pyroxenites in the lithosphere. The presence of lage amounts of mantle pyroxenites in old orogenic regions confers physical and chemical particularities to these domains. Among others, global solidus temperature of the whole lithospheric domain will be lowered; it follows that old orogenic regions such as FMC, Morocco, Jordan and Cameroon represent refertilized lithospheric zones in which magmatic activity will be facilitated.

Geophysical Research Abstracts,
Vol. 11, EGU2009-0, 2009
EGU General Assembly 2009

Dynamics of the Axial Melt Lens/Dike transition at fast spreading ridges: assimilation and hydrous partial melting

L. France (1,2), B. Ildefonse (1), and J. Koepke (2)

(1) Université de Montpellier 2, Géosciences Montpellier, Montpellier, France (lfrance@um2.fr), (2) Institut fuer Mineralogie, Universitaet Hannover, Germany

Recent detailed field studies performed in the Oman ophiolite on the gabbro/sheeted dike transition, compared to corresponding rocks from the EPR drilled by IODP (Site 1256), constrain a general model for the dynamics of the axial melt lens (AML) present at fast spreading ridges (France et al., 2008). This model implies that the AML/dike transition is a dynamic interface migrating up- and downward, and that the isotropic gabbro horizon on top of the igneous section represents its fossilization. It is also proposed that upward migrations are associated to reheating of the base of the sheeted dike complex and to assimilation processes. Plagiogranitic lithologies are observed close to the truncated base of the dikes and are interpreted to represent frozen melts generated by partial melting of previously hydrothermalized sheeted dikes. Relicts of previously hydrothermalized lithologies are also observed in the fossil melt lens, and are associated to lithologies that have crystallized under high water activities, with clinopyroxene crystallizing before plagioclase, and An-rich plagioclase.
To better understand our field data, we performed hydrous partial melting experiments at shallow pressures (0.1 GPa) under slightly oxidizing conditions (NNO oxygen buffer) and water saturated conditions on hydrothermalized sheeted dike sample from the Oman ophiolite. These experiments have been performed between 850°C and 1030°C; two additional experiments in the subsolidus regime were also conducted (750°C and 800°C). Clinopyroxenes formed during incongruent melting at low temperature (<910°C) have compositions that match those from the corresponding natural rocks (reheated base of the sheeted dike and relicts of assimilated lithologies). In particular, the characteristic low TiO2 and Al2O3 contents are reproduced. The experimental melts produced at low temperatures correspond to compositions of typical natural plagiogranites. In natural settings, these silicic liquids would be mixed with the basaltic melt of the AML, resulting in intermediate compositions that can be observed in the isotropic gabbro horizon.
Our study suggests that assimilation of previously hydrothermalized lithologies in the melt lens is a common process at fast spreading ridges. This process should consequently be carefully considered in geochemical studies that deal with the origin of MORB.

France L., Ildefonse B., Koepke J., (2008) The fossilisation of a dynamic melt lens at fast spreading centers: insights from the Oman ophiolite. Eos Trans. AGU, 89(53), Fall Meet. Suppl. Abstract V51F-2111

CONTROL ID:
708458
TITLE:
Melting the Hydrothermally Altered Sheeted Dike Complex: Experiments and Chemical Compositions
PRESENTATION TYPE:
Assigned by Committee
SECTION/FOCUS GROUP:
Ocean Sciences (OS)
SESSION:
New Insights from Integrated Multidisciplinary Studies of Oceanic Spreading Center Processes – Ridge 2000 Research (OS03)
AUTHORS (FIRST NAME, LAST NAME):
Lyderic France[1, 2], Benoit Ildefonse[1], Juergen Koepke[2], Christopher J MacLeod[3], Marguerite Godard[1]
INSTITUTIONS (ALL):
1. Géosciences Montpellier, CNRS - Université Montpellier 2, Montpellier, France.
2. Institut fur Mineralogie, Leibniz Universität Hannover, Hannover, Germany.
3. School of Earth, Ocean and Planetary Sciences, Cardiff University, Cardiff, United Kingdom.
Title of Team: ABSTRACT BODY:
Oceanic plagiogranites are ubiquitously sampled in oceanic crust. At fast spreading ridges, they are preferentially located close to the gabbro/sheeted dike transition. The origin of oceanic plagiogranites is still debated; the favored formation processes are late-stage fractionation of tholeiitic melt, and hydrous partial melting of mafic rocks. The hydrothermally altered base of the sheeted dike complex, which is often infiltrated by plagiogranitic veins, is locally recrystallized into granoblastic dikes that are commonly interpreted as a result of prograde granulitic metamorphism.
We present the results of hydrous melting experiments, performed using an IHPV (Institut für Mineralogie, Hannover, Germany) under conditions that match those prevailing at the base of the sheeted dike complex, using a natural hydrothermally altered dike as starting material. Chemical compositions of experimental products (melts and associated minerals) are compared to those of natural plagiogranites and granoblastic dikes.
Major element contents have been measured using a Cameca SX 100 electron microprobe (Institut für Mineralogie, Hannover, Germany). Trace element contents of experimental melts and natural plagiogranites/granoblastic rocks have been measured using a Cameca IMS4f ion probe (Géosciences Montpellier, France), and an ICP-MS (Department of Earth Sciences, Cardiff, UK), respectively.
All generated melts are water saturated, transitional between tholeiitic and calc-alkaline, and match the compositions of oceanic plagiogranites observed close to the base of the sheeted dike complex. Newly crystallized clinopyroxene and plagioclase have compositions that are characteristic of those of the same minerals in granoblastic dikes. Trace element contents of the experimental melts have been measured for experimental runs from 1030°C to 955°C. REE and other trace element contents continuously evolve with temperature, and match those of natural oceanic plagiogranite at low temperature.
Our results demonstrate that hydrous partial melting is a likely common process in the root zone of the sheeted dike complex, starting at temperatures above 850°C. These results support a model in which the top of the melt lens representing the interface between magmatic and hydrothermal system is a dynamic horizon that can migrates vertically and interact with the overlying sheeted dikes. The anatectic plagiogranitic melt formed during upward melt lens migrations represent the main crustal contaminant for the MORB-type melts filling the melt lens.

INDEX TERMS:
[3035] MARINE GEOLOGY AND GEOPHYSICS / Midocean ridge processes, [1032] GEOCHEMISTRY / Mid-oceanic ridge processes, [3614] MINERALOGY AND PETROLOGY / Mid-oceanic ridge processes, [3630] MINERALOGY AND PETROLOGY / Experimental mineralogy and petrology.
(No Table Selected)
(No Image Selected)

Additional Details

Previously Presented Material: not previously presented; one paper is submitted, another one in preparation.
Scheduling Request:

Annex E.

Samples locations and characteristics

Annex E: Samples locations and characteristics. Transverse Mercator projection; alt: altitude; SDC: sheeted-dike complex; RZSDC: root zone outcrop that shows the truncated base of the sheeted dike complex (gabbro intrusion).

Sample	Zone	type	Way-point	E	N	alt (m)	comment
07OL01a	Al Ahamadi Hills	SDC	07_05	647 652	2 520 726	513	core
07OL01b1	Al Ahamadi Hills	SDC	07_05	647 652	2 520 726	513	margin
07OL01b2	Al Ahamadi Hills	SDC	07_05	647 652	2 520 726	513	margin
07OL01c1	Al Ahamadi Hills	SDC	07_05	647 652	2 520 726	513	margin
07OL01c2	Al Ahamadi Hills	SDC	07_05	647 652	2 520 726	513	margin
07OL01d	Al Ahamadi Hills	fine-grained isotropic gabbro	07_06	647 642	2 520 744	516	
07OL01e	Al Ahamadi Hills	coarse-grained isotropic gabbro	07_07	647 598	2 520 857	521	
07OL01e2	Al Ahamadi Hills	plagiogranite	07_07	647 598	2 520 857	521	
07OL01f1	Al Ahamadi Hills	fine-grained isotropic gabbro	07_08	647 581	2 520 905	520	
07OL01f2	Al Ahamadi Hills	fine-grained isotropic gabbro	07_08	647 581	2 520 905	520	
07OL01g1	Al Ahamadi Hills	microgranular dike	07_10	647 631	2 520 751	519	+ fine-grained gabbro
07OL01g2	Al Ahamadi Hills	microgranular dike	07_10	647 631	2 520 751	519	core
07OL01g3	Al Ahamadi Hills	microgranular dike	07_10	647 631	2 520 751	519	margin
07OL02	Gideah	Composite	07_12	656 600	2 525 755	573	SDC+gabbro+plagiogranite
07OL03	Gideah	foliated gabbro	07_13	656 572	2 525 844	575	
07OL04	Gideah	SDC	07_14	656 529	2 526 092	580	
07OL05a	Gideah	microgranular dike	07_15	656 505	2 526 120	573	
07OL05b	Gideah	microgranular dike	07_15	656 505	2 526 120	573	
07OL05c	Gideah	microgranular dike	07_15	656 505	2 526 120	573	
07OL06	Gideah	Composite	07_16	656 542	2 526 466	574	SDC+gabbro+plagiogranite
07OL07a	Gideah	magmatic breccia	07_17	656 342	2 526 371	561	
07OL07b	Gideah	magmatic breccia	07_17	656 342	2 526 371	561	

07OL08a	Gideah	SDC	GUIDI 1	656 254	2 525 246	544	margin
07OL08b	Gideah	SDC	GUIDI 1	656 254	2 525 246	544	core
07OL08c	Gideah	fine-grained isotropic gabbro	GUIDI 1	656 254	2 525 246	544	
07OL08d	Gideah	coarse-grained isotropic gabbro	GUIDI 1	656 254	2 525 246	544	
07OL09	Gideah	wehrlites	07_105	656 411	2 526 710	573	
07OL10	Farah	fine-grained isotropic gabbro	07_18	666 518	2 529 598	572	
07OL10a1	Farah	fine-grained isotropic gabbro	07_18	666 518	2 529 598	572	
07OL10a2	Farah	fine-grained isotropic gabbro	07_18	666 518	2 529 598	572	
07OL10a3	Farah	fine-grained isotropic gabbro	07_18	666 518	2 529 598	572	
07OL10b	Farah	fine-grained isotropic gabbro	07_18	666 518	2 529 598	572	
07OL10a4	Farah	fine-grained isotropic gabbro	07_18	666 518	2 529 598	572	
07OL10c1	Farah	fine-grained isotropic gabbro	07_18	666 518	2 529 598	572	
07OL10c2	Farah	fine-grained isotropic gabbro	07_18	666 518	2 529 598	572	
07OL11a1	Farah	Composite	07_19	666 534	2 529 553	562	microgranular dike + coarse-grained gabbro
07OL11a2	Farah	Composite	07_19	666 534	2 529 553	562	microgranular dike + coarse-grained gabbro
07OL12	Farah	fine-grained isotropic gabbro	07_20	666 581	2 529 498	547	
07OL13	Farah	coarse-grained isotropic gabbro	07_21	666 600	2 529 497	541	
07OL13b	Farah	plagiogranite	07_21	666 600	2 529 497	541	
07OL14a	Farah	plagiogranite	07_21	666 600	2 529 497	541	
07OL14b	Farah	Composite	07_21	666 600	2 529 497	541	SDC + plagiogranite
07OL14c	Farah	SDC	07_21	666 600	2 529 497	541	core

07OL15	Sarur	fine-grained isotropic gabbro	07_30	613 692	2 583 897	277	
07OL15b	Sarur	xenolith	07_30	613 692	2 583 897	277	within foliated gabbros
07OL16	Sarur	fine-grained isotropic gabbro	07_31	614 110	2 583 949	293	
07OL16a	Sarur	layered gabbro	07_32	614 154	2 583 850	301	granular
07OL16b	Sarur	fine-grained isotropic gabbro	07_32	614 154	2 583 850	301	
07OL17a	Sarur	Composite	07_33	614 116	2 583 861	311	granular gabbro + xenolith
07OL18	Sarur	Composite	07_35	614 122	2 583 822	325	gabbro + microgranular dike
07OL19a	Luzugh	Composite	07_39	614 616	2 582 438	325	fine-grained gabbro + microgranular dike
07OL20	Luzugh	layered gabbro	07_41	614 807	2 582 755	369	granular
07OL21	Luzugh	Composite	07_44	614 941	2 582 626	324	coarse-grained gabbro + xenolith
07OL21a	Luzugh	RZSDC	07_44	614 941	2 582 626	324	
07OL21b	Luzugh	RZSDC	07_44	614 941	2 582 626	324	
07OL21c	Luzugh	foliated gabbro	07_44	614 941	2 582 626	324	
07OL22a	Luzugh	plagiogranite	07_47	615 172	2 582 281	295	
07OL22b	Luzugh	plagiogranite	07_47	615 172	2 582 281	295	
07OL23a	N Hilti	microgranular dike	07_49	444 383	2 679 011	334	core
07OL23b	N Hilti	microgranular dike	07_49	444 383	2 679 011	334	margin
07OL23c	N Hilti	Composite	07_49	444 383	2 679 011	334	microgranular dike + foliated gabbro
07OL23d	N Hilti	Composite	07_49	444 383	2 679 011	334	microgranular dike + foliated gabbro
07OL23e	N Hilti	Composite	07_49	444 383	2 679 011	334	microgranular dike + foliated gabbro
07OL23f	N Hilti	anorthosite	07_49	444 383	2 679 011	334	
07OL24	N Hilti	xenolith	07_50	443 887	2 678 169	362	
07OL26a	Sarami	coarse-grained isotropic gabbro	07_55	469 151	2 650 687	310	

07OL26b	Sarami	Composite	07_55	469 151	2 650 687	310	microgranular dike intruded by plagiogranite
07OL26c1	Sarami	fine-grained isotropic gabbro	07_56	468 376	2 650 085	344	
07OL26c2	Sarami	fine-grained isotropic gabbro	07_56	468 376	2 650 085	344	
07OL26c3	Sarami	fine-grained isotropic gabbro	07_56	468 376	2 650 085	344	
07OL27	Sarami	composite	07_57	468 229	2 650 041	366	fine & coarse-grained gabbro + microgranular dike
07OL28	Sarami	wehrlites	07_57	468 229	2 650 041	366	
07OL29b	Shaïq	SDC	07_59	443 973	2 707 651	162	margin
07OL29a	Shaïq	SDC	07_59	443 973	2 707 651	162	core
07OL29a’	Shaïq	SDC	07_59	443 973	2 707 651	162	core
07OL30a	Shaïq	SDC	07_59	443 973	2 707 651	162	
07OL30b	Shaïq	SDC	07_59	443 973	2 707 651	162	
07OL31a	Shaïq	RZSDC	07_62	444 878	2 707 586	149	
07OL31b	Shaïq	RZSDC	07_62	444 878	2 707 586	149	
07OL32	Shaïq	composite	07_63	445 578	2 707 539	151	microgranular dike + foliated gabbro
07OL32a	Shaïq	microgranular dike	07_64	431 210	2 723 757	260	core
O7OL32b1	Shaïq	microgranular dike	07_64	431 210	2 723 757	260	margin + gabbro
O7OL32b2	Shaïq	microgranular dike	07_64	431 210	2 723 757	260	margin + gabbro
07OL32c	Shaïq	magmatic breccia	07_64	431 210	2 723 757	260	
07OL32d1	Shaïq	magmatic breccia	07_64	431 210	2 723 757	260	
d2	Shaïq	magmatic breccia	07_64	431 210	2 723 757	260	
07OL33a	Rajmi	microgranular dike	07_65	431 029	2 724 346	269	margin
07OL33b	Rajmi	microgranular dike	07_65	431 029	2 724 346	269	core
07OL34	Rajmi	coarse-grained isotropic gabbro	07_66	431 157	2 724 497	261	
07OL35a	Rajmi	xenolith	07_68	430 517	2 723 711	285	
07OL35b	Rajmi	xenolith	07_68	430 517	2 723 711	285	

07OL36a	Rajmi	coarse-grained isotropic gabbro	07_70	430 565	2 723 695	285	
07OL36b	Rajmi	pegmatitic gabbro	07_70	430 565	2 723 695	285	
07OL36	Rajmi	plagiogranite	07_71	430 723	2 723 664	279	
07OL37	Rajmi	RZSDC	07_72	430 936	2 723 698	281	
07OL38a	Rajmi	microgranular dike	07_64	431 210	2 723 757	260	margin
07OL38b	Rajmi	microgranular dike	07_64	431 210	2 723 757	260	
07OL38f	Rajmi	microgranular dike	07_64	431 210	2 723 757	260	
07OL38c	Rajmi	RZSDC	07_64	431 210	2 723 757	260	
07OL38d	Rajmi	RZSDC	07_64	431 210	2 723 757	260	
07OL38e	Rajmi	RZSDC	07_64	431 210	2 723 757	260	
07OL38g	Rajmi	xenolith	07_64	431 210	2 723 757	260	core
07OL38h	Rajmi	xenolith	07_64	431 210	2 723 757	260	core
07OL39b	Rajmi	microgranular dike	07_73	433 116	2 724 012	246	
07OL39a	Rajmi	fine-grained isotropic gabbro	07_73	433 116	2 724 012	246	
07OL39c	Rajmi	SDC	07_73	433 116	2 724 012	246	core
07OL39d	Rajmi	SDC	07_73	433 116	2 724 012	246	margin
07OL40a	Rajmi	foliated gabbro	07_74	433 111	2 723 981	236	granular
07OL40b	Rajmi	foliated gabbro	07_74	433 111	2 723 981	236	granular
07OL41a1	Rajmi	fine-grained isotropic gabbro	07_75	433 205	2 723 771	221	
07OL41a2	Rajmi	fine-grained isotropic gabbro	07_75	433 205	2 723 771	221	
07OL41b	Rajmi	SDC	07_75	433 205	2 723 771	221	margin
07OL41c	Rajmi	SDC	07_75	433 205	2 723 771	221	core
07OL42	Rajmi	SDC	07_76	433 198	2 723 806	229	
07OL43	Rajmi	coarse-grained isotropic gabbro	07_77	433 175	2 723 866	229	
07OL44	Rajmi	SDC	07_77	433 175	2 723 866	229	core
07OL45a	Aswad	coarse-grained isotropic gabbro	07_78	624 228	2 557 071	800	
07OL45a1	Aswad	coarse-grained isotropic gabbro	07_78	624 228	2 557 071	800	

07OL45a1’	Aswad	coarse-grained isotropic gabbro	07_78	624 228	2 557 071	800	
07OL45a2	Aswad	coarse-grained isotropic gabbro	07_78	624 228	2 557 071	800	
07OL45b	Aswad	coarse-grained isotropic gabbro	07_78	624 228	2 557 071	800	
07OL45c	Aswad	RZSDC	07_78	624 228	2 557 071	800	
07OL45d	Aswad	RZSDC	07_78	624 228	2 557 071	800	
07OL45e	Aswad	RZSDC	07_78	624 228	2 557 071	800	
07OL45f	Aswad	RZSDC	07_78	624 228	2 557 071	800	
07OL45g	Aswad	RZSDC	07_78	624 228	2 557 071	800	
07OL45h	Aswad	RZSDC	07_78	624 228	2 557 071	800	
07OL45i	Aswad	RZSDC	07_78	624 228	2 557 071	800	
07OL45j = 45j1	Aswad	RZSDC	07_78	624 228	2 557 071	800	
07OL45j2	Aswad	microgranular dike	07_78	624 228	2 557 071	800	margin
07OL45k	Aswad	RZSDC	07_78	624 228	2 557 071	800	
07OL45l	Aswad	RZSDC	07_78	624 228	2 557 071	800	
07OL45n	Aswad	RZSDC	07_78	624 228	2 557 071	800	
07OL45p	Aswad	RZSDC	07_78	624 228	2 557 071	800	
07OL45q	Aswad	RZSDC	07_78	624 228	2 557 071	800	
07OL45r	Aswad	RZSDC	07_78	624 228	2 557 071	800	
07OL45s	Aswad	RZSDC	07_78	624 228	2 557 071	800	
07OL45t	Aswad	RZSDC	07_78	624 228	2 557 071	800	
07OL45u	Aswad	RZSDC	07_78	624 228	2 557 071	800	
07OL45v	Aswad	RZSDC	07_78	624 228	2 557 071	800	
07OL45w	Aswad	RZSDC	07_78	624 228	2 557 071	800	
07OL45x	Aswad	RZSDC	07_78	624 228	2 557 071	800	
07OL45y	Aswad	RZSDC	07_78	624 228	2 557 071	800	
07OL45z	Aswad	RZSDC	07_78	624 228	2 557 071	800	
07OL45v’	Aswad	RZSDC	07_78	624 228	2 557 071	800	
07OL46a	Aswad	SDC	07_79	624 102	2 556 847	787	core
07OL46b	Aswad	SDC	07_79	624 102	2 556 847	787	core
07OL47a	Aswad	microgranular dike	07_82	624 630	2 557 361	814	
07OL47b	Aswad	microgranular dike	07_82	624 630	2 557 361	814	

07OL47c	Aswad	fine-grained isotropic gabbro	07_91	624 654	2 557 157	800	
07OL47d	Aswad	microgranular dike	07_92	624 706	2 557 063	805	margin
07OL47e	Aswad	microgranular dike	07_92	624 706	2 557 063	805	core
07OL47f	Aswad	composite	07_93	624 810	2 556 937	806	microgranular dike + fine-grained gabbro
07OL48a	Gideah	SDC	07_102	656 238	2 524 895	554	
07OL48b	Gideah	SDC	07_102	656 238	2 524 895	554	core
07OL48c	Gideah	SDC	07_102	656 238	2 524 895	554	core
07OL48d	Gideah	plagiogranite	07_102	656 238	2 524 895	554	
07OL49a	Gideah	RZSDC	07_105	656 411	2 526 710	573	
07OL49b	Gideah	RZSDC	07_105	656 411	2 526 710	573	
07OL49c1	Gideah	coarse-grained isotropic gabbro	07_105	656 411	2 526 710	573	
07OL49c2	Gideah	coarse-grained isotropic gabbro	07_105	656 411	2 526 710	573	
07OL49d1	Gideah	wehrlites	07_105	656 411	2 526 710	573	
07OLd2	Gideah	wehrlites	07_105	656 411	2 526 710	573	
07OL50a	Zafani/Him	fine-grained isotropic gabbro	07_114	669 417	2 529 281	539	
07OL50b	Zafani/Him	xenolith	07_114	669 417	2 529 281	539	in plagiogranite
07OL50c1	Zafani/Him	composite	07_115	669 405	2 529 288	539	xenolith + plagiogranite
07OL50c2	Zafani/Him	composite	07_115	669 405	2 529 288	539	xenolith + plagiogranite
07OL50e	Zafani/Him	plagiogranite	07_116	669 425	2 529 344	535	
07OL50f	Zafani/Him	plagiogranite	07_116	669 425	2 529 344	535	
07OL51a	Gideah	RZSDC	07_102	656 238	2 524 895	554	
51b	Gideah	RZSDC	07_102	656 238	2 524 895	554	
07OL 52a	Kadir	plagiogranite	07_117	654 781	2 522 602	513	
07OL53a	Farah	doleritic micro-gabbro	07_131	666 535	2 529 307	538	
07OL54a	Aswad	RZSDC	07_137	623 690	2 557 313	876	+ coarse-grained gabbro

07OL55a1, 2, 3	Aswad	micrograniular dike	07_147	622 988	2 557 767	866	crosscut by plagiogranite
07OL55b	Aswad	RZSDC	07_147	622 988	2 557 767	866	+ plagiogranite
07OL55c	Aswad	micrograniular dike	07_147	622 988	2 557 767	866	
07OL56a	Aswad	composite	07_152	625 517	2 555 898	773	micrograniular dike + coarse-grained gabbro
07OL56b	Aswad	composite	07_152	625 517	2 555 898	773	micrograniular dike + coarse-grained gabbro
07OL56c	Aswad	composite	07_152	625 517	2 555 898	773	micrograniular dike + coarse-grained gabbro
07OL57a	Aswad	composite	07_150	625 292	2 556 087	768	micrograniular dike + coarse-grained gabbro
07OL58a	Aswad	foliated gabbro	07_160	626 195	2 555 531	759	
07OL59	Aswad	granular gabbro	07_173	626 533	2 556 691	842	
07OL60a	Aswad	composite	07_178	626 117	2 556 589	876	micrograniular dike + fine-grained gabbro
60b	Aswad	composite	07_178	626 117	2 556 589	876	micrograniular dike + fine-grained gabbro
07OL61	Aswad	composite	07_182	625 528	2 555 878	772	micrograniular dike + fine-grained gabbro
07OL62a	Aswad	granular gabbro	07_189	624 078	2 557 455	820	
07OL62b	Aswad	foliated gabbro	07_189	624 078	2 557 455	820	
07OL62c	Aswad	composite	07_193	624 283	2 557 584	872	micrograniular dike + foliated gabbro
07OL62d	Aswad	composite	07_194	624 310	2 557 588	861	fine & coarse-grained gabbro + micrograniular dike
07OL63a1	Luzugh	plagiogranite	07_205	614 991	2 582 268	301	
07OL63a2	Luzugh	plagiogranite	07_205	614 991	2 582 268	301	
07OL63b1	Luzugh	plagiogranite	07_205	614 991	2 582 268	301	
07OL63b2	Luzugh	plagiogranite	07_205	614 991	2 582 268	301	
07OL63c1	Luzugh	gabbro	07_205	614 991	2 582 268	301	

07OL63c2	Luzugh	gabbro	07_205	614 991	2 582 268	301	
07OL64a	Luzugh	tectonized gabbro	07_206	615 546	2 582 142	311	
07OL64b	Luzugh	tectonized gabbro	07_206	615 546	2 582 142	311	
07OL64c	Luzugh	tectonized gabbro	07_206	615 546	2 582 142	311	
08OL01a	Gideah	RZSDC	08_10	656 265	2 524 710	579	
08OL01b	Gideah	RZSDC	08_10	656 265	2 524 710	579	
08OL01c	Gideah	RZSDC	08_10	656 265	2 524 710	579	
08OL01d	Gideah	RZSDC	08_10	656 265	2 524 710	579	
08OL01e	Gideah	RZSDC	08_10	656 265	2 524 710	579	
08OL02	Gideah	"grey layer" (diorite)	08_22	656 164	2 525 190	552	subhorizontal
08OL02b	Gideah	coarse-grained isotropic gabbro	08_23	656 174	2 525 168	559	
08OL03	Gideah	RZSDC	07_104	656 248	2 524 892	559	
08OL03b	Gideah	gabbro	07_104	656 248	2 524 892	559	
08OL04a	Gideah	RZSDC	08_25	656 343	2 524 747	569	
08OL04b	Gideah	RZSDC	08_25	656 343	2 524 747	569	
08OL05a	Gideah	RZSDC	08_25	656 343	2 524 747	569	
08OL05b	Gideah	RZSDC	08_25	656 343	2 524 747	569	
08OL06a	Gideah	gabbro/gabbro contact	08_44	657 285	2 524 479	546	
08OL06b	Gideah	xenolith	08_44	657 285	2 524 479	546	
08OL06c	Gideah	xenolith	08_44	657 285	2 524 479	546	
08OL06d	Gideah	"grey layer" (diorite)	08_46	656 947	2 524 916	544	
08OL06e	Gideah	"grey layer" (diorite)	08_46	656 947	2 524 916	544	
08OL06f	Gideah	xenolith	08_48	656 692	2 525 069	555	within coarse-grained gabbro
08OL06g	Gideah	xenolith	08_51	656 812	2 525 668	559	
08OL06h	Gideah	foliated gabbro	08_01	656 714	2 525 177	550	
08OL06i	Gideah	RZSDC	08_52	655 920	2 525 586	566	
08OL06j	Gideah	gabbro/gabbro contact	08_54	656 000	2 525 683	564	
08OL07a	Al Ahamadi Hills	RZSDC	08_56	648 796	2 518 672	510	
08OL07b	Al Ahamadi Hills	RZSDC	08_56	648 796	2 518 672	510	
08OL08a	Aswad	RZSDC	08_59	624 400	2 556 684	772	
08OL08b	Aswad	RZSDC	08_59	624 400	2 556 684	772	
08OL09a	Aswad	microgranular	08_61	624 081	2 556 716	768	

		dike					
08OL09b	Aswad	microgranular dike	08_61	624 081	2 556 716	768	
08OL09c1	Aswad	microgranular dike	08_61	624 081	2 556 716	768	
08OL09c2	Aswad	microgranular dike	08_61	624 081	2 556 716	768	
08OL09c	Aswad	fine-grained isotropic gabbro	08_62	623 710	2 556 480	765	
08OL09d	Aswad	xenolith	08_62	623 710	2 556 480	765	within coarse-grained gabbro
08OL09e	Aswad	SDC	08_63	623 745	2 556 500	772	
08OL09f	Aswad	SDC	08_63	623 745	2 556 500	772	
08OL09g	Aswad	SDC	08_63	623 745	2 556 500	772	
08OL09h	Aswad	SDC	08_64	623 769	2 556 470	776	
08OL09i	Aswad	SDC	08_65	623 829	2 556 427	805	
08OL10a	Aswad	composite	08_66	622 465	2 556 383	760	microgranular dike + foliated gabbro
08OL10b	Aswad	xenolith	08_67	622 519	2 556 434	762	within coarse-grained gabbro
08OL10c	Aswad	SDC	08_68	622 608	2 556 419	761	
08OL10d	Aswad	RZSDC	08_77	623 122	2 556 474	748	
08OL10e	Aswad	RZSDC	08_77	623 122	2 556 474	748	
08OL10f	Aswad	RZSDC	08_81	623 191	2 556 386	751	
08OL10g	Aswad	RZSDC	08_81	623 191	2 556 386	751	
08OL10h	Aswad	xenolith	08_93	622 874	2 556 333	760	within fine-grained gabbro
08OL11	Aswad	microgranular dike	08_100	624 809	2 556 919	793	
08OL12a	Aswad	fine-grained isotropic gabbro	08_102	623 874	2 557 375	828	
08OL12b	Aswad	xenolith	08_106	623 836	2 557 293	871	within coarse-grained gabbro
08OL12c	Aswad	xenolith	08_106	623 836	2 557 293	871	within coarse-grained gabbro
08OL12d	Aswad	xenolith	08_113	623 614	2 557 420	809	within fine-grained gabbro
08OL12e1	Aswad	RZSDC	08_116	623 681	2 557 316	872	
08OL12e2	Aswad	RZSDC	08_116	623 681	2 557 316	872	

08OL12f	Aswad	RZSDC	08_151	623 546	2 557 459	782	
08OL13a	Aswad	microgranular dike	08_120	624 392	2 557 133	795	
08OL13b	Aswad	xenolith	08_126	624 268	2 557 408	871	within coarse-grained gabbro
08OL13c	Aswad	xenolith	08_126	624 268	2 557 408	871	within coarse-grained gabbro
08OL13d	Aswad	composite	08_129	624 240	2 557 578	896	fine & coarse-grained gabbro
08OL13e	Aswad	xenolith	08_131	624 164	2 557 764	921	within coarse-grained gabbro
08OL13f	Aswad	microgranular dike	08_133	624 154	2 557 857	917	
08OL13g	Aswad	composite	08_133	624 154	2 557 857	917	microgranular dike + gabbro
08OL13h	Aswad	composite	08_135	624 152	2 557 956	901	microgranular dike + gabbro
08OL14a	Aswad	composite	08_138	624 657	2 557 262	802	microgranular dike + gabbro
08OL13i	Aswad	microgranular dike	08_143	623 903	2 557 606	836	
08OL13j	Aswad	RZSDC	08_133	624 154	2 557 857	917	
08OL13k	Aswad	RZSDC	08_133	624 154	2 557 857	917	
08OL13l	Aswad	plagiogranite	08_133	624 154	2 557 857	917	
08OL13m	Aswad	SDC	08_144	624 155	2 557 937	918	core
08OL13n	Aswad	xenolith	08_147	624 206	2 558 550	869	
08OL13o	Aswad	xenolith	08_147	624 206	2 558 550	869	
08OL12f	Aswad	xenolith					
08OL15a	Gideah	RZSDC	08_08	656 266	2 525 065	582	
08OL15b	Gideah	RZSDC	08_08	656 266	2 525 065	582	
08OL15c	Gideah	RZSDC	08_08	656 266	2 525 065	582	
08OL15d	Gideah	RZSDC	08_08	656 266	2 525 065	582	
08OL15e	Gideah	RZSDC	08_08	656 266	2 525 065	582	
08OL15f	Gideah	RZSDC	08_09	656 246	2 525 063	582	
08OL15g	Gideah	RZSDC	08_09	656 246	2 525 063	582	
08OL15h	Gideah	RZSDC	08_14	656 288	2 524 730	584	
08OL15i	Gideah	RZSDC	08_14	656 288	2 524 730	584	
08OL15j	Gideah	xenolith	07Guidi1	656 254	2 525 246	544	
08OL15k	Gideah	xenolith	07Guidi1	656 254	2 525 246	544	

08OL15l	Gideah	fine-grained isotropic gabbro	07Guidi1	656 254	2 525 246	544	
08OL15m	Gideah	gabbro/gabbro contact	07Guidi1	656 254	2 525 246	544	
08OL15n	Gideah	gabbro/gabbro contact	07Guidi1	656 254	2 525 246	544	
08OL16	Aswad	composite	08_181	623 842	2 556 799	797	microgranular dike + gabbro
08OL16b	Aswad	xenolith	08_184	623 704	2 557 039	868	within coarse-grained gabbro
08OL17a	Aswad	RZSDC	08_185	623 726	2 557 205	924	
08OL17b	Aswad	xenolith	08_188	623 639	2 557 080	887	within coarse-grained gabbro
08OL17c	Aswad	RZSDC	08_189	623 610	2 557 047	906	
08OL18	Aswad	RZSDC	08_110	623 459	2 557 272	793	
08OL19a	Aswad	RZSDC	08_203	623 334	2 557 544	827	
08OL19b	Aswad	RZSDC	08_204	623 311	2 557 499	833	
08OL19c	Aswad	xenolith	08_213	623 024	2 557 684	813	
08OL19d	Aswad	xenolith	08_224	622 973	2 557 036	794	
08OL20	Aswad	composite	08_237	623 442	2 557 172	814	microgranular dike + coarse-grained gabbro
08OL21a	Aswad	RZSDC	08_243	623 884	2 556 686	785	
08OL21b	Aswad	RZSDC	08_247	623 774	2 556 776	833	
08OL21c	Aswad	RZSDC	08_247	623 774	2 556 776	833	dike margin
08OL21d	Aswad	SDC	08_248	623 752	2 556 783	852	dike core
08OL22a	Haymiliyah	xenolith	08_264	521 006	2 606 897	346	
08OL22b	Haymiliyah	xenolith	08_265	521 279	2 606 818	330	
08OL23a	Al Hoqayn	microgranular lens	pr Juergen	537 389	2 605 319	232	
08OL23b	Al Hoqayn	microgranular lens	pr Juergen	537 389	2 605 319	232	
08OL23c	Al Hoqayn	microgranular lens	pr Juergen	537 389	2 605 319	232	
08OL24a	Al Abyad	composite	Al Abiyad	569 300	2 597 000	190	fine and coarse-grained gabbro
08OL24b	Al Abyad	composite	Al Abiyad	569 300	2 597 000	190	fine and coarse-grained gabbro

08OL24c	Al Abyad	composite	Al Abiyad	569 300	2 597 000	190	fine and coarse-grained gabbro
08OL25a	Gideah	SDC	08_171	656 309	2 524 698	596	
08OL25b	Gideah	SDC	08_171	656 309	2 524 698	596	
08OL25c	Gideah	SDC	08_173	656 321	2 524 638	570	
08OL26	Gideah	gabbro/gabbro contact	07Guidi1	656 254	2 525 246	544	
08OL27	Aswad	RZSDC	08_266	lost	lost	lost	
08OL27b	Aswad	RZSDC	08_267	lost	lost	lost	
08OL27b'	Aswad	RZSDC	08_267	lost	lost	lost	
08OL28	Aswad	xenolith	08_268	lost	lost	lost	
08OL29a	Al Ahamadi Hills	foliated gabbro	08_270	lost	lost	lost	
08OL29b	Al Ahamadi Hills	foliated gabbro	08_271	lost	lost	lost	
08OL29c	Al Ahamadi Hills	microgranular dike	08_272	lost	lost	lost	margin
08OL29d	Al Ahamadi Hills	microgranular dike	08_272	lost	lost	lost	core
08OL29e	Al Ahamadi Hills	xenolith	08_276	lost	lost	lost	within coarse-grained gabbro
08OL29f	Al Ahamadi Hills	xenolith	08_277	lost	lost	lost	within coarse-grained gabbro
08OL29g	Al Ahamadi Hills	xenolith	08_279	lost	lost	lost	within coarse-grained gabbro
08OL29h	Al Ahamadi Hills	xenolith	08_280	lost	lost	lost	within coarse-grained gabbro
08OL29i	Al Ahamadi Hills	xenolith	08_262	648 541	2 519 969	528	
08OL30	Al Ahamadi Hills	SDC	08_281	lost	lost	lost	
08OL29j	Al Ahamadi Hills	fine-grained isotropic gabbro	08_260	648 430	2 520 243	519	
08OL29k	Al Ahamadi Hills	medium-grained gabbro	08_260	648 430	2 520 243	519	
08OL29l	Al Ahamadi Hills	foliated gabbro	08_283	lost	lost	lost	
08OL31	Aswad	medium-grained gabbro	08_291	lost	lost	lost	
08OL32a	Aswad	SDC	08_292	lost	lost	lost	
08OL32b	Aswad	SDC	08_292	lost	lost	lost	
08OLC06	Aswad	RZSDC	08_247	623 774	2 556 776	833	